

EISSN 1305-3612

# DIR

## Diagnostic and Interventional Radiology

**TSR**  
1924  
TURKISH SOCIETY  
OF RADIOLOGY

[dirjournal.org](http://dirjournal.org)

VOLUME 29  
ISSUE 2  
MARCH 2023

**Editor in Chief**

Mehmet Ruhi Onur, MD

Department of Radiology, Hacettepe University Faculty of Medicine, Ankara, Turkey

ORCID ID: 0000-0003-1732-7862

**Section Editors and Scientific Editorial Board**

**Abdominal Imaging**

İlkay S. İdilman, MD 

Department of Radiology, Hacettepe University Faculty of Medicine, Ankara, Turkey

ORCID ID: 0000-0002-1913-2404

Sonay Aydın, MD 

Department of Radiology, Erzincan Binali Yıldırım University Faculty of Medicine, Erzincan, Turkey

ORCID ID: 0000-0002-3812-6333

**Artificial Intelligence and Informatics**

Burak Koçak, MD 

Department of Radiology, University of Health Sciences, Başakşehir Çam and Sakura City Hospital, İstanbul, Turkey

ORCID ID: 0000-0002-7307-396X

**Breast Imaging**

Füsun Taşkın, MD 

Department of Radiology, Acıbadem University Faculty of Medicine, İstanbul, Turkey

ORCID ID: 0000-0001-7985-3660

**Chest and Cardiovascular Imaging**

Furkan Ufuk, MD 

Department of Radiology, Pamukkale University Faculty of Medicine, Denizli, Turkey

ORCID ID: 0000-0002-8614-5387

**Hybrid Imaging and Nuclear Medicine**

Evrin Bengi Türkbey, MD 

Radiology and Imaging Sciences, Clinical Center, National Institutes of Health Bethesda, Maryland, United States

ORCID ID: 0000-0002-5216-3528

**Interventional Radiology**

Barbaros Çil, MD, FCIRES 

Department of Radiology, Koç University School of Medicine, İstanbul, Turkey

ORCID ID: 0000-0003-1079-0088

Bahri Üstünsöz, MD 

Department of Radiology, LSUHSC (Louisiana State University Health Science Center) School of Medicine, New Orleans, United States

ORCID ID: 0000-0003-4308-6708

**Musculoskeletal Imaging**

Zeynep Maraş Özdemir, MD 

Department of Radiology, İnönü University Faculty of Medicine, Malatya, Turkey

ORCID ID: 0000-0003-1085-8978

**Neuroradiology**

Gülgün Yılmaz Ovalı, MD 

Department of Radiology, Celal Bayar University Faculty of Medicine, Manisa, Turkey

ORCID ID: 0000-0001-8433-5622

Erkan Gökçe, MD 

Department of Radiology, Tokat Gaziosmanpaşa University Faculty of Medicine, Tokat, Turkey

ORCID ID: 0000-0003-3947-2972

**Pediatric Radiology**

Meltem Ceyhan Bilgici, MD 

Department of Radiology, 19 Mayıs University Faculty of Medicine, Samsun, Turkey

ORCID ID: 0000-0002-0133-0234

Evrin Özmen, MD 

Department of Radiology, Koç University Hospital, İstanbul, Turkey

ORCID ID: 0000-0003-3100-4197

**Publication Coordinator**

Şükrü Mehmet Ertürk, MD 

Department of Radiology, İstanbul University, İstanbul Faculty of Medicine, İstanbul, Turkey

ORCID ID: 0000-0003-4086-675X

**Biostatistical Consultant**

İlker Ercan, PhD 

Department of Biostatistics, Uludağ University School of Medicine, Bursa, Turkey

ORCID ID: 0000-0002-2382-290X

**Publication Services**

Galenos Publishing, İstanbul, TR

**Past Editors**

**Editors in Chief**

Mustafa Seçil, MD (2016-2022)

Nevzat Karabulut, MD (2011-2016)

Üstün Aydingöz, MD (2010-2011)

Okan Akhan, MD (2001-2010)

Ferhun Balkancı, MD (1999-2001)

Aytekin Besim, MD (1994-1999)\*

\* Dr. Aytekin Besim actually served as the General Coordinator. His work in this capacity, however, was in effect that of an Editor in Chief.

**Editors**

Ayşenur Cila, MD (2001-2002)

Suat Kemal Aytaç, MD (1997-2001)

Erhan Ilgıt, MD (1994-2001)

Okan Akhan, MD (1994-2001)

Ferhun Balkancı, MD (1994-2000)

Serdar Akyar, MD (1994-1997)

**Section Editors**

Section Editorship was established in 2002 at the tenure of Dr Okan Akhan, Editor in Chief.

**Abdominal Imaging**

Bengi Gürses, MD (2020-2023)

Mehmet Ruhi Onur, MD (2016-2022)

Barış Türkbey, MD (2014-2020)

Mustafa N. Özmen, MD (2012-2018)

Murat Acar, MD (2015-2016)

Mustafa Seçil, MD (2011-2016)

Ahmet Tuncay Turgut, MD (2011)

Deniz Akata, MD (2007-2011)

Ayşe Erden, MD (2002-2011)

Okan Akhan, MD (2002-2010)

Hakan Özdemir, MD (2002-2010)

**Artificial Intelligence and Informatics**

Bariş Türkbey, MD (2020-2023)

**Breast Imaging**

Mustafa Erkin Arıbal, MD (2016-2023)

Sibel Kul (2015-2018)

Ayşenur Oktay, MD (2009-2014)

Ayşegül Özdemir, MD (2004-2009)

**Cardiovascular Imaging**

Uğur Bozlar, MD (2016-2023)

Muşturay Karçaaltıncaba, MD (2007-2010)

Mecit Kantarcı (2010-2016)

**Chest Imaging**

Nevzat Karabulut, MD (2010-2014)

Çetin Atasoy, MD (2007-2010)

Macit Arıyürek, MD (2002-2007)

Figen Demirkazık, MD, (2014-2018)

**General Radiology**

Ersin Öztürk, MD (2014-2017)

Utku Şenol, MD (2010-2013)

Oğuz Dicle, MD (2007-2010)

**Interventional Radiology**

Cüneyt Aytekin, MD (2016-2023)

Bora Peynircioğlu, MD (2012-2015)

Levent Oğuzkurt, MD (2011-2014)

Fatih Boyvat, MD (2007-2010)

İsmail Oran, MD (2015-2019)

**Musculoskeletal Imaging**

Hatice Tuba Sanal, MD (2016-2023)

Fatih Kantarcı, MD (2014-2016)

Ayşenur Oktay, MD (2011-2013)

Üstün Aydıngöz, MD (2002-2011)

Berna Dirim Mete (2016-2017)

**Neuroradiology and Head & Neck Imaging**

Kubilay Aydın, MD (2016-2023)

Nafi Aygün, MD (2016-2023)

Kader Karlı Oğuz, MD (2011-2015)

Süleyman Men, MD (2007-2013)

Muhteşem Ağıldere, MD (2002-2011)

**Nuclear Medicine**

A. Cahid Civelek, MD (2016-2023)

Oktay Sarı, MD (2015)

Akın Yıldız, MD (2011-2014)

**Pediatric Radiology**

Korgün Koral, MD (2016-2023)

Murat Kocaoğlu, MD (2016-2023)

Ensar Yekeler, MD (2014-2016)

Suat Fitöz, MD (2007-2013)

Diagnostic and Interventional Radiology (Diagn Interv Radiol) is a bimonthly periodical of the Turkish Society of Radiology and the content of the journal is available at <https://www.dirjournal.org/>. It is peer-reviewed and adheres to the highest ethical and editorial standards. The editors of the journal endorse the Editorial Policy Statements Approved by the Council of Science Editors Board of Directors ([www.councilscienceeditors.org/services/draft\\_approved.cfm](http://www.councilscienceeditors.org/services/draft_approved.cfm)). The journal is in compliance with the Recommendations for the Conduct, Reporting, Editing and Publication of Scholarly Work in Medical Journals published by the International Committee of Medical Journal Editors (updated May 2022, [www.icmje.org](http://www.icmje.org)).

First ten volumes of Diagnostic and Interventional Radiology have been published in Turkish under the name of Tanısal ve Girişimsel Radyoloji (Index Medicus® abbreviation: Tani Girişim Radyol), the current title's exact Turkish translation.

Diagnostic and Interventional Radiology is an open access publication, and the journal's publication model is based on Budapest Open Access Initiative (BOAI) declaration. All published content is available online, free of charge at <https://www.dirjournal.org/>. Authors retain the copyright of their published work in Diagnostic and Interventional Radiology. The journal's content is licensed under a Creative Commons Attribution-NonCommercial (CC BY-NC) 4.0 International License which permits third parties to share and adapt the content for non-commercial purposes by giving the appropriate credit to the original work.

Diagnostic and Interventional Radiology is indexed in **Pubmed/Medline, Pubmed Central, Web of Science, TUBITAK ULAKBIM TR Index, HINARI, EMBASE, CINAHL, Scopus, Gale and CNKI.**

**Contact Information**

Diagnostic and Interventional Radiology Turkish Society of Radiology

Hoşdere Cad., Güzelkent Sok., Çankaya Evleri, F/2, 06540

Ankara, Turkey

E-mail: [info@dirjournal.org](mailto:info@dirjournal.org)

Phone: +90 (312) 442 36 53 Fax: +90 (312) 442 36 54

**Publisher Contact**

Address: Molla Gürani Mah. Kaçamak Sk.

No: 21/1 34093 İstanbul, Turkey

Phone: +90 (530) 177 30 97

E-mail: [info@galenos.com.tr](mailto:info@galenos.com.tr)/[yayin@galenos.com.tr](mailto:yayin@galenos.com.tr)

Web: [www.galenos.com.tr](http://www.galenos.com.tr) Publisher Certificate Number: 14521

Online Publication Date: March 2023

EISSN 1305-3612

International scientific journal published bimonthly.



## Instructions to Authors

Diagnostic and Interventional Radiology (Diagn Interv Radiol) is a medium for disseminating scientific information based on research, clinical experience, and observations pertaining to diagnostic and interventional radiology. The journal is the double-blind peer-reviewed, bimonthly, open-access publication organ of the Turkish Society of Radiology and its publication language is English. Diagnostic and Interventional Radiology is currently indexed by Science Citation Index Expanded, PubMed MEDLINE, PubMed Central, TUBITAK ULAKBIM TR Index, HINARI, EMBASE, CINAHL, Scopus, Gale and CNKI.

The journal is a medium for original articles, reviews, pictorial essays, technical notes related to all fields of diagnostic and interventional radiology.

The editorial and publication process of the Diagnostic and Interventional Radiology are shaped in accordance with the guidelines of the International Committee of Medical Journal Editors (ICMJE), World Association of Medical Editors (WAME), Council of Science Editors (CSE), Committee on Publication Ethics (COPE), European Association of Science Editors (EASE), and National Information Standards Organization (NISO). The journal is in conformity with the Principles of Transparency and Best Practice in Scholarly Publishing.

### Authorship

Each individual listed as an author should fulfill the authorship criteria recommended by the International Committee of Medical Journal Editors (ICMJE - [www.icmje.org](http://www.icmje.org)). To be listed as an author, an individual should have made substantial contributions to all four categories established by the ICMJE: (a) conception and design, or acquisition of data, or analysis and interpretation of data, (b) drafting the article or revising it critically for important intellectual content, (c) final approval of the version to be published, and (d) agreement to be accountable for all aspects of the work in ensuring that questions related to the accuracy or integrity of any part of the work are appropriately investigated and resolved. Individuals who contributed to the preparation of the manuscript but do not fulfill the authorship criteria should be acknowledged in an acknowledgements section, which should be included in the title page of the manuscript. If the editorial board suspects a case of "gift authorship", the submission will be rejected without further review.

### Ethical standards

For studies involving human or animal participants, the authors should indicate whether the procedures followed were in accordance with the ethical standards of the responsible committee on human and animal experimentation (institutional or regional) and with the Helsinki Declaration). Application or approval number/year of the study should also be provided. The editorial board will act in accordance with COPE guidelines if an ethical misconduct is suspected.

It is the authors' responsibility to carefully protect the patients' anonymity and to verify that any experimental investigation with human subjects reported in the submission was performed with informed consent and following all the guidelines for experimental investigation with human subjects required by the institution(s) with which all the authors are affiliated with. For photographs that may reveal the identity of the patients, signed releases of the patient or of his/her legal representative should be enclosed.

Prospective human studies require both an ethics committee approval and informed consent by participants. Retrospective studies require an ethics committee approval with waiver of informed consent. Authors may be required to document such approval.

All submissions are screened by a similarity detection software (iThenticate by CrossCheck). Manuscripts with an overall similarity index of greater than 20%, or duplication rate at or higher than 5% with a single source are returned back to authors without further evaluation along with the similarity report.

In the event of alleged or suspected research misconduct, e.g., plagiarism, citation manipulation, and data falsification/fabrication, the Editorial Board will follow and act in accordance with COPE guidelines.

### Withdrawal Policy

Articles may be withdrawn under certain circumstances.

The article will be withdrawn if it;

- violates professional ethical codes,
- is subject to a legal dispute,
- has multiple submissions,
- includes fake claims of authorship, plagiarism, misleading data, and false data that may pose a severe health risk.

The editorial board will follow the principles set by COPE (Committee on Publication Ethics) in case of an article withdrawal.

### Manuscript Preparation

The manuscripts should be prepared in accordance with ICMJE-Recommendations for the Conduct, Reporting, Editing, and Publication of Scholarly Work in Medical Journals (updated in May 2022 - <https://www.icmje.org/recommendations/>).

Original Investigations and Reviews should be presented in accordance with the following guidelines: randomized study – CONSORT, observational study – STROBE, study on diagnostic accuracy – STARD, systematic reviews and meta-analysis PRISMA, nonrandomized behavioral and public health intervention studies – TREND.

Diagnostic and Interventional Radiology will only evaluate manuscripts submitted via the journal's self-explanatory online manuscript submission and evaluation system available at [mc04.manuscriptcentral.com/dir](http://mc04.manuscriptcentral.com/dir). Evaluation process of submitted manuscripts takes 4 weeks on average.

Manuscripts are evaluated and published on the understanding that they are original contributions, and do not contain data that have been published elsewhere or are under consideration by another journal. Authors are required to make a full statement at the time of submission about all prior reports and submissions that might be considered duplicate or redundant publication, and mention any previously published abstracts for meeting presentations that contain partial or similar material in the cover letter. They must reference any similar previous publications in the manuscript.

Authors must obtain written permission from the copyright owner to reproduce previously published figures, tables, or any other material in both print and electronic formats and present it during submission. The original source should be cited within the references and below the reprinted material.

**Cover letter:** A cover letter must be provided with all manuscripts. This letter may be used to emphasize the importance of the study. The authors should briefly state the existing knowledge relevant to the study and the contributions their study make to the existing knowledge. The correspondent author should also include a statement in the cover letter declaring that he/she accepts to undertake all the responsibility for authorship during the submission and review stages of the manuscript.

## *Instructions to Authors*

**Title page:** A separate title page should be submitted with all manuscripts and should include the title of the manuscript, name(s), affiliation(s), and major degree(s) of the author(s). The name, address, telephone (including the mobile phone number) and fax numbers and e-mail address of the corresponding author should be clearly listed. Grant information and other sources of support should also be included. Individuals who contributed to the preparation of the manuscript but do not fulfill the authorship criteria should also be acknowledged in the title page. Manuscripts should not be signed by more than 6 authors unless they are multicenter or multidisciplinary studies.

### **Main document**

**Abstract:** All submissions (except for Letters to the Editor) should be accompanied by an abstract limited to 400 words. A structured abstract is only required with original articles and it should include the following subheadings: PURPOSE, METHODS, RESULTS, CONCLUSION.

**Main points:** Each submission should be accompanied by 3 to 5 “main points”, which should emphasize the most striking results of the study and highlight the message that is intended to be conveyed to the readers. As these main points would be targeting radiology residents, experts and residents of other fields of medicine, as well as radiology experts, they should be kept as plain and simple as possible. These points should be constructed in a way that provides the readers with a general overview of the article and enables them to have a general idea about the article.

The main points should be listed at the end of the main text, above the reference list.

**Example:** Liu S, Xu X, Cheng Q, et al. Simple quantitative measurement based on DWI to objectively judge DWI-FLAIR mismatch in a canine stroke model. *Diagn Interv Radiol* 2015; 21:348–354.

- The relative diffusion-weighted imaging signal intensity (rDWI) of ischemic lesions might be helpful to identify the status of fluid attenuated inversion recovery (FLAIR) imaging in acute ischemic stroke.
- The relative apparent diffusion coefficient (rADC) value appears not useful to identify the status of FLAIR imaging in the acute period.
- Based on our embolic canine model, rDWI increased gradually in the acute period, while the rADC kept stable, which might explain why rDWI is helpful to identify the status of FLAIR imaging, while rADC is not.

### **Main text**

#### **Original Articles**

Original articles should provide new information based on original research. The main text should be structured with Introduction, Methods, Results, and Discussion subheadings. The number of cited references should not exceed 50 and the main text should be limited to 4500 words. Number of tables included in an original article should be limited to 4 and the number of figures should be limited to 7 (or a total of 15 figure parts).

#### **Introduction**

State briefly the nature and purpose of the work, quoting the relevant literature.

#### **Methods**

Include the details of clinical and technical procedures.

### **Research ethics standards compliance**

All manuscripts dealing with human subjects must contain a statement indicating that the study was approved by the Institutional Review Board or a comparable formal research ethics review committee. If none is present at your institution, there should be a statement that the research was performed according to the Declaration of Helsinki principles ([www.wma.net/e/policy/b3.htm](http://www.wma.net/e/policy/b3.htm)). There should also be a statement about whether informed consent was obtained from research subjects.

### **Results**

Present these clearly, concisely, and without comment. Statistical analysis results should also be provided in this section to support conclusions when available.

### **Discussion**

Explain your results and relate them to those of other authors; define their significance for clinical practice. Limitations, drawbacks, or shortcomings of the study should also be stated in the discussion section before the conclusion paragraph. In the last paragraph, a strong conclusion should be written.

### **Review Articles**

Review articles are scientific analyses of recent developments on a specific topic as reported in the literature. No new information is described, and no opinions or personal experiences are expressed. Reviews include only the highlights on a subject. Main text should be limited to 4000 words and the number of cited references should not exceed 75. Number of tables included in a review article should be limited to 4 and the number of figures should be limited to 15 (or a total of 30 figure parts).

### **Pictorial Essay**

This is a continuing medical education exercise with the teaching message in the figures and their legends. Text should include a brief abstract; there may be as many as 30 figure parts. No new information is included. The value of the paper turns on the quality of the illustrations. Authors can submit dynamic images (e.g. video files) or include supplemental image files for online presentation that further illustrate the educational purpose of the essay. Maximums: Pages of text – 4 (1,500 words); References – 20; Figures – 15 or total of 30 images; No table Main text should be limited to 1500 words and the number of cited references should not exceed 15.

### **Technical Notes**

Technical note is a brief description of a specific technique, procedure, modification of a technique, or new equipment of interest to radiologists. It should include a brief introduction followed by Technique section for case reports or Methods section for case series, and Discussion is limited to the specific message, including the uses of the technique, equipment, or software. Literature reviews and lengthy descriptions of cases are not appropriate.

Main text should be limited to 1500 words and the number of cited references should not exceed 8. Number of tables included in a technical note should be limited to 4 and the number of figures should be limited to 3 (or a total of 6 figure parts).

### Letter to the Editor and Reply

Letters to the Editor and Replies should offer objective and constructive criticism of published articles within last 6 months. Letters may also discuss matters of general interest to radiologists and may include images. Material being submitted or published elsewhere should not be duplicated in letters.

Main text should be limited to 500 words and the number of cited references should not exceed 6. No tables should be included and the number of figures should be limited to 2 (or a total of 4 figure parts).

### Recommendations for Manuscripts:

Type of manuscript	Word limit	Abstract word limit	Reference limit	Author limit	Table limit	Figure limit
Original Article	4500	400 (Structured)	50	6*	4	7 or total of 15 images
Review Article	4000	200	75	5	4	15 or total of 24 images
Pictorial Essay	1500	400	20	5	1	15 figures or total of 30 figure parts
Technical Note	1500	200	8	5	2	3 figures or total of 6 figure parts
Letter	500	N/A	6	4	No tables	2 figures or total of 4 figure parts

\*Manuscripts should not be signed by more than 6 authors unless they are multicenter or multidisciplinary studies.

\*\*Considering the specific condition of the manuscript, minor flexibilities may be applied for the recommendations upon the decision of Editor-in-Chief or the Section Editors.

### References

Both in-text citations and the references must be prepared according to the AMA Manual of style.

While citing publications, preference should be given to the latest, most up-to-date publications. Authors are responsible for the accuracy of references. If an ahead-of-print publication is cited, the DOI number should be provided. Journal titles should be abbreviated in accordance with the journal abbreviations in Index Medicus/MEDLINE/PubMed. When there are six or fewer authors, all authors should be listed. If there are seven or more authors, the first three authors should be listed followed by "et al." In the main text of the manuscript, references should be cited in superscript after punctuation. The reference styles for different types of publications are presented in the following examples.

**Journal Article:** Economopoulos KJ, Brockmeier SF. Rotator cuff tears in overhead athletes. *Clin Sports Med.* 2012;31(4):675-692.

**Book Section:** Fikremariam D, Serafini M. Multidisciplinary approach to pain management. In: Vadivelu N, Urman RD, Hines RL, eds. *Essentials of Pain Management.* New York, NY: Springer New York; 2011:17-28.

**Books with a Single Author:** Patterson JW. *Weedon's Skin Pathology.* 4th ed. Churchill Livingstone; 2016.

**Editor(s) as Author:** Etzel RA, Balk SJ, eds. *Pediatric Environmental Health.* American Academy of Pediatrics; 2011.

**Conference Proceedings:** Morales M, Zhou X. Health practices of immigrant women: indigenous knowledge in an urban environment. Paper presented at: 78th Association for Information Science and Technology Annual Meeting; November 6-10; 2015; St Louis, MO. Accessed March 15, 2016. <https://www.asist.org/files/meetings/am15/proceedings/openpage15.html>

**Thesis:** Maiti N. Association Between Behaviours, Health Characteristics and Injuries Among Adolescents in the United States. Dissertation. Palo Alto University; 2010.

**Online Journal Articles:** Tamburini S, Shen N, Chih Wu H, Clemente KC. The microbiome in early life: implications for health outcomes. *Nat Med.* Published online July 7, 2016. doi:10.1038/nm4142

**Epub Ahead of Print Articles: Websites:** International Society for Infectious Diseases. ProMed-mail. Accessed February 10, 2016. <http://www.promedmail.org>

### Tables

Tables should be included in the main document and should be presented after the reference list. Tables should be numbered consecutively in the order they are referred to within the main text. A descriptive title should be provided for all tables and the titles should be placed above the tables. Abbreviations used in the tables should be defined below by footnotes (even if they are defined within the main text). Tables should be created using the "insert table" command of the word processing software and they should be arranged clearly to provide an easy reading. Data presented in the tables should not be a repetition of the data presented within the main text but should be supporting the main text.

### Figures and figure legends

Figures, graphics, and photographs should be submitted as separate files (in TIFF or JPEG format) through the submission system. The files should not be embedded in a Word document or the main document. When there are figure subunits, the subunits should not be merged to form a single image. Each subunit should be submitted separately through the submission system. Images should not be labelled (a, b, c, etc.) to indicate figure subunits. Thick and thin arrows, arrowheads, stars, asterisks, abbreviations and similar marks can be used on the images to support figure legends. Like the rest of the submission, the figures too should be blind. Any information within the images that may indicate the institution or the patient should be removed.

Figure legends should be listed at the end of the main document.

### General

All acronyms and abbreviations used in the manuscript should be defined at first use, both in the abstract and in the main text. The abbreviation should be provided in parenthesis following the definition.

Statistical analysis should be performed in accordance with guidelines on reporting statistics in medical journals (Altman DG, Gore SM, Gardner MJ, Pocock SJ. Statistical guidelines for contributors to medical journals. *Br Med J* 1983; 7; 1489-1493.). Information on the statistical analysis process of the study should be provided within the main text.

When a drug, product, hardware, or software mentioned within the main text product information, the name and producer of the product should be provided in parenthesis in the following format: "Discovery St PET/CT scanner (GE Healthcare)."

## Instructions to Authors

All references, tables, and figures should be referred to within the main text and they should be numbered consecutively in the order they are referred to within the main text.

### Initial evaluation and Peer review process

Manuscripts submitted to Diagnostic and Interventional Radiology will first go through a technical evaluation process where the editorial office staff will ensure that the manuscript is prepared and submitted in accordance with the journal's guidelines. Submissions that do not conform to the journal's guidelines will be returned to the submitting author with technical correction requests.

All submissions are screened by a similarity detection software (iThenticate by CrossCheck), and those with an overall similarity index of greater than 20%, or duplication rate at or higher than 5% with a single source are returned back to authors without further evaluation along with the similarity report.

Manuscripts meeting the requirements mentioned in journal's guideline will go under the review process. The initial review will be performed by Editor-in-Chief and the Section Editor, which include the evaluation of the manuscript for its originality, importance of the findings, scientific merit, interest to readers and compliance with the policy of the journal in force. Manuscripts with insufficient priority for publication are not sent out for further review and rejected promptly at this level to allow the authors to submit their work elsewhere without delay.

Manuscripts that pass through the initial review are sent to peer review, which is performed in a blinded manner by at least two external and independent reviewers. During the review process, all original articles are evaluated by at least one senior consultant of statistics for proper handling and consistency of data, and use of correct statistical method. The Section Editor and / or Editor-in-Chief are the final authority in the decision-making process for all submissions.

### Revisions

When submitting a revised version of a paper, the author must submit a detailed "Response to reviewers" that states point by point how each issue raised by the reviewers has been covered and where it can be found (each reviewer's comment followed by the author's reply and line numbers where the changes have been made) as well as an annotated copy, and a clear copy of the main document.

Revised manuscripts must be submitted within 30 days from the date of the decision letter. If the revised version of the manuscript is not submitted within the allocated time, the revision option will be automatically cancelled by the submission system. If the submitting author(s) believe that additional time is required, they should request an extension before the initial 30-day period is over.

### Proofs and DOI Number

Accepted manuscripts are copy-edited for grammar, punctuation, and format by professional language editors. Following the copyediting process, the authors will be asked to review and approve the changes made during the

process. Authors will be contacted for a second time after the layout process and will be asked to review and approve the PDF proof of their article for publication. Once the production process of a manuscript is completed it is published online on the journal's webpage as an ahead-of-print publication before it is included in its scheduled issue.

### Publication Fee Policy

Diagnostic and Interventional Radiology (DIR) applies an Article Processing Charge (APCs) for only accepted articles. No fees are requested from the authors during submission and evaluation process. All manuscripts must be submitted via Manuscript Manager.

An APC fee of and local taxes will be applied depending on the article type (see Table 1)

Review	\$ 1250
Original Article	\$ 1000
Pictorial Essay	\$ 750
Technical Note	

**Table 1. Article Types and Fees**

The APCs will be accepted through the link that will be sent to the corresponding author of each article via the online article system. In the next step, the authors will be receiving a receipt of their payment.

\*Please note that the Article Processing Charge (APC) will not affect neither the editorial and peer-review process nor the priority of the manuscripts by no means. All submissions will be evaluated by the Editorial Board and the external reviewers in terms of scientific quality and ethical standards.

### Refund Policy:

Returning the article to the author; Diagnostic and Interventional Radiology (DIR) will refund the submission fees with a coupon code if the article is returned to the author. Using this code, authors can use the submission fees of different articles without making a new payment.

### Article Retraction:

Infringements of publication/research ethics, such as multiple submissions, bogus claims of authorship, plagiarism, and fraudulent use of data could lead to article retraction.

A retraction statement titled "Retraction: [article title]" must be signed by the authors and/or the editor. The original article is marked as retracted but a PDF version remains available to readers, and the retraction statement is linked to the original published paper.

## Contents

### EDITORIAL

203 **Editorial.** Letter from the New Editor-in-Chief. *Mehmet Ruhi Onur*

### ABDOMINAL IMAGING

205 **Original Article.** Four-phase computed tomography helps differentiation of renal oncocytoma with central hypodense areas from clear cell renal cell carcinoma. *Jian-Yi Qu, Hong Jiang, Xin-Hong Song, Jin-Kun Wu, Heng Ma*

212 **Original Article.** A comparison between the superb microvascular imaging technique and conventional Doppler ultrasound in evaluating chronic allograft damage in renal transplant recipients. *Ahmet Faruk Gürbüz, Ayşe Keven, Aygül Elmalı, Serap Toru, Ali Apaydın, Kağan Çeken*

219 **Original Article.** Diagnostic performance of magnetic resonance imaging in preoperative local staging of rectal cancer after neoadjuvant chemoradiotherapy. *Hakkı Çelik, Funda Barlık, Selman Sökmen, Cem Terzi, Aras Emre Canda, Özgül Sağol, Sülen Sarıoğlu, Mehtat Ünlü, İlnur Bilkay Görken, Zümre Arıcan Alicıkus, İlhan Öztıp*

228 **Original Article.** pT1-2 gastric cancer with lymph node metastasis predicted by tumor morphologic features on contrast-enhanced computed tomography. *Zhicong Wang, Qingyu Liu, Xiongjie Zhuang, Yan Yan, Qingqiang Guo, Junhong Lu, Qinchao Wu, Liqing Xie*

### ARTIFICIAL INTELLIGENCE AND INFORMATICS

234 **Original Article.** Machine learning analysis of adrenal lesions: preliminary study evaluating texture analysis in the differentiation of adrenal lesions. *Canan Altay, Işıl Başara Akın, Abdullah Hakan Özgül, Süleyman Cem Adıyaman, Abdullah Serkan Yener, Mustafa Seçil*

### BREAST IMAGING

244 **Original Article.** Contrast-enhanced spectral mammography: are kinetic patterns useful for differential diagnoses of enhanced lesions? *Xiaocui Rong, Yihe Kang, Jing Xue, Pengyin Han, Guang Yang, Zhigang Li*

251 **Original Article.** High-resolution diffusion-weighted imaging compared with conventional diffusion-weighted imaging and dynamic contrast-enhanced magnetic resonance imaging with regard to image quality and assessment of breast cancer morphology. *Yavuz Metin, Nurgül Orhan Metin, Sibel Kul, Filiz Taşçı, Oğuzhan Özdemir, Ali Küpeli*

260 **Original Article.** Prediction of malignancy upgrade rate in high-risk breast lesions using an artificial intelligence model: a retrospective study. *Özge Aslan, Ayşenur Oktay, Başak Katuk, Rıza Cenk Erdur, Oğuz Dikenelli, Levent Yeniay, Osman Zekioglu, Süha Süreyya Özbek*

### CARDIOVASCULAR IMAGING

268 **Original Article.** Low-dose ultra-high-pitch computed tomography coronary angiography: identifying the optimum combination of iteration strength and radiation dose reduction strategies to achieve true submillisievert scans. *Nidhi Kumari, Kartik P. Ganga, Vineeta Ojha, Sanjeev Kumar, Priya Jagia, Nitish Naik, Gurpreet Gulati, Sanjiv Sharma*

276 **Original Article.** The value of dual-energy computed tomography in the evaluation of myocarditis. *Mecit Kantarcı, Ümmügülsüm Bayraktutan, Abdusselam Akbulut, Onur Taydaş, Naci Ceviz, Fadime Güven, Hayri Oğul, Sonay Aydın*

### CHEST IMAGING

283 **Original Article.** Computed-tomography-based radiomic nomogram for predicting the risk of indeterminate small (5–20 mm) solid pulmonary nodules. *Chun-Ran Zhang, Qi Wang, Hui Feng, Yu-Zhi Cui, Xiao-Bo Yu, Gao-Feng Shi*

291 **Original Article.** Photon-counting computed tomography in the assessment of rheumatoid arthritis-associated interstitial lung disease: an initial experience. *Nikolett Marton, Janos Gyebnar, Kinga Fritsch, Judit Majnik, Gyorgy Nagy, Judit Simon, Veronika Müller, Adam Domonkos Tarnoki, David Laszlo Tarnoki, Pal Maurovich-Horvat*

### EMERGENCY RADIOLOGY

300 **Original Article.** Current practice of emergency radiology in Turkey and future expectations: a survey study. *Özüm Tuncyürek, Mehmet Ruhi Onur, Ersen Ertekin, Cem Çallı*

## Contents

### INTERVENTIONAL RADIOLOGY

**309 Technical Note.** A novel technique for the non-surgical management of inadvertent bowel catheterization during percutaneous abscess drainage: a technical note. *Okan Akhan, Duygu İmre Yetkin, Ferdi Çay, Emre Ünal, Türkmen Turan Çiftçi, Devrim Akıncı*

**312 Original Article.** Management of single double-J stent failure in malignant ureteral obstruction: tandem ureteral stenting with less frequent stent exchange. *Devrim Akıncı, Emre Ünal, Türkmen Turan Çiftçi, Orhan Şeref Özkan, Okan Akhan*

**318 Pictorial Essay.** Vascular complications related to image-guided percutaneous thermal ablation of hepatic tumors. *Sonam Tashi, Apoorva Gogna, Sum Leong, Nanda Venkatanarasimha, Sivanathan Chandramohan*

**326 Original Article.** Feasibility study of percutaneous thoracic duct embolization with lower-limb intermittent pneumatic compression devices. *Ravivarma Balasubramaniam, Mona Mossad*

**331 Original Article.** Embolization therapy for type 2 endoleaks after endovascular aortic aneurysm repair: imaging-based predictive factors and clinical outcomes on long-term follow-up. *Ruben Vandembulcke, Sabrina Houthoofd, Annouschka Laenen, Pieter-Jan Buyck, Hozan Mufty, Inge Fourneau, Geert Maleux*

**342 Original Article.** Long-term outcomes of combined radiofrequency ablation and multipronged ethanol ablation for the treatment of unfavorable hepatocellular carcinoma. *Ming Liu, Xiao-Ju Li, Xiao-Er Zhang, Ming Kuang, Xiao-Yan Xie, Guang-Liang Huang*

**350 Original Article.** Safety and efficacy of flow diverter stents in the treatment of middle cerebral artery aneurysms: a single-center experience and follow-up data. *Efe Soydemir, Cemal Aydın Gündoğmuş, Derya Türeli, Nurten Andaç Baltacıoğlu, Yaşar Bayri, Feyyaz Baltacıoğlu*

**359 Original Article.** Microwave ablation as a primary versus secondary treatment for hepatocellular carcinoma. *Philip Lee, Ajay Makkena, Mohamed Tantawi, Felipe Velasquez-Botero, John R. Eisenbrey, Colette M. Shaw*

**367 Original Article.** Percutaneous cholecystoduodenal stent as a definite treatment for acute cholecystitis in elderly or comorbid patients: a bicentric retrospective study. *Tae Yun Lee, Jong Woo Kim, Dong Jae Shim, Doyoung Kim, Young Chul Yoon, Edward Wolfgang Lee*

### MODALITY-BASED (UC, CT, MRI, PET-CT) IMAGING

**373 Original Article.** Did radiation exposure increase with chest computed tomography use among different ages during the COVID-19 pandemic? A multi-center study with 42028 chest computed tomography scans. *Mehmet Coşkun, Atilla H. Çilengir, Kenan Çetinoğlu, Merve Horoz, Ayberk Sinci, Betül Demircan, Engin Uluç, Fazıl Gelal*

**379 Original Article.** Multivariate analysis based on the maximum standard unit value of <sup>18</sup>F-fluorodeoxyglucose positron emission tomography/computed tomography and computed tomography features for preoperative predicting of visceral pleural invasion in patients with subpleural clinical stage IA peripheral lung adenocarcinoma. *Yun Wang, Deng Lyu, Taohu Zhou, Wenting Tu, Li Fan, Shiyuan Liu*

### MUSCULOSKELETAL IMAGING

**390 Original Article.** Sacroiliac joint involvement in osteochondromatosis: identifying its prevalence and characteristics from cross-sectional imaging. *Sevtap Arslan, Adalet Elçin Yıldız, Fatma Bilge Ergen, Üstün Aydıngöz*

### NEURORADIOLOGY

**396 Original Article.** Quantitative analysis of the olfactory system in pediatric epilepsy: a magnetic resonance imaging study. *Ali Haydar Baykan, Elçin Aydın, Şükri Şahin, Erman Altunışık*

**402 Original Article.** Radiomics analysis for predicting malignant cerebral edema in patients undergoing endovascular treatment for acute ischemic stroke. *Xuehua Wen, Xingfei Hu, Yanan Xiao, Junfa Chen*

### ABDOMINAL IMAGING

**410 Letter to the Editor.** Less known but important complications and associated anomalies of Abernethy malformation. *Ayşe Rüksan Ütebey, Furkan Ufuk, Muhammed Raşid Aykota*

**412 Letter to the Editor.** Letter to the Editor: "Prospective assessment of VI-RADS score in multiparametric MRI in bladder cancer: accuracy and the factors affecting the results". *Furkan Ufuk, Ahmet Baki Yağcı*

Full text of these articles can be accessed online at [www.dirjournal.org](http://www.dirjournal.org) or through PubMed ([www.pubmed.org](http://www.pubmed.org)).

Dear Reviewers,

Thank you for your invaluable contributions as reviewers to Diagnostic and Interventional Radiology in 2022. Your expertise and insightful feedback have helped to maintain our journal's high standards and ensure the quality of the articles we publish. We appreciate your interest in our journal and wish you every success in your academic career.

Sincerely,

Adnan Kabaalioglu  
Afak Durur Karakaya  
Ahmed Ba-Ssalamah  
Ahmet Erdemir  
Ahmet Sığirci  
Ahmet Yalçın  
Akira Yamada  
Alessandra Borgheresi  
Alessandro Posa  
Ambarish Bhat  
Andre Uflacker  
Andrea Borghesi  
Andrea Delli Pizzi  
Arzu Arslan  
Ashkan Malayeri  
Atilla Hikmet Çilengir  
Awais Ahmed  
Ayşe Keven  
Ayşe Seçil Ekşioğlu  
Ayşegül Akdoğan Gemici  
Ayşenur Oktay  
Aytül Hande Yardımcı  
Bahri Üstünsöz  
Beau Bosko Toskich  
Behnan Gülünay  
Bengi Gürses  
Berczi Bérczi  
Berna Dirim Mete  
Bernhard Gebauer  
Bernhard Maisch  
Betül Emine Derinkuyu  
Bilgin Kadri Arıbaş  
Bin Song  
Birkan Bozkurt  
Bülent Çekiç

Burak Kocak  
Burcu Alparslan  
Canan Altay  
Carlos Bileiro  
Caterina Gaudio  
Cem Yücel  
Cengiz Erol  
Christian Grieser  
Cihan Akgül Özmen  
Daisuke Tsurumaru  
Deniz Akata  
Derya Yakar  
Donghoon Choi  
Duygu Herek  
Ebru Ozan  
Eduardo de Faria Castro Fleury  
Elena Belloni  
Elias Kehagias  
Emre Bozkurt  
Eric James Monroe  
Eric K Hoffer  
Erwin Blessing  
Ezgi Güler  
Fabio Corvino  
Fatma Sen  
Faysal Ekici  
Fazıl Gelal  
Fei-Yun Wu  
Figen Demirkazık  
Filippo Piacentino  
Filiz Elbüken  
Francois Cornelis  
Fumio Chikamori  
Furkan Ufuk  
Füsün Taşkın

Gabriele Piffaretti  
Gamze Durhan  
Georgia Tsoumakidou  
Gökçe Kaan Ataç  
Gökçen Çoban  
Gonca Eldem  
Guang Yang  
Gül Ergör  
Güven Kahrıman  
H Shimuzu  
Hadi Sasani  
Hans-Jonas Meyer  
Hasan Dinç  
Hayato Abe  
Heron Rodriguez  
Hilal Şahin  
Hüseyin Tuğsan Ballı  
Hyungjin Rhee  
Ilias E. Gatos  
In Jae Lee  
Irmak Durur-Subasi  
Işıl Başara Akın  
İlkay Bayrak  
İlkay Çamlıdağ  
İlkay S. İdilman  
İlker Ercan  
İnci Kızıldağ Yırgın  
İsmail Oran  
Jafar Golzarian  
Ji Hye Min  
Jin-Xiang Zhang  
John Chang  
José Hugo Luz  
Juergen Machann  
Julian Hercun

Kader Oğuz  
Karin Horsthuis  
Kazuo Awai  
Kenneth Ouriel  
Kerim Aslan  
Korgun Koral  
Krishna Prasad Bellam Premnath  
Kubilay Aydın  
Kumble Seetharama Madhusudhan  
Laurens Hermie  
Levent Çelik  
Li Yang  
Lin Yang  
Luigi Larosa  
Lukas Luerken  
M Tsurusaki  
M. Yasemin Karadeniz Bilgili  
Maram Alakhras  
María Martín  
Marinos Kontzialis  
Mark Ahlman  
Marnix G. E. H. Lam  
Masaaki Takeuchi  
Massimo Galia  
Mecit Kantarcı  
Mehmet Akif Topçuoğlu  
Mehmet Barburoğlu  
Mehmet Coşkun  
Mehmet Ruhi Onur  
Mehmet Serkan Gür  
Meiyan Liao  
Meltem Gülsün Akpınar  
Menna Allah Mahmoud  
Mesude Tosun  
Michael Pavlides  
Michael R Narkewicz  
Miguel Angel De Gregorio  
Miran Jeromel  
Mohamed Elshikh  
Mohammad Eghtedari  
Muhammad Taha Hagar  
Müjdat Zeybel  
Murat Alp Öztekin  
Murat Fani Bozkurt

Mustafa Mahmut Barış  
Mutlu Hayran  
Naciye Sinem Gezer  
Nadine Abanador-Kamper  
Nail Bulakbasi  
Naim Ceylan  
Nakarin Inmutto  
Naofumi Matsunaga  
Nikolaos Achilleas Arkoudis  
Nuray Voyvoda  
Okan Akhan  
Olivier Detry  
Onur Taydaş  
Osman Ahmed  
Özge Aslan  
Özgür Tosun  
Özüm Yüksel  
Pankaj Gupta  
Patrick Krumm  
Philippe Dabadie  
Pierleone Lucatelli  
Pinggui Lei  
PinYi Chiang  
Qiang Huang  
Qiang Wang  
R Rajagopal  
Rafael De Freitas  
Rahmi Oklu  
Ran Luo  
Rathachai Kaewlai  
Regent Lee  
Rene Aschenbach  
Robert G Sawyer  
Roberto Cannella  
Rohini Gupta Ghasi  
Rong-Xin Chrn  
Sally Emad-Eldin  
Sang Yub Lee  
Sanjay Rastogi  
Satoshi Kobayashi  
Sebastiano Piana  
Seda Aladag Kurt  
Sen Jiang  
Serap Doğan

Serçin Özkök  
Serkan Arıbal  
Serkan Güneyle  
Sheng Liu  
Shintaro Ichikawa  
Shiro Miyayama  
Shorav Bhatnagar  
Shusen Zheng  
Sıla Ulus  
Sirish A Kishore  
Sonay Aydın  
Sophie I Mavrogeni  
Stavros Spiliopoulos  
Süha Süreyya Özbek  
Şükrü Mehmet Ertürk  
Sumit Singh  
Sungmin Woo  
Takayuki Shimizu  
Tao Gu  
Thomas Tu  
Tiago Bilhim  
Torsten Diekhoff  
Toshiya Kamiyama  
Tümay Bekçi  
Ulysses S. Torres  
Ural Oğuz  
Utku Şenol  
Valdair Francisco Muglia  
Venkatraman Bhat  
Wei Chen  
Weihua Dong  
Wen Zhang  
Xavier Adhoute  
Xiao Li  
Xingshun Qi  
Xu Wang  
Xubin Li  
Xuefeng Luo  
Ying Ding  
Yoshihisa Kodama  
Yoshiki Asayama  
Zhe Ji



## Letter from the New Editor-in-Chief

Mehmet Ruhi Onur   
Editor-in-Chief

It is a great honor and privilege for me to be appointed the editor-in-chief of our *Diagnostic and Interventional Radiology*, following my service as the section editor of abdominal radiology for 6 years. I want to express my heartfelt gratitude to all the members of the Board of Directors of the Turkish Society of Radiology.

*Diagnostic and Interventional Radiology* is a highly reputable scientific journal in our field and distinguished itself with its high scientific and quality standards. The key factor for this distinction is the careful evaluation process of the submitted articles. Applying the highest scientific and ethical standards is elemental in every step of this process, ensuring the maintenance of the high quality of our journal. Our priorities in the upcoming editorial period are to at least preserve and possibly improve the best practices pertaining to the scientific and stylistic evaluation of the submitted manuscripts, closely follow the innovations in the field of radiology, and further our publication standards.

The impact factor of *Diagnostic and Interventional Radiology* is 3.132 for the last five years, 3.346 for 2021 and an estimated 2.43 for 2022. The Scopus Cite Scores of our journal in 2021 and 2022 are 3.9 and 3.8, respectively. Although variable JCI scores are recorded, the rank of *Diagnostic and Interventional Radiology* among 200 journals in "Radiology, Nuclear Medicine and Medical Imaging" is 85 (70/136 among SCI-Expanded journals) (Table 1). Despite an abundance of manuscript submissions to all scientific journals during COVID-19 pandemic, evaluation processes were generally expedited, leading to a steep rise in the impact factor of many journals, including ours.<sup>1</sup> However, during the current normalization period which ensued the heyday of the pandemic, a decrease is expected with regard to the impact factor of our journal. Since we have a large backlog of accepted manuscripts that are pending publication, maintaining—let alone improving—our impact factor will be quite challenging. As of December 2022, there were around 80 accepted articles waiting to be published in our journal. This translated into a significant gap between the number of accepted and published manuscripts (Table 2). The first thing that we did following the most recent reshaping of our editorial board was to publish all these articles online in the first week of January 2023. We aspire to work hard for improving and streamlining this process of publishing already accepted articles as we move further along the way.

I would like to share several important changes that have been recently implemented in our journal as well as our future projections: first, the editorial board of *Diagnostic and Interventional Radiology* has been extensively changed in accordance with our societal bylaws with the addition of new colleagues who are, as have been the ones they have replaced, all reputable experts in their subspecialties. Second, an article publication fee has been started to be charged for articles accepted to be published in *Diagnostic and Interventional Radiology* as of October 2022. Details of this newly implemented policy are available in the author instruction section of our journal's website. Open-access peer-review policy of the journal will be continued. Third, we are working on changes in the article submission and reviewing system of our journal which will facilitate the submission process of manuscripts and will allow reviewers to evaluate the manuscripts in a more efficient way. These changes will be implemented into our system in a short period of time. With these changes, submission of manuscripts will be easier and publication of accepted manuscripts will be faster. The editorial board of *Diagnostic and Interventional Radiology* will be more than happy to hear opinions, suggestions and criticisms about the journal's publication policy, article evaluation and publishing processes from all our readers.



DOI: 10.4274/dir.2023.232228

**Table 1.** Journal citation and index ranking results of *Diagnostic and Interventional Radiology* between 2017 and 2021

JCR year	JIF	JCI	JIF rank	JCI rank	JIF quartile	JCI quartile
2017	1.618	0.63	85/129	85/181	Q3	Q2
2018	1.464	0.60	97/129	93/182	Q4	Q3
2019	1.871	0.59	85/134	98/184	Q3	Q3
2020	2.630	0.65	77/133	83/186	Q3	Q2
2021	3.346	0.69	70/136	85/206	Q3	Q2

JCR, Journal Citation Reports; JIF, Journal Impact Factor; JCI, Journal Citation Indicator (category of radiology, nuclear medicine and medical imaging)

**Table 2.** Some performance parameters of *Diagnostic and Interventional Radiology* in the evaluation and publication of all manuscripts between 2018 and 2022

Years	Manuscripts submitted (n)	Manuscript review time period (days)	Accepted manuscripts (n)	Published manuscripts (n)
2018	696	14.9	97	69
2019	685	19.7	84	72
2020	1280	11.8	165	105
2021	988	25.8	104	127
2022	498	39.8	67	87
Total			517	460

In conclusion, I would like to thank all our previous chief editors and section editors as well as all our colleagues who have generously donated their time as reviewers, as well as all the authors who contributed with

their scientific papers to our journal. Now is the time to work together to further improve the hard-earned reputation of *Diagnostic and Interventional Radiology* in the field of radiology.

## Reference

1. Delardas O, Giannos P. How COVID-19 Affected the Journal Impact Factor of High Impact Medical Journals: Bibliometric Analysis. *J Med Internet Res.* 2022;24(12):e43089. [\[CrossRef\]](#)



# Four-phase computed tomography helps differentiation of renal oncocytoma with central hypodense areas from clear cell renal cell carcinoma

Jian-Yi Qu\*   
 Hong Jiang\*   
 Xin-Hong Song   
 Jin-Kun Wu   
 Heng Ma 

\*Jian-Yi Qu and Hong Jiang contributed equally to this work.

## PURPOSE

To explore the utility of four-phase computed tomography (CT) in distinguishing renal oncocytoma with central hypodense areas from clear cell renal cell carcinoma (ccRCC).

## METHODS

Eighteen patients with oncocytoma and 63 patients with ccRCC presenting with central hypodense areas were included in this study. All patients underwent four-phase CT imaging including the excretory phases later than 20 min after contrast injection. Two blinded experienced radiologists visually reviewed the enhancement features of the central hypodense areas in the excretory phase images and selected the area demonstrating the greatest degree of enhancement of the tumor in the corticomedullary phase images. Regions of interest (ROIs) were placed in the same location in each of the three contrast-enhanced imaging phases. Additionally, ROIs were placed in the adjacent normal renal cortex for normalization. The ratio of the lesion to cortex attenuation (L/C) for the three contrast-enhanced imaging phases and absolute de-enhancement were calculated. The receiver operating characteristic curve was used to obtain the cut-off values.

## RESULTS

Complete enhancement inversion of the central areas was observed in 12 oncocytomas (66.67%) and 16 ccRCCs (25.40%) ( $P = 0.003$ ). Complete enhancement inversion combined with L/C in the corticomedullary phase lower than 1.0 ( $P < 0.001$ ) or absolute de-enhancement lower than 42.5 HU ( $P < 0.001$ ) provided 86.42% and 85.19% accuracy, 61.11% and 55.56% sensitivity, 93.65% and 93.65% specificity, 73.33% and 71.43% positive predictive value (PPV), and 89.39% and 88.06% negative predictive value (NPV), respectively, for the diagnosis of oncocytomas. Combined with complete enhancement inversion, L/C in the corticomedullary phase lower than 1.0 and absolute de-enhancement lower than 42.5 HU provided 87.65%, 55.56%, 96.83%, 83.33%, and 88.41% of accuracy, sensitivity, specificity, PPV, and NPV, respectively, for the diagnosis of oncocytomas.

## CONCLUSION

The combination of enhancement features of the central hypodense areas and the peripheral tumor parenchyma can help distinguish oncocytoma with central hypodense areas from ccRCC.

## KEYWORDS

Cancer, MDCT, oncology, radiology, renal

From the Department of Radiology (J.-Y.Q., H.J., X.-H.S., H.M. ✉ mahengdoctor@163.com), Yantai Yuhuangding Hospital, Qingdao University School of Medicine, Yantai, China; Department of Pathology (J.-K.W.), Yantai Yuhuangding Hospital, Qingdao University School of Medicine, Yantai, China.

Received 23 August 2021; revision requested 20 September 2021; last revision received 22 November 2021; accepted 16 December 2021.



Epub: 27.01.2023

Publication date: 29.03.2023

DOI: 10.5152/dir.2022.21834

Renal oncocytomas are virtually benign and account for 3%–7% of all renal tumors.<sup>1</sup> Based on the benign course and excellent prognosis of oncocytomas, partial nephrectomy and active surveillance are popular therapeutic options.<sup>2</sup> Accurate preoperative diagnosis is thus crucial. Although the features of oncocytoma shown on computed tomography (CT) and magnetic resonance imaging (MRI) have been extensively reported, these common imaging features have not been shown to accurately distinguished oncocytoma from

renal cell carcinoma (RCC), particularly from clear cell RCC (ccRCC), which is also a hyper-vascular tumor.<sup>3-7</sup>

Typical oncocytomas have previously been characterized by a central scar, which is seen in up to one-third of all cases.<sup>8</sup> However, this is not adequately specific, because the central scar is also present in three of the most common subtypes of RCC.<sup>1</sup> Moreover, the central necrotic areas within classic RCC can mimic a central scar; therefore, when central hypodense areas are observed on CT, they may indicate a central scar or necrosis. However, the contrast-enhanced CT features of the central scar within oncocytoma and the differences between oncocytoma and RCC central scar have not been studied in detail.

Several studies have focused on the differentiation of oncocytomas from ccRCCs on multiphase contrast-enhanced CT using different quantitative measures and enhancement correction methods.<sup>4,5,9-14</sup> However, these studies showed considerable overlap between oncocytomas and ccRCCs regarding their enhancement degree and pattern, making it difficult to confidently distinguish between them. In fact, many patients with benign renal tumors undergo unnecessary radical nephrectomy because the clinicians are unable to make an accurate preoperative diagnosis.

Different histopathologic structures of the central scar in oncocytomas and ccRCCs may lead to different appearances on CT; however, we hypothesized that if enhancement features of peripheral tumor paren-

chyma are also included, we can accurately distinguish typical oncocytoma with central scar from ccRCC.<sup>1</sup>

Therefore, we conducted this study to retrospectively explore whether oncocytomas with central hypodense areas can be differentiated from ccRCCs on four-phase CT based on enhancement features of the central hypodense areas and peripheral tumor parenchyma.

## Methods

### Patients

Our institutional review board approved the retrospective study (2019/298) and waived the requirement for informed consent owing to the retrospective nature of the study. We searched the radiology and pathology databases in our institution to identify all cases of histologically proven ccRCCs and oncocytomas between June 2013 and June 2019, in which all patients had undergone preoperative four-phase CT including the excretory phase later than 20 min after contrast injection. Two radiologists with three and five years of experience, respectively, reviewed all identified cases to select only tumors visually presenting central stellate or irregular hypodense areas compatible with central necrosis or scar in unenhanced or corticomedullary phase images. Cases without complete imaging or pathological data and central hypodense areas were excluded. In total, 81 patients and 81 tumors were included, of which 18 were oncocytomas and 63 were ccRCCs. Three patients each had two lesions (both of which were ccRCCs), but only one lesion in each patient was associated with central hypodensity.

### CT examination

All CT examinations were performed using Philips Brilliance 64or 256 detector row helical scanners (Philips Healthcare). The CT images were obtained while patients were holding their breath, using the following parameters: tube voltage of 120 kV, tube current of 150–250 mA, section thickness of 5 mm, and reconstruction interval of 5 mm. An 80–100 mL dose of iohexol (General Electric Pharmaceuticals Shanghai Co., Ltd.) was administered at a rate of 5 mL/s via injection into an antecubital vein by high-pressure automatic injectors. The enhanced CT scans were performed in the renal corticomedullary phase (delayed 25–30 s), nephrographic phase (delayed 60–90 s), and excretory phase (delayed >20 min).

### Image analysis

Another two radiologists with 10 and 20 years of experience, respectively, who were not involved in case selection, reviewed all selected cases in consensus on the picture archiving and communication system workstation. These two radiologists were blinded to the pathology results.

First, the two radiologists visually assessed the enhancement features of the central hypodense areas of these tumors. An enhancement inversion was considered to be present when the central hypodense areas enhanced slowly in a centripetal manner over time and showed higher attenuation than the peripheral tumor parenchyma in the excretory phase images. It was considered to be a complete enhancement inversion when the entire central hypodense areas were enhanced and showed higher attenuation and an incomplete enhancement inversion when only the periphery of the areas was enhanced and showed higher attenuation.

Second, the two radiologists selected the areas that demonstrated the maximum enhancement of the tumor in the corticomedullary phase images. Matching elliptical or round regions of interest (ROIs), approximately 8–15 mm<sup>2</sup> in size, were drawn in the same location in each of the three contrast-enhanced imaging phases. For each contrast-enhanced phase, two measurements of the same configuration and size were acquired on each lesion using a cursor, and the average value was recorded. Another ROI of the same size was drawn in the adjacent renal cortex to normalize variations in attenuation due to technical and individual factors. The ratio of lesion to cortex attenuation (L/C) was calculated using the formula (lesion ROI / cortex ROI) × 100%. In addition, the formula (lesion ROI<sub>corticomedullary</sub> – lesion ROI<sub>nephrographic</sub>) was used to calculate absolute de-enhancement.

Pathologic findings were used as the gold standard.

### Statistical analysis

Statistical analysis was conducted using SPSS for Windows software (ver. 25.0; IBM Inc.). Descriptive analyses used the mean and standard deviation (SD) for normally distributed numeric variables, median (min–max) values for non-normally distributed numeric variables, and n (%) for categorical variables. The enhancement inversion was compared between oncocytomas and ccRCCs using the Pearson chi-square test.

#### Main points

- A longer delay scanning time is valuable for distinguishing oncocytomas with a central scar from clear cell renal cell carcinomas (ccRCCs).
- The absence of enhancement inversion of the central hypodense areas in the excretory phase could be used to rule out oncocytoma.
- Quantitative analysis of the peripheral tumor parenchyma using the ratio of lesion to cortex attenuation in the corticomedullary phase and absolute de-enhancement showed significant value in differentiating oncocytomas from ccRCCs, but there were some overlaps.
- The combination of enhancement analysis of the central hypodense areas and peripheral tumor parenchyma provided high diagnostic specificity and negative predictive value.

The L/C and absolute de-enhancement were compared between oncocytomas and ccRCCs using the Student's t-test if normal distribution was achieved; otherwise, the non-parametric Mann-Whitney U test was used. The Kolmogorov-Smirnov test was used to evaluate the normality of quantitative data. A *P* value of <0.050 was considered to indicate a significant difference. Optimal cutoff values of L/C in the corticomedullary phase and absolute de-enhancement for identifying oncocytomas and ccRCCs were derived using receiver operating characteristic (ROC) curve analysis. To assess the diagnostic performance of these parameters for distinguishing oncocytomas from ccRCCs, accuracy, sensitivity, specificity, positive predictive value (PPV), and negative predictive value (NPV) were calculated.

## Results

The study population consisted of 44 men (54.32%) and 37 women (45.68%); the median (min-max) age was 60 (37-83) years. All patients underwent partial or total nephrectomy, and data on postoperative histological diagnosis were obtained. The mean size ± SD of oncocytomas and ccRCCs was 4.8 ± 2.2 and 4.9 ± 1.5 cm, respectively.

The enhancement inversion analysis of the central hypodense areas is shown in Table 1. The central hypodense areas of all tumors showed either slow enhancement in a centripetal manner over time and enhancement inversion or no enhancement, which was observed in 72 (88.89%) and 9 (11.11%) cases, respectively. A complete enhancement inversion was observed in 28 (34.57%) cases, and in all cases, it was observed in the excretory phase (Figures 1, 2). An incomplete enhancement inversion was observed in 44 (54.32%) cases (Figures 3, 4). Complete enhancement inversion was more common in oncocytomas than in ccRCCs (*P* = 0.003).

Results of the enhancement analysis of the peripheral parenchyma of tumors are shown in Table 2 and Figure 5. The L/C in the corticomedullary phase significantly differed between oncocytomas and ccRCCs (*P* < 0.001);

in the nephrographic and excretory phases, the L/C overlapped considerably between oncocytomas and ccRCCs (*P* = 0.533 and *P* = 0.794, respectively). Oncocytomas had a significantly lower absolute de-enhancement than ccRCCs (*P* < 0.001). Optimal cut-off values of the L/C in the corticomedullary phase of 1.0 and absolute de-enhancement of 42.5 HU were extracted using ROC curve analysis (Figure 6) for identifying oncocytomas and ccRCCs. These values suggest that a tumor with an L/C in the corticomedullary phase lower than 1.0 or absolute de-enhancement lower than 42.5 HU can be considered as an oncocytoma.

The accuracy, sensitivity, specificity, PPV, and NPV obtained by different parameters are shown in Table 3. The combination of complete enhancement inversion and the quantitative features of peripheral tumor parenchyma provided high specificity and NPV for distinguishing oncocytomas from ccRCCs.

## Discussion

The quantitative analysis of peripheral tumor parenchyma using the L/C in the corticomedullary phase and absolute de-enhancement showed significant value in identifying oncocytomas and ccRCCs, but there were some overlaps. The combination of enhancement features of central hypodense areas and peripheral tumor parenchyma provided high diagnostic specificity and NPV.

The central scar is an important radiological feature of oncocytomas, but it is not specific because the central necrosis that occurs within RCCs also shows hypodense areas on unenhanced CT, and the central scar also occurs in a small fraction of RCCs.<sup>15</sup> Moreover, the central scar does not always present a typical stellate pattern, making it more difficult to distinguish from irregular central necrosis within RCCs.<sup>16</sup> In our study, a longer delay scanning time (>20 min after injection) was used to evaluate the enhancement features of the central hypodense areas. Our study provides some important results. First, all oncocytomas presented complete or in-

complete enhancement inversion within the central hypodense areas in the excretory phase. This means that the absence of enhancement inversion of the central hypodense areas could be used to rule out oncocytoma. Second, complete enhancement inversion of the central areas was more common in oncocytomas than in ccRCCs. The difference may be related to different histopathologic structures of central areas in oncocytomas and ccRCCs.<sup>1</sup> Kim et al.<sup>17</sup> described the imaging feature of "segmental enhancement inversion" in homogeneous renal tumors smaller than 4 cm without a central scar; however, it is important to note that the segmental enhancement inversion was due to pathological differences in the stromal content within the tumor parenchyma, as opposed to the enhancement inversion of the central scar and peripheral tumor parenchyma in our study. Third, complete enhancement inversion was observed only in the excretory phase. This explains why it has never been mentioned with CT before, since a longer delay scanning time has not previously been used.<sup>5,18</sup>

Cornelis et al.<sup>1</sup> investigated the delayed enhancement features of central high T2-weighted signal intensity of oncocytomas and RCCs on MRI and first proposed the concept of enhancement inversion. In our study, the rate of complete enhancement inversion in ccRCCs was higher than that reported by Cornelis et al.<sup>1</sup> There are two possible explanations for this. First, we only included ccRCCs for our study, whereas the previous study included the three most common subtypes of RCCs. Second, in our study, the excretory phase images were obtained later than 20 min after contrast injection, whereas the late enhanced scanning was only carried out later than 5 min after contrast injection in the study by Cornelis et al.<sup>1</sup> We believe that a longer delay scanning time may result in a higher rate of complete enhancement inversion in ccRCCs. We speculate that there may be an optimal delay scanning time to better identify oncocytomas and ccRCCs based on enhancement features of the central hypodense areas, but solid evidence is needed to back this up.

The enhancement degree and pattern are valuable parameters for distinguishing oncocytoma from ccRCC.<sup>19</sup> Because there is no uniform standard, previous studies have used different measurement and enhancement correction methods, which has led to different and even completely opposing research results.<sup>4,5,13,20,21</sup> Wang et al.<sup>22</sup> reported that the degree of enhancement measured

**Table 1.** Enhancement analysis of the central hypodense areas of tumors

Enhancement of central hypodense areas	Type		<i>P</i> value
	Oncocytomas (n = 18)	ccRCCs (n = 63)	
None	0	9 (14.29%)	0.003 <sup>a</sup>
Complete	12 (66.67%)	16 (25.40%)	
Incomplete	6 (33.33%)	38 (60.32%)	

<sup>a</sup>, Pearson chi-square test; ccRCCs, clear cell renal cell carcinomas.

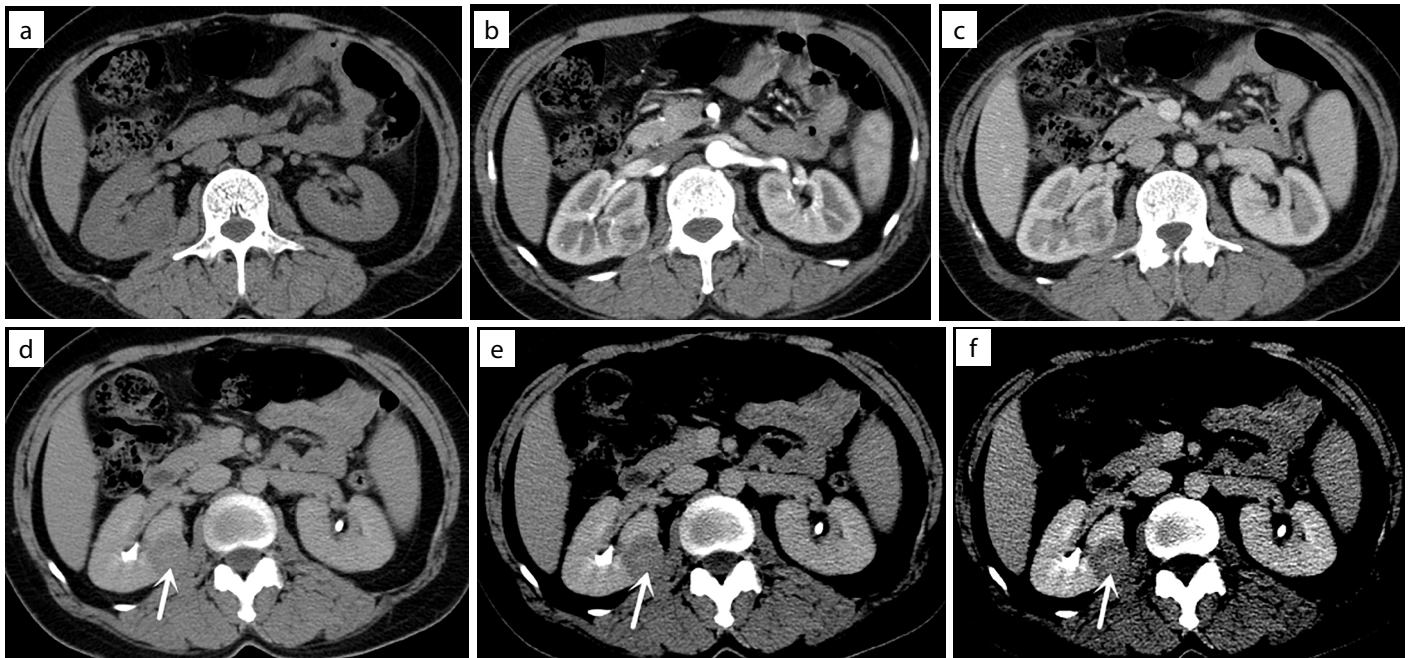


**Figure 1.** A 38-year-old woman with oncocytoma. (a) Axial unenhanced CT scan shows a 2.4 cm-diameter mass with central irregular hypodense areas. (b-d) Axial corticomedullary-, nephrographic-, and excretory-phase CT scans show that the central hypodense areas enhance slowly in a centripetal manner. The ratio of lesion to cortex attenuation in the corticomedullary phase and absolute de-enhancement are 0.66 and -44 HU, respectively. The excretory-phase CT scan shows that enhancement inversion is complete (arrow). (e, f) Axial excretory-phase CT scans with different windowing can better display the enhancement inversion of central hypodense areas (arrows). CT, computed tomography.

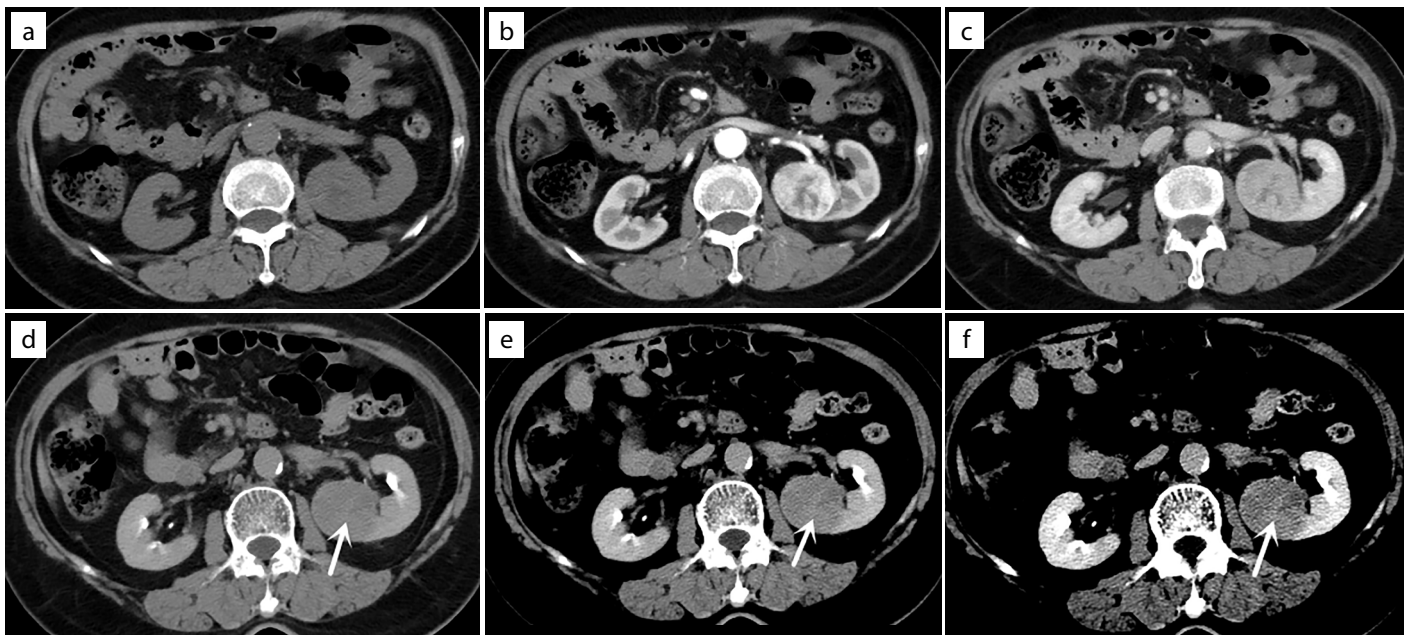


**Figure 2.** A 68-year-old woman with ccRCC. (a) Axial unenhanced CT scan shows a 3.9 cm-diameter mass with central irregular hypodense areas. (b-d) Axial corticomedullary-, nephrographic-, and excretory-phase CT scans show that the central hypodense areas appear slow with progressive enhancement in a centripetal manner. The ratio of lesion to cortex attenuation in the corticomedullary phase and absolute de-enhancement are 1.14 and 67 HU, respectively. The excretory-phase CT scan shows complete enhancement inversion of central areas (arrow). (e, f) Axial excretory-phase CT scans with different windowing can better display the complete enhancement inversion of central areas (arrows). ccRCC, clear cell renal cell carcinoma; CT, computed tomography.

using smaller ROIs (10–20 mm<sup>2</sup>) performed better than small ROIs (50–100 mm<sup>2</sup>) or large ROIs (included all components of the tumor on the largest cross-sectional images) for identifying renal angiomyolipoma without visible fat and small ccRCCs with CT. Therefore, in our study, we attempted to measure a smaller ROI (8–15 mm<sup>2</sup>) to avoid the influ-

ence of micronecrotic areas contained in ccRCCs and better reflect the enhancement degree of tumor. Our study showed that the L/C in the corticomedullary phase was significantly lower than the optimal cut-off value of 1.0 in nearly all oncocytomas (17/18, 94.44%) and higher than 1.0 in most ccRCCs (53/63, 84.13%). However, Bird et al.<sup>21</sup> meas-

ured a larger ROI (100 mm<sup>2</sup>) and reported that the L/C in the corticomedullary phase was highest for oncocytoma, followed by ccRCC. Gentili et al.<sup>5</sup> measured as large a tumor parenchyma as possible and concluded that oncocytomas are almost isodense and ccRCCs are mostly hypodense compared with the renal cortex in the corticomedul-

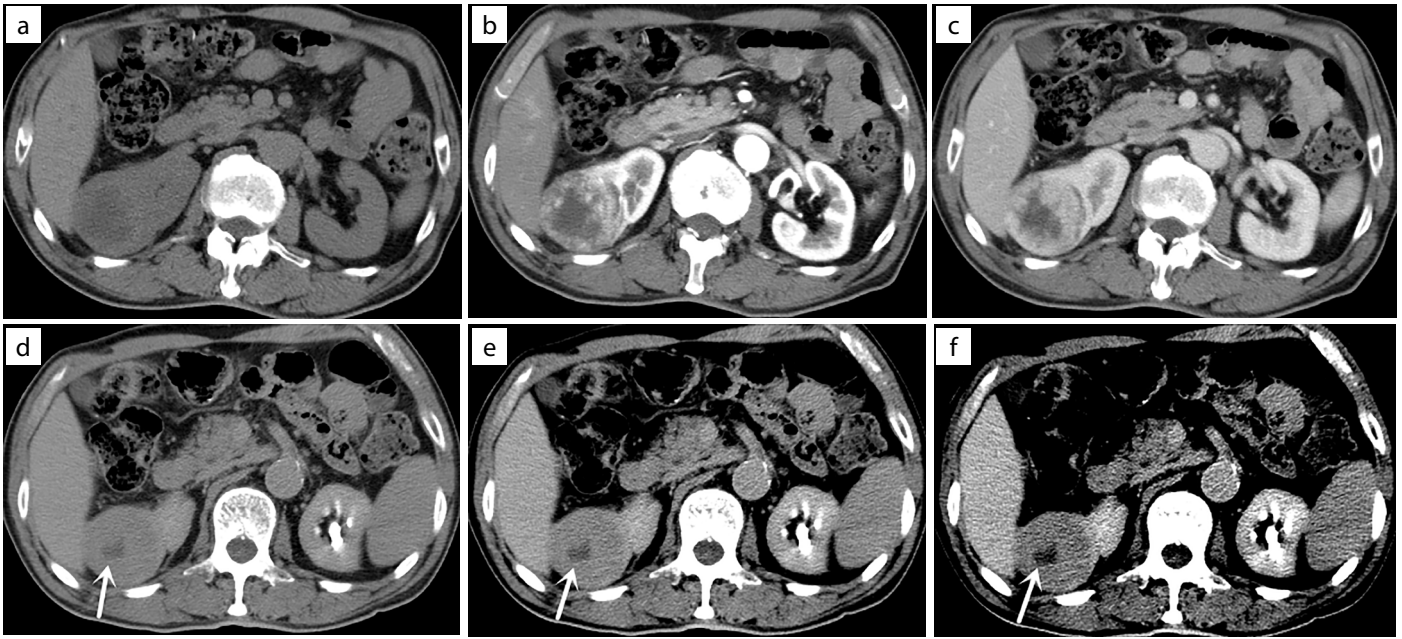


**Figure 3.** A 73-year-old man with oncocytoma. (a) Axial unenhanced CT scan shows a 4.9 cm-diameter mass with central irregular hypodense areas. (b-d) Axial corticomedullary-, nephrographic-, and excretory-phase CT scans show that the central hypodense areas enhance slowly in a centripetal manner except in the inner portion. The ratio of lesion to cortex attenuation in the corticomedullary phase and absolute de-enhancement are 0.62 and 15 HU, respectively. The excretory-phase CT scan shows that enhancement inversion appears incomplete. Note the higher enhancement at the junction between the central hypodense area and peripheral tumor component (arrow). (e, f) Axial excretory-phase CT scans with different windowing can better display the incomplete enhancement inversion of central areas (arrows). CT, computed tomography.

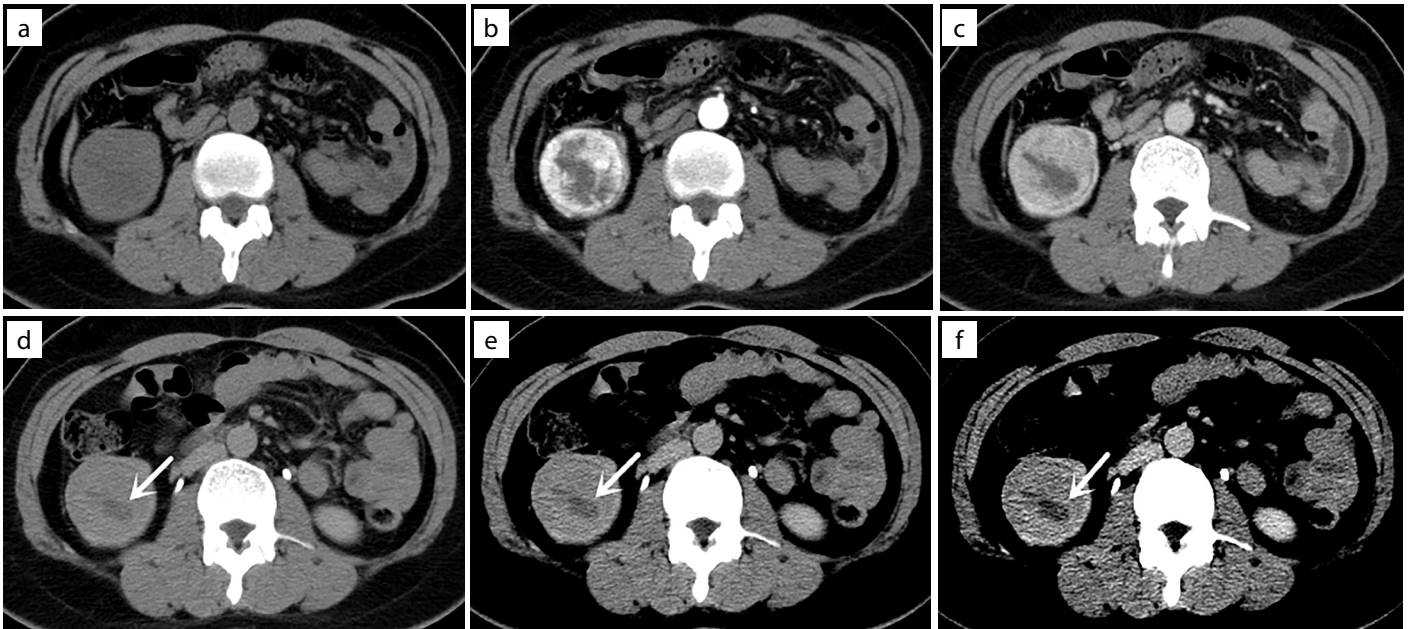


**Figure 4.** A 43-year-old woman with ccRCC. (a, b) Axial unenhanced and corticomedullary-phase CT scans show a 4.5 cm-diameter mass with central hypodense areas. The ratio of lesion to cortex attenuation in the corticomedullary phase is 1.23. (c, d) Axial nephrographic- and excretory-phase CT scans show that the central hypodense areas appear slow with progressive enhancement in a centripetal manner except in the inner portion. Absolute de-enhancement is 86 HU. The excretory-phase CT scan shows that enhancement inversion appears incomplete. Note the higher enhancement at the junction between the central hypodense areas and peripheral tumor component (arrow). (e, f) Axial excretory-phase CT scans with different windowing can better display the enhancement inversion of central hypodense areas (arrows). ccRCC, clear cell renal cell carcinoma; CT, computed tomography.

lary phase. Although Moldovanu et al.<sup>23</sup> also measured a smaller ROI (10 mm<sup>2</sup>) and found that oncocytoma had a higher enhancement change than ccRCC, the difference did not reach statistical significance. This suggests that different ROI sizes have a significant impact on the differentiation of oncocyto-

ma from ccRCC. In our study, the L/C in the corticomedullary phase measured by smaller ROIs showed high sensitivity and NPV for differentiating oncocytoma from ccRCC. Some studies have found rapid washout enhancement pattern in ccRCCs on multiphase contrast-enhanced CT.<sup>4,12</sup> Our study showed that

absolute de-enhancement was significantly lower than the optimal cutoff value of 42.5 HU in most oncocytomas (15/18, 83.33%) and higher than 42.5 HU in most ccRCCs (50/63, 79.37%), similar to the finding of Lee-Felker et al.<sup>13</sup> Using the combination of L/C in the corticomedullary phase and absolute

**Table 2.** Enhancement analysis of the peripheral parenchyma of tumors

Enhancement of the tumor parenchyma	Type		P value
	Oncocytomas (n = 18)	ccRCCs (n = 63)	
L/C in the corticomedullary phase, median (min–max)	0.83 (0.62–1.06)	1.15 (0.47–2.01)	<0.001 <sup>a</sup>
L/C in the nephrographic phase, mean ± SD	0.78 ± 0.12	0.76 ± 0.11	0.533 <sup>b</sup>
L/C in the excretory phase, mean ± SD	0.71 ± 0.07	0.72 ± 0.16	0.794 <sup>b</sup>
Absolute de-enhancement, median (min–max)	11 (–44–58)	67 (–12–220)	<0.001 <sup>a</sup>

<sup>a</sup>, Mann–Whitney U test; <sup>b</sup>, Student's t-test; ccRCCs, clear cell renal cell carcinomas; L/C, ratio of lesion to cortex attenuation; SD, standard deviation.

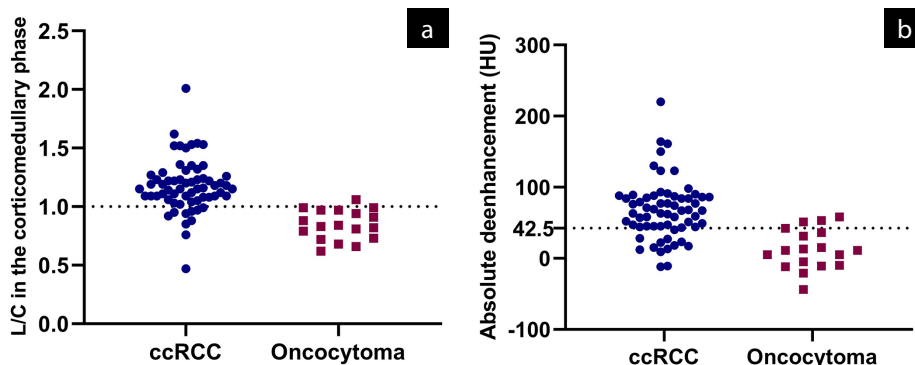


**Figure 5.** Scatterplots of the L/C in the corticomedullary phase and absolute de-enhancement for tumors of oncocytoma and ccRCC groups. (a) Scatterplot of the L/C in the corticomedullary phase. Most ccRCCs have an L/C higher than 1.0, whereas nearly all oncocytomas have a ratio lower than 1.0. (b) Scatterplot of absolute de-enhancement. Most ccRCCs have an absolute de-enhancement higher than 42.5 HU, whereas most oncocytomas have an absolute de-enhancement lower than 42.5 HU. L/C, ratio of lesion to cortex attenuation; ccRCC, clear cell renal cell carcinoma.

**Table 3.** Accuracy of differentiation of oncocytomas from ccRCCs for all criteria

Criteria	Differentiation	Accuracy (%)	Sensitivity (%)	Specificity (%)	PPV (%)	NPV (%)
Enhancement inversion	Complete	72.84	66.67	74.60	42.86	88.68
	Incomplete	38.27	33.33	39.68	13.64	67.57
Enhancement of the peripheral tumor parenchyma	Complete or incomplete	33.33	100.00	14.29	25.00	100.00
	L/C in the corticomedullary phase ≤1.0	86.42	94.44	84.13	62.96	98.15
	Absolute de-enhancement ≤42.5 HU	80.25	83.33	79.37	53.57	94.34
	Combination of both criteria	90.12	83.33	92.06	75.00	95.08
Combination of both criteria	Complete enhancement inversion and L/C in the corticomedullary phase ≤1.0	86.42	61.11	93.65	73.33	89.39
	Complete enhancement inversion and absolute de-enhancement ≤42.5 HU	85.19	55.56	93.65	71.43	88.06
	Complete enhancement inversion and L/C in the corticomedullary phase ≤1.0 and absolute de-enhancement ≤42.5 HU	87.65	55.56	96.83	83.33	88.41

ccRCC, clear cell renal cell carcinoma; PPV, positive predictive value; NPV, negative predictive value; L/C, ratio of lesion to cortex attenuation.

de-enhancement was better than using a single parameter for distinguishing oncocytomas from ccRCCs. In conclusion, L/C in the corticomedullary phase or absolute de-enhancement provided a simple method that can be applied in the clinic for differential diagnosis. The two parameters can be used in combination to differentiate oncocytomas from ccRCCs.

Our study has some limitations. First, owing to the retrospective design, the analysis is subjected to some selection bias. Second, our study only evaluated tumors with central hypodense areas, which increased the rate of oncocytomas by excluding ccRCCs that were not associated with the typical central scar or necrosis. We did not evaluate oncocytomas or ccRCCs with a homogeneous appearance

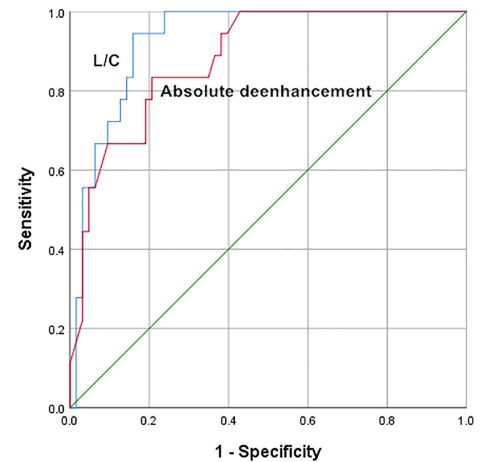


**Figure 6.** Receiver operating characteristic curve for the L/C in the corticomedullary phase and absolute de-enhancement for distinguishing oncocytomas from ccRCCs. The area under the receiver operating characteristic curve was 0.929 (95% CI, 0.874–0.983; SE, 0.028) for the L/C in the corticomedullary phase and 0.881 (95% CI, 0.802–0.959; SE, 0.040) for absolute de-enhancement. L/C, ratio of lesion to cortex attenuation; ccRCC, clear cell renal cell carcinoma; CI, confidence interval; SE, standard error.

or other subtypes of RCC. Third, although the two experienced radiologists reached a consensus when assessing the enhancement inversion, visual assessment could carry errors. Fourth, due to space constraints, we only chose simple and easy-to-operate measurement and enhancement correction methods; we did not compare the results with other measurement and enhancement correction

methods, and this might be an interesting future direction. Finally, because of the similar imaging features but different treatment strategies, most imaging studies on the differential diagnosis of benign and malignant renal tumors are based on the standard whose diameter are 4 cm or less. Though limiting the size of the lesions would add more value to our study, we did not do so because of the case number constraints.

In conclusion, a longer delay scanning time is valuable for distinguishing oncocytomas with a central scar from ccRCCs. Quantitative analysis of the peripheral tumor parenchyma showed some overlaps between oncocytomas and ccRCCs, and we provided optimal cutoff values. The addition of enhancement features of the central hypodense areas can provide high diagnostic specificity and NPV.

### Conflict of interest disclosure

The authors declared no conflicts of interest.

### References

- Cornelis F, Lasserre AS, Tourdias T, et al. Combined late gadolinium-enhanced and double-echo chemical-shift MRI help to differentiate renal oncocytomas with high central T2 signal intensity from renal cell carcinomas. *AJR Am J Roentgenol*. 2013;200(4):830-838. [\[CrossRef\]](#)
- Meagher MF, Lane BR, Capitanio U, et al. Comparison of renal functional outcomes of active surveillance and partial nephrectomy in the management of oncocytoma. *World J Urol*. 2021;39(4):1195-1201. [\[CrossRef\]](#)
- Guo K, Ren S, Cao Y, et al. Differentiation between renal oncocytomas and chromophobe renal cell carcinomas using dynamic contrast-enhanced computed tomography. *Abdom Radiol (NY)*. 2021;46(7):3309-3316. [\[CrossRef\]](#)
- Ren A, Cai F, Shang YN, et al. Differentiation of renal oncocytoma and renal clear cell carcinoma using relative CT enhancement ratio. *Chin Med J (Engl)*. 2015;128(2):175-179. [\[CrossRef\]](#)
- Gentili F, Bronico I, Maestroni U, et al. Small renal masses ( $\leq 4$  cm): differentiation of oncocytoma from renal clear cell carcinoma using ratio of lesion to cortex attenuation and aorta-lesion attenuation difference (ALAD) on contrast-enhanced CT. *Radiol Med*. 2020;125(12):1280-1287. [\[CrossRef\]](#)
- Zhong Y, Wang H, Shen Y, et al. Diffusion-weighted imaging versus contrast-enhanced MR imaging for the differentiation of renal oncocytomas and chromophobe renal cell carcinomas. *Eur Radiol*. 2017;27(12):4913-4922. [\[CrossRef\]](#)
- Akın IB, Altay C, Güler E, et al. Discrimination of oncocytoma and chromophobe renal cell carcinoma using MRI. *Diagn Interv Radiol*. 2019;25(1):5-13. [\[CrossRef\]](#)
- Sasaguri K, Takahashi N. CT and MR imaging for solid renal mass characterization. *Eur J Radiol*. 2018;99:40-54. [\[CrossRef\]](#)
- Grajo JR, Batra NV, Bozorgmehri S, et al. Validation of aorta-lesion-attenuation difference on preoperative contrast-enhanced computed tomography scan to differentiate between malignant and benign oncocytic renal tumors. *Abdom Radiol (NY)*. 2021;46(7):3269-3279. [\[CrossRef\]](#)
- Chen F, Gulati M, Hwang D, et al. Voxel-based whole-lesion enhancement parameters: a study of its clinical value in differentiating clear cell renal cell carcinoma from renal oncocytoma. *Abdom Radiol (NY)*. 2017;42(2):552-560. [\[CrossRef\]](#)
- Paño B, Soler A, Goldman DA, et al. Usefulness of multidetector computed tomography to differentiate between renal cell carcinoma and oncocytoma. A model validation. *Br J Radiol*. 2020;93(1115):20200064. [\[CrossRef\]](#)
- Zokalj I, Marotti M, Kolarić B. Pretreatment differentiation of renal cell carcinoma subtypes by CT: the influence of different tumor enhancement measurement approaches. *Int Urol Nephrol*. 2014;46(6):1089-1100. [\[CrossRef\]](#)
- Lee-Felker SA, Felker ER, Tan N, et al. Qualitative and quantitative MDCT features for differentiating clear cell renal cell carcinoma from other solid renal cortical masses. *AJR Am J Roentgenol*. 2014;203(5):W516-W524. [\[CrossRef\]](#)
- Grajo JR, Terry RS, Ruoss J, et al. Using aorta-lesion-attenuation difference on preoperative contrast-enhanced computed tomography scan to differentiate between malignant and benign renal tumors. *Urology*. 2019;125:123-130. [\[CrossRef\]](#)
- Giambelluca D, Pellegrino S, Midiri M, Salvaggio G. The "central stellate scar" sign in renal oncocytoma. *Abdom Radiol (NY)*. 2019;44(5):1942-1943. [\[CrossRef\]](#)
- Choudhary S, Rajesh A, Mayer NJ, Mulcahy KA, Haroon A. Renal oncocytoma: CT features cannot reliably distinguish oncocytoma from other renal neoplasms. *Clin Radiol*. 2009;64(5):517-522. [\[CrossRef\]](#)
- Kim JI, Cho JY, Moon KC, Lee HJ, Kim SH. Segmental enhancement inversion at biphasic multidetector CT: characteristic finding of small renal oncocytoma. *Radiology*. 2009;252(2):441-448. [\[CrossRef\]](#)
- Li X, Nie P, Zhang J, Hou F, Ma Q, Cui J. Differential diagnosis of renal oncocytoma and chromophobe renal cell carcinoma using CT features: a central scar-matched retrospective study. *Acta Radiol*. 2022;63(2):253-260. [\[CrossRef\]](#)
- Allgood E, Raman SS. Image interpretation: practical triage of benign from malignant renal masses. *Radiol Clin North Am*. 2020;58(5):875-884. [\[CrossRef\]](#)
- Kahn AE, Lomax SJ, Bajalia EM, Ball CT, Thiel DD. Utility of the aortic-lesion-attenuation-difference (ALAD) and peak early-phase enhancement ratio (PEER) to differentiate benign from malignant renal masses. *Can J Urol*. 2020;27(4):10278-10284. [\[CrossRef\]](#)
- Bird VG, Kanagarajah P, Morillo G, et al. Differentiation of oncocytoma and renal cell carcinoma in small renal masses (<4 cm): the role of 4-phase computerized tomography. *World J Urol*. 2011;29(6):787-792. [\[CrossRef\]](#)
- Wang X, Song G, Jiang H. Differentiation of renal angiomyolipoma without visible fat from small clear cell renal cell carcinoma by using specific region of interest on contrast-enhanced CT: a new combination of quantitative tools. *Cancer Imaging*. 2021;21(1):47. [\[CrossRef\]](#)
- Moldovanu CG, Petresc B, Lebovici A, et al. Differentiation of clear cell renal cell carcinoma from other renal cell carcinoma subtypes and benign oncocytoma using quantitative MDCT enhancement parameters. *Medicina (Kaunas)*. 2020;56(11):569. [\[CrossRef\]](#)



# A comparison between the superb microvascular imaging technique and conventional Doppler ultrasound in evaluating chronic allograft damage in renal transplant recipients

Ahmet Faruk Gürbüz

Ayşe Keven

Aygül Elmalı

Serap Toru

Ali Apaydın

Kağan Çeken

## PURPOSE

The present study comparatively evaluates the performance of conventional Doppler ultrasound and superb microvascular imaging (SMI) in delineating the cortical microvessels of the transplanted kidney and compares the chronic allograft damage index (CADI) based on the examination of biopsy specimens with Doppler ultrasound and SMI findings.

## METHODS

Sixty-eight renal transplant recipients underwent kidney biopsy with the pre-diagnosis of rejection before undergoing renal Doppler ultrasound examination between January 2020 and October 2020. The distance between the kidney capsule and the vascular structure closest to the kidney capsule was measured at the level of the lower pole in the transplanted kidney using color Doppler ultrasound (CDUS), power Doppler ultrasound (PDUS), and the SMI technique. The kidney size, resistive index at the level of the arcuate artery in the lower pole of the kidney, and renal artery flow rates were also measured.

## RESULTS

The mean distance between the kidney capsule and the vessel was  $2.44 \pm 2.0$  mm on CDUS,  $1.34 \pm 1.2$  mm on PDUS,  $0.99 \pm 1.8$  mm using the color SMI (cSMI) technique, and  $0.86 \pm 1.8$  mm using the monochrome SMI (mSMI) technique. The study found that the SMI technique was superior to CDUS and PDUS in delineating the cortical microvasculature of the kidney. Both Doppler ultrasound examinations and the SMI technique proved effective in predicting the CADI ( $P = 0.006$  for CDUS,  $P = 0.002$  for PDUS,  $P = 0.018$  for cSMI, and  $P = 0.027$  for mSMI).

Among conventional Doppler ultrasound examinations and the SMI technique, PDUS had the highest sensitivity, and cSMI had the highest specificity in differentiating high and low CADI values. Both the cSMI and mSMI techniques had similar sensitivity values, whereas only cSMI exhibited high specificity. CDUS had the lowest specificity value ( $P = 0.003$  for CDUS,  $P = 0.002$  for PDUS,  $P = 0.005$  for cSMI, and  $P = 0.004$  for mSMI).

## CONCLUSION

The present study is the first in the literature to demonstrate the utility of the distance between the kidney capsule and the vessels in predicting the CADI score and to compare the Doppler ultrasound examinations and SMI technique in doing so.

## KEYWORDS

Chronic allograft damage index, Doppler ultrasound, kidney, renal transplant, superb microvascular imaging

From the Department of Radiology (A.F.G., A.K. ✉ aysekeven@gmail.com, A.E., A.A., K.Ç.), Akdeniz University Faculty of Medicine, Antalya, Turkey; Department of Pathology (S.T.), Akdeniz University Faculty of Medicine, Antalya, Turkey.

Received 20 May 2021; revision requested 30 June 2021; last revision received 01 December 2021; accepted 29 December 2021.



Epub: 27.01.2023

Publication date: 29.03.2023

DOI: 10.5152/dir.2022.21555

You may cite this article as: Gürbüz AF, Keven A, Elmalı A, Toru S, Apaydın A, Çeken K. A comparison between the superb microvascular imaging technique and conventional Doppler ultrasound in evaluating chronic allograft damage in renal transplant recipients. *Diagn Interv Radiol.* 2023;29(2):212-218.

Chronic kidney disease is a significant public health concern because of its increasing incidence, associated high rates of morbidity and mortality, significant impairment in patients' quality of life, high treatment costs, and low level of public awareness. Hemodialysis, peritoneal dialysis, and renal transplantation are used in treating patients with kidney failure. Among these treatment modalities, renal transplantation is considered the ideal treatment method. Renal transplantation confers more prolonged survival and better quality of life compared with peritoneal dialysis and hemodialysis.<sup>1</sup>

The success of a renal transplant depends on the extent to which renal functions have been preserved. Kidney biopsy is the most crucial examination method in exploring renal dysfunction.<sup>2,3</sup> The chronic allograft damage index (CADI) is a scoring system developed in the early 1990s to numerically classify pathological lesions associated with the loss of kidney function in renal transplant recipients. There is a correlation between kidney survival and functions and the CADI, which is calculated using six histopathological lesions (interstitial inflammation, tubular atrophy, interstitial fibrosis, arterial fibrointimal thickening, glomerular mesangial matrix increase, and glomerular sclerosis). The CADI provides beneficial information to the clinician in deciding the treatment and follow-up of the patient, as the CADI is a numeric scoring system reflecting the extent of chronic kidney damage. This scoring system provides a quick overview of the severity of chronic alternations. Previous studies recommend using the CADI as a part of routine clinical assessment when interpreting transplanted kidney biopsies.<sup>4</sup> A strong relationship has been reported between the CADI and graft survival and functions.<sup>5</sup>

#### Main points

- The superb microvascular imaging (SMI) technique seems to be more sensitive than color Doppler ultrasound (CDUS) and power Doppler ultrasound (PDUS) in depicting the kidney cortical microvasculature in the transplanted kidney.
- The distance between the kidney capsule and the vessel measured by CDUS, PDUS, and SMI significantly differed between patients with low and high chronic allograft damage index (CADI) scores.
- CDUS and PDUS examinations and the SMI technique prove effective in predicting the CADI score in transplanted kidneys, and the SMI technique is the most specific in ruling out severe chronic rejection.

Histopathological examination of the transplanted kidney provides beneficial information about the precise diagnosis and treatment.<sup>6</sup> However, biopsy examination also has some known limitations. The examination of a small amount of kidney tissue may fail to detect many renal pathologies. The factors limiting the examination of the biopsy materials include the inability to collect a sufficient amount of kidney tissue, failure to recover cortical tissue, patchy involvement of the kidney in the disease, borderline lesions, therapies received, and the presence of parenchymal scarring.<sup>2</sup>

Some histologic features of chronic allograft nephropathy, such as vascular intimal proliferation and fibrosis, are related to tissue perfusion.<sup>7</sup> Assessing the cortical microvasculature blood flow representing kidney perfusion is challenging due to the small caliber of the vessels with a slow flow. Wang et al.<sup>8</sup> assessed cortical perfusion of renal transplants during acute rejection episodes using power Doppler quantification and found that acute antibody-mediated rejection is associated with significantly decreased cortical perfusion. Schwenger et al.<sup>7</sup> suggest that perfusion intensity assessed by dynamic color Doppler measurements is significantly reduced in allografts with grade 2 and 3 fibrosis compared to allografts without fibrosis.

Imaging techniques have become essential auxiliary diagnostic methods in kidney diseases. Doppler ultrasound is a valuable tool in the diagnosis and follow-up of complications and rejection after renal transplantation. However, color Doppler ultrasound (CDUS) assesses renal perfusion only in large arteries without giving any detailed information regarding the perfusion of preglomerular arterioles. Power Doppler ultrasound (PDUS) is reportedly sensitive to low-velocity and microvascular blood flow. The main drawback of PDUS, though, is its high sensitivity to tissue motion. Superb microvascular imaging (SMI) uses advanced ultrasound algorithms to preserve the subtlest slow-flow components that cannot be depicted using CDUS or PDUS techniques.

A study by Gao et al.<sup>9</sup> compared SMI and other Doppler ultrasound techniques in terms of their sensitivities in demonstrating microvasculature and concluded that SMI performs best in delineating kidney microvasculature. The authors of the present study consider that the superior performance of the SMI technique in demonstrating micro-

vasculature might provide new scientific data that allows insight into the effects of kidney rejection on peripheral vasculature and predicts the degree of rejection.

The studies in the literature have established a strong relationship between the CADI and graft survival and functions.<sup>4,5,10,11-13</sup> However, no radiological method currently exists that predicts the CADI. The present study aims to evaluate the effectiveness of the SMI technique in predicting the type and severity of rejection in renal transplant patients. It also compares the performances of the SMI technique and conventional Doppler ultrasound techniques in predicting the severity of rejection.

## Methods

### Study design and setting

The present study was designed as a single-center study approved by the hospital's ethics committee (23.10.2019/958). Informed consent forms were signed by all patients in line with the World Medical Association Declaration of Helsinki, revised in 2000 in Edinburgh. The study was financially supported by the Akdeniz University Scientific Research project fund (project no: 5146).

### Patient data

The study included patients who were examined by the physicians working at the hospital's transplantation unit and who underwent renal transplant biopsy between January 2020 and October 2020 due to recent-onset proteinuria, persistently elevated serum creatinine levels, and a lack of a decrease to basal levels of serum creatinine despite the therapies.

The biopsy materials consisted of core biopsy performed at different time points after transplantation. Sixty-eight patients were evaluated by renal Doppler ultrasound before undergoing renal biopsy. No glomeruli were observed in the biopsy specimen of one patient, two glomeruli were observed in two patients, three glomeruli were observed in one patient, and these four patients were excluded from the study, as a pathological examination could not be performed due to insufficient glomeruli in the specimens.

Age, gender, serum creatinine levels, the mean time elapsed since transplantation, and the results of a pathological examination evaluating renal allograft rejection were retrieved from the hospital's database (MIA

MED, 1.0.1.3295). Gray-scale ultrasound, CDSU, PDUS, and SMI examinations were performed using an Aplio i800 ultrasound scanner (Canon Medical Systems USA, Tustin, CA) equipped with a linear array transducer (PLT-1005BT, 10 MHz).

### Imaging parameters and technique

All patients underwent gray-scale ultrasound, PDUS, CDUS, and SMI in a supine position in a dimly lit ultrasound room before undergoing a biopsy. The results were recorded for later comparison with histopathological results. Table 1 presents the parameters used in the conventional Doppler ultrasound and SMI.

The longitudinal axis, parenchymal thickness, and echo pattern of the transplanted kidneys were evaluated on gray-scale ultrasound examination. Then, the resistive index (RI) was measured at the level of the arcuate artery in the lower pole of the kidney by switching to CDUS mode. Because biopsies were done, the lower pole for RI measurement was preferred. The renal artery flow rate was measured from the point closest to

the anastomosis line, and the Doppler angle was measured parallel to the vessel wall with a transducer angle of fewer than 60 degrees. The distance between the kidney capsule and the vascular structure closest to the kidney capsule (capsule-to-vessel distance) was measured by CDUS, PDUS, and SMI at the lower pole level in the transplanted kidney (Figure 1). A small color box in the cortical area and the pre-settings of the Doppler device recommended for renal examination were used to achieve a high frame rate and resolution. Each CDUS mode was performed once at the same region. A single operator who had five years of experience with kidney sonography performed renal CDUS in all patients.

### Statistical analysis

The sample size in the study was calculated using a power of at least 80% for each variable and a 5% type 1 error. The Kolmogorov–Smirnov ( $n > 50$ ) test and the Skewness–Kurtosis test were used to examine whether continuous variables were normally distributed, and parametric tests were applied due to the normal distribution of the measurements.

Descriptive statistics were used to express continuous variables, such as mean, standard deviation, minimum, and maximum; categorical variables were expressed as numbers and percentages. The independent-samples t-test was used to compare measurements between the CADI groups. A chi-squared test

**Table 1.** The parameters used in CDUS, PDUS, and SMI techniques

Parameter	Frequency	Pulse repetition frequency	Mechanical index	Color gain
CDUS	10 MHz	9–14	1.5–1.6	39
PDUS	10 MHz	10–15	1.5–1.6	47
SMI	10 MHz	0.8–1.2	1.5–1.6	40

CDUS, color Doppler ultrasound; PDUS, power Doppler ultrasound; SMI, superb microvascular imaging.

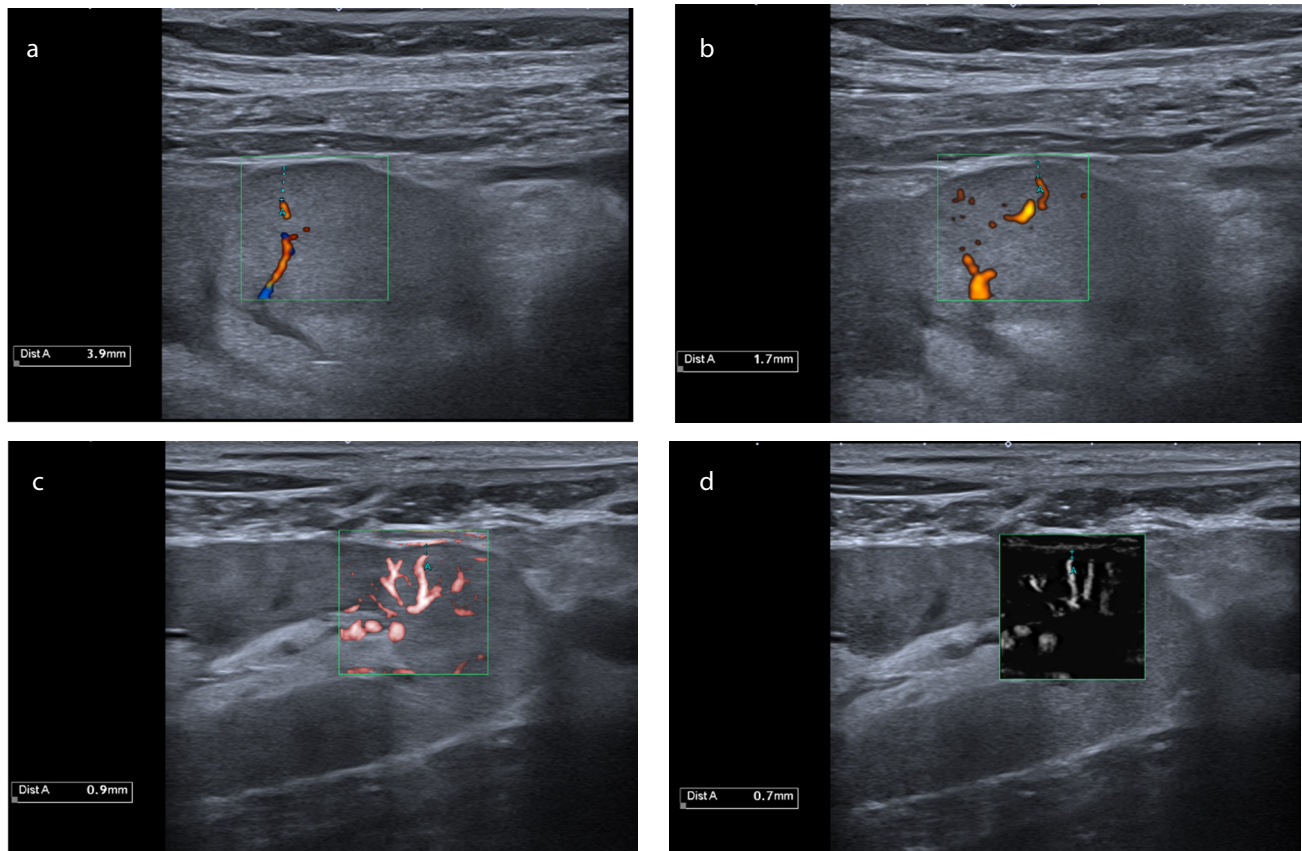


**Figure 1.** In a thirty-year-old male patient who underwent kidney transplantation five years ago, the distance between the kidney capsule and the vessel was measured as 3.9 mm on (a) color Doppler ultrasound, 1.7 mm on (b) power Doppler ultrasound, 0.9 mm on (c) color superb microvascular imaging examination, and 0.7 mm on (d) monochrome superb microvascular imaging examination. The chronic allograft damage index (CADI) score was calculated as 6. The patient was in the high CADI group. The capsule-vessel distances measured by the Doppler examinations were above the cut-off values and correlated with the pathology result. The resistive index was calculated as 0.58, and serum creatinine was 4.54 mg/dL.

was used to examine the relationship between the categorical variables. In receiver operating characteristic (ROC) curve analysis, the area under the curve (AUC), sensitivity, specificity, and cut-off values were calculated to determine the performance of the CADI in predicting the distance between the kidney capsule and the vessel measured by Doppler ultrasound examination.

The Statistical Package for the Social Sciences version 24 software package was used in the statistical analysis. A *P* value of less than 0.050 was considered statistically significant in all statistical analyses.

## Results

### Patient characteristics

The mean number of glomeruli was 14.36 (minimum: 7; maximum: 35) in biopsy

specimens recovered from 69 patients. The mean kidney size was 113.2 mm. Thirty patients were female (31.25), and 44 were male (68.75%). The mean age was 38.42 years, with a minimum of 8 years and a maximum of 64 years. The highest velocity in the renal artery was 201/43 cm/s, and the lowest was 45/15 cm/s.

The mean time elapsed since renal transplantation was 6.5 years. The time from renal transplantation was less than one year in 15 patients (23.44%), 1–3 years in 10 patients (15.62%), and more than three years in 39 patients (60.94%).

The histopathological CADI score was calculated for a total of 64 patients. Patients with a CADI score of 4 or less were allocated to the low CADI group, and those with a CADI score of greater than 4 were allocated to the high CADI group. The mean CADI score was

1.77 for 23 patients in the low CADI group and 8.49 for 41 patients in the high CADI group. The mean RI was 0.62 (0.4–0.77) and 0.66 (0.54–0.88) in the low and high CADI groups, respectively. The mean creatinine was 1.68 mg/dL in the low CADI group and 2.46 mg/dL in the high CADI group (Table 2).

### Results of color Doppler ultrasound, power Doppler ultrasound, and superb microvascular imaging

The RI was lower than 0.70 in 45 patients and 0.70 or higher in 19 patients. Among 19 patients with a high RI, five had low CADI scores, and 14 had high CADI scores. Among 45 patients with a low RI value, 18 had a low CADI score, and 27 had a high CADI score. The analysis of the relationship between the CADI score and the RI revealed no statistically significant relationship (*P* = 0.297).

The mean capsule-to-vessel distance on CDUS was significantly lower in the low CADI group (1.49 mm vs. 2.33 mm, *P* = 0.006) and was also lower on PDUS in the low CADI group (0.70 mm vs. 1.70 mm, *P* = 0.002) (Table 3).

The mean capsule-to-vessel distance on color SMI (cSMI) was significantly lower in the low CADI group (0.26 mm vs. 1.39 mm, *P* = 0.018) (Table 4). Finally, the mean distance between the kidney capsule and the vessel on monochrome SMI (mSMI) significantly dif-

**Table 2.** Age, female-to-male ratio, RI, creatinine, and time elapsed since transplantation in the low and high CADI groups

	CADI ≤4 (n = 23)	CADI >4 (n = 41)
CADI score	1.77	8.49
Age (year)	34.29	41.66
Female-to-male ratio	1/3.6	1/3.1
RI	0.62 (0.40–0.77)	0.66 (0.54–0.88)
Creatinine (mg/dL)	1.68	2.46
Time elapsed since transplantation (year)	3.48	7.92

CADI, chronic allograft damage index; RI, resistive index.

**Table 3.** Mean, standard deviation, minimum, and maximum values for the kidney capsule-to-vessel distance measured by CDUS, PDUS, cSMI, and mSMI techniques

	Mean ± SD	Min–max (mm)	* <i>P</i>
<b>CDUS</b>			
CADI ≤4 (n = 23)	1.50 ± 1.10	0–4.3	0.006
CADI >4 (n = 41)	2.96 ± 2.33	0.7–13	
Total (n = 64)	2.44 ± 2.09	0–13	
<b>PDUS</b>			
CADI ≤4 (n = 23)	0.70 ± 0.85	0–3.1	0.002
CADI >4 (n = 41)	1.70 ± 1.34	0–5.1	
Total (n = 64)	1.35 ± 1.28	0–5.1	
<b>cSMI</b>			
CADI ≤4 (n = 23)	0.27 ± 0.51	0–1.6	0.018
CADI >4 (n = 41)	1.40 ± 2.19	0–13	
Total (n = 64)	0.99 ± 1.85	0–13	
<b>mSMI</b>			
CADI ≤4 (n = 23)	0.20 ± 0.41	0–1.2	0.027
CADI >4 (n = 41)	1.23 ± 2.16	0–13	
Total (n = 64)	0.86 ± 1.81	0–13	

\*Independent-samples t-test. CDUS, color Doppler ultrasound; cSMI, color superb microvascular imaging; max, maximum distance between the kidney capsule and the vessel; Min, minimum distance between the kidney capsule and the vessel; mSMI, monochrome superb microvascular imaging; n, number; PDUS, power Doppler ultrasound; SD, standard deviation.

ferred between the low and high CADI groups ( $P = 0.027$ ) (Table 3).

In ROC curve analysis, conventional Doppler examinations and the SMI technique proved effective in predicting the CADI score. The calculated AUC value in ROC curve analysis was 0.722 for CDUS, 0.740 for PDUS, 0.712 for cSMI, and 0.718 for mSMI (Table 4). Although the values were close to each other, the highest AUC value was calculated for PDUS. According to ROC curve analysis, the cut-off value for the capsule-to-vessel distance in differentiating between a low and high CADI score was 1.90 mm (a sensitivity of 63% and a specificity of 65%) in CDUS, 1.15 mm (a sensitivity of 68% and a specificity of 70%) in PDUS, 0.85 mm (a sensitivity of 56% and a specificity of 87%) in cSMI, and 0.65 mm (a sensitivity of 56% and a specificity of 83%) in mSMI (Figure 2). PDUS had the highest sensitivity (68%), and cSMI had the highest specificity (87%). Although cSMI and mSMI yielded similar sensitivity rates (each 56%), the cSMI technique yielded higher specificity. CDUS had the lowest specificity.

## Discussion

Renal transplantation is a treatment method used in end-stage renal insufficiency. Successful renal transplantation improves patients' quality of life and decreases mortality. Renal transplantation is more valuable than dialysis due to its low cost.<sup>14</sup> Recognizing complications early after renal transplantation is crucial to prolonging graft survival. Early recognition will prevent the loss of health and eliminate the psychological, social, and economic burden of therapies that may be required after rejection.

Doppler ultrasound examination is used to recognize complications and evaluate the vascularity of the transplanted kidney after transplantation. A hemodynamic index, the RI, reflects the vascular compliance of the recipient. A persistently elevated RI has also been considered to be pathological. The RI represents the microcirculation status and provides information about the glomerular function and pathological conditions.<sup>15</sup> The correlation between the RI and glomerular sclerosis, tubulointerstitial, and vascular al-

terations has been demonstrated in various studies.<sup>16-18</sup> In a study comparing the RI with the transplanted kidney functions and biopsy results, Ikee et al.<sup>19</sup> followed up with 52 patients for two years, and a significant relationship was reported between the RI and age, creatinine clearance, and histopathological results. The RI has been employed as a useful marker in evaluating renal allograft function and the survival and long-term prognosis of the patients.<sup>20,21</sup> In the present study, patients with chronic kidney damage were divided into two groups according to the CADI score: patients with a CADI score of 4 or less were allocated to the group with mild chronic kidney damage, and patients with a CADI score of greater than 4 were allocated to the group with severe chronic kidney damage. The mean RI in the groups of patients with mild and severe chronic kidney damage was 0.62 (0.40–0.77) and 0.66 (0.54–0.88), respectively. In statistical analysis considering a cut-off value of 0.70 for RI, no significant relationship was found between the RI and the degree of chronic kidney damage ( $P > 0.050$ ).

Renal function is related to the hemodynamic status of the cortical microvasculature.<sup>22,23</sup> It is difficult to evaluate the blood flow in cortical microvessels representing kidney perfusion due to low flow velocity and the small diameter of the vessels.<sup>24</sup> The use of CDUS has been a standard approach for follow-up after renal transplantation and in evaluating possible complications.<sup>25-27</sup> However, CDUS fails to evaluate microvasculature and low flow velocity.<sup>28</sup> Additionally, PDUS is considered sensitive in evaluating the status of microvasculature but is affected by tissue movements.<sup>27</sup> The SMI technique, capable of differentiating tissue movement from low flow velocity due to improved Doppler algorithms and wall filters, was introduced into clinical practice in 2014.<sup>29</sup>

In a study comparing the SMI technique with conventional ultrasound techniques in evaluating the cortical microvasculature of the kidney, Gao et al.<sup>9</sup> reported significant differences in the renal capsule-vessel distances measured by the SMI, PDUS, and CDUS techniques ( $P < 0.001$ ). They found lower capsule-to-vessel distance in SMI than in the other two techniques. The capsule-to-vessel distance was reportedly  $1.06 \pm 0.43$  mm in SMI,  $2.11 \pm 1.0$  mm in PDUS, and  $4.5 \pm 2.1$  mm in CDUS. Consequently, they suggested that the SMI technique was superior to other Doppler ultrasound techniques in demonstrating the cortical microvasculature of the kidney in healthy individuals.<sup>9</sup> In the present study, 64 renal transplant recipients

**Table 4.** The diagnostic tests, AUC, and the cut-off values in renal transplant recipients with low and high CADI scores

Doppler technique	AUC	Sensitivity	Specificity	*Cut-off	P
CDUS	0.722	0.634	0.652	1.90	0.003
PDUS	0.740	0.683	0.696	1.15	0.002
cSMI	0.712	0.561	0.870	0.80	0.005
mSMI	0.718	0.561	0.826	0.65	0.004

\*The cut-off values in millimeters for the distance between the kidney capsule and the vessel measured by Doppler techniques. AUC, area under the curve; CADI, chronic allograft damage index; CDUS, color Doppler ultrasound; cSMI, color superb microvascular imaging; mSMI, monochrome superb microvascular imaging; PDUS, power Doppler ultrasound.

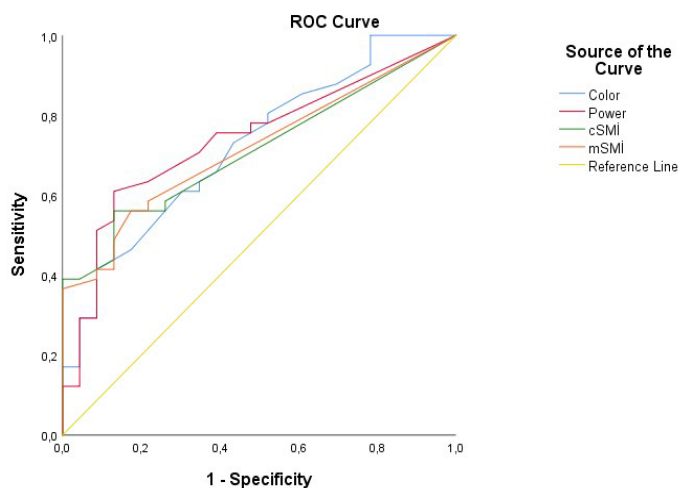


**Figure 2.** The receiver operating characteristic curve demonstrating the efficacies of Doppler ultrasound examinations in predicting the chronic allograft damage index score. ROC, receiver operating characteristic; cSMI, color superb microvascular imaging; mSMI, monochrome superb microvascular imaging.

underwent CDUS, PDUS, cSMI, and mSMI on the same day as the kidney biopsy procedure. The distance between the kidney capsule and vascular structures could not be observed in four patients using CDUS, 20 patients using PDUS, 34 patients using cSMI, and 36 patients using mSMI. The cSMI technique demonstrated the vascular structures in the subcapsular area, which could not be observed in 30 patients using CDUS and 14 patients using PDUS. The SMI technique also detected all those patients detected by CDUS and PDUS. The mean capsule-to-vessel distance was  $2.44 \pm 2.0$  mm in CDUS,  $1.34 \pm 1.2$  mm in PDUS,  $0.99 \pm 1.8$  mm in cSMI, and  $0.86 \pm 1.8$  mm in mSMI. The distance of the end vessels of the cortex to the kidney capsule represents the sensitivity of color Doppler images in depicting small vessels because vessels closer to the kidney capsule are smaller. In other words, the shorter distance of the cortical end vessel to the kidney capsule indicates the higher sensitivity of SMI in depicting smaller vessels in the cortex near to the kidney capsule. Similar to the studies in the literature, the present study reports the superiority of the SMI technique to CDUS and PDUS in demonstrating the cortical microvasculature of the kidney.

A transplanted kidney functions for approximately 10–20 years, and chronic kidney damage remains among the unresolved problems leading to the loss of kidney function. The histopathological alterations precede kidney function loss, and histopathological scoring of the damage in a functional kidney provides beneficial information to clinicians in predicting allograft prognosis.<sup>4</sup>

Nankivell et al.<sup>30</sup> suggest that the distance between the margin of the vascular structures and the kidney capsule can predict chronic allograft nephropathy. The present study is the first to evaluate the use of Doppler examinations and the SMI technique in predicting the CADI score. Patients were divided into two groups: patients with a CADI score of 4 or less and those with a CADI score of greater than 4. The reasons for selecting a CADI score of 4 as the cut-off level were the reports in the literature showing a significantly higher rate of graft loss and significantly higher serum creatinine levels in patients with a CADI score of greater than 4 compared with patients with a CADI score of 4 or less.<sup>5,10,12,13</sup> The capsule-to-vessel distance measured by CDUS, PDUS, and SMI significantly differed between the patients with low and high CADI scores, and it is found that these methods can effectively predict the score. The authors consider that this find-

ing will enable the provision of appropriate therapy to transplant recipients at a high risk of graft dysfunction before graft loss occurs and will inform the clinicians about the necessity of performing a renal biopsy in patients anticipated to have a high CADI score.

There are some limitations in the present study. One of the main limitations was the small sample size. To find a significant difference between the CADI groups, the sample size was calculated using the G power statistical program. According to this; with Power (test power) 0.80, Effect size 0.8, and Type-1 error ( $\alpha$ ) 0.05 (for 2 groups,  $CADI \leq 4$  and  $CADI > 4$ ), a total of 42 patients with “minimum 21 observations (patient data)” in each group determined as “. However, to ensure the number of samples and to keep the Power value high, the number of samples was increased and “ $CADI \leq 4$  n = 23” and “ $CADI > 4$  n = 41” patient data were obtained in our study. The power recalculated based on this new sample size was 91%. The scarcity of patients with a  $CADI \leq 4$  was the most important limitation of the sample size. When the contribution of Doppler ultrasound and the SMI technique in predicting the degree of rejection is investigated in a larger study sample, more appropriate cut-off values and optimal sensitivity and specificity values can be achieved. Another limitation of the study was that only one investigator was involved in collecting the study data, making it impossible to evaluate interobserver variability.

The flow data of the vessels are presented in color codes and gray-scale maps in the cSMI technique. In the mSMI technique, flow signals are received from small and large vessels, and a gray-scale flow map is created by removing the background data.<sup>8</sup> In comparing the cSMI and mSMI techniques, a limiting factor for measuring the distance between the kidney capsule and the vessel is the fact that gray-scale data are eliminated in the mSMI technique.

Furthermore, the time elapsed since transplantation was different between the study patients. The authors consider that the effectiveness of the SMI and conventional Doppler ultrasound techniques would be increased in future studies, provided that the study period covers a certain period after transplantation.

In conclusion, the present study is the first in the literature to demonstrate the utility of the capsule-to-vessel distance measured by Doppler ultrasound examinations and the SMI technique in predicting the CADI score, which is closely related to graft survival and

function. When compared with CDUS and PDUS, the SMI technique was found to be superior in delineating the cortical microvasculature of the kidney.

The statistical analyses in the present study suggest that both conventional Doppler ultrasound examinations and the SMI technique prove sensitive in predicting the CADI score. The study also finds that the SMI technique is the most specific in ruling out severe chronic rejection. There is, however, a need for further national and international studies involving larger patient groups.

### Conflict of interest disclosure

The authors declared no conflicts of interest.

### References

1. Çamsarı T, Sağlam F. Kronik Böbrek Yetmezliği. In: Erol Ç, Süleymanlar, ed. *İç Hastalıkları Nefroloji. Birinci Baskı*. Ankara: MN Medikal&Nobel Yayınevi, 2011; 85-97. [CrossRef]
2. Kasiske BL, Cangro CB, Hariharan S, et al. The evaluation of renal transplantation candidates: clinical practice guidelines. *Am J Transplant*. 2001;1 Suppl 2:3-95. [CrossRef]
3. Asadpour A, Molaei M, Yaghoobi S. Management of ureteral complications in renal transplantation: prevention and treatment. *Saudi J Kidney Dis Transpl*. 2011;22(1):72-74. [CrossRef]
4. Helanterä I, Ortiz F, Koskinen P. Chronic Allograft Damage Index (CADI) as a biomarker in kidney transplantation. *Biomarkers in Kidney Disease*. 2015;1-19. [CrossRef]
5. Isoniemi H, Taskinen E, Häyry P. Histological chronic allograft damage index accurately predicts chronic renal allograft rejection. *Transplantation*. 1994;58(11):1195-1198. [CrossRef]
6. Wilczek HE. Percutaneous needle biopsy of the renal allograft. A clinical safety evaluation of 1129 biopsies. *Transplantation*. 1990;50(5):790-797. [CrossRef]
7. Schwenger V, Korosoglou G, Hinkel UP, et al. Real-time contrast-enhanced sonography of renal transplant recipients predicts chronic allograft nephropathy. *Am J Transplant*. 2006;6(3):609-615. [CrossRef]
8. Wang HK, Chou YH, Yang AH, et al. Evaluation of cortical perfusion in renal transplants: application of quantified power Doppler ultrasonography. *Transplant Proc*. 2008;40(7):2330-2332. [CrossRef]
9. Gao J, Thai A, Erpelding T. Comparison of superb microvascular imaging to conventional color Doppler ultrasonography in depicting renal cortical microvasculature. *Clin Imaging*. 2019;58:90-95. [CrossRef]

10. Yilmaz S, Tomlanovich S, Mathew T, et al. Protocol core needle biopsy and histologic chronic allograft damage index (CADI) as surrogate end point for long-term graft survival in multicenter studies. *J Am Soc Nephrol*. 2003;14(3):773-779. [\[CrossRef\]](#)
11. Mengel M, Gwinner W, Schwarz A, et al. Infiltrates in protocol biopsies from renal allografts. *Am J Transplant*. 2007;7(2):356-365. [\[CrossRef\]](#)
12. Hayry P, Paavonen T, Taskinen E, et al. Protocol core needle biopsy and histological chronic allograft damage index as surrogate endpoint for Long-Term graft survival. *Transplant Proc*. 2004;36(1):89-91. [\[CrossRef\]](#)
13. Abbas TM, Wafa EW, Bakr MA, et al. Histologic and clinical findings in living donor allografts with long-term stable function. *Am J Nephrol*. 2006;26(5):491-496. [\[CrossRef\]](#)
14. Özdil G. Preoperative evaluation of renal transplantation: ultrasound and color Doppler ultrasound. *Türkiye Klinikleri J Radiol-Special Topics*. 2016;9:87-90. [\[CrossRef\]](#)
15. Krumme B, Grotz W, Kirste G, Schollmeyer P, Rump LC. Determinants of intrarenal Doppler indices in stable renal allografts. *J Am Soc Nephrol*. 1997;8(5):813-816. [\[CrossRef\]](#)
16. Platt JF, Ellis JH, Rubin JM, DiPietro MA, Sedman AB. Intrarenal arterial Doppler sonography in patients with nonobstructive renal disease: correlation of resistive index with biopsy findings. *AJR Am J Roentgenol*. 1990;154(6):1223-1227. [\[CrossRef\]](#)
17. Mostbeck GH, Kain R, Mallek R, et al. Duplex Doppler sonography in renal parenchymal disease. Histopathologic correlation. *J Ultrasound Med*. 1991;10(4):189-194. Erratum in: *J Ultrasound Med*. 1991;10(11):651. [\[CrossRef\]](#)
18. Platt JF, Rubin JM, Ellis JH. Lupus nephritis: predictive value of conventional and Doppler US and comparison with serologic and biopsy parameters. *Radiology*. 1997;203(1):82-86. [\[CrossRef\]](#)
19. Ikee R, Kobayashi S, Hemmi N, et al. Correlation between the resistive index by Doppler ultrasound and kidney function and histology. *Am J Kidney Dis*. 2005;46(4):603-609. [\[CrossRef\]](#)
20. Don S, Kopecky KK, Filo RS, et al. Duplex Doppler US of renal allografts: causes of elevated resistive index. *Radiology*. 1989;171(3):709-712. [\[CrossRef\]](#)
21. Drudi FM, Cascone F, Pretagostini R, et al. Ruolo dell'eco color-Doppler nella diagnostica del rene trapiantato [Role of color Doppler US in the evaluation of renal transplant]. *Radiol Med*. 2001;101(4):243-250. [\[CrossRef\]](#)
22. Shebel HM, Akl A, Dawood A, El-Diasty TA, Shokeir AA, Ghoneim MA. Power doppler sonography in early renal transplantation: does it differentiate acute graft rejection from acute tubular necrosis? *Saudi J Kidney Dis Transpl*. 2014;25(4):733-740. [\[CrossRef\]](#)
23. Wang HK, Chou YH, Yang AH, et al. Evaluation of cortical perfusion in renal transplants: application of quantified power Doppler ultrasonography. *Transplant Proc*. 2008;40(7):2330-2332. [\[CrossRef\]](#)
24. Rubin JM, Bude RO, Carson PL, Bree RL, Adler RS. Power Doppler US: a potentially useful alternative to mean frequency-based color Doppler US. *Radiology*. 1994;190(3):853-856. [\[CrossRef\]](#)
25. Gao J, Mennitt K, Belfi L, Zheng YY, Chen Z, Rubin JM. Green tagging in displaying color Doppler aliasing: a comparison to standard color mapping in renal artery stenosis. *Ultrasound Med Biol*. 2013;39(11):1976-1982. [\[CrossRef\]](#)
26. Chen P, Maklad N, Redwine M. Color and power Doppler imaging of the kidneys. *World J Urol*. 1998;16(1):41-45. [\[CrossRef\]](#)
27. Kuwa T, Cancio LC, Sondeen JL, et al. Evaluation of renal cortical perfusion by noninvasive power Doppler ultrasound during vascular occlusion and reperfusion. *J Trauma*. 2004;56(3):618-624. [\[CrossRef\]](#)
28. Shau YW, Pao SH, Chou NK, Chang KJ, Shyu JJ. Renal vascular perfusion index in a canine model. *Ultrasound Med Biol*. 2009;35(1):36-43. [\[CrossRef\]](#)
29. Park AY, Seo BK, Cha SH, Yeom SK, Lee SW, Chung HH. An innovative ultrasound technique for evaluation of tumor vascularity in breast cancers: superb micro-vascular imaging. *J Breast Cancer*. 2016;19(2):210-213. [\[CrossRef\]](#)
30. Nankivell BJ, Chapman JR, Gruenewald SM. Detection of chronic allograft nephropathy by quantitative doppler imaging. *Transplantation*. 2002;74(1):90-96. [\[CrossRef\]](#)



# Diagnostic performance of magnetic resonance imaging in preoperative local staging of rectal cancer after neoadjuvant chemoradiotherapy

Hakkı Çelik <sup>ID</sup>  
Funda Barlık <sup>ID</sup>  
Selman Sökmen <sup>ID</sup>  
Cem Terzi <sup>ID</sup>  
Aras Emre Canda <sup>ID</sup>  
Özgül Sağol <sup>ID</sup>  
Sülen Sarıoğlu <sup>ID</sup>  
Mehtat Ünlü <sup>ID</sup>  
İlknur Bilkay Görken <sup>ID</sup>  
Zümre Arıcan Alıcıkış <sup>ID</sup>  
İlhan Öztop <sup>ID</sup>

## PURPOSE

This paper aims to investigate the diagnostic performance of magnetic resonance imaging (MRI) in predicting the pathologic stage of locally advanced rectal cancer (LARC) after neoadjuvant chemoradiotherapy (CRT) and the role of MRI in selecting patients with a pathologic complete response (ypCR).

## METHODS

Restaging MRI (yMRI) examinations of 136 patients with LARC treated with neoadjuvant CRT followed by surgery were retrospectively analyzed by two radiologists. All examinations were performed on a 1.5 Tesla MRI machine with a pelvic phased-array coil. T2-weighted turbo spin-echo images and diffusion-weighted imaging were obtained. Histopathologic reports of the surgical specimens were the reference standard. The accuracy, sensitivity, specificity, positive and negative predictive values (PPV and NPV) of yMRI in predicting the pathologic T-stage (ypT), N-stage, and ypCR were calculated. The inter-observer agreement was evaluated using kappa statistics.

## RESULTS

The yMRI results showed 67% accuracy, 59% sensitivity, 80% specificity, 81% PPV, and 56% NPV in identifying ypT (ypT0-2 versus ypT3-4). In predicting the nodal status, the yMRI results revealed 63% accuracy, 60% sensitivity, 65% specificity, 47% PPV, and 75% NPV. In predicting ypCR, the yMRI results showed 84% accuracy, 20% sensitivity, 92% specificity, 23% PPV, and 90% NPV. The kappa statistics revealed substantial agreement between the two radiologists.

## CONCLUSION

Utilization of yMRI showed high specificity and PPV in predicting the tumor stage and high NPV in predicting the nodal stage; in addition, yMRI revealed moderate accuracy in the T and N classifications, mainly due to underestimating the tumor stage and overestimating the nodal status. Finally, yMRI revealed high specificity and NPV but low sensitivity in predicting the complete response.

## KEYWORDS

Rectal cancer, magnetic resonance imaging, neoadjuvant chemoradiotherapy, neoplasm staging, surgical pathology

From the Department of Radiology (H.Ç. ✉ dr.celik90@gmail.com, F.B.), Dokuz Eylül University Faculty of Medicine, İzmir, Turkey; Department of General Surgery (S.S., C.T., A.E.C.), Dokuz Eylül University Faculty of Medicine, İzmir, Turkey; Department of Pathology (Ö.S., S.Sa., M.Ü.), Dokuz Eylül University Faculty of Medicine, İzmir, Turkey; Department of Radiation Oncology (İ.B.G., Z.A.A.), Dokuz Eylül University Faculty of Medicine, İzmir, Turkey; Department of Medical Oncology (İ.Ö.), Dokuz Eylül University Faculty of Medicine, İzmir, Turkey.

Received 09 January 2022; revision requested 15 February 2022; last revision received 21 April 2022; accepted 13 May 2022.



Epub: 02.01.2023

Publication date: 29.03.2023

DOI: 10.4274/dir.2022.221333

**N**eoadjuvant chemoradiotherapy (CRT) is the standard initial treatment for patients with locally advanced rectal cancer (LARC). Neoadjuvant CRT induces tumor downstaging in approximately 50% of patients and creates a pathologic complete response (ypCR) in 15%–38% of LARC cases.<sup>1,2</sup> Neoadjuvant CRT provides the opportunity to perform sphincter-preserving surgery in patients with LARC by increasing the distance between the tumor and the anorectal junction. It can even offer a non-surgical treatment approach for some patients.<sup>3</sup> Additionally, it leads to a significant reduction in the number and size of metastat-

ic mesorectal lymph nodes.<sup>4</sup> Patients with LARC are restaged with a digital rectal examination, a colonoscopy, and rectal magnetic resonance imaging (MRI) after receiving neoadjuvant CRT.<sup>5,6</sup> Proper staging after CRT is essential to determine the optimal surgical strategy, such as sphincter-sparing surgery for tumors in the lower rectum or local excision for tumors confined to the rectal wall.<sup>7</sup>

MRI is the technique of choice for local staging, while positron emission tomography and computed tomography are more often used to detect distant metastases.<sup>8</sup> However, the reliability of restaging MRI (yMRI) remains controversial. Restaging with MRI after CRT is more challenging than the initial staging of cancer with MRI since it is difficult to distinguish small residual tumor areas from edema, fibrosis, and normal mucosa. Although the residual tumor has intermediate signal intensity, whereas fibrosis and scarring have low signal intensity on T2-weighted (T2W) images, the differentiation is still not easy, as the residual tumor may be found within scar tissue. Diffusion-weighted imaging (DWI) is useful in differentiating between viable residual tumor and treatment-related tissue changes.<sup>9-11</sup> Many studies have suggested that DWI plays a remarkable role in restaging.<sup>12-17</sup>

Restaging rectal cancer with MRI remains a challenge.<sup>18-20</sup> Studies that have investigated the performance of MRI in the staging of LARC after CRT revealed substantial discrepancies regarding tumor and lymph node staging and complete response evaluation.<sup>15</sup> Thus, this study investigates the diagnostic performance of MRI in predicting the pathologic stage of rectal cancer after CRT using histopathology as the gold standard. Additionally, the performance of MRI in selecting pathologic complete responders after CRT is analyzed.

### Main points

- Restaging magnetic resonance imaging (MRI) showed high specificity and positive predictive value in predicting the tumor stage and high negative predictive value (NPV) in predicting the nodal stage.
- Restaging MRI revealed moderate accuracy in the T-stage and N-stage classifications, mainly due to underestimating the tumor stage and overestimating the nodal status.
- Restaging MRI revealed high specificity and NPV but low sensitivity in predicting the complete response.

## Methods

### Study population

The institutional review board approved this retrospective study (2021/28-11) and waived the informed consent requirement. Consecutive patients diagnosed with LARC who underwent neoadjuvant CRT followed by total mesorectal excision between December 2012 and January 2020 were retrieved from our hospital database. Patients who underwent rectal MRI after CRT were included in the study. The exclusion criteria were distant metastases, insufficient image quality, incomplete CRT, and mucinous tumors. The patient accrual is summarized in Figure 1.

All patients underwent rectal high-resolution MRI and DWI after neoadjuvant CRT. For all patients, 45-Gy radiotherapy to the pelvis was administered before surgery. Consequently, a 5.4-Gy boost in three fractions was applied to the primary tumor. After the first and fifth weeks of radiation therapy, patients received 400 mg/m<sup>2</sup>/day fluorouracil and 20 mg/m<sup>2</sup>/day leucovorin over three days. The yMRI was performed at approximately 6–8 weeks after the completion of neoadjuvant CRT.

### Image acquisition

To minimize bowel motility, 20 mg of scopolamine butylbromide was injected in-

travenously 10 min before scanning, unless contraindicated. All examinations were performed on a 1.5-T MR machine (Philips Achi-va Release 1.8, Eindhoven, The Netherlands) with a pelvic phased-array coil. The T2W turbo spin-echo images were obtained in sagittal, para-axial (perpendicular to the long axis of the tumor), and para-coronal (parallel to the long axis of the tumor) planes using a repetition time of 4,500 ms, a field of view (FOV) of 180–220 mm, a matrix size of 256 × 512, a slice thickness of 3 mm, an intersection gap of 0.8 mm, and an echo train length of 16. Fat-suppression techniques and contrast agents were not used. Diffusion-weighted (b: 0 and b: 1.000 s/mm<sup>2</sup>) images were obtained in the sagittal and axial planes with a single-shot echo-planar sequence using a TR/TE of 4.200/95, a bank angle of 90°, a slice thickness of 5 mm, and a FOV of 350–400 mm. The in-line software automatically generated apparent diffusion coefficient (ADC) maps.

### Image interpretation

Rectal MRI examinations performed after CRT for yMRI were evaluated independently by two radiologists who were blinded to the histopathologic staging (ypTNM) results. Initially, an independent blinded evaluation of the yMRI images of each patient was performed by two radiologists [F.O. (radiologist-1), H.C. (radiologist-2), with 22 and 6 years of experience reading rectal MR images, respectively], who had no knowledge of the results of the histopathologic exam-

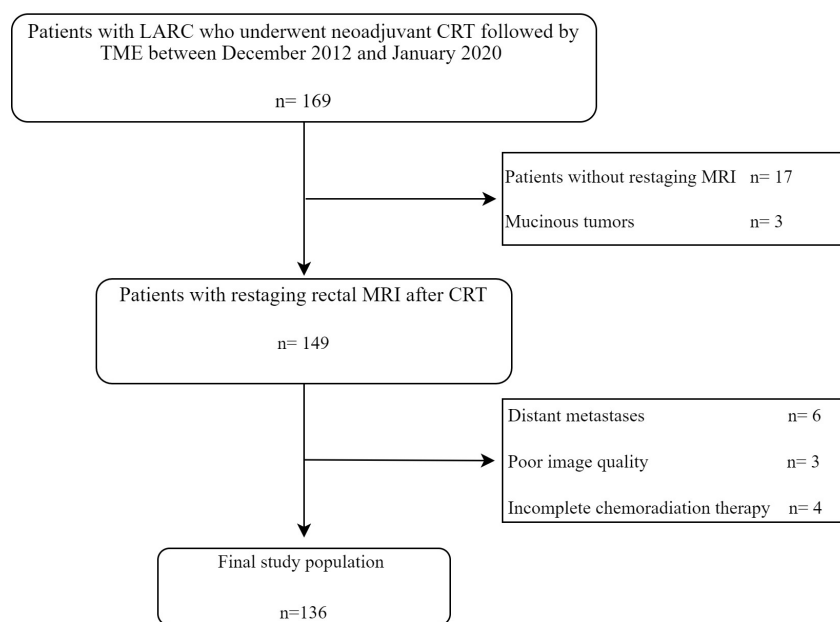


Figure 1. Flow chart of the study population.

LARC, locally advanced rectal cancer; CRT, chemoradiotherapy; MRI, magnetic resonance imaging; TME, total mesorectal excision

ination. The observers reached a consensus by discussing cases where they did not fully agree on the findings. The observers were able to review the rectal MRI obtained before neoadjuvant CRT to identify the treated tumor. The yT-stage (ypT), yN-stage (ypN), and the presence of radiologic complete response (ymrCR) were assessed using MRI. The yT-stages were defined according to the depth of tumor penetration into the rectal wall, mesorectum, and adjacent pelvic structures as follows: T1, infiltration into the submucosa; T2, infiltration into the muscularis propria; T3, infiltration beyond muscularis propria; and T4, infiltration to peritoneal reflection or other pelvic organs. The T-stage was primarily evaluated using high-resolution T2W images. On the T2W images, DWI and ADC maps were also evaluated to distinguish residual tumor from fibrosis. The signal intensity on DWI is usually high in the residual tumor and low in fibrosis. Subgroups of yT were defined as yT0-2 representing the early stage versus yT3-4 representing LARC.

According to the latest ESGAR guidelines, nodes with a short-axis diameter of <5 mm on yMRI are considered benign.<sup>21</sup> Nodes with a short-axis diameter of ≥5 mm are considered malignant in yMRI since there are no reliable criteria other than size for irradiated nodes. Only the T2W-MR images were evaluated for deciding on the nodal status.

The tumor response to neoadjuvant CRT was mainly evaluated qualitatively using DWI images and ADC maps. Neverthe-

less, the lack of anatomical details and the greater vulnerability to artifacts of DWI can introduce inaccuracy and variability in interpretation. Therefore, T2W images were reviewed to accurately assess the former tumor location. Lesions were considered to have restricted diffusion when the signal intensities on DWIs were higher than those of the prostate or small intestine.<sup>22</sup> The absence of any hyperintense signal that may belong to a residual tumor on DWI was accepted as a radiologic complete response (Figure 2). The patients who were qualitatively classified as ymrCR were compared with those reported to have ypCR.

### Histopathologic evaluation

All histopathologic interpretations were conducted by pathologists experienced in rectal cancer (O.S., S.S., and M.U.; 22, 24, and 15 years of experience, respectively). Histopathology records were reviewed for the ypT, ypN, and presence of complete response. Pathologic T0-2 (ypT0-2) stages were accepted as early stage, while ypT3-4 stages were accepted as LARC. Subgroups of ypT included ypT0-2 representing the early stage and ypT3-4 representing LARC. Lymph nodes were grouped as ypN- and ypN+.

### Statistical analysis

The reference standard was the histopathologic reports of the surgical specimens. The accuracy, sensitivity, specificity, positive predictive value (PPV), and negative predic-

tive value (NPV) of MRI in predicting ypT, ypN, and ypCR were calculated. Kappa statistics were used to evaluate agreement among the observers.

## Results

Of the 136 patients included in this study, 50 (37%) were female and 86 (63%) were male, with a mean age of 63.2 ± 11.2 years (range: 33–88 years).

Regarding yMRI, early T-stage (yT0-2) was detected in 53.7% (n = 73) of the patients, while LARC (yT3-4) was detected in 46.3% (n = 63) of them. Regarding histopathology, ypT0-2 was found in 39.7% (n = 54) patients, and ypT3-4 was found in 60.3% (n = 82) patients. Correlations between the MRI-based T classification after CRT and ypT-stages are summarized in Table 1.

Regarding the lymph node assessment on yMRI, 43.4% (n = 59) of the patients had at least one lymph node metastasis, and 56.6% (n = 77) of the patients had no metastatic lymph node. Assessment of the surgical resection specimens revealed that 34.6% (n = 47) of patients had at least one metastatic lymph node, and 65.4% (n = 89) of patients had no metastatic lymph node. The correlation between the results of yMRI and histopathology for the nodal status is summarized in Table 2.

The radiologic complete response to CRT was detected in 9.6% (n = 13) of the patients

**Table 1.** Comparison of MRI-based T-stage classification after chemoradiation and postoperative pathologic T classification

ymrT-stage	ypT-stage						
	ypT0	ypT1	ypT2	ypT0-2	ypT3	ypT4	ypT3-4
ymrT0	2	0	4	6	1	0	1
ymrT1	1	0	0	1	1	0	1
ymrT2	9	4	21	34	28	2	30
ymrT0-2	12	4	25	41	30	2	32
ymrT3	3	1	8	12	38	2	40
ymrT4	0	0	1	1	6	4	10
ymrT3-4	3	1	9	13	44	6	50

The overall accuracy of yMRI in the T-staging of rectal cancer: 48%. MRI, magnetic resonance imaging; yMRI, restaging MRI; ymrT, MRI-based T classification after chemoradiation; ypT, postoperative pathologic T classification.

**Table 2.** Comparison of MRI-based N-stage classification after chemoradiation and postoperative pathologic N classification

ymrN	ypN	
	ypN+	ypN-
ymrN+	28	31
ymrN-	19	58

MRI, magnetic resonance imaging; ymrN, MRI-based N classification after chemoradiation; ypN, postoperative pathologic N classification.

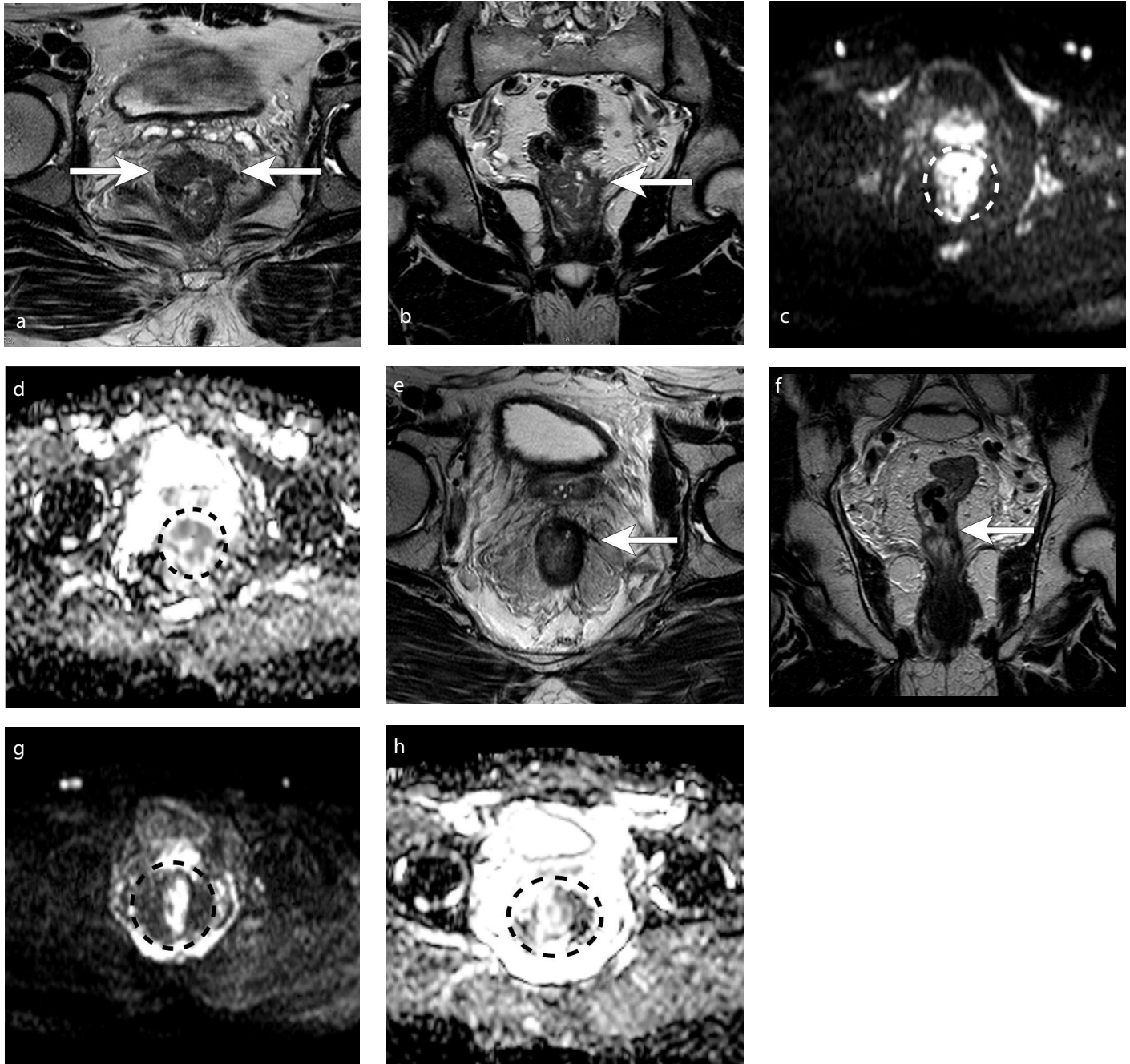


**Figure 2.** A 42-year-old man with locally advanced rectal cancer, treated with neoadjuvant chemoradiotherapy followed by total mesorectal excision. (a-d) Baseline rectal magnetic resonance (MR) images. T2W MR images in axial (a) and coronal planes (b) demonstrate the tumor infiltrating beyond muscularis propria (arrows). Axial diffusion-weighted (DW) image (c) and ADC map (d) demonstrate restricted diffusion (dashed circles). (e-h) Restaging MR images. T2-weighted MRI images in the axial (e) and coronal planes (f) show that the tumor is completely replaced by low-signal-intensity fibrosis (arrows). The axial DW image (g) and ADC map (h) reveal no restricted diffusion in the former tumor location (dashed circles). A complete tumor response (ypT0N0) was confirmed at histopathology.

on yMRI. The ypCR to neoadjuvant treatment was detected in 11% (n = 15) of patients. The correlation between the radiologic and histopathologic complete responses is summarized in Table 3.

The yMRI results showed 67% accuracy, 59% sensitivity, 80% specificity, 81% PPV, and 56% NPV in predicting ypT (ypT3-4 versus ypT0-2). The overall accuracy of yMRI in predicting each T-stage (T0/1/2/3/4) was 48%.

In predicting the nodal status, yMRI revealed 63% accuracy, 60% sensitivity, 65% specificity, 47% PPV, and 75% NPV. In predicting the complete response to neoadjuvant CRT, yMRI showed 84% accuracy, 20% sensitivity, 92% specificity, 23% PPV, and 90% NPV. The value of kappa was 0.82 in T-staging, 0.79 in N-staging, and 0.74 in predicting ypCR according to the agreement analysis of the observers. The diagnostic performance of yMRI is summarized in Table 4.

## Discussion

This study investigated the efficacy of yMRI in predicting the histopathologic stage after neoadjuvant CRT. In this study, the moderate accuracy of MRI in predicting the histopathologic stage can be related to understaging in the T-stage and overstaging in the N-stage. The yMRI results showed high specificity and moderate sensitivity in predicting the pathologic T-stage, whereas it showed moderate

**Table 3.** Comparison of radiologic and pathologic complete response

ymrCR	ypCR	
	ypCR+	ypCR–
ymrCR+	3	10
ymrCR–	12	111

ymrCR, radiologic complete response; ypCR, pathologic complete response.

**Table 4.** Diagnostic performance of MRI performed after chemoradiotherapy in the evaluation of the T-stage (ypT3-4 versus ypT0-2), N-stage (ypN-positive versus ypN0), and complete response (ypCR+ versus ypCR–)

	Sensitivity (%)			Specificity (%)			PPV (%)			NPV (%)			Accuracy (%)			IOA (kappa)
	R1	R2	C	R1	R2	C	R1	R2	C	R1	R2	C	R1	R2	C	R1-R2
T-staging	59	57	59	80	70	80	81	75	81	56	52	56	67	63	67	0.82
N-staging	60	54	60	65	58	65	47	40	47	75	71	75	63	57	63	0.79
CR	20	14	20	92	87	92	23	11	23	90	89	90	84	78	84	0.74

MRI, magnetic resonance imaging; PPV, positive predictive value; NPV, negative predictive value; IOA, interobserver agreement; CR, complete response; R1, radiologist 1; R2, radiologist 2; C, consensus.

sensitivity and specificity in nodal staging. A qualitative assessment of DWI revealed high specificity but low sensitivity in predicting ypCR. Interobserver agreements were significant, but an experienced observer revealed a higher performance in all statistical measures (Table 4).

The pathologic examination of the treated tumor revealed fibrosis and/or mucin production. On T2W and high b-value DWI, fibrosis presents as low-signal intensity areas, while mucin-containing areas appear hyperintense. Both fibrotic and mucinous tissue changes may obscure small areas of residual tumor, reducing the accuracy of yMRI.<sup>23</sup> In the present study, the tumor stage was understaged in 25% of patients on yMRI (Figure 3). We hypothesized that a viable residual tumor concealed in the hypointense scar was the main reason for underestimating the T-stages. In contrast, Lee et al.<sup>19</sup> suggested that diffusely infiltrated hypointense tissue in the mesorectal fascia secondary to CRT causes T-overstaging and decreases the accuracy of yMRI. Moreover, the submucosal edema adjacent to the tumor presented as a hyperintense signal on T2W images and may be misinterpreted as a residual tumor.<sup>23</sup> The combination of T2W imaging and DWI can be helpful to circumvent these pitfalls for response evaluation after neoadjuvant CRT.<sup>23</sup> The T2W images should be used as a reference for accurate identification of the tumor site when assessing DWI and ADC maps (Figures 2, 4).<sup>24</sup>

After CRT, both benign and malignant nodes shrank, and approximately 44% disappeared.<sup>25</sup> There are no specific morphological characteristics for characterizing metastatic and benign nodes on yMRI.<sup>21</sup> In

addition, morphology may be difficult to assess due to the shrinkage of the lymph nodes after CRT. Note that DWI successfully detects lymph nodes, but it is insufficient to distinguish between benign and malignant tumors.<sup>26</sup> After CRT, node size in the short axis is more reliable than other criteria for assessing residual metastatic disease.<sup>8</sup> Staging the N-classification on yMRI was more challenging than T-staging, and the accuracy of N-staging was slightly lower than T-staging. The yMRI results showed moderate accuracy, sensitivity, and specificity in predicting the metastatic lymph nodes in our study. The overall accuracy of yMRI in predicting ypN was 63%, which is similar to Lee et al.<sup>19</sup> The NPV for nodal restaging was high (up to 75%) in our study, which is partly due to the high chance of sterilization of the remaining nodes after irradiation.<sup>27</sup> According to the literature, 25% of nodes are overstaged.<sup>21</sup> In the present study, the overstaging rate was 22.8% for ypN classification. Representative T2W images are shown in Figure 5. Despite technological advances in MRI, the accuracy of post-CRT lymph node characterization remains low.<sup>15</sup> We suggest that the reason for the reduced accuracy of yMRI is the lack of reliable criteria other than size for evaluating the irradiated lymph nodes after CRT.

An accurate assessment of the clinical response to neoadjuvant CRT is essential, as the non-surgical approach is now an option for selected patients with clinical complete response.<sup>28</sup> In selected patients with LARC, the “watch and wait” strategy is associated with good cancer control, along with lower morbidity and better quality of life than conventional treatment.<sup>29</sup> However, an in-depth analysis of this strategy is still needed, as

there are controversies that can be resolved by consensus among the specialists involved in treating these patients.

Histopathologic complete response rates reported in previous studies range from 15% to 38%.<sup>1,2,6,30,31</sup> In this study, ypCR was present in 15 (11%) of 136 patients, and the accuracy of MRI in predicting the complete response was 84%. In general, the diagnostic performance of MRI in detecting the complete response in our study is consistent with similar studies in the literature, although the accuracy of these studies varies between 50% and 90%.<sup>15,18</sup> Utilization of yMRI revealed high specificity and NPV and low sensitivity and PPV in the assessment of ypCR. Compared to T2W images, DWI can display smaller tumor sizes, but higher interobserver agreement can be achieved.<sup>32</sup> In our experience, the presence of diffusion restriction in post-CRT DWI is useful in demonstrating the presence of a residual tumor. The specificity and NPV of DWI in anticipating the complete response were high (92% and 90%, respectively) since the presence of a residual tumor can be demonstrated with a high b-value DWI. Potential explanations for the low sensitivity and PPV of restaging DWI in this study include the possibility of small residual tumor foci, even in the absence of diffusion restriction, and the low rate of ypCR (11%) in our patient population. The poor spatial resolution of DWI obtained using the 1.5 T MR scanner may have led to misinterpretations in estimating ypCR. Increased spatial resolution and higher SNR can be achieved with 3T MR systems. The misinterpretation of the T2 shine-through is a major pitfall for DWI.<sup>27</sup> ADC maps were inspected in each case to look for a corresponding area of low signal to

avoid this pitfall. T2 dark-through is another trap that is attributed to hypointensity that can sometimes be seen on the ADC maps in fibrotic areas.<sup>33</sup> The reason for this low signal is the high amount of collagen rather than the residual tumor (Figure 4). It is essential to evaluate the ADC maps with high b-value DW images, as fibrosis will be hypointense on DWI, while viable residual tumor will be hyperintense.

It is challenging to anticipate the histopathologic stage by evaluating only conventional MRI. Given the importance of a reliable diagnosis of complete response, new techniques are being studied, including dynamic contrast imaging,<sup>34</sup> magnetic transfer ratio,<sup>35</sup> and texture analyses.<sup>36-38</sup> Further, positron emission tomography and T1 mapping may help predict and evaluate tumor response to

CRT.<sup>39,40</sup> More accurate restaging can be performed with MRI by utilizing treatment-related changes in the tumor volume and metabolism.<sup>40</sup> However, these techniques are still not used in routine practice, as there is not enough evidence to prove their effectiveness.

Our study has several limitations. First, this is a retrospective, single-center study. Therefore, further studies, especially prospective and multicentric ones, are needed to evaluate the diagnostic performance of yMRI and define the most reliable parameters in predicting the ypT, ypN, and complete response after CRT. Second, some patients did not receive scopolamine butylbromide intravenously due to contraindications. In addition, our 1.5 T MR scanner is routinely scheduled for a software upgrade, which

might have improved the image quality over time. However, these changes did not affect or change the main protocol parameters. Additionally, poor spatial resolution of DWI was a potential challenge that may have caused misinterpretations in predicting ypCR.

In conclusion, yMRI revealed moderate accuracy in the T and N classifications, mainly due to underestimating the tumor stage and overestimating the nodal status. The yMRI results showed high specificity and PPV in predicting the tumor stage and high NPV in predicting the nodal stage; in addition, yMRI revealed high specificity and NPV but low sensitivity in predicting the complete response. Estimating the nodal stage and complete response using MRI after CRT remains a major challenge.

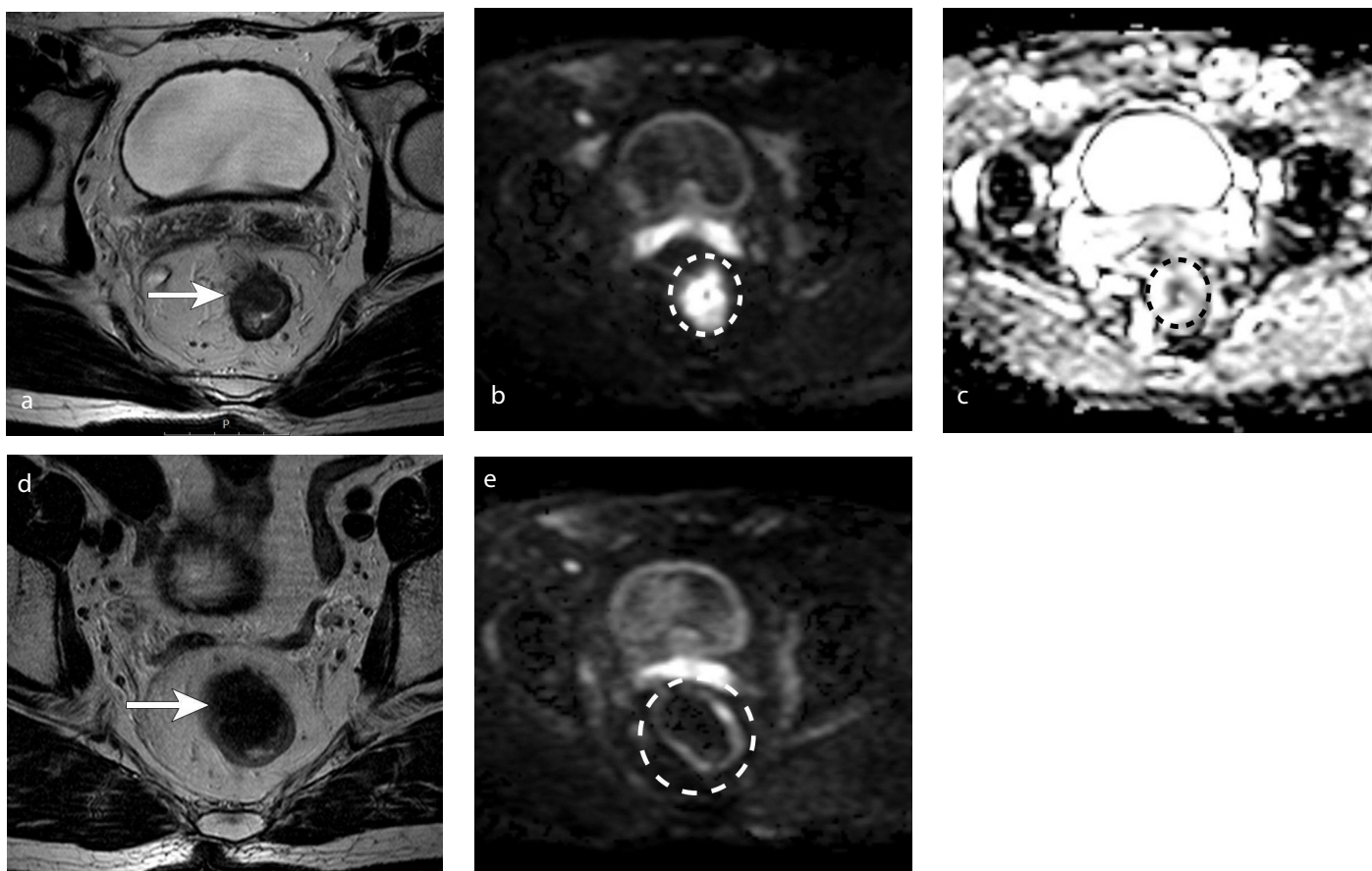


**Figure 3.** A 57-year-old man with rectal adenocarcinoma who underwent neoadjuvant chemoradiotherapy. (a-c) Baseline rectal magnetic resonance (MR) images. Axial T2-weighted (T2W) MR image (a) demonstrates a stage T3 tumor with intermediate signal (arrow). Axial diffusion-weighted (DW) image (b) and apparent diffusion coefficient (ADC) map (c) reveal restricted diffusion (dashed circles) in the tumor location. (d-e) Restaging MR images of the patient. The axial T2W MR image (d) reveals complete disappearance of the tumor signal with fibrotic low signal change. The axial DW image (e) shows no hyperintense signal in the former tumor location (dashed circle), and the patient was classified as complete response. The histopathologic staging was postoperative pathologic T classification 2.

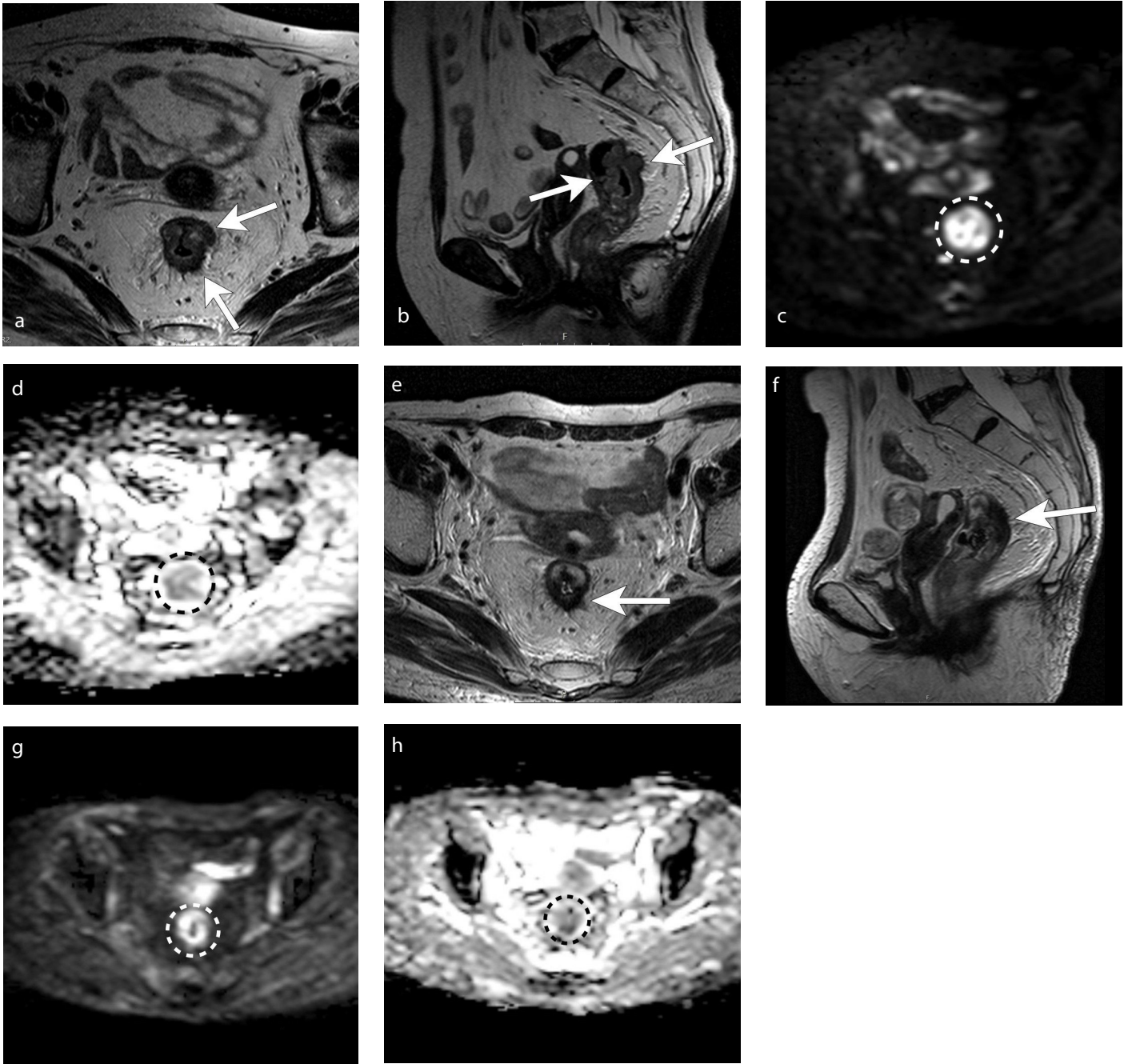


**Figure 4.** An 83-year-old woman with rectal adenocarcinoma. (a-d) Baseline rectal magnetic resonance (MR) images. T2-weighted (T2W) MR images in axial (a) and coronal planes (b) demonstrate the tumor infiltrating the mesorectal fat (arrows). Axial diffusion-weighted (DW) image (c) and apparent diffusion coefficient (ADC) map (d) demonstrate restricted diffusion (dashed circles). (e-h) Restaging MR images. The T2W MR images in the axial (e) and coronal planes (f) reveal that the tumor is smaller and confined to the muscularis propria (arrows). The axial DW image (g) and ADC map (h) reveal persistent restricted diffusion (dashed circles). The patient was classified as , MR imaging-based T classification 2 after chemoradiation, which is consistent with histopathology (postoperative pathologic T classification 2).

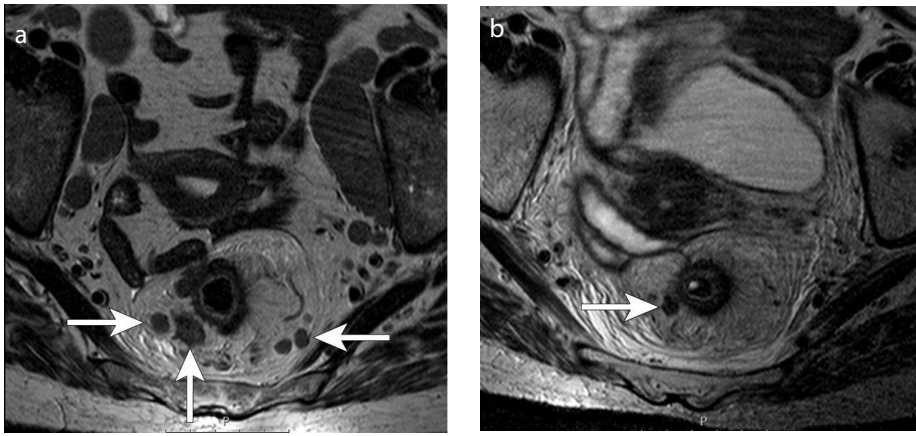


**Figure 5.** A 75-year-old female with locally advanced rectal cancer. (a) Baseline axial T2-weighted (T2W) magnetic resonance (MR) image (a) shows multiple metastatic mesorectal lymph nodes (arrows). Post-treatment axial T2W MR image (b) shows a lymph node with a short axis >5 mm (arrow), and the patient was classified as MRI-based N classification after chemoradiation +, and the histopathologic staging was post-operative pathologic N classification 0.

### Conflict of interest disclosure

The authors declared no conflicts of interest.

### References

- Maas M, Nelemans PJ, Valentini V, et al. Long-term outcome in patients with a pathological complete response after chemoradiation for rectal cancer: a pooled analysis of individual patient data. *Lancet Oncol.* 2010;11(9):835-844. [CrossRef]
- Garcia-Aguilar J, Marcet J, Coutsoftides T, et al. Impact of neoadjuvant chemotherapy following chemoradiation on tumor response, adverse events, and surgical complications in patients with advanced rectal cancer treated with TME. *J Clin Oncol.* 2011;29(15):3514. [CrossRef]
- Krdzalic J, Beets-Tan RGH, Engelen SME, et al. MRI predicts increased eligibility for sphincter preservation after CRT in low rectal cancer. *Radiother Oncol.* 2020;145:223-228. [CrossRef]
- Koh DM, Chau I, Tait D, Wotherspoon A, Cunningham D, Brown G. Evaluating mesorectal lymph nodes in rectal cancer before and after neoadjuvant chemoradiation using thin-section T2-weighted magnetic resonance imaging. *Int J Radiat Oncol Biol Phys.* 2008;71(2):456-461. [CrossRef]
- Habr-Gama A, Perez R, Proscurshim I, Gama-Rodrigues J. Complete clinical response after neoadjuvant chemoradiation for distal rectal cancer. *Surg Oncol Clin N Am.* 2010;19(4):829-845. [CrossRef]
- Nahas SC, Rizkallah Nahas CS, Sparapan Marques CF, et al. Pathologic complete response in rectal cancer: can we detect it? Lessons learned from a proposed randomized trial of watch-and-wait treatment of rectal cancer. *Dis Colon Rectum.* 2016;59(4):255-263. [CrossRef]
- Patel UB, Taylor F, Blomqvist L, et al. Magnetic resonance imaging-detected tumor response for locally advanced rectal cancer predicts survival outcomes: MERCURY experience. *J Clin Oncol.* 2011;29(28):3753-3760. [CrossRef]
- Horvat N, Rocha CCT, Oliveira BC, Petkovska I, Gollub MJ. MRI of rectal cancer: tumor staging, imaging techniques, and management. *Radiographics.* 2019;39(2):367-387. [CrossRef]
- Nerad E, Delli Pizzi A, Lambregts DMJ, et al. The apparent diffusion coefficient (ADC) is a useful biomarker in predicting metastatic colon cancer using the ADC-value of the primary tumor. *PLoS One.* 2019;14(2):e0211830. [CrossRef]
- Haak HE, Maas M, Lahaye MJ, et al. Selection of patients for organ preservation after chemoradiotherapy: MRI identifies poor responders who can go straight to surgery. *Ann Surg Oncol.* 2020;27:2732-2739. [CrossRef]
- Moreno CC, Sullivan PS, Kalb BT, et al. Magnetic resonance imaging of rectal cancer: staging and restaging evaluation. *Abdom Imaging.* 2015;40(7):2613-2629. [CrossRef]
- Delli Pizzi A, Caposiena D, Mastrodicasa D, et al. Tumor detectability and conspicuity comparison of standard b1000 and ultrahigh b2000 diffusion-weighted imaging in rectal cancer. *Abdom Radiol (NY).* 2019;44(11):3595-3605. [CrossRef]
- Van Heeswijk MM, Lambregts DMJ, Palm WM, et al. DWI for assessment of rectal cancer nodes after chemoradiotherapy: Is the absence of nodes at DWI proof of a negative nodal status? *AJR Am J Roentgenol.* 2017;208(3):W79-W84. [CrossRef]
- Iannicelli E, Di Pietropaolo M, Pillozzi E, et al. Value of diffusion-weighted MRI and apparent diffusion coefficient measurements for predicting the response of locally advanced rectal cancer to neoadjuvant chemoradiotherapy. *Abdom Radiol (NY).* 2016;41(10):1906-1917. [CrossRef]
- Van Der Paardt MP, Zagers MB, Beets-Tan RGH, Stoker J, Bipat S. Patients who undergo preoperative chemoradiotherapy for locally advanced rectal cancer restaged by using diagnostic MR imaging: a systematic review and meta-analysis. *Radiology.* 2013;269(1):101-112. [CrossRef]
- Lambregts DM, Vandecaveye V, Barbaro B, et al. Diffusion-weighted MRI for selection of complete responders after chemoradiation for locally advanced rectal cancer: A multicenter study. *Ann Surg Oncol.* 2011;18(8):2224-2231. [CrossRef]
- Barbaro B, Vitale R, Leccisotti L, et al. Restaging locally advanced rectal cancer with MR imaging after chemoradiation therapy. *Radiographics.* 2010;30(3):699-716. [CrossRef]
- Van Den Broek JJ, Van Der Wolf FSW, Lahaye MJ, et al. Accuracy of MRI in restaging locally advanced rectal cancer after preoperative chemoradiation. *Dis Colon Rectum.* 2017;60(3):274-283. [CrossRef]
- Lee JH, Jang HS, Kim JG, et al. Prediction of pathologic staging with magnetic resonance imaging after preoperative chemoradiotherapy in rectal cancer: pooled analysis of KROG 10-01 and 11-02. *Radiother Oncol.* 2014;113(1):18-23. [CrossRef]
- Kim DJ, Kim JH, Lim JS, et al. Restaging of rectal cancer with MR imaging after concurrent chemotherapy and radiation therapy. *Radiographics.* 2010;30(2):503-516. [CrossRef]
- Beets-Tan RGH, Lambregts DMJ, Maas M, et al. Magnetic resonance imaging for clinical management of rectal cancer: Updated recommendations from the 2016 European Society of Gastrointestinal and Abdominal Radiology (ESGAR) consensus meeting. *Eur Radiol.* 2018;28(4):1465-1475. Erratum in: *Eur Radiol.* 2018. [CrossRef]
- Kim SH, Lee JM, Hong SH, et al. Locally advanced rectal cancer: added value of diffusion-weighted MR imaging in the evaluation of tumor response to neoadjuvant chemo- and radiation therapy. *Radiology.* 2009;253(1):116-125. [CrossRef]
- Cianci R, Cristel G, Agostini A, et al. MRI for rectal cancer primary staging and restaging after neoadjuvant chemoradiation therapy: how to do it during daily clinical practice. *Eur J Radiol.* 2020;131:109238. [CrossRef]
- Lambregts DMJ, van Heeswijk MM, Delli Pizzi A, et al. Diffusion-weighted MRI to assess response to chemoradiotherapy in rectal cancer: main interpretation pitfalls and their use for teaching. *Eur Radiol.* 2017;27(10):4445-4454. [CrossRef]

25. Heijnen LA, Maas M, Beets-Tan RG, et al. Nodal staging in rectal cancer: why is restaging after chemoradiation more accurate than primary nodal staging? *Int J Colorectal Dis.* 2016;31(6):1157-1162. [\[CrossRef\]](#)
26. Heijnen LA, Lambregts DM, Mondal D, et al. Diffusion-weighted MR imaging in primary rectal cancer staging demonstrates but does not characterise lymph nodes. *Eur Radiol.* 2013;23(12):3354-3360. [\[CrossRef\]](#)
27. Maas M, Dijkhoff RAP, Beets-Tan R. Rectal cancer: assessing response to neoadjuvant therapy. *Magn Reson Imaging Clin N Am.* 2020;28(1):117-126. [\[CrossRef\]](#)
28. Smith JJ, Paty PB, Garcia-Aguilar J. Watch and wait in rectal cancer or more wait and see? *JAMA Surg.* 2020;155(7):657-658. [\[CrossRef\]](#)
29. López-Campos F, Martín-Martín M, Fornell-Pérez R, et al. Watch and wait approach in rectal cancer: current controversies and future directions. *World J Gastroenterol.* 2020;26(29):4218-4239. [\[CrossRef\]](#)
30. Habr-Gama A, Perez RO, Nadalin W, et al. Operative versus nonoperative treatment for stage 0 distal rectal cancer following chemoradiation therapy: long-term results. *Ann Surg.* 2004;240(4):711-717; discussion 717-718. [\[CrossRef\]](#)
31. Sclafani F, Brown G, Cunningham D, et al. Comparison between MRI and pathology in the assessment of tumour regression grade in rectal cancer. *Br J Cancer.* 2017;117(10):1478-1485. [\[CrossRef\]](#)
32. Rosa C, Caravatta L, Delli Pizzi A, et al. Reproducibility of rectal tumor volume delineation using diffusion-weighted MRI: Agreement on volumes between observers. *Cancer Radiother.* 2019;23(3):216-221. [\[CrossRef\]](#)
33. Lambregts DMJ, Boellaard TN, Beets-Tan RGH. Response evaluation after neoadjuvant treatment for rectal cancer using modern MR imaging: a pictorial review. *Insights Imaging.* 2019;10(1):15. [\[CrossRef\]](#)
34. Dijkhoff RAP, Beets-Tan RGH, Lambregts DMJ, Beets GL, Maas M. Value of DCE-MRI for staging and response evaluation in rectal cancer: a systematic review. *Eur J Radiol.* 2017;95:155-168. [\[CrossRef\]](#)
35. Martens MH, Lambregts DM, Papanikolaou N, et al. Magnetization transfer imaging to assess tumour response after chemoradiotherapy in rectal cancer. *Eur Radiol.* 2016;26(2):390-397. [\[CrossRef\]](#)
36. Delli Pizzi A, Chiarelli AM, Chiacchiaretta P, et al. MRI-based clinical-radiomics model predicts tumor response before treatment in locally advanced rectal cancer. *Sci Rep.* 2021;11(1):5379. [\[CrossRef\]](#)
37. Liu Z, Zhang XY, Shi YJ, et al. Radiomics analysis for evaluation of pathological complete response to neoadjuvant chemoradiotherapy in locally advanced rectal cancer. *Clin Cancer Res.* 2017;23(23):7253-7262. [\[CrossRef\]](#)
38. Horvat N, Veeraraghavan H, Khan M, et al. MR imaging of rectal cancer: Radiomics analysis to assess treatment response after neoadjuvant therapy. *Radiology.* 2018;287(3):833-843. [\[CrossRef\]](#)
39. Kremser C, Trieb T, Rudisch A, Judmaier W, de Vries A. Dynamic T(1) mapping predicts outcome of chemoradiation therapy in primary rectal carcinoma: sequence implementation and data analysis. *J Magn Reson Imaging.* 2007;26(3):662-671. [\[CrossRef\]](#)
40. Buijsen J, van den Bogaard J, van der Weide H, et al. FDG-PET-CT reduces the interobserver variability in rectal tumor delineation. *Radiother Oncol.* 2012;102(3):371-376. [\[CrossRef\]](#)



# pT1-2 gastric cancer with lymph node metastasis predicted by tumor morphologic features on contrast-enhanced computed tomography

Zhicong Wang   
 Qingyu Liu   
 Xiongjie Zhuang   
 Yan Yan   
 Qingqiang Guo   
 Junhong Lu   
 Qinchao Wu   
 Liqing Xie 

Zhicong Wang and Qingyu Liu contributed equally to this study.

From the Department of Radiology (Z.W., X.Z., Y.Y., Q.G., J.L.), The First Affiliated Hospital of Xiamen University, Xiamen, China; Department of Ultrasound (Q.L.), The First Affiliated Hospital of Xiamen University, Xiamen, China; Department of Pathology (Q.W.), The First Affiliated Hospital of Xiamen University, Xiamen, China; Department of Child Healthcare (L.X. ✉ 838937405@qq.com), Children's Hospital of Fudan University, Xiamen, China.

Received 07 October 2021; revision requested 05 November 2021; last revision received 05 May 2022; accepted 30 May 2022.



Epub: 28.12.2022

Publication date: 29.03.2023

DOI: 10.4274/dir.2021.21286

## PURPOSE

To investigate the value of tumor morphologic features of pT1-2 gastric cancer (GC) on contrast-enhanced computed tomography (CT) in assessing lymph node metastasis (LNM) with reference to histopathological results.

## METHODS

Eighty-six patients seen from October 2017 to April 2019 with pT1-2 GC proven by histopathology were included. Tumor volume and CT densities were measured in the plain scan and the portal-venous phase (PVP), and the percent enhancement was calculated. The correlations between tumor morphologic features and the N stages were analyzed. The diagnostic capability of tumor volume and enhancement features in predicting the LN status of pT1-2 GCs was further investigated using receiver operating characteristic (ROC) analysis.

## RESULTS

Tumor volume, CT density in the PVP, and tumor percent enhancement in the PVP correlated significantly with the N stage ( $\rho$ : 0.307, 0.558, and 0.586, respectively). Tumor volumes were significantly lower in the LNM- group than in the LNM+ group (14.4 mm<sup>3</sup> vs. 22.6 mm<sup>3</sup>,  $P = 0.004$ ). The differences between the LNM- and LNM+ groups in the CT density in the PVP and the percent enhancement in the PVP were also statistically significant (68.00 HU vs. 87.50 HU,  $P < 0.001$ ; and 103.06% vs. 179.19%,  $P < 0.001$ , respectively). The area under the ROC curves for identifying the LNM+ group was 0.69 for tumor volume and 0.88 for percent enhancement in the PVP, respectively. The percent enhancement in the PVP of 145.2% and tumor volume of 17.4 mL achieved good diagnostic performance in determining LNM+ (sensitivity: 71.4%, 82.1%; specificity: 91.4%, 58.6%; and accuracy: 84.9%, 66.3%, respectively).

## CONCLUSION

Tumor volume and percent enhancement in the PVP of pT1-2 GC could improve the diagnostic accuracy of LNM and would be helpful in image surveillance of these patients.

## KEYWORDS

Computed tomography, contrast enhancement, gastric cancer, lymph node metastasis, tumor volume

**G**astric cancer (GC) is the most common type of malignant tumor in Eastern Asia, the region with the highest incidence and mortality of GC.<sup>1,2</sup> The mortality rate for early gastric cancer (EGC) is still relatively high, and only approximately one-third of these patients survive for more than five years. The five-year survival rate for GC has increased significantly.<sup>3</sup> However, some patients present with metastasis, which is still concerning. Lymph node (LN) staging is based on the number of metastatic LNs and has been shown to help predict patient prognosis and guide treatment. The N stage is classified according to the number of lymph nodes metastatic (LNM) (N0, no metastatic regional lymph nodes; N1, 1–2 metastatic regional lymph nodes; N2, 3–6 metastatic regional lymph nodes; N3, >6 metastatic regional lymph nodes). EGCs in any location are seldom assumed to cause nodal metasta-

You may cite this article as: Wang Z, Liu Q, Zhuang X, et al. pT1-2 gastric cancer with lymph node metastasis predicted by tumor morphologic features on contrast-enhanced computed tomography. *Diagn Interv Radiol.* 2023;29(2):228-233.

ses. In the literature, however, LNM incidence ranges from 2% to 5% in EGCs confined to the mucosal layer, rising to 10% to 25% when the disease invades the submucosa.<sup>4,5</sup> The incidence of LNM in stage T2 GCs in the right gastroepiploic and para-aortic nodes is 10% and 26%, respectively,<sup>6</sup> which is still considerably high. In Asia, D2 dissection is a conventional surgical approach involving the resection of lymph nodes along the perigastric region, including the left gastric, splenic, celiac, and hepatic arteries. The National Comprehensive Cancer Network recommends D2 dissection as the preferred mode of treatment for these cancers.<sup>7</sup> However, for patients with stage pT1-2 GC, uniform application of this highly invasive surgery may result in overtreatment, increased morbidity and mortality, and a decreased quality of life postoperatively.<sup>8-10</sup>

This aggressive surgical method should be reserved only for patients with pT1-2 GC with a high risk of LNM. Alternatively, minimally invasive surgeries, such as endoscopic submucosal dissection and endoscopic mucosal resection, could be chosen in those patients with LN non-metastatic EGC.<sup>11</sup> Therefore, accurate preoperative diagnoses of LNM are essential in deciding treatment strategies and predicting the prognosis of patients with pT1-2 cancer.

Predicting LNM in pT1-2 GCs is still an arduous task. Fluorodeoxyglucose positron emission tomography (FDG-PET), endoscopic ultrasonography, and computed tomography (CT) are available methods for diagnosing LNM. However, FDG-PET is unreliable in predicting LNM due to its low sensitivity.<sup>12,13</sup> Endoscopic ultrasonography defines LN status depending on LN size, morphology, and echogenicity, but its accuracy is only 64% for predicting LN presence.<sup>14</sup> CT is another

anatomical imaging method to define metastasis in clinical practice, mainly based on LN size. Although CT, in combination with multiplanar reformation, can show the location and size of LNs, differentiating between hyperplastic, metastatic, and inflammatory LNs is still unreliable since it depends solely on LN size as a criterion.<sup>15,16</sup> Thus, other parameters are needed to improve the accuracy of CT for diagnosing LNM. Tumor volume and enhancement features can be used to identify LNM. Tumor size has been reported to correlate significantly with the likelihood of LNM in EGC;<sup>17,18</sup> however, tumor volume may be a better preoperative parameter than size. Size cannot be defined on axial images as GC always involves the gastric wall circumferentially. Tumor percent enhancement has also helped determine LN status in rectal cancer.<sup>19</sup> In light of these considerations, this study aims to investigate the diagnostic value of CT tumor volume and enhancement in predicting LNM in stage pT1-2 GC.

## Methods

### Patients

Our institutional review board approved this retrospective study and waived the requirement for informed consent (approval ID: KY027-01). This study enrolled consecutive patients from October 2017 to April 2019 with pathologically proven stage T1-2 GC confined to the mucosa or submucosa and the muscularis propria. The inclusion criteria were as follows: (1) patients with histopathological confirmation of T1-2 GC, regardless of N and M stage; (2) those who underwent multislice CT scanning before surgery; (3) those who had no radiotherapy or chemotherapy before surgery; and (4) those who underwent surgical resection with extensive LN excision. For further confirmation of LNM, surgically excised LNs were fixed and stained with hematoxylin and eosin. LNM was defined as the presence of tumor cells or tissue in LNs at magnifications of 10× and 40×. Eleven patients were excluded because the filling state of the stomach was unsatisfactory or they lacked a contrast-enhanced CT. Finally, a total of 86 patients were enrolled, including 28 patients with LNM+ and 58 patients without LNM– (Figure 1).

### Computed tomography acquisition

All patients underwent CT with multislice equipment (Siemens Somatom Sensation 64), with a tube voltage of 120 kV, a tube current of 200 mAs, a collimator width of 16 × 0.75 mm, a screw pitch of 0.750, a slice

thickness of 5 mm, and a slice interval of 5 mm. Each patient who completed breathing exercises was requested to fast for at least eight hours and received 800 mL of water orally and an intramuscular injection of 10 mg of anisodamine to achieve gastric distension approximately 20 minutes before the examination. The CT scan covered the upper or entire abdomen. The iodinated contrast material was administered at a dose of 1.5 to 2.0 mL/kg (Omnipaque 350 mg I/mL) and an injection flow rate of 3.0 mL/s using a high-pressure syringe. Images were obtained in the arterial phase (30 s) and portal-venous phase (80 s) after initiation of contrast material injection.

### Tumor analyses

The CT images of the PVP were sent to the workstation, and the GC lesions were determined by two radiologists (with at least eight years of experience in abdominal imaging) who were blind to the clinicopathological stage. They analyzed the images together to determine the outline of the tumor. Disagreement was resolved by discussion, and a consensus was reached, ensuring the accuracy of the tumor volume measurement. The tumors were manually drawn by tracing the lesion edge (Figure 2). Focal thickening of the gastric wall by 6 mm or greater with noticeable enhancement was included in the region of interest (ROI) if it was difficult to differentiate tumor tissue from the adjacent normal gastric wall;<sup>20,21</sup> the gastric lumen and artifacts were excluded. The radiologists then calculated the tumor volume by multiplying the area of each ROI by the slice thickness (5 mm). Percent enhancement in the PVP was calculated according to the following equation:  $(\text{Val-p} - \text{Val-0})/\text{Val-0} \times 100\%$ , where Val-0 and Val-p represented the CT density in Hounsfield units (HU) of the ROI of the lesion on the largest slice before contrast enhancement and in the PVP, respectively.

### Statistical analysis

Spearman's rank correlation test was applied to analyze the correlation between tumor morphologic features and different N stages (0.00–0.20, poor; 0.21–0.40, fair; 0.41–0.60, moderate; 0.61–0.80, good; and 0.81–1.00, excellent). The differences between tumor volume, CT density in the PVP, and tumor percent enhancement in the PVP of different N stage groups (LNM+ vs. LNM–) were compared using the Mann-Whitney U test. The diagnostic efficacy of significant features predicting LNM in T1-2 GC was evaluated using receiver operating characteristic

### Main points

- Accurate prediction of lymph node metastasis (LNM) of pT1-2 gastric cancer (GC) through imaging is crucial in deciding treatment strategies.
- The pathologic N stage of pT1-2 GC significantly correlated with computed tomography (CT) tumor volume, density, and tumor percent enhancement.
- CT tumor volumetry and enhancement features of pT1-2 GC provided useful adjunct information for predicting LNM.
- Percent enhancement of portal-venous phase achieved better diagnostic performance than tumor volume in determining LNM.

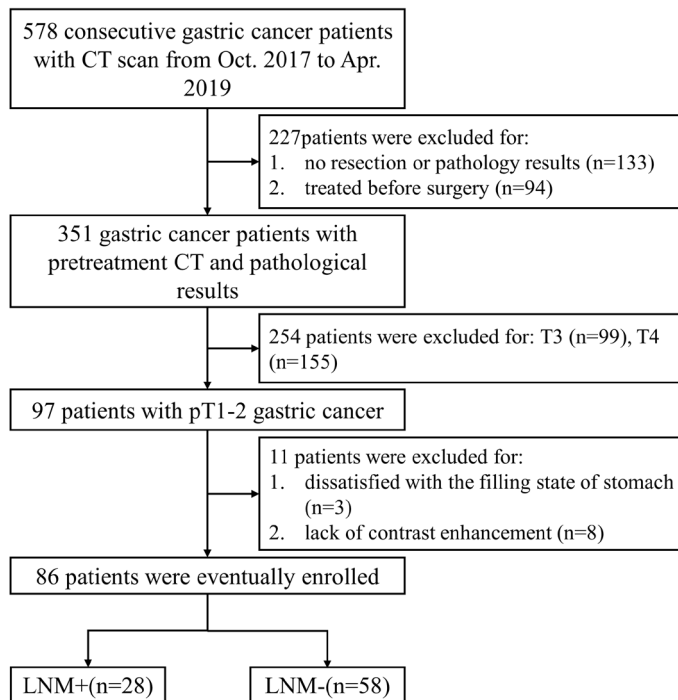


**Figure 2.** Shows the computed tomography (CT) images of a 56-year-old man with poorly differentiated adenocarcinoma and signet ring cell carcinoma, the lesion infiltrating the submucosa. The CT image of the portal-venous phase shows a thickened wall with heterogeneous enhancement in the stomach. The region of interest was manually drawn along the margin of the lesion (white line).

percent enhancement in the PVP were also statistically significant ( $P < 0.001$ ). However, there was no statistically significant difference between pre-contrast CT density and nodal involvement ( $P = 0.40$ ). Table 3 shows the tumor volume, CT density, and percent enhancement in the PVP in the LNM+ and LNM- groups.

#### Receiver operating characteristic analysis

The diagnostic efficacy of tumor volume, CT density in the PVP, and percent enhancement in the PVP for differentiating between the LNM+ and LNM- groups were further evaluated using ROC analysis. The area under the ROC curve (AUC) for determining LNM+ in stage T1-2 GC was highest for the percent enhancement in the PVP (AUC= 0.883,  $P = 0.001$ ), followed by CT density in the PVP (AUC= 0.865,  $P < 0.001$ ) and tumor volume (AUC= 0.693,  $P < 0.001$ ) (Figure 3). The percent enhancement in the PVP of 145.2% achieved good diagnostic performance in determining LNM+ (sensitivity: 71.43%, specificity: 91.38%, and accuracy: 84.88%). The CT density of 76 HU in the PVP predicted LNM+ with 89.29% sensitivity and 75.86% specificity, while a tumor volume of 17.35 mm<sup>3</sup> predicted LNM+ with 82.14% sensitivity and 58.62% specificity. Table 4 shows the

**Figure 1.** Patient selection flowchart. CT, computed tomography, LNM, lymph node metastasis.

(ROC) analysis. A value of  $P < 0.05$  was considered statistically significant. All statistical analyses were performed using MedCalc version 15.2.2 (MedCalc Software, Mariakerke, Belgium).

## Results

### Patient characteristics

The study group comprised 86 patients ranging in age from 27–80 years (median age, 59 years); 56 of the 86 patients were men (median age, 61 years), and 30 were women (median age, 56 years). Regarding the T stage, 57 patients (57/86, 66.3%) were T1, and 29 patients (29/86, 33.7%) were T2; and regarding the N stage, 58 patients (58/86, 67.4%) were N0, 12 patients (12/86, 14.0%) were N1, seven patients (7/86, 8.1%) were N2, and nine patients (9/86, 10.5%) were N3. Regarding the number of lymph nodes available for histopathological examination in resection specimens, 15 patients had 15–20 lymph nodes (15/86, 17.4%), 50 patients had 21–40 lymph nodes (50/86, 58.1%), and 21 patients had 41–63 lymph nodes (21/86, 24.4%) (Table 1).

### Relationship between morphologic features and N stage

Tumor volume, CT density in the PVP, and percent enhancement in the PVP correlated significantly with the pathologic N stage. The correlation factor ( $\rho$ ) was highest for

the percent enhancement in the PVP ( $\rho = 0.586$ ,  $P < 0.001$ ), followed by CT density in the PVP ( $\rho = 0.558$ ,  $P < 0.001$ ) and tumor volume ( $\rho = 0.307$ ,  $P = 0.004$ ). However, CT density on non-contrast images did not correlate with the N stage ( $\rho = -0.076$ ,  $P = 0.49$ ) (Table 2).

### Lymph node metastasis plus versus lymph node metastasis minus groups

The LNM+ group had twenty-eight patients (28/86, 32.6%) with stage N1, N2, or N3 disease, while the LNM- group had 58 patients (58/86, 67.4%) with stage N0 disease. The median tumor volumes in the LNM+ and LNM- groups were 22.6 mm<sup>3</sup> and 14.4 mm<sup>3</sup>, respectively. Tumor volume was significantly less in the LNM- group than in the LNM+ group ( $P = 0.004$ ). The median percent enhancement in the PVP in the LNM+ and LNM- groups was 179.19% and 103.06%, respectively. Differences between the two groups in CT density in the PVP and

**Table 1.** Clinicopathological characteristics of patients

	LNM-	LNM+			Total
		N1	N2	N3	
Patient, n (%)	58 (67.4%)	12 (14.0%)	7 (8.1%)	9 (10.5%)	86 (100%)
Age, y*	59 ± 11	62 ± 6	60 ± 9	56 ± 13	59 ± 10
Male/female, n	37/21	8/4	7/0	4/5	56/30
T1/T2, n	44/14	5/7	4/3	4/5	57/29

\*Data are presented as mean ± SD. SD, standard deviation; LNM+, lymph node metastasis present; LNM-, no lymph node metastasis.

**Table 2.** Median values and correlation between morphologic features and N stage

	N stage				Rho (95% CI)	P
	N0	N1	N2	N3		
<b>Tumor volume median mm<sup>3</sup></b>	14.4	22.4	24.7	22.8	0.307	0.004
Range	(1.9–63.0)	(10.7–102.2)	(7.6–65.0)	(12.8–94.6)	(0.102–0.487)	
<b>CT density on non-contrast images: median</b>	34.0	31.5	31.0	34.0	-0.076	0.49
Range (HU)	(15.0–56.0)	(25.0–43.0)	(24.0–39.0)	(22.0–42.0)	(-0.283–0.139)	
<b>CT density in PVP: median</b>	68.0	95.0	90.0	81.0	0.558	< 0.001
Range (HU)	(23.0–97.0)	(65.0–120.0)	(78.0–105.0)	(71.0–149.0)	(0.393–0.689)	
<b>Percent enhancement %</b>	103.1	202.9	190.3	150.0	0.586	< 0.001
Median (range)	(14.3–304.3)	(116.7–314.3)	(135.9–258.3)	(91.9–304.5)	(0.427–0.710)	

Rho, correlation coefficient; CI, confidence interval; PVP, portal-venous phase; HU, Hounsfield units.

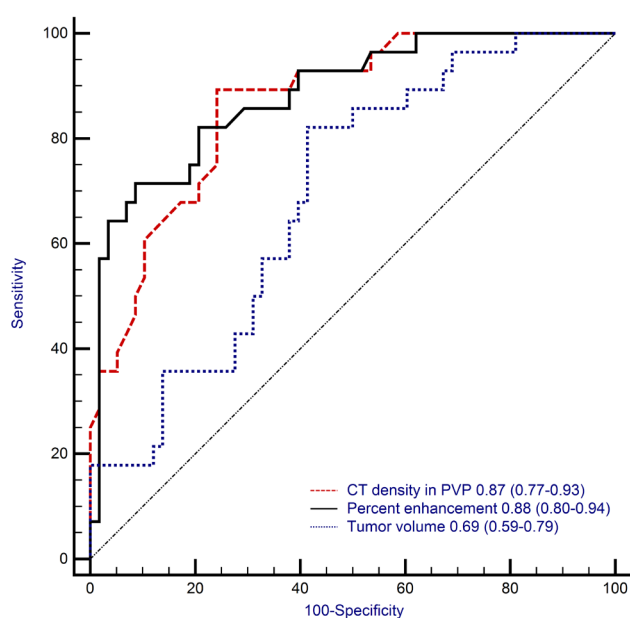


**Figure 3.** Shows the receiver operating characteristic (ROC) curves of tumor volume, computed tomography density in the portal venous phase, and percent enhancement for identification of lymph node metastases in pT1-2 gastric cancers. The area under the curve and 95% confidence interval are shown in the lower right corner of the figure. PVP, portal-venous phase; CT, computed tomography.

**Table 3.** Median values and interquartile ranges between the LNM+ and LNM– groups

	LNM+ (n = 28)	LNM– (n = 58)	Z	P
<b>Tumor volume in mm<sup>3</sup></b>	22.6	14.4	2.894	0.004
Interquartile range	18.3–38.6	8.8–26.2		
<b>CT density on non-contrast images in HU</b>	33.0	34.0	0.844	0.40
Interquartile range	29.0–37.0	30.0–37.0		
<b>CT density in the PVP in HU</b>	87.5	68.0	5.461	< 0.001
Interquartile range	79.5–101.0	59.0–76.0		
<b>Percent enhancement %</b>	179.2	103.1	5.737	< 0.001
Interquartile range	134.1–232.3	83.3–123.5	-	-

LNM+, lymph node metastasis; LNM–, lymph node non-metastasis; PVP, portal-venous phase; HU, Hounsfield units.

sensitivities, specificities, negative and positive predictive values, and accuracy.

## Discussion

Individualized treatment is set to become the cornerstone for more effective cancer therapy. Patients with early-stage GC are frequently overtreated because of a lack of available detection methods that are robust and accurate in identifying LN metastasis before surgery. Our study indicated that tumor volume, CT density in the PVP, and percent enhancement in the PVP significantly correlated with the pathologic N stage in pT1-2 GC. These variables were useful for accurate preoperative diagnosis of LN metastasis and may improve the prognosis of patients with GC.

Previously published studies have shown that tumor volume measured using CT was reproducible and valuable as an additional parameter for TNM staging in GC.<sup>22,23</sup> They showed that tumor volume significantly correlated with the N stage in GC with an AUC of 0.75 for stage  $\geq$  N1. Our study also showed similar results. Our study found that gastric tumors with larger volumes are related to an increased likelihood of invasion and LNM, i.e., higher T and N stages.

Various studies have reported that tumor percent enhancement could help in evaluating the prognosis of hepatocellular carcinoma,<sup>24</sup> distinguishing the histological type of GC,<sup>25</sup> predicting synchronous and metachronous hepatic metastasis in GC,<sup>26</sup> and determining LNM of rectal cancer.<sup>19,27</sup> These studies revealed that enhancement features of tumors play an essential role in assessing tumor prognosis and clinical stage. Our study also showed that tumor CT den-

**Table 4.** Diagnostic performance of whole tumor volume and enhancement features in predicting lymph node metastasis in pT1-2 stage gastric cancers by receiver operating characteristic curve analyses

	AUC (95% CI)	Cut-off values	Sensitivity (%)	Specificity (%)	PPV (%)	NPV (%)	Accuracy (%)
<b>Tumor volume</b>	0.69 (0.59–0.79)	17.4 mm <sup>3</sup>	82.1 (23/28)	58.6 (34/58)	48.9 (23/47)	87.2 (34/39)	66.3 (57/86)
<b>CT density in the PVP</b>	0.87 (0.77–0.93)	76 HU	89.3 (25/28)	75.9 (44/58)	64.1 (25/39)	93.6 (44/47)	80.2 (69/86)
<b>Percent enhancement</b>	0.88 (0.80–0.94)	145.2%	71.4 (20/28)	91.4 (53/58)	80.0 (20/25)	86.9 (53/61)	84.9 (73/86)

AUC, area under the curve; CI, confidence interval; PPV, positive predictive value; NPV, negative predictive value; PVP, portal-venous phase; CT, computed tomography.

sity in the PVP and percent enhancement in the PVP could help assess LNMs in pT1-2 GC by obtaining appropriate cut-off values. The growth of solid tumors depends heavily on surrounding angiogenesis, which accelerates tumor growth and increases the likelihood of tumor metastasis. Moreover, in the progression of malignant tumors, increased leakage of arteriovenous shunts and neo-vascularization often occur, leading to early enhancement of tumors on CT/magnetic resonance imaging (MRI). In addition, compared with normal vessels, the endothelial cells of tumor capillaries have a wider gap, and the basement membrane is discontinuous, making it easier for tumor cells to penetrate.<sup>28</sup> Our research also indicated that tumors with higher percent enhancement were more likely to metastasize to LNMs, which might attract the attention of radiologists and gastric surgeons. Notably, CT density in the PVP and percent enhancement in N1 was higher than in N2 and N3. We speculated that once tumor cells have metastasized to sentinel lymph nodes, the increase in metastatic LNMs no longer depends on the tumor itself but on metastasis from one LN to another.

In clinical practice, the abnormalities of LNMs on CT/MRI are generally evaluated using the Response Evaluation Criteria in Solid Tumors, which has adopted the short-axis diameter (SAD) of LNMs as a criterion.<sup>29</sup> However, the definition of LNM varies, and different cut-off values have been used in various studies.<sup>30-34</sup> Ahn et al.<sup>34</sup> determined LNM as an SAD  $\geq 8$  mm, while Tokunaga et al.<sup>31</sup> suggested an SAD cut-off of  $\geq 15$  mm. Saito et al.<sup>35</sup> showed that the accuracy of individual SAD cut-off values in diagnosing LNM was 71.1% based on pathological type. More recently, however, Kim and Kim<sup>16</sup> reported that the largest LN was the metastatic LN in only a small percentage of patients with EGC. In other words, the largest diameter LN may only be an inflamed lymph node. Relying solely on the size of the LN to diagnose metastatic LN would lead to a lack of optimal disease treatment. Long and short diameter values were also used to assess LNM; nevertheless, there is still no defined size stan-

dard.<sup>36</sup> In addition to size, other CT features of the LN can also be used to evaluate the nodal status, such as morphology (long/short diameter ratio  $<1.5$ ), uneven enhancement, and clustered nodes.<sup>33,34,37</sup>

In this study, we only enrolled pT1-2 patients because the lymph nodal status of these patients is crucial in deciding treatment strategies. To the best of our knowledge, there are currently no defined reliable criteria for nodal involvement based on CT features. To obtain multiple additional quantifiable indicators, we combined the morphologic parameters of gastric tumors to determine the LNM status - an innovative aspect of our research.

This study has several limitations. First, it was based in a single center, had a relatively small sample size (especially when considering patients with LNM), and had an inevitable selection bias. Second, the reproducibility of data measurement between reviewers was not evaluated. Finally, manual measurement of gastric tumor volume might be subjective. With the development of artificial intelligence, graphics-processing capabilities have become more powerful. We believe that an automatized tool will take the place of manual tracing and be a better option to circumvent this limitation. Tumor volume could then be more readily and precisely assessed.

In conclusion, we have established that tumor volume, CT density in the PVP, and percent enhancement in the PVP, could be used to determine LNMs in pT1-2 GC, with percent enhancement in the PVP achieving better diagnostic performance than tumor volume. Identifying an appropriate cut-off value for percent enhancement and tumor volume can improve the diagnostic accuracy for LNM.

#### Acknowledgements

We would like to extend our sincere gratitude to our friends who have put considerable time and effort into their comments on the draft. We are deeply grateful of their help in the completion of this paper. Specially, we are indebted to Shengxiang Rao for his

continuous support and encouragement. We would like to thank Editage (www.editage.cn) for English language editing.

#### Conflict of interest disclosure

The authors declared no conflicts of interest.

#### References

1. Global Burden of Disease Cancer Collaboration, Fitzmaurice C, Dicker D, et al. The Global Burden of Cancer 2013. *JAMA Oncol.* 2015;1(4):505-527. [CrossRef]
2. Sugano K. Screening of gastric cancer in Asia. *Best Pract Res Clin Gastroenterol.* 2015;29(6):895-905. [CrossRef]
3. Khan U, Shah MA. Optimizing therapies in the perioperative management of gastric cancer. *Curr Treat Options Oncol.* 2019;20(7):57. [CrossRef]
4. Lee KS, Oh DK, Han MA, et al. Gastric cancer screening in Korea: report on the national cancer screening program in 2008. *Cancer Res Treat.* 2011;43(2):83-88. [CrossRef]
5. Kwee RM, Kwee TC. Predicting lymph node status in early gastric cancer. *Gastric Cancer.* 2008;11(3):134-148. [CrossRef]
6. Di Leo A, Marrelli D, Roviello F, et al. Lymph node involvement in gastric cancer for different tumor sites and T stage: Italian Research Group for Gastric Cancer (IRGGC) experience. *J Gastrointest Surg.* 2007;11(9):1146-1153. [CrossRef]
7. Ajani JA, D'Amico TA, Almhanna K, et al. Gastric Cancer, version 3.2016, NCCN Clinical Practice Guidelines in Oncology. *J Natl Compr Canc Netw.* 2016;14(10):1286-1312. [CrossRef]
8. Bonenkamp JJ, Hermans J, Sasako M, et al. Extended lymph-node dissection for gastric cancer. *N Engl J Med.* 1999;340(12):908-914. [CrossRef]
9. Brennan MF. Current status of surgery for gastric cancer: a review. *Gastric Cancer.* 2005;8(2):64-70. [CrossRef]
10. Mocellin S, McCulloch P, Kazi H, Gama-Rodrigues JJ, Yuan Y, Nitti D. Extent of lymph node dissection for adenocarcinoma of the stomach. *Cochrane Database Syst Rev.* 2015;(8):CD001964. [CrossRef]
11. Soetikno R, Kaltenbach T, Yeh R, Gotoda T. Endoscopic mucosal resection for early cancers of the upper gastrointestinal tract. *J*

- Clin Oncol.* 2005;23(20):4490-4498. [\[CrossRef\]](#)
12. Mukai K, Ishida Y, Okajima K, Isozaki H, Morimoto T, Nishiyama S. Usefulness of preoperative FDG-PET for detection of gastric cancer. *Gastric Cancer.* 2006;9(3):192-196. [\[CrossRef\]](#)
  13. Dassen AE, Lips DJ, Hoekstra CJ, Pruijt JF, Bosscha K. FDG-PET has no definite role in preoperative imaging in gastric cancer. *Eur J Surg Oncol.* 2009;35(5):449-455. [\[CrossRef\]](#)
  14. Cardoso R, Coburn N, Seevaratnam R, et al. A systematic review and meta-analysis of the utility of EUS for preoperative staging for gastric cancer. *Gastric Cancer.* 2012;15(Suppl 1):19-26. [\[CrossRef\]](#)
  15. Nakamura K, Morisaki T, Noshiro H, Torata N, Kinukawa N, Tanaka M. Morphometric analysis of regional lymph nodes with and without metastasis from early gastric carcinoma. *Cancer.* 2000;88(11):2438-2442. [\[CrossRef\]](#)
  16. Kim DJ, Kim W. Is lymph node size a reliable factor for estimating lymph node metastasis in early gastric cancer. *J Gastric Cancer.* 2018;18(1):20-29. [\[CrossRef\]](#)
  17. An JY, Baik YH, Choi MG, Noh JH, Sohn TS, Kim S. Predictive factors for lymph node metastasis in early gastric cancer with submucosal invasion: analysis of a single institutional experience. *Ann Surg.* 2007;246(5):749-753. [\[CrossRef\]](#)
  18. Park DJ, Lee HK, Lee HJ, et al. Lymph node metastasis in early gastric cancer with submucosal invasion: feasibility of minimally invasive surgery. *World J Gastroenterol.* 2004;10(24):3549-3552. [\[CrossRef\]](#)
  19. Tang Y, Rao S, Yang C, Hu Y, Sheng R, Zeng M. Value of MRI morphologic features with pT1-2 rectal cancer in determining lymph node metastasis. *J Surg Oncol.* 2018;118(3):544-550. [\[CrossRef\]](#)
  20. Kim HJ, Kim AY, Oh ST, et al. Gastric cancer staging at multi-detector row CT gastrography: comparison of transverse and volumetric CT scanning. *Radiology.* 2005;236(3):879-885. [\[CrossRef\]](#)
  21. Kawanami S, Komori M, Tsurumaru D, Matsuura S, Nishie A, Honda H. Description of early gastric cancer with wall-carving technique on multidetector computed tomography. *Jpn J Radiol.* 2011;29(1):76-82. [\[CrossRef\]](#)
  22. Hallinan JT, Venkatesh SK, Peter L, Makmur A, Yong WP, So JB. CT volumetry for gastric carcinoma: association with TNM stage. *Eur Radiol.* 2014;24(12):3105-3114. [\[CrossRef\]](#)
  23. Wang ZC, Wang C, Ding Y, Ji Y, Zeng MS, Rao SX. CT volumetry can potentially predict the local stage for gastric cancer after chemotherapy. *Diagn Interv Radiol.* 2017;23(4):257-262. [\[CrossRef\]](#)
  24. Hu XX, Yang ZX, Liang HY, et al. Whole-tumor MRI histogram analyses of hepatocellular carcinoma: correlations with Ki-67 labeling index. *J Magn Reson Imaging.* 2017;46(2):383-392. [\[CrossRef\]](#)
  25. Tsurumaru D, Miyasaka M, Muraki T, et al. Histopathologic diversity of gastric cancers: relationship between enhancement pattern on dynamic contrast-enhanced CT and histological type. *Eur J Radiol.* 2017;97:90-95. [\[CrossRef\]](#)
  26. Tsurumaru D, Nishimuta Y, Muraki T, et al. Gastric cancer with synchronous and metachronous hepatic metastasis predicted by enhancement pattern on multiphasic contrast-enhanced CT. *Eur J Radiol.* 2018;108:165-171. [\[CrossRef\]](#)
  27. Alberda WJ, Dassen HP, Dwarkasing RS, et al. Prediction of tumor stage and lymph node involvement with dynamic contrast-enhanced MRI after chemoradiotherapy for locally advanced rectal cancer. *Int J Colorectal Dis.* 2013;28(4):573-580. [\[CrossRef\]](#)
  28. Zhang H, Pan Z, Du L, et al. Advanced gastric cancer and perfusion imaging using a multidetector row computed tomography: correlation with prognostic determinants. *Korean J Radiol.* 2008;9(2):119-127. [\[CrossRef\]](#)
  29. Eisenhauer EA, Therasse P, Bogaerts J, et al. New response evaluation criteria in solid tumours: revised RECIST guideline (version 1.1). *Eur J Cancer.* 2009;45(2):228-247. [\[CrossRef\]](#)
  30. Yan C, Zhu ZG, Yan M, et al. Size of the largest lymph node visualized on multi-detector-row computed tomography (MDCT) is useful in predicting metastatic lymph node status of gastric cancer. *J Int Med Res.* 2010;38(1):22-33. [\[CrossRef\]](#)
  31. Tokunaga M, Sugisawa N, Tanizawa Y, Bando E, Kawamura T, Terashima M. The impact of preoperative lymph node size on long-term outcome following curative gastrectomy for gastric cancer. *Ann Surg Oncol.* 2013;20(5):1598-1603. [\[CrossRef\]](#)
  32. Kim HJ, Kim AY, Oh ST, et al. Gastric cancer staging at multi-detector row CT gastrography: comparison of transverse and volumetric CT scanning. *Radiology.* 2005;236(3):879-885. [\[CrossRef\]](#)
  33. Chen CY, Hsu JS, Wu DC, et al. Gastric cancer: preoperative local staging with 3D multi-detector row CT--correlation with surgical and histopathologic results. *Radiology.* 2007;242(2):472-482. [\[CrossRef\]](#)
  34. Ahn HS, Lee HJ, Yoo MW, et al. Diagnostic accuracy of T and N stages with endoscopy, stomach protocol CT, and endoscopic ultrasonography in early gastric cancer. *J Surg Oncol.* 2009;99(1):20-27. [\[CrossRef\]](#)
  35. Saito T, Kurokawa Y, Takiguchi S, et al. Accuracy of multidetector-row CT in diagnosing lymph node metastasis in patients with gastric cancer. *Eur Radiol.* 2015; 25(2):368-374. [\[CrossRef\]](#)
  36. Lee SL, Lee HH, Ku YM, Jeon HM. Usefulness of two-dimensional values measured using preoperative multidetector computed tomography in predicting lymph node metastasis of gastric cancer. *Ann Surg Oncol.* 2015;22(Suppl 3):786-793. [\[CrossRef\]](#)
  37. Kim YN, Choi D, Kim SH, et al. Gastric cancer staging at isotropic MDCT including coronal and sagittal MPR images: endoscopically diagnosed early vs. advanced gastric cancer. *Abdom Imaging.* 2009;34(1):26-34. [\[CrossRef\]](#)



# Machine learning analysis of adrenal lesions: preliminary study evaluating texture analysis in the differentiation of adrenal lesions

Canan Altay   
Işıl Başara Akın   
Abdullah Hakan Özgül   
Süleyman Cem Adıyaman   
Abdullah Serkan Yener   
Mustafa Seçil 

## PURPOSE

This study aimed to determine the accuracy of texture analysis in differentiating adrenal lesions on unenhanced computed tomography (CT) images.

## METHODS

In this single-center retrospective study, 166 adrenal lesions in 140 patients (64 women, 76 men; mean age  $56.58 \pm 13.65$  years) were evaluated between January 2015 and December 2019. The lesions consisted of 54 lipid-rich adrenal adenomas, 37 lipid-poor adrenal adenomas (LPAs), 56 adrenal metastases (ADM), and 19 adrenal pheochromocytomas (APhs). Each adrenal lesion was segmented by manually contouring the borders of the lesion on unenhanced CT images. A texture analysis of the CT images was performed using Local Image Feature Extraction software. First-order and second-order texture parameters were assessed, and 45 features were extracted from each lesion. One-Way analysis of variance with Bonferroni correction and the Mann-Whitney U test was performed to determine the relationships between the texture features and adrenal lesions. Receiver operating characteristic curves were performed for lesion discrimination based on the texture features. Logistic regression analysis was used to generate logistic models, including only the texture parameters with a high-class separation capacity (i.e.,  $P < 0.050$ ). SPSS software was used for all statistical analyses.

## RESULTS

First-order and second-order texture parameters were identified as significant factors capable of differentiating among the four lesion types ( $P < 0.050$ ). The logistic models were evaluated to ascertain the relationships between LPA and ADM, LPA and APh, and ADM and APh. The sensitivity, specificity, positive predictive value (PPV), negative predictive value (NPV), and accuracy of the first model (LPA vs. ADM) were 85.7%, 70.3%, 81.3%, 76.4%, and 79.5%, respectively. The sensitivity, specificity, PPV, NPV, and accuracy of the second model (LPA vs. APh) were all 100%. The sensitivity, specificity, PPV, NPV, and accuracy of the third model (ADM vs. APh) were 87.5%, 82%, 36.8%, 98.2%, and 82.7%, respectively.

## CONCLUSION

Texture features may help in the characterization of adrenal lesions on unenhanced CT images.

## KEYWORDS

Adrenal adenoma, adrenal glands, adrenal mass, computed tomography, texture analysis

From the Department of Radiology (C.A. ✉ drcananaltay@gmail.com, I.B.A., A.H.Ö., M.S.), Dokuz Eylül University Faculty of Medicine, Izmir, Turkey; Department of Endocrinology (S.C.A., A.S.Y.), Dokuz Eylül University Faculty of Medicine, Izmir, Turkey.

Received; 04 April 2021, revision requested; 02 May 2021, last revision received; 05 December 2021, accepted 10 January 2022.



Epub: 06.02.2023

Publication date: 29.03.2023

DOI: 10.5152/dir.2022.21266

Incidental adrenal masses are common lesions, with a rate of detection of 4%–6% using abdominal computed tomography (CT) in patients undergoing abdominal imaging.<sup>1</sup> Adrenal adenomas are the most common adrenal lesions, with a prevalence up to 9% in the general population.<sup>2</sup> The rate of adrenal adenomas increases with age.<sup>3</sup> Nearly 25% of adrenal adenomas have insufficient intracytoplasmic lipid content for accurate detection using conventional CT, rendering these lesions difficult to differentiate from malignant adrenal lesions and

You may cite this article as: Altay C, Başara Akın I, Özgül AH, Adıyaman SC, Yener AS, Seçil M. Machine learning analysis of adrenal lesions: preliminary study evaluating texture analysis in the differentiation of adrenal lesions. *Diagn Interv Radiol.* 2023;29(2):234-243.

adrenal pheochromocytomas (APhs).<sup>3</sup> This can ultimately lead to unnecessary surgical resection of these benign adrenal lesions. Clinical findings and radiological features in unenhanced CT images have a limited ability to differentiate lipid-poor adrenal adenomas (LPAs) from malignant adrenal lesions and APhs because they are in the same density spectrum range. CT washout imaging and magnetic resonance imaging (MRI) are non-invasive imaging techniques used for the differential diagnosis of adrenal lesions.<sup>4-6</sup>

Lipid-rich adrenal adenomas (LRAs) can be easily recognized in unenhanced CT, with homogeneous and relatively low attenuation values [ $<10$  Hounsfield units (HU)], due to their high fat content.<sup>7</sup> LRAs can also be diagnosed through MRI with high sensitivity and specificity.<sup>1</sup> Most LRAs show a loss of signal intensity ( $>20\%$ ) in out-of-phase images from conventional dual-phase T1-weighted imaging and using the Dixon technique due to intratumoral microscopic fat content.<sup>4</sup> LPAs, however, may have a diagnostic overlap with other lipid-poor adrenal lesions, such as adrenal metastasis (ADM) and APhs, in unenhanced CT or MRI images.<sup>8</sup> Washout CT of the adrenal gland is the most reliable imaging method for differentiating adrenal adenomas from other lesions. Most adrenal adenomas show a rapid washout pattern after administration of the contrast agent.<sup>4</sup> However, hypervascular ADM, especially from hepatocellular carcinoma or renal cell carcinoma, may also show a rapid washout pattern.<sup>9</sup> Therefore, the definitive preoperative diagnosis of adrenal lesions is not always possible.

Texture analysis (TA), performed using several complex mathematical processes, is an objective assessment of the structure, gray-level intensity, and pixel position of a le-

sion.<sup>10</sup> The TA parameters of the radiological images can be divided into first-order and second-order statistics. First-order TA parameters consist of the uniformity (in gray-level dispersion), skewness (histogram asymmetry), entropy (irregularity in gray-level dispersion), kurtosis (histogram flatness), energy (uniformity of the distribution), mean/minimum/maximum density, and standard deviation of the gray-level histogram dispersion.<sup>11</sup> Second-order TA, used to assess the spatial relationships among pixels, includes the following parameters: gray-level co-occurrence matrix (GLCM), neighborhood gray-level difference matrix (NGLDM), gray-level run-length matrix (GLRLM), gray-level zone length matrix (GLZLM), and their subgroup parameters.<sup>12</sup> First-order and second-order TA parameters in adrenal lesions may help physicians to differentiate subgroup lesions based on the underlying histopathological composition. This study investigated the role of TA in differentiating adrenal lesions in unenhanced CT images.

## Materials and Methods

### Patient selection

The protocol of this retrospective study was approved by our institutional review board (approval number: 2020/20-31; date: 2020-08-31), and written informed consent was obtained from each patient. The endocrinology department database was reviewed to identify patients with LRA, LPA, ADM, or APh between January 2015 and December 2019. The inclusion criteria were age  $\geq 19$  years, histopathologically proven APh, diagnosis of LRA, LPA, or ADM based on radiological features, positron emission tomography (PET)-CT features, long-term follow-up, histopathological diagnosis, or biopsy, and unenhanced CT performed before resection or during follow-up screening. Eligible patients had an adrenal lesion determined by unenhanced CT or PET-CT to be ADM (for those with known primary tumors with standardized uptake value (SUV)<sub>max</sub> ratio  $>2.5$  [the accepted value for distinguishing between benign and cancerous lesions], and SUV<sub>max</sub> values of ADM were higher than those of normal liver parenchyma), LRA ( $\leq 10$  HU in unenhanced CT images), or LPA (diagnosis made by histopathological or radiological follow-up at least 36 months following initial CT).<sup>13</sup>

Histopathological diagnosis of adrenal lesions is made by surgical intervention, and adrenal lesion biopsy should only be considered for making a diagnosis of metastatic

disease in patients with known or suspected non-adrenal cancer.<sup>14</sup> The exclusion criteria were adrenal lesion  $<1$  cm ( $n = 18$ ), lack of unenhanced CT images ( $n = 82$ ), CT images with severe motion or other artifacts ( $n = 7$ ), and CT imaging performed at another institution ( $n = 23$ ). Both lesions of patients with bilateral adrenal lesions were included in the study. We were unable to confirm a diagnosis of adenoma versus ADM histopathologically in three patients, and these patients were also excluded. After these criteria had been applied, a total of 140 patients with 166 adrenal lesions were included (Figure 1). All patients were evaluated through non-contrast abdominal CT using the CT devices available in our department (Supplementary Table 1).

Endocrinological examinations were performed in all cases preoperatively. Metanephrine and normetanephrine were measured in 24-h urine for a differential diagnosis of pheochromocytoma in all patients. Basal plasma levels of adrenocorticotropic hormone and serum levels of cortisol, the dexamethasone suppression test, plasma renin activity, and the aldosterone/renin ratio were used to evaluate adrenal adenoma.

### Texture analysis

The unenhanced CT images of each patient were reviewed by three radiologists (HAÖ, IBA, and CA) with 4, 15, and 20 years of experience in abdominal radiology, respectively. The selected images of all adrenal lesions were decided by consensus. For each adrenal lesion, a selected axial image was obtained through CT for use in TA. The selected images for the 166 adrenal masses were anonymized and exported from Sectra IDS7 PACS (Sectra AB, Linköping, Sweden). The image selection was made in the largest diameter of the lesion. Reprocessing of the images was performed using standardization: (gray value-average value)/standard deviation. The images were examined and segmented using Local Image Feature Extraction (LIFEX) software (version 5.1; <http://www.lifexsoft.org>) independently by two radiologists (IBA and CA) with 15 and 20 years of experience in abdominal radiology, respectively. Regions of interest (ROIs) were drawn manually on each CT image for the measurements (Figures 2, 3). To provide uniformity, the number of gray levels was adjusted to 128 (7 bits). Furthermore, to homogenize the voxel sizes in the XYZ directions, they were adjusted as X, 0.5 mm; Y, 0.5 mm; and Z, 2.5 mm after calculating their mean  $\pm 3$  standard deviations. First-order and second-order TA features were calculated in each adrenal lesion.

### Main points

- Adrenal masses are commonly encountered in daily practice, and it can be difficult to distinguish between lipid-poor adenoma and masses that may require surgical treatment based on non-contrast computed tomography (CT).
- Texture analysis reveals minor differences in gray levels, which can provide guidance in the differential diagnosis of visceral neoplasms.
- This study suggests that lipid-poor adenoma, adrenal metastasis, and pheochromocytoma can be distinguished through an analysis of textural features in non-contrast CT images

## Statistical Analysis

IBM SPSS software for Windows, version 24.0 (IBM Corporation, Armonk, NY), was used for all statistical analyses. We recorded demographic data, including the patient's age, sex, diagnosis, and TA measurements. Interobserver variability between the two radiologists was evaluated using intraclass correlation coefficients (0–0.4, poor agreement; 0.41–0.6, moderate agreement; 0.61–0.8, good agreement; 0.81–1, excellent agreement). We performed One-Way analysis of variance (ANOVA) with Bonferroni correction to compare the differences in the TA parameters of LRA, LPA, ADM, and APh. The non-parametric Mann–Whitney U test was performed to detect significant associations between the texture parameters and each adrenal subgroup. LPAs were excluded from the statistical evaluation because they are easily recognized in non-contrast CT examinations and do not cause diagnostic difficulties. Receiver operating characteristic (ROC) curve analysis was performed to evaluate the

diagnostic performance of the parameters in differentiating among the adrenal lesion subgroups by calculating the area under the ROC curve (AUC). A *P* value <0.050 was considered statistically significant.

Next, we developed three models to identify texture features predicting LPA, ADM, and APh, with *P* < 0.050 in the univariate analysis. A logistic regression model was developed based on the qualitative features. In the final logistic regression model, statistically significant texture parameters were used for the three comparisons (12 for LPA vs. ADM, 15 for LPA vs. APh, and 4 for ADM vs. APh). The model performance was assessed according to sensitivity, specificity, negative predictive value (NPV), positive predictive value (PPV), and accuracy.

## Results

The final study population consisted of 140 patients (64 men, 76 women; mean age,  $56.58 \pm 13.65$  years) with 166 adrenal lesions.

Fifty-four adrenal lesions were diagnosed with LRA, 37 were diagnosed with LPA, 56 were diagnosed with ADM, and 19 were diagnosed with APh (Table 1). There were no significant differences in age or sex among the subgroups. In our series of 91 adrenal adenomas, 76% were non-functioning. The total interobserver agreement between two radiologists (IBA and CA) was  $\kappa = 0.73$  in the TA calculation. Due to the high level of interobserver agreement and the large amount of numerical data, the data of observer 1 are presented in the tables. Twenty-seven texture parameters, consisting of 11 histogram features, 7 GLCM features, 3 GLRLM features, 3 NGLDM features, and 3 GLZLM features, showed statistically significant differences. The One-Way ANOVA identified 16 second-order texture parameters that were significantly different among all adrenal lesion subgroups (Table 2). The Mann–Whitney U test identified 12 texture parameters that could differentiate between LPA and ADM (*P* = 0.000–0.032), 15 that

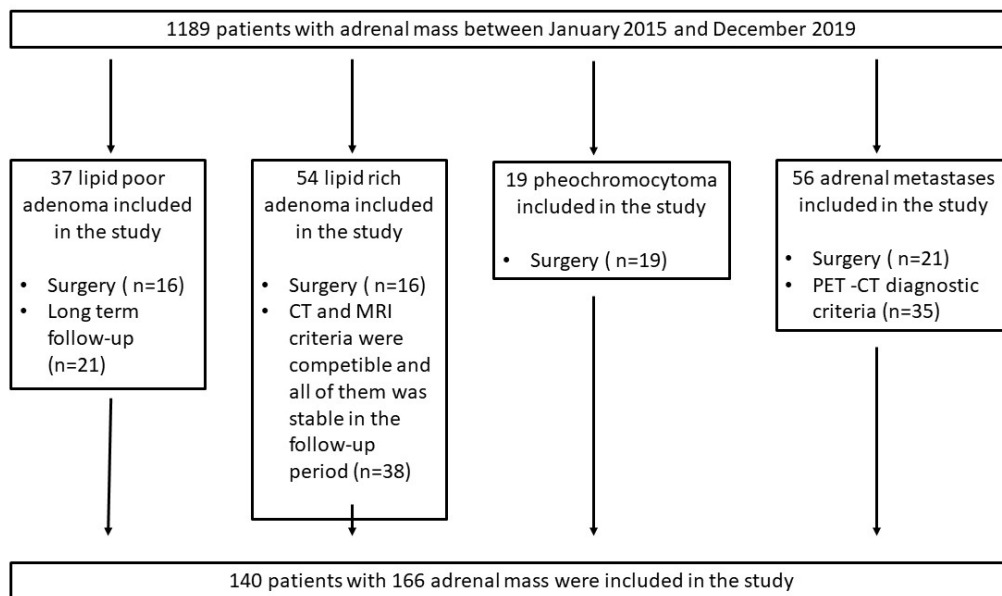


**Figure 1.** Flowchart of patients with adrenal lesions. CT, computed tomography; MRI, magnetic resonance imaging; PET-CT, positron emission tomography-computed tomography.

**Table 1.** Imaging characteristics of adrenal lesions

Imaging characteristics	Lipid-rich adenoma (n = 54)	Lipid-poor adenoma (n = 37)	Metastasis (n = 56)	Pheochromocytoma (n = 19)
HU <sub>min</sub>	-70.57 ± 22.9	-57.12 ± 32.7	-32.90 ± 30.2	-30.67 ± 34.7
HU <sub>mean</sub>	-9.84 ± 13.9	14.60 ± 14.6	30.32 ± 13.9	33.47 ± 11.9
HU <sub>max</sub>	49.56 ± 141.2	74 ± 98.9	83.5 ± 26.4	89 ± 19.4
Mean lesion size (cm)	5.4	5.9	7.8	4.9
Mean SUV <sub>max</sub>	-	-	8.6	-

SUV<sub>max</sub>, maximum standardized uptake value; HU<sub>min</sub>, Hounsfield unit minimum; HU<sub>mean</sub>, Hounsfield unit mean; HU<sub>max</sub>, Hounsfield unit maximum.

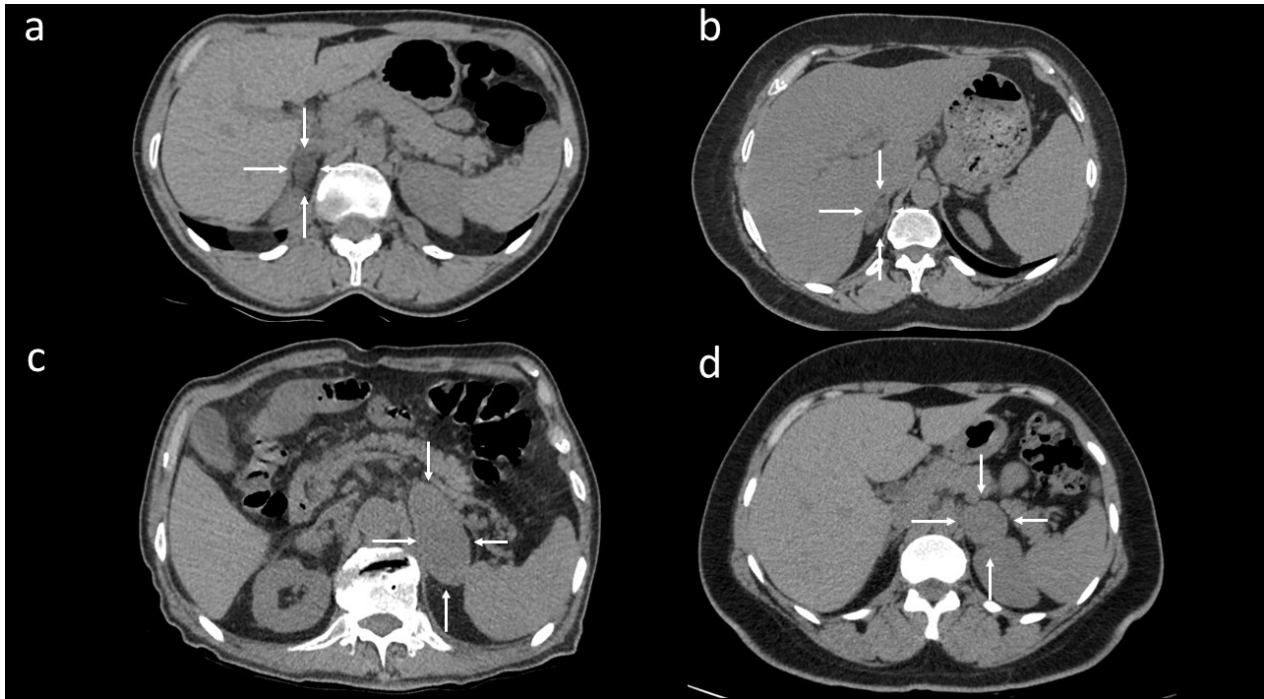


**Figure 2.** (a) Lipid-rich adenoma in a 49-year-old woman. A well-circumscribed and low-density lesion was observed in the right adrenal gland in axial computed tomography (CT) (white arrows). (b) A 37-year-old woman with lipid-poor adenoma diagnosed histopathologically. Axial unenhanced CT showed a lipid-poor right adrenal mass (white arrows). The mass with a density of 22–56 Hounsfield unit (HU) had a heterogeneous internal structure. (c) Adrenal metastases were diagnosed through surgery in a 56-year-old man with lung cancer. Axial unenhanced CT showed a large, well-defined, homogenous left adrenal mass with a density of 54 HU (white arrows). (d) Surgically resected pheochromocytoma in a 32-year-old man. Axial unenhanced CT showed a well-defined, homogenous, spherical left adrenal mass with a density of 46 HU (white arrows).

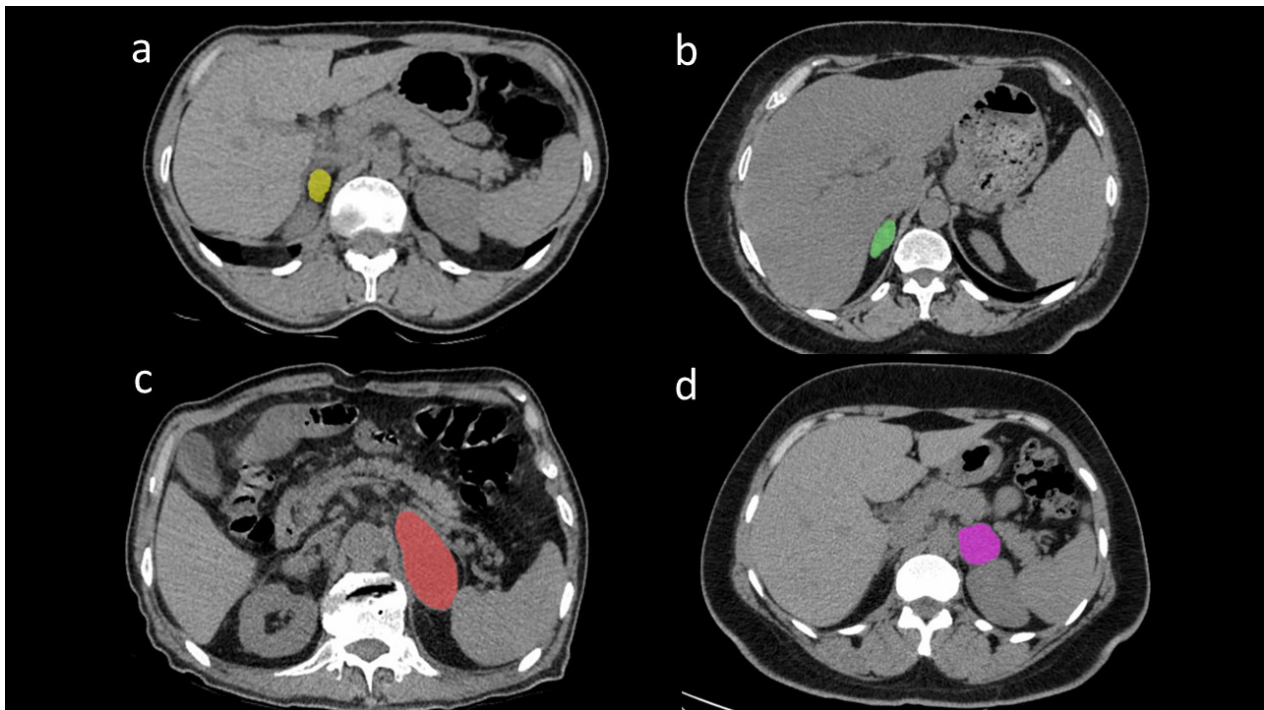


**Figure 3.** Segmentation examples of reader 1 (a) and reader 2 (b). (a) Texture analyses of the lipid-rich adrenal adenoma using local image feature extraction (LIFEx) software [lesion tagged with a yellow region of interest (ROI)]. (b) Texture analyses of the lipid-poor adrenal adenoma using LIFEx software (lesion tagged with a green ROI). (c) Texture analyses of the adrenal metastasis using LIFEx software (lesion tagged with a red ROI). (d) Texture analyses of the adrenal pheochromocytoma using LIFEx software (lesion tagged with a pink ROI).

**Table 2.** Differences in texture parameters for differentiating adrenal lesions on non-enhanced computed tomography

Texture analysis parameters	1-lipid-rich adenoma (n = 54)			2-lipid-poor adenoma (n = 37)			3-metastasis (n = 56)			4-pheochromocytoma (n = 19)			P value
	Median	Q1 (IQR 25%)	Q3 (IQR 75%)	Median	Q1 (IQR 25%)	Q3 (IQR 75%)	Median	Q1 (IQR 25%)	Q3 (IQR 75%)	Median	Q1 (IQR 25%)	Q3 (IQR 75%)	
HU <sub>min</sub>	-70.57	-87.59	-54.44	-57.12	-79.71	-34.92	-32.90	-51.02	-22.63	-30.67	-52	-14	<0.001
HU <sub>mean</sub>	-9.84	-18.05	-0.17	14.60	-0.51	24.98	30.32	23.50	35.13	33.47	28.16	38.91	<0.001
HU <sub>max</sub>	49.56	35.86	60.29	74	62.72	92.03	83.5	68.59	107.50	89	74.8	98.6	0.015
HUQ1	-20.21	-30.71	-12.62	1.0	-12.29	14.12	18.30	10.73	22.20	21	16.53	28.14	<0.001
HUQ2	-10.03	-17.43	-0.34	14.57	-0.74	25.83	30.18	23.33	35.84	33	28.18	38.25	<0.001
HUQ3	2.91	-4.25	13.79	27.36	16.99	39.28	42.51	35.48	47.84	44.49	37.77	53.66	<0.001
HU-Skewness	-0.014	-0.012	-0.12	-0.065	-0.27	-0.025	-0.079	-0.21	-0.025	-0.101	-0.17	-0.022	0.068
HU-Kurtosis	3.15	2.96	3.53	3.16	2.92	3.63	3.21	3.03	3.57	3.20	3.04	3.61	0.896
HU-Excess Kurtosis	0.15	-0.034	0.53	0.167	-0.71	0.64	0.217	0.039	0.578	0.20	0.041	0.612	0.896
HU peak sphere 0.5 mL	0.46	0.46	0.46	0.470	0.46	0.46	0.46	0.46	0.46	0.46	0.46	0.46	0.010
HU peak sphere 1 mL	1.00	1.00	1.00	1.00	1.00	1.00	1.00	1.00	1.00	1.01	1.00	1.00	0.110
GLCM-homogeneity	0.1235	0.1186	0.1325	0.1287	0.1222	0.1361	0.1288	0.123	0.140	0.122	0.115	0.133	0.101
GLCM-energy	0.0011	0.0007	0.0016	0.0010	0.0005	0.0017	0.0008	0.0005	0.0012	0.0005	0.0004	0.0007	0.001
GLCM-contrast	473.94	378.78	532.39	412.12	351.81	489.62	429.78	356.13	494.84	503.14	408.77	580.48	0.058
GLCM-correlation	0.46	0.404	0.544	0.55	0.44	0.60	0.517	0.442	0.595	0.434	0.354	0.524	0.022
GLCM-entropy log10	2.97	2.79	3.17	2.99	2.79	3.28	3.14	2.92	3.38	3.30	3.17	3.43	<0.001
GLCM-entropy log2	9.90	9.29	10.54	9.94	9.29	10.90	10.45	9.70	11.22	10.98	10.53	11.41	<0.001
GLCM-dissimilarity	17.12	15.23	18.20	15.86	14.98	17.40	16.26	14.69	17.48	17.51	15.94	18.91	0.053
GLRLM-LRLGE	0.00304	0.0006	0.0048	0.0024	0.0009	0.0047	0.0058	0.0021	0.0083	0.0037	0.0018	0.0056	0.061
GLRLM-GLNU	9.67	6.49	14.89	8.69	5.36	17.44	13.85	7.64	28.70	25.84	14.90	34.45	<0.001
GLRLM-RLNU	638.61	384.49	1011.57	612.07	375.34	1340.15	936.18	490.26	1973.91	1630.25	1040.04	2418.51	<0.001
NGLDM-coarseness	0.0114	0.760	1.155	0.0106	0.0034	0.017	0.0091	0.0042	0.0137	0.0045	0.0029	0.0065	0.001
NGLDM-contrast	0.926	0.404	0.544	0.913	0.637	1.07	0.765	0.636	0.944	0.785	0.694	1.114	0.027
NGLDM-busyness	0.015	0.011	0.022	0.012	0.009	0.027	0.017	0.0126	0.0313	0.031	0.023	0.043	<0.001
GLZM-LZLGE	0.0032	0.0007	0.0071	0.0034	0.0010	0.0084	0.0063	0.0024	0.0146	0.0039	0.0025	0.0161	0.030
GLZM-GLNU	9.00	5.97	13.91	8.11	4.94	16.46	12.81	7.12	26.65	25.35	14.64	32.99	<0.001
GLZM-ZLNU	488.62	320.81	851.50	506.1	306.4	1163.5	763.88	414.42	1656.78	1321.87	874.36	2022.33	<0.001

GLCM, gray-level co-occurrence matrix; GLRLM, gray-level run-length matrix; GLNU, gray-level non-uniformity; NGLDM, neighborhood gray-level difference matrix; HU<sub>min</sub>, hounsfield unit minimum; HU<sub>mean</sub>, hounsfield unit mean; HU<sub>max</sub>, hounsfield unit maximum.

could differentiate between LPA and APh ( $P = 0.000-0.039$ ), and 7 that could differentiate between ADM and APh ( $P = 0.002-0.042$ ) (Table 3). Texture parameters that were significantly different between LPA and ADM,

between LPA and APh, and between ADM and APh were identified by ROC analysis. The AUCs for all independent factors distinguishing the lesions in these three comparisons were between 0.25 and 0.87. The AUCs, 95%

confidence intervals, optimal cut-off values, sensitivities, and specificities for each of the three comparisons are listed in Tables 3-5, respectively. Logistic regression analyses produced three logistic models. The logis-

**Table 3.** First-order and second-order radiomic features with significant differences between LRA, LPA, ADM, and APh

First- and second-order texture parameters	1-2*	1-3*	1-4*	2-3*	2-4*	3-4*
HU <sub>min</sub>	0.032	<0.001	<0.001	0.001	0.007	0.443
HU <sub>mean</sub>	<0.001	<0.001	<0.001	<0.001	<0.001	0.116
H <sub>Ustd</sub>	0.021	0.995	0.138	0.032	0.003	0.144
HU <sub>max</sub>	<0.001	<0.001	<0.001	0.027	0.036	0.692
HUQ1	<0.001	<0.001	<0.001	<0.001	<0.001	0.075
HUQ2	<0.001	<0.001	<0.001	<0.001	<0.001	0.144
HUQ3	<0.001	<0.001	<0.001	<0.001	<0.001	0.348
HU-skewness	0.067	0.032	0.028	0.100	0.869	0.635
HU peak sphere 0.5 mL	0.822	0.292	0.013	0.254	0.038	0.002
HU peak sphere 1 mL	0.181	0.306	0.033	0.624	0.206	0.100
GLCM-homogeneity	0.170	0.037	0.497	0.689	0.191	0.073
GLCM-energy	0.539	0.006	<0.001	0.101	0.011	0.095
GLCM-contrast	0.098	0.047	0.327	0.100	0.079	0.040
GLCM-correlation	0.025	0.031	0.346	0.510	0.033	0.053
GLCM-entropy log10	0.545	0.005	<0.001	0.103	0.009	0.093
GLCM-entropy log2	0.545	0.005	<0.001	0.103	0.009	0.093
GLCM-dissimilarity	0.106	0.035	0.365	0.826	0.085	0.040
GLRLM-LRLGE	0.904	0.021	0.315	0.031	0.222	0.407
GLRLM-GLNU	0.704	0.008	<0.001	0.023	0.002	0.042
GLRLM-RLNU	0.765	0.006	<0.001	0.089	0.005	0.062
NGLDM-coarseness	0.314	0.055	<0.001	0.666	0.039	0.008
NGLDM-contrast	0.450	0.002	0.191	0.124	0.697	0.355
NGLDM-busyness	0.359	0.061	<0.001	0.024	0.001	0.005
GLZM-LZLGE	0.790	0.009	0.163	0.031	0.121	0.526
GLZM-GLNU	0.710	0.008	<0.001	0.023	<0.001	0.007

(1) lipid-rich adrenal adenoma, (2) lipid-poor adrenal adenoma, (3) adrenal metastasis, (4) adrenal pheochromocytoma \* $P < 0.050$ . LRA, lipid-rich adrenal adenomas; LPA, lipid-poor adrenal adenoma, ADM, adrenal metastase; APh, adrenal pheochromocytoma; HU<sub>min</sub>, hounsfield unit minimum; HU<sub>mean</sub>, hounsfield unit mean; HU<sub>max</sub>, hounsfield unit maximum; GLCM, gray-level co-occurrence matrix; GLRLM, gray-level run-length matrix; GLNU, gray-level non-uniformity; NGLDM, neighborhood gray-level difference matrix.

**Table 4.** Accuracy of radiomic features for differentiating between lipid-poor adrenal adenoma and adrenal metastasis

	AUC $\pm$ std (95% confidence interval)	P value	Cut-off value	Sensitivity (%)	Specificity (%)
HU <sub>min</sub>	0.71 $\pm$ 0.054 (0.61–0.81)	0.012	–44.61	64.3	64.8
HU <sub>mean</sub>	0.78 $\pm$ 0.051 (0.69–0.88)	<0.001	24.00	73.2	72.9
HU <sub>std</sub>	0.37 $\pm$ 0.058 (0.25–0.48)	0.032	19.16	62.2	37.8
HU <sub>max</sub>	0.63 $\pm$ 0.060 (0.52–0.75)	0.027	80.32	58.9	59.4
HUQ1	0.78 $\pm$ 0.052 (0.68–0.88)	<0.001	12.54	73.2	72.9
HUQ2	0.76 $\pm$ 0.051 (0.68–0.88)	<0.001	23.86	73.2	72.9
HUQ3	0.63 $\pm$ 0.052 (0.66–0.86)	<0.001	35.75	71.4	70.2
GLRLM-LRLGE	0.63 $\pm$ 0.060 (0.51–0.75)	0.031	0.0036	58.9	59.4
GLRLM-GLNU	0.64 $\pm$ 0.061 (0.52–0.76)	0.023	10.71	60.7	59.4
NGLDM-busyness	0.64 $\pm$ 0.061 (0.52–0.76)	0.024	0.0124	76.8	45.9
GLZM-LZLGE	0.63 $\pm$ 0.059 (0.52–0.75)	0.031	0.0022	76.8	59.5
GLZM-GLNU	0.64 $\pm$ 0.060 (0.52–0.76)	0.023	6.75	76.8	62.2

HU<sub>min</sub>, Hounsfield unit minimum; HU<sub>mean</sub>, Hounsfield unit mean; HU<sub>max</sub>, Hounsfield unit maximum; AUC, area under the ROC curve; GLCM, gray-level co-occurrence matrix; GLRLM, gray-level run-length matrix; GLNU, gray-level non-uniformity; NGLDM, neighborhood gray-level difference matrix; std, standard.

tic models were evaluated to ascertain the relationships between LPA and ADM, LPA and APh, and ADM and APh (Tables 4-6). The sensitivity, specificity, PPV, NPV, and accuracy of the first model (LPA vs. ADM) were 85.7%, 70.3%, 81.3%, 76.4%, and 79.5%, respectively ( $P = 0.050$ ). The sensitivity, specificity, PPV,

NPV, and accuracy of the second model (LPA vs. APh) were all 100% ( $P < 0.001$ ). The sensitivity, specificity, PPV, NPV, and accuracy of the third model (ADM vs. APh) were 87.5%, 82%, 36.8%, 98.2%, and 82.7%, respectively ( $P = 0.018$ ). We present all values of our logistic regression models in Table 7. The first lo-

gistic model found that  $HU_{\text{mean}}$ , GLRLM-long run low gray-level emphasis (GLRLM-LGE), and NGLDM-Busyness were significant factors differentiating LPA from ADM, with odds ratios (ORs) of 3.87, 2.64, and 5.07, respectively. In the second model, GLRLM-gray-level non-uniformity (GLRLM-GLNU) and  $HU_{\text{mean}}$

**Table 5.** Accuracy of radiomic features for differentiating between lipid-poor adrenal adenoma and adrenal pheochromocytoma

	AUC $\pm$ std (95% confidence interval)	<i>P</i> value	Cut-off value	Sensitivity (%)	Specificity (%)
$HU_{\text{min}}$	0.72 $\pm$ 0.079 (0.57–0.88)	0.071	–41.05	68.4	67.5
$HU_{\text{mean}}$	0.86 $\pm$ 0.048 (0.77–0.96)	<0.001	26.96	78.9	78.4
$HU_{\text{std}}$	0.25 $\pm$ 0.076 (0.10–0.40)	0.003	18.49	31.6	32.4
$HU_{\text{max}}$	0.67 $\pm$ 0.071 (0.53–0.81)	0.040	82.26	63.2	62.1
HUQ1	0.87 $\pm$ 0.048 (0.77–0.96)	<0.001	15.22	78.9	78.37
HUQ2	0.85 $\pm$ 0.051 (0.75–0.95)	<0.001	24.42	78.9	78.4
HUQ3	0.83 $\pm$ 0.054 (0.72–0.94)	<0.001	37.41	78.9	75.6
GLCM energy	0.29 $\pm$ 0.072 (0.15–0.43)	0.013	0.00066	36.8	32.4
GLCM correlation	0.32 $\pm$ 0.079 (0.17–0.48)	0.030	0.49	36.8	35.1
GLCM-entropy log 10	0.72 $\pm$ 0.072 (0.58–0.86)	0.001	3.203	68.4	67.6
GLCM-entropy log 2	0.72 $\pm$ 0.072 (0.58–0.86)	0.001	10.63	68.4	67.5
GLRLM-GLNU	0.76 $\pm$ 0.070 (0.62–0.89)	0.002	15.19	73.7	72.9
GLRLM-RLNU	0.73 $\pm$ 0.072 (0.59–0.87)	0.005	1046.48	73.7	70.2
NGLDM-coarseness	0.33 $\pm$ 0.074 (0.18–0.47)	0.040	0.0045	47.4	32.4
NGLDM-busyness	0.78 $\pm$ 0.065 (0.65–0.91)	0.001	0.022	78.9	72.9
GLZLM-GLNU	0.81 $\pm$ 0.058 (0.69–0.92)	<0.001	14.29	78.6	73.9
GLZLM-ZLNU	0.73 $\pm$ 0.072 (0.58–0.87)	0.006	896.77	73.7	70.3

$HU_{\text{min}}$ , hounsfield unit minimum;  $HU_{\text{mean}}$ , hounsfield unit mean;  $HU_{\text{max}}$ , hounsfield unit maximum; AUC, area under the ROC curve; GLCM, gray-level co-occurrence matrix; GLRLM, gray-level run-length matrix; GLNU, gray-level non-uniformity; NGLDM, neighborhood gray-level difference matrix; std, standard.

**Table 6.** Accuracy of radiomic features for differentiating between adrenal metastasis and adrenal pheochromocytoma

	AUC $\pm$ std (95% confidence interval)	<i>P</i> value	Cut-off value	Sensitivity (%)	Specificity (%)
HU peak sphere 0.5 mL	0.68 $\pm$ 0.083 (0.51–0.84)	0.023	0.456	89.3	10.7
GLCM-contrast	0.66 $\pm$ 0.079 (0.50–0.81)	0.040	462.22	63.2	62.5
GLCM-dissimilarity	0.66 $\pm$ 0.078 (0.50–0.81)	0.040	16.85	63.2	62.5
GLRLM-GLNU	0.66 $\pm$ 0.067 (0.52–0.79)	0.042	20.35	63.2	64.2
NGLDM-coarseness	0.29 $\pm$ 0.065 (0.16–0.42)	0.008	0.0030	73.7	19.6
NGLDM-busyness	0.72 $\pm$ 0.064 (0.59–0.84)	0.005	0.0249	68.4	64.2
GLZLM-GLNU	0.71 $\pm$ 0.059 (0.59–0.82)	0.007	19.16	68.4	64.3

HU, hounsfield unit; AUC, area under the ROC curve; GLCM, gray-level co-occurrence matrix; GLRLM, gray-level run-length matrix; GLNU, gray-level non-uniformity; NGLDM, neighborhood gray-level difference matrix; std, standard.

**Table 7.** Statistical values of logistic regression models

	Model 1*	Model 2**	Model 3***
Sensitivity (%)	85.7	100	87.5
Specificity (%)	70.3	100	82
Positive predictive value (%)	81.3	100	36.8
Negative predictive value (%)	76.4	100	98.2
Accuracy (%)	79.5	100	82.7
<i>P</i> value	0.050	<0.001	0.018

\*, statistical model between lipid-poor adrenal adenoma and adrenal metastasis; \*\*, statistical model between lipid-poor adrenal adenoma and adrenal pheochromocytoma; \*\*\*, statistical model between adrenal metastasis and adrenal pheochromocytoma).

were identified as factors differentiating LPA from APH, with ORs of 119.09 and 4.98, respectively. An HU peak sphere of 0.5 mL was identified as a factor differentiating ADM from APH, with an OR of 4.2.

## Discussion

We evaluated the performance of CT-based TA for differentiating adrenal lesions in unenhanced CT images. The results indicate that TA in unenhanced CT images may help to differentiate adrenal lesion subgroups. Numerous TA parameters can be useful for the differential diagnosis of adrenal lesions. GLCM-homogeneity, GLCM-contrast, GLRLM-LGE, and NGLDM-contrast are unique identifiers for discrimination, demonstrating the highest sensitivity and specificity rates (Table 1).

Unenhanced CT, CT washout, and adrenal MRI have been used to differentiate LRAs from other adrenal masses, with high sensitivities and specificities.<sup>3,4</sup> However, there are occasionally false-positive diagnoses of LRAs that mimic ADM or APH.<sup>15</sup> Adrenal LRAs are easily identified through contrast-enhanced CT using a cut-off of 10 HU.<sup>3</sup> Washout CT is widely used to differentiate LRA and LPA from other adrenal lesions. Johnson et al.<sup>16</sup> reported a sensitivity of 88% and specificity of 96% for diagnosing adrenal adenomas using absolute percentage washout in CT. However, Patel et al.<sup>17</sup> revealed that LPA and APH have a diagnostic overlap with CT attenuation and washout criteria. Seo et al.<sup>18</sup> compared the ability of MRI and washout CT to diagnose LPA and reported sensitivities of 75.7% and 100% and specificities of 60% and 80%, respectively. Hypervascular metastases in the adrenal gland show a rapid washout pattern in CT and cannot be differentiated from adrenal adenomas.<sup>19</sup> Another diagnostic issue is that hepatocellular carcinomas and renal cell carcinomas are rich in intracytoplasmic fat, resulting in difficult differentiation from LRAs based on chemical-shift MRI.<sup>19</sup> Therefore, the diagnostic capabilities of unenhanced CT, washout CT, and adrenal MRI are limited in terms of definitive differentiation among LPA, ADM, and APH.

TA enables the evaluation of a variety of image pixels used to describe the relationships among their gray-level intensity positions within an image.<sup>20</sup> To evaluate the internal architecture of adrenal lesions, TA can be used to quantify intratumoral heterogeneity based on the distribution of gray-level values and the spatial arrangement of the pixels within a given region of interest.<sup>20</sup> Previous

studies have demonstrated that TA helps distinguish among adrenal lesions. Shi et al.<sup>1</sup> performed TA using CT to distinguish ADM from benign adrenal masses; they used support vector machine modeling and reported an AUC of  $0.85 \pm 0.03$  and accuracy of 77% for distinguishing metastatic from benign adrenal masses. Yi et al.<sup>21</sup> used a texture software program (MaZda, version 4.6) to analyze CT images to differentiate LPA from APH. Their logistic regression model based on four texture parameters differentiated LPA from APH, with a sensitivity, specificity, and accuracy of 86.2%, 97.5%, and 94.4%, respectively. Sensitivity and specificity were higher in the present study; the difference may be related to the differences in the software used and the higher number of second-order parameters in our study. Elmohr et al.<sup>22</sup> used TA in 54 cases of adrenal adenomas and carcinomas. Using Boruta random forest modeling, they achieved a validated accuracy of 82% for differentiating benign from malignant adrenal lesions. Ho et al.<sup>23</sup> performed a multivariate logistic analysis of 21 texture features, which were combined for each modality, to show that contrast-enhanced CT and chemical-shift MRI could identify malignant lesions, whereas unenhanced CT could not, in 23 patients (malignant adrenal lesions in 8 and LRAs in 15). We included more patients in our study and a significant difference was found between adenomas and malignant lesions. Torresan et al.<sup>24</sup> used a cutoff mean densitometry value of 22.5 HU for contrast-enhanced CT TA with a sensitivity and specificity of 95% and 100%, respectively.

To differentiate LRAs from other adrenal lesions (ADMs and APHs) using TA, 10 first-order and 16 second-order texture parameters were identified as statistically significant in our study. HU-Skewness, GLCM-Homogeneity, and NGLDM-Contrast were the most significantly different texture parameters between LRA and ADM. LRAs are easily differentiated from other lipid-poor adrenal lesions using conventional adrenal imaging techniques.

It is often difficult to differentiate LPA from ADM or APH in daily radiological practice. LPA is a benign condition that does not require surgical treatment. In contrast to previous studies, we focused on comparisons of first-order and second-order texture parameters to distinguish among LPA, ADM, and APH.

In our study, LPA was significantly different from ADM in appearance, based on 12 texture parameters in unenhanced CT im-

ages, with high sensitivity and specificity of 85.7% and 70.3%, respectively. The first-order texture parameters GLRLM-LGE, GLRLM-GLNU, NGLDM-Busyness, GLZLM low gray-level zone emphasis, and GLZLM-GLNU calculated on enhanced CT images had positive correlations with ADM. Moreover,  $HU_{mean}$  (OR: 3.87), GLRLM-LGE (OR: 2.64), and NGLDM-Busyness (OR: 5.07) were the texture parameters that best differentiated LPA from ADM. Our study included a sufficient number of cases to evaluate TA using 45 parameters and to construct a logistic model based on these texture parameters, allowing us to predict malignancy using TA.

We also evaluated the relationship between LPA and APH. A comparison of our results with those in recent studies that evaluated CT for the same clinical questions revealed higher sensitivity and specificity values for our TA results than those identified by Yi et al.<sup>21</sup> In this study, sensitivity and specificity for distinction between LPA and APH were 86.2% and 97.5%, respectively. In addition, our model predicts APH with high accuracy using conventional assessment methods in unenhanced CT. Moreover, the GLRLM-GLNU value in the second-order TA was a statistically significant factor differentiating LPA from APH, with a high OR of 119.09.

Finally, we also evaluated the role of TA in differentiating ADM from APH in unenhanced CT images. Our logistic regression analysis identified an HU peak sphere of 0.5 mL (OR: 4.2) as a more robust factor differentiating these two lesion types compared with the other texture parameters. Our study has several limitations. First, the retrospective study design was potentially subject to bias. Previous studies have indicated that the reproducibility and variability of TA are affected by the CT device and technique used. To overcome these limitations, we included 140 patients who underwent unenhanced CT using the same acquisition protocol performed by two different CT scanners. Additional studies involving a larger number of cases and standardized CT acquisition protocols will provide more reliable results. Second, we did not include any primary malignant adrenal tumors. Although malignant adrenal tumors are rare, ADM being the most common, the inclusion of malignant adrenal tumors of different histopathological types, especially adrenocortical cancer, is needed to improve the reliability of our results. Another limitation is that we used two-dimensional analysis, which may have resulted in less available information during the data transfer compared with three-dimensional analysis.<sup>25</sup> Fi-

nally, our machine learning program used logistic regression analysis and SPSS software, whereas recent studies have used additional texture parameters and specialized machine learning programs (i.e., random forest, GBM), which can improve the results.

In conclusion, TA parameters in unenhanced CT images can be used to differentiate among the four most frequently encountered adrenal tumors, LRA, LPA, ADM, and APH. Differences in texture parameters may be related to differences in tumor cellularity, lipid content, and biological behavior. The addition of TA parameters to CT findings may improve the ability of radiologists to distinguish LPA from ADM or APH. Unenhanced CT-based TA has potential for the diagnosis of incidental adrenal lesions, leading to accurate diagnoses and preventing unnecessary surgical treatment. Further prospective trials in larger populations are needed to verify the role and performance of TA in patients with adrenal masses.

#### Conflict of interest disclosure

The authors declared no conflicts of interest.

#### References

1. Shi B, Zhang GM, Xu M, Jin ZY, Sun H. Distinguishing metastases from benign adrenal masses: what can CT texture analysis do? *Acta Radiol.* 2019;60(11):1553-1561. [\[CrossRef\]](#)
2. Song JH, Chaudhry FS, Mayo-Smith WW. The incidental indeterminate adrenal mass on CT (> 10 H) in patients without cancer: is further imaging necessary? Follow-up of 321 consecutive indeterminate adrenal masses. *AJR Am J Roentgenol.* 2007;189(5):1119-1123. [\[CrossRef\]](#)
3. Schieda N, Siegelman ES. Update on CT and MRI of Adrenal Nodules. *AJR Am J Roentgenol.* 2017;208(6):1206-1217. [\[CrossRef\]](#)
4. Albano D, Agnello F, Midiri F, et al. Imaging features of adrenal masses. *Insights Imaging.* 2019;10(1):1. [\[CrossRef\]](#)
5. Bharwani N, Rockall AG, Sahdev A, et al. Adrenocortical carcinoma: the range of appearances on CT and MRI. *AJR Am J Roentgenol.* 2011;196(6):W706-W714. [\[CrossRef\]](#)
6. Leung K, Stamm M, Raja A, Low G. Pheochromocytoma: the range of appearances on ultrasound, CT, MRI, and functional imaging. *AJR Am J Roentgenol.* 2013;200(2):370-378. Erratum in: *AJR Am J Roentgenol.* 2013;200(3):705. [\[CrossRef\]](#)
7. Johnson PT, Horton KM, Fishman EK. Adrenal imaging with multidetector CT: evidence-based protocol optimization and interpretative practice. *Radiographics.* 2009;29(5):1319-1331. Erratum in: *Radiographics.* 2009;29(7):2198. [\[CrossRef\]](#)
8. Schieda N, Al Dandan O, Kielar AZ, Flood TA, McInnes MD, Siegelman ES. Pitfalls of adrenal imaging with chemical shift MRI. *Clin Radiol.* 2014;69(11):1186-1197. [\[CrossRef\]](#)
9. Choi YA, Kim CK, Park BK, Kim B. Evaluation of adrenal metastases from renal cell carcinoma and hepatocellular carcinoma: use of delayed contrast-enhanced CT. *Radiology.* 2013;266(2):514-520. [\[CrossRef\]](#)
10. Kato H, Kanematsu M, Zhang X, et al. Computer-aided diagnosis of hepatic fibrosis: preliminary evaluation of MRI texture analysis using the finite difference method and an artificial neural network. *AJR Am J Roentgenol.* 2007;189(1):117-122. [\[CrossRef\]](#)
11. Basara Akin I, Ozgul H, Simsek K, Altay C, Secil M, Balci P. Texture analysis of ultrasound images to differentiate simple fibroadenomas from complex fibroadenomas and benign phyllodes tumors. *J Ultrasound Med.* 2020;39(10):1993-2003. [\[CrossRef\]](#)
12. Koçak B, Durmaz EŞ, Ateş E, Kılıçkesmez Ö. Radiomics with artificial intelligence: a practical guide for beginners. *Diagn Interv Radiol.* 2019;25(6):485-495. [\[CrossRef\]](#)
13. Xu B, Gao J, Cui L, et al. Characterization of adrenal metastatic cancer using FDG PET/CT. *Neoplasma.* 2012;59(1):92-99. [\[CrossRef\]](#)
14. Mazzaglia PJ, Monchik JM. Limited value of adrenal biopsy in the evaluation of adrenal neoplasm. *Arch Surg.* 2009;144(5):465-470. [\[CrossRef\]](#)
15. Nioche C, Orlhac F, Boughdad S, et al. LIFEX: a freeware for radiomic feature calculation in multimodality imaging to accelerate advances in the characterization of tumor heterogeneity. *Cancer Res.* 2018;78(16):4786-4789. [\[CrossRef\]](#)
16. Johnson PT, Horton KM, Fishman EK. Adrenal mass imaging with multidetector CT: pathologic conditions, pearls, and pitfalls. *Radiographics.* 2009;29(5):1333-1351. [\[CrossRef\]](#)
17. Patel J, Davenport MS, Cohan RH, Caoili EM. Can established CT attenuation and washout criteria for adrenal adenoma accurately exclude pheochromocytoma? *AJR Am J Roentgenol.* 2013;201(1):122-127. [\[CrossRef\]](#)
18. Seo JM, Park BK, Park SY, Kim CK. Characterization of lipid-poor adrenal adenoma: chemical-shift MRI and washout CT. *AJR Am J Roentgenol.* 2014;202(5):1043-1050. Erratum in: *AJR Am J Roentgenol.* 2019;212(1):232. [\[CrossRef\]](#)
19. Elbanan MG, Javadi S, Ganeshan D, et al. Adrenal cortical adenoma: current update, imaging features, atypical findings, and mimics. *Abdom Radiol (NY).* 2020;45(4):905-916. [\[CrossRef\]](#)
20. Ursprung S, Beer L, Bruining A, et al. Radiomics of computed tomography and magnetic resonance imaging in renal cell carcinoma—a systematic review and meta-analysis. *Eur Radiol.* 2020;30(6):3558-3566. [\[CrossRef\]](#)
21. Yi X, Guan X, Chen C, et al. Adrenal incidentaloma: machine learning-based quantitative texture analysis of unenhanced CT can effectively differentiate sPHEO from lipid-poor adrenal adenoma. *J Cancer.* 2018;9(19):3577-3582. [\[CrossRef\]](#)
22. Elmohr MM, Fuentes D, Habra MA, et al. Machine learning-based texture analysis for differentiation of large adrenal cortical tumours on CT. *Clin Radiol.* 2019;74(10):818.e1-818.e7. [\[CrossRef\]](#)
23. Ho LM, Samei E, Mazurowski MA, et al. Can texture analysis be used to distinguish benign from malignant adrenal nodules on unenhanced CT, contrast-enhanced CT, or in-phase and opposed-phase MRI? *AJR Am J Roentgenol.* 2019;212(3):554-561. [\[CrossRef\]](#)
24. Torresan F, Crimi F, Geccato F, et al. Radiomics: a new tool to differentiate adrenocortical adenoma from carcinoma. *BJS Open.* 2021;5(1):zraa061. [\[CrossRef\]](#)
25. Soni N, Priya S, Bathla G. Texture analysis in cerebral gliomas: a review of the literature. *AJNR Am J Neuroradiol.* 2019;40(6):928-934. [\[CrossRef\]](#)

**Supplementary Table 1.** Abdominal CT examination protocols used in patients included in the study

	CT scanner I	CT scanner II
CT scanner brand	Brilliance 16; Philips Medical Systems, best the Netherlands	Brilliance 64; Philips Medical Systems, best the Netherlands
Reconstructed slice thickness in 3 plane	2.0 mm	2.0 mm
Tube voltage	120	120
mA	Automatic tube current modulation activated, 100–350 mA	Automatic tube current modulation activated, 100–350 mA
Detector configuration	16 x 1.25	64 x 0.625
Detector collimation	4 x 1.25	16 x 0.625
Effective section thickness	1.25 mm	1.24 mm
Reconstruction interval	2 mm	2 mm
Pitch	1.375	1.75
CT, computed tomography.		



# Contrast-enhanced spectral mammography: are kinetic patterns useful for differential diagnoses of enhanced lesions?

Xiaocui Rong

Yihe Kang

Jing Xue

Pengyin Han

Guang Yang

Zhigang Li

## PURPOSE

To investigate the diagnostic efficiency of the kinetic curves of enhanced lesions on contrast-enhanced spectral mammography (CESM) and whether they were similar to those of magnetic resonance imaging (MRI).

## METHODS

Two hundred and twelve patients with 222 enhanced lesions were included in this prospective study. Single-view craniocaudal of an affected breast was acquired at 3, 5, and 7 min after contrast media injection. The kinetic patterns of each lesion were evaluated and classified as elevated (type I), steady (type II), and depressed (type III). Statistical comparison used the chi-squared test, the receiver operating characteristic (ROC) curve, and Cohen's kappa.

## RESULTS

Of 222 enhanced lesions, 140 were breast cancers, and 82 were benign lesions. The distribution of the kinetic curves for breast cancer was type I, 3.57%, type II, 35.71%, and type III, 60.72%. As for benign lesions, the distribution was type I, 43.90%, type II, 45.12%, and type III, 10.98%. The difference in the enhancement patterns between benign lesions and breast cancers was significant ( $P < 0.001$ ). The likelihood of breast cancer related to a type I, II, and III curve was 12.20%, 57.47%, and 90.43%, respectively. For the enhancement intensity, the area under curve (AUC) of the ROC curves was  $0.702 \pm 0.036$ ; for enhancement patterns, the AUC increased to  $0.819 \pm 0.030$ . Cohen's kappa coefficient was 0.752 ( $P < 0.001$ ) regarding the kinetic curves for CESM and MRI.

## CONCLUSION

The kinetic patterns on CESM show promise in differentiating between benign lesions and breast cancers, with good agreement, when compared with MRI.

## KEYWORDS

Breast cancer, contrast-enhanced spectral mammography, contrast agents

From the Department of Radiology (X.R., Y.K., J.X., P.H., G.Y., Z.L. ✉ zhigangli050011@163.com), Hebei Medical University Fourth Affiliated Hospital, Shijiazhuang, China.

Received 15 June 2021; revision requested 14 July 2021; last revision received 21 December 2021; accepted 27 December 2021.



Epub: 27.02.2023

Publication date: 29.03.2023

DOI: 10.5152/dir.2022.21562

**B**reast cancer is now the most common cancer and the main cause of cancer-related death in women. About 2.3 million new breast cancer cases are diagnosed worldwide, accounting for nearly 25% of all cancer cases among females.<sup>1</sup> Full-field digital mammography (FFDM) and digital breast tomosynthesis are widely used in the screening and diagnosis of breast cancer, but some tumors, surrounded mostly by glandular tissue, might be missed with both techniques.<sup>2</sup> Ultrasound is a commonly used imaging examination for dense breasts, but its diagnostic efficacy is operator-dependent.<sup>3</sup>

Traditionally, dynamic contrast-enhanced magnetic resonance imaging (DCE-MRI) has been considered a sensitive imaging examination for breast cancer detection, and the types of the time-intensity curve (TIC) can be used as differential diagnostic criteria for breast-enhancing lesions.<sup>4,5</sup> However, DCE-MRI has a lengthy examination time and a relatively large number of false positive results, leading to additional examinations and biopsies. It is also

You may cite this article as: Rong X, Kang Y, Xue J, Han P, Yang G, Li Z. Contrast-enhanced spectral mammography: are kinetic patterns useful for differential diagnoses of enhanced lesions? *Diagn Interv Radiol.* 2023;29(2):244-250.

expensive and not available for all patients.<sup>6</sup> Contrast-enhanced spectral mammography (CESM) is a promising new technology. Similar to MRI, CESM reflects the angiogenesis associated with breast cancer. Fallenberg et al.<sup>7</sup> and Kim et al.<sup>8</sup> showed that CESM and MRI had comparable accuracy for breast cancer detection. Clauser et al.<sup>9</sup> also demonstrated that CESM had a higher specificity than MRI. However, some benign enhanced lesions such as fibroadenomas, papillomas, hamartomas, intra-mammary nodes, and fat necrosis were misdiagnosed as breast cancer on CESM.<sup>10,11</sup> CESM is a suitable alternative to MRI if it can provide morphological and kinetic information equivalent to DCE-MRI.

This pilot study aims to evaluate the diagnostic efficacy of kinetic curves of enhanced lesions on CESM and whether they are similar to those on MRI.

## Methods

### Patients

This prospective study was approved by the Fourth Hospital of Hebei Medical University ethics committee (no: 2020KY182). Written informed consent was obtained from all patients. The inclusion criteria were: (1) suspected lesions determined by breast sonography, mammography, or both; (2) all breast lesions confirmed by pathology via either percutaneous breast core needle biopsy or excision surgery; (3) cases where CESM were conducted according to our standardized protocol: conducting craniocaudal (CC) views of the normal breast first and CC views of the affected breast later acquired at 3, 5, and 7 min after a contrast agent injection. Patients who did not meet the inclusion criteria and those who met the following exclusion criteria were not accepted to this study: contraindications to iodinated contrast media and poor image quality. As the study flow chart (Figure 1) shows, a total of 212 patients (mean age, 48.09 ± 10.17 years; range, 21–74 years) with 222 lesions were included in this study from April 2019 to June 2020.

### Main points

- The kinetics of the contrast agent can be evaluated using contrast-enhanced spectral mammography (CESM).
- Contrast agent kinetic patterns on CESM show good performance in differentiating between benign and malignant breast-enhanced lesions.
- The kinetic patterns on CESM are similar to those on magnetic resonance imaging.

## Image acquisition and assessment

### CESM

CESM was conducted using the Senographe Essential (GE Healthcare), which is equipped with an amorphous silicon flat panel detector. All patients received an intravenous injection of iodine contrast media (370 mg iodine/mL, 1.22 mL/kg body weight, flow rate 3 mL/s) through the antecubital vein. Two min after the injection, bilateral breast images were obtained by the sequence of contralateral CC projection, and ipsilateral CC projection acquired at 3 (a relatively early phase), 5, and 7 min (a relatively late phase) with the breast compressed after a contrast agent injection. For each exposure, both the low-energy and high-energy images were obtained. The recombined images were acquired by automated post-processing. In the recombined CESM images, a region of interest (ROI) was manually delineated by two radiologists (readers A and B), and the signal values of enhanced lesions and the percentage signal difference between the enhanced lesion and the background (%RS), according to the enhancement formula  $(S'c - S'b) / S'b \times 100\%$ ,<sup>12</sup> were measured to evaluate enhancement intensity, where  $S'c$  and  $S'b$  were signal values in the ROI of the breast lesion and the background, respectively. The enhancement formula  $(\%RS1 - \%RS2) / \%RS2 \times 100\%$  was applied to calculate the value of the pattern of kinetics curves, where  $\%RS1$  and  $\%RS2$  were  $\%RS$  values measured

in the CC projection at 3 and 7 min after the injection, respectively. An ROI was selectively placed in the areas of the breast lesion with the fastest and strongest enhancement, and its size varied with the size of the enhanced lesion ranging from 5 to 216 mm<sup>2</sup>. Attention was given to keeping the ROI in the same location of the lesion and at the exact sizes at each time point to ensure the accuracy of the curve measurement. The ROI of the background was placed in an area of the most homogeneous fatty tissue, far away from the enhanced focus or breast parenchyma. The enhancement intensity was measured at the first postcontrast image (3 min). The patterns of the kinetic curve were classified into three categories: (1) type I, elevated pattern (the enhancement increased more than 10%), (2) type II, steady pattern (the enhancement changed within 10%), and (3) type III, depressed pattern (the enhancement decreased more than 10%) (Figure 2).

### MRI

All breast MRI examinations were conducted on a 1.5T MR scanner (Signa HDe, GE Healthcare) with dedicated phased-array breast-surface coils. Patients were in a prone position, with naturally sagging breasts. The DCE-MRI was performed using volume imaging for the breast assessment (VIBRANTI) and fat-suppressed technology with the following scanning parameters: repetition time 5.6 ms, echo time 1.0 ms, the field of view 320 mm, flip angle 15°, matrix 320 × 288, slice

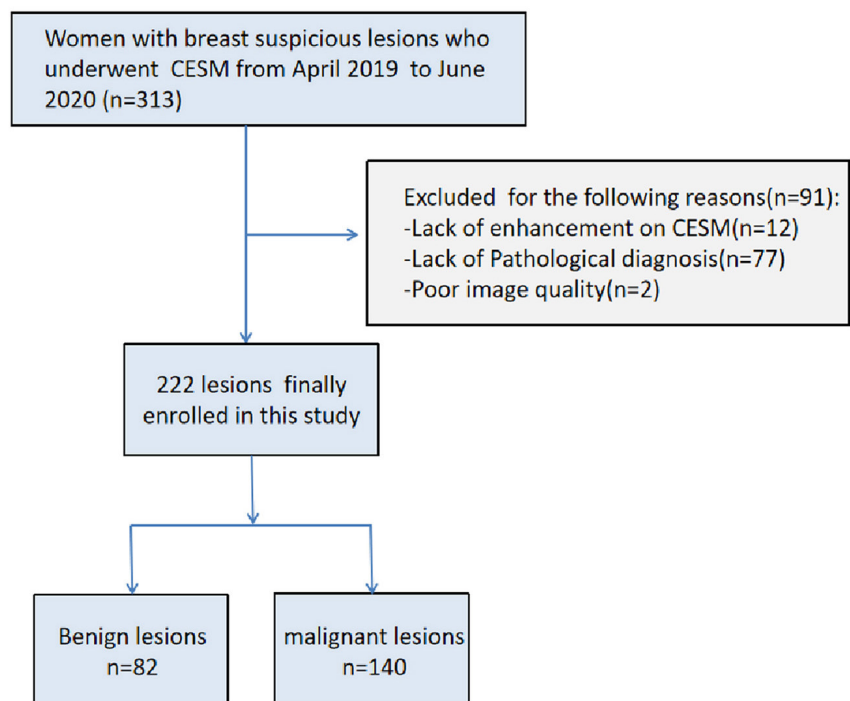


Figure 1. The flow of the study. CESM, contrast-enhanced spectral mammography.

thickness 1.2 mm without an intersection gap, and an imaging time of 62 s per dynamic image. The dynamic series included eight dynamic images: one was acquired before and seven following a 30 s delay after the intravenous injection of Gadoterate meglumine (0.1 mmol/kg body weight) at a flow rate of 3 mL/s. The MRI-enhanced images were acquired between 1 min and 7 min 12 s.

### Statistical analysis

Data analysis and graphical work were performed using SPSS Statistics (version 21.0, IBM, Armonk, NY) and GraphPad Prism 8.0. The Kolmogorov–Smirnov test was used to assess the normality of the data. Descriptive data statistics were presented with n (%), and normal distributions were shown as mean ± standard deviation. The independent samples t-test and the One-Way analysis of variance were used to compare the difference in enhancement degree (%RS) in different lesion types, followed by multiple comparisons using the least significant difference test. A chi-squared test was used to test the significance of the curve-type distribution in benign and malignant breast lesions. The receiver operating characteristic (ROC) analysis was performed to evaluate the diagnostic performance of enhancement intensity and patterns on the CESH, and the areas under the curve (AUCs) were calculated and shown as AUC ± standard error. The best cut-off value was determined using the Youden index. Qualitative agreement between CESH and MRI and the inter-reader agreement in contrast agent kinetics were analyzed using Cohen’s kappa. A kappa coefficient of ≤0.20 indicated poor agreement; 0.21–0.40, fair agreement; 0.41–0.60, moderate agreement; 0.61–0.80, good agreement; and >0.80, excellent agreement.<sup>13</sup> For all tests, a two-sided P value of <0.050 was considered statistically significant.

## Results

### Diagnosis of lesions

Of the 222 enhanced lesions, 140 (63.06%) were breast cancers, consisting of 116 (52.25%) infiltrating cancers and 24 (10.81%) non-infiltrating cancers (ductal carcinoma *in situ*). The infiltrating cancers included 104 invasive ductal cancers not otherwise specified, 8 papillary carcinomas, 1 metaplastic carcinoma, 1 apocrine carcinoma, 1 mucinous cancer, and 1 invasive lobular cancer. Of the 82 (36.94%) benign lesions, 24 were adenosis, 23 fibroadenomas, 19 intraductal papillomas, 11 inflammatory lesions, 3

cysts with infection, 1 phyllodes tumor, and 1 myofibroblastic neoplasia. All the diagnoses were confirmed by core needle biopsy or excisional biopsy.

### Enhancement intensity on CESH

The comparison of %RS by lesion type is presented in Figure 3. In the malignant lesion group, the mean %RS was 4.50 ± 2.20 (4.77 ± 2.18 for infiltrating cancers, 3.58 ± 2.02 for non-infiltrating cancers), while in the benign lesion group, the mean %RS was 3.19 ± 1.81. The comparison between %RS for the benign and malignant groups was statistically significant ( $P < 0.001$ ). There was a significant statistical difference in %RS among the benign lesions, non-infiltrating cancers, and infiltrating cancers groups ( $P < 0.001$ , Table 1). The

%RS of infiltrating cancers was higher than non-infiltrating and benign lesions ( $P = 0.004$ ,  $P < 0.001$ ). There was no significant difference between %RS for the non-infiltrating cancers and benign lesions ( $P = 0.337$ ).

### Enhancement patterns of CESH

Among breast cancers, a type III curve accounted for 60.72% (85 of 140), a type II curve for 35.71% (50 of 140), and a type I curve for 3.57% (5 of 140). As for benign lesions, a type I curve occurred in 43.90% (36 of 82), a type II curve was seen in 45.12% (37 of 82), and a type III curve presented in 10.98% (9 of 82). The difference in enhancement patterns between malignant and benign lesions was significant ( $P < 0.001$ , Table 2). Table 3 provides the enhancement patterns of CESH in differ-

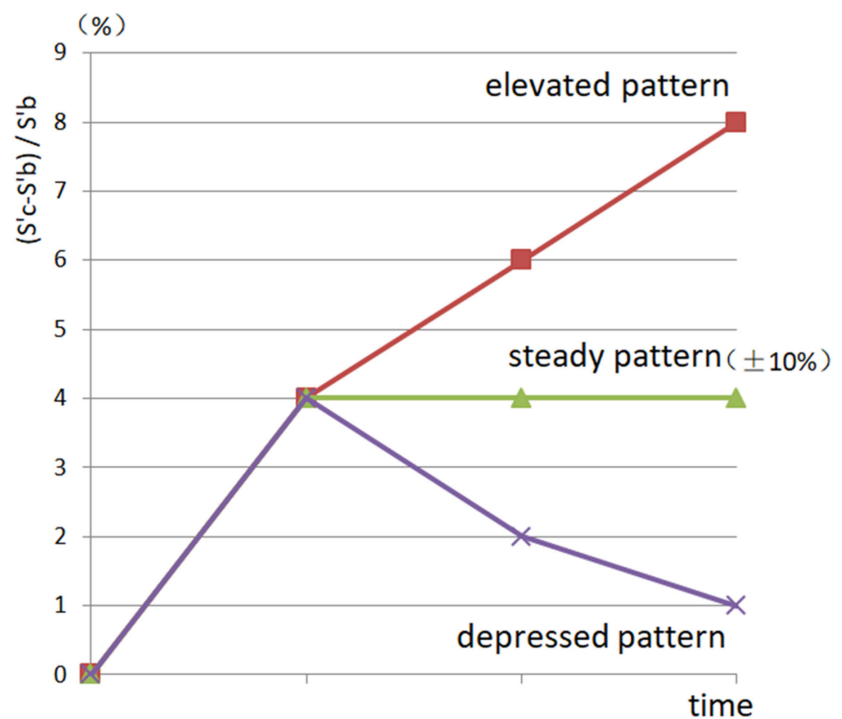


**Figure 2** The patterns of the kinetic curve. Any change from –10% to 10% was considered a steady pattern, more than 10% was considered an elevated pattern, and less than –10% was considered a decreased pattern.

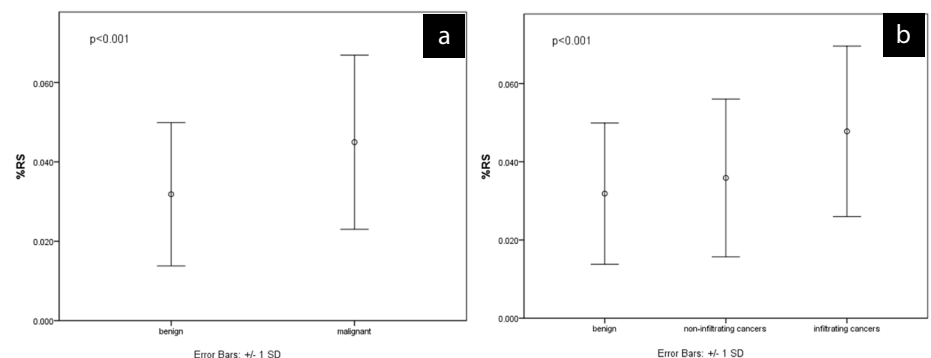


**Figure 3.** (a, b) Comparison of %RS with lesion type. SD, standard deviation.

**Table 1.** Descriptive and multiple comparison statistics

	Type of lesion			P (ANOVA)	P (LSD)		
	Benign (A)	Non-infiltrating cancers (B)	Infiltrating cancers (C)		A vs. B	A vs. C	B vs. C
%RS (mean ± SD)	3.19 ± 1.81	3.58 ± 2.02	4.77 ± 2.18	<0.001	0.337	<0.001	0.004

A, benign; ANOVA, One-Way analysis of variance; B, non-infiltrating cancers; C, infiltrating cancers; LSD, least significant difference; SD, standard deviation.

**Table 2.** Kinetic patterns on CESH between benign and malignant breast lesions

Kinetic pattern	Benign lesions n (%)	Malignant lesions n (%)	P value
Type I	36 (43.90)	5 (3.57)	<0.001
Type II	37 (45.12)	50 (35.71)	
Type III	9 (10.98)	85 (60.72)	

CESM, contrast-enhanced spectral mammography.

**Table 3.** Enhancement patterns on CESH in different histopathological results

Type of lesion		Type of curve			
		Type I n (%)	Type II n (%)	Type III n (%)	Total n (%)
Benign	Adenosis	8 (22.22)	15 (40.54)	1 (11.11)	24 (29.27)
	Fibroadenoma	16 (44.44)	4 (10.81)	3 (33.33)	23 (28.05)
	Intraductal papilloma	4 (11.11)	11 (29.73)	4 (44.45)	19 (23.17)
	Inflammatory lesion	4 (11.11)	6 (16.22)	1 (11.11)	11 (13.41)
	Cysts with infection	3 (8.34)	0 (0.00)	0 (0.00)	3 (3.66)
	Phyllodes tumor	0 (0.00)	1 (2.70)	0 (0.00)	1 (1.22)
	Myofibroblastic neoplasia	1 (2.78)	0 (0.00)	0 (0.00)	1 (1.22)
Total		36	37	9	82
Malignant	Invasive ductal cancer	2 (40.00)	30 (60.00)	72 (84.70)	104 (74.29)
	Ductal carcinoma in situ	3 (60.00)	15 (30.00)	6 (7.06)	24 (17.15)
	Papillary carcinoma	0 (0.00)	3 (6.00)	5 (5.88)	8 (5.72)
	Metaplastic carcinoma	0 (0.00)	0 (0.00)	1 (1.18)	1 (0.71)
	Apocrine carcinoma	0 (0.00)	0 (0.00)	1 (1.18)	1 (0.71)
	Mucinous cancer	0 (0.00)	1 (2.00)	0 (0.00)	1 (0.71)
	Invasive lobular cancer	0 (0.00)	1 (2.00)	0 (0.00)	1 (0.71)
Total		5	50	85	140

CESM, contrast-enhanced spectral mammography.

tion. Comparing the types of kinetic curves on CESH and MRI, the results showed that the accordance rate between the two examination methods was 85.00%, of which 10.00% (12 of 120) were type I curve, 35.83% (43 of 120) were type II, 39.17% (47 of 120) were type III (Figure 5), and the other 15.00% (18 of 120) had inconsistent kinetic curves (Table 5). Cohen's kappa coefficient for CESH and MRI was 0.752 ( $P < 0.001$ ), indicating good agreement (0.6–0.8).

## Discussion

The CESH technique is an emerging modality that combines traditional mammography with administering an intravenous contrast agent and is increasingly being used in diagnostics to differentiate benign lesions from breast cancers. Most malignant lesions are hypervascular, with immature tumor blood vessels. Hence, malignant lesions usually exhibit earlier and stronger enhancement than benign lesions.<sup>4,14</sup> This study showed a significant correlation between a lesion's enhancement intensity (%RS) on CESH and malignancy. The enhancement intensity of benign lesions was lower than that of malignant tumors, and the degree of enhancement of benign lesions and non-invasive cancers was lower than invasive cancers, consistent with the results of Rudnicki et al.<sup>12,15</sup> Nonetheless, the diagnostic efficiency is low (accuracy was 66.20%, AUC was  $0.702 \pm 0.036$ ) if the differentiation between benign and malignant lesions depends on the enhancement intensity. To further improve the diagnostic efficiency of CESH, this study investigated enhancement patterns on CESH between benign lesions and breast cancers. The preliminary research indicated that the difference in enhancement patterns on CESH between malignant and benign lesions was significant, and the AUC was  $0.819 \pm 0.030$ . In breast cancers, the steady or depressed patterns (type II or III) were dominant. On the contrary, benign lesions mainly showed an elevated and steady pattern (type I or II). According to the results of this study, the likelihood of breast cancer related to a type III curve was 90.43%, whereas the likelihood of breast cancer related to a type I curve was only 12.20%.

ent histopathological results. The likelihood of breast cancer related to a type I, II, and III curve was 12.20% (5 of 41), 57.47% (50 of 87), and 90.43% (85 of 94), respectively.

### The ROC analysis results

For the enhancement intensity, the AUC was  $0.702 \pm 0.036$  [95% confidence interval (CI) from 0.631 to 0.773,  $P < 0.001$ ]. According to the Youden index, the optimal cut-off value of %RS for the differentiation between benign and malignant lesions was 3.60, sensitivity was 64.00%, specificity was 72.00%, accuracy was 66.20%, positive likelihood ratio was 2.14, and negative likelihood ratio was 0.50. For enhancement patterns, the AUC increased to  $0.819 \pm 0.030$  (95% CI from 0.761 to 0.877,  $P < 0.001$ ). Figure 4 shows the ROC curves. The difference between the two

AUC values was statistically significant ( $P < 0.001$ ).

### Inter-reader variability of enhancement pattern classification

In 91.89% (204 of 222) of cases, the two readers had consistent results in enhancement patterns. In the 18 (8.11%) cases with inconsistent classification, there were differences between type I and type II or type II and type III. There was no difference in classification between type I and type III (Table 4). The kappa coefficient was 0.873 ( $P < 0.001$ ), indicating excellent inter-reader agreement.

### Comparison of enhancement patterns in CESH and MRI

One hundred twenty patients with 120 lesions underwent CESH and MRI examina-

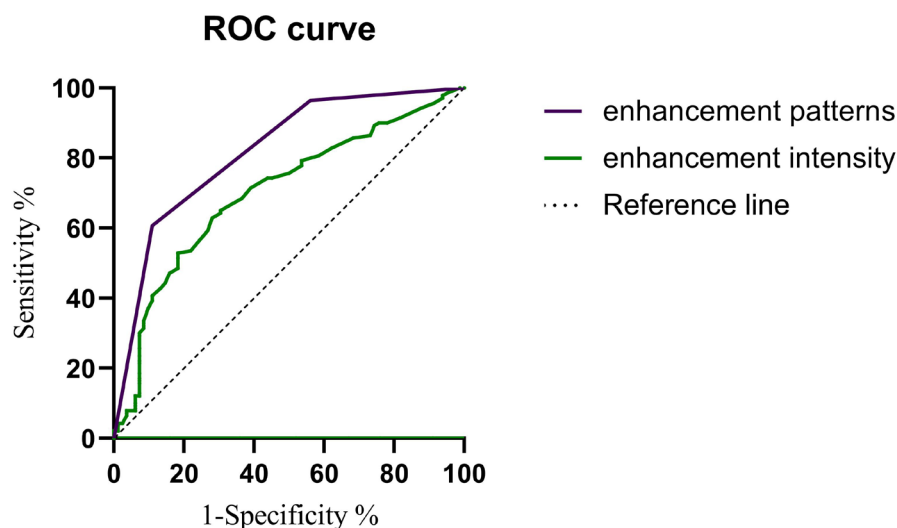


**Figure 4.** Receiver operating characteristic curves for enhancement intensity and enhancement patterns. ROC, receiver operating characteristic.

**Table 4.** Comparison of enhancement patterns between reader 1 and reader 2

Reader 1	Reader 2			Total
	Type I	Type II	Type III	
Type I	41	1	0	42
Type II	2	78	9	89
Type III	0	6	85	91
Total	43	85	94	222

Until now, there have been only a few studies about the kinetic investigation of CESM. Jong et al.<sup>16</sup> and Dromain et al.<sup>17</sup> conducted a small sample study using a temporal subtraction method instead of a dual-energy approach to CESM. In their studies, a mask image and a post-contrast image were obtained before and after the injection of a contrast agent, and a subtraction image was derived from imaging post-processing. Their technique was more susceptible to motion. Jong et al.<sup>16</sup> showed that 4 of 10 (40%) breast cancer lesions had a plateau curve, 3 of 10 (30%) presented with a washout curve, 1 of 10 (10%) had increasing enhancement, and 2 of 10 (20%) had no enhancement. Due to a limited number of patients, statistical significance was not measured in that study. In the study by Dromain et al.<sup>17</sup>, they acquired the images from 30 s to 7 min and considered early if the enhancement peak was before 1 min 30 s. In their few cases, gradually increasing enhancement (35%, 7/20) was the most common kinetic curve observed in breast cancers, and a washout curve was only found in 20% of cases. They considered that the discrepancy between kinetic curves observed using CESM and MRI might be due to the compression of the breast, which may alter blood flow. In addition, the different kinetic patterns may be caused by the differ-

ence in acquisition times. Recent studies<sup>18-20</sup> showed that the comparison of enhancement patterns on CESM between malignant and benign lesions was significant. Deng et al.<sup>18</sup> used the time interval between the CC projection and mediolateral (MLO) projection to assess relative enhancement patterns. Among the relative enhancement patterns, the incidence of malignant and benign lesions was 73.08% (19/26) and 26.92% (7/26) in the elevated pattern, 92.86% (13/14) and 7.14% (1/14) in the steady pattern, 94.29% (66/70) and 5.71% (4/70) in the depressed pattern, and 20.0% (32/40) and 80.00% (8/40) in non-enhancement lesions, respectively. Liu et al.<sup>19</sup> also evaluated the enhancement patterns based on two different views of CC and MLO. This may affect the results since the tissues superimposed and adjacent to the lesions will be different in different positions. Reported in their study was an accordance rate of 64.2% for enhancement patterns on CESM and MRI. The study by Huang et al.<sup>20</sup> demonstrated that the washout pattern was significantly associated with malignant lesions at 2–4 and 2–10 min frames based on two readers' interpretations. However, they did not evaluate the diagnostic efficacy of enhancement patterns on CESM in detail, nor did they compare it with TIC on MRI. All images in that study were obtained on MLO view

without releasing the paddle. The enhancement of suspicious lesions was semi-quantitatively analyzed using a 10-point grayscale reference bar.

In the present study, the CC view was used because it was easier for the patients to remain motionless in this projection.<sup>16,17</sup> The patients' motion can cause faulty kinetic curves. Thus, care was taken to keep the ROI at the same position of the lesion at each imaging time point.<sup>21</sup> Only three CC views were performed on the affected breast to reduce the patients' radiation dose. Because the signal value differences of the lesions at different time points after enhancement were small in absolute values, and the pre-contrast signal values on the recombined images of breast lesions were roughly equal to the post-contrast signal values of background, the %RS on CESM was used to make it comparable to DCE-MRI.<sup>12</sup>

Some studies have shown a significant correlation between enhancement patterns and a moderate agreement (Cohen's kappa coefficient was 0.438 and 0.515) between contrast-enhanced digital breast tomosynthesis or CESM and MRI.<sup>19,22</sup> By comparing the enhancement patterns of CESM and MRI, we found that the accordance rate of the two examination methods was 85.0%, and the agreement was good (Kappa coefficient: 0.752).

The present study had some limitations. Firstly, this study had a limited number of patients from a single institution. Nonetheless, the sample size in this study was the largest for kinetic curves on CESM. Secondly, the radiation dose of CESM was not considered. Previous studies have shown that the combined radiation dose estimated from low- and high-energy views is about 1.2 times that of conventional FFDM.<sup>11,23</sup> The dose values of CESM meet the recommendations for the maximum dose in mammography.<sup>24</sup> Although the radiation dose is increased, CESM provides radiologists with a standard low-energy image (similar to FFDM) and a recombined image highlighting angiogenesis areas. In the future, when a CESM examination is planned, additional FFDM can be avoided, with the possibility of saving up to 48.5% of the radiation dose (depending on the system used).<sup>25</sup> This study's authors plan to explore ways to reduce radiation doses in further studies. Thirdly, CESM was not arranged according to the patients' menstrual cycles. The background parenchymal enhancement may be more obvious in patients with CESM before menstruation, which will

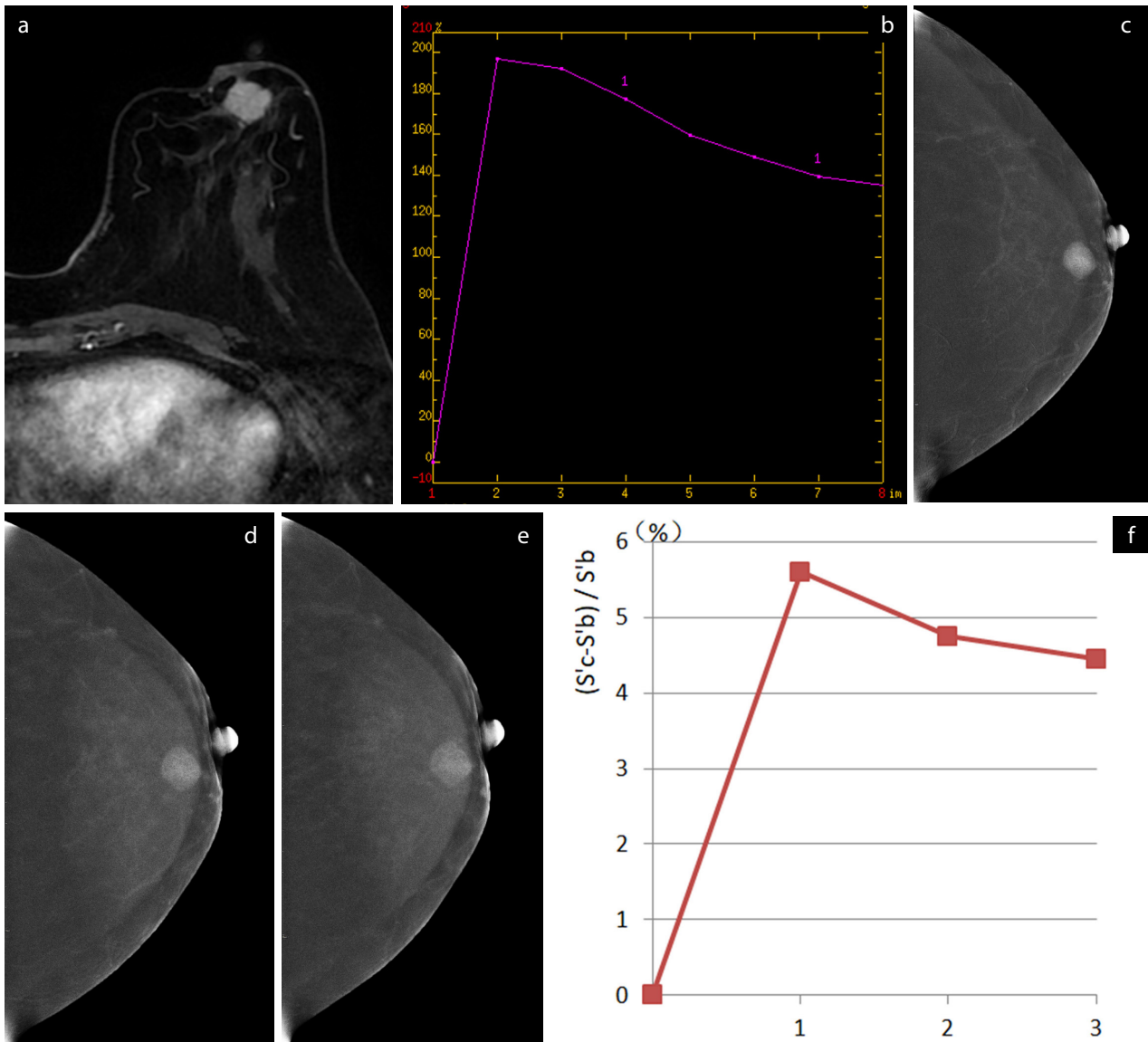


**Figure 5.** An invasive ductal carcinoma in the left breast of a 45-year-old woman. An early post-contrast magnetic resonance image depicts a strongly enhancing lesion (a). The time-signal intensity curve of the mass on magnetic resonance imaging shows a washout time course (b). The subtraction images of contrast-enhanced spectral mammography (CESM) obtained 3, 5, and 7 min after the contrast agent injection show a round circumscribed mass, and the enhancement intensity decreases with time (c-e). The kinetic curve of contrast enhancement derived from the receiver operating characteristics drawn in this lesion on CEM shows a depressed pattern (f).

**Table 5.** Comparison of enhancement patterns between CESM and MRI

CESM	MRI			Total
	Type I	Type II	Type III	
Type I	12	3	0	15
Type II	4	43	4	51
Type III	0	7	47	54
Total	16	53	51	120

CESM, contrast-enhanced spectral mammography; MRI, magnetic resonance imaging.

affect the accuracy of the measurement results. In addition, the enhancement patterns in breast cancers with different histopathology were not discussed because of the small number of patients in each subtype. Finally, there is no commercial tool for the quantitative analysis of the kinetic curve on CESM.

The ROI was drawn manually, which was subjective and time-consuming. The inter- and intra-observer reproducibility may be poor. Nevertheless, this study demonstrated that the agreement was excellent (Kappa coefficient: 0.873) for the curve types between the two readers.

In conclusion, our results showed that the kinetic pattern of enhanced lesions on CESM effectively differentiates benign from malignant breast lesions, with good agreement, when compared with MRI.

#### Acknowledgments

The authors would like to thank Junjing Zhao and Xiujian Liu for their help in creating this article.

#### Conflict of interest disclosure

The authors declared no conflicts of interest.

## References

1. Sung H, Ferlay J, Siegel RL, et al. Global Cancer Statistics 2020: GLOBOCAN estimates of incidence and mortality worldwide for 36 cancers in 185 countries. *CA Cancer J Clin.* 2021;71(3):209-249. [\[CrossRef\]](#)
2. Lee SH, Jang MJ, Kim SM, et al. Factors affecting breast cancer detectability on digital breast tomosynthesis and two-dimensional digital mammography in patients with dense breasts. *Korean J Radiol.* 2019;20(1):58-68. [\[CrossRef\]](#)
3. Abdullah N, Mesurolle B, El-Khoury M, Kao E. Breast imaging reporting and data system lexicon for US: interobserver agreement for assessment of breast masses. *Radiology.* 2009;252(3):665-672. [\[CrossRef\]](#)
4. Kuhl CK, Mielcareck P, Klaschik S, et al. Dynamic breast MR imaging: are signal intensity time course data useful for differential diagnosis of enhancing lesions? *Radiology.* 1999;211(1):101-110. [\[CrossRef\]](#)
5. Mann RM, Kuhl CK, Kinkel K, Boetes C. Breast MRI: guidelines from the European Society of Breast Imaging. *Eur Radiol.* 2008;18(7):1307-1318. [\[CrossRef\]](#)
6. Ghaderi KF, Phillips J, Perry H, Lotfi P, Mehta TS. Contrast-enhanced mammography: current applications and future directions. *Radiographics.* 2019;39(7):1907-1920. [\[CrossRef\]](#)
7. Fallenberg EM, Schmitzberger FF, Amer H, et al. Contrast-enhanced spectral mammography vs. mammography and MRI - clinical performance in a multi-reader evaluation. *Eur Radiol.* 2017;27(7):2752-2764. [\[CrossRef\]](#)
8. Kim EY, Youn I, Lee KH, et al. Diagnostic value of contrast-enhanced digital mammography versus contrast-enhanced magnetic resonance imaging for the preoperative evaluation of breast cancer. *J Breast Cancer.* 2018;21(4):453-462. [\[CrossRef\]](#)
9. Clauser P, Baltzer PAT, Kapetas P, et al. Low-dose, contrast-enhanced mammography compared to contrast-enhanced breast MRI: a feasibility study. *J Magn Reson Imaging.* 2020;52(2):589-595. [\[CrossRef\]](#)
10. James JJ, Tennant SL. Contrast-enhanced spectral mammography (CESM). *Clin Radiol.* 2018;73(8):715-723. [\[CrossRef\]](#)
11. Dromain C, Thibault F, Diekmann F, et al. Dual-energy contrast-enhanced digital mammography: initial clinical results of a multireader, multicase study. *Breast Cancer Res.* 2012;14(3):R94. [\[CrossRef\]](#)
12. Rudnicki W, Heinze S, Niemiec J, et al. Correlation between quantitative assessment of contrast enhancement in contrast-enhanced spectral mammography (CESM) and histopathology-preliminary results. *Eur Radiol.* 2019;29(11):6220-6226. [\[CrossRef\]](#)
13. Landis JR, Koch GG. The measurement of observer agreement for categorical data. *Biometrics.* 1977;33(1):159-174. [\[CrossRef\]](#)
14. Watt AC, Ackerman LV, Windham JP, et al. Breast lesions: differential diagnosis using digital subtraction angiography. *Radiology.* 1986;159(1):39-42. [\[CrossRef\]](#)
15. Rudnicki W, Heinze S, Popiela T, Kojs Z, Luczynska E. Quantitative assessment of contrast enhancement on contrast enhancement spectral mammography (CESM) and comparison with qualitative assessment. *Anticancer Res.* 2020;40(5):2925-2932. [\[CrossRef\]](#)
16. Jong RA, Yaffe MJ, Skarpathiotakis M, et al. Contrast-enhanced digital mammography: initial clinical experience. *Radiology.* 2003;228(3):842-850. [\[CrossRef\]](#)
17. Dromain C, Balleyguier C, Muller S, et al. Evaluation of tumor angiogenesis of breast carcinoma using contrast-enhanced digital mammography. *AJR Am J Roentgenol.* 2006;187(5):W528-W537. [\[CrossRef\]](#)
18. Deng CY, Juan YH, Cheung YC, et al. Quantitative analysis of enhanced malignant and benign lesions on contrast-enhanced spectral mammography. *Br J Radiol.* 2018;91(1086):20170605. [\[CrossRef\]](#)
19. Liu Y, Zhao S, Huang J, et al. Quantitative analysis of enhancement intensity and patterns on contrast-enhanced spectral mammography. *Sci Rep.* 2020;10(1):9807. [\[CrossRef\]](#)
20. Huang JS, Pan HB, Yang TL, et al. Kinetic patterns of benign and malignant breast lesions on contrast enhanced digital mammogram. *PLoS One.* 2020;15(9):e0239271. [\[CrossRef\]](#)
21. Kuhl CK, Jost P, Morakkabati N, Zivanovic O, Schild HH, Gieseke J. Contrast-enhanced MR imaging of the breast at 3.0 and 1.5 T in the same patients: initial experience. *Radiology.* 2006;239(3):666-676. [\[CrossRef\]](#)
22. Froeling V, Diekmann F, Renz DM, et al. Correlation of contrast agent kinetics between iodinated contrast-enhanced spectral tomosynthesis and gadolinium-enhanced MRI of breast lesions. *Eur Radiol.* 2013;23(6):1528-1536. [\[CrossRef\]](#)
23. Lobbes MB, Smidt ML, Houwers J, Tjan-Heijnen VC, Wildberger JE. Contrast enhanced mammography: techniques, current results, and potential indications. *Clin Radiol.* 2013;68(9):935-944. [\[CrossRef\]](#)
24. Jeukens CR, Lalji UC, Meijer E, et al. Radiation exposure of contrast-enhanced spectral mammography compared with full-field digital mammography. *Invest Radiol.* 2014;49(10):659-665. [\[CrossRef\]](#)
25. Fallenberg EM, Dromain C, Diekmann F, et al. Contrast-enhanced spectral mammography: does mammography provide additional clinical benefits or can some radiation exposure be avoided? *Breast Cancer Res Treat.* 2014;146(2):371-381. [\[CrossRef\]](#)



# High-resolution diffusion-weighted imaging compared with conventional diffusion-weighted imaging and dynamic contrast-enhanced magnetic resonance imaging with regard to image quality and assessment of breast cancer morphology

Yavuz Metin   
Nurgül Orhan Metin   
Sibel Kul   
Filiz Taşçı   
Oğuzhan Özdemir   
Ali Küpeli 

From the Department of Radiology (Y.M. ✉ ymetin53@gmail.com), Ankara University Faculty of Medicine, Ankara, Turkey; Clinic of Radiology (N.O.M.), Beytepe Murat Erdi Eker State Hospital, Ankara, Turkey; Department of Radiology (S.K.), Karadeniz Technical University Faculty of Medicine, Trabzon, Turkey; Department of Radiology (F.T.), Recep Tayyip Erdoğan University Faculty of Medicine, Rize, Turkey; Clinic of Radiology (O.Ö.), Keçiören Medical Park Hospital, Ankara, Turkey; Clinic of Radiology (A.K.), Trabzon Kanuni Training and Research Hospital, Trabzon, Turkey

Received 24 April 2021; revision requested 28 May 2021; last revision received 29 November 2021; accepted 30 December 2021.



Epub: 10.02.2023

Publication date: 29.03.2023

DOI: 10.5152/dir.2022.21362

## PURPOSE

To evaluate the image quality and tumor morphology depiction ability of high resolution (HR) diffusion-weighted imaging (f-DWI) in comparison to conventional DWI (c-DWI) and dynamic contrast-enhanced magnetic resonance imaging (DCE-MRI) in the primary breast cancer setting.

## METHODS

The f-DWI, c-DWI, and DCE-MRIs of 160 malignant breast masses were evaluated retrospectively by two independent radiologists. Data on image quality [sharpness, distortion, and perceived signal-to-noise ratio (SNR)], apparent diffusion coefficient (ADC) value, lesion size, and tumor morphology (shape, margin, and internal pattern) obtained on f-DWI, c-DWI, and DCE-MRI were compared. Consistency between the readers and imaging methods for morphological parameters was analyzed.

## RESULTS

The ADC values measured on f-DWI were significantly lower than those measured on c-DWI for both readers ( $P < 0.001$  for each), whereas mean lesion size was significantly larger in c-DWI than in f-DWI and DCE-MRI for both readers ( $P < 0.001$  for each). Higher consistency values were obtained for f-DWI compared with c-DWI when correlated with DCE-MRI for each morphological parameter. The least distorted images were obtained using DCE-MRI compared with c-DWI and f-DWI for both readers, whereas the highest distortion scores were obtained using c-DWI. Sharpness and perceived SNR scores were rated as significantly higher for f-DWI and DCE-MRI images compared with c-DWI by both readers ( $P < 0.001$  for all). The concordance between c-DWI and DCE-MRI was fair to slight ( $\kappa = 0.15$  to  $0.41$ ), whereas concordance between f-DWI and DCE-MRI was significantly better ( $\kappa = 0.68$  to  $0.87$ ) for each reader and for all morphological parameters ( $P < 0.001$ ). The highest concordance between the readers was achieved in margin assessment ( $\kappa = 0.87$  to  $0.89$ ) regardless of the MRI method, followed by shape and internal pattern parameters ( $\kappa = 0.63$  to  $0.79$ ).

## CONCLUSION

The results demonstrated that f-DWI produces higher-quality images than c-DWI, enabling the morphological features to be identified in similar detail to that offered by HR DCE-MRI. Accordingly, f-DWI, as a method that highly correlates with DCE in determining the morphological characteristics of breast cancers, seems to have potential in the evaluation of breast tumors in patients for whom the use of contrast media is contraindicated.

## KEYWORDS

Breast cancer, conventional, high resolution diffusion weighted, magnetic resonance imaging, tumor morphology

You may cite this article as: Metin Y, Orhan Metin N, Kul S, Taşçı F, Özdemir O, Küpeli A. High-resolution diffusion-weighted imaging compared with conventional diffusion-weighted imaging and dynamic contrast-enhanced magnetic resonance imaging with regard to image quality and assessment of breast cancer morphology. *Diagn Interv Radiol.* 2023;29(2):251-259.

**M**agnetic resonance imaging (MRI) techniques have become increasingly used as the preferred imaging modality for the diagnosis, staging, and follow-up of breast cancer.<sup>1,2</sup> Dynamic contrast-enhanced (DCE) MRI series are routinely used because of their high contrast and spatial resolution; however, contrast agent-related side effects or contraindications such as renal insufficiency or known allergic reactions are the major drawbacks of this technique.<sup>3,4</sup> Diffusion-weighted imaging (DWI), a non-contrast-MRI method based on the production of images from the random Brownian motion of water molecules, is considered highly effective in the differential diagnosis of breast tumors and is commonly applied as an adjunct to DCE-MRI for breast imaging.<sup>5,6</sup>

Conventional DWI (c-DWI), applied using single-shot echo-planar imaging (ss-EPI) in most cases, is considered favorable because of its speed. However, low spatial resolution; the high frequency of distortion, blurring, and artifacts; and low signal-to-noise ratio (SNR) are some of the major disadvantages of this technique.<sup>7,8</sup> With recent technological advances, high-resolution (HR) DWI has become a popular method with its increased spatial resolution and reduction in artifacts and distortions, compared with c-DWI.<sup>9-11</sup>

One of the improved HR-DWI approaches is to implement a reduced field-of-view (rFOV) acquisition. This is a technique called focus DWI (f-DWI), which aims to shorten the required readout duration for ss-EPI.<sup>2,12,13</sup> The manner in f-DWI differs from other rFOV techniques in terms of active excitation of the imaging region of interest (ROI) itself, which does not necessitate outer-volume suppression pulses, with a likelihood of potentially higher specific absorption rates.<sup>14</sup> In contrast to inner-volume methods, this technique allows contiguous multislice imaging without

the need for a slice skip<sup>15</sup> and concomitantly suppresses the signal from fat, which is considered to be important in breast imaging.<sup>2</sup>

Although HR-DWI is mainly used in the field of neuroradiology, its importance in breast imaging has also been emphasized in recent years.<sup>9-11</sup> In breast imaging, c-DWI has mainly been used for the quantitative evaluation [determination of apparent diffusion coefficient (ADC) values] of breast lesions. However, obtaining high-quality images using HR-DWI demonstrated that DWIs can also be used qualitatively, such as for determining tumor morphology. In this context, there are a few publications comparing the compatibility of HR-DWI with c-DWI and DCE-MRI in determining the morphological features of breast lesions. However, in these studies, conducted with small numbers of patients, the aim was to compare the image quality rather than evaluate the morphological features in detail.<sup>2,11,16-20</sup>

In this study with the participation of a large number of patients with breast cancer, the aim was to compare f-DWI with both c-DWI and DCE-MRI in characterizing all morphological features (shape, margin, internal pattern, and size) of the tumor and in terms of image quality.

## Methods

### Study population

A total of 175 patients who had undergone breast MRI, including both f-DWI and c-DWI, using a 3T MRI scanner and who had a pathologically proven breast cancer diagnosis were included in this retrospective study conducted between November 2014 and September 2017. Patients with available data on three methods (f-DWI, c-DWI, and DCE-MRI) of imaging with sufficient image quality were included in the study. Non-mass enhancement, focus-type lesions, cysts, concomitant neoadjuvant chemotherapy, and insufficient image quality were the exclusion criteria of the study. After the exclusion of 11 patients in the c-DWI group, 5 patients in the f-DWI group, and 4 patients in the DCE-MRI group upon detection of motion artifacts affecting image quality, a total of 155 consecutive patients with 160 breast tumors comprised the study population.

The ethics committee of our university hospital approved this study (date of approval: 16/06/2017; reference number/protocol no: 2017/96). Informed consent was waived due to the retrospective design of the study.

### Study parameters

Data on ADC values ( $10^{-3}$  mm<sup>2</sup>/s), lesion size (mm), tumor morphology (shape, margin, and internal pattern), image quality (sharpness, distortion, and perceived SNR) obtained using f-DWI, c-DWI, and DCE-MRI were compared. Consistency analyses between the two DWI methods and DCE-MRI were performed for both morphological parameters and image quality. Interobserver agreement was also analyzed.

### Magnetic resonance imaging methods

MRI scanning was performed using a 3.0-T MR (GE Healthcare Discovery MR750, Waukesha, WI, USA) together with a 16-channel dedicated breast coil. Patients lay in a prone position, with the breasts inside the breast coil. A survey sequence was followed by axial T1-weighted (T1W) sequence and fat-saturated T2-weighted (T2W) fast spin-echo sequence for both breasts prior to contrast administration to avoid signal alteration as a result of the injected gadolinium. For DCE-MRI, the contrast agent gadobutrol (Gadovist, Bayer Schering Pharma, Berlin, Germany) was injected (0.1 mmol/kg bolus injection, flow rate of 2 mL/s), and then the residual contrast agent in the catheter was rinsed with 20 mL of saline at the same rate. After the injection, six phases of volume imaging for breast assessment (VIBRANT-Flex) were employed, with approximately 60-s intervals between each phase and a total scanning of 410 s [repetition time (TR) 3.9 ms, shortest echo time TE, flip angle 12, FOV 360–360 mm, matrix 320–320, layer thickness 1.4 mm].

Subsequently, c-DWI and then f-DWI were performed before the contrast injection by using the same b-values (0–800 s/mm<sup>2</sup>). The target for f-DWI was determined by reviewing the clinical and conventional imaging findings and with the assistance of non-contrast MRI (axial fat-saturated T2W and T1W images). A combined sequence using the array spatial sensitivity encoding technique was conducted prior to scanning. The scanning parameters of c-DWI and f-DWI were a TR of 3600 ms, FOV of 360–360 mm, matrix of 160–160 of matrix, shortest TE, 1 mm gap, 4 mm slice thickness, bandwidth of 250, and 6 excitations. The scanning time was 76 s for c-DWI and 164 s for f-DWI.

### Morphological analysis

All MR images were reviewed retrospectively by two dedicated breast radiologists (YM and NOM, who had 6-years' and 4-years'

#### Main points

- In determining the morphological characteristics of primary breast cancer, high-resolution (HR) diffusion-weighted imaging (f-DWI) shows good consistency with dynamic contrast-enhanced magnetic resonance imaging and is superior to conventional DWI (c-DWI).
- Having less distortion and obtaining a higher perceived signal-to-noise ratio and sharpness significantly increases the image quality of f-DWI images compared with c-DWI.
- High-quality images obtained with f-DWI will positively increase the problem-solving ability of c-DWI, especially in situations where contrast material cannot be used.

experience of breast imaging, respectively) blinded to the clinical history and other primary imaging findings. The radiologists independently evaluated the morphological features of the masses in separate sessions for f-DWI, c-DWI, and DCE-MRI at 3-week intervals on a GE Healthcare workstation (ADW 4.5, GE Healthcare, Waukesha, WI, USA). The shape, margin, and internal pattern of each case were evaluated on high *b* value (800 s/mm<sup>2</sup>) f-DWI and c-DWI images and on subtracted and non-subtracted DCE-MR images obtained in the second minute postcontrast. Morphological descriptors defined in the fifth edition of the American College of Radiology Breast Imaging Reporting and Data System (BI-RADS)<sup>21</sup> were used. Accordingly, the shapes of the masses were categorized as round, oval, and irregular. The margins of the masses were categorized as circumscribed and non-circumscribed, and the internal patterns of the masses were categorized as homogeneous, heterogeneous, and rim type. The internal enhancement pattern was arranged as an internal pattern to be compatible with DWI, which is an unenhanced imaging method. The ADC values on the DWIs and the longest diameter of the masses on the axial slices in each imaging method (high *b* values of DWIs and subtracted postcontrast 2<sup>nd</sup> minute images of DCE) were measured. The ADC measurement was performed by placing circular ROIs within the targeted lesion on ADC maps. The portion of the lesion showing the most diffusion restriction was determined visually, and the mean ADC measurements were performed from this area. A

circular ROI was placed inside the lesion and made as large as possible while avoiding cystic, necrotic or hemorrhagic areas and obvious artifacts. The ROI size was set at ≥2 cm<sup>2</sup>. For each lesion, at least three measurements were taken, and the lowest value was used.

### Analysis of image quality

After the analysis of the morphological features of the breast tumors, another session was organized to evaluate the quality of the f-DWI, c-DWI, and DCE-MR images. Both readers independently evaluated all imaging methods simultaneously. Image quality was evaluated in three categories: sharpness (5 point scale: 1 = unsharp to 5 = very sharp), distortion (4-point scale: 0 = no distortion to 3 = severe distortion), and perceived SNR (5-point scale: 1 = very poor to 5 = excellent).

### Statistical analysis

Statistical analysis was performed using SPSS 15.0 software (SPSS Inc., Chicago, IL, USA) and the MedCalc package (version 16.8, Ostend, Belgium). Descriptive statistics of the data are presented as n (%). Non-normalized variables are presented as median (range), and normal distributions are presented as mean ± standard deviation. The Kolmogorov–Smirnov test was used to show deviation from the normal distribution. The non-parametric Wilcoxon test (Table 1) was used by each reader to compare the ADC values obtained in c-DWI and f-DWI. A paired t-test (Table 2) was used to compare lesion size measured on f-DWI and DCE-MRI with lesion size measured on c-DWI for the same reader.

The Freidman test with the Bonferroni correction was used to compare the sharpness, distortion, and perceived SNR scores (categorized in Table 3; the readers rated image quality on point scales) measured on f-DWI, c-DWI, and DCE-MRI by the same reader. The Wilcoxon test was used for pairwise comparisons. Agreement between methods and readers was evaluated using Cohen's kappa coefficients and intraclass correlation (ICC), and expressed using kappa and ICC values, with 0.81–1.00, 0.61–0.80, 0.41–0.60, 0.21–0.40, and 0.10–0.20 indicating a very good, good, moderate, fair, and slight strength of agreement, respectively.<sup>22,23</sup> *P* < 0.05 was considered significant.

## Results

In the current study, 160 malignant breast mass lesions (multifocal tumors in four patients and bilateral breast cancer in one patient) were evaluated, including invasive ductal carcinoma with no special type (*n* = 135), invasive lobular carcinoma (*n* = 9), mucinous carcinoma (*n* = 8), ductal carcinoma *in situ* (*n* = 3), malignant phyllodes tumor (*n* = 2), medullary carcinoma (*n* = 2), and tubular carcinoma (*n* = 1). The median age of the patients was 52 years (range 17–87 years).

### Breast lesion characteristics on imaging analysis

The ADC values measured on f-DWI were significantly lower than those measured on c-DWI for both readers (*P* < 0.001) (Table 1).

The tumor shape was considered to be

**Table 1.** Breast tumor characteristics on c-DWI, f-DWI, and DCE-MRI

	Reader 1			Reader 2		
	c-DWI	f-DWI	DCE-MRI	c-DWI	f-DWI	DCE-MRI
ADC (x10 <sup>-3</sup> mm <sup>2</sup> /s), median (range)	0.95 (0.55–1.97)	0.83 (0.24–1.82)	-	0.93 (0.55–1.90)	0.88 (0.24–1.87)	-
<i>P</i> value of ADC	<0.001			<0.001		
<b>Tumor morphology, n (%)</b>						
<b>Shape</b>						
Round	54 (33.75)	16 (10.00)	13 (8.12)	52 (32.50)	31 (19.38)	27 (16.88)
Oval	37 (23.12)	18 (11.25)	26 (16.25)	26 (16.25)	21 (13.12)	21 (13.12)
Irregular	69 (43.13)	126 (78.75)	121 (75.63)	82 (51.25)	108 (67.50)	112 (70.00)
<b>Margin</b>						
Circumscribed	92 (57.50)	47 (29.37)	52 (32.50)	100 (62.50)	68 (42.50)	60 (37.50)
Non-circumscribed	68 (42.50)	113 (70.63)	108 (67.50)	60 (37.50)	92 (57.50)	100 (62.50)
<b>Internal pattern</b>						
Homogeneous	93 (58.13)	24 (15.00)	20 (12.50)	82 (51.25)	45 (28.12)	48 (30.00)
Heterogeneous	37 (23.12)	56 (35.00)	60 (37.50)	50 (31.25)	64 (40.00)	67 (41.88)
Rim type	30 (18.75)	80 (50.00)	80 (50.00)	28 (17.50)	51 (31.88)	45 (28.12)
c-DWI, conventional diffusion-weighted imaging; f-DWI, focus diffusion-weighted imaging; DCE-MRI, dynamic contrast-enhanced magnetic resonance imaging; ADC, apparent diffusion coefficient.						

irregular in most cases regardless of the MRI method; however, the tumor margin was defined as circumscribed in c-DWIs (57.50% of cases for reader 1; 62.50% of cases for reader 2) and non-circumscribed in f-DWI (70.63%

of cases for reader 1; 57.50% of cases for reader 2) and DCE-MRI (67.50% of cases for reader 1; 62.50% of cases for reader 2) by both readers. The tumor internal pattern was defined as homogeneous in c-DWI by both

readers (58.13% of cases for reader 1; 51.25% of cases for reader 2), whereas reader 1 defined it as rim type (50% of cases with both methods) and reader 2 as heterogeneous in f-DWI (40% of cases) and DCE-MRI (41.88% of

**Table 2.** Comparison of lesion dimensions (mm) of c-DW with f-DW and DCE-MRI

	Reader 1			Reader 2		
	f-DWI	c-DWI	DCE-MRI	f-DWI	c-DWI	DCE-MRI
mean ± SD	27 ± 16	28 ± 17	27 ± 16	27 ± 16	28 ± 17	27 ± 15
<i>P</i> value		<0.001			<0.001	

c-DWI, conventional diffusion-weighted imaging; f-DWI, focus diffusion-weighted imaging; DCE-MRI, dynamic contrast-enhanced magnetic resonance imaging; SD, standard deviation.

**Table 3.** Frequencies of image quality analysis scores on c-DWI, f-DWI, and DCE-MRI images

	Reader 1			Reader 2		
	c-DWI	f-DWI	DCE-MRI	c-DWI	f-DWI	DCE-MRI
<b>Image quality, n (%)</b>						
<b>Sharpness</b>						
Median (range)	3 (1–5)	5 (3–5)	5 (4–5)	4 (1–5)	5 (3–5)	5 (4–5)
1 = unsharp	1 (1%)	-	-	1 (1%)	-	-
2 = somewhat unsharp	25 (16%)	-	-	18 (11%)	-	-
3 = moderately sharp	63 (39%)	9 (6%)	-	65 (40%)	8 (5%)	-
4 = sharp	62 (38%)	60 (37%)	32 (20%)	67 (42%)	51 (32%)	32 (20%)
5 = very sharp	9 (6%)	91 (57%)	128 (80%)	9 (6%)	101 (63%)	128 (80%)
<i>P</i> value		<0.001			<0.001	
<i>P</i> value (sharp dw-sharp focus)		<0.001			<0.001	
<i>P</i> value (sharp dw-sharp c)		<0.001			<0.001	
<i>P</i> value (sharp focus-sharp c)		0.013			0.082	
<b>Distortions</b>						
Median (range)	2 (0–3)	0 (0–2)	0 (0–1)	2 (0–3)	1 (0–2)	0 (0–1)
0 = no distortions	25 (16%)	77 (48%)	142 (89%)	24 (15%)	75 (47%)	139 (87%)
1 = some, interpretable	58 (35%)	76 (47%)	18 (11%)	58 (36%)	77 (48%)	21 (13%)
2 = severe, interpretable	68 (43%)	7 (5%)	-	69 (43%)	8 (5%)	-
3 = severe, uninterpretable	9 (6%)	-	-	9 (6%)	-	-
<i>P</i> value		<0.001			<0.001	
<i>P</i> value (sharp dw-sharp focus)		<0.001			<0.001	
<i>P</i> value (sharp dw-sharp c)		<0.001			<0.001	
<i>P</i> value (sharp focus-sharp c)		<0.001			<0.001	
<b>Perceived SNR</b>						
Median (range)	4 (1–5)	5 (3–5)	5 (3–5)	4 (1–5)	5 (3–5)	5 (3–5)
1 = very poor	2 (1%)	-	-	2 (1%)	-	-
2 = poor	21 (13%)	-	-	19 (12%)	-	-
3 = acceptable	56 (35%)	4 (3%)	1 (1%)	56 (35%)	3 (2%)	1 (1%)
4 = good	66 (42%)	59 (37%)	31 (19%)	68 (42%)	57 (36%)	28 (17%)
5 = excellent	15 (9%)	97 (60%)	128 (80%)	15 (9%)	100 (62%)	131 (82%)
<i>P</i> value		<0.001			<0.001	
<i>P</i> value (sharp dw-sharp focus)		<0.001			<0.001	
<i>P</i> value (sharp dw-sharp c)		<0.001			<0.001	
<i>P</i> value (sharp focus-sharp c)		0.088			0.108	

Bonferroni correction adjusted *P* value was 0.0167 for Table 3. c-DWI, conventional diffusion-weighted imaging; f-DWI, focus diffusion-weighted imaging; DCE-MRI, dynamic contrast-enhanced magnetic resonance imaging; SNR, signal-to-noise ratio.

cases) (Table 1).

The mean lesion size was significantly larger in c-DWI than in f-DWI and DCE-MRI for both readers ( $P < 0.001$ ) (Table 2).

### Image quality analysis

The findings on image quality analysis based on each method are provided in Table 3. The quality analysis on c-DWI demonstrated that 12%–16% of images were unsharp, a total of 5% of images were uninterpretable due to distortions, and 13%–14% of cases had poor perceived SNR. However, unsharp, uninterpretable due to severe distortion, and poorly perceived SNR images were not detected in f-DWI and DCE-MRI (Table 3).

The least distorted images were obtained in DCE-MRI for both readers, whereas the highest distortion scores were obtained in c-DWI (Table 3, Figure 1). Sharpness and perceived SNR scores were rated as significantly higher for f-DWI and DCE-MRI images than for c-DWI by both readers ( $P < 0.001$  for all). No significant difference was noted between f-DWI and DCE-MRI in terms of sharpness and perceived SNR scores for both readers (for reader 1,  $P = 0.083$  and  $P = 0.157$ , and for reader 2,  $P = 0.059$  and  $P = 0.102$ , respectively) (Table 3). However, when f-DWI and DCE-MRI were compared in terms of distortion scores, it was found that both readers determined statistically lower distortion scores for DCE-MR images than for f-DWIs ( $P < 0.001$ ).

When the interreader agreement was evaluated in terms of image quality, excellent agreement was found for sharpness (ICC: 0.95, 0.97, and 0.94;  $P < 0.001$ ), distortion (ICC: 0.98, 0.99, and 0.95;  $P < 0.001$ ), and perceived SNR scores (ICC: 0.98, 0.99, and 0.97;  $P < 0.001$ ) for f-DWI, c-DWI, and DCE-MRI, respectively.

### Consistency of diffusion-weighted imaging methods with dynamic contrast-enhanced magnetic resonance imaging in terms of tumor morphology

Because of their high spatial resolution, contrast-enhanced series are the images most commonly chosen for determining the morphological features of breast tumors, and thus consistency analyses were performed between DCE-MRI and both DWIs. In evaluations made independently of lesion size, consistency between f-DWI and DCE-MRI was significantly better ( $\kappa$  value range between 0.68 and 0.87 for reader 1 and between 0.72 and 0.80 for reader 2) compared with the consistency between c-DWI and DCE-MRI ( $\kappa$

value range between 0.15 and 0.24 for reader 1 and between 0.23 and 0.46 for reader 2) for all parameters (shape, margin, and internal pattern) ( $P < 0.001$  for both readers) (Table 4).

Based on the measurements made by reader 1 (the more experienced radiologist) in DCE-MRI, when the sizes of the lesions were grouped into three main groups, 36 (22%) of the lesions were  $< 15$  mm (group 1), 56 (35%) were between 16 and 25 mm (group 2), and the remaining 68 (43%) were  $> 25$  mm (group 3). According to this classification, in determining the tumor shape, concordance between DCE-MRI and DWIs increased with increasing lesion size for both readers (for reader 1,  $\kappa = 0.06, 0.20,$  and  $0.23$ , and for reader 2,  $\kappa = 0.23, 0.37,$  and  $0.41$  on c-DWI; for reader 1,  $\kappa = 0.77, 0.82,$  and  $0.93$ , and for reader 2,  $\kappa = 0.72, 0.73,$  and  $0.94$  on f-DWI; respectively;  $P < 0.001$  for both readers). Similarly, the consistency in the determination of lesion margins increased with increasing lesion size (for reader 1,  $\kappa = 0.13,$

0.17, and 0.20 and  $\kappa = 0.12, 0.22,$  and  $0.25$  on c-DWI; for reader 2,  $\kappa = 0.70, 0.77,$  and  $0.90$  and  $\kappa = 0.71, 0.77,$  and  $0.86$  on f-DWI, respectively;  $P < 0.001$  for both readers). When the compatibility in the determination of tumor internal patterns was evaluated, an increase was found in c-DWIs for both readers as the tumor size increased (for reader 1,  $\kappa = 0.09, 0.12,$  and  $0.27$ , and for reader 2,  $\kappa = 0.12, 0.15,$  and  $0.38$ , respectively) ( $P < 0.001$  for both readers). In f-DWI, the highest agreement was found in tumors ranging from 16 to 25 mm (for reader 1,  $\kappa = 0.62, 0.76,$  and  $0.55$  and for reader 2,  $\kappa = 0.64, 0.77,$  and  $0.64$ , respectively;  $P < 0.001$  for both readers) (Table 5).

### Interobserver agreement in assessing tumor morphology

Considering the interobserver agreement, the highest concordance between readers was achieved in assessing the margin parameter ( $\kappa = 0.87$  to  $0.89$ ;  $P < 0.001$ ) regardless of the MRI method, followed by shape and internal pattern parameters ( $\kappa = 0.63$  to  $0.79$ ;  $P < 0.001$ ). However, higher interobserver agreement values were obtained for c-DWI, particularly for shape and internal pattern ( $P < 0.001$  for each) (Table 6, Figures 2, 3).

## Discussion

Our findings revealed that f-DWI shows good consistency with DCE-MRI and is superior to c-DWI in assessing tumor morphology in primary breast cancer settings. Thus, even in cases where contrast material cannot be used, it will be possible to evaluate tumor morphology and size in a more detailed and clearer manner in a short time, with higher quality, less distortion, higher perceived SNR, and greater sharpness on HR-DWI. It is thought that employing f-DWI together with c-DWI will be of great benefit for increasing diagnostic accuracy.

As a HR imaging technique, DCE-MRI provides information about enhancement patterns of breast lesions and a detailed assessment of tumor morphology, allowing these lesions to be categorized accurately in the BI-RADS classification.<sup>24</sup> In fact, in a study by Goto et al.<sup>25</sup>, breast lesions were reported as likely to be diagnosed as benign and malignant based on only morphological assessment, regardless of the kinetic enhancement patterns obtained on DCE-MRI.

However, contrast-enhanced series cannot be obtained in the presence of a known contrast material allergy or renal dysfunction. In these cases, the importance and use of unenhanced series increases. In c-DWI, which

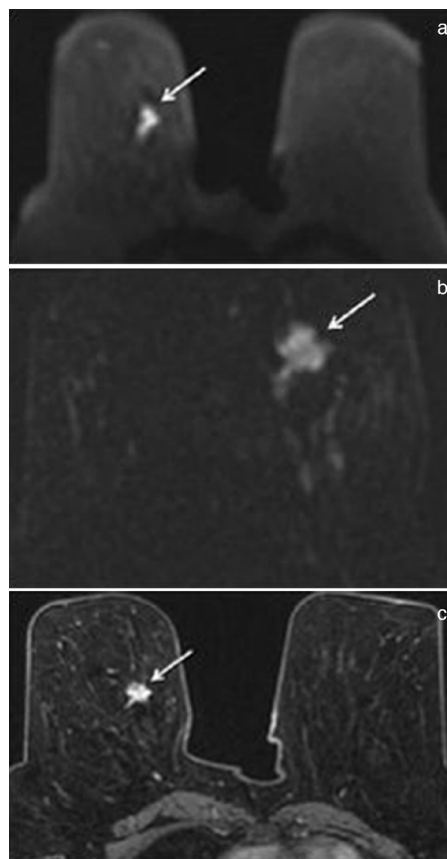


**Figure 1.** A 58-year-old female patient with a diagnosis of invasive ductal cancer in the lower outer quadrant of the right breast is observed. In conventional diffusion-weighted image (a), the marginal feature of the lesion is difficult to identify due to distortion. Due to HR in focus diffusion-weighted (b) and dynamic contrast-enhanced imaging (c), the marginal features of the lesion can be determined more clearly.

is one of the preferred unenhanced MRI methods, we attempted to obtain information about the quantitative values of breast lesions rather than their qualitative characteristics.<sup>26,27</sup> However, in recent years, there have been various publications investigating the diagnostic contribution of DWIs in determining the morphological features of breast lesions.<sup>16,17,19,20,28</sup> Kang et al.<sup>16</sup> highlighted the potential utility of c-DWI in assessing morphological features of lesions with high accuracy rates, which can be used for benign-malignant differentiation or for prognostic predictions. We have also previously reported the favorable utility of c-DWI in assessing the size and morphology of breast masses, along with a good consistency between c-DWI and DCE-MRI.<sup>17</sup> In addition, Radovic et al.<sup>19</sup> conducted a comparison of DCE-MRI

and c-DWI to evaluate the morphological features of breast lesions, reporting the presence of a moderate-to-substantial consistency between c-DWI and DCE-MRI along with similar values of interobserver agreement for each method. If the morphological features of breast masses could be obtained accurately using DWI, as in DCE-MRI, based on BI-RADS descriptors, this information could be used in the further characterization of breast masses and the prognostication and prediction of the response to breast cancer treatment using an unenhanced MRI method.

Despite all these data, the key reason why c-DWI is still less desirable than DCE-MRI in the qualitative evaluation of breast lesions is because it has disadvantages, such as low SNR, low resolution, and relatively low-quality images caused by magnetic susceptibility and chemical shift artifacts.

HR-DWI is a new technique developed to increase diagnostic accuracy, both quantitatively and qualitatively, by minimizing the disadvantages of experience in c-DWI.<sup>2</sup> In the literature, there are studies showing

that HR-DWI provides higher-quality images than c-DWI and is a more effective method for categorizing breast lesions according to the BI-RADS classification and also for determining their morphological features. Similarly, it has been reported that HR-DWI is more compatible with DCE-MRI in determining the qualitative characteristics of breast lesions compared with c-DWI. For example, in a previous study by Dong et al.<sup>29</sup> comparing rFOV DWI and c-DWI of breast tissue, rFOV DWI was reported to be associated with a significantly higher image quality score and higher resolution. The authors also considered rFOV DWI to be a potentially helpful technique in the diagnosis of breast cancer. Again, in a study using readout-segmented EPI, another HR-DWI method,<sup>30</sup> it was reported that obtaining higher-quality images compared with c-DWI is convenient and contributes greatly to the identification of breast tumors and the determination of their morphological features. In another study, Kishimoto et al.<sup>20</sup> reported a high agreement between HR-DWI and DCE-MRI in the assessment of morphological features and extent of malignant breast lesions. This study concluded that HR-DWIs can improve the diagnostic accuracy of unenhanced MRI. Barentsz et al.<sup>18</sup> reported that HR-DWI provided greater sharpness and perceived SNR than c-DWI, and as a result, the BI-RADS classification of breast lesions was achieved more accurately. By contrast, in the present study, with the participation of more patients, not only the shape features of the breast lesions but also the margin and internal pattern features were evaluated. As a result of our study, consistent with the findings of Barentsz et al.<sup>18</sup>, we determined that all breast lesion morphological features could be determined in detail, similar to contrast-enhanced series, with f-DWI providing higher-quality images.

One of the key results of our study is that although the best agreement among readers in determining tumor morphology was obtained for c-DWI, better agreement was found between f-DWI and DCE-MRI when the consistency between the methods was examined. This is mainly due to the fact that f-DWI provides high-quality images, which reveals tumor morphology more clearly and results in higher intermethod agreement with DCE-MRI. However, the fact that images with less clarity were obtained with c-DWIs compared with f-DWIs meant the readers were able to determine the morphological features in detail, resulting in better interobserver compatibility. Thus, it is thought that high-quality images obtained in f-DWIs

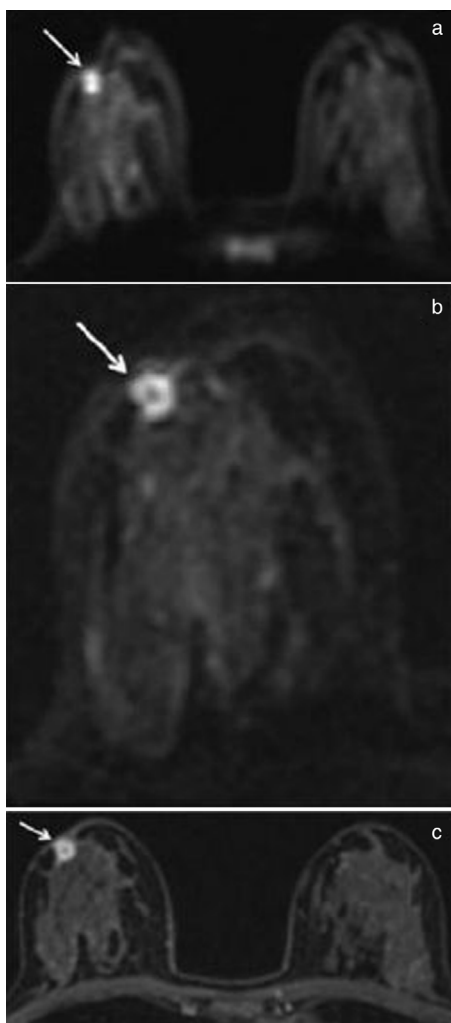


**Figure 2.** A 46-year-old female patient with a diagnosis of invasive ductal cancer in the retroareolar area of the right breast. Conventional diffusion-weighted image (a) showed homogeneous diffusion restriction in the lesion. Focus diffusion-weighted image (b) showed ring-shaped diffusion restriction in the lesion. In dynamic contrast-enhanced image (c), there is a circular pattern of enhancement in the lesion.

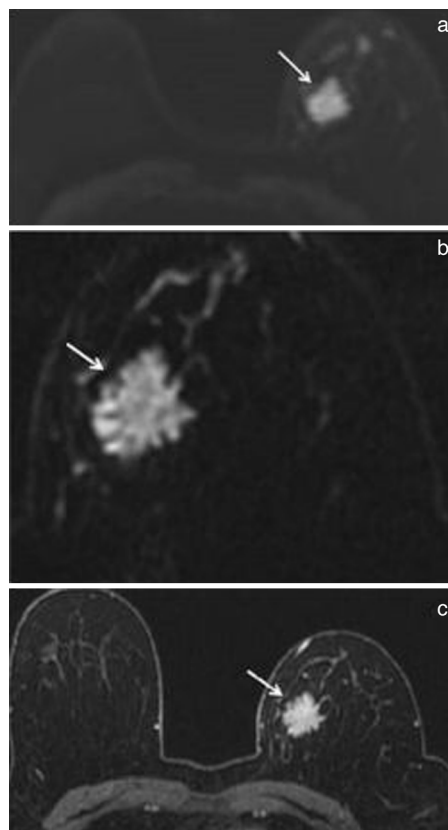


**Figure 3.** A 75-year-old female patient with a diagnosis of invasive ductal cancer in the upper inner quadrant of the left breast is observed. In conventional diffusion-weighted image (a), the shape of the mass was evaluated as lobulated. Focus diffusion-weighted (b) and dynamic contrast-enhanced images (c) revealed irregular shape of the lesion.

**Table 4.** Intermethod agreement for assessment of tumor morphology

		Reader 1		Reader 2	
		Kappa	P value	Kappa	P value
<b>Shape</b>	c-DWI and DCE-MRI	0.24	<0.001	0.41	<0.001
	f-DWI and DCE-MRI	0.87	<0.001	0.78	<0.001
<b>Margin</b>	c-DWI and DCE-MRI	0.22	<0.001	0.26	<0.001
	f-DWI and DCE-MRI	0.81	<0.001	0.80	<0.001
<b>Internal pattern</b>	c-DWI and DCE-MRI	0.15	<0.001	0.23	<0.001
	f-DWI and DCE-MRI	0.68	<0.001	0.72	<0.001

c-DWI, conventional diffusion-weighted imaging; f-DWI, focus diffusion-weighted imaging; DCE-MRI, dynamic contrast-enhanced magnetic resonance imaging.

**Table 5.** Determining the consistency of DWI methods with DCE-MRI in terms of tumor morphology according to lesion size

<b>Tumor size grouping</b>													
Group	Count (Percentage)	Reader 1 Kappa values of shapes	P	Reader 2 Kappa values of shapes	P	Reader 1 Kappa values of margins	P	Reader 2 Kappa values of margins	P	Reader 1 Kappa values of internal patterns	P	Reader 2 Kappa values of internal patterns	P
Group 1 (<15mm)	36 (22%)												
Group 2 (16–25 mm)	56 (35%)												
Group 3 (>25 mm)	68 (43%)												
Group 1 (DCE-MRI with c-DWI)		0.061	0.52	0.227	<0.001	0.134	0.03	0.116	0.37	0.091	0.01	0.120	0.051
Group 2 (DCE-MRI with c-DWI)		0.203	0.02	0.373	<0.001	0.167	0.02	0.216	0.01	0.120	0.03	0.152	0.02
Group 3 (DCE-MRI with c-DWI)		0.227	0.03	0.408	<0.001	0.203	0.04	0.253	0.01	0.266	0.01	0.383	<0.001
Group 1 (DCE-MRI with f-DWI)		0.769	<0.001	0.719	<0.001	0.771	<0.001	0.712	<0.001	0.616	<0.001	0.642	<0.001
Group 2 (DCE-MRI with f-DWI)		0.819	<0.001	0.729	<0.001	0.700	<0.001	0.768	<0.001	0.758	<0.001	0.772	<0.001
Group 3 (DCE-MRI with f-DWI)		0.934	<0.001	0.935	<0.001	0.899	<0.001	0.861	<0.001	0.552	<0.001	0.636	<0.001

c-DWI, conventional diffusion-weighted imaging; f-DWI, focus diffusion-weighted imaging; DCE-MRI, dynamic contrast-enhanced magnetic resonance imaging.

**Table 6.** Interobserver agreement for assessment of tumor morphology

	Reader 1	Reader 2
<b>Shape</b>		
c-DWI	0.75	<0.001
f-DWI	0.63	<0.001
DCE-MRI	0.65	<0.001
<b>Margin</b>		
c-DWI	0.89	<0.001
f-DWI	0.87	<0.001
DCE-MRI	0.89	<0.001
<b>Internal</b>		
c-DWI	0.79	<0.001
<b>Pattern</b>		
f-DWI	0.71	<0.001
DCE-MRI	0.70	<0.001

c-DWI, conventional diffusion-weighted imaging; f-DWI, focus diffusion-weighted imaging; DCE-MRI, dynamic contrast-enhanced magnetic resonance imaging.

caused a higher rate of disagreement among readers and therefore lower intraobserver agreement. Based on these results, f-DWI can be considered a potential competitor to DCE-MRI in evaluating the morphological features and extent of breast masses, and the use of HR DWI together with c-DWI could increase diagnostic accuracy, especially in patients who cannot undergo contrast-enhanced imaging.

Another key result of our study, consistent with findings in the literature, is the determination of the ADC values obtained on f-DWIs as statistically lower than the ADC values obtained on c-DWIs.<sup>28,31,32</sup> Although this effect has been suggested to be secondary to a reduced partial volume effect of normal fibroglandular tissue and residual fat in HR images, the exact mechanism has not yet been fully clarified.<sup>2,11</sup> One of the reasons for the emergence of this difference with f-DWIs is that tumor heterogeneity and tumor in-

ternal pattern can be defined more clearly, and thus, the area of the tumor that exhibits the most prominent diffusion restriction can be accurately determined. A more accurate determination of ADC values may provide important benefits for tumor prognosis and an evaluation of response to treatment. For example, Wilmes et al.<sup>2</sup> compared changes in ADC values measured by HR-DWI and c-DWIs, revealing that lower ADC values obtained with HR-DWI were better correlated with regression in tumor size. Consistent with these findings, we believe that the more accurate ADC values obtained with HR-DWI will enable a more accurate assessment of tumor prognosis or response to treatment.

To our knowledge, this is the largest study population comparing c-DWI, HR-DWI, and DCE-MRI in determining the morphological characteristics of breast cancers. However, certain limitations should be considered.

First, due to the evaluation of only the morphological features of malignant tumors, the diagnostic capability of f-DWI in the differentiation of benign and malignant tumors could not be evaluated. Second, image quality analysis was based on the simultaneous evaluation of all the c-DWI, f-DWI, and DCE series side by side. This may have led to the emergence of biases that better quality images are obtained with f-DW and/or DCE-MR images. Therefore, it would be more appropriate to evaluate all three methods separately in future studies. Third, it may not be possible to determine the morphological features of all multifocal and multicentric lesions due to the examination of a limited area with f-DWI. For this reason, attempts should be made to define the most suspicious lesions more clearly using f-DWIs, especially in conjunction with c-DWIs. Finally, f-DWIs have a longer imaging time than c-DWIs.

In conclusion, our findings revealed the favorable utility of f-DWI in the detailed evaluation of the morphological features of primary breast cancer as a method that is not inferior to DCE-MRI and is superior to c-DWI. Especially in cases where dynamic contrast sequences cannot be obtained, it is possible to characterize suspicious lesions detected in conventional imaging more clearly and in detail with f-DWIs, which provide high-quality images due to greater sharpness, perceived SNR and lower distortion. This may enable more accurate diagnoses to be made.

### Conflict of interest disclosure

The authors declare that they have no conflicts of interest.

### References

- Partridge SC, Gibbs JE, Lu Y, et al. MRI measurements of breast tumor volume predict response to neoadjuvant chemotherapy and recurrence-free survival. *AJR Am J Roentgenol*. 2005;184(6):1774-1781. [\[Crossref\]](#)
- Wilmes LJ, McLaughlin RL, Newitt DC, et al. High-resolution diffusion-weighted imaging for monitoring breast cancer treatment response. *Acad Radiol*. 2013;20(5):581-589. [\[CrossRef\]](#)
- Orel SG. High-resolution MR imaging for the detection, diagnosis, and staging of breast cancer. *Radiographics*. 1998;18(4):903-912. [\[CrossRef\]](#)
- Kuhl CK, Schild HH, Morakkabati N. Dynamic bilateral contrast-enhanced MR imaging of the breast: trade-off between spatial and temporal resolution. *Radiology*. 2005;236(3):789-800. [\[CrossRef\]](#)
- Woodhams R, Ramadan S, Stanwell P, et al. Diffusion-weighted imaging of the breast: principles and clinical applications. *Radiographics*. 2011;31(4):1059-1084. [\[CrossRef\]](#)
- Ei Khouli RH, Jacobs MA, Mezban SD, et al. Diffusion-weighted imaging improves the diagnostic accuracy of conventional 3.0-T breast MR imaging. *Radiology*. 2010;256(1):64-73. [\[CrossRef\]](#)
- Mansfield P. Multi-planar image-formation using NMR spin echoes. *J Phys C: Solid State Phys*. 1977;10(3):55-58. [\[CrossRef\]](#)
- Turner R, Le Bihan D. Single-shot diffusion imaging at 2.0 Tesla. *J Magn Reson Imaging*. 1990;86(3):445-452. [\[CrossRef\]](#)
- Zaharchuk G, Saritas EU, Andre JB, et al. Reduced field-of-view diffusion imaging of the human spinal cord: comparison with conventional single-shot echo-planar imaging. *AJNR Am J Neuroradiol*. 2011;32(5):813-820. [\[CrossRef\]](#)
- Karampinos DC, Van AT, Olivero WC, Georgiadis JG, Sutton BP. High resolution reduced-FOV diffusion tensor imaging of the human pons with multi-shot variable density spiral at 3T. *Annu Int Conf IEEE Eng Med Biol Soc*. 2008;2008:5761-5764. [\[CrossRef\]](#)
- Singer L, Wilmes LJ, Saritas EU, et al. High-resolution diffusion-weighted magnetic resonance imaging in patients with locally advanced breast cancer. *Acad Radiol*. 2012;19(5):526-534. [\[CrossRef\]](#)
- Saritas EU, Cunningham CH, Lee JH, Han ET, Nishimura DG. DWI of the spinal cord with reduced FOV single-shot EPI. *Magn Reson Med*. 2008;60(2):468-473.
- Finsterbusch J. High-resolution diffusion tensor imaging with inner field-of-view EPI. *J Magn Reson Imaging*. 2009;29(4):987-993. [\[CrossRef\]](#)
- Wilm BJ, Svensson J, Henning A, Pruessmann KP, Boesiger P, Kollias SS. Reduced field-of-view MRI using outer volume suppression for spinal cord diffusion imaging. *Magn Reson Med*. 2007;57(3):625-630. [\[CrossRef\]](#)
- Wheeler-Kingshott CA, Hickman SJ, Parker GJ, et al. Investigating cervical spinal cord structure using axial diffusion tensor imaging. *Neuroimage*. 2002;16(1):93-102. [\[CrossRef\]](#)
- Kang BJ, Lipson JA, Planey KR, et al. Rim sign in breast lesions on diffusion-weighted magnetic resonance imaging: diagnostic accuracy and clinical usefulness. *J Magn Reson Imaging*. 2015;41(3):616-623. [\[CrossRef\]](#)
- Kul S, Metin Y, Kul M, Metin N, Eyuboglu I, Ozdemir O. Assessment of breast mass morphology with diffusion-weighted MRI: Beyond apparent diffusion coefficient. *J Magn Reson Imaging*. 2018;48(6):1668-1677. [\[CrossRef\]](#)
- Barentsz MW, Taviani V, Chang JM, et al. Assessment of tumor morphology on diffusion-weighted (DWI) breast MRI: diagnostic value of reduced field of view DWI. *J Magn Reson Imaging*. 2015;42(6):1656-1665. [\[CrossRef\]](#)
- Radovic N, Ivanac G, Divjak E, Biondic I, Bulum A, Brkljacic B. Evaluation of breast cancer morphology using diffusion-weighted and dynamic contrast-enhanced MRI: intermethod and interobserver agreement. *J Magn Reson Imaging*. 2019;49(5):1381-1390. [\[CrossRef\]](#)
- Kishimoto AO, Kataoka M, Lima M, et al. The comparison of high-resolution diffusion weighted imaging (DWI) with high-resolution contrast-enhanced MRI in the evaluation of breast cancers. *Magn Reson Imaging*. 2020;71:161-169. [\[CrossRef\]](#)
- American College of Radiology. ACR BI-RADS magnetic resonance imaging. Reston, VA: American College of Radiology. Website: www.acr.org. Published 2013. Accessed June 20, 2016. [\[CrossRef\]](#)
- McHugh ML. Interrater reliability: the kappa statistic. *Biochem Med (Zagreb)*. 2012;22(3):276-282. [\[CrossRef\]](#)
- Koo TK, Li MY. A guideline of selecting and reporting intraclass correlation coefficients for reliability research. *J Chiropr Med*. 2016;15(2):155-163. Erratum in: *J Chiropr Med*. 2017;16(4):346. [\[CrossRef\]](#)
- Liu PF, Debatin JF, Caduff RF, Kacal G, Garzoli E, Krestin GP. Improved diagnostic accuracy in dynamic contrast enhanced MRI of the breast by combined quantitative and qualitative analysis. *Br J Radiol*. 1998;71(845):501-509. [\[CrossRef\]](#)
- Goto M, Ito H, Akazawa K, et al. Diagnosis of breast tumors by contrast-enhanced MR imaging: comparison between the diagnostic performance of dynamic enhancement patterns and morphologic features. *J Magn Reson Imaging*. 2007;25(1):104-112. [\[CrossRef\]](#)
- Park MJ, Cha ES, Kang BJ, Ihn YK, Baik JH. The role of diffusion-weighted imaging and the apparent diffusion coefficient (ADC) values for breast tumors. *Korean J Radiol*. 2007;8(5):390-396. [\[CrossRef\]](#)
- Yabuuchi H, Matsuo Y, Okafuji T, et al. Enhanced mass on contrast-enhanced breast MR imaging: lesion characterization using combination of dynamic contrast-enhanced and diffusion-weighted MR images. *J Magn Reson Imaging*. 2008;28(5):1157-1165. [\[CrossRef\]](#)
- Kishimoto AO, Kataoka M, Lima M, et al. Evaluation of malignant breast lesions using high-resolution readout-segmented diffusion-weighted echo-planar imaging: comparison with pathology. *Magn Reson Med Sci*. 2021;20(2):204-215. [\[CrossRef\]](#)
- Dong H, Li Y, Li H, Wang B, Hu B. Study of the reduced field-of-view diffusion-weighted imaging of the breast. *Clin Breast Cancer*. 2014;14(4):265-271. [\[CrossRef\]](#)

30. McKay JA, Church AL, Rubin N, et al. A comparison of methods for high-spatial-resolution diffusion-weighted imaging in breast MRI. *Radiology*. 2020;297(2):304-312. [\[CrossRef\]](#)
31. Wisner DJ, Rogers N, Deshpande VS, et al. High-resolution diffusion-weighted imaging for the separation of benign from malignant BI-RADS 4/5 lesions found on breast MRI at 3T. *J Magn Reson Imaging*. 2014;40(3):674-681. [\[CrossRef\]](#)
32. Yamaguchi K, Nakazono T, Egashira R, et al. Diagnostic performance of diffusion tensor imaging with readout-segmented echo-planar imaging for invasive breast cancer: correlation of ADC and FA with pathological prognostic markers. *Magn Reson Med Sci*. 2017;16(3):245-252. [\[CrossRef\]](#)



# Prediction of malignancy upgrade rate in high-risk breast lesions using an artificial intelligence model: a retrospective study

Özge Aslan   
Ayşenur Oktay   
Başak Katuk   
Rıza Cenk Erdur   
Oğuz Dikenelli   
Levent Yeniay   
Osman Zekioğlu   
Süha Süreyya Özbek 

## PURPOSE

High-risk breast lesions (HRLs) are associated with future risk of breast cancer. Considering the pathological subtypes, malignancy upgrade rate differs according to each subtype and depends on various factors such as clinical and radiological features and biopsy method. Using artificial intelligence and machine learning models in breast imaging, evaluations can be made in terms of risk estimation in different research areas. This study aimed to develop a machine learning model to distinguish HRL cases requiring surgical excision from lesions with a low risk of accompanying malignancy.

## METHODS

A total of 94 patients who were diagnosed with HRL by image-guided biopsy between January 2008 and March 2020 were included in the study. A structured database was created with clinical and radiological characteristics and histopathological results. A machine learning prediction model was created to make binary classifications of lesions as malignant or benign. Random forest, decision tree, K-nearest neighbors, logistic regression, support vector machine (SVM), and multilayer perceptron machine learning algorithms were used. Among these algorithms, SVM was the most successful. The estimations of malignancy for each case detected by artificial intelligence were combined and statistical analyses were performed.

## RESULTS

Considering all cases, the malignancy upgrade rate was 24.5%. A significant association was observed between malignancy upgrade rate and lesion size ( $P = 0.004$ ), presence of mammography findings ( $P = 0.022$ ), and breast imaging-reporting and data system category ( $P = 0.001$ ). A statistically significant association was also found between the artificial intelligence prediction model and malignancy upgrade rate ( $P < 0.001$ ). With the SVM model, an 84% accuracy and 0.786 area-under-the-curve score were obtained in classifying the data as benign or malignant.

## CONCLUSION

Our artificial intelligence model (SVM) can predict HRLs that can be followed up with a lower risk of accompanying malignancy. Unnecessary surgeries can be reduced, or second line vacuum excisions can be performed in HRLs, which are mostly benign, by evaluating on a case-by-case basis, in line with radiology-pathology compatibility and by using an artificial intelligence model.

## KEYWORDS

Artificial intelligence, breast, cancer, high risk lesion of breast, image-guided biopsy

From the Department of Radiology (Ö.A. ✉), dr.ozgeaslan@gmail.com, A.O., S.S.Ö.), Ege University Faculty of Medicine, Izmir, Turkey; Department of Computer Engineering (B.K., R.C.E., O.D.), Ege University Engineering Faculty, Izmir, Turkey; Department of General Surgery (L.Y.), Ege University Faculty of Medicine, Izmir, Turkey; Department of Medical Pathology (O.Z.), Ege University Faculty of Medicine, Izmir, Turkey.

Received 21 November 2021; revision requested 20 December 2021; last revision received 13 March 2022; accepted 16 March 2022.



Epub: 24.01.2023

Publication date: 29.03.2023

DOI: 10.5152/dir.2022.211047

The increase in breast cancer screening with mammography increases the rate of non-palpable lesions detected in the breast.<sup>1,2</sup> In the diagnosis of these lesions, percutaneous biopsy methods are increasingly applied under the guidance of imaging methods. Percutaneous needle biopsy is a fast, easy-to-apply, inexpensive, and well-tolerated biopsy alternative to open surgical biopsies.<sup>1,3</sup> The prevalence of high-risk breast lesion (HRL) detection with core needle biopsy (CNB) is 5–9% in all breast biopsies.<sup>2,4,5</sup> HRLs are defined as lesions with a high risk of malignant transformation and the possibility of synchronous or ad-

You may cite this article as: Aslan Ö, Oktay A, Katuk B, et al. Prediction of malignancy upgrade rate in high-risk breast lesions by an artificial intelligence model: a retrospective study. *Diagn Interv Radiol.* 2023;29(2):260-267.

adjacent breast malignancy.<sup>6</sup> They are detected together with breast malignancy by imaging-guided percutaneous breast biopsies as well as by excisional biopsies and during surgical procedures.<sup>5,7,8</sup> Additionally, HRLs are a heterogeneous group of proliferative lesions with variable malignant potential and can be considered as falling in a “gray zone” between benign and malignant lesions (Figure 1).

HRLs are associated with future breast cancer risk and are precursors of breast carcinogenesis.<sup>5,9</sup> Lesions defined as high-risk in thick-needle biopsies [CNB and vacuum assisted biopsy (VAB)] may upgrade to malignancy when a surgical excision is performed. The overall positive predictive value (PPV) for malignancy is approximately 10–30%. After detecting an HRL in a thick-needle biopsy, a clinical decision is required between surgical excision or follow-up of the lesion to avoid unnecessary surgery due to the possibility of concomitant malignancy based on radiology–pathology compatibility. As a general approach, surgical excision is often recommended for most of these lesions because of the risk of malignancy.<sup>10</sup> However, the malignancy upgrade rate of HRLs reported in the literature is varied and depends on various factors such as pathological subtype, clinical and radiological features, and biopsy method.<sup>2</sup> In recent studies, a case-by-case approach was recommended. Upgrade rates are higher in lesions with atypia compared to other HRLs.<sup>7</sup> The Second International B3 Lesions Consensus Conference recommends excision with vacuum biopsy as an alternative to open surgery in HRLs except atypical ductal hyperplasia (ADH) and phyllodes tumors.<sup>11</sup>

The success of image-guided needle biopsies depends on the evaluation after the biopsy as well as the biopsy procedure. When evaluating biopsy results, radiopathological compatibility is considered. Pathology

results can be expected to adequately explain imaging findings.<sup>2</sup> A multidisciplinary case-based approach is key to optimal patient care.<sup>2</sup>

Previous research suggests that artificial intelligence (AI) algorithms can support breast radiologists in diagnosis, treatment, and case follow-up management by using large quantities of high-quality imaging data, however more studies are needed into this.<sup>12</sup> Using AI and machine learning models in breast imaging, evaluations can be made in terms of risk estimation in different research areas.<sup>13</sup> In the literature, there are many examples of successful computer-aided diagnosis systems that have used traditional machine learning and deep learning algorithms to classify breast cancer.<sup>14</sup> However, there is insufficient research into risk determination in HRLs.

In this study, we aimed to develop a machine learning model to distinguish HRLs with a low risk of accompanying malignancy from cases requiring surgical excision. For this purpose, a structured dataset consisting of HRL patients with known surgical outcomes was created. Then, a machine learning model was trained with this dataset to develop a model for classifying patients whose surgical outcomes were unknown.

## Methods

Approval for this study was obtained from the ethics committee of our institution (approval no: 20-11.1T/42, date: 25.11.2020). Before the biopsies were performed, the procedure was explained to all patients, and they signed a consent form. The pathology results of 2,249 patients who underwent image-guided thick-needle biopsy between January 2008 and March 2020 in our breast

radiology clinic were retrospectively evaluated, and 120 patients diagnosed with high-risk lesion were identified from these cases. The pathology results of those who underwent surgical excision and the radiological follow-up results of those who were followed-up without surgery were evaluated. A total of 26 patients, who were followed up for less than one year after having a thick-needle biopsy or whose pathology results were unknown were excluded from the study. A structured database was created with the following information: age at the time of diagnosis, breast cancer history and family history, age of menarche, hormonal therapy history, other cancer history, smoking status, lesion size, radiological imaging features, breast imaging reporting and data system (BI-RADS) category, biopsy type, needle thickness, sampling number (<4 or ≥4), biopsy histopathology result, excision histopathology results, and follow-up findings (Figure 2).

Mammographic images were obtained with full-field digital mammography and digital breast tomosynthesis mammograms (Lorad Selenia and Selenia Dimensions, Hologic). Stereotactic VABs were performed on a prone table unit (Multicare Platinum; Hologic), with a 9-G needle (Encore biopsy probe; Bard). Magnetic resonance imaging (MRI) were performed with 1.5T (Magnetom Amira, Symphony Siemens) and 3T (Magnetom Verio Siemens) MRI devices using conventional and dynamic contrast sequences. Ultrasonography (US) and US-guided biopsy procedures were performed with Hitachi and Siemens devices using a high-frequency linear probe. A 14-G needle was used in US-guided thick-needle biopsy. The BI-RADS category was determined according to the American College of Radiology BI-RADS Atlas

**Main points**

- High-risk breast lesions are associated with future risk of breast cancer.
- The malignancy upgrade rate of high-risk breast lesions is diverse and depends on several factors such as pathological subtype, clinical and radiological features, and biopsy method.
- In high-risk lesions, which are mostly benign, unnecessary surgeries can be reduced or excision can be performed with second line vacuum biopsy in line with radiology–pathology compatibility and by using an artificial intelligence prediction model.

### High risk breast lesion subtypes

Ductal proliferative lesions	Atypical ductal hyperplasia (ADH), Columnar cell lesions
Lobular proliferative lesions (Lobular neoplasia)	Atypical lobular hyperplasia (ALH), Lobular carcinoma in situ (LCIS)
Radial sclerosing lesions	Radial scar, complex sclerosing lesion
Papillary lesions	Intraductal papilloma, Atypical intraductal papilloma (AIP)
Cellular fibroepithelial tumor	Flat epithelial atypia (FEA)

Figure 1. Classification of high-risk breast lesion subtypes.

5<sup>th</sup> edition classification, based on mammography, US, and MRI findings.

Morphology and distribution features of microcalcification, structural distortion, asymmetry, and mass opacity were evaluated in the mammography. Lesions were classified as mass and non-mass (abnormal echogenicity and structural distortion) findings on the US and recorded. The presence of mass and non-mass enhancement in the MRI was evaluated. In cases diagnosed with more than one HRL by biopsy, diagnoses that included atypia and had a higher risk of

malignancy were accepted as the main lesion. Those who had a malignant diagnosis (invasive ductal carcinoma, ductal carcinoma *in situ*, or invasive lobular carcinoma) with surgical excision were accepted as upgraded to malignancy.

Patients with benign histopathology results and those who were stable in the long-term follow-up were included in the benign group, and those with a malignant excision diagnosis were included in the malignant group. The upgrade rate of existing HRLs to malignancy in the AI prediction model was

defined from the highest to the lowest, considering the ranges specified in the literature [ADH > atypical intraductal papilloma (AIP) > lobular neoplasia > radial scar > intraductal papilloma without atypia].<sup>2,7,15,16</sup>

### Artificial intelligence model technique

#### Libraries and technologies used

Python programming language and related libraries (Numpy, Pandas, and Scikit-learn) were used in data preprocessing and training the machine learning algorithms.

#### Pre-processing of data

Data were preprocessed prior to the creation of the AI prediction model. The data set contained columns with numerical data and categorical data. Pre-processing steps were carried out on these columns. In the preprocessing stage, categorical data were digitized, and all data were normalized. For digitization, a one-hot encoding scheme or a custom encoding scheme was used depending on the type of categorical data (nominal or ordinal) (Figure 3).

For example, in the mammography findings column, which contains nominal categorical data, one-hot vectors were created for each of the column values of asymmetry, mass opacity, microcalcification, and structural distortion (Figure 3). These vectors were added to the data set as a new feature, and the original column was removed from the dataset.

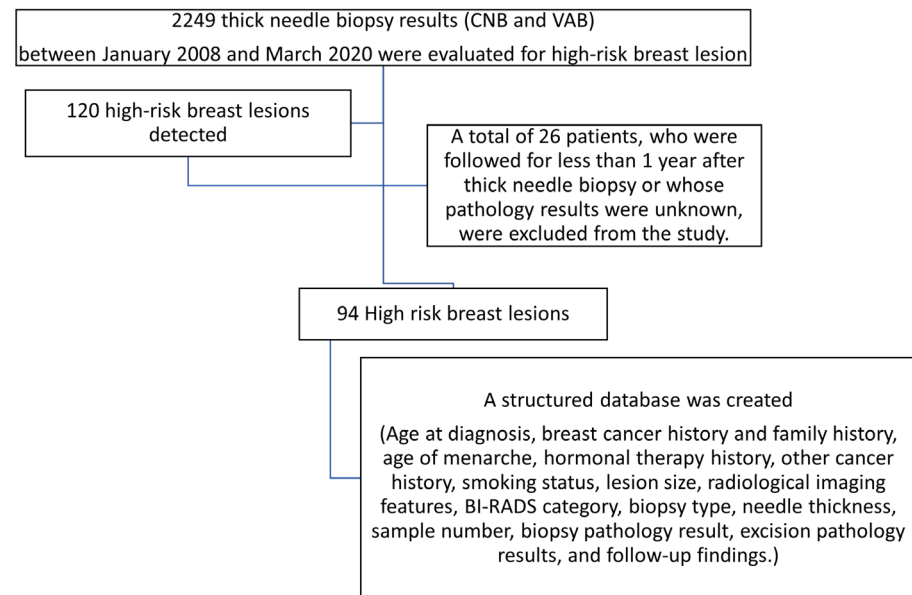
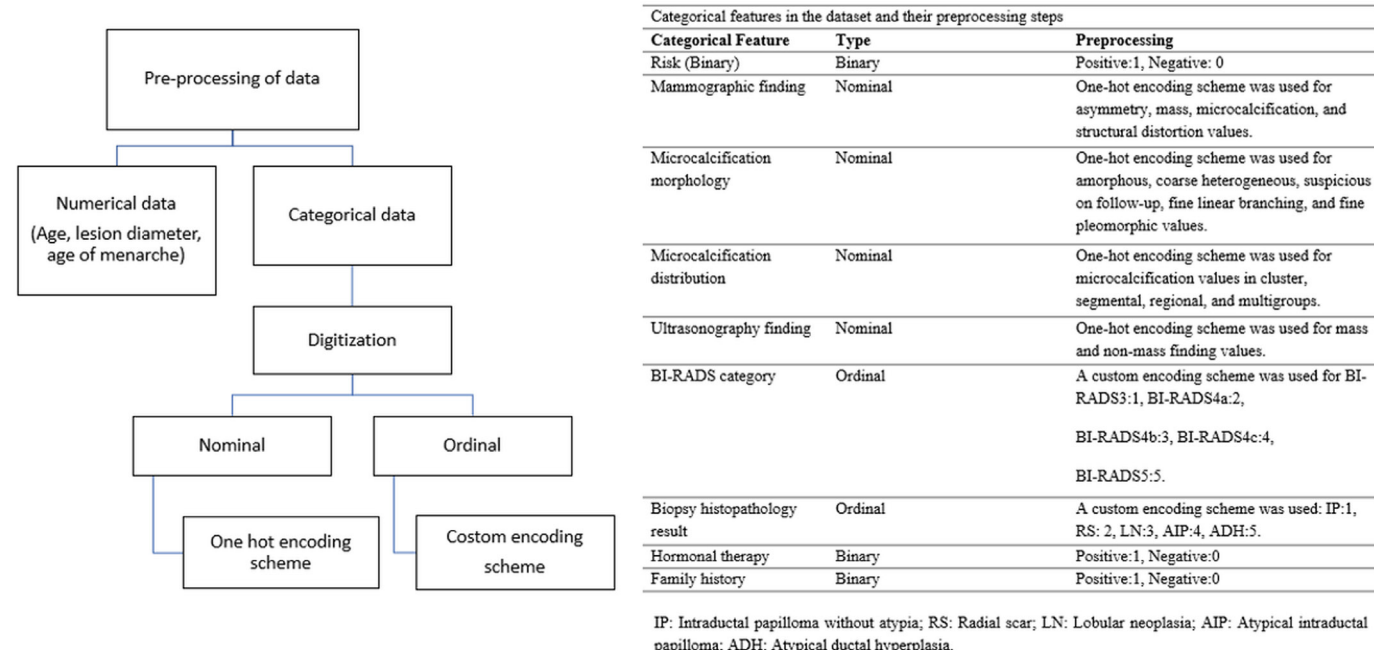


**Figure 2.** Flow chart of the steps followed while creating the database. CNB, core needle biopsy; VAB, vacuum assisted biopsy; BI-RADS, breast imaging reporting and data system.



Categorical features in the dataset and their preprocessing steps		
Categorical Feature	Type	Preprocessing
Risk (Binary)	Binary	Positive:1, Negative: 0
Mammographic finding	Nominal	One-hot encoding scheme was used for asymmetry, mass, microcalcification, and structural distortion values.
Microcalcification morphology	Nominal	One-hot encoding scheme was used for amorphous, coarse heterogeneous, suspicious on follow-up, fine linear branching, and fine pleomorphic values.
Microcalcification distribution	Nominal	One-hot encoding scheme was used for microcalcification values in cluster, segmental, regional, and multigroups.
Ultrasonography finding	Nominal	One-hot encoding scheme was used for mass and non-mass finding values.
BI-RADS category	Ordinal	A custom encoding scheme was used for BI-RADS3:1, BI-RADS4a:2, BI-RADS4b:3, BI-RADS4c:4, BI-RADS5:5.
Biopsy histopathology result	Ordinal	A custom encoding scheme was used: IP:1, RS: 2, LN:3, AIP:4, ADH:5.
Hormonal therapy	Binary	Positive:1, Negative:0
Family history	Binary	Positive:1, Negative:0

IP: Intraductal papilloma without atypia; RS: Radial scar; LN: Lobular neoplasia; AIP: Atypical intraductal papilloma; ADH: Atypical ductal hyperplasia.

**Figure 3.** Categorical features in the dataset and their preprocessing steps.

In the BI-RADS category column, which contains ordinal categorical data, a custom encoding scheme was used to match BI-RADS3:1, BI-RADS4a:2, BI-RADS4b:3, BI-RADS4c:4, and BI-RADS5:5. Minimum-maximum normalization was used for normalization of the data.

### Machine learning model development

The data passed through the preprocessing stage were divided into training and test datasets. The test data set comprised 20% of the entire data set (19 samples). In splitting the dataset, the proportions of samples in each class observed in the original dataset were preserved, and a stratified train–test split was applied.

The prepared data sets were used to create a machine learning prediction model to make binary classification as “malignant” or “benign.” Random forest, decision tree, K-nearest neighbor, logistic regression, support vector machine (SVM), and multilayer perceptron machine learning algorithms were run with the training data set, and their performances were measured with the test data set (Figure 4). In the specified machine learning algorithms trained by hyperparameter optimization and using cross-validation, the models were compared by looking at the accuracy and area under the curve (AUC) score. Although the AUC scores of the logistic regression (0.743) and SVM (0.786) models are relatively close, SVM made a more accurate prediction for the “malign” samples. In addition, the accuracy of SVM (0.84) was 0.05 points higher than the logistic regression (0.79). The AUC score and accuracy of the K-nearest neighbor model was lower than the SVM model (Figures 5-7).

The SVM, which gave the most successful results, was selected. For the hyperparameters of the SVM algorithm, the C, gamma, and kernel parameters were optimized for various values (Figure 4). In the fine-tuning of the hyperparameters, five-fold cross-validation was performed with the grid search algorithm.

The performance of the SVM classification model was measured by using the metrics accuracy, sensitivity, specificity, and F1 Score (Figure 5), and a confusion matrix was obtained (Figure 6). The AUC score of the model was then calculated (Figure 7).

The estimation of malignancy of each case detected by AI and clinical and radiological case features were combined and statistical analyses were performed with the IBM SPSS 25.0 program.

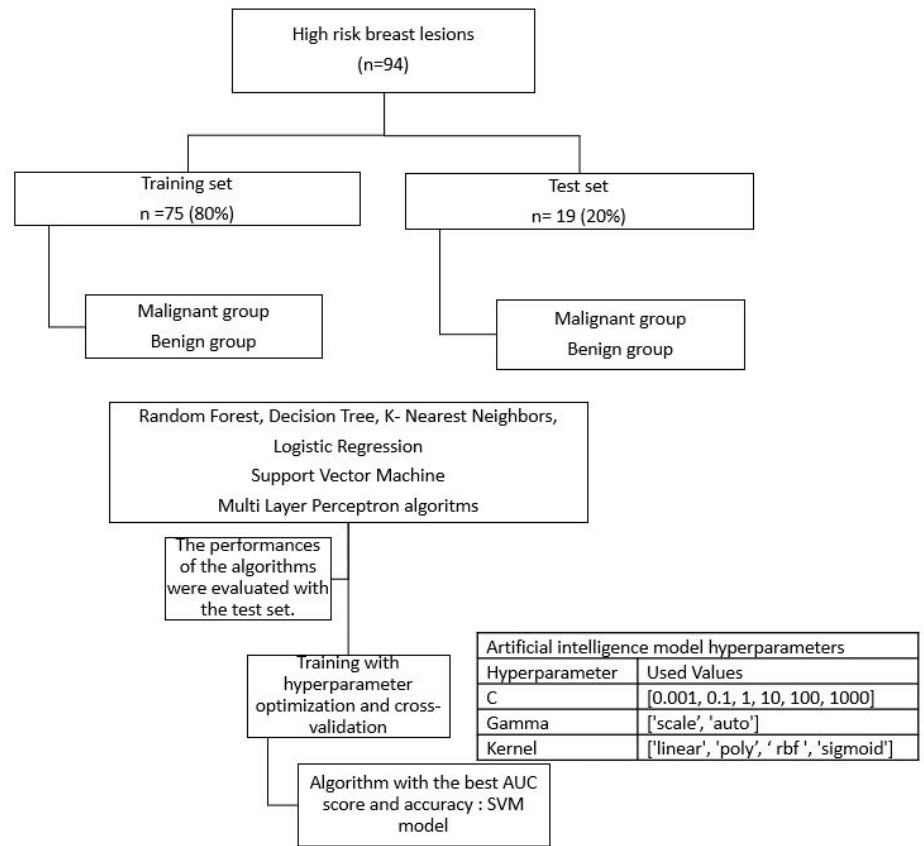


**Figure 4.** Machine learning model development stages. AUC, area-under-the-curve; SVM, support vector machine.

Best Parameters for <b>Logistic regression</b> (random_state=0): ['clf__C':10, 'clf__solver': 'scale', 'Newton-cg']					
Detailed classification report:					
		precision	recall	f1-score	support
Benign	0	0.78	1.00	0.88	14
Malignant	1	1.00	0.20	0.33	5
Accuracy				0.79	19
Macro avg		0.89	0.60	0.60	19
Weighted avg		0.84	0.79	0.73	19

Best Parameters for <b>K-Neighbours Classifier</b> (): ['clf__algorithm': 'auto', 'clf__n_neighbors':3, 'clf__p':2, 'clf__weights': 'uniform']					
Detailed classification report:					
		precision	recall	f1 score	support
Benign	0	0.76	0.93	0.84	14
Malignant	1	0.50	0.20	0.29	5
Accuracy				0.74	19
Macro avg		0.63	0.56	0.56	19
Weighted avg		0.70	0.74	0.69	19

Best Parameters for <b>Support Vector Machine</b> (probability=True, random state=0): ['clf__C':1, 'clf__gamma': 'scale', 'clf__kernel': 'poly']					
Detailed classification report:					
		precision	recall	f1-score	support
Benign	0	0.82	1.00	0.90	14
Malignant	1	1.00	0.40	0.57	5
Accuracy				0.84	19
Macro avg		0.91	0.70	0.74	19
Weighted avg		0.87	0.84	0.82	19

**Figure 5.** Logistic regression, support vector machine, and K-nearest neighbors model detailed classification reports.

The estimation of malignancy upgrade was evaluated in all cases according to each HRL pathological subtype.

### Statistical analysis

The distribution of cases across the age groups was expressed as the mean ± stan-

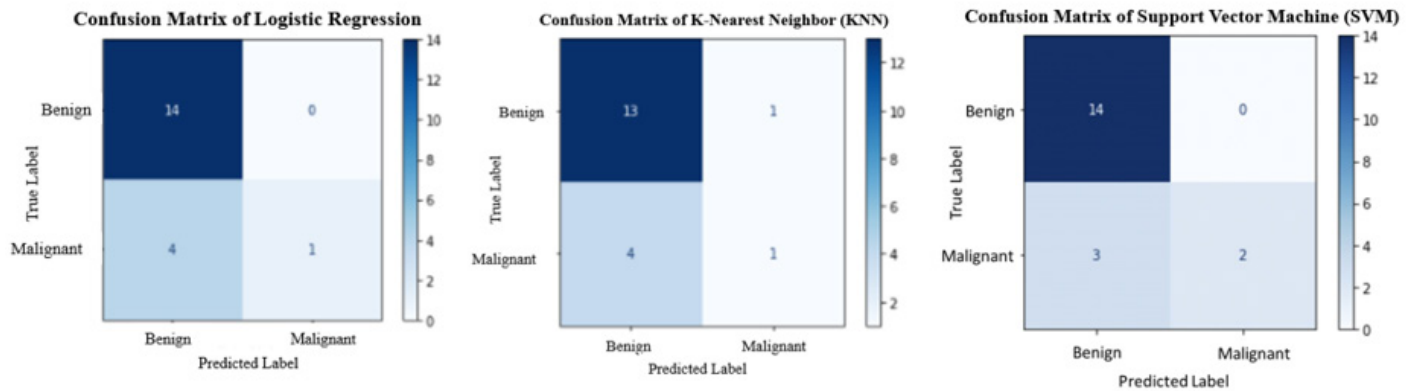


**Figure 6.** Confusion matrices of the logistic regression, support vector machine, and K-nearest neighbors.

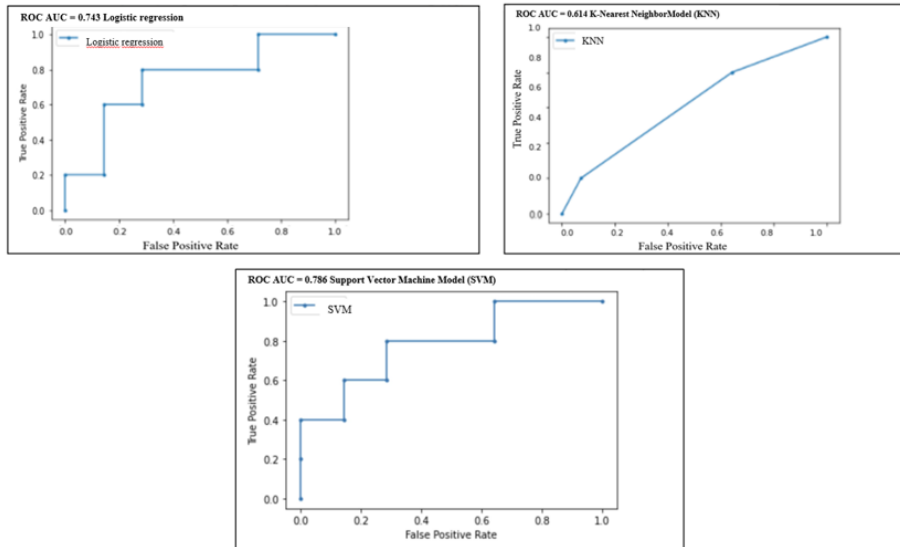


**Figure 7.** Logistic regression, support vector machine, and K-nearest neighbors algorithm area-under-the-curve scores. AUC, area-under-the-curve; ROC, receiver operating characteristic curve; SVM, support vector machine.

dard deviation, and categorical data were expressed as frequencies (n) and percentages (%). All statistical analyses were performed with SPSS software version 25.0 (IBM). Kolmogorov–Smirnov and Shapiro–Wilk tests were used to assess the normal distribution of data. Pearson’s chi-square and Fisher’s exact tests were employed to compare the malignancy upgrade rate and AI SVM model assessment. Student’s t-tests were used to compare differences in continuous variables. Pearson’s chi-square test was used to evaluate the relationship between the AI SVM model assessment and radiological–clinical features of cases.

## Results

In the 94 female patients, the mean age was  $47.22 \pm 10.7$ ; range: 17–73 years, the mean lesion size was  $1.8 \pm 4.9$  cm; range: 5–100 cm, and the mean age of menarche was  $13.26 \pm 1.4$ ; range: 10–18 years.

A rate of 25.5% (n = 24) of the patients

had a positive family history of breast cancer. Hormonal therapy was applied in 26.6% (n = 25). When evaluated in terms of family history, hormonal therapy, previous breast cancer and HRL history, risk factor status of breast cancer was positive in 35% (n = 33) of the patients. There was a history of smoking in 36% (n = 34). Considering the imaging characteristics, 53% (n = 50) had positive mammography findings (microcalcification, asymmetry, structural distortion, and mass opacity). Suspicious microcalcification was present in 31% (n = 29). The most common microcalcification morphology was amorphous (14%; n = 13), and the most common distribution pattern was clustered type (17%; n = 16). The most common BI-RADS category was 4A (55.3%; n = 52). US findings [53% (n = 50) with a mass and 22% (n = 21) without a mass] were observed in 75.5%. MRI findings [20.2% (n = 19) mass enhancement or 21.3% (n = 20) non-mass enhancement] were present in 41.5% of the cases (Table 1). Of the mass-shaped lesions (n = 19), 47.4% (n = 9)

had smooth contours and 52.6% (n = 10) had irregular contours in MRI. In the pharmacokinetic evaluation of lesions, 92.3% (n = 36) type-1 and type-2 curves and 7.7% (n = 3) type-3 curve patterns were observed.

Mammography-guided (stereotactic) VAB was performed on 25.5% (n = 24) of the patients, and US-guided CNB was performed on 75.5% (n = 70). Vacuum biopsies were performed using 9-G needles, and 14-G needles were used in CNBs. The number of samples was below four in 20% of the patients and four or more in 80% of the patients (Table 1).

According to the thick-needle biopsy histopathology results, the pathological subtypes of the cases were ADH (44.7%; n = 42), intraductal papilloma (37.2%; n = 35), AIP (10.6%; n = 10), radial scar (5.3%; n = 5), and lobular neoplasia (2.1%; n = 2). Of the cases, 84% were removed by surgical excision, and 16% were followed up. Of the 79 excised cases, 41% were diagnosed as benign, 30% with atypia, and 29% as malignant. Fifteen patients who were followed up without surgery were stable in clinical and radiological follow-up, and these cases were placed in the benign group.

Considering all cases, the malignancy upgrade rate was 24.5% (n = 23). According to the pathological subtypes, the malignancy upgrade rates were 50% (n = 1) for lobular neoplasia, 40% (n = 2) for radial scar, 31% (n = 13) for ADH, 30% (n = 3) for AIP, and 11.4% (n = 4) for intraductal papilloma (Table 2).

When evaluated with Pearson’s chi-square test for the upgrade rate to malignancy with all variables, a statistically significant association was found with the variables of BI-RADS category, lesion diameter, and presence of mammographic findings ( $P < 0.05$ ; Table 3). No statistically significant relationship was found between family history and smoking and upgrade to malignancy ( $P = 0.631$ ,  $P = 0.247$ , respectively).

		Benign group	Malignant group	SVM model prediction result (n)		Total
		n (%)	n (%)	Wrong	Right	n (%)
Biopsy type	CNB	55 (59)	15 (16)	8	62	70 (74)
	VAB	16 (17)	8 (9)	1	23	24 (26)
Risk	Positive	25 (27)	8 (9)	1	32	33 (35)
	Negative	46 (49)	15 (16)	8	53	61 (65)
Needle thickness	9 G	16 (17)	8 (9)	1	23	24 (26)
	14 G	55 (59)	15 (16)	8	62	70 (74)
Sampling number	<4	15 (16)	4 (4)	3	16	19 (20)
	≥4	56 (60)	19 (20)	6	69	75 (80)
Lesion diameter	<1.5 cm	46 (49)	7 (7)	4	49	53 (56)
	≥1.5 cm	25 (27)	16 (17)	5	36	41 (44)
Mammography finding	Microcalcification	19 (40)	10 (21)	1	28	29 (62)
	Mass	6 (13)	3 (6)	1	8	9 (19)
	Non-mass	6 (13)	3 (6)	2	7	9 (19)
US finding	Mass	40 (56)	10 (14)	4	46	50 (70)
	Non-mass	14 (20)	7 (10)	4	17	21 (30)
MRI finding	Mass	16 (41)	3 (8)	1	18	19 (49)
	Non-mass	13 (33)	7 (18)	5	15	20 (51)
Microcalcification morphology	Amorphous, coarse heterogeneous	11 (38)	4 (14)	1	14	15 (52)
	Fine linear branching, fine pleomorphic	8 (28)	6 (21)	-	14	14 (48)

CNB, core needle biopsy; VAB, vacuum assisted biopsy; SVM, support vector machine; US, ultrasonography; MRI, magnetic resonance imaging.

Pathologic subgroups	Benign group n (%)	Malignant group n (%)	Total n (%)	Malignancy upgrade rate (%)
IP	31 (33)	4 (4)	35 (37)	11.4
ADH	29 (31)	13 (14)	42 (45)	31
AIP	7 (7)	3 (3)	10 (11)	30
Radial scar	3 (3)	2 (2)	5 (5)	40
Lobular neoplasia	1 (1)	1 (1)	2 (2)	50
Total	71 (76)	23 (24)	94 (100)	24.5

IP, intraductal papilloma without atypia; ADH, atypical ductal hyperplasia; AIP, atypical intraductal papilloma.

		Benign group n (%)	Malignant group n (%)	Total n (%)	P value
BI-RADS category	3-4A-4B	64 (68)	14 (15)	78 (83)	0.003
	4C-5	7 (7)	9 (10)	16 (17)	
Lesion diameter	<1.5 cm	46 (49)	7 (7)	53 (56)	0.004
	≥1.5 cm	25 (27)	16 (17)	41 (44)	
Mammographic finding	Positive	33 (35)	17 (18)	50 (53)	0.022
	Negative	38 (40)	6 (6)	44 (47)	

BI-RADS, breast imaging reporting and data system.

The AI analysis identified 85 cases correctly and 9 cases incorrectly (Tables 1 and 4). The SVM AI model, which was trained using

certain hyperparameters, had 84% accuracy (Figure 5) and an AUC score of 0.786 (Figure 7) in classifying the data as benign or malignant.

No statistically significant difference was found between needle thickness/biopsy type and erroneous AI estimation ( $P = 0.297$ ).

A statistically significant difference was found between the AI prediction and the malignancy upgrade rate of the patients ( $P < 0.001$ ). The sensitivity of the malignant case prediction set of the AI model was 60.87%, the specificity was 100%, PPV was 100%, and negative predictive value was 88.75%.

## Discussion

The most significant problem in the management of HRLs is upgrading to malignancy. The upgrade rate to malignancy in this study was 24.5%, which is similar to the rates reported in the literature.<sup>10</sup>

Considering pathological subtypes, the rate of upgrade to malignancy differs according to each subtype. The malignancy upgrade rate of ADH, which was the most common lesion subtype among our cases, was similar to the literature. A wide range of malignancy upgrade rates for ADH and AIP has been reported in the literature.<sup>2,7</sup> In this study, for AIP, as in ADH, there were erroneous AI predictions in three of the patients,

**Table 4.** Distribution characteristics of pathological subgroups malignancy upgrade rates and the accuracy of the SVM model in subtypes

Pathologic subgroup	True malignancy upgrade rates n (%)	SVM model malignancy upgrade rates n (%)	SVM model accuracy (%)
ADH (n = 42)	13 (31)	10 (23.8)	92.8
AIP (n = 10)	3 (30)	-	70
LN (n = 2)	1 (50)	1 (50)	100
RS (n = 5)	2 (40)	-	60
IP (n = 35)	4 (11.4)	3 (8.6)	97.1
Total	23 (24.5)	14 (14.9)	90.4

ADH, atypical ductal hyperplasia; AIP, atypical intraductal papilloma; LN, lobular neoplasia; RS, radial scar; IP, intraductal papilloma without atypia; SVM, support vector machine.

and biopsies were performed with tru-cut in both groups.

The malignancy upgrade rates for radial scar and lobular neoplasia were in the upper limit of the rates stated in the literature.<sup>7</sup> This may be due to the low number of cases in these subgroups.

The SVM model made an incorrect prediction in nine malignant cases in total (Tables 1 and 4). One of these cases was diagnosed by VAB with a 9-G needle, and all others were diagnosed by CNB with a 14-G needle. No statistically significant correlation was found between needle thickness/biopsy type and erroneous AI estimation, but the low number of cases is a limitation in the evaluation of this variable. In the study of Bahl et al.<sup>13</sup>, which included 1,006 HRLs, the AI prediction model had a prediction accuracy of 97.4% in malignant cases and 69.4% in benign cases, and they reported that unnecessary surgeries could be reduced in benign cases. In the present study, the AI model made a correct prediction in all cases that were diagnosed as benign by surgical excision and considered as stable in long-term follow-up. More than half of the patients who underwent surgical excision were diagnosed as benign. Considering the radiopathological fit and AI model estimation, if these cases had been followed up radiologically and clinically, the rate of unnecessary surgery could have been reduced by 71%.

The majority of HRLs are benign but most are surgically excised because of the associated risk of malignancy. Post-biopsy evaluation and biopsy procedure are important in the management of these lesions.<sup>1,15</sup>

Comparable to the literature, there was a statistically significant relationship between VAB as a biopsy guide method, 9-G needle thickness, and sufficient number of samples

with the malignancy upgrade rate. In cases that have these features, a more appropriate decision can be made in terms of follow-up and excision. In order to increase the correct prediction rates with the AI model, studies containing more cases and data sets are needed.

There are some further limitations to this study. Firstly, it is a retrospective study. The differences in the number of pathological subtypes and the low number of patients were our biggest limitations. Significant results could not be obtained in many statistical analyses due to the differences in the number of pathological subtypes such as lobular neoplasia and radial scar, and the low number of cases. In addition, due to the small number of cases and the limited number of histopathological features in terms of the degree of atypia, a clear analysis of the variables that may be effective in the erroneous predictions of the SVM model could not be made. For this reason, better statistical results can be obtained by adding features such as the degree of pathological atypia, which will further strengthen the data set, and by including more patients.

In conclusion, this study's AI model (SVM) can predict HRLs that can be followed up with a lower risk of accompanying malignancy. Both ADH and AIP cases should be surgically excised because of the high risk of malignancy associated with them. Apart from these subtypes, HRLs, which are mostly benign, can be evaluated on a case-by-case basis, in line with radiology-pathology compatibility and using an AI prediction model, to reduce unnecessary surgeries, or excision can be performed with second-line VAB.

#### Conflict of interest disclosure

The authors declare no conflicts of interest.

## References

1. Oktay A. Meme hastalıklarında görüntüleme. İçinde: Tunacı M, ed. Radyoloji-patoloji sonuçlarının korelasyonu, bölüm 7. 2nd ed. Ankara: *Dünya Tıp Kitabevi*; 2020:249-255. [Crossref]
2. Neal L, Sandhu NP, Hieken TJ, et al. Diagnosis and management of benign, atypical, and indeterminate breast lesions detected on core needle biopsy. *Mayo Clin Proc.* 2014;89(4):536-547. [Crossref]
3. Liberman L. Clinical management issues in percutaneous core breast biopsy. *Radiol Clin North Am.* 2000;38(4):791-807. [Crossref]
4. Oktay A. Radyolojik-patolojik korelasyon: yüksek risk lezyonlarda ne yapmalıyız? *Türk Radyoloji Seminerleri.* 2014;2:217-229. [Crossref]
5. Gulla S, Lancaster R, De Los Santos J. High-risk breast lesions and current management. *Semin Roentgenol.* 2018;53(4):252-260. [Crossref]
6. Bianchi S, Caini S, Renne G, et al. Positive predictive value for malignancy on surgical excision of breast lesions of uncertain malignant potential (B3) diagnosed by stereotactic vacuum-assisted needle core biopsy (VANCB): a large multi-institutional study in Italy. *Breast.* 2011;20(3):264-270. [Crossref]
7. Nakhli F. How do we approach benign proliferative lesions? *Curr Oncol Rep.* 2018;20(4):34. [Crossref]
8. Georgian-Smith D, Lawton TJ. Controversies on the management of high-risk lesions at core biopsy from a radiology/pathology perspective. *Radiol Clin North Am.* 2010;48(5):999-1012. [Crossref]
9. Thomas PS. Diagnosis and management of high-risk breast lesions. *J Natl Compr Canc Netw.* 2018;16(11):1391-1396. [Crossref]
10. Boateng S, Tirada N, Khorjekar G, Richards S, Ioffe O. Excision or observation: the dilemma of managing high-risk breast lesions. *Curr Probl Diagn Radiol.* 2020;49:124-132. [Crossref]
11. Rageth CJ, O'Flynn EAM, Pinker K, et al. Second international consensus conference on lesions of uncertain malignant potential in the breast (B3 lesions). *Breast Cancer Res Treat.* 2019;174(2):279-296. [Crossref]
12. Mendelson EB. Artificial intelligence in breast imaging: potentials and limitations. *AJR Am J Roentgenol.* 2019;212(2):293-299. [Crossref]
13. Bahl M, Barzilay R, Yedidia AB, Locascio NJ, Yu L, Lehman CD. High-risk breast lesions: a machine learning model to predict pathologic upgrade and reduce unnecessary surgical excision. *Radiology.* 2018;286(3):810-818. [Crossref]
14. Murtaza G, Shuib L, Wahab AWA, et al. Deep learning-based breast cancer classification through medical imaging modalities: state of

the art and research challenges. *Artif Intell Rev.* 2019;53:1655-1720. [\[Crossref\]](#)

15. Krishnamurthy S, Bevers T, Kuerer H, Yang WT. Multidisciplinary considerations in the management of high-risk breast lesions.

*AJR Am J Roentgenol.* 2012;198(2):132-140. [\[Crossref\]](#)

16. Armes JE, Galbraith C, Gray J, Taylor K. The outcome of papillary lesions of the breast diagnosed by standard core needle biopsy

within a BreastScreen Australia service. *Pathology.* 2017;49(3):267-270. [\[Crossref\]](#)



# Low-dose ultra-high-pitch computed tomography coronary angiography: identifying the optimum combination of iteration strength and radiation dose reduction strategies to achieve true submillisievert scans

Nidhi Kumari\*

Kartik P. Ganga\*

Vineeta Ojha

Sanjeev Kumar

Priya Jagia

Nitish Naik

Gurpreet Gulati

Sanjiv Sharma

\*Contributed equally and share first authorship.

From the Department of Cardiovascular Radiology and Endovascular Interventions (N.K., K.P.G., V.O., S.K., P.J., G.G. [✉ gulatigurpreet@rediffmail.com](mailto:gulatigurpreet@rediffmail.com), S.S.), All India Institute of Medical Sciences, New Delhi, India; Department of Cardiology (N.N.), All India Institute of Medical Sciences, New Delhi, India.

Received 09 October 2020; revision requested 16 December 2020; last revision received 30 June 2021; accepted 01 July 2021.



Epub: 20.03.2023

Publication date: 29.03.2023

DOI: 10.4274/dir.2021.0849

## PURPOSE

To identify the optimum strength of advanced modeled iterative reconstruction (ADMIRE) to achieve the best subjective and objective image quality when combining three-dose reduction strategies, ultra-high-pitch computed tomography coronary angiography (FLASH CTCA; with single-dose ivabradine to lower heart rate), low tube voltage, and ADMIRE.

## METHODS

Sixty consecutive patients underwent FLASH CTCA at 100 kVp in this single-center prospective study. Single-dose ivabradine was administered to patients whose heart rate was above 75 bpm. Images were reconstructed using the three highest strengths of ADMIRE (A3, A4, and A5). Objective and subjective image quality (using a Likert scale) were evaluated in the three datasets.

## RESULTS

The signal strength remained unchanged but mean noise significantly reduced across the increasing strengths of ADMIRE [signal:  $513.78 \pm 101.7$  Hounsfield units (HU) at A3,  $515.6 \pm 100.5$  HU at A4, and  $519.7 \pm 107.9$  HU at A5; noise:  $23.4 \pm 4.5$  HU at A3,  $20.2 \pm 3.6$  HU at A4, and  $17.2 \pm 3.3$  HU at A5]. Signal-to-noise and contrast-to-noise ratios were the highest at A5, and A5 offered significantly higher Likert scores in image noise, vessel sharpness, and overall image quality than A3 or A4. Additionally, A5 did not interfere with image interpretation in any patient.

## CONCLUSION

Using all three dose reduction strategies during FLASH CTCA along with single-dose ivabradine administration ensures minimal radiation exposure in daily practice. In this study, A5 datasets had the best overall subjective and objective image quality despite their “plastic appearance”. In the future, enhanced dose reduction can be obtained by further lowering tube voltages.

## KEYWORDS

Advanced modeled iterative reconstruction, ultra-high-pitch computed tomography coronary angiography, computed tomography angiography, cardiac, dose reduction strategies

The main disadvantage of computed tomography coronary angiography (CTCA), despite its non-invasive nature, is radiation exposure. With increasing concerns regarding the accurate estimation of the “true” radiation burden of CTCA caused by the challenges in determining the cardiac-specific conversion factor (k factor), the need to devise new strategies and incorporate multiple dose reduction techniques is of paramount importance. With the newly proposed k factors, even the lower radiation burden of prospectively gated CTCA can no longer be considered “low dose” per se, indicating an urgent need to use all avail-

You may cite this article as: Kumari N, Ganga KP, Ojha V, et al. Low-dose ultra-high-pitch computed tomography coronary angiography: identifying the optimum combination of iteration strength and radiation dose reduction strategies to achieve true submillisievert scans.

*Diagn Interv Radiol.* 2023;29(2):268-275.

able advanced techniques for every patient to undergo “true” submillisievert CTCAs.<sup>1</sup>

Lowering the tube potential as a stand-alone measure leads to a decrease in image quality. The current guidelines recommend 100 kVp for patients with a body mass index (BMI) <30 kg/m<sup>2</sup>, making an approximate reduction of 50%–60% in radiation dose possible using these strategies compared with strategies using 120 kVp.<sup>2</sup> Additional dose reduction may be possible by further reducing the tube voltage and using iterative reconstruction (IR), which permits the decoupling of spatial resolution and noise to offset the noisier image quality obtained with lower tube voltages. IR has rapidly replaced the more archaic filtered back projection (FBP) by enabling the drastic reduction in image noise inherent in the use of low tube voltage.<sup>3,4</sup> As a result of advances in computer processing technologies, current generation IR, such as model-based IR, is now available on all vendor platforms and is no longer limited by the absence and expense of the faster computational requirements that IR requires. Previous generations of IR have been shown to reduce image noise by 70%–80% compared with FBP in CT.<sup>5,6</sup> The latest generation advanced modeled IR (ADMIRE) is a hybrid technique that removes noise more rapidly by using statistical modeling in both the raw and image domain. Although different strengths of ADMIRE have been shown to deliver a better signal-to-noise ratio (SNR) and contrast-to-noise ratio (CNR) even for CTCA, the best strength of iteration that is optimal remains undetermined. This is because higher strengths of iteration can lead to an excessive smoothing of the image, which degrades subjective image quality.<sup>7</sup>

Another dose reduction strategy that can be used is high-pitch (>3) prospective electrocardiogram (ECG)-triggered helical data

acquisition (FLASH CTCA), which can acquire the complete volumetric dataset within a fraction of a cardiac cycle. The high pitch leads to very low radiation dose (0.5–1 mSv) as long as the patient has low, regular heart rates (HRs).

Prospective ECG-gated CTCA, which is the default “lower-dose CTCA”, is a well-utilized technique. By using forward-looking ECG prediction and step/shoot non-spiral acquisition, it requires the X-ray beam to be turned on for only a small portion of the cardiac cycle. In FLASH CTCA, by using a higher pitch and faster table movement, the beam is switched on for even shorter periods, enabling it to be genuinely “low dose” or “ultra-low dose”.

Combining the three techniques (low tube voltage, FLASH CTCA, and IR) could lead to a significant reduction in radiation exposure and still deliver diagnostic image quality. The objective of this study was to identify the optimum strength of ADMIRE to achieve the best SNR and CNR when using FLASH CTCA at a tube voltage of 100 kVp because the strength of ADMIRE that provides the optimum subjective image quality is still contested. This study also evaluated the role of a single dose of the novel HR-lowering drug ivabradine in decreasing and stabilizing the HR to rates required for FLASH CTCA.

## Methods

This study was a prospective single-center study involving 66 consecutive adult patients who underwent CTCA for suspected coronary artery disease. The study was approved by the Institutional Ethics Committee (IECPG-96/21.03.2018), and informed consent was obtained. All studies were conducted after documenting baseline HR and blood pressure and assessing left ventricular ejection fraction through echocardiography. A 384 -slice (192\*2) dual-source scanner (Siemens Somatom Force, Erlangen, Germany) was used to perform FLASH CTCA. The acquisition parameters were 2 × 192 × 0.6 mm for detector collimation (Siemens Healthcare Sector, Forchheim, Germany), rotation time of 0.25 s, temporal resolution of 66 ms, pitch of 3.2 mm, and tube voltage of 100 kVp. In cases where the HR was greater than 75 bpm, a single 10 mg dose of ivabradine (in patients without any contraindications for the drug) was administered to the patient, and CTCA was acquired if the HR was less than 75 bpm after 2 h. Ivabradine was not administered to any of the patients already on beta-blockers.

Subsequently, 50–60 mL of iodinated contrast media (350 mg I/mL) was injected, followed by a 30 mL saline chaser at a flow rate of 3.6–3.8 mL/s through the antecubital vein. Scans were automatically triggered after an attenuation threshold of 100 Hounsfield units (HU) was reached in the descending thoracic aorta using bolus tracking. Automatic exposure control (CARE kV, Siemens) and attenuation-based tube current modulation (CAREdose, Siemens) was enabled. A dual FLASH protocol was performed using one set of images acquired in the strongest systolic phase (35% of RR interval) and one set of images acquired in the strongest diastolic phase (65% of RR interval). All patients, including those who were given ivabradine, were observed carefully for adverse effects before, during, and after the CTCA. Patients with HRs above 75 bpm, despite being on oral beta-blockers, and patients with hypersensitivity to iodinated contrast were excluded from the study.

## Computed tomography image reconstruction

CTCA images were reconstructed using ADMIRE (Siemens, Germany). Both the systolic and diastolic phases were reconstructed using three increasing strengths of noise reduction: ADMIRE 3 (A3), ADMIRE 4 (A4), and ADMIRE 5 (A5). The parameters for reconstruction for both the systolic and diastolic datasets were a 0.75 mm slice thickness with 0.5 mm increments and a 512 × 512 matrix using a medium soft tissue reconstruction kernel (Bv-40).

The resulting six series of images were archived and then evaluated using a commercially available software (Siemens Syngo.via VB10B).

Regions of interest (ROIs) of 1 cm<sup>2</sup> drawn in the aortic root at the level of the left main coronary artery on an axial image were used to measure signal strength (mean HU value). The standard deviation (SD) obtained from the same ROI represented the objective image noise (Figure 1). Similar ROIs (as large as possible) were drawn on the right coronary, proximal left main, left anterior descending, and left circumflex arteries (within 1 cm of their origins on axial images).

Only one phase, either the highest quality diastolic or systolic images, were chosen for the assessment of subjective and objective image analysis based on which had the least cardiac motion in the preliminary analysis of both datasets.

### Main points

- Signal strength remains unchanged but mean noise significantly decreases with increasing advanced modeled iterative reconstruction (ADMIRE) strengths (A3 to A5).
- Signal-to-noise and contrast-to-noise ratios are the highest at A5.
- The A5 datasets have the best overall subjective and objective image quality despite producing a “plastic appearance” when combining three-dose reduction strategies: ultra-high-pitch computed tomography coronary angiography (with single-dose ivabradine to lower heart rate), low tube voltage, and ADMIRE.

## Quantitative analysis

An automated copy/paste tool ensured that all measurements were performed in an

identical location for all three datasets (A3, A4, and A5), which were viewed side by side simultaneously by NK (Figures 2-4).

Mean signal strength and noise were calculated by averaging the values obtained from the five vessels mentioned above.

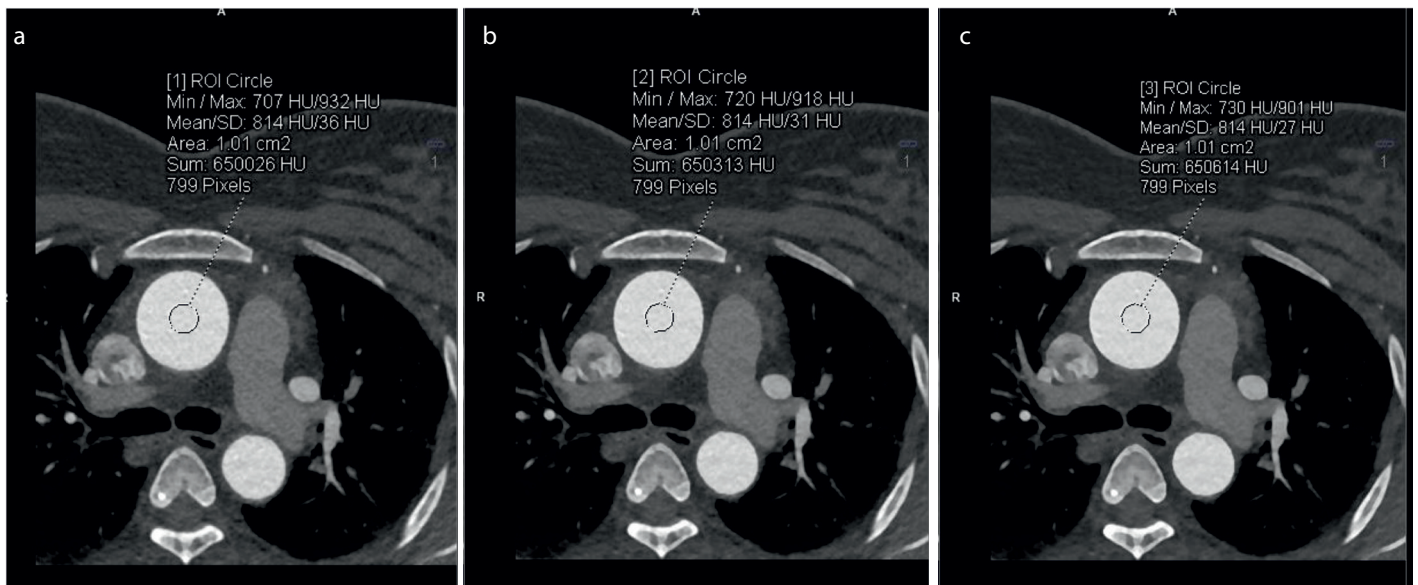


**Figure 1.** (a-c) Axial computed tomography images showing image noise measurements in the aortic root in a 45-year-old female patient (62 kg, 150 cm) at advanced modeled iterative reconstruction (ADMIRE) 3 [image noise: 36 Hounsfield units (HU)], ADMIRE 4 (image noise: 31 HU), and ADMIRE 5 (image noise: 27 HU). ROI, Regions of interest; SD, standard deviation.

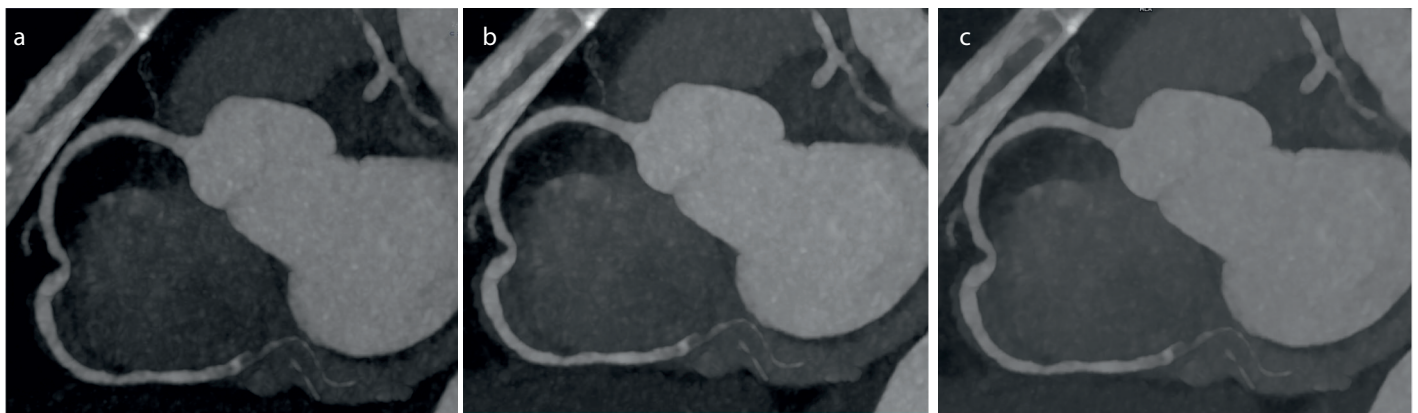


**Figure 2.** (a-c) Curved multiplanar computed tomography images of the right coronary artery of a 45-year-old female patient (62 kg, 150 cm, heart rate: 69 bpm) obtained through electrocardiogram-triggered high-pitch acquisition at advanced modeled iterative reconstruction (ADMIRE) 3 (a), ADMIRE 4 (b), and ADMIRE 5 (c).

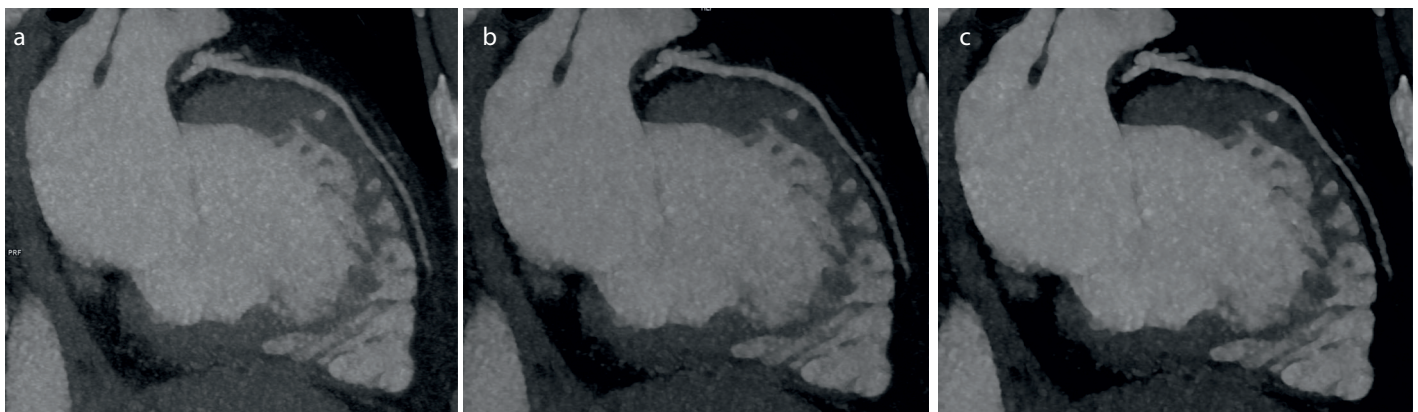


**Figure 3.** (a-c) Curved multiplanar computed tomography images of the left anterior descending artery of a 45-year-old male patient (88 kg, 170 cm, heart rate: 66 bpm) obtained through electrocardiogram-triggered high-pitch acquisition at advanced modeled iterative reconstruction (ADMIRE) 3 (a), ADMIRE 4 (b), and ADMIRE 5 (c).

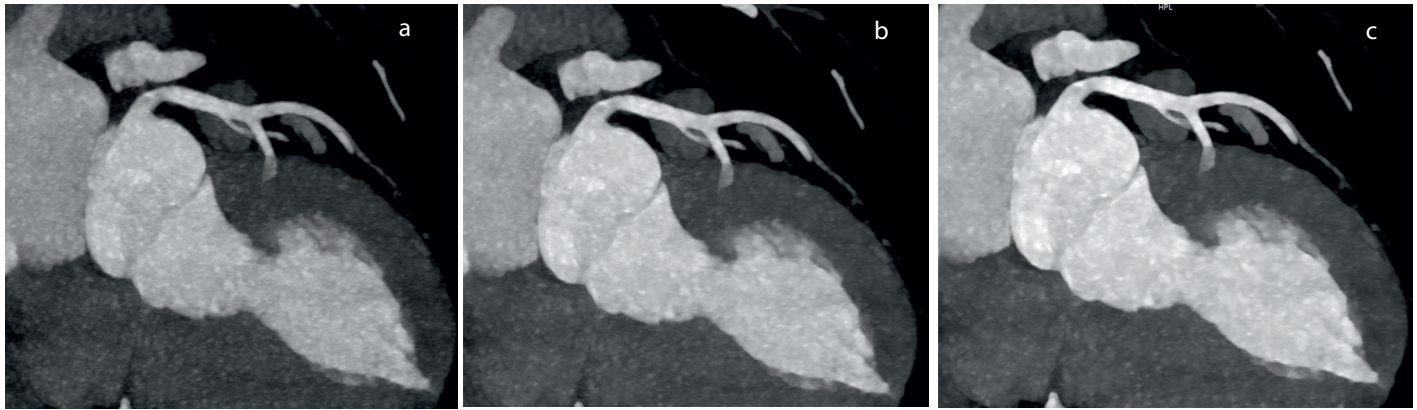


**Figure 4.** (a-c) Curved multiplanar computed tomography images of the left main coronary artery of a 45-year-old male patient (88 kg, 170 cm, heart rate: 66 bpm) obtained through electrocardiogram-triggered high-pitch acquisition at advanced modeled iterative reconstruction (ADMIRE) 3 (a), ADMIRE 4 (b), and ADMIRE 5 (c).

In addition, SNR was defined as the ratio of the mean HU value of the coronary artery and its SD (noise), and CNR was calculated by dividing the contrast attenuation by image noise.

### Qualitative analysis

Two independent and blinded cardiothoracic radiologists (GG and KG, with 20 and 6 years of experience, respectively, in cardiac imaging) performed the qualitative image analysis at a different time from the quantitative measurements. The ADMIRE strengths used on each dataset were hidden from the readers to prevent bias.

Maximum intensity projections, curved multiplanar images, and routine axial datasets were used at the discretion of the individual readers. A Likert score was assigned for each dataset with respect to 1) subjective image noise, 2) coronary wall definition (sharpness), 3) beam-hardening artifacts, and 4) overall subjective image quality. The readers ignored artifacts resulting from motion and poor gating that were not caused by the reconstruction algorithm.

These four parameters were assessed using a single score on a 4-point Likert scale (range 1–4) based on the segment of the coronary artery with the poorest appearance. The Likert scale was defined as follows: image noise and beam-hardening artifacts were assessed as (1) present and not acceptable, (2) present and interfering with assessment, (3) present but not interfering with assessment, and (4) minimal or absent; vessel sharpness was defined as (1) blurry, (2) poorer than average, (3) better than average, and (4) the sharpest; overall image quality was graded as (1) unacceptable (inadequate to evaluate coronary stenosis), (2) fair (sufficient for evaluating coronary stenosis), (3) good, and (4)

excellent quality. The Likert scores from both readers were averaged and used for statistical analysis.

### Estimation of radiation dose

The CT volume dose index and dose-length product (DLP) were obtained from the scanner. The effective dose was derived from the product of DLP and the conversion coefficient (k) for the chest.<sup>8</sup> To make our study more comparable with previous studies, a coefficient of  $0.014 \text{ mSv mGy}^{-1} \text{ cm}^{-1}$  was used

### Statistical analysis

Data were analyzed using SPSS version 23.0 (SPSS, Chicago, IL, USA). Descriptive statistics are presented in frequencies with percentages, mean $\pm$  SD, or median (min–max), depending on the distribution of the data. For the assessment of image quality score and quantitative parameters between the three reconstruction algorithms, a One-Way analysis of variance (for normal data) and Kruskal–Wallis tests (for non-normal data) were used. For pairwise comparisons, a post hoc test (Dunn's test) was applied. Student's test (paired) was used for comparing HRs in patients who had been administered ivabradine (before or after ivabradine administration). Interobserver reliability was assessed using the Kappa coefficient. A *P* value < 0.05 was considered statistically significant.

## Results

In total, 66 patients were enrolled, with 6 patients excluded because of an elevated preprocedural HR above 75 bpm despite being on routine beta-blocker therapy. The mean age of the 33 men and 27 women was  $49.9 \pm 9.6$  years (range: 30–75). The mean BMI and average HR during CTCA were  $27.4 \pm 4.1 \text{ kg/m}^2$  (range: 19.5–40.9) and  $69 \pm 5.7$  bpm

(range: 50–75), respectively. Ivabradine was administered to 31 patients, after which the average HR was  $67.9 \pm 6.2$  bpm compared with  $87.3 \pm 7.8$  bpm (*P* = 0.038) prior to administration. No adverse effect was identified in any patient.

### Quantitative analysis

Mean signal strength (averaged value of the ROIs in the five vessels) remained unchanged across the three datasets reconstructed at the different strengths of ADMIRE ( $513.78 \pm 101.7$  HU in A3,  $515.6 \pm 100.5$  HU in A4, and  $519.7 \pm 107.9$  HU in A5) (*P* = 0.976).

Mean image noise (averaged value of the ROIs in the five vessels) significantly decreased with increasing strengths of ADMIRE ( $23.4 \pm 4.5$  HU in A3,  $20.2 \pm 3.6$  HU in A4, and  $17.2 \pm 3.3$  HU in A5) (*P* = 0.033), although pairwise comparison produced varying results in different vessels (Table 1). Mean noise was reduced by 13.66% at A4 compared with A3, 14.83% at A5 compared with A4, and 26.49% at A5 compared with A3 (Table 1). Thus, a linear improvement in the mean SNR and CNR was observed with increasing iterations, with an improvement of 39.91% and 37.12%, respectively, at A5 compared with A3 (*P* < 0.0001) (Table 1).

### Qualitative analysis

The optimal overall image quality was obtained at A5, with readers 1 and 2 rating 96.67% (58/60) and 98.33% (59/60), respectively, of the A5 images as excellent (Table 2).

Subjective image noise was at its maximum at A3, with readers 1 and 2 grading it as minimal or absent only in 58.33% and 18% of the A3 datasets. Subjective image noise was at a minimum at A5, with both readers grading it as minimal or absent in 95% of the A5 datasets.

**Table 1.** Objective image quality parameters in the study population

Variables	ADMIRE 3 (A3)	ADMIRE 4 (A4)	ADMIRE 5 (A5)	P value <sup>#</sup>	P (A3–A4)*	P (A4–A5)*	P (A3–A5)*
<b>I. Aorta</b>							
Aorta signal (HU)	546.12 ± 105.0	546.5 ± 105	546.5 ± 106.5	0.999	-	-	-
Aorta noise (HU)	42.5 ± 9.3	37.5 ± 8.4	32.3 ± 8.3	<0.0001	0.004	0.001	0.0001
Aorta SNR	13.3 ± 3.4	15.1 ± 4.2	17.7 ± 5.3	<0.001	0.104	0.084	0.029
Aorta CNR	15.4 ± 3.8	17.5 ± 4.6	20.5 ± 5.7	<0.001	0.076	0.040	0.011
<b>II. Left main (LM) coronary artery</b>							
LM signal (HU)	524.2 ± 117.1	525.3 ± 116.0	526.0 ± 117	0.998	-	-	-
LM noise (HU)	18.7 ± 8.8	16.1 ± 7.5	13.1 ± 6.4	<0.001	0.143	0.031	<0.0001
LM SNR	29.39 (9.9–178.6)	35 (9.8–200)	45.6 (10.3–149.2)	0.028	0.912	0.310	0.025
LM CNR	34.9 (11.0–217.3)	41.2 (11.4–226)	51.4 (11.5–168.7)	0.027	0.931	0.292	0.025
<b>III. Left anterior descending artery (LAD)</b>							
LAD signal (HU)	510.7 ± 108.7	513.4 ± 105.4	513.0 ± 177	0.984	-	-	-
LAD noise (HU)*	15 (4–46)	14 (3–38)	12 (2–31)	0.014	0.384	0.476	0.011
LAD SNR*	327 (11.1–89)	35.7 (13.4–179.6)	41.2 (16.5–271)	0.017	0.506	0.409	0.013
LAD CNR*	38.6 (14.1–95.3)	41.7 (17.1–190.3)	49.4 (00.9–288)	0.138	-	-	-
<b>IV. Left circumflex artery (LCX)</b>							
LCX signal (HU)	486.7 ± 112.8	491.0 ± 110	492.2 ± 112	0.966	-	-	-
LCX noise (HU)*	18.5 (3–51)	15 (4–44)	13 (3–38)	0.003	0.203	0.168	0.003
LCX SNR*	24.7 (8.5–82)	30.9 (14.5–119.5)	43.0 (16.8–142.3)	0.007	0.524	0.211	0.005
LCX CNR*	28.9 (12.4–96.6)	35.5 (14.5–119.7)	43.0 (16.8–142.3)	0.004	0.468	0.173	0.003
<b>V. Right coronary artery (RCA)</b>							
RCA signal (HU)	500.9 ± 125.7	502.4 ± 122.9	503.1 ± 124	0.997	-	-	-
RCA noise (HU)	19.2 ± 8.9	16.0 ± 7.9	13.3 ± 7.2	<0.001	0.063	0.058	<0.0001
RCA SNR*	26.3 (3.4–94.4)	32.8 (4.6–95.5)	40.7 (7.5–166)	0.001	0.335	0.093	0.001
RCA CNR*	30.4 (10.16–105.3)	39.6 (123.6–124.3)	49.3 (15.5–196.3)	0.0007	0.301	0.084	<0.0001
<b>VI. Averaged values from 5 vessels</b>							
Signal (HU)	513.78 ± 101.77	515.68 ± 100.53	519.78 ± 107.92	0.976	-	-	-
Noise (HU)	23.47 ± 4.5	20.28 ± 3.6	17.21 ± 3.38	<0.001	<0.001	<0.001	<0.001
SNR	31.94 ± 19.89	38.14 ± 25.19	46.35 ± 31.83	<0.001	<0.001	<0.001	<0.001
CNR	37.34 ± 22.85	44.42 ± 28.28	53.89 ± 35.05	<0.001	<0.001	<0.001	<0.001

Values are expressed as mean ± standard deviation or median (min–max), depending on the normality of the data. #One-Way analysis of variance or Kruskal–Wallis test, depending on the normality of the data,  $P < 0.05$  for statistically significant difference, \*Dunn's test,  $P < 0.05$  for statistically significant difference. ADMIRE, advanced modeled iterative reconstruction; SNR, signal-to-noise ratio; CNR, contrast-to-noise ratio; HU, Hounsfield unit. Mean signal reflects the averaged value from the regions of interest in the five vessels.

Beam-hardening artifacts were minimal or absent in almost all the datasets for both readers at all three ADMIRE strengths and did not interfere in the interpretation in any of the datasets for either reader.

Vessel sharpness in all 60 patients was lowest at A3 [14/60 (23.33%) for reader 1, 19/60 (31.67%) for reader 2] and highest in those reconstructed at A5 [60/60 (100%) for both readers]. Interobserver reliability was excellent for subjective image noise, vessel sharpness, and overall image quality at A5 (Table 3). Poor agreement for subjective image noise was determined at A3. This may be because the more experienced reader 1 (GG) was more accepting of image noise. Howev-

er, image noise did not interfere with image interpretation for either reader.

Pairwise comparisons revealed that A4 and A5 offered significantly higher Likert scores for image noise, vessel sharpness, and overall image quality compared with A3 (Table 4), and A5 was associated with a significant increase in all three of the aforementioned parameters according to the Likert scale (all  $P < 0.0001$ ). Likert scores for beam-hardening artifacts were not significantly different between the groups ( $P = 0.999$ ).

The average effective radiation dose was  $1.6 \pm 0.29$  mSv (range 1.2–2.5 mSv; dual FLASH protocol). The radiation dose with

a single FLASH scan was  $0.60 \pm 0.09$  mSv [an average of the radiation dose from the strongest diastolic dataset that was most frequently (59/60) used for interpretation].

## Discussion

High CTCA accuracy is desirable when using conventional angiography only in patients requiring revascularization therapy. FBP, which is usually used for CTCA, is fast, requires less computing power, and is more easily implemented, but it leads to noisier images with artifacts at reduced doses because of its inherent mathematical assumptions of the CT system. FBP ignores essential information such as the Poisson distribution

**Table 2. Subjective comparison between different strengths of ADMIRE**

Variables	Reader 1			Reader 2		
	ADMIRE 3 (total n = 60)	ADMIRE 4 (total n = 60)	ADMIRE 5 (total n = 60)	ADMIRE 3 (total n = 60)	ADMIRE 4 (total n = 60)	ADMIRE 5 (total n = 60)
<b>Image noise</b>						
Present and unacceptable	-	-	-	-	-	-
Present and interfering	1 (1.67%)	-	-	-	-	-
Present and not interfering	24 (40.00%)	13 (21.67%)	3 (5.00%)	49 (81.67%)	11 (18.33%)	3 (5.00%)
Minimal/absent	35 (58.33%)	47 (78.33%)	57/60 (95.00%)	11/60 (18.33%)	49 (81.67%)	57 (95.00%)
<b>Beam-hardening artifact</b>						
Present and unacceptable	-	-	-	-	-	-
Present and interfering	-	-	-	-	-	-
Present and not interfering	1 (1.67%)	1 (1.67%)	1 (1.67%)	-	-	-
Minimal/absent	59 (98.33%)	59 (98.33%)	59 (98.33%)	60 (100.00%)	60 (100.00%)	60 (100.00%)
<b>Vessel sharpness</b>						
Blurry	-	-	-	-	-	-
Poorer than average	3 (5%)	-	-	1 (1.67%)	-	-
Better than average	43 (71.66%)	16 (26.66%)	-	40 (66.66%)	7 (11.67%)	-
Sharpest	14 (23.34%)	44 (73.34%)	60 (100.00%)	19 (31.67%)	53 (88.33%)	60 (100.00%)
<b>Overall image quality</b>						
Unacceptable	-	-	-	-	-	-
Fair	4 (6.67%)	-	-	12 (20.00%)	-	-
Good	17 (28.33%)	6 (10.00%)	2 (2.33%)	21 (35.00%)	3 (5.00%)	1 (1.67%)
Excellent	39 (65.00%)	54 (90.00%)	58 (96.67%)	27 (45.00%)	57 (95.00%)	59 (98.33%)

ADMIRE, advanced modeled iterative reconstruction.

**Table 3. Interobserver variability between readers 1 and 2**

Variables	ADMIRE 3		ADMIRE 4		ADMIRE 5	
	Agreement (%)	κ value*	Agreement (%)	κ value*	Agreement (%)	κ value*
Image noise	58.3	0.26	86.6	0.58	100	1
Beam hardening	98.3	0.001	98.3	0.001	98.3	0.001
Vessel sharpness	81.6	0.59	81.3	0.43	100	1
Overall image quality	86.6	0.73	95.3	0.64	98.3	0.65

\*All P values of the kappa coefficient were significant (P < 0.001). ADMIRE, advanced modeled iterative reconstruction.

**Table 4. Likert scores for different ADMIRE strengths**

Variables	ADMIRE 3 (A3)	ADMIRE 4 (A4)	ADMIRE 5 (A5)	P (A3–A4–A5) <sup>#</sup>	P (A3–A4)*	P (A4–A5)*	P (A3–A5)*
Image noise	3.5 ± 0.5	3.7 ± 0.4	3.9 ± 0.2	<0.0001	<0.0001	0.04	<0.0001
Beam-hardening artifact	3.9 ± 0.1	3.9 ± 0.1	3.9 ± 0.2	0.999	-	-	-
Vessel sharpness	3.1 ± 0.5	3.7 ± 0.4	4.0 ± 0.1	<0.0001	<0.0001	0.005	<0.0001
Overall image quality	3.5 ± 0.6	3.9 ± 0.3	3.9 ± 0.1	<0.0001	<0.0001	0.999	<0.0001

<sup>#</sup>One-Way analysis of variance, P < 0.05 for statistically significant difference, \*post-hoc analysis (Bartlett's test), P < 0.05 for statistically significant difference. ADMIRE, advanced modeled iterative reconstruction.

of photons and CT hardware details (focal spot size, active detector area, and image voxel shape). The more complex IR has been reintroduced for CT imaging as advances in computer hardware and processing have overcome its traditional time and processing-intensive drawbacks. It has since become routine<sup>9</sup> and can compensate for a lower

tube potential or even tube current, which are associated with noisier images, by producing images of higher quality in the setting of a very low SNR, as demonstrated by multiple authors.<sup>10</sup> To further lower the patient's radiation burden, CTCA acquisition is, in the current era, primarily performed using the prospective "step-and-shoot" acquisition

and by lowering the tube current and using tube current modulation. The resulting incremental increase in noise and decrease in spatial resolution is negated by shifting from FBR to IR. Further advances in IR with the development of hybrid-IR algorithms (e.g., ASIR, AIDR 3D, and iDose) and model-based IR algorithms (e.g., ADMIRE, IMR, VEO, and

FIRST) have demonstrated that a “virtually noise-free” image with a higher CNR can be obtained.<sup>11</sup> Second-generation dual-source prospective FLASH CTCA provides an additional opportunity to combine all three techniques to obtain a maximum reduction in radiation dose with excellent image quality, mainly by lowering the tube voltage/current and using IR. The low radiation exposure results from the absent slice overlap of the FLASH CTCA protocol compared with the conventional prospectively triggered protocols. Nearly all unnecessary radiation exposure is eliminated when FLASH CTCA is used only at the beginning and end of the scanned volume. With a pitch of 3.4, time resolution of 75 ms, and full heart coverage in <0.25 s, FLASH CTCA has a reported success rate of 100% in the delineation of coronary arteries up to 1.5 mm.<sup>12</sup> FLASH CTCA is, therefore, an acceptable angiographic method for reducing radiation dose without compromising image quality. The challenge with using FLASH CTCA is that it requires a stable and low HR. HR control medications such as beta-blockers have long attempted to achieve this objective, but they have numerous drawbacks and contraindications. However, newer drugs such as ivabradine, a funny channel blocker, have recently been successfully used and have proved in studies more efficacious at lowering and stabilizing the HR.<sup>13–15</sup> We therefore incorporated this into the protocol to establish the utility of a single dose of ivabradine in lowering the HR.

Studies have also demonstrated that it is possible to perform CTCA with ultra-low-dose radiation exposure in the order of 0.1–0.5 mSv.<sup>16,17</sup> What remains unanswered is if the higher iteration strength images interfere with interpretation because of their extreme smoothing effect and the possibility of achieving the low HR required for these studies in daily routine clinical practice. The apparent subjective degradation is likely caused by the reader’s preference for obtaining images that have been used to receive FBP, indicating the need for a more conscious and concerted shift toward higher IR strengths despite the “apparent” degradation, which is an opinion shared by other authors.<sup>18</sup>

In our study, the image noise was lowest at A5 among the three IR datasets (23.4 ± 4.5 HU at A3, 20.2 ± 3.6 HU at A4, and 17.2 ± 3.3 HU at A5). The SNR was 21.3 ± 9.4 at A3, 25.9 ± 5.6 at A4, and 30.6 ± 6.9 at A5, and CNR was 26.1 ± 5.1 at A3, 30.2 ± 5.9 at A4, and 36.5 ± 7.36 at A5. Both SNR and CNR were highest at A5. The subjective image noise was high-

est at A3 and lowest at A5. Vessel sharpness and overall subjective image quality increased with the higher ADMIRE strengths and were highest at A5. These results are similar to those of the studies by Gordic et al.<sup>16</sup>, who found that both the objective as well as subjective image noise decreased with higher ADMIRE strengths. Although A4 (selected in 84%) was the preferred dataset in their study for making the diagnosis, our readers preferred A5 (selected in >96%). Images with excessive smoothing and a plastic appearance at A5, which was cited as a drawback in the previous studies, was not a disadvantage in this study. This is consistent with another study by Scholtz et al.<sup>19</sup>, who opined that despite an artificially smoothed image appearance in CT angiographies of the neck, CNR and overall quality were rated better at A5 than at A3; however, the difference was non-significant. The conclusion of both the previous and present studies is that higher strengths of iteration do not degrade image quality nor interfere with coronary assessment despite the images having a more plastic appearance. The dual FLASH protocol, consisting of two high-pitch CTCA scans performed sequentially, achieves good image quality despite an unexpectedly high HR (caused by anxiety or pain during contrast injection) and occasional premature ventricular contractions. In this study, however, we concluded that a single FLASH is sufficient for an evaluation of all the coronary vessels because, in our sample, only one patient (1/60, 1.67%) required an evaluation of both systolic and diastolic datasets for the depiction of all coronary arteries. This was likely possible because we followed a strict protocol of performing the FLASH technique only after ensuring a stable or regular HR of <75 bpm. If the patient’s HR was >75 bpm, a single 10 mg dose of ivabradine was administered 2 h before examination. In the small subset of patients receiving ivabradine, a significant reduction in the HR was noted. To the best of our knowledge, this is the first study to suggest that a single 10 mg dose of ivabradine may be efficacious in lowering the HR. A recently published abstract by Baig et al.<sup>20</sup> revealed similar results with the administration of a 15 mg dose of ivabradine. However, larger randomized studies are required to verify that this is a valid method and not confounded by the 2 h interval period prior to CTCA.

The mean radiation dose per patient was 1.6 and 0.6 mSv when only one scan (systole or diastole) was considered, which demonstrates that FLASH CTCA, when used with a low tube voltage and IR, can lead to submil-

lisievert scans and still obtain diagnostic image quality. Earlier studies have demonstrated that diagnostic image quality can also be achieved with 80 kVp using similar high-pitch techniques with exposure levels as low as 0.1–0.3 mSv despite using lower levels of IR, such as A3 or A4.<sup>19,20,23</sup> Based on the findings of our study, we hypothesize that these remarkably low exposure levels can become routinely feasible and be applied to larger subsets of the general population if adequate attention is paid to HR control (with novel and safe drugs such as ivabradine), using FLASH CTCA at 70–80 kVp, and using higher strengths of iteration to compensate for the noisy image. In routine daily practice, coronary artery evaluation is feasible with good-to-excellent image quality while simultaneously reducing radiation exposure significantly.

This study has limitations. First, this was a single vendor study from a single center only; thus, the replication of our results to other scanners and centers may be limited. Second, although anonymized images were used, the differences in image quality between reconstruction methods were at times apparent and may have impacted observer blinding. Third, quantitative noise assessment in IR can be inaccurate when using the SD from ROIs because noise is unequally distributed in the images; however, this is still an accepted criterion for noise estimation. Fourth, the effect of higher grades of iteration on the quantitative assessment of the degree of coronary artery stenosis was not assessed in this study. However, other studies have conclusively proved that stenosis assessment is not hampered with the higher iteration grade of images.<sup>19,20,23</sup> Finally, the role played by a single dose of ivabradine needs further validation through trials. The small study group is also a limitation of our study.

In conclusion, we conclude that combining FLASH CTCA, lowering tube voltage, and using IR leads to a significant reduction in radiation dose exposure closer to “true” submillisievert levels in patients, especially if combined with novel drugs such as ivabradine to lower the HR. The highest strength of IR, despite the plastic appearance of the images, does not interfere with image interpretation and leads to a significant increase in SNR and CNR. The higher strengths of iteration with its superior noise-reducing capabilities but the consequent plastic/smoothed appearance is likely the lesser of two evils because it improves diagnostic image quality, allowing for a greater reduction in tube voltage and consequent radiation exposure.

## Conflict of interest disclosure

The authors declared no conflicts of interest.

## References

1. Trattner S, Halliburton S, Thompson CM, et al. Cardiac-specific conversion factors to estimate radiation effective dose from dose-length product in computed tomography. *JACC Cardiovasc Imaging*. 2018;11(1):64-74. [\[CrossRef\]](#)
2. Abbara S, Blanke P, Maroules CD, et al. SCCT guidelines for the performance and acquisition of coronary computed tomographic angiography: a report of the society of cardiovascular computed tomography guidelines committee: endorsed by the North American Society for Cardiovascular Imaging (NASCI). *J Cardiovasc Comput Tomogr*. 2016;10(6):435-449. [\[CrossRef\]](#)
3. Deseive S, Pugliese F, Meave A, et al. Image quality and radiation dose of a prospectively electrocardiography-triggered high-pitch data acquisition strategy for coronary CT angiography: the multicenter, randomized PROTECTION IV study. *J Cardiovasc Comput Tomogr*. 2015;9(4):278-285. [\[CrossRef\]](#)
4. Tayal U, King L, Schofield R, et al. Image reconstruction in cardiovascular CT: part 2 - iterative reconstruction; potential and pitfalls. *J Cardiovasc Comput Tomogr*. 2019;13(3):3-10. [\[CrossRef\]](#)
5. Naoum C, Blanke P, Leipsic J. Iterative reconstruction in cardiac CT. *J Cardiovasc Comput Tomogr*. 2015;9(4):255-263. [\[CrossRef\]](#)
6. Halliburton SS, Tanabe Y, Partovi S, Rajiah P. The role of advanced reconstruction algorithms in cardiac CT. *Cardiovasc Diagn Ther*. 2017;7(5):527-538. [\[CrossRef\]](#)
7. Pontana F, Castellano I, Ismail T, Gartland N, Rubens M, Nicol E. 131 reduced-dose dual-source coronary computed tomography angiography (CCTA): is raw-data-based iterative reconstruction able to maintain diagnostic confidence? *Heart*. 2015;101:A75. [\[CrossRef\]](#)
8. Bongartz G, Golding SJ, Jurik AG, et al. European guidelines for multislice computed tomography. Luxembourg: European Commission, 2004. [\[CrossRef\]](#)
9. Padole A, Ali Khawaja RD, Kalra MK, Singh S. CT radiation dose and iterative reconstruction techniques. *AJR Am J Roentgenol*. 2015;204:W384-W392. [\[CrossRef\]](#)
10. Moscariello A, Takx RA, Schoepf UJ, et al. Coronary CT angiography: image quality, diagnostic accuracy, and potential for radiation dose reduction using a novel iterative image reconstruction technique-comparison with traditional filtered back projection. *Eur Radiol*. 2011;21(10):2130-2138. [\[CrossRef\]](#)
11. Ippolito D, Riva L, Talei Franzesi CR, et al. Diagnostic efficacy of model-based iterative reconstruction algorithm in an assessment of coronary artery in comparison with standard hybrid-iterative reconstruction algorithm: dose reduction and image quality. *Radiol Med*. 2019;124(5):350-359. [\[CrossRef\]](#)
12. Zhao RP, Hao ZR, Song ZJ. Diagnostic value of Flash dual-source CT coronary artery imaging combined with dual-energy myocardial perfusion imaging for coronary heart disease. *Exp Ther Med*. 2014;7(4):865-868. [\[CrossRef\]](#)
13. Adile KK, Kapoor A, Jain SK, et al. Safety and efficacy of oral ivabradine as a heart rate-reducing agent in patients undergoing CT coronary angiography. *Br J Radiol*. 2012;85(1016):e424-e428. [\[CrossRef\]](#)
14. Saburudin A, Chan AL, Nasir NM. Ivabradine as an effective heart rate controlling agent in coronary computed tomography angiography: a systematic review. *J Hear Health*. 2016;2(2). [\[CrossRef\]](#)
15. Qiu S, Shi S, Ping H, Zhou S, Wang H, Yang B. Efficacy of ivabradine versus  $\beta$ -blockers for heart rate reduction during computed tomography coronary angiography: a meta-analysis of randomized controlled trials. *Cardiology*. 2016;135(3):133-140. [\[CrossRef\]](#)
16. Gordic S, Desbiolles L, Sedlmair M, et al. Optimizing radiation dose by using advanced modelled iterative reconstruction in high-pitch coronary CT angiography. *Eur Radiol*. 2016;26(2):459-468. [\[CrossRef\]](#)
17. Cha MJ, Seo JS, Yoo DS, Chong S. Knowledge-based iterative model reconstruction in coronary computed tomography angiography: comparison with hybrid iterative reconstruction and filtered back projection. *Acta Radiol*. 2018;59(3):280-286. [\[CrossRef\]](#)
18. Schofield R, King L, Tayal U, et al. Image reconstruction: part 1 - understanding filtered back projection, noise and image acquisition. *J Cardiovasc Comput Tomogr*. 2020;14(3):219-225. [\[CrossRef\]](#)
19. Scholtz JE, Wichmann JL, Hüsers K, et al. Third-generation dual-source CT of the neck using automated tube voltage adaptation in combination with advanced modeled iterative reconstruction: evaluation of image quality and radiation dose. *Eur Radiol*. 2016;26(8):2623-2631. [\[CrossRef\]](#)
20. Baig M, Ahmed H, Nazir A, Anwar A, Raja Y. Single dose ivabradine (15 mg single dose 2 hours before the scan) is safe & effective in reducing heart rate before cardiovascular Ct angiogram (ctca). *J Cardiovasc Comput Tomogr*. 2019;13:S10. [\[CrossRef\]](#)
21. Chaosuwanakit N, Makarawate P. Reduction of radiation dose for coronary computed tomography angiography using prospective electrocardiography-triggered high-pitch acquisition in clinical routine. *Pol J Radiol*. 2018;83:e260-e267. [\[CrossRef\]](#)
22. Yin WH, Lu B, Li N, et al. Iterative reconstruction to preserve image quality and diagnostic accuracy at reduced radiation dose in coronary CT angiography: an intraindividual comparison. *JACC Cardiovasc Imaging*. 2013;6(12):1239-1249. [\[CrossRef\]](#)
23. Lee J, Kim TH, Lee BK, et al. Diagnostic accuracy of low-radiation coronary computed tomography angiography with low tube voltage and knowledge-based model reconstruction. *Sci Rep*. 2019;9(1):1308. [\[CrossRef\]](#)



# The value of dual-energy computed tomography in the evaluation of myocarditis

Mecit Kantarcı   
Ümmügülsüm Bayraktutan   
Abdusselam Akbulut   
Onur Taydaş   
Naci Ceviz   
Fadime Güven   
Hayri Oğul   
Sonay Aydın 

## PURPOSE

The inflammation of the heart muscle is referred to as acute myocarditis. Cardiac magnetic resonance imaging (CMR) has become the primary method for a non-invasive assessment of myocardial inflammation. However, there are several drawbacks of CMR. During the last decade, dual energy computed tomography (DECT) has been used in cardiac imaging. The current study aims to assess the efficacy and feasibility of DECT in acute myocarditis and compare the results to CMR.

## METHODS

This prospective study included patients who had myocarditis but no coronary artery pathology. Two observers evaluated the patients for acute myocarditis using DECT and CMR. CMR was performed on 22 patients within 24 hours of DECT, which was administered within 12 hours following the onset of chest pain. Inter-observer agreement was tested with Cohen's Kappa coefficient, and Spearman's correlation was used to examine the possible correlations. A *P* value of <0.050 was accepted as statistically significant.

## RESULTS

The DECT and CMR agreement was significant for transmural diagnoses, excellent for subepicardial and intramyocardial diagnoses, and perfect for nodular and band-like patterns.

## CONCLUSION

The findings of this study showed that the dark areas on the color-coded iodine map created with DECT were strongly correlated with CMR in acute cases of myocarditis. In addition, DECT is a robust imaging method that can also be used in the diagnosis of acute myocarditis. Furthermore, it provides information about coronary arteries faster and more reliably than magnetic resonance imaging without any limitations.

## KEYWORDS

Dual-energy computed tomography, cardiac magnetic resonance imaging, magnetic resonance imaging, myocarditis

From the Department of Radiology (M.K. ✉ akkanrad@hotmail.com, Ü.B., A.A., F.G., H.O.), Atatürk University Faculty of Medicine, Erzurum, Turkey; Department of Radiology (O.T.), Sakarya University Faculty of Medicine, Sakarya, Turkey; Department of Pediatric Cardiology (N.C.), Atatürk University Faculty of Medicine, Erzurum, Turkey; Department of Radiology (S.A.), Erzincan Binali Yıldırım University Faculty of Medicine, Erzincan, Turkey.

Received 23 July 2021; revision requested 19 September 2021; last revision received 13 November 2021; accepted 16 December 2021.



Epub: 27.01.2023

Publication date: 29.03.2023

DOI: 10.5152/dir.2022.21749

The inflammation of the heart muscle is referred to as acute myocarditis. The etiology of this condition is influenced by infections, toxins, hypersensitivity/autoimmune factors, and drugs. Myocarditis can cause a variety of symptoms, including sudden death or cardiogenic shock, recent onset heart failure due to ventricular dysfunction, chest pain, ventricular arrhythmias, and atrial arrhythmias.<sup>1,2</sup>

Electrocardiography (ECG) findings in some cases of focal myopericarditis are indistinguishable from myocardial infarction with ST segment elevation.<sup>3</sup>

The gold standard for diagnosing myocarditis is an endomyocardial biopsy (EMB).<sup>4</sup> The role of an EMB in diagnosing pathologic entities has evolved over time. The Dallas criteria are controversial because many patients who did not meet the Dallas criteria were eventu-

You may cite this article as: Kantarcı M, Bayraktutan Ü, Akbulut A, et al. The value of dual-energy computed tomography in the evaluation of myocarditis. *Diagn Interv Radiol.* 2023;29(2):276-282.

ally diagnosed with myocarditis.<sup>5</sup> Because of the risk of complications and the low sensitivity of histological studies due to the small sampling area, non-invasive diagnostic tests are required.<sup>6</sup> According to one study, increased myocardial delayed enhancement with cardiac magnetic resonance imaging (CMR) correlates well with the presence of an active inflammatory process detected in the histopathology of EMBs.<sup>7</sup> In patients with suspected myocarditis, CMR has become the primary method for a non-invasive assessment of myocardial inflammation.<sup>7-11</sup> Following the introduction of myocardial mapping, new Lake Louise Criteria (nLLC) were recently published, which redefined imaging diagnoses based on the presence of a T1 criterion [presence of late gadolinium enhancement (LGE) or increased T1 mapping or extracellular volume values] and a T2 criterion (hyperintensity in T2 weighted Short tau inversion recovery or increased T2 mapping values). Results revealed that nLLC improved the CMR diagnostic performance for the diagnosis of acute myocarditis, particularly in cases with unusual clinical presentation.<sup>12</sup> However, there are several drawbacks of CMR, such as the long scan time, the fact that it is not universally available, the high cost, claustrophobia, incompatibility with pacemakers, and the incompatibility of prostheses with this technique.<sup>13,14</sup>

Dual-energy computed tomography (DECT) is a developing technology that provides information about the material composition via image acquisition by varying photon energy levels.<sup>15</sup> During the last decade, DECT has been used in cardiac imaging.<sup>16,17</sup> When different energy levels of X-ray spectra penetrate through iodine as a contrast material, it exhibits unique absorption characteristics. As a result, iodine mapping reveals the distribution of iodine in the myocardium,<sup>16</sup> where the dark areas indicate a lack of iodine,

and DECT precisely detects cardiac perfusion defects.<sup>18,19</sup>

The current study aims to assess the efficacy and feasibility of DECT in acute myocarditis and compare the results to CMR.

## Methods

### Study population

The institutional ethics committee approved the study (ATAUNI-KAEK-19-1-13). All participants were enrolled in the study after providing written informed consent, which was obtained from the parents in pediatric cases.

This prospective study began with the recruitment of 41 consecutive patients admitted to our hospital over a 30-month period for acute chest pain mimicking acute coronary syndrome, with high troponin levels but no specific ECG findings indicating typical ischemia.

Exclusion criteria for coronary diseases included the following: (1) a history of cardiac bypass surgery (one patient); (2) a history of coronary stenting (two patients); and (3) the presence of coronary stenosis or occlusion on DECT (two patients). Another five patients were ruled out due to chronic renal failure an unstable hemodynamic state (one patient), and a high heart rate (>80 beats per minute) that made them susceptible to DECT artifacts (three patients). In addition, seven cases (four DECT studies and three CMR studies) with poor image quality and numerous artifacts were eliminated from further consideration. Two patients were ruled out due to claustrophobia. The study group included 22 patients who met the selection criteria (13 males, 9 females; median age, 14 years; range, 1–22 years).

### Study design

Within 12 hours of the onset of chest pain, DECT was used to assess these patients. Following DECT, all patients were evaluated by CMR within a maximum of 24 hours. All patients' creatine kinase (CK), CK-muscle/brain (CKMB), troponin I, ECG, and transthoracic echocardiography (TTE) results were recorded.

To assess the image quality of each coronary segment on DECT, the following five-point scale was used: 5, no motion artifacts; 4, minor artifacts (mild blurring); 3, moderate artifacts (moderate blurring without discontinuity); 2, severe artifacts (doubling or discontinuity along the coronary segments);

and 1, unreadable (vessel structures not differentiable). A score of  $\geq 4$  was considered to indicate acceptable image quality.<sup>20</sup>

### DECT protocol

The DECT examinations were carried out using a 64-slice dual-source multi detector CT scanner (Somatom Definition Flash, Siemens Healthcare, Forchheim, Germany). At a flow rate of 5 mL/s, 70 mL of iopromide (ultravist 370 mg/mL, Bayer Schering Pharma, Berlin, Germany) was injected into the right antecubital vein, followed by 60 mL of saline. The region of interest (ROI) was located in the left ventricle using a bolus tracking technique (CARE-bolus, Siemens Healthcare, Forchheim, Germany). The data collection began at a specific time determined by a single ROI system with a trigger threshold of 200 HU in the left ventricle blood pool. Data collection began 8 s after triggering, with data collected in the arterial phase. The scan mode was a retrospective low-pitch ECG-gated scan with ECG pulsing (a prospective protocol could not be applied to the artifacts during the dual-energy protocol). In the retrospective protocol, ECG dose modulation was used for all patients. For each patient, the CT dose index volume and the dose-length product of the DECT scans were recorded.

During the procedure, the patients were instructed to use the deep-inspiration breath-hold technique, and the scan was performed craniocaudally from the subcarinal level to the diaphragm. For the cardiac cycle, the reconstruction window of the initial axial images was set to 75% (end of diastolic phase) and 45% (end of the systolic phase).

The high- and low-voltage data were reconstructed for the myocardial evaluation using a dual-energy convolution core (D30f) with a temporal resolution of 140 ms and a thickness of 1.5 mm, with 1 mm increments used to optimize the signal/noise ratio. The reconstructed data sets were then tested with a three-material decomposition software analysis platform (Syngo Multimodality Workplace; Siemens, Erlangen, Germany).

### CMR protocol

A 3.0 T magnetic resonance imaging (MRI) device (Magnetom Skyra, Siemens Healthcare, Berlin, Germany) with a 16-channel cardiac coil was used to examine all the patients. All the scans were conducted with the patient in the supine position, and the images were taken during a single breath hold. Gadolinium-enhanced T1-weighted

#### Main points

- Dual energy computed tomography (DECT) is increasingly used for the diagnosis of cardiac pathologies with a reasonable radiation dose, including acute myocarditis. In addition, DECT is strongly correlated with cardiac magnetic resonance imaging in acute cases of myocarditis.
- The combination of a computed tomography coronary angiography and an iodine map with DECT within a single examination can accurately diagnose malignant coronary artery anomalies, coronary artery disease, and acute myocarditis, which can cause symptoms of acute coronary syndrome.

and T2-weighted CMR sequences were obtained by matching with routine short-axis images. After bolus infusion, first-pass perfusion sequences were obtained by injecting 0.1 mmol (i.e., 10–20 mL) of gadoterate dimeglumine (Dotarem; Guerbet, Aulnay-sous-Bois, France) at a rate of 3–4 mL/s, followed by a 30 mL saline flush at the same rate. Next, LGE CMR was performed 10 minutes after the contrast agent was administered intravenously. A two-dimensional phase-sensitive inversion recovery breath-hold sequence was used for LGE imaging at least 10 minutes after the last gadolinium administration. All images were uploaded to the Syngo Multimodality Workplace for review.

### Image analysis

Two radiologists (M.K. and Ü.B., with 13 and 6 years of experience in cardiac CT and MRI, respectively), who were blinded to the clinical data, first independently reviewed the CT images using the 17-segment model according to the American Heart Association classification of the segmentation of the left ventricular myocardium. The main coronary arteries and branches were also evaluated for intraluminal pathologies and anomalies. Before evaluating the myocardium using DECT, on the workstation, the “DE normalize contrast” procedure was applied to standardize the visual evaluation to remove any bias related to inter-observer variability (Figure 1). Arterial phase images were used for the myocardial evaluation. The dark areas on the color-coded iodine map were accepted as pathological fields and recorded for each patient and segment. The two radiologists reached a consensus for the protocol concerning the evaluation of myocarditis when examining the CMR findings of the patients according to the segments at two-day intervals after the DECT evaluation of the combination of coronary CT angiography and iodine map images in a single examination.

A CMR diagnosis of myocarditis was made based on the updated LLC (2018) (Table 1).

The dark areas on the iodine map images on DECT and increased signal intensity areas on the T2-weighted images and LGE in CMR

were noted following a segment-by-segment analysis and visually compared. The number of segments involved, anatomic location (transmural, intramyocardial, subepicardial, subendocardial), and pattern of involvement (nodular, band-like) were also recorded for each segment.

### Statistical analysis

Statistical analyses were performed using SPSS v. 20.0 software (SPSS Inc, Chicago, IL, U.S.A.). Conformity of the data to normal distribution was assessed using the Kolmogorov–Smirnov test. Numerical variables with normal distribution were shown as mean  $\pm$  standard deviation values, variables without normal distribution as median (minimum–maximum) values, and categorical variables as numbers (n) and percentages (%). The sensitivity, specificity, and positive and negative predictive values of observer 1 and observer

2 were calculated according to the segments, location, and pattern obtained from the CMR results. Observers 1 and 2 independently evaluated the CT images for the presence of myocarditis. Cohen’s Kappa coefficient was used to assess the agreement between Observers 1 and 2 regarding the myocarditis diagnosis in terms of the segments, location, and pattern. Accordingly, the degree of agreement was evaluated as slight if the coefficient was 0 to 0.20, fair if it was 0.21 to 0.40, moderate if it was 0.41 to 0.60, substantial if it was 0.61 to 0.80, and almost perfect if it was 0.81 to 1.00.<sup>21</sup> According to the normality assessment of the Kolmogorov–Smirnov test, a Spearman Correlation coefficient was performed for Observer 1, Observer 2, DECT, and CMR data in terms of the total number of segments detected for each patient. A *P* value of <0.005 was accepted as statistically significant.

### Results

An evaluation was made in a total of 22 patients, comprising 13 (59.11%) males and nine (40.90%) females. The mean age of the population and serum concentrations of CK, CKMB, and troponin are shown in detail in Table 2. An infectious episode less than three weeks before admission was reported in 19 patients. For the remaining patients, the primary symptoms were restlessness and acute chest pain. No patient showed signs of cardiac failure or dyspnea. In the ECG, ST-segment elevation was observed in one patient, ST depression was found in three patients, and T-wave inversion was present in five patients. The ECG showed mild tricuspid insufficiency in four patients and left ventricular hypokinesia in five patients. All examinations were completed on time and without any complications. One of the patients had a coronary

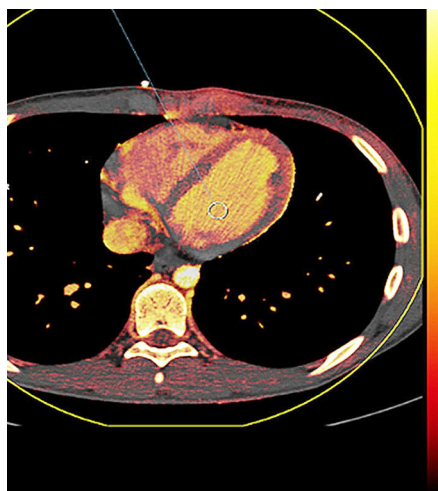


**Figure 1.** The procedure of “DE normalize contrast” (indicated by arrows) in the iodine map on dual energy computed tomography using a dedicated workstation. DE, dual energy.

**Table 2.** Distribution of cardiac enzymes and ages in patients

	Number	Mean $\pm$ SD	Median (min–max)
CK (UI/L)	22	351.18 $\pm$ 75.39	149 (39–3691)
CKMB (UI/L)	22	43.54 $\pm$ 3.81	33 (10–203)
Troponin (ng/mL)	22	8.26 $\pm$ 2.41	0.15 (0.04–85)
Age (years)	22	13.50 $\pm$ 6.62	14 (1–32)

SD, standard deviation; CK, creatine kinase; CKMB, creatine kinase-muscle/brain.

**Table 1.** Updated Lake Louise Criteria (2018)

CMR provides strong evidence for myocardial inflammation with increasing specificity and demonstrates the combination of myocardial edema and inflammatory myocardial injury if both of the following criteria (T1 and T2) are present:

- Regional or global increase of native T2 times or regional or global increase of T2 signal intensity
- Regional or global increase of T1 times, regional or global increase of ECV, or regional non-ischemic LGE signal pattern

Supportive criteria: pericardial effusion, pericardial signal abnormalities, or systolic left ventricle dysfunction

CMR, cardiac magnetic resonance; ECV, extracellular volume; LGE, late gadolinium enhancement.

anomaly. Left anterior descending artery had a course between the aorta and the pulmonary artery. A catheter angiography was not performed since no intraluminal pathology was observed in DECT. All patients were discharged without complications. The patients were checked by laboratory tests (troponin I) and ECG three weeks after the treatment, and no pathology was detected. The cases that previously had pathological findings on TTE also showed improvement. The effective radiation dose of DECT was calculated using a technique proposed by the European

Guidelines on Quality Criteria. The radiation dose parameters for the DECT scans were 315 mGy × cm in the dose-length product, and 7.05 mGy in volume CT dose index.

The dark areas on the iodine map images on DECT and the corresponding increased intensity areas on the T2-weighted scans and LGE in CMR appeared to be nodular or band-like with a subepicardial, intramyocardial, or transmural anatomical location within the left ventricular wall (Figures 2-4). No patient had subendocardial involvement. The dark and normal areas on the iodine map imag-

es on DECT were measured using ROI. The mean value of the dark areas was  $125.67 \pm 40.02$  HU (range, 68–200), while that of the normal areas was  $49.08 \pm 12.90$  HU (range, 30–70).

The involved segments on DECT and CMR are shown in Table 3 according to the evaluation based on the number of segments. Table 4 shows the sensitivity, specificity, and positive and negative predictive values of both observers for the CT diagnosis based on CMR data.

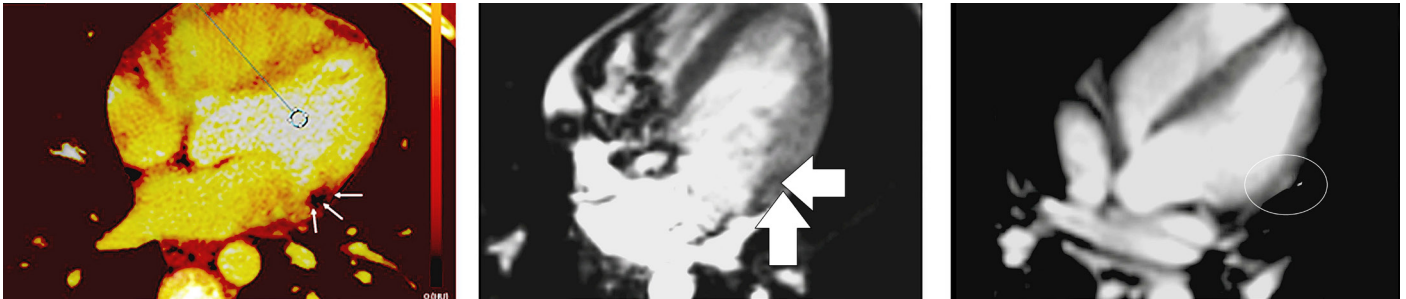


**Figure 2.** Nodular transmural involvement of acute myocarditis. The dark areas on the iodine map on the dual energy computed tomography image (thin arrows), the corresponding edema on the T2-weighted image (thick arrows), and hyperenhancement on the late gadolinium enhancement image (in the circle) in the cardiac magnetic resonance image.

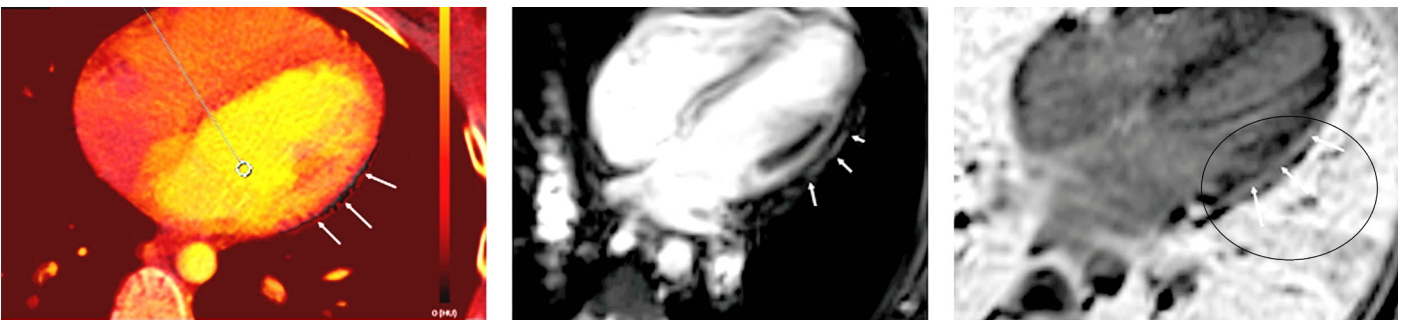


**Figure 3.** Band-like intramyocardial involvement of acute myocarditis. The dark areas on the iodine map on the dual energy computed tomography image (long arrows), the corresponding edema on T2-weighted image (short arrows), and hyperenhancement on the late gadolinium enhancement image (in the circle with arrows) in the cardiac magnetic resonance image. The arrows indicate the band-like intramyocardial involvement of acute myocarditis.

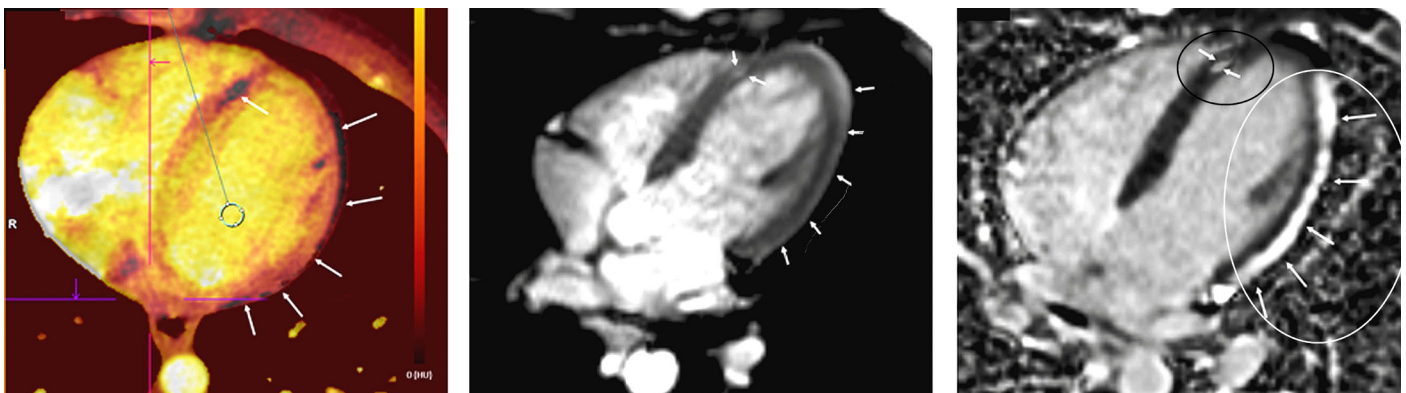


**Figure 4.** Band-like subepicardial involvement of the lateral wall and nodular intramyocardial involvement of the septum of the left ventricle in acute myocarditis. The dark areas on the iodine map on the dual energy computed tomography (DECT) image (single long arrow), the corresponding edema on the T2-weighted image (double short arrow), and hyperenhancement on the late gadolinium enhancement (LGE) image (in the dark circle with arrows) in the cardiac magnetic resonance image (CMR) for nodular intramyocardial involvement of the septum of the left ventricle. The dark areas on the iodine map on the DECT image (multiple long arrows), the corresponding edema on the T2-weighted image (multiple short arrows), and hyperenhancement on the LGE image (in the white circle with arrows) in CMR for band-like subepicardial involvement of the lateral wall.

**Table 3.** Distribution of segments determined by observer 1 and observer 2 on the DECT and consensus MRI findings

Patient	Observer 1 segments on DECT	Observer 2 segments on DECT	Segments on MRI
1	5	5	5
2	4, 5, 6	4, 5, 6	4, 6
3	17, 16, 11, 12, 5, 6	17, 16, 11, 12, 5, 6	17, 16, 11, 12, 5, 6
4	16	16	16
5	6, 12, 4, 10, 2	6, 12, 4, 10, 2	6, 12, 4, 10
6	14, 2	14	14
7	8, 12, 14	8, 12, 14	8, 12, 14
8	14, 8, 9, 3	14, 8, 9	14, 8
9	8, 14, 6	8, 14	8, 14
10	9, 10, 14, 3	9, 10, 14	9, 10, 14
11	2, 3	2, 3	2, 3
12	8, 12	8, 12	8, 12
13	14, 8, 12	14, 8, 12	14, 8, 12
14	12, 14, 1, 2	12, 14	12, 14
15	8, 12	12	12
16	14, 16, 17, 8, 9	14, 16, 17, 8, 9	14, 16, 17
17	12	12	12
18	12, 16	12, 16	12
19	5, 11, 4	5, 11, 4	5, 11
20	11, 12, 16, 8	11, 12, 16	11, 12, 16
21	5, 6, 10, 11	5, 6, 10, 11	5, 6
22	3, 8, 9	3, 8, 9	8, 9

DECT, dual-energy computed tomography; MRI, magnetic resonance imaging.

**Table 4.** Sensitivity, specificity, and positive and negative predictive values of both observers

Observers	Sensitivity (%)	Specificity (%)	Negative predictive value (%)	Positive predictive value (%)
Observer 1	83	87	91	93
Observer 2	89	91	94	96

For observer 1, there was low to moderate agreement between the DECT and CMR findings of segments 2 and 3; substantial agreement for segments 4, 8, 9, and 10; and nearly perfect agreement for segments 5, 6, 11, 12, 14, 16, and 17.

For observer 2, there was low to moderate agreement between the DECT and CMR findings of segment 9; moderate agreement for segment 16; and nearly perfect agreement for segments 5, 8, 11, 12, 14, and 17.

According to the evaluation based on the anatomic location and pattern, the agreement between DECT and CMR was substantial for the diagnosis of transmural involvement, excellent for subepicardial and intramyocardial diagnoses, and almost perfect for nodular and band-like patterns for both observers.

In segments 2, 3 and 16, there was substantial agreement between observer 1 and observer 2, while nearly perfect agreement

was found in the remaining segments (coefficient was 0 to 0.20 fair, 0.21 to 0.40 moderate, 0.41 to 0.60 substantial, 0.61 to 0.80; and almost perfect 0.81 to 1.00) (Table 5).

There was a statistically significant correlation between the total number of segments individually identified on DECT and CMR by observer 1 and observer 2.

**Table 5.** Consensus between observers regarding computed tomography segments

Segment	Kappa	P value
2	0.621	0.002
3	0.621	0.002
4	1.000	<0.001
5	1.000	<0.001
6	0.861	<0.001
8	0.805	<0.001
9	0.831	<0.001
10	1.000	<0.001
11	1.000	<0.001
12	1.000	<0.001
14	1.000	<0.001
16	0.699	0.001
17	1.000	<0.001

**Table 6.** Distribution of correlation between the DECT findings of the observers and the consensus MRI in terms of the total number of segments

	r*	P
Observer 1 DECT - MRI	0.712	<0.001
Observer 2 DECT - MRI	0.769	<0.001
Observer 1 DECT - observer 2 DECT	0.830	<0.001

\*r, correlation coefficient; DECT, dual-energy computed tomography; MRI, magnetic resonance imaging.

The inter-observer agreement was substantial, and the correlation between the total number of segments on DECT identified by both observers was statistically significant.

The correlation was found to be statistically significant in terms of the total number of segments diagnosed between the DECT and CMR findings for both observer 1 and observer 2, as well as in the comparison between the two observers ( $P < 0.001$ ) (Table 6).

## Discussion

In this study, the dark areas on the color-coded iodine map on DECT, which represent pathological myocardial tissue, were compared with the increased intensity areas on the T2-weighted scans and gadolinium enhancement in CMR.

Acute myocarditis is relatively uncommon, and EMB is the gold standard in diagnosis; however, due to its invasiveness and lack of sensitivity, non-invasive techniques have become more popular.<sup>22</sup> Therefore, CMR, with T2-weighted imaging and LGE, has become more widely adopted. Previous studies have shown that CMR correlates with acute inflammation sites histopathologically.<sup>7,9,10</sup> Some studies that use cardiac CT demonstrated that the delayed enhancement areas were similar to those seen on CMR in acute myocarditis.<sup>7,9,10,23</sup>

The DECT technique is used in cardiac imaging to provide information about the coronary artery system and myocardial perfusion with a single contrast-enhanced CT scan obtained within a few seconds using a reasonable radiation dose.<sup>18,24,25</sup> The DECT scans can be obtained with suitable doses similar to single-energy CT.<sup>26</sup> A previous study on cardiac contusion showed the efficiency and feasibility of DECT with a reasonable radiation dose.<sup>27</sup> Moreover, the radiation doses in the current study were lower than those reported in the literature.<sup>28</sup>

A case study of two patients with acute myocarditis showed focal myocardial hypoenhancement areas on an early-phase rou-

tine cardiac CT corresponding to high signals on the T2-weighted MR images and LGE,<sup>29</sup> which were attributed to edema. In another case report, it was found that abnormally delayed iodine enhancement areas on DECT showed an excellent topographic match with CMR.<sup>30</sup>

In the present study, DECT was used to evaluate coronary arteries and myocardial abnormalities. None of the patients had a coronary artery anomaly or pathology. Since malignant coronary artery anomalies and coronary artery disease may lead to similar clinical features to acute myocarditis, it is important to also confirm their presence on DECT. Although DECT is not sufficient to show intraluminal pathologies in distal branches, this study demonstrated its ability to easily show coronary anomalies and intraluminal pathologies in the main branches. In addition, no patient in the current study had a history of coronary artery disease, and the dark areas observed on DECT did not correspond to a coronary artery territory.

Both observers noted that more segments were involved in cardiac DECT than CMR. They were both found to have false positive results. Some of these segments found by observer 1 could be interpreted as beam-hardening artifacts where the heart muscle was thinner. In addition, the literature emphasized that to optimize virtual monoenergetic imaging, the width/length (W/L) setting is crucial.<sup>31,32</sup> Additional research to standardize W/L settings may improve the reliability of DECT in myocarditis imaging.

Some patients in this study had black areas in the late phase on DECT. Early and late enhancements of CMR in myocarditis have been reported in the literature.<sup>33,34</sup> In a comprehensive study by Aquaro et al.<sup>35</sup>, various enhancement patterns in different areas of myocarditis were detected and found to be related to the prognosis. In the current study, although these areas were considered to correspond to early enhancement areas in CMR, the HU values that were measured from these areas were higher than those of the normal myocardium, which creates confusion. Therefore, a histopathological cor-

relation is needed for a clear understanding of this pathophysiology.

There were several limitations to this study, primarily the small patient group. A non-trivial number of initially selected patients were excluded for various reasons, the key subcohort of these patients being those with an inadequate heart rate or suboptimal scan quality. An inadequate heart rate can cause explicit artifacts, which can potentially limit the wider applicability of this technique in this setting. However, this limitation can be overcome by the administration of beta blockers. Larger multicentric and collaborative investigations are required to define the clinical value of DECT and confirm the findings of the current study. Further studies are needed to determine the contrast pattern of the black areas seen in the late phase on DECT. Another limitation was that the distal branches of the coronary arteries could not be assessed due to the technical incompatibility of DECT. Finally, in areas other than the left ventricular free wall, the evaluation was suboptimal due to the beam-hardening artifacts. These limitations could be overcome using advanced technological developments in further DECT studies.

In conclusion, the results of this study showed that the dark areas on the color-coded iodine map on DECT were strongly correlated with CMR in acute cases of myocarditis. The combination of CT coronary angiography and an iodine map with a DECT in a single examination can accurately diagnose malignant coronary artery anomalies, coronary artery disease, and acute myocarditis that can cause symptoms of acute coronary syndrome.

## Conflict of interest disclosure

The authors declared no conflicts of interest.

## References

1. McCarthy RE 3rd, Boehmer JP, Hruban RH, et al. Long-term outcome of fulminant myocarditis as compared with acute (nonfulminant) myocarditis. *N Engl J Med.* 2000;342(10):690-695. [CrossRef]
2. Feldman AM, McNamara D. Myocarditis. *N Engl J Med.* 2000;343(19):1388-1398. [CrossRef]
3. Munguti CM, Akidiva S, Wallace J, Farhoud H. ST segment elevation is not always myocardial infarction: a case of focal myopericarditis. *Case Rep Cardiol.* 2017;2017:3031792. [CrossRef]
4. Aretz HT, Billingham ME, Edwards WD, et al. Myocarditis. A histopathologic definition and classification. *Am J Cardiovasc Pathol.* 1987;1(1):3-14. [CrossRef]

5. Ahmed T, Goyal A. Endomyocardial Biopsy. StatPearls [Internet]. 2021. [\[CrossRef\]](#)
6. Ammirati E, Veronese G, Bottiroli M, et al. Update on acute myocarditis. *Trends Cardiovasc Med.* 2021;31(6):370-379. [\[CrossRef\]](#)
7. Mahrholdt H, Goedecke C, Wagner A, et al. Cardiovascular magnetic resonance assessment of human myocarditis: a comparison to histology and molecular pathology. *Circulation.* 2004;109(10):1250-1258. [\[CrossRef\]](#)
8. Friedrich MG, Sechtem U, Schulz-Menger J, et al. Cardiovascular magnetic resonance in myocarditis: A JACC White Paper. *J Am Coll Cardiol.* 2009;53(17):1475-1487. [\[CrossRef\]](#)
9. Friedrich MG, Strohm O, Schulz-Menger J, Marciniak H, Luft FC, Dietz R. Contrast media-enhanced magnetic resonance imaging visualizes myocardial changes in the course of viral myocarditis. *Circulation.* 1998;97(18):1802-1809. [\[CrossRef\]](#)
10. Laissy JP, Hyafil F, Feldman LJ, et al. Differentiating acute myocardial infarction from myocarditis: diagnostic value of early- and delayed-perfusion cardiac MR imaging. *Radiology.* 2005;237(1):75-82. [\[CrossRef\]](#)
11. Laissy JP, Messin B, Varenne O, et al. MRI of acute myocarditis: a comprehensive approach based on various imaging sequences. *Chest.* 2002;122(5):1638-1648. [\[CrossRef\]](#)
12. Cundari G, Galea N, De Rubeis G, et al. Use of the new Lake Louise Criteria improves CMR detection of atypical forms of acute myocarditis. *Int J Cardiovasc Imaging.* 2021;37(4):1395-1404. [\[CrossRef\]](#)
13. Saeed M, Van TA, Krug R, Hetts SW, Wilson MW. Cardiac MR imaging: current status and future direction. *Cardiovasc Diagn Ther.* 2015;5(4):290-310. [\[CrossRef\]](#)
14. Stokes MB, Nerlekar N, Moir S, Teo KS. The evolving role of cardiac magnetic resonance imaging in the assessment of cardiovascular disease. *Aust Fam Physician.* 2016;45(10):761-764. [\[CrossRef\]](#)
15. Karçaaltıncaba M, Aktaş A. Dual-energy CT revisited with multidetector CT: review of principles and clinical applications. *Diagn Interv Radiol.* 2011;17(3):181-194. [\[CrossRef\]](#)
16. Vliegenthart R, Pelgrim GJ, Ebersberger U, Rowe GW, Oudkerk M, Schoepf UJ. Dual-energy CT of the heart. *AJR Am J Roentgenol.* 2012;199(Suppl 5):S54-S63. [\[CrossRef\]](#)
17. McCollough CH, Leng S, Yu L, Fletcher JG. Dual- and multi-energy ct: principles, technical approaches, and clinical applications. *Radiology.* 2015;276(3):637-653. [\[CrossRef\]](#)
18. Ruzsics B, Lee H, Zwerner PL, Gebregziabher M, Costello P, Schoepf UJ. Dual-energy CT of the heart for diagnosing coronary artery stenosis and myocardial ischemia-initial experience. *Eur Radiol.* 2008;18(11):2414-2424. [\[CrossRef\]](#)
19. Zhao RP, Hao ZR, Song ZJ. Diagnostic value of Flash dual-source CT coronary artery imaging combined with dual-energy myocardial perfusion imaging for coronary heart disease. *Exp Ther Med.* 2014;7(4):865-868. [\[CrossRef\]](#)
20. Bayraktutan U, Kantarci M, Gundogdu F, et al. Efficacy of ivabradin to reduce heart rate prior to coronary CT angiography: comparison with beta-blocker. *Diagn Interv Radiol.* 2012;18(6):537-541. [\[CrossRef\]](#)
21. McHugh ML. Interrater reliability: the kappa statistic. *Biochem Med (Zagreb).* 2012;22(3):276-282. [\[CrossRef\]](#)
22. Felker GM, Thompson RE, Hare JM, et al. Underlying causes and long-term survival in patients with initially unexplained cardiomyopathy. *N Engl J Med.* 2000;342(15):1077-1084. [\[CrossRef\]](#)
23. Dambrin G, Laissy JP, Serfaty JM, Caussin C, Lancelin B, Paul JF. Diagnostic value of ECG-gated multidetector computed tomography in the early phase of suspected acute myocarditis. A preliminary comparative study with cardiac MRI. *Eur Radiol.* 2007;17(2):331-338. [\[CrossRef\]](#)
24. Schwarz F, Ruzsics B, Schoepf UJ, et al. Dual-energy CT of the heart--principles and protocols. *Eur J Radiol.* 2008;68(3):423-433. [\[CrossRef\]](#)
25. Srichai MB, Lim RP, Donnino R, et al. Low-dose, prospective triggered high-pitch spiral coronary computed tomography angiography: comparison with retrospective spiral technique. *Acad Radiol.* 2012;19(5):554-561. [\[CrossRef\]](#)
26. Forghani R, De Man B, Gupta R. Dual-energy computed tomography: physical principles, approaches to scanning, usage, and implementation: part 2. *Neuroimaging Clin N Am.* 2017;27(3):385-400. [\[CrossRef\]](#)
27. Sade R, Kantarci M, Ogul H, et al. The feasibility of dual-energy computed tomography in cardiac contusion imaging for mildest blunt cardiac injury. *J Comput Assist Tomogr.* 2017;41(3):354-359. [\[CrossRef\]](#)
28. Hausleiter J, Meyer T, Hermann F, et al. Estimated radiation dose associated with cardiac CT angiography. *JAMA.* 2009;301(5):500-507. [\[CrossRef\]](#)
29. Brett NJ, Strugnell WE, Slaughter RE. Acute myocarditis demonstrated on CT coronary angiography with MRI correlation. *Circ Cardiovasc Imaging.* 2011;4(3):e5-e6. [\[CrossRef\]](#)
30. Baudry G, Bouleti C, lung B, et al. Diagnosis of acute myocarditis with dual source cardiac tomography. *Int J Cardiol.* 2015;179:256-257. [\[CrossRef\]](#)
31. Caruso D, Parinella AH, Schoepf UJ, et al. Optimization of window settings for standard and advanced virtual monoenergetic imaging in abdominal dual-energy CT angiography. *Abdom Radiol (NY).* 2017;42(3):772-780. [\[CrossRef\]](#)
32. D'Angelo T, Bucher AM, Lenga L, et al. Optimisation of window settings for traditional and noise-optimised virtual monoenergetic imaging in dual-energy computed tomography pulmonary angiography. *Eur Radiol.* 2018;28(4):1393-1401. [\[CrossRef\]](#)
33. Bondarenko O, Beek AM, Hofman MB, et al. Standardizing the definition of hyperenhancement in the quantitative assessment of infarct size and myocardial viability using delayed contrast-enhanced CMR. *J Cardiovasc Magn Reson.* 2005;7(2):481-485. [\[CrossRef\]](#)
34. Bouleti C, Baudry G, lung B, et al. Usefulness of late iodine enhancement on spectral CT in acute myocarditis. *JACC Cardiovasc Imaging.* 2017;10(7):826-827. [\[CrossRef\]](#)
35. Aquaro GD, Perfetti M, Camastra G, et al. Cardiac MR with late gadolinium enhancement in acute myocarditis with preserved systolic function: ITAMY study. *J Am Coll Cardiol.* 2017;70(16):1977-1987. [\[CrossRef\]](#)



# Computed-tomography-based radiomic nomogram for predicting the risk of indeterminate small (5–20 mm) solid pulmonary nodules

Chun-Ran Zhang\*

Qi Wang\*

Hui Feng

Yu-Zhi Cui

Xiao-Bo Yu

Gao-Feng Shi

\*Contributed equally to this work.

## PURPOSE

This study aims to develop a diagnostic model that combines computed tomography (CT) images and radiomic features to differentiate indeterminate small (5–20 mm) solid pulmonary nodules (SSPNs).

## METHODS

This study retrospectively enrolled 413 patients who had had SSPNs surgically removed and histologically confirmed between 2017 and 2019. The SSPNs included solid malignant pulmonary nodules (n = 210) and benign pulmonary nodules (n = 203). The least absolute shrinkage and selection operator was used for radiomic feature selection, and random forest algorithms were used for radiomic model construction. The clinical model and nomogram were established using univariate and multivariable logistic regression analyses combined with clinical symptoms, subjective CT findings, and radiomic features. The area under the curve (AUC) of the receiver operating characteristic curve was used to evaluate the performance of the models.

## RESULTS

The AUC for the clinical model was 0.77 in the training cohort [n = 289; 95% confidence interval (CI): 0.71–0.82; P = 0.001] and 0.75 in the validation cohort (n = 124; 95% CI: 0.66–0.83; P = 0.016). The AUCs for the nomogram were 0.92 (95% CI: 0.89–0.95; P < 0.001) and 0.85 (95% CI: 0.78–0.91; P < 0.001), respectively. The radiomic score (Rad-score), sex, pleural indentation, and age were the independent predictors that were used to build the nomogram.

## CONCLUSION

The radiomic nomogram derived from clinical features, subjective CT signs, and the Rad-score can potentially identify the risk of indeterminate SSPNs and aid in the patient's preoperative diagnosis.

## KEYWORDS

Computed tomography, solid pulmonary nodules, lung cancer, nomogram, radiomics

From the Department of Radiology (C-R.Z., Q.W., H.F., Y-Z.C., G-F.S. ✉ gaofengs62@sina.com), Hebei Medical University Fourth Affiliated Hospital and Hebei Provincial Tumor Hospital, Shijiazhuang, China; Siemens Healthineers Ltd. (X-B.Y.), Beijing, China.

Received 30 April 2021; revision requested 02 June 2021; last revision received 30 March 2022; accepted 30 April 2022.



Epub: 27.01.2023

Publication date: 29.03.2023

DOI: 10.4274/dir.2022.22395

With the wide application of computed tomography (CT) in pulmonary nodule screening and the improvement of public health awareness, an increasing number of small solid pulmonary nodules (SSPNs) are being detected.<sup>1,2</sup> According to the Fleischner guidelines, the nodules are categorized into solid and subsolid nodules depending on their density. Solid nodules are dense enough to mask the traveling blood vessels and bronchial shadows, while subsolid nodules refer to the ground glass density containing the lesion density that is not enough to mask the traveling blood vessels and bronchial shadows. Nodules with different densities have different malignant probabilities. A survey found that the malignant probability of small nodules (SNs) in patients undergoing surgical resection ranged from 5% to 70%.<sup>3,4</sup> The classic definition of indeterminate solitary pulmonary nodules (which may be malignant) is pulmonary nodules that do not meet the quintessential benign radiological criteria.<sup>5</sup> Currently, the incidence of lung carcinoma both in China and globally remains high.<sup>6,7</sup> In the early stage, lung carcinoma is often found in the form of pulmonary

nodules. Assessing the nature of the nodules is an essential step in making SN management decisions. One study showed that solid nodules smaller than 5 mm had a malignancy rate of 0.4%, solid nodules larger than 20 mm had a malignancy rate of 31%,<sup>8</sup> and solid nodules between 5 and 20 mm were difficult to diagnose.<sup>9</sup>

A computer-aided diagnosis is increasingly used in the diagnosis of pulmonary nodules. Some people build clinical models to diagnose hamartoma and adenocarcinoma, and some use radiomics to distinguish between benign and malignant pulmonary nodules.<sup>10,11</sup> The latest research techniques, such as the use of radiomic features and the attached vessel tortuosity, are also used to distinguish between lung adenocarcinoma and granuloma. We developed a nomogram to predict the risk probability of indeterminate solid lung nodules, which combined clinical data, subjective CT signs, and radiomics, and included nodules ranging from 5 to 20 mm.

## Methods

### Patient selection

Our retrospective study was approved (approval no: 2020KY082) by the Hospital Institutional Review Committee, and the requirement for informed consent was waived. Two radiologists (with 3 and 10 years of working experience, respectively) who were blinded to the final pathological diagnosis and clinical data, independently reviewed the CT images of all patients with SSPNs between January 2017 and December 2019. Interpretation discrepancy, if any, was resolved by consensus. The admission criteria for patients were as follows: (1) SSPNs 5–20 mm in diameter; (2) aged older than 15 years; (3) no history of malignant tumors in the past 5 years; (4) confirmation by surgical or CT-guided biopsy pathology; (5) no radiotherapy or chemotherapy before the exam-

ination; (6) preoperative chest thin-layer CT image ( $\leq 1.25$  mm); and (7) interval between chest CT scan and surgery of less than one month. The exclusion criteria were as follows: (1) SPNs (non-solid and part-solid); (2) impacts of diffuse pulmonary disease on imaging diagnosis; (3) lesions accompanied by a cavity; and (4) pathologically confirmed metastatic carcinoma.

In total, 413 participants were enrolled in this study ( $58.0 \pm 10.5$  years old), including 199 (48.18%) women and 214 (51.82%) men. The prevalence of malignant SSPNs was 50.85%. The most malignant SSPN was lung adenocarcinoma with 196 (93.33%) cases, while the others included 8 (3.81%) squamous cell carcinomas, 5 (2.38%) adenosquamous carcinomas, and 1 (0.48%) neuroendocrine carcinoma. Figure 1 shows a flowchart for nodule screening.

### Chest CT scanning technology and image analysis

A thoracic spiral CT was performed from the apex pulmonis to the costophrenic angle using the second-generation Somatom

Definition Flash CT scanner of Siemens or a GE Revolution Spiral system (GE Healthcare). The enhanced scan was performed using a high-pressure syringe, injecting non-ionic iodine (iohexol; 350 mg/mL; injection amount, 1.5–2 mL/kg; injection rate, 3 mL/s) intravenously through the elbow. The arterial phase scan was performed 25 s after injection of the contrast agent. The acquisition parameters were set as follows: tube voltage, 120 kV; tube current, 80–300 mAs; pitch, 0.2; and scanning matrix,  $512 \times 512$ . The scanning layer thickness was 5.0 mm, and the reconstruction layer thickness of the standard algorithm was 1.0–1.25 mm. The mediastinum window was set [width, 350 Hounsfield unit (HU); level, 40 HU], and the lung window was also set (width, 1.200 HU; level, –600 HU). The picture archiving and communication system was used to store the images and export them in the Digital Imaging and Communications in Medicine format.

Two radiologists analyzed the characteristics of each SSPN while blinded to the patients' pathological results, including their age, sex, smoking history, clinical symptoms,

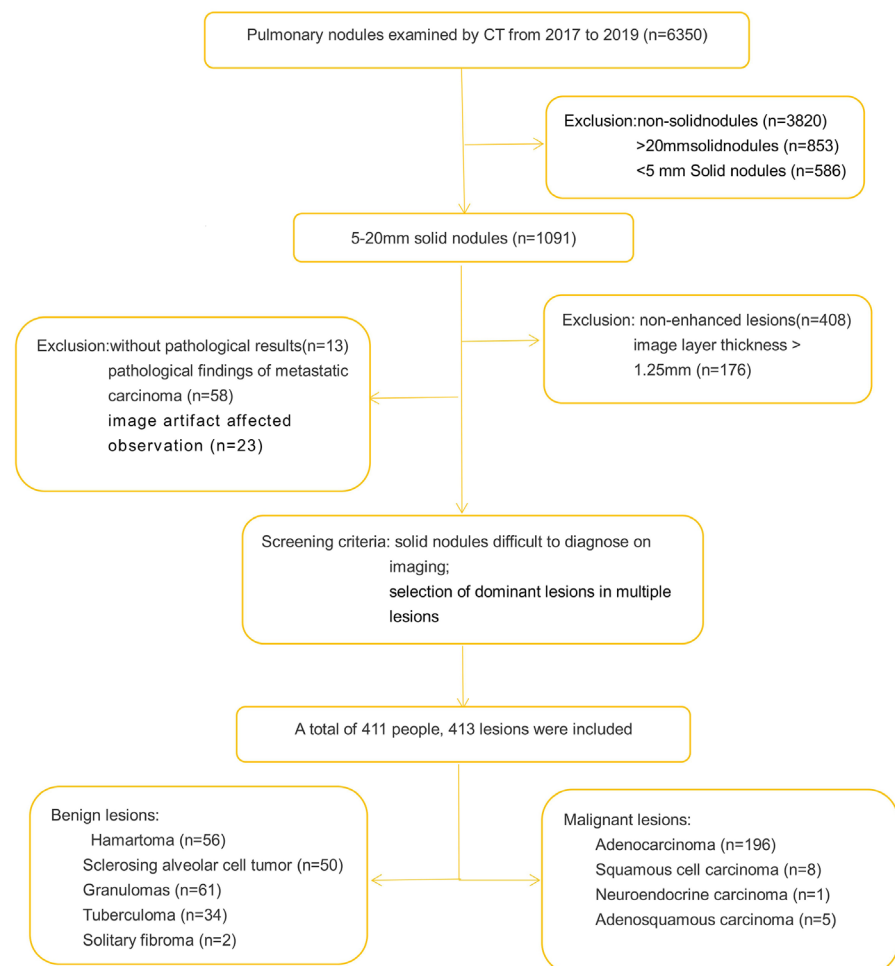


Figure 1. Nodule screening flow chart. CT, computed tomography.

### Main points

- Radiomics has great advantages in assessing the risk of indeterminate small solid pulmonary nodules (SSPNs).
- The radiomic nomogram derived from clinical features, subjective computed tomography signs, and the radiomic score (Rad-score) is superior to the clinical model in evaluating the risk of indeterminate SSPNs.
- The Rad-score, sex, age, and pleural indentation are independent predictors in assessing the risk of indeterminate SSPNs.

respiratory disease history, family history of lung cancer, and extrathoracic malignancy history (>5 years ago). The image-based features included the size, location (whether located in the upper lobe), density, shape, margin (regular or irregular), marginal spiculation, pleural indentation, pulmonary nodules significantly enhanced [yes (>15 HU) or no ( $\leq$ 15 HU)], and emphysema. Nodule size was defined as the mean of the longest diameter and vertical diameter of the largest plane of the nodule on the axial CT image. The regular margin was determined to have circular or elliptical smooth shapes. The marginal spiculation sign was a straight-line shadow from the margins of the lesion to the surroundings, which were radial and unbranched. Pleural indentation, also known as pleural traction, was due to the formation of fibrosis in the tumor, which pulls the visceral pleura toward the tumor. The enhancement index was measured as the difference between the enhancement scan and plain scan at the CT central level of nodules. If the diameter of the nodule was less than 1 cm, the two radiologists measured the CT value independently three times and took the average value.

### Nodule segmentation and feature extraction

Dedicated radiomic software (Radiomics, version 1.0.3, Siemens, Forchheim, Germany) was used for semiautomatic lesion segmentation. The accuracy of the segmentation was confirmed layer by layer from the axial, coronal, and sagittal positions (Figure 2). Pleural indentation, the long cords around the lesion, and the blood vessels and trachea at the edge of the lesion were not delineated, and any non-conforming layers were manually erased or filled.

Feature extraction was performed for each lung nodule, and 1,691 features were computed, including first-order statistical features, shape-based features, and texture features based on the gray-level co-occurrence matrix and gray-level size zone matrix. The interobserver reproducibility of segmentation was evaluated using 50 randomly selected cases that were re-segmented by the same radiologist following the same delineation principle one week later.

### Data Analysis

#### Radiomic feature selection and radiomic feature model construction

An intraclass correlation coefficient (ICC) threshold of 0.8 was used to evaluate the

reproducibility of the radiomic features. The ICC of a radiomic feature of  $>0.8$  was considered stable and selected for subsequent analysis. Next, the least absolute shrinkage and selection operator (LASSO) method was used to further select the features using the five-fold cross-validation method. The prediction model was constructed using the random forest (RF) method, which is a categorization method that involves multiple nodes of a decision tree and bootstrap resampling technology. Each tree uses a stochastically selected input variable or each node variable combination to form a forest.<sup>12,13</sup> The RF has the potential to overcome the overfitting problem with high accuracy and a robust anti-interference ability. Each nodule's characteristic radiomic score (Rad-score) was calculated using the constructed model. The radiomic model was developed using the Python Scikit-learn package (Python 3.6; Scikit-learn version 0.24.0; <http://scikit-learn.org/>).

#### Construction and evaluation of the nomogram

The Rad-scores, clinical features, and subjective CT signs were analyzed in the training cohort, and the nomogram was established with univariate and multivariable logistic regressions. The backward stepwise multivariable logistic regression was utilized to obtain similar results with fewer variables. The area under the curve (AUC) of each prediction model was estimated using bootstrapping (1,000 times) based on the prediction score.

#### Clinical value of the radiological nomogram

A decision curve analysis (DCA) was performed to evaluate the nomogram's clinical efficacy, which was calculated as a series benefit of the model under a series of threshold probabilities. Figure 3 shows the flow chart of the data process.

#### Statistical analysis

In this study, continuous variables conforming to a normal distribution were expressed as the mean  $\pm$  standard deviation; otherwise, they were expressed as the median (the first quantile; the third quantile). Categorical variables were presented as frequencies with percentages. The Wilcoxon rank-sum test was used for continuous variables, and  $\chi^2$  or Fisher's exact test was used for categorical variables. The performance of the models in the training and validation cohorts was quantified by the receiver operating characteristic (ROC) analysis of the AUC, accuracy, sensitivity, specificity, positive predictive value, and negative predic-

tive value. A 95% confidence interval (CI) for each feature was also recorded. The calibration curve was used to evaluate the consistency between the observed outcomes and predicted results, and the Hosmer-Lemeshow test was performed to evaluate the fit. The AUC comparison was examined using the DeLong test. We evaluated the performance of the model with the Nagelkerke R-squared and omnibus tests. Statistical analyses in this study were performed using R software (version 4.0.3; R Foundation for Statistical Computing, Vienna, Austria, <http://www.Rproject.org>) and SPSS 24.0 software (SPSS Inc., Chicago, IL, USA). The R package information is shown in Appendix 1. The reported statistical significance levels were both two-sided with  $P < 0.050$  but  $P < 0.100$  in the univariate logistic regression analysis.

## Results

#### Clinical feature analysis and clinical model establishment

The patients were randomized in a 7:3 ratio into the training and validation cohorts. The patient's clinical characteristics are described in Table 1. In the training cohort, potential predictors were determined using a univariate logistic regression analysis and incorporated into a multivariable logistic regression analysis. Sex [odds ratio (OR): 0.46; 95% CI: 0.27–0.81;  $P = 0.007$ ], morphology (OR: 2.07; 95% CI: 1.23–3.49;  $P = 0.006$ ), age (OR: 1.04; 95% CI: 1.01–1.07;  $P = 0.004$ ), pleural indentation (OR: 3.16; 95% CI: 1.86–5.39;  $P < 0.001$ ), emphysema (OR: 2.63; 95% CI: 1.07–6.48;  $P = 0.036$ ), and significant lung nodule enhancement (OR: 2.11; 95% CI: 1.25–3.57;  $P = 0.005$ ) were malignancy-independent predictors, and a clinical model was constructed using these six independent predictors (Table 2). The AUCs for the clinical model in the training and validation cohorts were 0.77 (95% CI: 0.71–0.82;  $P < 0.001$ ) and 0.75 (95% CI: 0.66–0.83;  $P < 0.001$ ), respectively.

#### Establishment and verification of the radiomic model

In total, 1,691 radiological features were abstracted from each patient's lung image. The radiological features of 29 non-zero coefficients were selected using LASSO regression in the training cohort and included in the Rad-score calculation. Figure 4 shows the distribution of the Rad-scores of benign and malignant SSPNs in the training and validation cohorts. No significant differences were

found in the Rad-scores between the benign ( $P = 0.448$ ) and validation ( $P = 0.055$ ) cohorts, and malignant nodule groups in the training but the Rad-scores of the malignant nodule

group [0.72 (0.62; 0.78) vs. 0.64 (0.57; 0.74);  $P < 0.001$ ] and benign nodule group [0.34 (0.23; 0.51) vs. 0.38 (0.25; 0.53);  $P < 0.001$ ] in the training and validation cohorts were significantly different.

Malignant pulmonary nodules typically have higher Rad-scores than benign pulmonary nodules. The AUC values of the radiomic model in the training and validation groups were 0.90 (95% CI: 0.86–0.93) and 0.83 (95% CI: 0.76–0.91), respectively, which showed good performance in predicting SSPNs.

### Establishment and verification of the nomogram

The multivariable logistic regression analysis showed that the Rad-score, sex (OR: 0.23; 95% CI: 0.10–0.49;  $P < 0.001$ ), age (OR: 1.05; 95% CI: 1.02–1.09;  $P = 0.004$ ), and pleural indentation (OR: 2.42; 95% CI: 1.20–4.87;  $P = 0.013$ ) were independent predictors. By integrating these four independent factors, a combined model was constructed and presented in the form of a nomogram (Figure 5). The AUC of the nomogram was 0.92 (95% CI: 0.89–0.95);  $P < 0.001$ ) in the training cohort and 0.85 (95% CI: 0.78–0.91);  $P < 0.001$ ) in the validation cohort. The calibration curve showed that the predicted results of the nomogram were in good agreement with the actual results in the training and verification queues. The Hosmer–Lemeshow test yielded a non-significant statistic ( $P = 0.584$  and  $P = 0.716$  for the training and validation cohorts, respectively), which suggests a good fit for probability.

### Model performance comparison

Table 3 shows the clinical model and nomogram's diagnostic performance, and Figures 6 and 7 show the ROC curves of these models. The cut-off values for the clinical model and nomogram AUCs were 0.49 and 0.56, respectively. Using the omnibus test with the model coefficients, the nomogram was significantly improved compared to the clinical model ( $P < 0.001$ ). Based on the DeLong test, statistically significant differences were found between the clinical model and nomogram in predicting the risk of SSPNs (Figure 8). The DCA curve (Figure 9) shows that the nomogram increases the net benefit more than the clinical model in distinguishing indeterminate SSPNs.

## Discussion

In the present retrospective study, we developed and verified a nomogram combining routine clinical features, subjective

**Table 1.** Clinical characteristics and subjective CT findings of the SSPN patients

	Test	Train	P value
	n = 124	n = 289	
<b>Sex</b>			0.485
Female	63 (50.81%)	136 (47.06%)	
Male	61 (49.19%)	153 (52.94%)	
<b>Age</b>	57.50 (52.00; 64.00)	60.00 (52.00; 66.00)	0.157
<b>Location</b>			0.230
Upper	65 (52.42%)	133 (46.02%)	
Middle and lower	59 (47.58%)	156 (53.98%)	
<b>Average diameter</b>	1.25 (1.04; 1.55)	1.25 (0.98; 1.53)	0.280
<b>Density</b>			0.316
Uniform	62 (50.00%)	129 (44.64%)	
Non-uniform	62 (50.00%)	160 (55.36%)	
<b>Morphology</b>			0.194
Regular	67 (54.03%)	136 (47.06%)	
Irregular	57 (45.97%)	153 (52.94%)	
<b>Boundary</b>			0.119
Clear	94 (75.81%)	197 (68.17%)	
Unclear	30 (24.19%)	92 (31.83%)	
<b>Spicule sign</b>			0.990
No	76 (61.29%)	177 (61.25%)	
Yes	48 (38.71%)	112 (38.75%)	
<b>Pleural indentation</b>			0.370
No	64 (51.61%)	163 (56.40%)	
Yes	60 (48.39%)	126 (43.60%)	
<b>Emphysema</b>			0.844
No	109 (87.90%)	256 (88.58%)	
Yes	15 (12.10%)	33 (11.42%)	
<b>Significant lung nodule enhancement</b>			0.459
No	68 (54.84%)	147 (50.87%)	
Yes	56 (45.16%)	142 (49.13%)	
<b>Clinical symptoms</b>			0.049
No	101 (81.45%)	209 (72.32%)	
Yes	23 (18.55%)	80 (27.68%)	
<b>Smoking history</b>			0.882
No	81 (65.32%)	191 (66.09%)	
Yes	43 (34.68%)	98 (33.91%)	
<b>Respiratory disease history</b>			1.000
No	121 (97.58%)	282 (97.58%)	
Yes	3 (2.42%)	7 (2.42%)	
<b>Lung cancer history</b>			0.229
No	108 (87.10%)	263 (91.00%)	
Yes	16 (12.90%)	26 (9.00%)	
<b>Extrathoracic malignancy history</b>			0.850
No	117 (94.35%)	274 (94.81%)	
Yes	7 (5.65%)	15 (5.19%)	

CT, computed tomography; SSPN, small solid pulmonary nodule.

findings from CT images, and radiomic features to distinguish indeterminate SSPNs. Our results suggest that the performance of a nomogram is superior to the clinical model in predicting the risk of indeterminate SSPNs.

The DCA curve demonstrates the clinical usefulness of a nomogram.

Radiomics is a rapidly developing field that can extract thousands of quantitative image features from images and describe

the biological characteristics and heterogeneity of lesions by analyzing these features. Radiomics identifies information from conventional images that are not visible to the naked eye or limited by the size or shape of the lesion.<sup>14-16</sup> In recent years, using a radiomic texture feature analysis for lung nodule assessments has received increased attention. Most studies have focused on general small pulmonary nodules (including solid and subsolid nodules) or used radiomics and clinical features to identify the nature of pulmonary nodules,<sup>17-19</sup> for which CT signs have not been included. We constructed an integrated model combining clinical features, subjective CT signs, and the Rad-scores for indeterminate SSPNs (5–20 mm). SNs require stricter research standards and are more challenging to diagnose through imaging.

Our study revealed that sex, age, shape, pleural indentation, emphysema, and enhancement are independent predictors of indeterminate SSPNs. This finding is consistent with the findings of previous studies.<sup>20-24</sup> However, we also found that in most previous studies, the position of the upper lobe and smoking history were independent predictors of the malignancy of pulmonary nodules. This finding differs from those in previous studies. First, the discrepancy may be caused by regional differences. The incidence of tuberculosis in China is very high and mainly affects the upper lobe. Additionally, according to our previous statistics on the risk factors for lung cancer screening in the Hebei province, smoking history is not an independent predictor. This may be due to air pollution, which has caused the incidence of nodules in non-smokers to increase significantly. Additionally, malignant pulmonary nodules may be mostly adenocarcinoma, which has a higher incidence in women than in men, and smoking is rare in women.

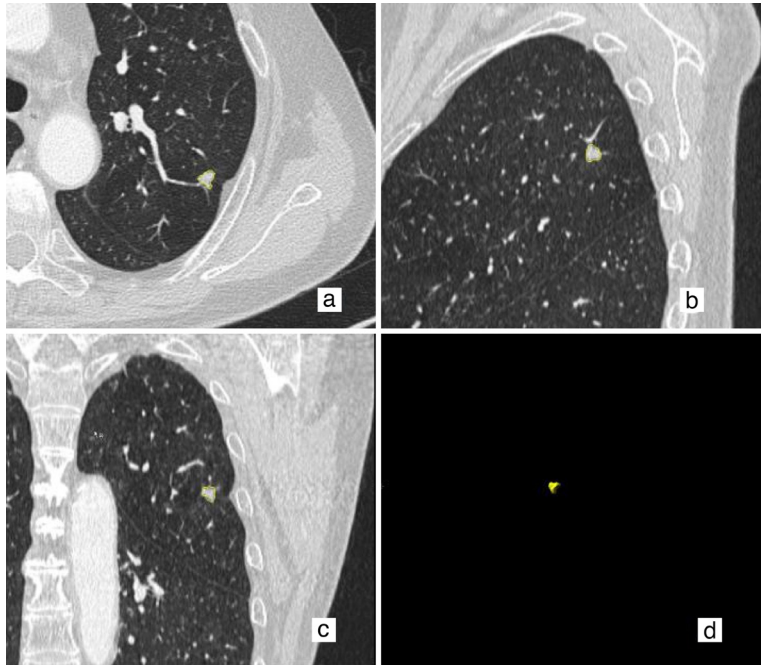


**Figure 2.** (a, b, and c) are used to determine the region of interest boundary layer by layer from the axial, sagittal, and coronal positions, respectively. (d) Is a three-dimensional diagram of the nodule segmentation.

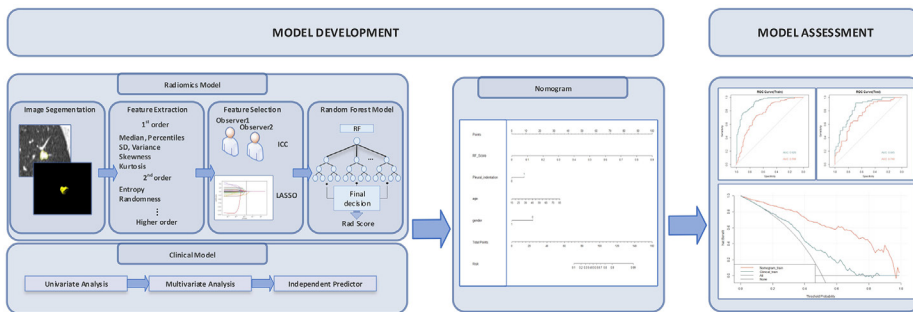


**Figure 3.** Flow chart of data processing. RF, random forest; ICC, intraclass correlation coefficient; LASSO, least absolute shrinkage and selection operator; B, regression coefficient.

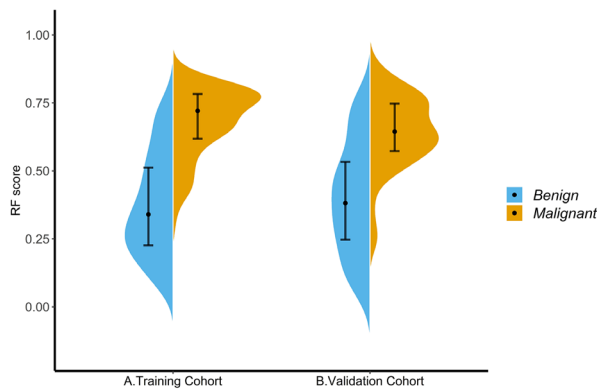


**Figure 4.** Distribution of the radiomic scores between benign and malignant nodules in the training and validation cohorts, with the ordinate representing the ability to differentiate between benign and malignant nodules.

Our model covers various pathological types, such as adenocarcinoma, squamous cell carcinoma, small cell carcinoma, inflammation, tuberculosis, hamartoma, and other pathological types. We extracted 1,691 features from each nodule, and the most critical and reproducible features were selected to construct the prediction model. However, our results were not significantly different from those of other studies. Because the SSPNs included in our study were difficult to diagnose on imaging, we excluded 20–30 mm nodules and subsolid nodules. Larger-diameter nodules and subsolid nodules are more likely to become

**Table 2.** Clinical model screening results

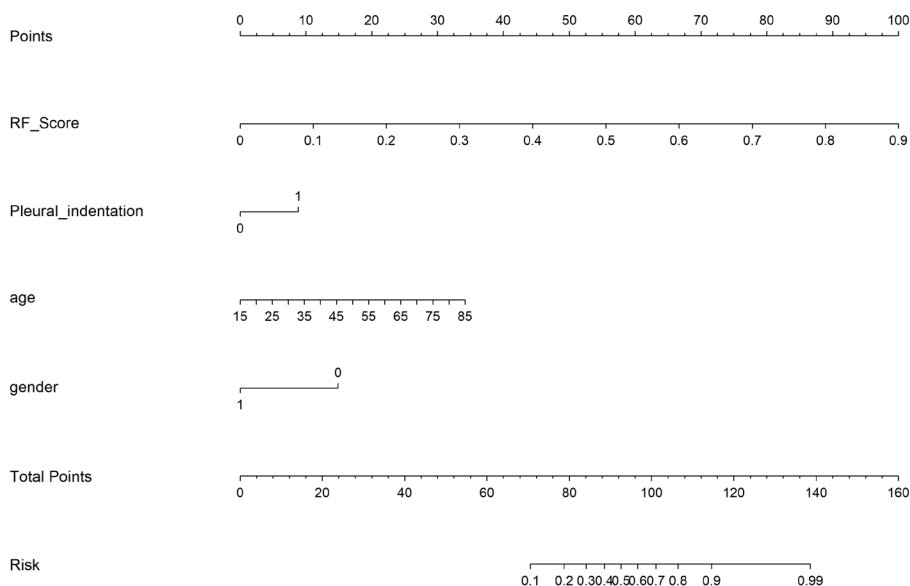
Variables	Variable category		Univariate logistic regression			Multivariable logistic regression		
	Reference category	Other category	B	OR (95% CI)	P value	B	OR (95% CI)	P value
Sex	Female	Male	-0.55	0.58 (0.36-0.92)	0.021	-0.77	0.46 (0.270-0.81)	0.007
Age	-	-	0.04	1.04 (1.02-1.07)	<0.001	0.04	1.04 (1.01-1.07)	0.004
Morphology	Regular	Irregular	0.97	2.65 (1.65-4.28)	<0.001	0.73	2.07 (1.23-3.49)	0.006
Pleural indentation	No	Yes	1.16	3.17 (1.96-5.2)	<0.001	1.15	3.16 (1.86-5.39)	<0.001
Emphysema	No	Yes	0.9	2.45 (1.15-5.58)	0.021	0.97	2.63 (1.07-6.48)	0.036
Significant lung nodule enhancement	No	Yes	0.83	2.29 (1.44-3.69)	0.001	0.75	2.11 (1.25-3.57)	0.005
Density	Uniform	Non-uniform	0.83	2.29 (1.43-3.7)	0.001	-	-	-
Boundary	Clear	Unclear	0.59	1.81 (1.10-3.02)	0.02	-	-	-
Spicule sign	No	Yes	0.53	1.70 (1.06-2.75)	0.029	-	-	-
Location	Middle and lower	Upper	0.41	1.51 (0.95-2.41)	0.083	-	-	-
Average diameter	-	-	-0.03	0.97 (0.63-1.45)	0.865	-	-	-
Clinical symptoms	No	Yes	0.23	1.26 (0.75-2.12)	0.384	-	-	-
Smoking history	No	Yes	-0.18	0.84 (0.51-1.37)	0.479	-	-	-
Lung cancer history	No	Yes	-0.04	0.96 (0.43-2.17)	0.926	-	-	-
Respiratory disease history	No	Yes	0.26	1.30 (0.28-6.68)	0.737	-	-	-
Extrathoracic malignancy history	No	Yes	1.03	2.79 (0.93-10.26)	0.074	-	-	-

OR, odds ratio; CI, confidence interval; B, regression coefficient.

**Table 3.** Performance comparison between different models

		AUC	Sensitivity	Specificity	Accuracy	PPV	NPV	Cut-off	R <sup>2</sup>	P value
Training cohort	Clinical model	0.77	0.70	0.73	0.72	0.72	0.71	0.49	0.28	<0.001
	Nomogram	0.92	0.82	0.82	0.82	0.83	0.81	0.56	0.61	<0.001
Validation cohort	Clinical model	0.75	0.66	0.70	0.68	0.68	0.68	0.49	0.24	<0.001
	Nomogram	0.85	0.74	0.81	0.77	0.76	0.79	0.56	0.46	<0.001

AUC, area under the curve; NPV, negative predictive value; PPV, positive predictive value. R<sup>2</sup>, Nagelkerke R-square.

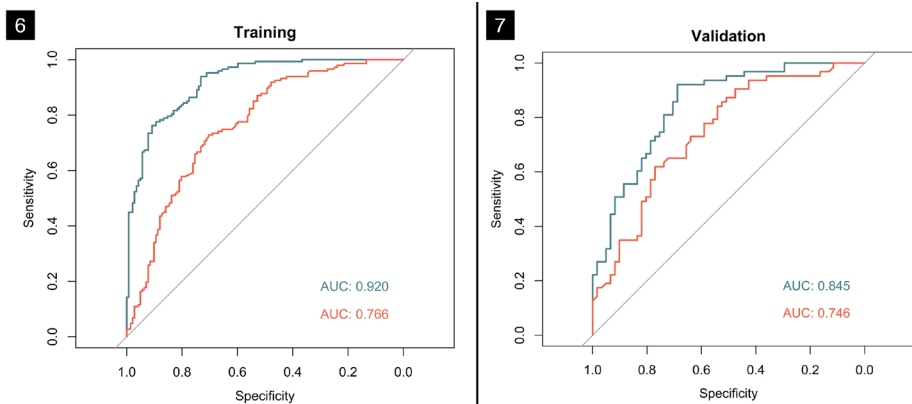


malignant. Models containing these factors may show better efficacy.<sup>25,26</sup>

Our research has several limitations. First, this is a retrospective study, but our results are further verified in the internal cohort. Second, we only included nodules with pathological results from surgery or biopsy, indicating selection bias. Additionally, our model was established based on clinical, radiomic, and image features of the pulmonary nodules. In addition, some other articles have applied other information, such as the nodules with attached vessel tortuosity and topological skeleton of the nodules.<sup>27,28</sup> In future studies, our model may be further improved if these latest research results are combined.

In conclusion, in this retrospective study, we constructed a nomogram combining clinical features, subjective CT imaging find-

**Figure 5.** Nomogram for predicting the risk of indeterminate small solid pulmonary nodules.



**Figures 6, 7.** Receiver operating characteristic curves of the two prediction models in the training and verification queues when predicting uncertain small solid pulmonary nodules.

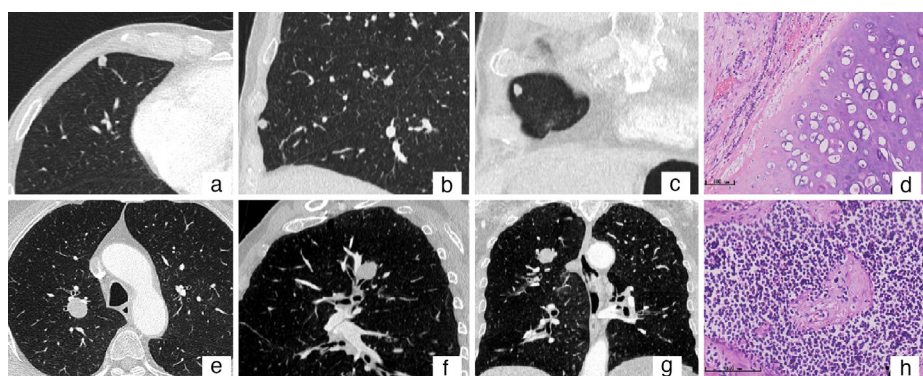


**Figure 8.** From left to right: axial computed tomography images, predicted results of the nomogram, and pathological diagnosis images of uncertain pulmonary nodules (hematoxylin and eosin staining,  $\times 400$ ). First row: a 74-year-old man presented with a small nodule (approximately 7.5 mm in diameter) in the middle lobe of his right lung (a-c), with a total nomogram score of 56.3, a 0.01 probability of malignancy, and a pathologically proven hepatocellular tumor (d). Second row: a 69-year-old man presented with a nodule (approximately 18.5 mm in diameter) in the superior lobe of his right lung (e-g), which had a total nomogram score of 107.5 and a probability of malignancy of 0.81. Pathology confirmed a small cell carcinoma (h).

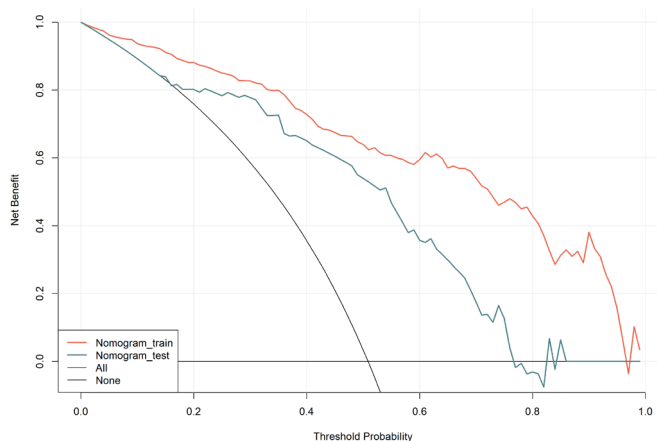


**Figure 9.** Decision curve analysis of the nomogram. The x-axis represents the threshold probability, and the y-axis represents the net-income benefit. The red line represents the clinical benefits of small solid pulmonary nodules (SSPNs) predicted by the nomogram in the training group. The blue line indicates the clinical benefits of SSPNs predicted by the nomogram in the validation group. The black slash represents the assumption that all nodules are malignant. The black horizontal line represents the assumption that all nodules are benign. The decision curve shows that the nomogram increases the net benefits in forecasting uncertain SSPNs.

ings, and radiomic features to differentiate indeterminate SSPNs. This nomogram is non-invasive and repeatable and has high predictive accuracy to help with the preoperative diagnosis of patients.

### Conflict of interest disclosure

The authors declared no conflicts of interest.

### References

- Hassannezhad R, Vahed N. Prediction of the risk of malignancy among detected lung nodules in the National Lung Screening Trial. *J Am Coll Radiology*. 2018;15(11):1529-1535. [\[CrossRef\]](#)
- Leleu O, Basille D, Auquier M, et al. Lung cancer screening by low-dose CT scan: baseline results of a french prospective study. *Clin Lung Cancer*. 2020;21(2):145-152. [\[CrossRef\]](#)
- McWilliams A, Tammemagi MC, Mayo JR, et al. Probability of cancer in pulmonary nodules detected on first-screening CT. *N Eng J Med*. 2013;369(10):910-919. [\[CrossRef\]](#)
- White CS, Dharaiya E, Campbell E, Boroczky L. The vancouver lung cancer risk prediction model: assessment by using a subset of the National Lung Screening Trial cohort. *Radiology*. 2017;283(1):264-272. [\[CrossRef\]](#)
- Erasmus JJ, McAdams HP, Connolly JE. Solitary pulmonary nodules: part II. Evaluation of the indeterminate nodule. *Radiographics*. 2000;20:59-66. [\[CrossRef\]](#)
- Chen WQ, Li H, Sun KX, et al. Report of cancer incidence and mortality in China, 2014. *Zhonghua Zhong Liu Za Zhi*. 2018;40(1):5-13. [\[CrossRef\]](#)
- Qu RY, Zhou BS. Analysis of the distribution and trend of lung cancer mortality in China between 2004 and 2010 [in Chinese]. *Chin J Health Stat*. 2014;31:932-5. [\[CrossRef\]](#)
- Swensen SJ, Jett JR, Hartman TE, et al. CT screening for lung cancer: five-year prospective experience. *Radiology*. 2005;235(1):259-265. [\[CrossRef\]](#)
- Liu X, Liang M, Wang Y, et al. The outcome differences of CT screening for lung cancer pre and post following an algorithm in Zhuhai, China. *Lung Cancer*. 2011;73(2):230-236. [\[CrossRef\]](#)
- Liu A, Wang Z, Yang Y, et al. Preoperative diagnosis of malignant pulmonary nodules in lung cancer screening with a radiomics nomogram. *Cancer Commun (Lond)*. 2020;40(1):16-24. [\[CrossRef\]](#)
- Chen X, Feng B, Chen Y, et al. A CT-based radiomics nomogram for prediction of lung adenocarcinomas and granulomatous lesions in patient with solitary sub-centimeter solid nodules. *Cancer Imaging*. 2020;20(1):45. [\[CrossRef\]](#)

12. Mei X, Wang R, Yang W, et al. Predicting malignancy of pulmonary ground-glass nodules and their invasiveness by random forest. *J Thorac Dis.* 2018;10(1):458-463. [\[CrossRef\]](#)
13. Li XX, Li B, Tian LF, Zhang L. Automatic benign and malignant classification of pulmonary nodules in thoracic computed tomography based on RF algorithm. *IET Image Processing.* 2018;12(7):1253-1264. [\[CrossRef\]](#)
14. Yang M, Ren Y, She Y, et al. Imaging phenotype using radiomics to predict dry pleural dissemination in non-small cell lung cancer. *Ann Transl Med.* 2019;7(12):259. [\[CrossRef\]](#)
15. Xu X, Huang L, Chen J, et al. Application of radiomics signature captured from pretreatment thoracic CT to predict brain metastases in stage III/IV ALK-positive non-small cell lung cancer patients. *J Thorac Dis.* 2019;11:4516-4528. [\[CrossRef\]](#)
16. Shen Y, Xu F, Zhu W, Hu H, Chen T, Li Q. Multiclassifier fusion based on radiomics features for the prediction of benign and malignant primary pulmonary solid nodules. *Ann Transl Med.* 2020;8(5):171. [\[CrossRef\]](#)
17. Ruilong Z, Daohai X, Li G, Xiaohong W, Chunjie W, Lei T. Diagnostic value of 18F-FDG-PET/CT for the evaluation of solitary pulmonary nodules: a systematic review and meta-analysis. *Nucl Med Commun.* 2017;38(1):67-75. [\[CrossRef\]](#)
18. Swensen SJ, Silverstein MD, Ilstrup DM, Schleck CD, Edell ES. The probability of malignancy in solitary pulmonary nodules. Application to small radiologically indeterminate nodules. *Arch Intern Med.* 1997;157(8):849-855. [\[CrossRef\]](#)
19. Li Y, Chen KZ, Wang J. Development and validation of a clinical prediction model to estimate the probability of malignancy in solitary pulmonary nodules in Chinese people. *Clin Lung Cancer.* 2011;12(5):313-319. [\[CrossRef\]](#)
20. Swensen SJ, Viggiano RW, Midthun DE, et al. Lung nodule enhancement at CT: multicenter study. *Radiology.* 2000;214(1):73-80. [\[CrossRef\]](#)
21. Soardi GA, Perandini S, Larici AR, et al. Multicentre external validation of the BIMC model for solid solitary pulmonary nodule malignancy prediction. *Eur Radiol.* 2017;27(5):1929-1933. [\[CrossRef\]](#)
22. Ruilong Z, Daohai X, Li G, Xiaohong W, Chunjie W, Lei T. Diagnostic value of 18F-FDG-PET/CT for the evaluation of solitary pulmonary nodules: a systematic review and meta-analysis. *Nucl Med Commun.* 2017;38(1):67-75. [\[CrossRef\]](#)
23. Xiang Y, Sun Y, Liu Y, et al. Development and validation of a predictive model for the diagnosis of solid solitary pulmonary nodules using data mining methods. *J Thorac Dis.* 2019;11(3):950-958. [\[CrossRef\]](#)
24. She Y, Zhao L, Dai C, et al. Development and validation of a nomogram to estimate the pretest probability of cancer in Chinese patients with solid solitary pulmonary nodules: a multi-institutional study. *J Surg Oncol.* 2017;116(6):756-762. [\[CrossRef\]](#)
25. Chu ZG, Zhang Y, Li WJ, Li Q, Zheng YN, Lv FJ. Primary solid lung cancerous nodules with different sizes: computed tomography features and their variations. *BMC Cancer.* 2019;19(1):1060. [\[CrossRef\]](#)
26. McWilliams A, Tammemagi MC, Mayo JR, et al. Probability of cancer in pulmonary nodules detected on first screening CT. *N Eng J Med.* 2013;369(10):910-919. [\[CrossRef\]](#)
27. Mahdi MBT, Orooji M, Teimouri M, Shahabifar R. Segmentation of the pulmonary nodule and the attached vessels in the CT scan of the chest using morphological features and topological skeleton of the nodule. *IET Image Processing.* 2020;14(87):1520-1528. [\[CrossRef\]](#)
28. Tavakoli MB, Orooji M, Teimouri M, Shahabifar R. Distinguishing adenocarcinomas from granulomas in the CT scan of the chest: performance degradation evaluation in the automatic segmentation framework. *BMC Res Notes.* 2021;14(1):87. [\[CrossRef\]](#)

Appendix 1. Packages used in this study			
Statistical analysis	Packages	Version	Web
Feature selection: LASSO	"glmnet" in R	4.1-1	<a href="https://CRAN.R-project.org/package=glmnet">https://CRAN.R-project.org/package=glmnet</a>
Radiomic model establishment: random forest	"randomForestSRC" in R	2.11.0	<a href="https://CRAN.R-project.org/package=randomForestSRC">https://CRAN.R-project.org/package=randomForestSRC</a>
Descriptive table	"compareGroups" in R	4.5.1	<a href="https://CRAN.R-project.org/package=compareGroups">https://CRAN.R-project.org/package=compareGroups</a>
Clinical model and nomogram establishment: logistic regression and nomogram	"rms" in R	6.0-1	<a href="https://CRAN.R-project.org/package=rms">https://CRAN.R-project.org/package=rms</a>
Model performance evaluation: DeLong test and 95% CI for ROC curve analysis	"pROC" in R	1.18.0	<a href="https://CRAN.R-project.org/package=pROC">https://CRAN.R-project.org/package=pROC</a>
Model performance evaluation: decision curve analysis	"rmda" in R	1.6	<a href="https://CRAN.R-project.org/package=rmda">https://CRAN.R-project.org/package=rmda</a>
Model performance evaluation: Hosmer–Lemeshow Goodness of Fit test	"ResourceSelection" in R	0.3-5	<a href="https://CRAN.R-project.org/package=ResourceSelection">https://CRAN.R-project.org/package=ResourceSelection</a>

CI, confidence interval; ROC, receiver operating characteristic curve.



# Photon-counting computed tomography in the assessment of rheumatoid arthritis-associated interstitial lung disease: an initial experience

Nikolett Marton   
 Janos Gyebnar   
 Kinga Fritsch   
 Judit Majnik   
 Gyorgy Nagy   
 Judit Simon   
 Veronika Müller   
 Adam Domonkos Tarnoki   
 David Laszlo Tarnoki   
 Pal Maurovich-Horvat 

From the Department of Radiology (N.M., J.G., J.S., A.D.T., D.L.T., P.M.-H. ✉ maurovich-horvat.pal@semmelweis.hu), Medical Imaging Centre, Semmelweis University, Budapest, Hungary; Department of Rheumatology (K.F., J.M., G.N.), Buda Hospital of the Hospitaller Order of Saint John of God, Budapest, Hungary; Department of Rheumatology and Clinical Immunology (J.M., G.N.), Semmelweis University, Budapest, Hungary; MTA-SE Cardiovascular Imaging Research Group (J.S., P.M.-H.), Semmelweis University, Budapest, Hungary; Department of Pulmonology (V.M.), Semmelweis University, Budapest, Hungary; Department of Oncologic Imaging and Invasive Diagnostic Radiology (A.D.T., D.L.T.), National Institute of Oncology, Budapest, Hungary.

Received 25 October 2022; revision requested 16 November 2022; last revision received 05 January 2023; accepted 22 January 2023.



Epub: 08.03.2023

Publication date: 29.03.2023

DOI: 10.4274/dir.2023.221959

## PURPOSE

Interstitial lung disease (ILD) accounts for a significant proportion of mortality and morbidity in patients with rheumatoid arthritis (RA). The aim of this cross-sectional study is to evaluate the performance of novel photon-counting detector computed tomography (PCD-CT) in the detection of pulmonary parenchymal involvement.

## METHODS

Sixty-one patients with RA without a previous definitive diagnosis of ILD underwent high-resolution (HR) (0.4 mm slice thickness) and ultra-high-resolution (UHR) (0.2 mm slice thickness) PCD-CT examination. The extent of interstitial abnormalities [ground-glass opacity (GGO), reticulation, bronchiectasis, and honeycombing] were scored in each lobe using a Likert-type scale. Total ILD scores were calculated as the sum of scores from all lobes.

## RESULTS

Reticulation and bronchiectasis scores were higher in the UHR measurements taken compared with the HR protocol [median (quartile 1, quartile 3): 2 (0, 3.5) vs. 0 (0, 3),  $P < 0.001$  and 2 (0, 2) vs. 0 (0, 2),  $P < 0.001$ , respectively]; however, GGO and honeycombing scores did not differ [2 (2, 4) vs. 2 (2, 4),  $P = 0.944$  and 0 (0, 0) vs. 0 (0, 0),  $P = 0.641$ , respectively]. Total ILD scores from both HR and UHR scans showed a mild negative correlation in diffusion capacity for carbon monoxide (HR:  $r = -0.297$ ,  $P = 0.034$ ; UHR:  $r = -0.294$ ,  $P = 0.036$ ). The pattern of lung parenchymal involvement did not differ significantly between the two protocols. The HR protocol had significantly lower volume CT dose index [0.67 (0.69, 1.06) mGy], total dose length product [29 (24.48, 33.2) mGy\*cm] compared with UHR scans [8.18 (6.80, 9.23) mGy,  $P < 0.001$  and 250 (218, 305) mGy\*cm,  $P < 0.001$ ].

## CONCLUSION

UHR PCD-CT provides more detailed information on ILD in patients with RA than low-dose HR PCD-CT. HR PCD-CT image acquisition with a low effective radiation dose may serve as a valuable, low-radiation screening tool in the selection of patients for further, higher-dose UHR PCD-CT screening.

## KEYWORDS

CT, high-resolution, low-dose, lung, photon-counting, ultra-high-resolution

Contrary to conventionally utilized energy-integrating detectors (EIDs), photon-counting detectors (PCDs) are able to directly convert X-ray photons into electric pulses.<sup>1</sup> This process leads to better spatial resolution, decreased beam hardening, reduced noise and radiation dose, and to register the energy of photons.<sup>2-4</sup> PCD-computed tomography (PCD-CT) has gained increasing interest in pulmonary imaging due to its high spatial resolution.<sup>5</sup> To date, preclinical studies have mostly investigated lung PCD-CT imaging by analyzing optimal reconstruction parameters, such as matrix size, optimal slice thickness, and iterative reconstruction algorithms.<sup>6,7</sup>

Rheumatoid arthritis (RA) is a systemic autoimmune disease associated with several pathologies, including parenchymal and pleural involvement, bronchiolitis, rheumatoid nodules, and vascular abnormalities. Interstitial lung abnormalities (ILA) occur in 1.8%–67% of patients with RA, among whom established interstitial lung disease (ILD) accounts for a significant proportion of mortality and morbidity.<sup>8,9</sup> High-resolution (HR) CT remains the main imaging modality for the evaluation of lung involvement in RA.<sup>10</sup> The spectrum of RA-related interstitial abnormalities in parenchymal involvement includes ground-glass opacity (GGO), fibroreticular changes, bronchiectasis, and honeycombing. The most frequent phenotype of RA-ILD is usual interstitial pneumonitis (UIP).<sup>11</sup> It has been demonstrated that the early identification of subclinical ILAs (which show a tendency to progress to ILD) by CT promotes early intervention that stabilizes further interstitial changes and, thus, significantly improves prognosis.<sup>12</sup>

The primary goal of this study is to evaluate the performance of PCD-CT in the detection of early and subclinical parenchymal lung involvement in patients with RA.

## Methods

### Patients

From February 2022 to November 2022, 334 patients were enrolled in this study (Figure 1). Inclusion criteria were as follows: (i) patients diagnosed with RA (according to 2010 American College of Rheumatology/European League Against Rheumatism classification criteria); and (ii) patients >40 years of age. Exclusion criteria were as follows: (i) patients with pulmonary infection, lung malignancies, or previously diagnosed ILD. The demographic data, clinical manifestations,

and routine laboratory test results of study participants were recorded. All patients were checked regularly and received medical treatment as recommended by the attending rheumatologist, following standards of care. First second of forced expiration, forced vital capacity, and diffusion capacity for carbon monoxide (DLCO) were measured by pulmonologists via pulmonary function tests. Patients underwent yearly chest X-rays following their RA diagnosis; however, based on earlier radiographs, none had an HR CT-based indication to rule out ILD. Written informed consent was obtained from all study participants. Three hundred twenty-six patients underwent HR CT imaging, and, following the detection of abnormalities by the attending radiologist, 61 patients underwent a subsequent ultra-high resolution (UHR) CT on the same day for further evaluation of lung parenchyma (Figure 1).

### Research ethics

This trial was registered on the clinicaltrials.gov website (IV-2683-1/2022/EKU) and approved by the local ethical review board (2021, National Scientific and Research Ethics

Committee, Hungary). This work was carried out in accordance with the Helsinki Declaration (JAMA 2000; 284:3043–3049).<sup>13</sup>

### Patient PCD-CT measurements

HR (slice thickness: 0.4 mm) and UHR (slice thickness: 0.2 mm) CT scans were carried out with a PCD-CT scanner (Naeotom Alpha<sup>®</sup>, Siemens Healthineers, Erlangen, Germany). Both imaging techniques were performed with a large field of view (FOV) [median (quartile 1, quartile 3): 35 (32, 38) cm] and 1024 × 1024 matrix. Additionally, quantitative iterative reconstruction algorithms were utilized to enhance image quality (Table 2). To exclude GGO from dependent atelectasis, prone inspiratory HR CT measurements were performed.

### Phantom studies

To compare the image quality of PCD- and EID-CT methods, prone chest region measurements with matched parameters (similar slice thicknesses and equivalent rotation times, voltage and current, pitch values, and scan lengths) were taken of a

### Main points

- Cross-sectional study shows that ultra-high-resolution (UHR) photon-counting detector computed tomography (PCD-CT) imaging provides more detailed information regarding interstitial lung disease (ILD) in patients with rheumatoid arthritis (RA) than HR PCD-CT.
- PCD-CT might be a promising tool in the early diagnosis of subclinical ILD and bronchiectasis in patients with RA.
- Low-dose, HR PCD-CT could serve as a means of preselecting candidates for more detailed, UHR measurements in the assessment of RA-related ILD.

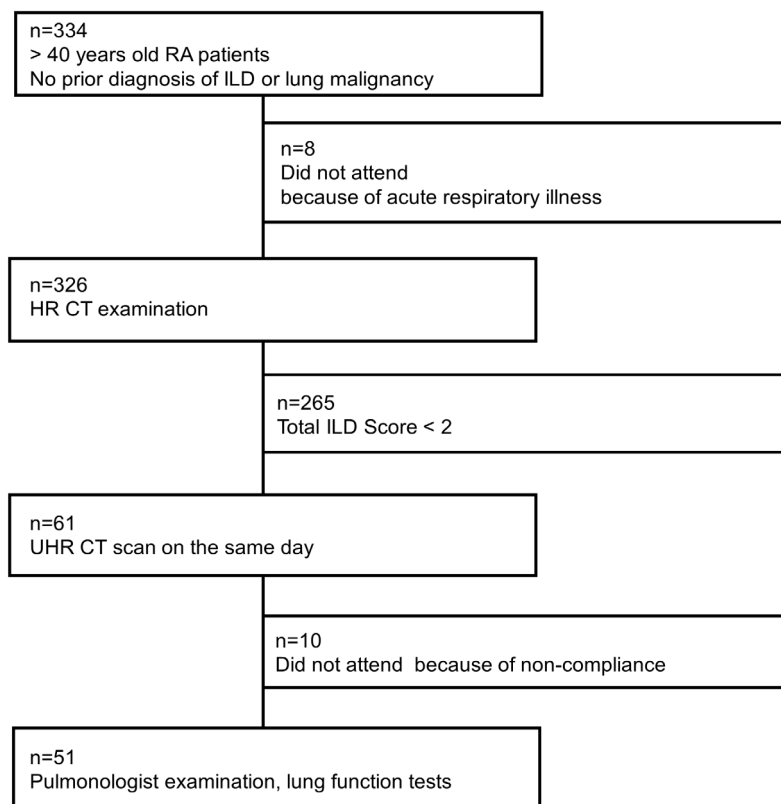


**Figure 1.** Flow chart of study sample and processing. Patients with rheumatoid arthritis who were <40 years of age, had pneumonia in the previous 3 months, or suffered from an already diagnosed interstitial lung disease or lung tumor were excluded. After the first low-dose, high-resolution (HR) chest computed tomography (CT) scan, radiologist specialists scored interstitial lung abnormalities (ground-glass opacity, reticulation, bronchiectasis, and honeycombing) based on a Likert-type scale. If these were absent or very low (scores <2), no ultra-high-resolution (UHR) measurement was conducted (n = 265), resulting in our final cohort with both HR and UHR CT (n = 61). RA, rheumatoid arthritis; ILD, interstitial lung disease.

phantom (CT Whole Body Phantom, PBU-60) with a 1-year-old PCD-CT scanner (Naeotom Alpha<sup>®</sup>, Siemens Healthineers, Erlangen, Germany), a 2.5-year-old 128-slice EID-CT scanner (Philips Incisive<sup>®</sup>, Philips, Amsterdam, The Netherlands), and a 2-year-old 128-slice EID-CT scanner (GE Revolution EVO<sup>®</sup>, GE Healthcare, Chicago, Illinois, USA). Subjective image quality was rated independently by four radiologists on a five-point scale (5 being best, 1 being worst). Contrast-to-noise ratio (CNR) was calculated based on the formula: [average pixel values in signal region of interest (ROI) (bronchial wall) – average pixel values of background ROI (air)] / standard deviation (SD) of background ROI (air). Signal-to-noise ratio (SNR) was calculated based on the formula: average pixel values in signal ROI (bronchial wall)/SD of background ROI (air).

### Dose values

Volume CT dose index (CTDIvol) and total dose length product (TDLP) values were extracted from patient protocol data (syngo.

via software, Siemens Healthineers). Approximate effective dose values were calculated from TDLP values as follows: Effective dose = TDLP × *k*-factor (0.014 mSv/mGy\*cm).<sup>14,15</sup>

### Evaluation of parenchymal abnormalities

All PCD-CT images were reviewed, and specific ILD patterns were determined by consensus, by two radiologists with 6 and 13 years of experience. A third thoracic radiologist with 13 years of experience then reviewed the images and spoke with the ILD board to reach an agreement with the pulmonologists. Interstitial abnormalities were classified into four categories: GGO (parenchymal opacity with perceptible underlying bronchovascular structure without architectural distortion), reticulation (thickening of interlobular septae or intralobular septae and traction), bronchiectasis (dilatation of bronchial tree), and honeycombing (clustered, subpleural, multilayered, cystic air-spaces).

To test whether the UHR protocol provided additional information about interstitial pathologies, a semiquantitative scoring system was utilized. The extent of pulmonary parenchymal abnormalities for each lobe was scored using a Likert-type scale (0 = absent; 1 = 1%–25%; 2 = 26%–50%; 3 = 51%–75%; 4 = 76%–100%). Total GGO, reticulation, bronchiectasis, and honeycombing scores were calculated by adding up the scores of all five lung lobes, with final values ranging from 0–20. All scores were combined to produce a total ILD HR CT score ranging from 0–80 (Figure 2).<sup>16,17</sup>

As ILD is a heterogeneous group of parenchymal lung disorders, observed abnormalities were classified into patterns defined in Table 3.

### Statistical analysis

Distribution was defined by the Kolmogorov–Smirnov test. Descriptive statistics (median and quartiles) and mean ± SD were used to represent abnormally and normally distributed variables, respectively. A paired t-test was used to compare normally distributed data, and the Wilcoxon test was used to compare non-parametric data. In the case of parenchymal changes with a definitive ILD pattern, Cohen’s kappa ( $\kappa$ ) was used to test agreement between readers (0–0.20 = poor agreement; 0.21–0.40 = fair agreement; 0.41–0.60 = moderate agreement; 0.61–0.80 = substantial agreement; and 0.81–1.00 = almost perfect agreement).<sup>18</sup> The Pearson correlation coefficient was used to find correlations between total lung HR CT scores and pulmonary function tests. Differences between the image quality parameters of different CTs were evaluated using a One-Way ANOVA test with a subsequent Tukey post-hoc analysis. Significance was established at *P* values <0.05 were considered statistically significant. Categorical variables were reported as frequencies and percentages. Statistical analyses were performed using GraphPad Prism v. 6.0 software.

## Results

### Demographic and clinical characteristics

Of the 334 patients initially enrolled, eight were excluded due to the presence of an acute lung infection, and 265 were excluded due to the absence of significant interstitial changes in the initial HR CT scan (total ILD score <2) (detailed descriptions in the section entitled: assessment of parenchymal abnormalities). Sixty-one patients underwent

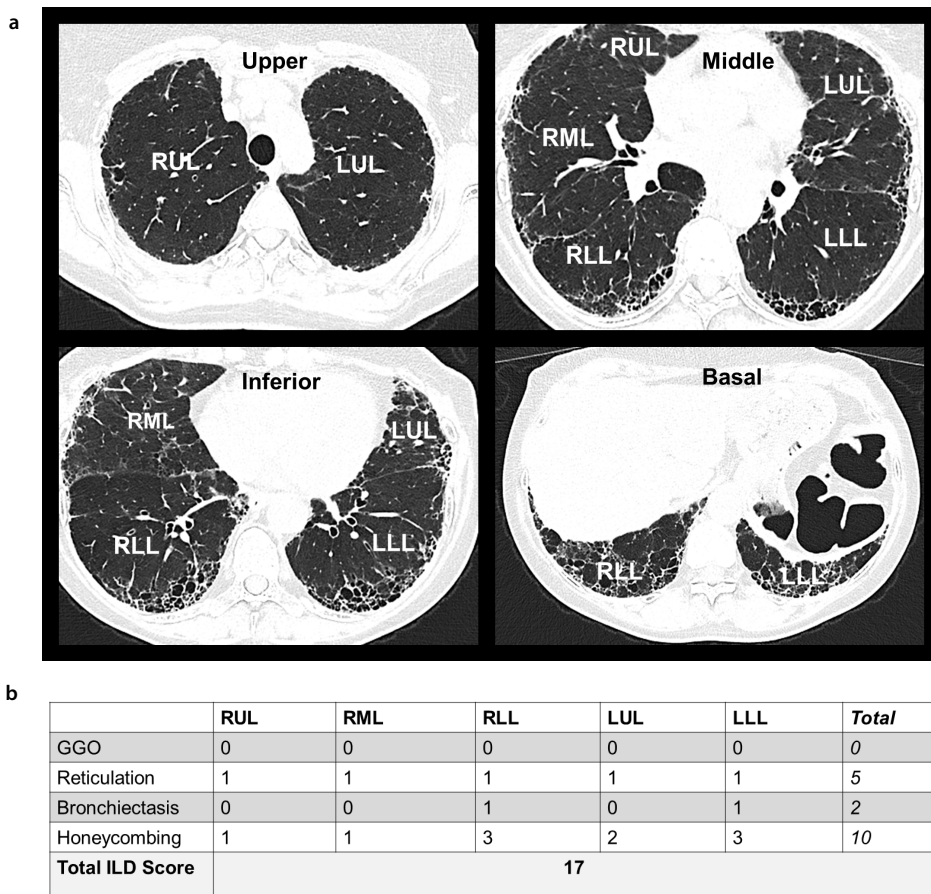


**Figure 2.** Four UHR CT images of a 68-year-old woman with RA at upper- and mid-level, inferior, and basal costophrenic angles revealed honeycombing, peripheral diffuse reticulation, and traction bronchiectasis with lower-zone dominance consistent with the pattern of definitive usual interstitial pneumonia (a). Lung HR CT score was calculated based on Wangkaew et al.<sup>20</sup> (b). RUL, right upper lobe; RML, right middle lobe; RLL, right lower lobe; LUL, left upper lobe; LLL, left lower lobe; RA, rheumatoid arthritis; ILD, interstitial lung disease; UHR, ultra-high-resolution; HR, high-resolution; CT, computed tomography; GGO, ground-glass opacity.

**Table 1.** Patient characteristics and pulmonary function test results

Patient characteristics (n = 61, both HR and UHR scans)	
Gender [n (%)]	40 (65.60%) females; 21 (34.40%) males
Age (y) (mean ± SD)	68.6 ± 9.73
Time since disease onset (y) (mean ± SD)	15.75 ± 12.85
Rheumatoid factor positivity [n (%)]	42 (68.85%)
Anti-citrullinated protein antibody positivity [n (%)]	36 (59.01%)
Smoking history (ever-smokers) [n (%)]	33 (54.10%)
Pack-year among smokers (mean ± SD)	23.66 ± 20.40
Body mass index (kg/m <sup>2</sup> ) (mean ± SD)	27.4 ± 3.96
Previous COVID-19 pneumonia (not in the prior 3 months) [n (%)]	6 (9.83%)
Cough [n (%)]	16 (26.22%)
Dyspnea [n (%)]	18 (29.50%)
Fatigue [n (%)]	26 (42.62%)
Pulmonary function tests (n = 51)	
FVC (%) (mean ± SD)	90 ± 17.89
FEV1 (%) (mean ± SD)	93.23 ± 14.30
FEV1/FVC (%) (mean ± SD)	101.39 ± 9.66
DLCO (%) (mean ± SD)	108.39 ± 19.61

Age, duration from disease onset, smoking history, and body mass index are expressed as mean ± standard deviation. The proportion of seropositivity, smokers, and clinical symptoms are presented as percentages. COVID-19, coronavirus disease 2019; DLCO, diffusion capacity for carbon monoxide; FEV1, first second of forced expiration; FVC, forced vital capacity; HR, high-resolution; ILD, interstitial lung disease; SD, standard deviation; UHR, ultra-high-resolution.

both HR and UHR scans, and 51 patients underwent pulmonary function tests (Table 1). The mean age of study participants was 68.6 ± 9.73 years, and 40 (65.57%) were female. Average time since disease onset was 15.75 ± 12.85 years. Forty-two (68.85%) patients were seropositive, and 33 (53.22%) had previously been smokers. The detailed characteristics of the study population are summarized in Table 1.

### Assessment of parenchymal abnormalities

Parenchymal abnormalities were visually recognizable on both HR and UHR scans (Figure 3). UHR CTs yielded higher total ILD scores than HR CTs [6 (4, 9) vs. 4 (2.5, 8),  $P < 0.001$ ]. Additionally, bronchiectasis and reticulation scores were significantly higher in the UHR protocol compared with the HR protocol [2 (0, 2) vs. 0 (0, 2),  $P < 0.001$  and 2 (0, 3.5) vs. 0 (0, 3)  $P < 0.001$ , respectively]; however, GGO and honeycombing scores did not differ [2 (2, 4) vs. 2 (2, 4),  $P = 0.944$  and 0 (0, 0) vs. 0 (0, 0),  $P = 0.641$ , respectively] (Figure 4). Visually identified patterns did not differ significantly between UHR and HR PCD-CT protocols (Figure 5). UIP patterns, non-specific interstitial pneumonia, desquamate interstitial pneumonia, respiratory bronchiolitis-ILD, pleuroparenchymal fibroelastosis, and post-coronavirus disease-2019 parenchymal changes were registered in the examined population on both HR and UHR protocols (Figure 5). No patterns of lympho-

cytic interstitial pneumonitis or organizing pneumonia were identified on the scans. Inter-reader reliability pattern scores varied

between moderate and perfect agreement (Figure 5). Most cases were small-extent, otherwise non-specified parenchymal ab-

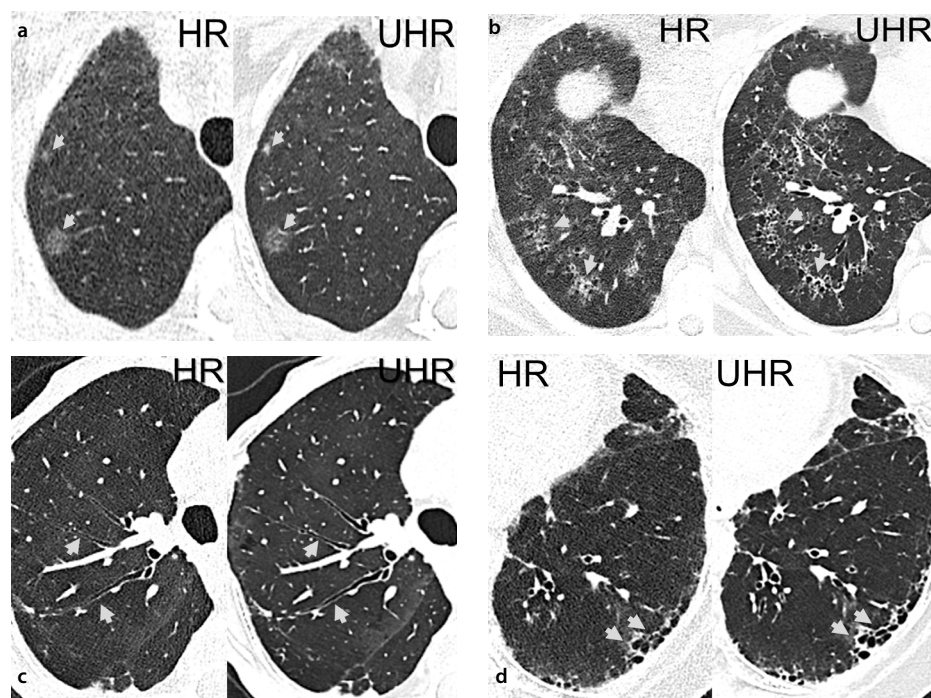


**Figure 3.** Non-contrast HR (left) and UHR (right) chest photon-counting detector CT scans at the same level represent interstitial abnormalities (indicated by gray arrows): upper-zone GGO (a), middle-zone peribronchovascular fibrosis (b), middle-zone bronchiectasis (c), and lower-zone honeycombing (d). Images are derived from four different RA patients with different patterns of parenchymal involvement: respiratory bronchiolitis interstitial lung disease (ILD) (a); desquamate interstitial pneumonia-ILD (b); non-specified ILA (c); and dUIP (d). UHR, ultra-high-resolution; HR, high-resolution; CT, computed tomography; GGO, ground-glass opacity; RA, rheumatoid arthritis; ILA, interstitial lung abnormalities; dUIP, definitive usual interstitial pneumonia.

normalities. Total ILD scores of both HR and UHR protocols showed a mild but significant negative correlation with DLCO values (HR:  $r = -0.297$ ,  $P = 0.034$ ; UHR:  $r = -0.294$ ;  $P = 0.036$ ) (Figure 6).

### Dose considerations and phantom studies

Reduced-dose, 0.4 mm scans had significantly lower CTDIvol values [median (quartile 1, quartile 3): 0.67 (0.69, 1.06) mGy] compared with non-reduced, 0.2 mm scans [8.18 (6.80, 9.23) mGy,  $P < 0.001$ ]. The 0.4 mm

slice thickness HR acquisitions had approximately  $8.6 \times$  lower TDLP [29.0 (24.48, 33.20) mGy\*cm] compared with 0.2 mm slice thickness, non-reduced-dose UHR scans [250 (218, 305) mGy\*cm,  $P < 0.001$ ]. Median effective radiation doses were  $\sim 0.4$  mSv for low-dose (LD) HR CT scans and 3 mSv for UHR CT scans (Table 2). Dose-matched phantom studies confirmed that, compared with EID-CT scans, PCD-CT measurements had improved subjective and objective image quality values (Figure 7).

## Discussion

A relatively small number of studies on the clinical application of PCD-CT in lung diseases have been published. This current work extends previous observations. This study demonstrates that LD PCD-CT chest scans could be used to evaluate the quality and extent of ILA in a majority of patients with RA, and higher-accuracy UHR imaging can add further information about lung parenchymal involvement. Thus, HR PCD-CT with a low effective radiation dose may serve as a valuable screening tool in the selection of RA-ILD patients for a more detailed, higher-dose UHR PCD-CT screening.

RA is a systemic autoimmune disease, and lung involvement may be its most frequent extra-articular manifestation and highest contributor to a worsening prognosis.<sup>19</sup> The prevalence of interstitial lung involvement is reported in a wide spectrum of patients with RA, and ILD can be a predictor of the development of articular manifestations.<sup>9,20,21</sup> Some forms of ILD are progressive, and, in addition to their patterns, the ILD board considers the extent of lung involvement an important parameter in its multidisciplinary discussion.<sup>22,23</sup> Screening for ILD may be advisable in select cases of RA, as early detection of parenchymal changes could help direct antirheumatic treatment.<sup>24</sup>

The identification of interstitial lung involvement requires high spatial resolution scans, as the subtlety of parenchymal changes (e.g., intralobular reticulations, bronchiectasis, and honeycombing) are frequently

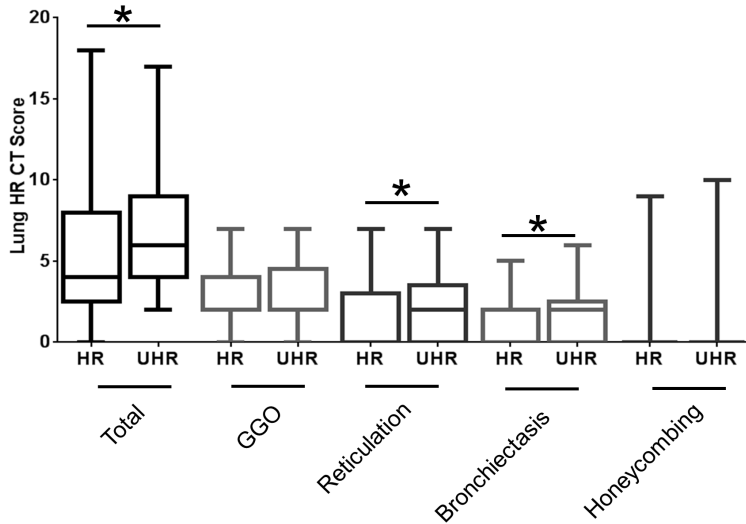


**Figure 4.** Box and whiskers diagram of interstitial lung disease scores.<sup>17</sup> GGO, reticulation, bronchiectasis, and honeycombing values represent scores from all the five lobes. Total scores were calculated from the sum of GGO, reticulation, bronchiectasis, and honeycombing values. UHR measurements had slightly higher total, reticulation, and bronchiectasis scores. Inner horizontal lines indicate median values. Whiskers represent minimum to maximum range. Results were considered statistically significant at  $P < 0.05$  (asterisk marks). GGO, ground-glass opacity; UHR, ultra-high-resolution; HR, high-resolution; CT, computed tomography.

Total number of examined patients $n=61$	Radiologist 1,2 (number of diagnosed patterns)			Radiologist 3 (number of diagnosed patterns)			Interobserver agreement (Cohen's Kappa)	
	HR	UHR	$p$	HR	UHR	$p$	HR	UHR
<b>Pattern</b>								
dUIP	8	8	(HR vs. UHR)	8	8	(HR vs. UHR)	1	1
pUIP	4	4		3	4		0.65	1
iUIP	1	0	0.97	0	0	1	0.65	1
NSIP	3	3	(ns)	5	5	(ns)	0.73	0.73
OP	0	0		0	0		1	1
LIP	0	0		0	0		1	1
RB-ILD	2	1		3	2		0.79	0.65
DIP	0	1		0	1		1	1
PPFE	2	1		2	1		1	1
postCOVID	2	2		2	2		1	1
otherwise non-specified	41	41		38	38		0.89	0.89

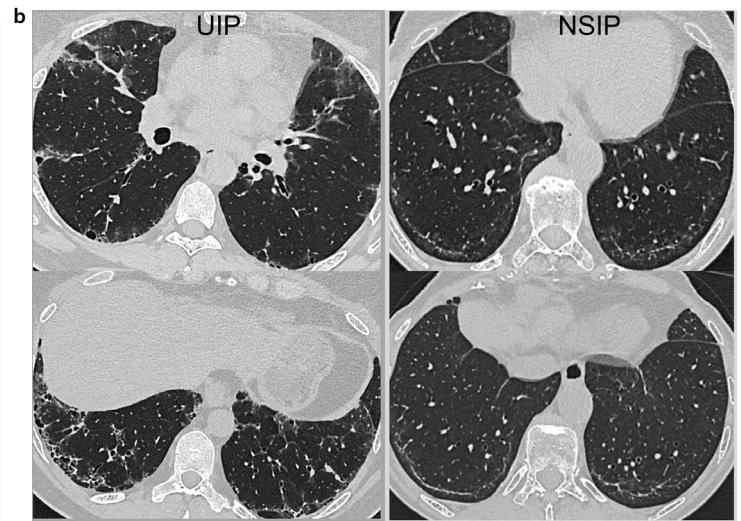


**Figure 5.** Patterns of ILD identified (a) in the examined RA population ( $n = 61$ ). Axial 0.2 mm slice thickness chest PCD-CT images representing the most common ILD patterns patients with RA (b) usual interstitial pneumonia (left), non-specific interstitial pneumonia (right). ILD, interstitial lung disease; PCD-CT, photon-counting detector-computed tomography; RA, rheumatoid arthritis; UHR, ultra-high-resolution; HR, high-resolution; dUIP, definitive usual interstitial pneumonia; pUIP, probable usual interstitial pneumonia; iUIP, indeterminate usual interstitial pneumonia; OP, organizing pneumonia; LIP, lymphocytic interstitial pneumonia; DIP, desquamative interstitial pneumonia; PPFE, pleuro-parenchymal fibroelastosis; COVID, coronavirus; NSIP, non-specific interstitial pneumonia; ns, non-significant.

indefinite.<sup>25</sup> To date, there is no worldwide consensus on screening recommendations because the benefits of lung parenchymal involvement screening have had to be balanced with the inherent risks of ionizing radiation. Large FOV chest PCD-CT scans with 1024 × 1024 matrix sizes conferred better overall image quality and SNR than standard EID-CT scans.<sup>6,26</sup> According to previous studies, LD image acquisition with PCD-CT showed better SNR and attenuation accuracy

compared with conventional CT, especially at lower doses, where attenuation decreased significantly with EID-CT.<sup>7</sup> Better image quality was also observed, especially in areas with known beam hardening (e.g., paravertebral spaces). Prior investigations have shown that PCD-CT images have 15.2%–16.8% less noise at two different dose levels. Furthermore, studies have proven that HR parameters could be preserved while applying LD protocols in lung evaluation.<sup>26</sup> In this examination,

fast gantry rotation times (0.25–0.5 s) were used to reduce scanning time and motion artifacts.<sup>27</sup> We used a 1024 × 1024 matrix, large FOV (35 ± 3 cm, depending on the size of the patient), and 0.2 or 0.4 mm slice thickness parameter protocols and found a satisfactory detection of parenchymal pathologies, including GGOs, fibrotic reticulations, bronchiectasis, and subpleural cysts (Table 2, Figure 4). According to the literature, lower tube currents are optimal for pulmonary nodule detection (approximately 25 mA).<sup>28</sup> However, for subtle parenchymal anomalies, higher currents are inevitable to reach better resolutions. In the case of this study, 100 kV (for HR) and 120 kV (for UHR) voltages, as well as automated mA parameters, were utilized to obtain a HR image with reduced dose values (Table 2).

Optimized dose efficiency, combined with iterative reconstruction algorithms, can decrease noise levels and allow for large matrix reconstructions that lead to ultra-LD protocols.<sup>29,30</sup> Due to increased data complexity and spectral information, a novel algorithm, quantum iterative reconstruction, with four strength levels (QIR-1–4) has been developed for PCD-CT.<sup>29</sup> According to a preceding article, QIR-3 dispensed the highest spatial resolution and noise texture; thus, we applied QIR-3 for our protocols.<sup>29</sup> Additionally, it has been described that significant dose reduction and conservation of HR parameters for lung parenchyma assessment is possible with PCD-CT, either with or without iterative reconstruction.

In a pilot study, Inoue et al.<sup>31</sup> demonstrated that PCD-CT produced better image qual-

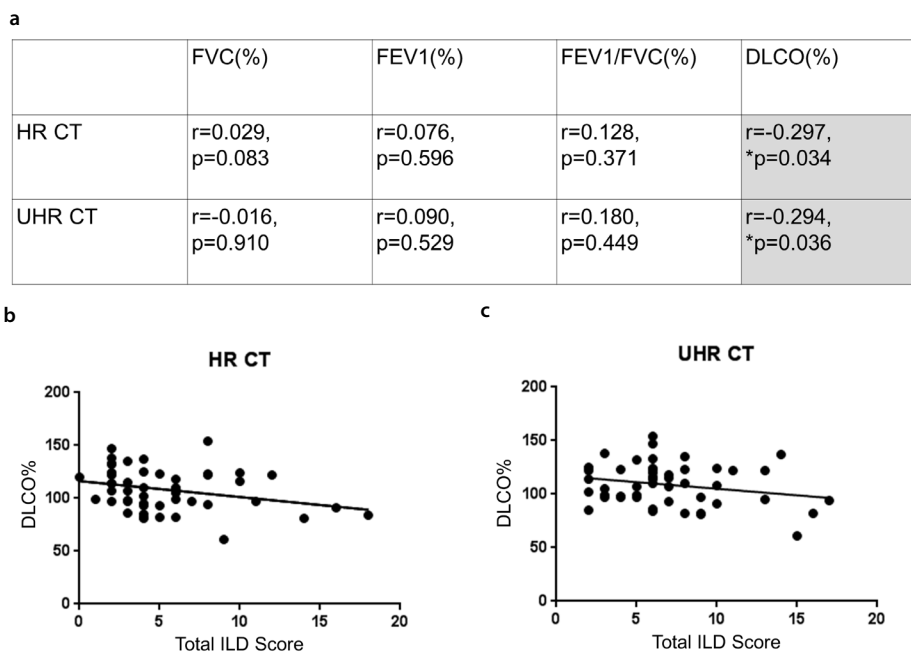


**Figure 6.** Correlation values of pulmonary function tests and total ILD scores (a). Both HR (b) and UHR (c) total ILD scores show a mild, significant negative correlation with DLCO values (%). \*,  $P < 0.05$ ; UHR, ultra-high-resolution; HR, high-resolution; CT, computed tomography; FVC, forced vital capacity; FEV1, first second of forced expiration; DLCO, diffusion capacity for carbon monoxide; ILD, interstitial lung disease.

**Table 2.** RA patient PCD-CT chest protocol characteristics

	HR	UHR
Rotation time (s)	0.25	0.5
Collimation	144 × 0.4	120 × 0.2
Pitch	1.5	0.85
kV	100	120
Filter	Standard	Standard
mA based on size (automated) (mean ± SD)	96 ± 25.2	86 ± 21.6
Total mAs based on size (automated) (mean ± SD)	217 ± 75.6	194.36 ± 64.8
Quantitative iterative reconstruction algorithm/strength	3	3
Matrix size	1024 × 1024	1024 × 1024
Kernel	Bl60	Bl60
Slice thickness (mm)	0.4	0.2
Slice increment (mm)	0.4	0.2
Pixel size (mm)	FOV/matrix size	FOV/matrix size
Care keV IQ level	15	100

LD, low dose; HR scan and sequential UHR scan was carried out without the administration of contrast media. HR, high-resolution; UHR, ultra-high-resolution; SD, standard deviation; RA, rheumatoid arthritis; PCD-CT, photon-counting detector computed tomography; BL, body lung kernel; FOV, field of view.

**a**

	PCD_A	PCD_B	EID1_A	EID1_B	EID2_A	EID2_E
Slice thickness (mm)	0.6	1	0.67	1	0.625	1
Rotation time (s)	0.5	0.5	0.5	0.5	0.5	0.5
Nominal single collimation	0.2	0.2	0.625	0.625	0.625	0.625
Pitch	1	1	1	1	1	1
kV	100	100	100	100	100	100
mA	100	100	100	100	100	100
Matrix size	512x512	512x512	512x512	521x512	512x512	521x512
Kernel	Bl60	Bl60	Lung	Lung	Lung	Lung
Scan length (cm)	31.00	31.00	32.00	32.00	32.00	32.00
Scan time (s)	2.3	2.6	6	6.5	8.5	8.8
TDLP (mGy*cm)	29.40	29.50	187	187	70.7	101
CTDIvol	0.83	0.84	4.84	4.83	2.98	2.98
Subjective Score (median [Q1;Q3])	4 [4;4]	4 [4.5;5]	2.5 [2;3]	3 [2;3]	4 [3;4]	4 [4;4]
Subjective Score/ TDLP	<b>0.14*</b>	<b>0.16*</b>	0.01	0.02	0.06	0.04
Subj Score Median/ CTDI	<b>4.82*</b>	<b>5.35*</b>	0.51	0.62	1.34	1.34
SNR	6.06	7.38	1.02	1.72	5.69	1.15
CNR	21.93	29.11	19.98	38.47	26.60	33.87
SNR/TDLP	<b>0.20*</b>	<b>0.25*</b>	0.01	0.01	0.08	0.01
SNR/CTDI	<b>7.30*</b>	<b>8.79*</b>	0.21	0.36	1.91	0.38
CNR/TDLP	<b>0.74*</b>	<b>0.98*</b>	0.11	0.21	0.08	0.06
CNR/CTDI	<b>26.43*</b>	<b>34.65*</b>	4.13	7.96	1.91	0.38

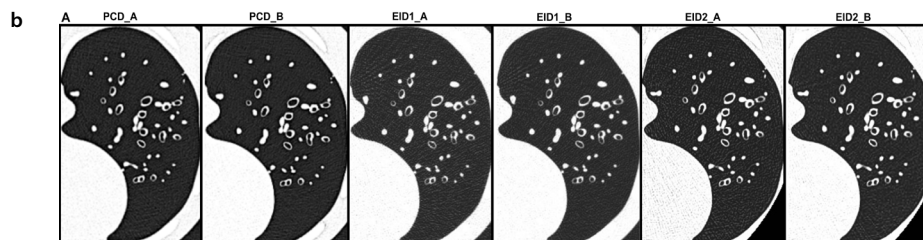


**Figure 7.** Matched-parameter scan protocols, dose values, and image quality parameters of different PCD and energy-integrating detector (EID) scans (a). Axial images of identical inferior chest regions (b) PCD-CT images have proven ( $P < 0.05$ ) dose-matched subjective and objective image quality compared with EID-CT images. \*,  $P < 0.05$ ; PCD-CT, photon-counting detector-computed tomography; CTDIvol, volume CT dose index; TDLP, total dose length product; CNR, contrast-to-noise-ratio; SNR, signal-to-noise ratio; BL, body lung kernel.

ity and enhanced diagnostic confidence for lung parenchymal abnormalities at reduced radiation doses. Jungblut et al.<sup>32</sup> further confirmed that PCD-CT provides good image quality with lower radiation doses, compared with EID-CT. Our phantom studies confirmed that, compared with EID-CT measurements, PCD-CT protocols produce improved dose-matched CNR and SNR values (Figure 7). Previous LD EID-CT protocols (i.e.,  $< 1$  mSv) are not recommended for diagnostic use, as their impaired image quality could lead to the misclassification of ILD.<sup>33</sup> Chest HR EID-CT has an effective dose of approximately 6–9 mSv, according to the literature, while

in our study, the effective dose of PCD-CT was 0.4 mSv for HR scans and 3.5 mSv for UHR scans. Previously reported average LD EID-CT protocols had an effective dose of 2.1–2.4 mSv, significantly higher than our HR PCD-CT dose value.<sup>13,26,32,34</sup> LD CT has been increasingly used in the assessment of pulmonary cancer; however, this is not the only pulmonary disorder in which the risk–benefit ratio could be positive. For instance, the follow-up of ILD at low doses of radiation could be of interest.<sup>33,35,36,37,38</sup> Our data suggest that PCD-CT is a promising tool in radiation dose optimization, which is crucial in optimizing the risk–benefit ratio of CT lung screening.<sup>39</sup>

UHR scans proved to be more sensitive in the detection of bronchiectasis and reticulation; hence, their total score values were slightly higher. However, the identification of GGO and honeycombing values was the same between protocols (Figure 4). The UHR protocol was slightly more sensitive to interstitial pathologies; however, the magnitude of differences was not protruding. Moreover, the same ILD patterns were identified with both protocols. Taking into consideration the dose values that were notably lower ( $\sim 7.4\times$ ) in LD HR scans, the LD measurements were able to assess interstitial changes with good proximity.

While this study has limitations (e.g., the relatively low number of patients enrolled), it is comparable to other international investigations. Furthermore, it would be interesting to set against our results from other PCD-CT protocols with different parameters. However, the benefits of better image quality need to be balanced with the risks of higher radiation exposure in these patients. Phantom studies to compare different detector-type CT protocols can be conducted to avoid increased radiation doses for patients. Additionally, ILD multidisciplinary team discussions are needed to gauge the difference between these two CT modalities in clinical settings to improve team diagnosis, especially of early cases. Longitudinal radiological data on natural behavior and disease-specific treatment of early RA-ILD are also needed.

In conclusion, wide-scale clinical experience with UHR CT imaging to assess lung involvement in patients with RA does not exist. In this proof-of-concept study, we found that a UHR PCD-CT protocol provided more detailed images compared with an HR PCD-CT protocol. The HR PCD-CT protocol provided detailed information regarding interstitial lung involvement; however, in the case of an extended or complex pathology, additional UHR imaging may prove beneficial. Further studies are needed to determine if an HR PCD-CT protocol, with its reduced radiation doses, could serve as an initial screening tool before selecting patients for further UHR imaging. From a clinical perspective, the higher effective radiation dose of UHR PCD-CT is balanced by its better characterization of pulmonary involvement, which provides the potential for earlier anti-fibrotic treatment, a very important intervention in RA patients with ILD.

**Table 3. Patterns of interstitial lung involvement**

Pattern name	Main characteristics (based on HR CT)
Definitive usual interstitial pneumonia	Honeycombing, +/- traction bronchiectasis, reticular abnormalities, distribution: subpleural, basal dominant; absence of features suggestive of an alternative diagnosis.
Probable usual interstitial pneumonia	Reticulations, +/- superimposed GGO, peripheral traction bronchiectasis/bronchiolectasis, distribution: subpleural, basal dominant; absence of features suggestive of an alternative diagnosis.
Indeterminate usual interstitial pneumonia	Subtle reticular abnormalities, +/- superimposed GGO, distribution: does not suggest different pathology.
Non-specific interstitial pneumonia	GGOs with basal predominance and subpleural sparing, subpleural reticulations, thickening of bronchovascular bundles in fibrotic type, traction bronchiectasis, distribution: subpleural, symmetrical, apicobasal gradient.
Organizing pneumonia	Patchy consolidation with a predominantly subpleural and/or peribronchial distribution, peribronchial or peribronchiolar nodules, thickened interlobular septae, bronchial wall thickening, GGO or crazy paving.
Desquamative interstitial pneumonia	Bilateral symmetric GGO, mostly basal and peripheral, irregular linear opacities, small cystic spaces (occasional).
Respiratory bronchiolitis interstitial lung disease	Slight upper-zone predilection of GGOs, poorly defined centrilobular nodules, smoking-related changes.
Pleuro-parenchymal fibroelastosis	Bilateral apical pleural thickening, architectural distortion, reticular abnormalities, peripheral consolidation, traction bronchiectasis, pneumothorax (occasional).
Lymphocytic interstitial pneumonia	Diffuse to mid- and lower-zone dominance, peribronchovascular thickening, reticulation, subpleural or centrilobular nodules, GGOs, scattered, thin-walled cysts.
Otherwise non-classifiable pattern	None of the above and/or cannot be characterized due to small extent ( $\leq 5\%$ ).

Interstitial lung disease is a heterogeneous group of chronic parenchymal diseases. The specific patterns listed belong to the ILD category. GGO, ground glass opacity<sup>10</sup>; HR, high-resolution; CT, computed tomography; ILD, interstitial lung disease.

## Acknowledgements

We would like to thank for the help and support of the colleagues mentioned afterwards:

Hanna Balogh MD<sup>1</sup>, Leila Szeibel MD<sup>1</sup>, Tamas Purczel MD<sup>1</sup>, Tamas Munkacsi MD<sup>1</sup>, Nora Kerkovits MD<sup>1</sup>, Klaudia Borbely MD<sup>1</sup>, Laszlo Szakacs<sup>1</sup>, Aniko Kubovje<sup>1</sup>, Kinga Karlinger MD, PhD<sup>1</sup>, Dora Sarvari MD<sup>2</sup>, Timea Petri MD<sup>2</sup>

<sup>1</sup>Department of Radiology, Medical Imaging Centre, Semmelweis University, Budapest, Hungary

<sup>2</sup>Buda Hospital of the Hospitaller Order of Saint John of God, Budapest, Hungary

## Conflict of interest disclosure

The authors declared no conflicts of interest.

## Funding

Nikolett Marton MD, PhD (first author) received a Bolyai Research Scholarship from the Hungarian Academy of Sciences.

## References

1. Taguchi K, Iwanczyk JS. Vision 20/20: single photon counting x-ray detectors in medical imaging. *Med Phys.* 2013;40(10):100901. [\[CrossRef\]](#)
2. Willemink MJ, Persson M, Pourmorteza A, Pelc NJ, Fleischmann D. Photon-counting CT: technical principles and clinical prospects. *Radiology.* 2018;289(2):293-312. [\[CrossRef\]](#)
3. Danielsson M, Persson M, Sjölin M. Photon-counting X-ray detectors for CT. *Phys Med Biol.* 2021;66(3):03TR01. [\[CrossRef\]](#)
4. Rajendran K, Petersilka M, Henning A, et al. First clinical photon-counting detector CT system: technical evaluation. *Radiology.* 2022;303(1):130-138. [\[CrossRef\]](#)
5. Ferda J, Vendiš T, Flohr T, et al. Computed tomography with a full FOV photon-counting detector in a clinical setting, the first experience. *Eur J Radiol.* 2021;137:109614. [\[CrossRef\]](#)
6. Hata A, Yanagawa M, Honda O, et al. Effect of matrix size on the image quality of ultra-high-resolution CT of the lung: comparison of 512×512, 1024×1024, and 2048×2048. *Acad Radiol.* 2018;25(7):869-876. [\[CrossRef\]](#)
7. Symons R, Pourmorteza A, Sandfort V, et al. Feasibility of dose-reduced chest CT with photon-counting detectors: initial results in humans. *Radiology.* 2017;285(3):980-989. [\[CrossRef\]](#)
8. Jacob J, Hirani N, van Moorsel CHM, et al. Predicting outcomes in rheumatoid arthritis related interstitial lung disease. *Eur Respir J.* 2019;53(1):1800869. [\[CrossRef\]](#)
9. Fazeli MS, Khaychuk V, Wittstock K, et al. Rheumatoid arthritis-associated interstitial lung disease: epidemiology, risk/prognostic factors, and treatment landscape. *Clin Exp Rheumatol.* 2021;39(5):1108-1118. [\[CrossRef\]](#)
10. Raghu G, Remy-Jardin M, Richeldi L, et al. Idiopathic pulmonary fibrosis (an update) and progressive pulmonary fibrosis in adults: an official ATS/ERS/JRS/ALAT clinical practice guideline. *Am J Respir Crit Care Med.* 2022;205(9):18-47. [\[CrossRef\]](#)
11. Spagnolo P, Lee JS, Sverzellati N, Rossi G, Cottin V. The lung in rheumatoid arthritis: focus on interstitial lung disease. *Arthritis Rheumatol.* 2018;70(10):1544-1554. [\[CrossRef\]](#)
12. Juge PA, Crestani B, Dieudé P. Recent advances in rheumatoid arthritis-associated interstitial lung disease. *Curr Opin Pulm Med.* 2020;26(5):477-486. [\[CrossRef\]](#)
13. No authors listed. World Medical Association Declaration of Helsinki: ethical principles for medical research involving human subjects. *JAMA.* 2000;284(23):3043-3045. [\[CrossRef\]](#)
14. Smith-Bindman R, Lipson J, Marcus R, et al. Radiation dose associated with common computed tomography examinations and the associated lifetime attributable risk of cancer. *Arch Intern Med.* 2009;169(22):2078-2086.

- [CrossRef]
15. Larke FJ, Kruger RL, Cagnon CH, et al. Estimated radiation dose associated with low-dose chest CT of average-size participants in the National Lung Screening Trial. *AJR Am J Roentgenol.* 2011;197(5):1165-1169. [CrossRef]
  16. Kazerooni EA, Martinez FJ, Flint A, et al. Thin-section CT obtained at 10-mm increments versus limited three-level thin-section CT for idiopathic pulmonary fibrosis: correlation with pathologic scoring. *AJR Am J Roentgenol.* 1997;169(4):977-983. [CrossRef]
  17. Wangkaew S, Euathrongchit J, Wattanawittawas P, Kasitanon N. Correlation of delta high-resolution computed tomography (HRCT) score with delta clinical variables in early systemic sclerosis (SSc) patients. *Quant Imaging Med Surg.* 2016;6(4):381-390. [CrossRef]
  18. McHugh ML. Interrater reliability: the kappa statistic. *Biochem Med (Zagreb).* 2012;22(3):276-282.
  19. Turesson C. Extra-articular rheumatoid arthritis. *Curr Opin Rheumatol.* 2013;25(3):360-366. [CrossRef]
  20. Mori S, Cho I, Koga Y, Sugimoto M. Comparison of pulmonary abnormalities on high-resolution computed tomography in patients with early versus longstanding rheumatoid arthritis. *J Rheumatol.* 2008;35(8):1513-1521. [CrossRef]
  21. Turesson C, O'Fallon WM, Crowson CS, Gabriel SE, Matteson EL. Occurrence of extraarticular disease manifestations is associated with excess mortality in a community based cohort of patients with rheumatoid arthritis. *J Rheumatol.* 2002;29(1):62-67. [CrossRef]
  22. Robles-Perez A, Luburich P, Rodriguez-Sanchon B, et al. Preclinical lung disease in early rheumatoid arthritis. *Chron Respir Dis.* 2016;13(1):75-81. [CrossRef]
  23. American Thoracic Society; European Respiratory Society. American Thoracic Society/European Respiratory Society International Multidisciplinary Consensus Classification of the Idiopathic Interstitial Pneumonias. This joint statement of the American Thoracic Society (ATS), and the European Respiratory Society (ERS) was adopted by the ATS board of directors, June 2001 and by the ERS Executive Committee, June 2001. *Am J Respir Crit Care Med.* 2002;165(2):277-304. [CrossRef]
  24. Picchianti Diamanti A, Markovic M, Argento G, et al. Therapeutic management of patients with rheumatoid arthritis and associated interstitial lung disease: case report and literature review. *Ther Adv Respir Dis.* 2017;11(1):64-72. [CrossRef]
  25. Watadani T, Sakai F, Johkoh T, et al. Interobserver variability in the CT assessment of honeycombing in the lungs. *Radiology.* 2013;266(3):936-944. [CrossRef]
  26. Bartlett DJ, Koo CW, Bartholmai BJ, et al. High-resolution chest computed tomography imaging of the lungs: impact of 1024 matrix reconstruction and photon-counting detector computed tomography. *Invest Radiol.* 2019;54(3):129-137. [CrossRef]
  27. Mohamed SS, Ness DB, Sigovan M, et al. Review of an initial experience with an experimental spectral photon-counting computed tomography system. *Nucl Inst Methods Phys Res.* 2017;873:27-35. [CrossRef]
  28. Beeres M, Wichmann JL, Paul J, et al. CT chest and gantry rotation time: does the rotation time influence image quality? *Acta Radiol.* 2015;56(8):950-954. [CrossRef]
  29. Oguchi K, Sone S, Kiyono K, et al. Optimal tube current for lung cancer screening with low-dose spiral CT. *Acta Radiol.* 2000;41(4):352-356. [CrossRef]
  30. Sartoretti T, Racine D, Mergen V, et al. Quantum iterative reconstruction for low-dose ultra-high-resolution photon-counting detector CT of the lung. *Diagnostics (Basel).* 2022;12(2):522. [CrossRef]
  31. Inoue A, Johnson TF, Voss BA, et al. A pilot study to estimate the impact of high matrix image reconstruction on chest computed tomography. *J Clin Imaging Sci.* 2021;11:52. [CrossRef]
  32. Jungblut L, Euler A, von Spiczak J, et al. Potential of photon-counting detector CT for radiation dose reduction for the assessment of interstitial lung disease in patients with systemic sclerosis. *Invest Radiol.* 2022;57(12):773-779. [CrossRef]
  33. Raghu G, Remy-Jardin M, Myers JL, et al. Diagnosis of idiopathic pulmonary fibrosis. An official ATS/ERS/JRS/ALAT clinical practice guideline. *Am J Respir Crit Care Med.* 2018;198(5):44-68. [CrossRef]
  34. Sartoretti T, Landsmann A, Nakhostin D, et al. Quantum iterative reconstruction for abdominal photon-counting detector CT improves image quality. *Radiology.* 2022;303(2):339-348. [CrossRef]
  35. Demb J, Chu P, Yu S, et al. Analysis of computed tomography radiation doses used for lung cancer screening scans. *JAMA Intern Med.* 2019;179(12):1650-1657. [CrossRef]
  36. Ataç GK, Parmaksız A, İnal T, et al. Patient doses from CT examinations in Turkey. *Diagn Interv Radiol.* 2015;21(5):428-434. [CrossRef]
  37. Molinari F, Tack DM, Boiselle P, et al. Radiation dose management in thoracic CT: an international survey. *Diagn Interv Radiol.* 2013;19(3):201-209. [CrossRef]
  38. Topçuoğlu OM, Sarıkaya B. Fast kilovoltage-switching dual-energy CT offering lower x-ray dose than single-energy CT for the chest: a quantitative and qualitative comparison study of the two methods of acquisition. *Diagn Interv Radiol.* 2019;25(3):204-209. [CrossRef]
  39. National Lung Screening Trial Research Team; Aberle DR, Berg CD et al. The National Lung Screening Trial: overview and study design. *Radiology.* 2011;258(1):243-253. [CrossRef]



# Current practice of emergency radiology in Turkey and future expectations: a survey study

Özüm Tunçyürek   
Mehmet Ruhi Onur   
Ersen Ertekin   
Cem Çallı 

## PURPOSE

The development of emergency radiology (ER) in Turkey has accelerated with the increase in the number of patients admitted to emergency departments. We aimed to present and discuss the responses to a survey distributed to radiologists in Turkey, which included questions about the current practice of ER and future expectations.

## METHODS

A survey with 29 questions enquiring about the infrastructure of respondents' hospitals and radiology units, information about emergency services and ER (including patient volume), the number of staff and equipment, the ER working plan and reporting method, and training in the field of ER were distributed to members of the Turkish Radiological Society by email.

## RESULTS

The response rate was 21.97% (328/1.493). The presence of distinct ER units in radiology departments was confirmed by 40.55% of respondents, while for 34.25%, ER was located inside the emergency room. Of the respondents, 26.96% stated they believed that emergency cases should be reported by emergency radiologists, and the necessity for an ER subunit in the emergency room was agreed upon by 58.64% of contributors. The majority of respondents (69.54%) agreed with the opinion that residents should receive their ER training in an ER unit.

## CONCLUSION

Keeping abreast of current ER practices and radiologists' expectations may be helpful for improving national ER practices and academic studies.

## KEYWORDS

Emergency, improvement, practice, radiology, survey

From the Department of Radiology (Ö.T. ozum. ✉ tuncyurek@gmail.com), Cyprus International University Faculty of Medicine, Nicosia, Cyprus; Department of Radiology (M.R.O.), Hacettepe University Faculty of Medicine, Ankara, Turkey; Department of Radiology (E.E.), Hitit University Faculty of Medicine, Çorum, Turkey; Department of Radiology (C.Ç.), Ege University Faculty of Medicine, İzmir, Turkey.

Received 27 August 2021; revision requested 05 November 2021; accepted 28 January 2022.



Epub: 27.01.2023

Publication date: 29.03.2023

DOI: 10.5152/dir.2022.21913

**E**mergency radiology (ER), a relatively new subspecialty in the radiology area, is unique in its emphasis on the imaging of acutely ill or injured patients.<sup>1</sup> The number of patients and volume of images taken by emergency services has risen in recent years due to the wide use of ER, which often requires a rapid report turnaround on a round-the-clock basis. Optimizing patient outcomes in high-volume emergency services can be accomplished by emergency radiologists through the triage of patients.<sup>2</sup>

Although the need for ER is clear, specialization in ER and/or ER policy, including the management of emergency imaging and education, is not yet established in most countries. In various countries, ER is not recognized as a distinct category within the radiology community. Compared with other subspecialties, ER has the fewest number of fellowship training programs in developed countries.<sup>1</sup>

Teaching the importance of ER may be accomplished through learning initiatives with radiologists and clinicians, which could increase awareness about its functional requirements and advantages. In recent years, radiology societies have introduced surveys that examine

You may cite this article as: Tunçyürek Ö, Onur MR, Ertekin E, Çallı C. Current practice of emergency radiology in Turkey and future expectations: a survey study. *Diagn Interv Radiol.* 2023;29(2):300-308.

radiologists' levels of awareness and knowledge regarding ER. These surveys reveal the current situation of ER in radiology departments, along with the expectations of radiologists working in ER, and they provide an in-depth, multifaceted review of several topics of critical importance to trauma and emergency imaging.<sup>3,4</sup> However, needs, expectations, and recommended actions are often based on local circumstances, which may necessitate the use of nation-specific surveys to implement appropriate policies for ER management and the establishment of ER units.

In this study, we present the results of an ER survey distributed to radiologists in Turkey. The results of the survey are then discussed in relation to the current situation of ER in Turkey, the radiologists' points of view, and expectations for the future development of ER practice and education in Turkey.

## Methods

### Survey construction

Institutional review board approval was obtained for this study (2021/92-1369). An anonymous digital survey consisting of 29 questions was developed by a team of four practicing academic emergency radiologists based in part on the methods undertaken by Scaglione et al.<sup>3</sup> The survey was first reviewed by 22 members of the Emergency Radiology Research and Education Study Group, which is one of the radiology study groups of the Turkish Radiological Society (TRS). The TRS Board of Directors also reviewed the survey and permitted the distribution of the survey to their members by using their email lists. Survey questions were designed to be

responded to by all types of radiologists, including residents, fellows, consultants, academic radiologists, and chairpersons of radiology departments. Questions that were designed to probe the current practice of ER and radiologists' points of view about the future of the ER were sub-grouped to investigate the respondent's position, hospital infrastructure, emergency service, and ER workload, including patient volume, the number of staff, equipment, work planning and reporting methods in ER, and educational and academic activities in ER.

The format of the survey questions consisted of yes/no and multiple-choice selection questions.

### Survey distribution

The digital survey was made available to radiologists via a web link to Survey Monkey (Palo Alto, CA). Initial emails accompanying the survey and reminder emails one week after its introduction directed that radiologists should complete the survey only once.

Since this distribution approach would potentially result in duplicate responses across different platforms, initial emails accompanying the survey and reminder emails one week after its introduction directed that radiologists should complete the survey only once. The survey was conducted between April 15<sup>th</sup> and May 4<sup>th</sup>, 2021.

### Statistical analysis

All available data were analyzed on a question-by-question basis; relevant frequencies for each question are provided in the results. Survey data were exported into Excel (Microsoft Inc., Redmond, WA) and analyzed using descriptive statistics; categorical variables were expressed as frequencies and percentages. The responses to some questions that investigated the opinions of radiologists about ER were assessed according to the rank and workplace of radiologists. All data were collected and descriptive metrics calculated using IBM SPSS statistics software, version 25 (IBM Software, New York, USA).

## Results

The survey questions and corresponding results with respondents' rates are presented in Table 1. The response rate of the survey was 21.97% (n = 328). Although survey announcement emails were sent to 4,213 members of TRS, it was confirmed that 1,493 recipients read the emails and became aware of the survey. The highest participation was

achieved the second day after the survey was sent. The average completion time of the survey was 4 minutes and 36 seconds.

### Respondents' positions and hospital infrastructure

Most of the respondents of the survey were practicing radiologists (n = 143, 43.6%), followed by residents (n = 100, 30.49%), academics in universities (n = 60, 18.29%), chairpersons (n = 13, 3.96%), and academics in state hospitals (n = 12, 3.66%) (Figure 1). The number of beds in the hospitals where most of the participants worked was between 100 vs 500 (32.21%), followed by >1000 (28.83%) and >500 (28.53%). Most of the respondents were from university hospitals (37.80%). The majority of the hospitals were training hospitals (70.12%) and major trauma-treating hospitals (96.95%).

It was determined that more than one participant participated in the survey in some hospitals. There were 19, 12, and five responses from one hospital, four respondents from six hospitals, three respondents from eight hospitals, and two respondents from 13 hospitals. The remaining 280 responses were from distinct hospitals. Analysis of the responses from those working at the same hospital yielded no discrepancies in terms of the structuring of units and departments, bed capacity, or the number of cases admitted to the radiology department.

### Patient volume, staff, and equipment in emergency departments (ED) and emergency radiology

More than half of the respondents (51.38%) revealed that the number of patients admitted to the ED daily was >400. A separate ER unit was available in 40.55% of radiology departments, while 34.25% of respondents declared that ER units resided within the ED. The need to establish a distinct ER unit in the ED was agreed upon by 58.64% of all respondents, with the highest rate reported for academics at training and research hospitals (81.82%) and the lowest rate for radiologists (49.65%) (Table 2). Based on hospital types, this suggestion received the greatest level of approval in university hospitals (66.13%).

The presence of imaging equipment used for only emergency patients and the presence of equipment in ER units varied widely between hospitals. One-quarter of radiologists stated that X-ray, ultrasonography

#### Main points

- This study reveals the current practices of emergency radiology (ER) in Turkey and radiologists' perspectives and expectations regarding ER.
- Current infrastructure, staff, and academic personnel of radiology departments need to be improved to establish ER divisions in radiology departments.
- Absence of ER units in radiology departments results in drawbacks not only in ER practice but also regarding the education of radiology residents in terms of emergency settings management.
- ER practice may be better managed by radiologists who undergo dedicated ER subspecialty training with a distinct ER study area as part of the core curriculum.

**Table 1. Respondents' answers to the survey**

Q1. What position do you have in the field of radiology?	n - %
Radiology resident	100-30.5%
Radiologist	143-43.6%
Radiology educator	12-3.7%
Academician	60-18.3%
Chairperson/head of department	13-3.9%
<b>Total</b>	<b>328-100%</b>
<b>Q2. What is the status of the hospital where you work?</b>	
State hospital	52-15.9%
Training-research hospital	96-29.3%
City hospital*	29-8.8%
University hospital	124-37.8%
Private hospital	27-8.2%
<b>Total</b>	<b>328-100%</b>
<b>Q3. What is the name of the hospital where you work?</b>	
Institution name	235-74.8%
If you do not wish to notify your institution, please specify	79-25.2%
<b>Total</b>	<b>314-100%</b>
<b>Q4. What is the bed capacity of your hospital?</b>	
<100	34-10.4%
100-500	105-32.2%
>500	93-28.6%
>1000	94-28.8%
<b>Total</b>	<b>326-100%</b>
<b>Q5. Does your hospital provide medical student or radiology residency training?</b>	
Yes	230-70.1%
No	98-29.9%
<b>Total</b>	<b>328-100%</b>
<b>Q6. Are major emergencies (arrest, stroke, myocardial infarction, acute abdomen) and major trauma cases accepted?</b>	
Yes	318-96.9%
No	10-3.1%
<b>Total</b>	<b>328-100%</b>
<b>Q7. What is the daily number of cases admitted to the ED?</b>	
<100	30-9.2%
100-200	37-11.4%
200-300	44-13.5%
300-400	47-14.5%
>400	167-51.4%
<b>Total</b>	<b>325-100%</b>
<b>Q8. Does your ED have a separate ER department that evaluates emergency patients?</b>	
Yes	133-40.6%
No	195-59.4%
<b>Total</b>	<b>328-100%</b>
<b>Q9. If you have an ER department, is this department located in the ED?</b>	
Yes	100-34.2%
No	192-65.8%
<b>Total</b>	<b>292-100%</b>
<b>Q10. Should ER departments be included in the ED?</b>	
Yes	190-58.6%
No	134-41.4%
<b>Total</b>	<b>324-100%</b>

**Table 1. Continued**

<b>Q11. Which devices do you have reserved for ER?</b>		
X-ray		43-13.6%
X-ray + US		15-4.8%
X-ray + CT		35-11.1%
X-ray + US + CT		74-23.4%
X-ray + US + CT + MRI		81-25.6%
X-ray + US + IR		0-0.0%
X-ray + US + CT + IR		6-1.9%
X-ray + US + CT + MRI + IR		62-19.6%
	<b>Total</b>	316-100%
<b>Q12. If there is no US device in the emergency room, how do you do these procedures?</b>		
It is done in the radiology department		290-94.5%
The patient is referred to an external center		11-3.6%
Evaluated by teleradiology		6-1.9%
	<b>Total</b>	307-100%
<b>Q13. If there is no CT device in the emergency room, how do you do these procedures?</b>		
It is done in the radiology department		268-89.3%
The patient is referred to an external center		13-4.3%
Evaluated by teleradiology		19-6.4%
	<b>Total</b>	300-100%
<b>Q14. If there is no MRI device in the emergency room, how do you do these procedures?</b>		
It is done in the radiology department		270-86.8%
The patient is referred to an external center		25-8.1%
Evaluated by teleradiology		16-5.1%
	<b>Total</b>	311-100%
<b>Q15. If there are no IR devices in the emergency room, how do you do these procedures?</b>		
It is done in the radiology department		235-74.1%
The patient is referred to an external center		82-25.9%
	<b>Total</b>	317-100%
<b>Q16. How many radiologists work in your RD?</b>		
1-10		123-37.5%
10-20		101-30.8%
20-30		53-16.2%
>30		51-15.5%
	<b>Total</b>	328-100%
<b>Q17. In your hospital, is there a radiologist who only deals with ER?</b>		
Yes		63-19.2%
No		265-80.8%
	<b>Total</b>	328-100%
<b>Q18. How many radiologists are working only in ER in your hospital?</b>		
0		247-76.2%
1-3		55-17.0%
3-5		17-5.3%
5-10		1-0.3%
>10		4-1.2%
	<b>Total</b>	324-100%
<b>Q19. Are there any rotating doctors in ER in your hospital?</b>		
All radiologists work in the emergency room in rotation		186-63.9%
Some of the radiologists rotate in the emergency room		71-24.4%
Only emergency radiologists work in the emergency room		34-11.7%
	<b>Total</b>	291-100%
<b>Q20. Which radiologists should report emergency imaging examinations in RD?</b>		
Subspecialists according to anatomic area (brain → neuroradiology; lung → chest radiologists etc.)		106-33.2%
Radiologists at emergency radiology rotation		127-39.8%
Emergency radiologists		86-27.0%
	<b>Total</b>	319-100%

**Table 1. Continued**

<b>Q21. How many radiologists report emergency imaging examinations during the daytime (8:00–17:00)</b>		
1		120-36.8%
1-4		139-42.6%
5-10		49-15.1%
10-15		18-5.5%
	<b>Total</b>	326-100%
<b>Q22. How many radiologists report emergency imaging examinations during nightshifts (17:00–8:00) and weekends (24 hours)?</b>		
1		172-53.9%
1-3		104-32.6%
3-5		12-3.8%
>5		31-9.7%
	<b>Total</b>	319-100%
<b>Q23. If consultant radiologists work only in the daytime, how are emergency imaging examinations reported?</b>		
		0-0.0%
Residents prepare the draft of the report		76-25.5%
Residents prepare the draft of the report; difficult cases are reported by on-duty consultant radiologist		
All imaging examinations are reported by on-duty consultant radiologists		2-9.4%
All imaging examinations are reported via teleradiology		96-32.3%
Residents prepare the draft of the report, and main report is prepared the following day		4-15.2%
All imaging examinations are assessed by on-duty consultant radiologist; short review notes, including imaging findings, are illustrated on hospital information system and images are sent to teleradiology for final report		
Residents prepare the draft of the report; difficult cases are reported by on-duty consultant radiologists and images are sent to teleradiology for final report		26-8.8%
		26-8.8%
	<b>Total</b>	297-100%
<b>Q24. Are emergency US examinations performed by non-radiologists in EDs?</b>		
Yes		16-4.9%
No		214-65.4%
Only FAST, other US examinations are performed by radiologists		97-29.7%
	<b>Total</b>	327-100%
<b>Q25. Do you agree with the suggestion that radiology residents should have their ER education in ER units settled in emergency medicine service?</b>		
Yes		226-69.5%
No		99-30.5%
	<b>Total</b>	325-100%
<b>Q26. Is it necessary to include ER as a separate subject in the core curriculum of radiology resident education?</b>		
Yes		289-88.1%
No		39-11.9%
	<b>Total</b>	328-100%
<b>Q27. Do you have regular (weekly or monthly) multidisciplinary case-based discussion meetings with the ED in your hospital?</b>		
Yes		24-7.3%
No		303-92.7%
-		
	<b>Total</b>	327-100%
<b>Q28. Do you think that a sufficient number of academic studies about ER are performed in your department?</b>		
Yes		31-9.5%
No		297-90.5%
	<b>Total</b>	328-100%
<b>Q29. Which one of the following is correct?</b>		
In our country, the number of neuro, chest, and abdomen radiologists are sufficient Emergency radiology practice and education should be performed by these radiologists. There is no need for a separate emergency radiology unit.		
Optimization of emergency imaging examination protocols and assessment of these imaging examinations should be performed by radiologists who have emergency radiology education or experience in this field		83-25.5%
		243-74.5%
	<b>Total</b>	326-100%

\*City hospital: large regional health institutions that include state hospitals and training and research hospitals affiliated to the Ministry of Health. ED, emergency department; ER, emergency radiology; RD, radiology department; US, ultrasonography; CT, computed tomography; MRI, magnetic resonance imaging; IR, interventional radiology; FAST, focused assessment with sonography for trauma.

(US), computed tomography (CT), magnetic resonance imaging (MRI), and interventional radiology (IR) equipment in their hospitals could be used for patients presenting to the ED (Table 1).

US, CT, MRI, or IR examinations were reported to be performed in the radiology department separate to the ED in 94.46%, 89.33%, 86.82%, and 74.13% of responses, respectively, where equipment for such imaging examinations was not located in the ED (Figure 2). If US, CT, MRI, or IR was not available in the ED, patients were referred to another hospital in 3.58%, 4.33%, 8.04%, and 25.87% of respondents' hospitals, respectively.

The number of radiologists in respondents' radiology departments varied between 1–10 (37.50%) and >30 (15.55%). Few respondents (19.21%) declared that a dedicated emergency radiologist was work-

ing in their department, with the number of radiologists working only in ER being 1–3 in 16.98% of cases, 3–5 in 5.25% of cases, 5–10 in 0.31% of cases, and >10 in 1.23% of cases. In 63.92% of respondents' hospitals, all radiologists were doing ER work on rotation.

### Emergency radiology work planning and reporting

The number of radiologists involved in reporting ER examinations during the day time (8:00–17:00) was one in 36.81% of hospitals, 1–4 in 42.64% of hospitals, and 5–10 in 15.03% of hospitals, while ER reports during night shifts (17:00–8:00) and weekends were performed by one radiologist in 53.92% of cases and 1–3 radiologists in 32.60% of cases. In the absence of consultant radiologists on night shifts and weekends, ER examinations were mostly reported via teleradiology (32.32%), followed by residents' draft report-

ing systems, with difficult cases being discussed with the on-duty consultant radiologist (25.59%). In the ED, all US examinations and focused assessment with sonography for trauma were reported to be performed by non-radiologist physicians in 4.89% and 29.66% of respondents' hospitals, respectively. Reporting of ER examinations by emergency radiologists, radiologists on ER rotation, or subspecialists other than emergency radiologists according to their interest area was approved by 26.96%, 39.81%, and 33.23% of respondents, respectively.

Reporting ER examinations by emergency radiologists was approved by 41.67% of academics in training and research hospitals, 28.68% of radiologists, 27.27% of residents, and 15.38% of the chairpersons of the departments. The suggestion received the highest approval from respondents who worked in city hospitals (51.72%), followed by private hospitals (37.50%), and university hospitals (25.20%). A higher percentage (74.54%) of radiologists agreed with the opinion that the optimization of emergency imaging examination protocols and assessments should be performed by radiologists with a specialized ER education or experience in ER. Support for this was highest among residents (79%) and lowest among department chairpersons (53.85%).

### Emergency radiology education

The majority of respondents (69.54%), including 73.27% of residents and 53.85% of department chairpersons, agreed that residents should receive their ER training in the ER unit. Additionally, 88.11% of contributors, 91.09% of residents, and 92.31% of department chairpersons declared that ER should be a separate subspecialty in the curriculum of radiology training. There was no regular multidisciplinary meeting conducted within the ED in 92.66% of respondents' radiology departments, with only 11.20% of respondents from university hospitals declaring that they have such meetings. The number of academic studies on ER in their departments was insufficient, according to 90.55% of respondents, 75% of academics in university, and 84.62% of department chairpersons. Only 20.80% of respondents from university hospitals stated that the number of academic studies in their departments was sufficient.

### Discussion

The results of this survey explained some current ER practice issues and the scope of radiologists' perspectives concerning ER in

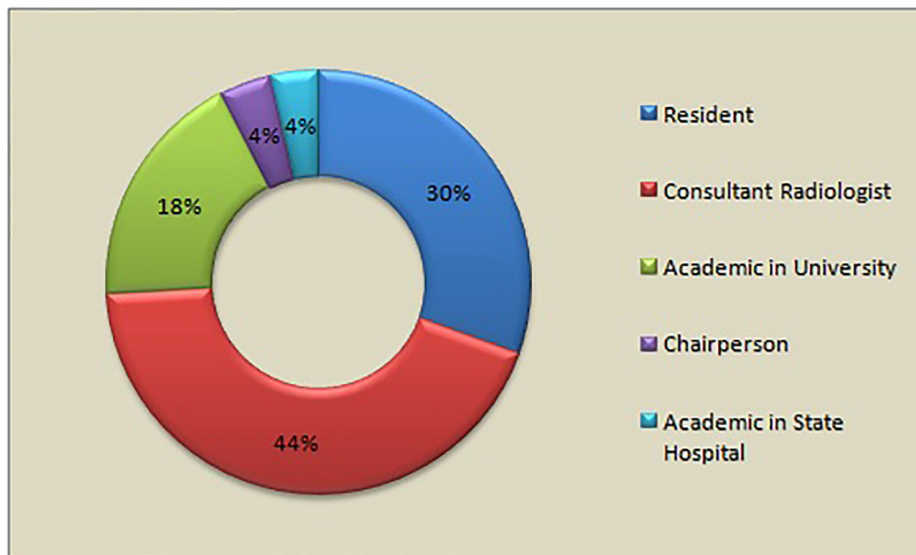


Figure 1. Circle diagram of distribution of the respondents

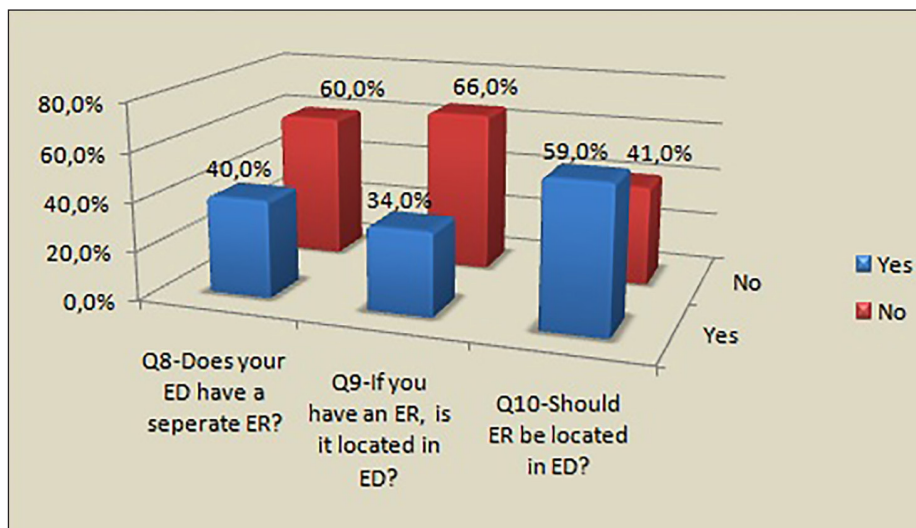


Figure 2. The distribution of the ER location. ER, emergency radiology; ED, emergency department.

**Table 2.** The responses to some questions in the survey according to the positions of radiologists

	Residents (n=101)	Consultants (n=143)	Academics in state hospital (n=12)	Academics in university (n = 60)	Chairpersons (n=13)
<b>Q10- Should ER be included in ED?</b>					
Yes	57-57.0%	70-49.6%	9	46-76.7%	9
No	43-43.0%	71-50.4%	2	14-23.3%	4
<b>Q20- Which radiologists should report emergency imaging examinations in RD?</b>					
Subspecialists according to anatomic area	29-29.3%	34-25.0%	3	36-60.0%	5
Radiologists at ER rotation	43-43.4%	63-46.3%	4	11-18.3%	6
ER radiologists	27-27.3%	39-28.7%	5	13-21.7%	2
<b>Q25- Do you agree with the suggestion that radiology residents should have their emergency radiology education in ER units settled in emergency medicine service?</b>					
Yes	74-73.3%	96-68.6%	10	40-66.7%	7
No	27-26.7%	44-31.4%	2	20-33.3%	6
<b>Q26- Is it necessary to include emergency radiology as a separate subject in the core curriculum of radiology resident education?</b>					
Yes	92-91.1%	126-88.1%	10	50-83.3%	12
No	9-8.9%	17-11.9%	2	10-16.7%	1
<b>Q28- Do you think that a sufficient number of academic studies about emergency radiology are performed in your department?</b>					
Yes	13-12.9%	2-1.4%	0	15-25.0%	2
No	88-87.1%	141-98.6%	12	45-75.0%	11
<b>Q29- Which one of the following is correct?</b>					
In our country, the number of neuro, chest, and abdomen radiologists is sufficient. ER practice and education should be performed by these radiologists. There is no need for a separate ER unit	21-21.0%	39-27.3%	3	14-23.7%	6
Optimization of emergency imaging examination protocols and assessment of these examinations should be performed by radiologists who have ER education or experience in this field	79-79.0%	104-72.7%	9	45-76.3%	7

Some questions were not answered by some respondents (four answers in Q10, nine in Q20, three in Q25, and two in Q29 were skipped). ER, emergency radiology; ED, emergency department; RD, radiology department.

Turkey. In their responses, radiologists noted the current drawbacks of ER practice, training, and the academic situation in Turkey and stated their opinions on improving these issues.

The response rate of our survey (21.97%) was fair compared with previous survey studies regarding ER.<sup>1,3-5</sup> However, we calculated this rate based on the information that 1.493 of 4.213 members read the survey emails and became aware of the survey. If all members are taken into account, then the response rate of the survey is approximately 6%. A previous survey study regarding ER practice across Europe had a 10% response rate, while another in the United States had a 29.6% response rate.<sup>3,4</sup> The variation in response rates to ER surveys may have resulted from undelivered emails, inadequate reminders, the time needed to complete the survey, or the disinterest of some radiologists. The distribution of the radiologists according to their positions in radiology (resident, academic, radiologist, chairperson of the department) allowed the study to represent the opinions

of different stakeholders in the field. Importantly, one-third of respondents of this survey were residents, which suggests a willingness by this group to announce their ideas, recommendations, and expectations on ER. Learning the ideas of this younger population may open new frontiers and help to further develop policies regarding radiology subspecialties.

A subspecialty in radiology departments may be improved by having the appropriate infrastructure.<sup>2,6</sup> Less than half of radiologists in Turkey revealed that there was a distinct ER unit in their departments, and ER units were located in ED in only 34.25% of respondents' hospitals. Approval for a distinct ER unit within the ED was highest among university hospital respondents (66.13%), which suggests that an ER unit within an ED improves patient management but is also necessary for training and academic purposes. The establishment of a distinct ER unit in a radiology department or ED may be insufficient to handle the imaging examinations of patients presenting to the ED. According to respon-

dents, 13.6% of radiology departments had only X-ray units, which may diminish the diagnostic capability of ER practice in these hospitals. CT in EDs was only present in 60% of respondents' hospitals. Emergency radiography units should be equipped with appropriate imaging equipment that meets ED requirements.<sup>7</sup> In this survey, we found that 8.04% of patients needing MRI and 25.87% of patients needing IR were sent to another hospital due to the inability to perform these in the ED. These high rates of patient loss may decrease the efficiency of ER and ED practice, along with decreasing educational and academic activities. The absence of imaging equipment in ER units affects not only radiology practice and training but also the ED and other departments that may be affected in terms of their practice and training. It is well known that emergency radiologists' efficiency and communication skills, and therefore management of patients' imaging, can be facilitated by placing the emergency radiologist in close proximity to the radiology technologist and the ED.<sup>2</sup> The results of the survey also showed that the number of

radiologists involved in the reporting of ER significantly decreased during night shifts and weekends compared with daytime practice. However, this practice manner is not compatible with the nature of ER since the number of patients and severity of illnesses and traumatic cases do not decrease during night shifts and weekends. Approximately one-third of respondents declared that the imaging examinations of patients presented during these time periods are assessed via teleradiology. This drawback in ER practice can be overcome with a specific staffing structure that includes dedicated ER radiologists who are familiar with the workload and requirements of the ED.<sup>8,9</sup> Scaglione et al.<sup>3</sup> also reported that X-ray, US, and CT equipment were sufficient in ER units of European centers; however, the absence of MRI and IR units caused patient discharges, according to their survey study. They suggest that the presence of MRI and IR units near the ED may also be helpful in evaluating these patients if it is not possible to assess them in the ED.<sup>3</sup>

For 63.92% of respondents' hospitals, the hospital was stated to have ER rotation, which suggests awareness about the importance of ER in radiology practice. However, the results of this survey also revealed that although most radiologists agreed with the necessity of an ER unit in the hospitals, they did not have the same level of approval for the reporting of ER examinations by emergency radiologists. Low approval rates of ER reporting by emergency radiologists in respondents (26.96%), academics in university (21.67%), and chairpersons of departments (15.38%) were surprising and need to be discussed to discover their underlying reasons. One of the reasons for this may be the unwillingness of radiologists to lose an area of their practice and other associated benefits.<sup>10</sup> Another reason for this approach may be that some patients presenting to the ED have chronic medical conditions rather than emergency conditions. Evaluation of these patients' imaging examinations may be better performed by radiologists rather than emergency radiologists. This drawback may be more critical in countries where indications of ER imaging are not well established and clinical decision support systems are not used. In Turkey, EDs have no limitation policy regarding ordering CT examinations, and there is no clinical decision support system used generally within the country, which causes the over-ordering of image examinations and the assessment of non-emergency cases by emergency radiologists. This clinical practice results in radiologists having less

confidence in ER assessments. Radiologists are also not used to responding to clinicians' requirements in common practice. Usually, radiologists need sufficient time to evaluate the images before reporting. However, ER practice necessitates fast and accurate responses, suggestions, comments, and reports so that decisions can be made regarding emergency treatment. This requirement may also be one of the underlying reasons for the unwillingness of some radiologists to conduct ER. For department chairpersons, it may be difficult to establish a new ER unit and manage the distribution of imaging workload between subspecialties. However, this point of view may hinder the improvement of the ER subspecialty in Turkey, which would be significantly improved by the allocation of emergency radiologists who are trained and only work in this area.

One of the interesting results of the survey was that 30% agreed that ER training of residents in ER units was unnecessary. This percentage is high from our point of view. Also, the majority of the respondents (88.11%) suggested that ER training should be taught as a distinct part of the curriculum embedded in radiology training. The responses of radiology department chairpersons to the question on ER training were interesting. Although 53.85% of department chairpersons agreed with the opinion that residents should receive their ER training in the ER unit, 92.31% of them declared that ER should exist as a separate subject like other subspecialties in the core curriculum of radiology training. Differences between these responses point to a discrepancy. We think that this subspecialty, as part of the core curriculum, deserves to be performed in a distinct unit, and training in this subspecialty should be performed by emergency radiologists who are educated in this area. The education of ER residents also presents an academic point of view regarding ER. As an academic activity, multidisciplinary meetings regarding ER are not performed in radiology departments according to 92.7% of respondents. Also, 90.55% of respondents stated that the number of academic studies about ER is not sufficient within their department. An insufficiency of these academic activities in radiology departments may be caused by the inadequate numbers of dedicated emergency radiologists. An absence of academic studies and an insufficient number of emergency radiologists leads to an unwillingness to pursue ER fellowship or training among radiology residents. The establishment of na-

tionally based ER training guidelines, maintaining principles of ER fellowship programs, and encouraging radiology residents to pursue ER as a specialty may be helpful in overcoming these obstacles. A previous survey study showed that radiology residents with the greatest exposure to ER during residency were more familiar with ER training and career opportunities.<sup>5</sup> One way to encourage residents to become more familiar with ER may be to increase the number of ER questions on board examinations. Improvement of ER is maintained in developed countries where ER is accepted as a distinct academic discipline by the community of radiologists.<sup>6</sup> One of the ways to make improvements in ER may be for emergency medicine societies to declare the necessity of distinct ER units in EDs with dedicated emergency radiologists. Because emergency radiologists focus on the needs of emergency physicians, the importance of collaboration between emergency physicians and emergency radiologists may be more objectively evaluated by the radiology community.<sup>2</sup> However, a key way to improve ER within a radiology community may be by attracting radiology residents to specialized fellowship programs. A previous survey conducted among radiology residents revealed that the two most important factors in selecting a subspecialty were whether it would be intellectually stimulating and whether respondents had a strong personal interest in it.<sup>5</sup>

Our study has some limitations. The response rate in this survey may be thought of as relatively low if all members of TRS are taken into account. However, the response rate was higher than in some previous surveys regarding ER.<sup>3,4</sup> The low response rate in this survey may have resulted in selection bias and overrepresentation of some respondent groups, such as residents and university employees. Some responses to survey questions about ER unit infrastructure (Q11–15), ER practice (Q17–24), and ER education (Q25–28) may have been more representative of residents' and university employees' opinions. We could not obtain responses from some institutes that have distinct ER units and/or emergency radiologists for the survey. Some of the questions, including Q10, Q20, Q25, Q26, and Q28, may be considered as directives from respondents. There are overlaps in categories of questions, such as Q4, Q7, Q16, Q18, Q21, and Q22. These overlaps may have caused confusion among respondents when it came to selecting the category that their department or ER unit belonged to. We did not classify the radiol-

ogists or residents according to their length of experience in radiology, and therefore we could not analyze their responses according to their level of expertise.

In conclusion, infrastructural, educational, and academic drawbacks in radiology departments affect the orientation of radiologists in ER. The scarcity of emergency radiologists feeds the shortcomings of ER. To contribute to ER improvement in the country, ER should be nationally structured as a subspecialty in radiology, radiology departments should be encouraged to establish distinct ER units with dedicated emergency radiologists, and ER units should be structured in line with international guidelines.

#### Conflict of interest disclosure

The authors declared no conflicts of interest.

## References

1. Chahine AH, Hanna TN, Myers L, Kumaravel M, Herr KD. The state of emergency radiology fellowships in North America and the development of a standardized curriculum. *Emerg Radiol.* 2019;26(1):53-58. [\[CrossRef\]](#)
2. Chong ST, Robinson JD, Davis MA, et al. Emergency radiology: current challenges and preparing for continued growth. *J Am Coll Radiol.* 2019;16(10):1447-1455. [\[CrossRef\]](#)
3. Scaglione M, Basilico R, Delli Pizzi A, et al. The practice of emergency radiology throughout Europe: a survey from the European Society of Emergency Radiology on volume, staffing, equipment, and scheduling. *Eur Radiol.* 2021;31(5):2994-3001. Erratum in: *Eur Radiol.* 2020. [\[CrossRef\]](#)
4. Hanna TN, Shekhani H, Lamoureux C, et al. Emergency radiology practice patterns: shifts, schedules, and job satisfaction. *J Am Coll Radiol.* 2017;14(3):345-352. [\[CrossRef\]](#)
5. Herr KD, Risk B, Hanna TN. Diagnostic radiology resident perspectives on fellowship training and career interest in emergency radiology. *Emerg Radiol.* 2018;25(6):653-658. [\[CrossRef\]](#)
6. Baker SR. Emergency radiology in the United States--a stepchild finding its way. *Br J Radiol.* 2016;89(1061):20150867. [\[CrossRef\]](#)
7. Huang J, Patel S, Scruggs R, Levin D. In pursuit of fellowship: results from a 2016 survey of US trainees. *Curr Probl Diagn Radiol.* 2019;48(1):22-26. [\[CrossRef\]](#)
8. Hatem SF, Novelline RA. Looking back, moving forward: 1988-2013. The first 25 years of the American Society of Emergency Radiology. *Emerg Radiol.* 2014;21(2):115-132. [\[CrossRef\]](#)
9. Hanna TN, Lamoureux C, Krupinski EA, Weber S, Johnson JO. Effect of shift, schedule, and volume on interpretive accuracy: a retrospective analysis of 2.9 million radiologic examinations. *Radiology.* 2018;287(1):205-212. [\[CrossRef\]](#)
10. Liebscher L, Sherry C, Breslau J, et al. The general radiologist in the 21st century. *J Am Coll Radiol.* 2012;9(8):554-559. [\[CrossRef\]](#)



# A novel technique for the non-surgical management of inadvertent bowel catheterization during percutaneous abscess drainage: a technical note

Okan Akhan   
Duygu İmre Yetkin   
Ferdî Çay   
Emre Ünal   
Türkmen Turan Çiftçi   
Devrim Akıncı 

## ABSTRACT

Percutaneous abscess drainage-related inadvertent bowel catheterization is an undesired complication that requires treatment. In two cases without signs of peritonitis that we examined, it was possible to achieve successful abscess drainage, and to treat abscess-related inadvertent bowel catheterization by using a novel technique without surgery.

## KEYWORDS

Abscess, catheter, CT, fluoroscopy, non-surgical management, ultrasound

Percutaneous abscess drainage (PAD) has been proven to be safe and effective as both a curative and temporizing means.<sup>1,2</sup> In addition, PAD can be used for abscesses in different localization like intraperitoneal, retroperitoneal, and inaccessible postoperative collections.<sup>3-5</sup> Although complications related to PAD are uncommon (in most series, the complication rate is 5%),<sup>1</sup> they can be life threatening. These complications range from minor issues, like pain and vasovagal syncope, to major complications, such as active bleeding and bowel perforation.<sup>6</sup> It has been reported that the small-bowel catheterization can be treated with conservative approach when there are no signs of peritonitis. It is also possible to wait until the tract maturation of the catheter, whereas emergency surgical intervention is required in cases of colonic catheterization.<sup>7</sup> In this paper, an outline of the non-surgical management of inadvertent bowel catheterization during PAD is shared by describing a novel technique.

## Methods

### Case 1

A 61-year-old male patient underwent computed tomography (CT)-guided PAD for an acute diverticulitis abscess. A fistula formation between the cavity and the sigmoid colon was viewed. After 31 days following medical therapy and PAD, the CT showed complete drainage of the cavity and the catheter was removed. Four days later, the patient had a fever, and the CT showed the recurrence of the abscess. It was thought possible to find the same tract that had been formed by the previous catheterization using ultrasound (US) guidance to carry out the PAD procedure. An 8F catheter was placed into the cavity with the Seldinger technique. Access was gained using a 19-G needle under US guidance, and contrast injection with fluoroscopy confirmed the cavity and showed there was no leakage to the adjacent structures. Subsequently, a 0.035-in Amplatz guidewire was advanced into the cavity after serial fascial dilatation had been performed. An 8F locking loop pigtail catheter with a stiffener was advanced over the wire into the collection. The stiffener and wire were removed, and the catheter was locked. The first day after catheter insertion, although the patient had no symptoms, we decided to perform a control CT to observe the collection and the inserted catheter to

From the Department of Radiology (O.A. ✉ akhano@tr.net, F.Ç., E.Ü., T.T.Ç., D.A.), Hacettepe University Faculty of Medicine, Ankara, Turkey; Clinic of Radiology (D.İ.Y.), Midyat State of Hospital, Mardin, Turkey.

Received 03 November 2021; revision requested 10 November 2021; accepted 12 December 2021.



Epub: 07.03.2023

Publication date: 29.03.2023

DOI: 10.5152/dir.2022.211104

You may cite this article as: Akhan O, Yetkin Dİ, Çay F, Ünal E, Çiftçi TT, Akıncı D. A novel technique for the non-surgical management of inadvertent bowel catheterization during percutaneous abscess drainage: a technical note. *Diagn Interv Radiol.* 2023;29(2):309-311.

avoid the risk of possible complications. The CT showed the catheter was traversing an ileal segment (Figure 1a). We decided to keep the catheter in place and wait for tract maturation. At the same time, a second (12F) catheter was placed into the abscess cavity using CT guidance (Figure 1b). Contrast injection via 8F catheter 22 days after the first intervention showed contrast filling of the ileal segment. Then the 8F catheter was pulled back to the entry side of the ileal segment with the intention of keeping the catheter tip just outside of the bowel wall (Figure 1c). On the following day, injection of contrast media via the 8F catheter showed neither contrast entry into the bowel nor free contrast flow into the peritoneal cavity. The injected contrast agent was released from the side holes of the catheter, and it did not fill the ileal loops (Figure 1d). Then, the 8F catheter tip was removed. Meanwhile, contrast injection via the 12F catheter showed a fistula between the abscess cavity and sigmoid colon, while there was no filling of the ileal segment. The 12F catheter was withdrawn 10 days later after the fistula between the abscess cavity and sigmoid colon was sealed. It was concluded that the fistula was closed because it was not visible after contrast administration in fluoroscopy. Daily drainage had also dropped below 3 cc.

## Case 2

A 55-year-old female patient was referred to our hospital for a bladder rupture. The abdomen CT showed multiple collections in the lower abdomen. Percutaneous aspiration of the two collections were performed under US guidance without catheterization. For the third collection that located in the right lower quadrant, a catheter was placed under

US guidance. There was a possibility that the catheter could pass through the colon during the procedure. The patient had no symptom at that time. A 10F pigtail catheter was inadvertently advanced into the caecum, which was confirmed by contrast injection under fluoroscopic guidance (Figure 2a). As a first step, the targeted collection was evacuated by needle aspiration. The decision was made to wait for tract maturation and to follow up the patient for signs of peritonitis. After 19 days, the control cavitography via 10F pigtail catheter showed contrast filling of the caecum. The pigtail catheter was changed with an 8F straight-tip catheter (Figure 2b). The straight-tip catheter was then pulled back with the technique as described below (Figure 2c). The patient was free of symptoms on the following day, and the control abdominal US examination showed no collection. The control CT examination obtained one month after the patient's discharge was normal.

## Technique

In case of bowel transgression during PAD, a new catheter (12F pigtail) was immediately inserted into the abscess cavity by using a safe tract under CT guidance when

required—as occurred in case 1. On the other hand, the first catheter, which had transgressed the bowel loop, was maintained in the same location for tract maturation for approximately three weeks. After three weeks, the pigtail catheter inside the bowel loop was exchanged with a thin catheter (preferably an 8F straight-tip catheter) when needed—as seen in case 2. We pulled back the tip of the catheter to just outside the bowel loop to confirm there was no drainage from the catheter. We kept the catheter in the same position within close proximity of the bowel wall for possible drainage for one to two days. When there was no daily drainage, the catheter was pulled back by 1–2 cm the following day. The integrity of the catheter tract was evaluated by injecting contrast material under fluoroscopy guidance. When the injection of contrast media via 8F catheter showed no filling of the bowel loop, we confirmed that the tract maturation was complete, and the catheter was removed.

## Discussion

To the best of our knowledge, this is the first study to outline a novel technique for

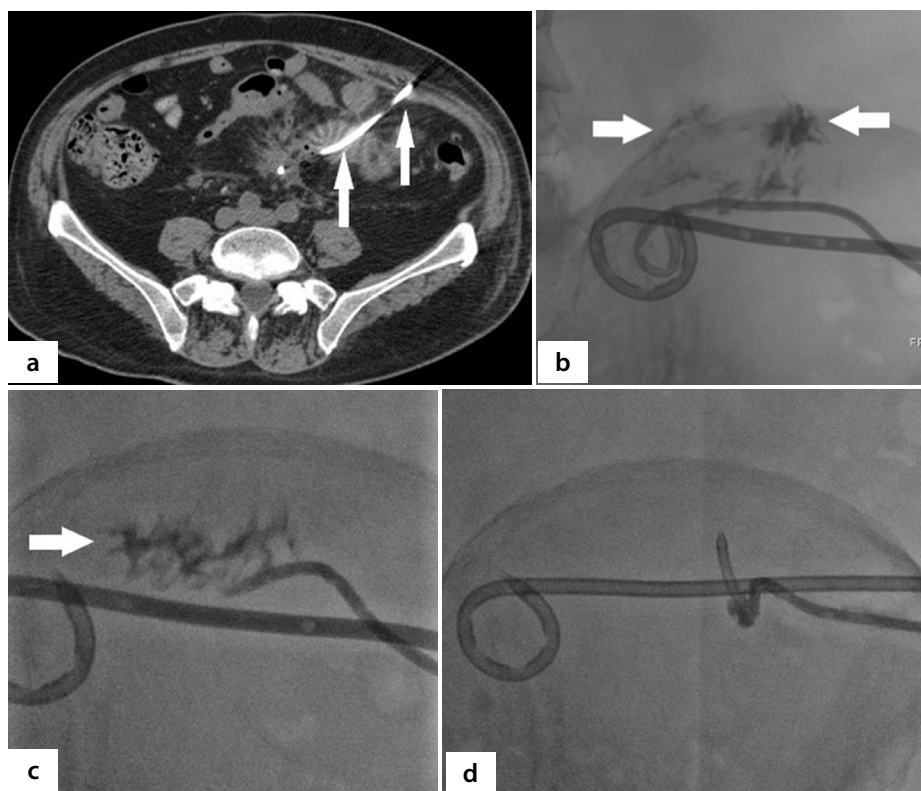


**Figure 1.** (a) Sixty-one-year-old male patient, who was followed up for acute diverticulitis-related abscess, an 8F catheter was inserted due to recurrence of the abscess. One day later, an unenhanced abdomen computed tomography showed the catheter was traversing the ileal segment (arrows). On the same day, a 12F catheter was placed into the abscess cavity (not shown). (b) On 22<sup>nd</sup> after catheterization, contrast injection via 8F catheter showed filling of the ileal segment (arrows). (c) Then, on the same day, the 8F catheter was pulled back to just proximal to the ileal segment (arrow). (d) After two days, contrast injection via the 8F catheter showed no filling of the ileal segment, and the 8F catheter was removed.

### Main points

- Percutaneous abscess drainage-related inadvertent bowel catheterization is an undesired complication.
- This complication can be treated without surgery.
- Keeping the catheter in the cavity, waiting for tract maturation, using a straight-tip catheter, pulling the catheter back to close proximity of the bowel wall, following up fluid volume and filling of the cavity with cavitography is a novel technique
- When no filling is detected by cavitography, the fluid level has dropped under 3 cc, and after checking with ultrasound and a computed tomography scan, we can remove the straight-tip catheter and treat this complication.

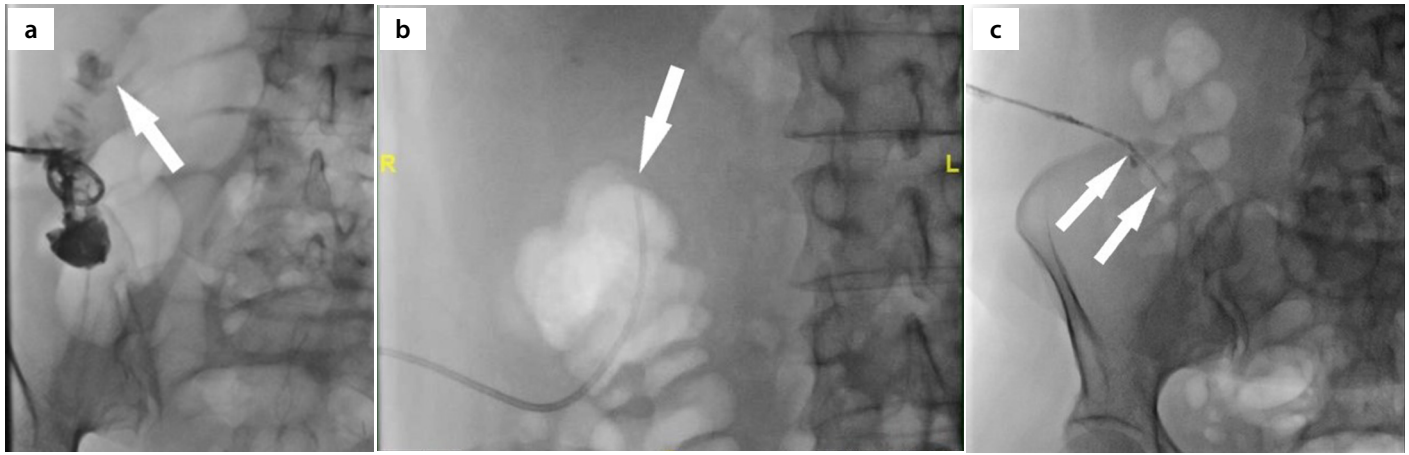


**Figure 2.** (a) The patient was followed up for bladder rupture and multiple collections, and a 10F pigtail catheter was inserted into the right lower quadrant-located collection. Contrast injection via the inserted catheter showed that the catheter tip was located in the colon (arrow). (b) Nineteen days after the initial treatment, the pigtail catheter was replaced with a straight-tip catheter in the cecum (arrow). (c) One day later on the 20<sup>th</sup> day of the treatment, the tip of the catheter was pulled back to just outside the bowel loop (arrows).

the non-surgical management of abscess-related inadvertent bowel catheterization that occurs as a complication of PAD.

There are multiple types of radiologic approaches, techniques, and imaging guidance for carrying out PAD. The choice of drainage technique and imaging guidance depends on the type and location of the collection as well as the experience and habits of the operator.<sup>6</sup> It is recommended that intervening structures such as the bowel, pleura, kidney, spleen, bladder, uterus, nerves, and vessels must be avoided while performing PAD to reduce the risk of complications.<sup>6</sup> However, inadvertent bowel catheterization might occur as a serious complication while performing PAD, especially for deeply located collections.<sup>7,8</sup> In the cases managed in the present study, inadvertent bowel puncture and catheterization occurred as both procedures were carried out under US and fluoroscopic guidance. The CT provides more detailed data about intraabdominal collections or abscesses in terms of their location, relationship with the surrounding organs, and intervening structures than US does;<sup>2</sup> therefore, it is preferable to perform PAD procedures with CT guidance to avoid complications, especially for the deeply located abscesses.

The key point of the management technique outlined in this paper is waiting for tract maturation before catheter removal to avoid leakage of bowel content into the outside of the bowel loop. Waiting approximately three weeks before catheter removal and after tract maturation to avoid bile leakage is a common method used during percutaneous cholecystostomy procedures.<sup>9</sup> It is also recommended to wait for tract maturation when pleural transgression is detected

while performing percutaneous subphrenic collection drainage or percutaneous cholecystostomy.<sup>10,11</sup> The same procedure was performed for the patients with bowel transgression in the current study. It was essential to constantly evaluate tract maturation before catheter removal because, as Picus et al.<sup>11</sup> showed, tract maturation may be incomplete even after waiting for what is deemed a sufficient length of time. This is especially true in predominantly transperitoneal tracts.<sup>11</sup>

Removal of the catheter before tract maturation can lead to bowel perforation and require surgery. Therefore, in the cases featured in this study, the catheters were removed after the confirmation of complete tract maturation by contrast injection under fluoroscopy guidance. Although there are some studies related to PAD that report bowel transgression during procedures,<sup>1</sup> there is no paper that provide a detailed non-surgical management plan for inadvertent bowel catheterization. The novel technique described in the present study is recommended for the non-surgical management of cases with abscess drainage-related inadvertent bowel catheterization.

#### Conflict of interest disclosure

The authors declared no conflicts of interest.

#### References

1. vanSonnenberg E, Wittich GR, Goodacre BW, Casola G, D'Agostino HB. Percutaneous abscess drainage: update. *World J Surg.* 2001;25(3):362-369; discussion 370-372. [\[CrossRef\]](#)
2. Men S, Akhan O, Köroğlu M. Percutaneous drainage of abdominal abscess. *Eur J Radiol.* 2002;43(3):204-218. [\[CrossRef\]](#)

3. Ciftci TT, Akinci D, Akhan O. Percutaneous transhepatic drainage of inaccessible postoperative abdominal abscesses. *AJR Am J Roentgenol.* 2012;198(2):477-481. [\[CrossRef\]](#)
4. Akhan O, Durmaz H, Balci S, Birgi E, Çiftçi T, Akinci D. Percutaneous drainage of retroperitoneal abscesses: variables for success, failure, and recurrence. *Diagn Interv Radiol.* 2020;26(2):124-130. [\[CrossRef\]](#)
5. Akinci D, Akhan O, Ozmen MN, et al. Percutaneous drainage of 300 intraperitoneal abscesses with long-term follow-up. *Cardiovasc Intervent Radiol.* 2005;28(6):744-750. [\[CrossRef\]](#)
6. Robert B, Yzet T, Regimbeau JM. Radiologic drainage of post-operative collections and abscesses. *J Visc Surg.* 2013;150(3 Suppl):S11-S18. [\[CrossRef\]](#)
7. Lorenz J, Thomas JL. Complications of percutaneous fluid drainage. *Semin Intervent Radiol.* 2006;23(2):194-204. [\[CrossRef\]](#)
8. Maher MM, Gervais DA, Kalra MK, et al. The inaccessible or undrainable abscess: how to drain it. *Radiographics.* 2004;24(3):717-735. [\[CrossRef\]](#)
9. Akhan O, Akinci D, Ozmen MN. Percutaneous cholecystostomy. *Eur J Radiol.* 2002;43(3):229-236. [\[CrossRef\]](#)
10. Maher MM, Kealey S, McNamara A, O'Laoide R, Gibney RG, Malone DE. Management of visceral interventional radiology catheters: a troubleshooting guide for interventional radiologists. *Radiographics.* 2002;22(2):305-322. [\[CrossRef\]](#)
11. Picus D, Burns MA, Hicks ME, Darcy MD, Vesely TM. Percutaneous management of persistently immature cholecystostomy tracts. *J Vasc Interv Radiol.* 1993;4(1):97-101; discussion 101-102. [\[CrossRef\]](#)



# Management of single double-J stent failure in malignant ureteral obstruction: tandem ureteral stenting with less frequent stent exchange

Devrim Akıncı   
Emre Ünal   
Türkmen Turan Çiftçi   
Orhan Şeref Özkan   
Okan Akhan 

## PURPOSE

To evaluate the safety and efficacy of the placement and exchange of tandem ureteral stents (TUS) under fluoroscopic guidance in the management of indwelling single double-J stent (DJS) failure in patients with malignant ureteral obstruction. We also aimed to investigate whether the generally accepted exchange period of DJSs could be extended using TUS.

## METHODS

This retrospective study involved 11 patients (10 female) with an age range of 27–64 years, median of 49 years, who underwent TUS (ipsilateral two 8F DJSs) placement due to indwelling single DJS failure occurring in less than 3 months. TUS exchanges were performed initially at 6-month intervals, and subsequent exchange intervals were extended to 9 and 12 months for seven patients. The interval from initial TUS placement to percutaneous nephrostomy, repeat exchange, or death was defined as the duration of stent patency.

## RESULTS

Indwelling single DJS failure occurred during a median follow-up of 45 days (range, 35–60 days) in 14 ureters of 11 patients. TUS were successfully placed and exchanged with a technical success rate of 100% without any early major complications. Thirty-nine procedures (11 placement and 28 exchange procedures) in 55 ureters were performed. The median duration of urinary patency was significantly higher with TUS [300 days (range, 60–440 days)] compared with single DJSs [45 days (range, 35–60 days)] ( $P < 0.001$ ).

## CONCLUSION

The placement and exchange of TUS can be safely and effectively performed under fluoroscopic guidance. The need for frequent DJS exchange could be reduced with increased duration of stent patency using TUS.

## KEYWORD

Tandem ureteral stents, double-J stent, malignant ureteral obstruction, retrograde exchange, stent failure

From the Department of Radiology (D.A. ✉ akincid@hotmail.com, E.Ü., T.T.Ç., O.A.), Hacettepe University Faculty of Medicine, Ankara, Turkey; Department of Radiology (O.Ş.Ö.), University of Wisconsin, Wisconsin, United States.

Received 03 July 2021; revision requested 06 August 2021; last revision received 08 November 2021; accepted 16 January 2022.



Epub: 28.02.2023

Publication date: 29.03.2023

DOI: 10.5152/dir.2022.21638

**M**alignant ureteral obstruction (MUO) is a common manifestation of metastatic disease and requires urinary diversion. Ureteral stenting in an antegrade or retrograde fashion is an effective and safe method of choice in such cases, offering superior quality of life compared with percutaneous nephrostomy.<sup>1-3</sup> Nevertheless, ureteral polymeric double-J stent (DJS) malfunction rates are between 19% and 58%.<sup>4-6</sup> Metal-mesh stents, metallic stents, and tandem stents (two ipsilateral DJSs) are alternative options to maintain urinary diversion and percutaneous nephrostomy in cases of single DJS malfunction.<sup>7-12</sup>

You may cite this article as: Akıncı D, Ünal E, Çiftçi TT, Özkan OŞ, Akhan O. Management of single double-J stent failure in malignant ureteral obstruction: tandem ureteral stenting with less frequent stent exchange. *Diagn Interv Radiol.* 2023;29(2):312-317.

Tandem ureteral stenting (TUS) has been shown to have good clinical success by providing extra space and drainage capacity between the stents and ureteral wall in a limited number of studies.<sup>8,10,12,13</sup> However, these studies recommended the frequent exchange of the TUS every 3–6 months, similar to single DJS, and did not investigate whether the routine exchange period could be extended by using TUS.

In this study, our aim was to evaluate the safety and efficacy of the placement and exchange of TUS under fluoroscopic guidance in the management of indwelling single DJS failure in patients with MUO. We also aimed to investigate whether the generally accepted exchange period of DJSs could be extended with TUS, which might eliminate the need for frequent stent exchanges.

## Methods

This retrospective study was approved by our institutional review board (HEK 09/64-3, 02/07/2009). Informed consent for each procedure was obtained prior to the procedure for all patients.

### Patients

Eleven (10 female) patients with an age range of 27–64 years, median of 49 years, underwent TUS placement due to single DJS failure occurring in less than 3 months. An exchange of TUS was also performed in seven patients. TUS exchanges were performed initially at 6-month intervals, and subsequent exchange intervals were extended to 9 and 12 months after observing the patency of TUS. Ultrasound examinations were routinely performed on follow-up every 3 months after TUS placement; each patient had an empty bladder and was in a supine position to check for the presence of hydronephrosis.

#### Main points

- Ureteral stenting with a single double-J stent (DJS) is an established method of choice in the management of malignant ureteral obstruction.
- Tandem ureteral stents (TUS) have been shown to have better clinical success and higher patency rates. However, previous studies suggest the frequent exchange of TUS every 3–6 months, similar to single DJSs.
- The need for frequent DJS exchange could be reduced with TUS, which may maintain ureteral patency for up to 9–12 months.

The time interval from the initial TUS placement to percutaneous nephrostomy, exchange time, or death was defined as the duration of stent patency. The results of the treatment were evaluated by reviewing patients' electronic records through the Picture Archiving and Communication System. Complications were classified according to the Cardiovascular and Interventional Radiological Society of Europe classification system.<sup>14</sup>

### Technique

Routine hemogram, blood biochemistry, and the coagulation profile were checked before each procedure.

All patients received prophylactic broad-spectrum antibiotics prior to the procedure. All procedures, including antegrade single DJS placements, were performed in the interventional radiology unit with the patient under conscious sedation. A combination of fentanyl (50–100 µg), midazolam (3–4 mg), ketamine (10–20 mg), and propofol (20–50 mg) was used for sedation.

The TUS placement was performed using the access route gained by retrieving the indwelling single DJS using the guide wire lasso technique.<sup>2</sup> First, a 9-10F vascular sheath was placed inside the bladder over a 0.035-inch hydrophilic guide wire (Terumo, Japan). A 0.035-inch guide wire (Starter Guide Wire, Bentson; Boston Scientific, USA), folded in two, was then inserted to create a lasso in the bladder. One end of the folded wire was advanced while holding the other steady to manipulate the lasso to pass through the pigtail or around the shaft of the stent. Once the indwelling stent was retrieved from the bladder, care was taken not to lose access to the renal pelvis by maintaining the upper end of the DJS in the ureter. A 0.035-inch guide wire (Terumo, Japan) was inserted through the withdrawn stent to reach the renal pelvis. After reaching the renal pelvis, a 5F catheter (Imager II Angiographic Catheter, Bern; Boston Scientific, USA) was placed over the hydrophilic guide wire, and this was exchanged for a stiff guide wire (Amplatz, Super Stiff; Boston Scientific USA). Dilatation of the ureteral stricture with an 8 mm balloon catheter was performed. After advancing the sheath to the distal ureter to maintain access for the second stent, a 5F catheter and a hydrophilic guide wire were inserted in retrograde fashion through the sheath, and the ureteral stricture was passed. After reaching the collecting system, the second stiff guide wire was left there. Two parallel 8F DJ stents (Flexima Ureteral Stent, Boston Scientific, USA)

were inserted separately with the support of pushers through a sheath that had been advanced over one of the wires. The nylon thread attached to the proximal part of the first stent was held tightly to prevent migration while pushing the second stent through the ureter. After obtaining the desired position of both stents, the nylon threads of both stents were removed (Figure 1). To exchange the TUS, the same retrograde approach was used (Supplementary Video 1).

For the male patient, the technique was the same, except a longer introducer sheath and a longer nylon thread were used to compensate for the longer urethra.

If the occluded stent lumen and pores precluded the advancement of a guide wire through the stent, a vascular sheath with the valve end cut off was advanced over the occluded stent into the distal ureter. A hydrophilic guide wire was then inserted beside the occluded stent through the lumen of the sheath, and access to the collecting system was achieved. All ureteral stents, including initial failed ones and tandem stents, were 8F in size.

### Statistical analysis

SPSS version 22.0 (IBM Corporation, Armonk, NY, USA) was used for statistical analysis. The Shapiro–Wilk test was used for normality analyses. Descriptive statistics of the data are presented as frequencies and percentages. Variables with normal distribution are shown as mean ± standard deviation, whereas non-normalized distributions are reported as median (min–max). The Mann–Whitney U test was used to investigate whether the duration of urinary patency could be increased with TUS;  $P < 0.05$  was taken as the level of significance.

## Results

A total of 11 patients (10 women) with an age range of 27–64 years, median of 49 years, were enrolled. Indwelling single DJS failure occurred at a median follow-up of 45 days (range, 35–60 days) in 11 patients with 14 ureters. In these patients, the single DJSs were exchanged for TUS, with a technical success rate of 100% in retrograde fashion. TUS were placed bilaterally in three patients. The most common history of malignancy was cervix carcinoma ( $n = 7$ , 60%) followed by breast carcinoma ( $n = 2$ , 20%) ovarian carcinoma ( $n = 1$ , 10%), and sacral Ewing sarcoma ( $n = 1$ , 10%).

After the initial placement of TUS in 14 ureters, 41 exchange procedures were per-

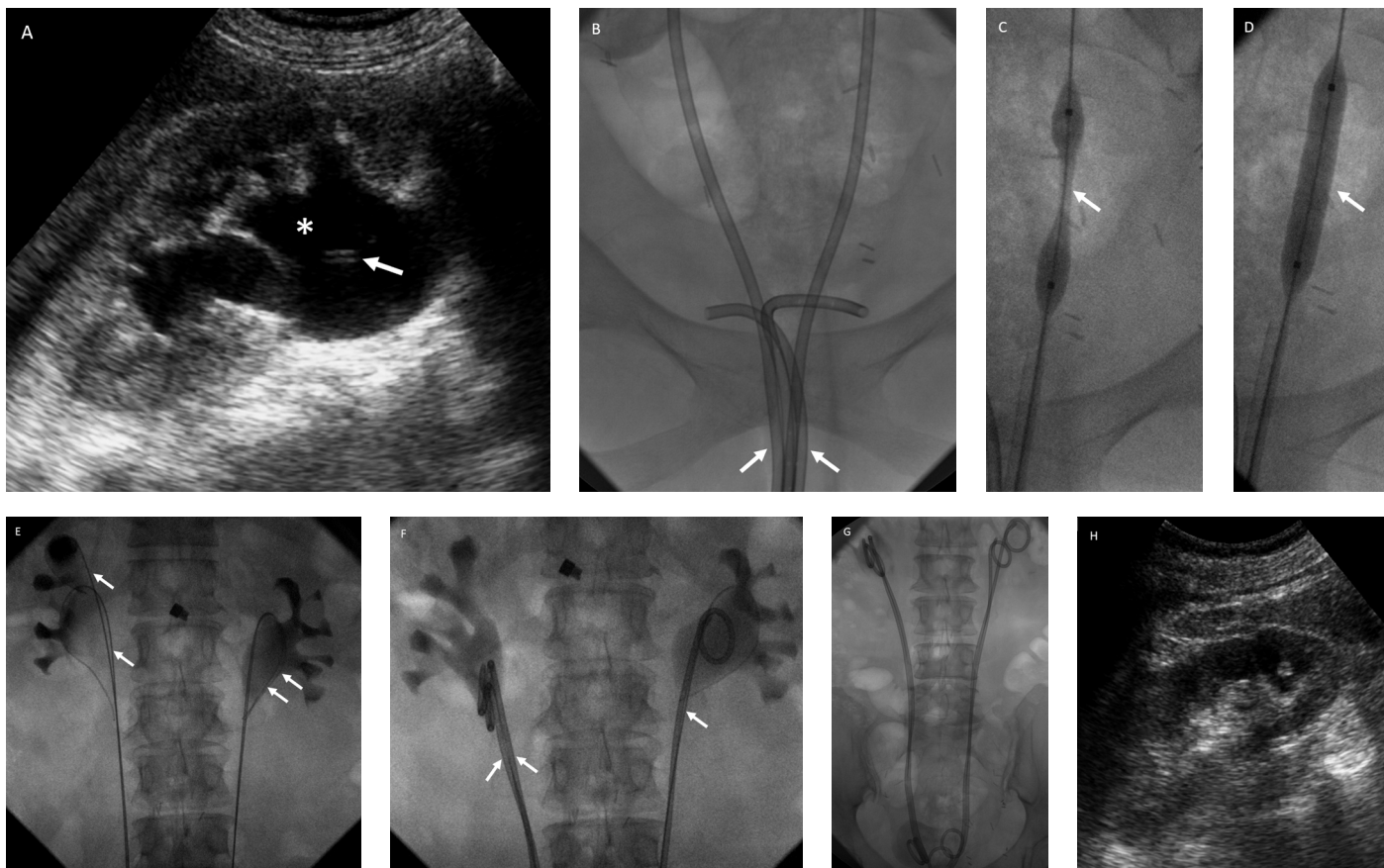


**Figure 1.** A 49-year-old woman with a previous history of cervix carcinoma underwent tandem ureteral stent (TUS) placement due to failure of indwelling single double-J stent (DJS). (a) Grayscale sonogram demonstrates presence of hydronephrosis (asterisk) due to non-functioning DJS (arrow). (b) First, the indwelling DJSs (arrows) were retrieved (retrograde fashion). (c, d) Prior to TUS placement, the ureteral strictures were dilated with balloon catheters (arrows). (e) Following balloon dilatation, bilateral guide wires (arrows) were guided into the renal pelvis. (f, g) Consequently, the ureteral stents were placed separately in retrograde fashion. (h) Grayscale sonogram obtained after the TUS placement reveals no hydronephrosis.

formed in 10 ureters of seven patients on 28 occasions, with a technical success rate of 100% (Figure 2). TUS exchange procedures were performed 22 times in one patient for both ureters (11 times each), eight times in one patient, five times in one patient, once in two patients, and once in two patients for both ureters (total of four procedures in two patients) (Figure 3).

In the remaining four patients, TUS exchange was not performed. Two of these patients died within a short time of follow-up after TUS placement (60 and 122 days); this was due to underlying disease progression, without any complications related to TUS. One patient is alive with patent TUS, and the other patient had a poor treatment response and underwent permanent percutaneous nephrostomy due to TUS occlusion 210 days after placement (Figure 3).

The median duration of urinary patency was significantly higher with TUS [300 days (range, 60–440 days)] compared with single DJSs [45 days (range 35–60 days)] ( $P < 0.001$ ).

In 9 out of 55 ureters with TUS, patients presented with hydronephrosis due to stent

occlusion at a median follow-up of 315 days (range, 210–365 days). In three ureters of two patients with TUS occlusion, temporary nephrostomy was performed due to pyonephrosis. After 1 month with temporary nephrostomy and subsequent TUS exchange, these two patients were catheter free with normal renal function on follow-up. However, one of these two patients underwent permanent nephrostomy 1535 days after temporary nephrostomy and five TUS exchange procedures because of borderline renal function. Further exchange procedures were not considered in this patient (patient no: 1). However, the remaining patient is still alive with normal renal function and patent TUS. Other patients underwent permanent nephrostomy because of infravesical obstruction caused by tumor progression (patient no: 4) and borderline renal function (patient no: 5) (Figure 2).

Neither mortality nor early complications related to TUS procedures occurred. Pyonephrosis was detected in 5 out of 55 ureters with TUS (9%) in two patients as a grade 3 late complication after 210, 335, and 365

days of patency; this was managed with percutaneous nephrostomy and TUS exchange procedures. Urinary tract infection ( $n = 4$ , 36.36%), lower urinary tract symptoms ( $n = 3$ , 27.27%), and hematuria ( $n = 3$ , 27.27%) were the grade 2 late complications. Hematuria was managed conservatively and resolved over time. Urinary tract infection was managed with outpatient oral antibiotic therapy.

## Discussion

The results of our study reveal that the placement and exchange of TUS can be safely and successfully performed under fluoroscopic guidance to increase the duration of stent patency. Our results reporting a median duration of stent patency of 300 days also suggest that TUS might be changed at greater intervals than 3–6 months, as previously reported.<sup>10,13,15</sup>

A limited number of studies have reported the efficacy of TUS in indwelling single DJS failure.<sup>8,10,12,13</sup> These studies are summarized in Table 1. First, Liu and Hrebinko<sup>13</sup> used two 4.8F DJSs and reported no need for percuta-

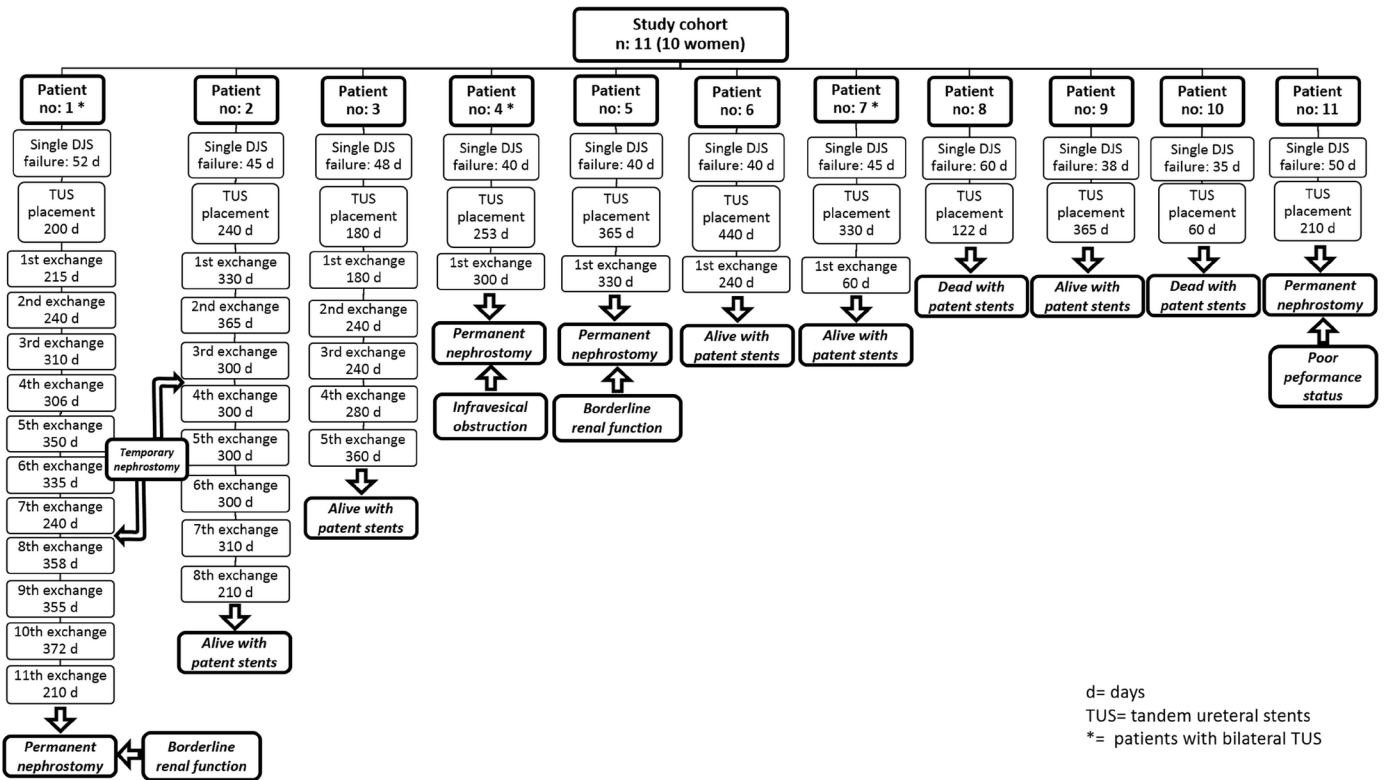


Figure 2. Patient outcomes after single double-J stent failure, tandem ureteral stent (TUS) placement, and TUS exchange procedures.

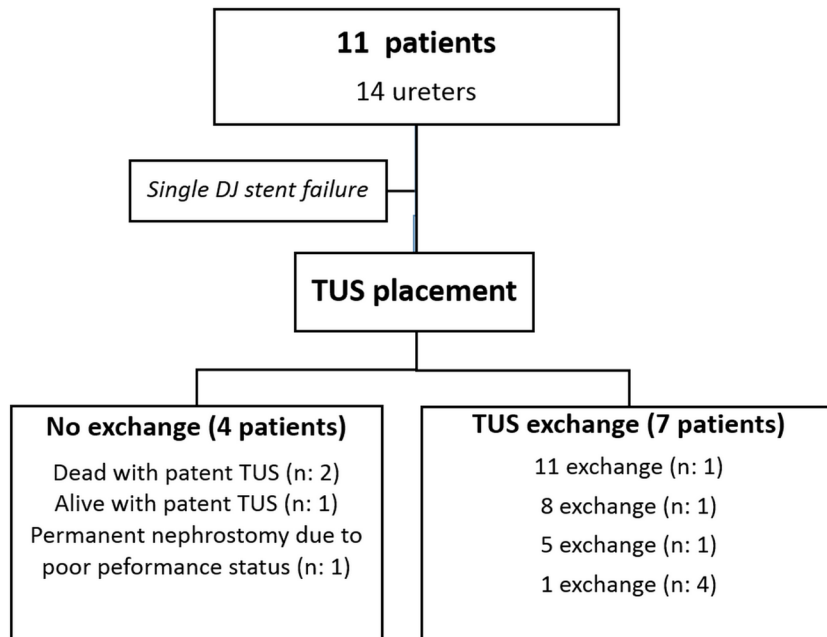


Figure 3. Study flowchart.

**Table 1.** Literature summary for the use of tandem ureteral stents in malignant ureteral obstruction

	Our results	Varnavas et al. <sup>12</sup>	Haifler et al. <sup>17</sup>	Ozyer and Dirim <sup>10</sup>	Elsamra et al. <sup>16</sup>	Liu et al. <sup>9</sup>	Chen et al. <sup>18</sup>	Rotariu et al. <sup>15</sup>	Fromer et al. <sup>8</sup>	Liu and Hrebinko <sup>13</sup>
Year	2020	2016	2020	2017	2013	2019	2011	2001	2002	1998
Number of patients	11	15	81	14	34	48	17	7	5	4
Number of exchanges	41	7	NA	7	15 pts (2–16 times)	NA	NA	NA	NA	NA
Stent size	2 8F	28F	2 6F	2 8/2 10F	2 6F	2 7F	2 6F	2 7F/ 8–6F	2x8F	2 4.7F
Mean dwell time of TUS between exchange	300 days*	156 days*	NA	181 days	128 days	214.7 days	NA	4–6 months	2–3 months	3 months
Technical success rate	100%	100%	100%***	95%	100%	95.2%	94.1%	100%	100%	100%
Method for placement	Retrograde	Retrograde	Retrograde	Antegrade/retrograde	Retrograde	Antegrade	Antegrade	Retrograde	Retrograde	Retrograde
Guide for procedure	Fluoroscopy	Cystoscopy	Cystoscopy	Fluoroscopy	Cystoscopy	Fluoroscopy/cystoscopy**	Fluoroscopy	Cystoscopy	Cystoscopy	Cystoscopy
Type of anesthesia	IV sedation	General	General	IV sedation	NA	Local analgesia	NA	General	NA	IV sedation

\*median; \*\*for exchange; \*\*\*procedure failed for three patients, who were excluded from the study cohort. Pts, patients; TUS, tandem ureteral stent.

neous nephrostomy, with a mean follow-up of 5.8 months in four patients. Rotariu et al.<sup>15</sup> achieved marked improvement in hydronephrosis and the alleviation of flank pain in seven patients with urinary diversion failure with indwelling single ureteral stents during a mean follow-up of 16 months. They used two 7F stents or a combination of 8F/6F DJSts, and the routine exchange period was every 4 to 6 months.<sup>15</sup> Fromer et al.<sup>8</sup> were able to successfully manage hydronephrosis and renal insufficiency by using two 8F DJSts in five patients and eight ureters with indwelling single DJS failure. The mean follow-up period was 12 months in their study. One patient developed pyonephrosis and underwent permanent nephrostomy.<sup>8</sup> Elsamra et al.<sup>16</sup> reported a 13% TUS failure rate in 34 patients (39 renal units) who underwent a total of 132 procedures for MUO. Mean stent duration was 128 days (4.3 months) with a mean follow-up of 23 months. Varnavas et al.<sup>12</sup> performed 15 cystoscopic primary TUS insertions and 7 subsequent exchanges in 15 patients with MUO. The failure rate was 20% at 3 months, and the median stent patency was 156 days. Haifler et al.<sup>17</sup> performed cystoscopic two-6F TUS placement in 81 patients with MUO and reported a 27.1% failure rate during a median follow-up of 32 weeks.

Ozyer and Dirim<sup>10</sup> investigated the efficacy and safety of TUS in 14 women experiencing gynecological malignancies. They reported a stent failure rate of 21.4% during a mean follow-up of 180.1 days; the median exchange time was 181 days. They suggested that the routine exchange of TUS might

be extended to 6 months.<sup>10</sup> Chen et al.<sup>18</sup> reported a higher failure rate of 72.7% with TUS at 3 months after placement in patients with MUO. In contrast to our study and previous ones, they inserted a new DJS alongside the indwelling malfunctioning ureteral stent instead of inserting two new stents. Their higher failure rate might be attributed to this technique because an indwelling malfunctioning ureteral stent could be a source of infection and encrustation and a reason for obstruction. Liu et al.<sup>9</sup> recently compared antegrade single and TUS in the management of MUO. They reported significantly improved ureteral patency with TUS (214.7 ± 21.0 days) compared with single ureteral stents (176.7 ± 21.3 days), with technical success rates of 93.6% and 95.2%, respectively. However, they did not mention the failure rates and exchange times of single and TUS in the follow-up period.

Metallic stents have also been used to maintain patency in MUO, and most studies have reported failure rates of approximately 20% to 40%.<sup>4,7,19</sup> With metallic spiral-coiled double-pigtail stents (Resonance, Cook Medical), a 79% overall success rate and 1% migration rate have been reported.<sup>20</sup> Self-expandable coated metallic stents (Uventa, Taewong Medical) have been found to be superior to DJSts in terms of patency in MUO.<sup>7</sup> Despite the increased patency rates of metallic stents compared with single DJSts, their cost effectiveness remains questionable, and there can also be issues with difficult technical insertion, exchange, and high migration rates.<sup>21–24</sup> We can conclude that TUS seems

to be a strong alternative to metallic ureteral stents in patients with single DJS failure, offering a long duration of ureteral patency for up to 9–12 months. Because single DJS exchange every 3–4 months is associated with increased cost and procedural risks, Taylor et al.<sup>11</sup> compared the costs associated with metallic resonance ureteral stents and single DJSts. They found a cost reduction of roughly 48%, 61%, and 74% with metal stents for 3, 4, and 6 DJS exchanges per year, respectively.<sup>11</sup> However, no study has investigated the additional benefit of TUS in reducing the frequency of stent exchange and the financial cost savings to patients. Elsamra et al.<sup>16</sup> reported the average exchange of TUS at a mean of 4.3 months (128 days) for MUO. They also hypothesized that TUS could be exchanged at greater intervals than 4 months; thus, the cost analysis might no longer favor metallic stents.<sup>4</sup> Herein, our results support this hypothesis, demonstrating an increased median dwell time of TUS of approximately 10 months (300 days). In our study, initial TUS exchanges were performed at 6 months with no failure. After observing the efficacy of TUS in durations of 6 months, subsequent exchanges were performed at greater intervals of up to 9 and 12 months. This is the longest duration of ureteral patency with TUS in patients with indwelling single DJS failure. Our longer patency rate might be attributed to assessing the presence of hydronephrosis every 3 months after TUS placement rather than conducting a routine exchange.

Our study has several limitations including its retrospective nature with a relatively

small patient population. Another potential limitation is the heterogeneity of etiologies of MUO. However, our study has the longest follow-up and dwell time of TUS, showing an increased stent patency rate (300 days).

In conclusion, the placement and retrograde exchange of TUS are safe and effective in patients with MUO. The need for frequent DJS exchange could be reduced with TUS, which may maintain ureteral patency for up to 9–12 months. This might be helpful in reducing health-care costs.

### Conflict of interest disclosure

The authors declared no conflicts of interest.

### References

1. Hyams ES, Shah O. Malignant extrinsic ureteral obstruction: a survey of urologists and medical oncologists regarding treatment patterns and preferences. *Urology*. 2008;72(1):51-56. [CrossRef]
2. Ozkan O, Akinci D, Bozlar U, Ustünsöz B, Ozmen M, Akhan O. Retrograde ureteral stent exchange under fluoroscopic guidance. *Diagn Interv Radiol*. 2009;15(1):51-56. [CrossRef]
3. Song Y, Fei X, Song Y. Percutaneous nephrostomy versus indwelling ureteral stent in the management of gynecological malignancies. *Int J Gynecol Cancer*. 2012;22(4):697-702. [CrossRef]
4. Elsamra SE, Leavitt DA, Motato HA, et al. Stenting for malignant ureteral obstruction: tandem, metal or metal-mesh stents. *Int J Urol*. 2015;22(7):629-636. [CrossRef]
5. Feng MI, Bellman GC, Shapiro CE. Management of ureteral obstruction secondary to pelvic malignancies. *J Endourol*. 1999;13(7):521-524. [CrossRef]
6. Yossepowitch O, Lifshitz DA, Dekel Y, et al. Predicting the success of retrograde stenting for managing ureteral obstruction. *J Urol*. 2001;166(5):1746-1749. [CrossRef]
7. Chung HH, Kim MD, Won JY, et al. Multicenter experience of the newly designed covered metallic ureteral stent for malignant ureteral occlusion: comparison with double J stent insertion. *Cardiovasc Intervent Radiol*. 2014;37(2):463-470. [CrossRef]
8. Fromer DL, Shabsigh A, Benson MC, Gupta M. Simultaneous multiple double pigtail stents for malignant ureteral obstruction. *Urology*. 2002;59(4):594-596. [CrossRef]
9. Liu KL, Lee BC, Ye JD, et al. Comparison of single and tandem ureteral stenting for malignant ureteral obstruction: a prospective study of 104 patients. *Eur Radiol*. 2019;29(2):628-635. [CrossRef]
10. Ozyer U, Dirim A. Tandem ureteral stents in the management of double-J stent dysfunction in gynecological malignancies. *Diagn Interv Imaging*. 2017;98(9):601-608. [CrossRef]
11. Taylor ER, Benson AD, Schwartz BF. Cost analysis of metallic ureteral stents with 12 months of follow-up. *J Endourol*. 2012;26(7):917-921. [CrossRef]
12. Varnavas M, Bolgeri M, Mukhtar S, Anson K. The role of tandem double-J ureteral stents in the management of malignant ureteral obstruction. *J Endourol*. 2016;30(4):465-468. [CrossRef]
13. Liu JS, Hrebinko RL. The use of 2 ipsilateral ureteral stents for relief of ureteral obstruction from extrinsic compression. *J Urol*. 1998;159(1):179-181. [CrossRef]
14. Filippiadis DK, Binkert C, Pellerin O, Hoffmann RT, Krajina A, Pereira PL. Cirse quality assurance document and standards for classification of complications: the cirse classification system. *Cardiovasc Intervent Radiol*. 2017;40(8):1141-1146. [CrossRef]
15. Rotariu P, Yohannes P, Alexianu M, et al. Management of malignant extrinsic compression of the ureter by simultaneous placement of two ipsilateral ureteral stents. *J Endourol*. 2001;15(10):979-983. [CrossRef]
16. Elsamra SE, Motato H, Moreira DM, et al. Tandem ureteral stents for the decompression of malignant and benign obstructive uropathy. *J Endourol*. 2013;27(10):1297-1302. [CrossRef]
17. Haifler M, Shvero A, Zilberman D, et al. Tandem ureteral stents for malignant ureteral obstruction. *J Endourol*. 2020;34(2):222-226. [CrossRef]
18. Chen HC, Shen SH, Wang JH, et al. Parallel second stent placement for refractory ureteral stent malfunction in malignant ureteral obstruction. *J Vasc Interv Radiol*. 2011;22(7):1012-1016. [CrossRef]
19. Kim KH, Cho KS, Ham WS, Hong SJ, Han KS. Early application of permanent metallic mesh stent in substitution for temporary polymeric ureteral stent reduces unnecessary ureteral procedures in patients with malignant ureteral obstruction. *Urology*. 2015;86(3):459-464. [CrossRef]
20. Khoo CC, Abboudi H, Cartwright R, El-Husseiny T, Dasgupta R. Metallic ureteric stents in malignant ureteric obstruction: a systematic review. *Urology*. 2018;118:12-20. [CrossRef]
21. Goldsmith ZG, Wang AJ, Bañez LL, et al. Outcomes of metallic stents for malignant ureteral obstruction. *J Urol*. 2012;188(3):851-855. [CrossRef]
22. Lang EK, Irwin RJ, Lopez-Martinez RA, LaNasa J Jr, Kasabian N, Watson RA. Placement of metallic stents in ureters obstructed by carcinoma of the cervix to maintain renal function in patients undergoing long-term chemotherapy. *AJR Am J Roentgenol*. 1998;171(6):1595-1599. [CrossRef]
23. Liatsikos EN, Kagadis GC, Barbalias GA, Siablis D. Ureteral metal stents: a tale or a tool? *J Endourol*. 2005;19(8):934-939. [CrossRef]
24. vanSonnenberg E, D'Agostino HB, O'Laoidhe R, et al. Malignant ureteral obstruction: treatment with metal stents--technique, results, and observations with percutaneous intraluminal US. *Radiology*. 1994;191(3):765-768. [CrossRef]

Supplementary Video 1. <https://www.youtube.com/watch?v=QjFWQ0CprFO>



# Vascular complications related to image-guided percutaneous thermal ablation of hepatic tumors

Sonam Tashi

Apoorva Gogna

Sum Leong

Nanda Venkatanarasimha

Sivanathan Chandramohan

## ABSTRACT

Percutaneous thermal ablation of hepatic tumors is accepted as a safe, reliable, and cost-effective therapeutic option for treating hepatocellular carcinoma and hepatic metastases. However, operators should be familiar with the myriad of vascular and non-vascular complications that can occur post-ablation and that are described in the literature. This review will focus on the various vascular complications related to percutaneous thermal ablation of hepatic tumors and discuss strategies to avoid and manage these complications.

## KEYWORDS

Ablation, complications, hepatic tumors, microwave ablation, radiofrequency ablation

Minimally invasive therapies like image-guided percutaneous thermal ablation have gained widespread acceptance as a method for treating focal primary and secondary hepatic malignancies. This review will focus only on radiofrequency ablation (RFA) and microwave ablation (MWA). These are the most frequently used modalities for thermal ablation of hepatic malignancies. The other less common modalities are laser thermal ablation, cryoablation, and irreversible electroporation.

Several studies, trials, and meta-analyses comparing thermal ablation with surgical resection of small hepatic tumors have shown that thermal ablation is less expensive and invasive. It also has a lower complication rate but a comparable survival rate.<sup>1</sup> Additionally, RFA and MWA are the most cost-effective treatment modalities for patients with very early and early-stage hepatocellular carcinoma (HCC).<sup>2</sup> According to the Barcelona Clinic Liver Cancer (BCLC) staging system, these patients are classified as BCLC-0 (very early-stage HCC) and BCLC-A (early-stage HCC). Thermal ablation is currently the standard of care for patients with oligo-metastases or those with BCLC-0 and BCLC-A HCC who are not well suited for surgical resection.<sup>3</sup> It is also used as a “bridging therapy” to prevent patient dropout from the liver transplantation waiting list.<sup>3</sup>

Vascular complications are usually due to vessel damage caused by either direct mechanical insertion of the ablation needle or by indirect thermal injury.<sup>4</sup> The complications encountered are needle tract bleeding, hepatic artery damage, venous thrombosis, hepatic infarction, hemobilia, arterioportal fistula (APF) formation, and cardiac tamponade. Vascular complications of MWA and RFA are similar since both modalities require insertion of needles and can result in heat-based damage.

From the Division of Radiological Sciences, Department of Vascular and Interventional Radiology (S.T. sonam. [✉ tashi@singhealth.com.sg](mailto:tashi@singhealth.com.sg), A.G., S.L., N.V., S.C.), Singapore General Hospital; Radiological Sciences Academic Clinical Program, SingHealth-Duke-NUS Academic Medical Centre, Outram Road, Singapore 169608.

Received 29 July 2021; revision requested 31 October 2021; last revision received 22 December 2021; accepted 16 January 2022.



Epub: 13.03.2023

Publication date: 29.03.2023

DOI: 10.5152/dir.2022.21809

You may cite this article as: Tashi S, Gogna A, Leong S, Venkatanarasimha N, Chandramohan S. Vascular complications related to image-guided percutaneous thermal ablation of hepatic tumors. *Diagn Interv Radiol.* 2023;29(2):318-325.

## Complications

### Needle tract bleeding

Significant needle tract bleeding is a major complication (Common Terminology Criteria for Adverse Events grade 3 or higher) of percutaneous thermal ablation of hepatic tumors, as it can be immediately life-threatening and may lead to prolonged hospitalization.<sup>5</sup> It is also one of the more frequent major complications of thermal ablation, with a prevalence ranging from 0.37% to 2.0%.<sup>4,6</sup> A greater risk of bleeding has been reported in patients with liver cirrhosis, given the higher degree of clinical or subclinical coagulation disorders in these patients. There is also greater vascularity when comparing HCC with metastases.<sup>7</sup>

Needle tract bleeding is also the most common vascular complication related to percutaneous thermal ablation of hepatic tumors. It often results from direct mechanical injury to the vasculature caused by the insertion of the needle rather than because of thermal damage to the vessels.<sup>4</sup>

Most bleeding during thermal ablation is minor and self-limited; it is usually of little clinical significance and can be managed expectantly.<sup>7</sup> The bleeding can result in the formation of regional hematomas (intrahepatic, subcapsular, or perihepatic) along the ablation needle pathway (Figure 1) or extend into the adjacent body cavities, such as the hemoperitoneum or hemothorax.

#### Main points

- There should be stringent criteria for patient selection and meticulous preprocedural planning and evaluation. Coagulopathy should be corrected before ablation is performed.
- Choose the most optimal imaging modality for ensuring a safe needle trajectory. To approach centrally located tumors more cautiously, avoid tumors abutting large major blood vessels and biliary ducts.
- Ensure patient cooperation and comfort during ablation. Thermal ablation should preferably be performed under general anesthesia or intravenous sedation.
- There should be vigilant postprocedural monitoring. Watch out for abdominal pain with increasing intensity, sustained tachycardia (>100 beats/min), and/or hypotension (systolic blood pressure <90 mmHg or drop in the systolic blood pressure by >40 mmHg).
- Well-timed follow-up imaging should be used for early detection of vascular complications.

Venous bleeding is usually self-limited and is mainly treated conservatively with occasional blood transfusions (Figure 2).<sup>4</sup> However, if arterial bleeding is suspected, this would require vigilant clinical evaluation and monitoring along with a low threshold to intervene if active bleeding is established.

Multiphase contrast-enhanced computed tomography (CT) should be routinely performed as it helps recognize immediate post-ablation bleeding and can determine whether the ablation procedure was effective. Close and vigilant monitoring of the patient's symptoms and vital signs are also indispensable for the early detection and proper management of such a potentially life-threatening complication. Prompt transcatheter arterial embolization should be performed if there is clinical or imaging evidence of continued arterial bleeding.

In addition to multiphase CT, interrogation of the needle track with either color Doppler study or contrast-enhanced ultrasound can be performed in cases where intravenous CT contrast media is contraindicated. This can be helpful in the early de-

tection of arterial bleeding along the needle track immediately after removal of the ablation needle.<sup>4,8</sup> In such cases, a repeat cauterization can be performed by immediately reintroducing the needle to the entry point at the liver's surface, and this can be done under real-time ultrasound guidance (Figure 3).<sup>9</sup>

### Hepatic artery damage

Hepatic artery damage has an incidence of 0.2%.<sup>10</sup> As mentioned previously, damage to the hepatic artery is usually by direct mechanical injury during the placement of the ablation needle, and this typically manifests as acute bleeding.<sup>4</sup> However, the formation and subsequent rupture of a hepatic artery pseudoaneurysm can also manifest as delayed hemorrhage and be potentially catastrophic (Figure 4).<sup>10,11</sup> Hepatic artery thrombosis is also very rare. Preclinical studies suggest that hepatic arteries are less likely to thrombose due to their high flow state.<sup>12</sup>

### Venous thrombosis

The reported incidence of venous thrombosis is 0.1% to 1.08%.<sup>10,13</sup> Portal and hepat-



**Figure 1.** (a-d) Chest wall hematoma due to active bleeding from the intercostal artery after radiofrequency ablation (RFA) of a segment 8/5 hepatocellular carcinoma. Plain axial computed tomography image (a) at the entry point level of the RFA needle (arrow). Axial contrast-enhanced computed tomography image (b) in the arterial phase demonstrates a right chest wall hematoma with active contrast extravasation (arrow). Selective angiogram (c) of the right 8<sup>th</sup> intercostal artery shows active contrast extravasation (arrow). Post-embolization angiogram (d) shows complete cessation of the active contrast extravasation after embolization with 2 mm coils (arrow).

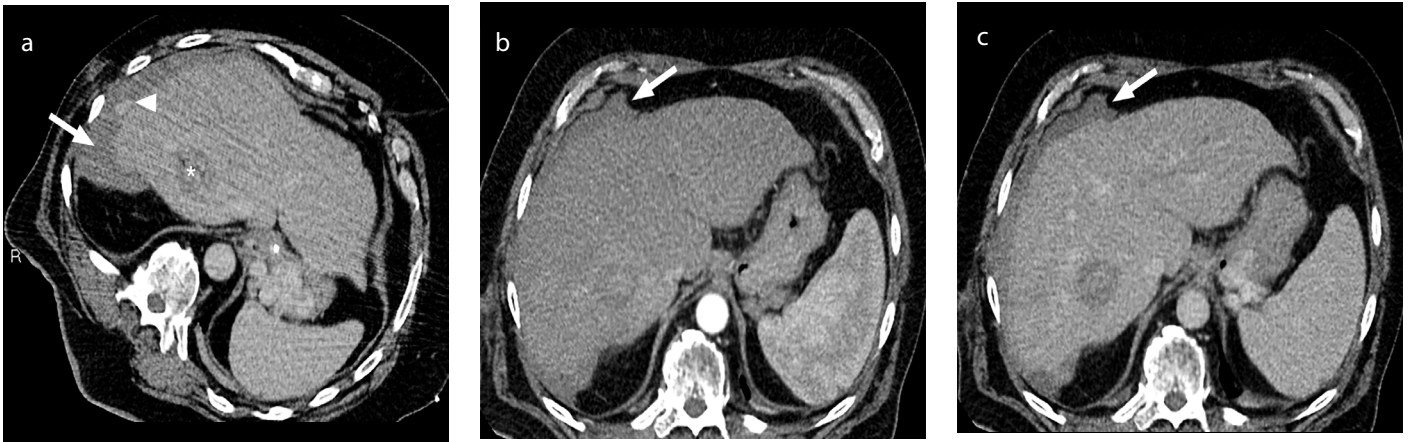


**Figure 2.** (a-c) Perihepatic hematoma after microwave ablation of a segment 7/8 hepatocellular carcinoma. Axial contrast-enhanced computed tomography (CECT) image (a) showing a perihepatic hematoma (arrow) with a focus on extracapsular contrast extravasation (arrowhead) seen only in the venous phase due to bleeding. Site of ablation (asterisk). The patient's hemodynamic status remained stable and unchanged during close monitoring. Repeat axial CECT images in the arterial (b) and venous (c) phases two hours post-procedure demonstrate a stable perihepatic hematoma (arrow) with the disappearance of the contrast extravasation.

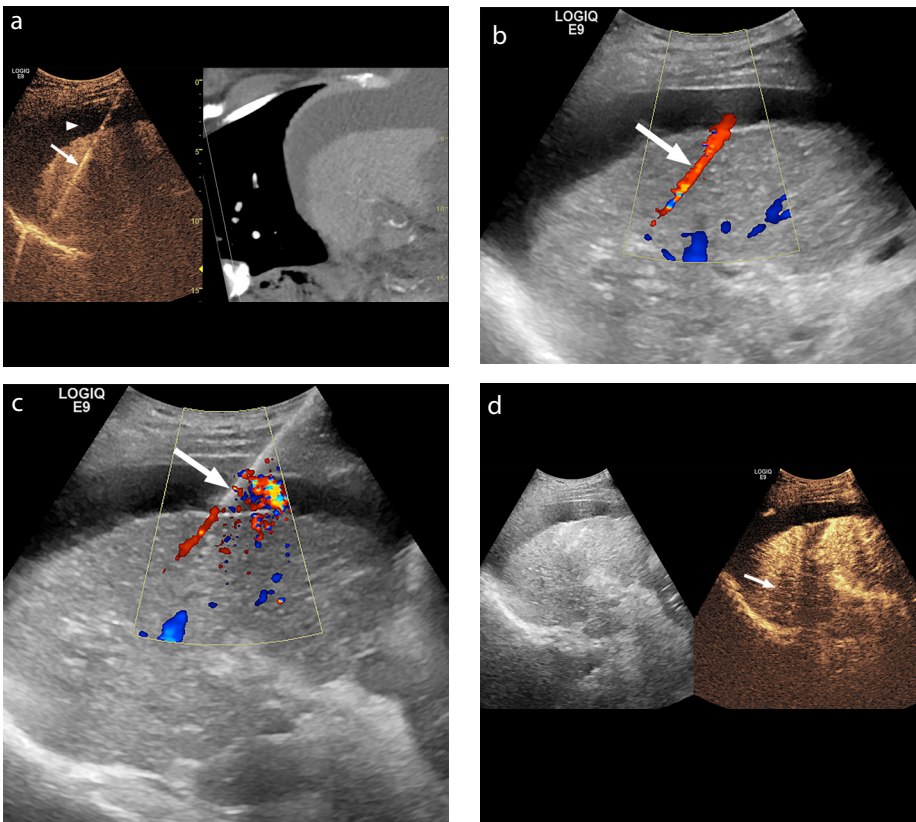


**Figure 3.** (a-d) Repeat cauterization of the needle tract bleeding after microwave ablation (MWA) of a recurrent segment 7 hepatocellular carcinoma. Fusion contrast-enhanced ultrasound (CEUS) with computed tomography (a) was performed to guide the MWA needle (arrow). Concomitant ascites (arrowhead). After removing the ablation needle, Doppler interrogation of the needle track (b) demonstrates a linear color Doppler flow (arrow) along the needle tract, indicating active bleeding. (c) The ablation needle (arrow) was immediately reintroduced under real-time ultrasound guidance to the needle entry point at the liver's surface, and repeat cauterization was performed. Post-ablation CEUS (d) demonstrates complete ablation of the lesion (arrow) with no evidence of active bleeding from the needle tract.

ic vein thrombosis is mainly caused by heat damage to the endothelium of these veins near the ablation zone.<sup>13</sup>

*In vivo* studies have shown that smaller vessels (with a diameter of <3 mm) encompassed by the ablation zone are more prone to thrombosis from thermal injury. This is due to the absence of vascular perfusion-mediated heat sink effect, which is mainly dependent on the vessel size.<sup>14</sup>

After ablation, thrombosis of larger vessels (with a diameter of >3 mm) is uncommon when the blood flow is normal;<sup>15</sup> however, thermal damage may cause thrombosis if the flow is compromised. Hence, other factors besides portal hypertension that can potentially decrease the blood flow in the portal venous system should be considered before ablation. Some factors include pre-existing thrombosis and compression of the vein by the tumor.<sup>16</sup>

Most patients with portal and hepatic vein thromboses are asymptomatic even when larger segmental vessels are thrombosed, and they require no specific therapy (Figure 5). However, extensive portal vein thrombosis can result in potentially fatal complications, such as hepatic failure or the worsening of portal hypertension, especially in patients with insufficient hepatic reserves.<sup>13,15,16</sup> Systemic anticoagulation or local thrombolysis may be necessary if the liver function is affected.<sup>14,16</sup>

Moreover, the presence of post-ablation portal and hepatic vein thrombosis warrants further investigation and follow-up imaging to rule out tumor progression within the venous system.<sup>13</sup>

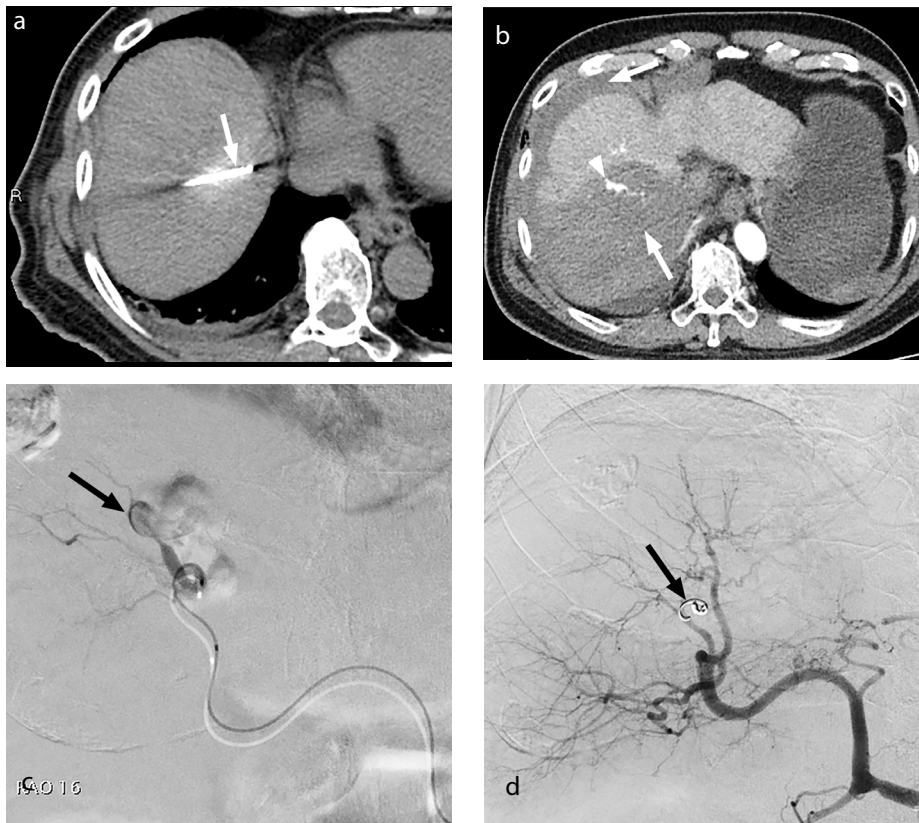


**Figure 4.** (a-d) Ruptured hepatic artery pseudoaneurysm with delayed presentation after radiofrequency ablation (RFA) of a segment 7 hepatocellular carcinoma. Axial plain computed tomography image (a) shows the final position of the RFA needle (arrow) before ablation. Axial contrast-enhanced computed tomography (six days post ablation) image (b) in the arterial phase demonstrates large intrahepatic and perihepatic hematomas (arrows) with a focus on active contrast extravasation (arrowhead). Selective angiogram (c) of the offending branch of the right hepatic artery shows a ruptured pseudoaneurysm (arrow) with active contrast extravasation. Post-embolization angiogram (d) shows successful embolization with 3 mm coils (arrow).

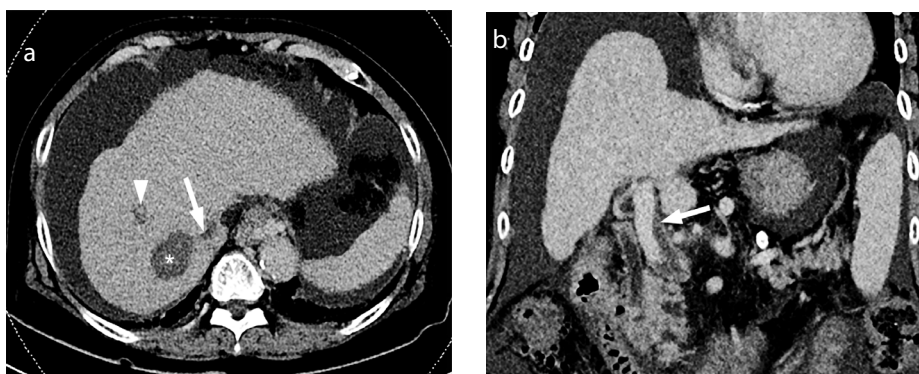


**Figure 5.** (a, b) Portal vein and hepatic vein thrombosis after microwave ablation of a segment 7 hepatocellular carcinoma. Axial contrast-enhanced computed tomography (CECT) (one month follow up) image (a) in the venous phase shows adequate ablation of the lesion (asterisk) with the formation of partial thrombus within the adjacent right hepatic vein (arrow) and portal vein (arrowhead). Coronal CECT image (b) in the venous phase demonstrates the extension of the partial thrombus into the main portal vein (arrow).

### Hepatic infarction

Hepatic infarction is an uncommon complication with an incidence of up to 0.07%.<sup>17</sup> It is uncommon because of the dual blood supply to the liver and the organ's ability to develop extensive collateral pathways. Nevertheless, hepatic infarction can occur from insult to both the hepatic arterial and portal venous systems.<sup>17,18</sup>

Most of these patients can be managed conservatively and may be treated with prophylactic antibiotics until the infarcted tissue heals (Figure 6). However, there can be accompanied complications, such as biloma or abscess formation, portal vein thrombosis, and rarely death from hepatic failure due to lobar infarction.<sup>16</sup>

### Hemobilia

Another hemorrhagic complication is hemobilia, with an incidence of 0.1% to 0.5%.<sup>6,10</sup> It usually occurs from a concomitant puncture of the biliary tract and blood vessel with the ablation needle. The presenting symptoms are typically upper abdominal pain, hematemesis, and melena.<sup>6</sup> Additional laboratory tests may show elevated levels of bilirubin and biliary enzymes. Clots may be visualized within the gallbladder or biliary tree on imaging.

No treatment is necessary for asymptomatic patients, but endoscopic or percutaneous drainage may be required for those with symptoms and biochemical evidence of biliary obstruction (total bilirubin concentration exceeding 4 mg/dL). Drainage may be necessary since there is a risk of liver failure or potentially fatal acute obstructive suppurative cholangitis caused by biliary obstruction from blood clots (Figure 7).<sup>6</sup>

Hence, careful selection of an appropriate needle pathway with real-time visualization of the needle trajectory is paramount to avoid puncturing biliary radicles, especially those that may be locally dilated because of tumor compression. Since the hepatic artery, portal vein, and intrahepatic bile duct run together, it is crucial to avoid these structures during needle insertion.<sup>6</sup> If a large arterio-biliary fistula is present, transcatheter arterial embolization may be performed to arrest any bleeding.<sup>7</sup>

### Arterioportal fistula

In a multicenter study of RFA complications, the incidence of APF formation was reported to be about 0.4%.<sup>18</sup> However, the ac-

tual incidence could have been higher since most patients are asymptomatic and APF formation is discovered on follow-up CT imaging (Figure 8).<sup>19</sup> The majority of small APFs heal spontaneously post ablation.<sup>10</sup>

However, APFs can potentially exacerbate portal hypertension symptoms and lead to the rupture of gastroesophageal varices, the worsening of ascites, and the deterioration of liver function (Figure 9). In such cases, a comprehensive evaluation of the APF should be performed, and it should be treated with transcatheter embolization.<sup>20</sup>

### Cardiac tamponade

Hemorrhagic cardiac tamponade is an extremely rare but potentially fatal complication that can be successfully treated if detected promptly. To date, about six cases have been reported in the literature.<sup>21</sup> Tumors located in the liver's left lobe near the pericardium (namely in segments II and IVa) are considered pertinent risk factors for this complication (Figure 10).<sup>21</sup> Emergency pericardiocentesis (with the placement of a drainage catheter into the pericardial space) should be performed if the post-procedure hemodynamic parameters and imaging favor a pericardial effusion.

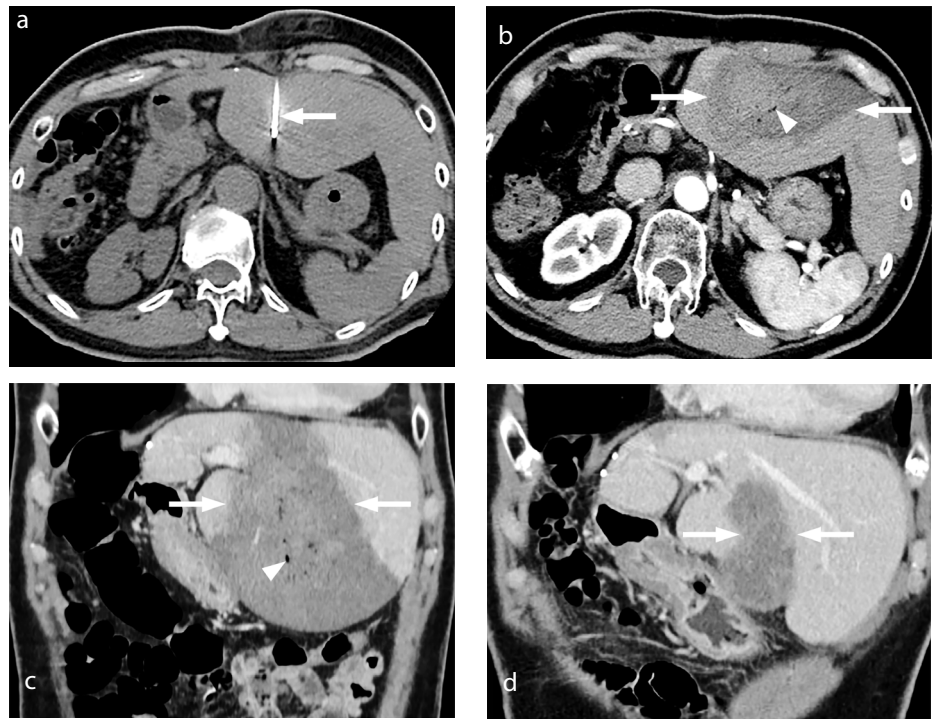


**Figure 6.** (a-d) Hepatic infarction after radiofrequency ablation (RFA) of a segment 3 metastasis from rectal carcinoma. Prior right hepatectomy was performed for hepatic metastases. Axial plain computed tomography (CT) image (a) shows the final position of the RFA needle (arrow) pre-ablation. Axial contrast-enhanced computed tomography (CECT) (two days post ablation) image in the arterial phase (b) and coronal CT image in the venous phase (c) demonstrate a large, well-defined hypodense area in the liver's left lobe, in keeping with hepatic infarction (arrows). Small, scattered pockets of gas (arrowhead) within this infarcted area suggest a concurrent infection. The patient was treated conservatively with antibiotics. Coronal CECT (six months follow up) image (d) in the venous phase demonstrates retraction and reduction in size (arrows).

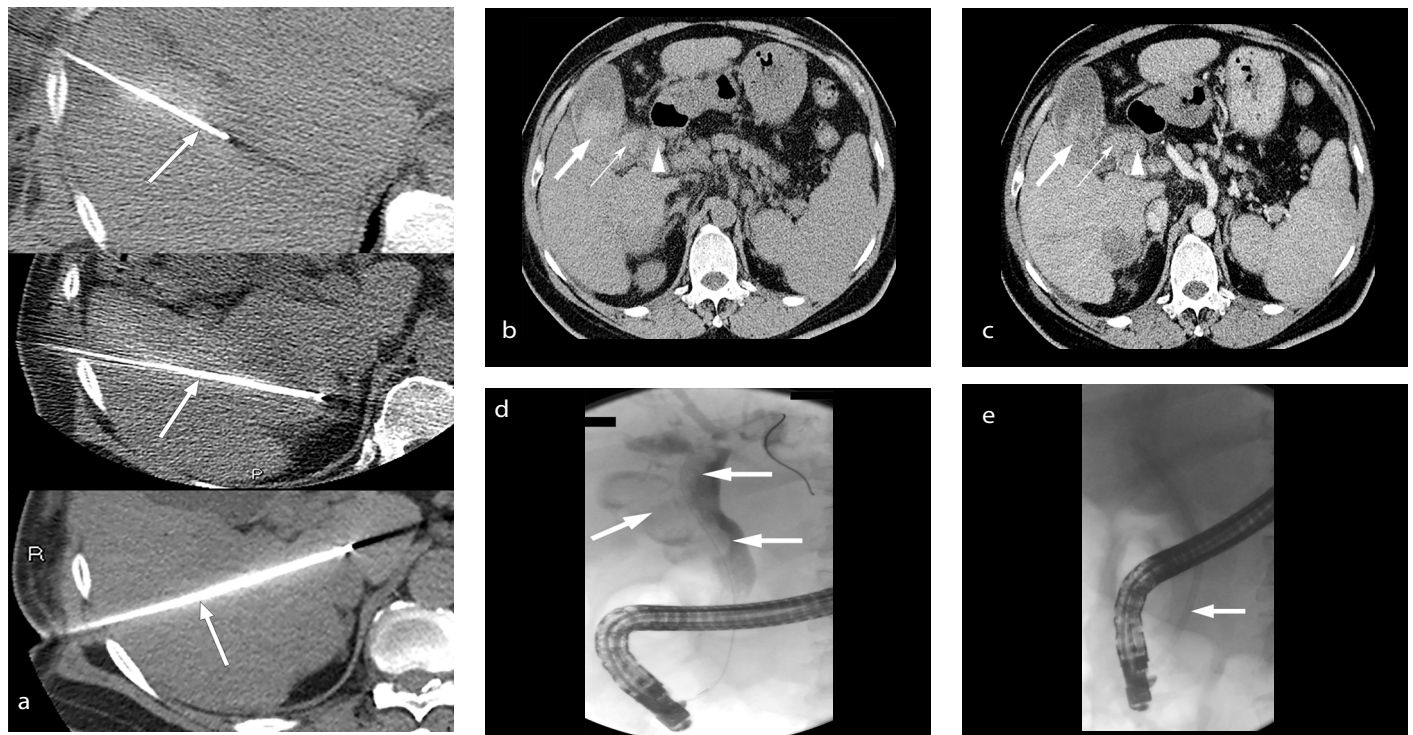


**Figure 7.** (a-e) Hemobilia presenting as melena with hemoglobin drop. The patient underwent sequential radiofrequency ablation (RFA) of three hepatocellular carcinomas in the same setting. Axial plain computed tomography (CT) images (a) show the RFA needle's position (arrows) in the segments 5/8, 5, and the caudate lobe. Axial CT (one week post ablation) images in the plain (b) and arterial (c) phases demonstrate hyperdense material within the gallbladder (thick arrow), cystic duct (thin arrow), and common bile duct (arrowhead), likely representing blood clots. No active contrast extravasation was noted on the CT scan. An endoscopic retrograde cholangiography (ERCP) was performed since the serum bilirubin level was markedly elevated. Fluoroscopic spot image from the ERCP (d) shows filling defects (arrows) within the opacified common bile duct, cystic duct, and gallbladder, likely caused by blood clots. (e) A plastic biliary stent (arrow) was deployed endoscopically for drainage of the biliary system.

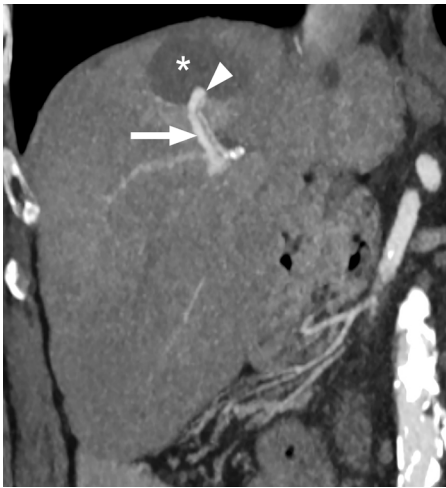


**Figure 8.** Arterioportal fistula (APF) formation after microwave ablation of a segment 8 hepatocellular carcinoma. Coronal maximum intensity projection contrast-enhanced computed tomography image in the arterial phase displays the APF (arrowhead) with early opacification of the adjacent segmental portal vein (arrow). Note the ablation zone (asterisk).

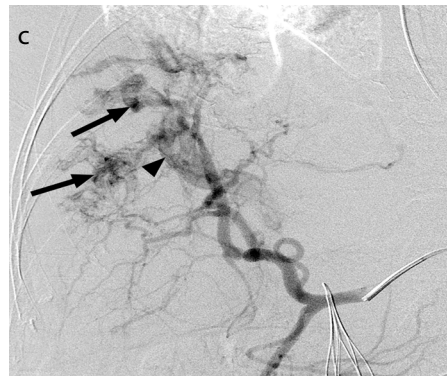
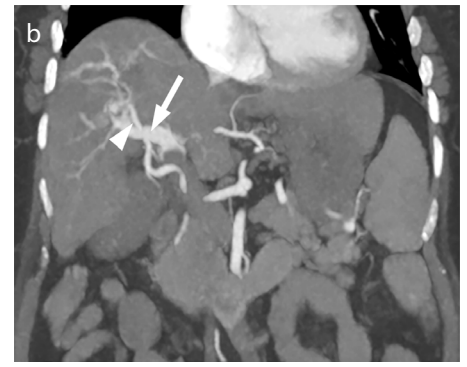
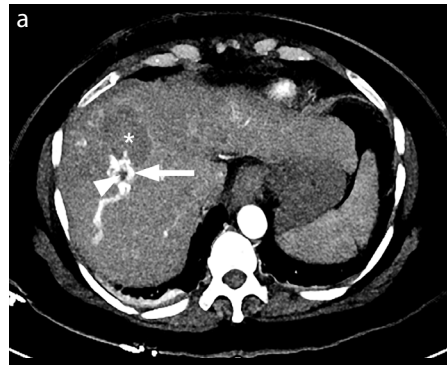


**Figure 9. (a-d)** Arterioportal fistula (APF) with exacerbation of portal hypertension. Massive hematemesis due to esophageal variceal bleed after microwave ablation of a segment 8 hepatocellular carcinoma. Axial (a) and coronal (b) maximum intensity projection contrast-enhanced computed tomography in the arterial phase demonstrates opacification of the right portal vein (arrow) adjacent to the ablation site (asterisk) due to APF. A non-occlusive thrombus in the opacified right portal vein is evident (arrowhead). The variceal bleeding was controlled with endoscopic band ligation. Angiogram (c) of the right hepatic artery demonstrates APF formation (arrows) with immediate opacification of the right portal vein (arrowhead). The APF was embolized with a mixture of histoacryl (n-butyl-2-cyanoacrylate) and lipiodol in a 1:2 ratio. Post-embolization angiogram (d) shows complete occlusion of the feeding artery with no evidence of APF.

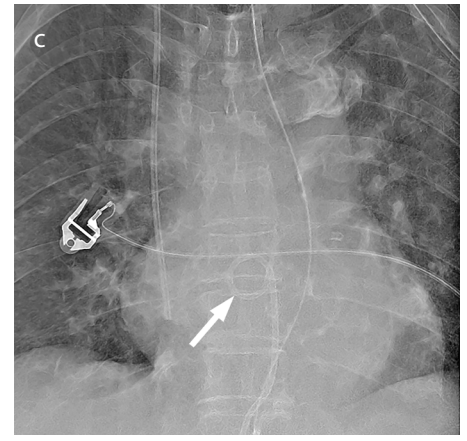
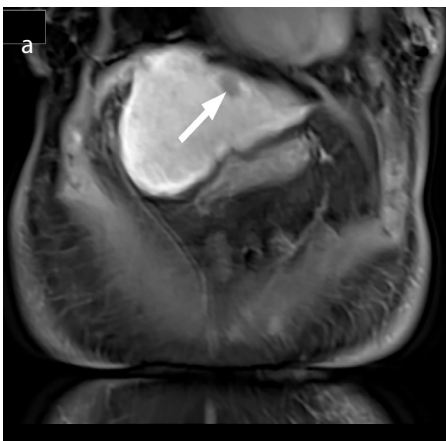


**Figure 10. (a-c)** Cardiac tamponade. Coronal fat-suppressed post-contrast T1-weighted image (a) shows a hepatocellular carcinoma (arrow) with washout in segment 2 of the liver near the pericardium. The patient became hypotensive after insertion of the radiofrequency ablation (RFA) needle and developed increased central venous pressure suggestive of cardiac tamponade. Sagittal plain computed tomography image (b) demonstrates the RFA needle's tip (arrowhead) abutting the pericardium with adjacent pericardial effusion (arrow). An 8-French pigtail catheter was immediately inserted into the pericardial space via the subcostal route. Fluoroscopic spot image (c) shows the position of the pigtail drainage catheter (arrow).

## Discussion

Meticulous preprocedural planning and evaluation are indispensable. A detailed assessment of the coagulation profile, tumor location, and hepatic reserve is essential.<sup>4</sup>

The risk factors for increased risk of bleeding include:

- coagulopathy,
- the size of the ablation needle,
- the tumor size,
- multiple punctures or electrodes,
- tumor location (tumors behind major blood vessels<sup>6,16</sup> or located superficially are at greater risk of bleeding).

Various periprocedural strategies can be taken to minimize the risk of bleeding. Preprocedural correction of underlying coagulopathy should be carried out. This can be done by administering the appropriate blood products, such as fresh frozen plasma, cryoprecipitate, and platelet concentrate, along with the appropriate withholding of antiplatelet or anticoagulant drugs.<sup>6,8</sup> Ablation should be judiciously deferred until all parameters are corrected in patients with coagulopathy.<sup>4</sup>

Careful selection of the needle path during the procedure is also paramount. It is crucial to select a path that traverses sufficient normal liver parenchyma and avoids transgressing any major vessels or biliary ducts near the index tumors.<sup>6,8</sup> Sufficient cauterization of the needle tract during withdrawal is also an effective method to prevent or reduce the risk of bleeding.<sup>8,10</sup> Finally, ablation should be avoided in patients with poor hepatic reserve.<sup>7</sup>

Some tumors are better visualized by a specific imaging modality; hence, to reduce the risk of damage to adjacent structures, the operator should choose the best modality for optimal visualization of the target tumor.<sup>4</sup>

Sometimes patients exhibit uncooperative breath-holding due to pain and anxiety, and this can result in difficulty targeting the lesion and misplacement of the ablation needle. Therefore, performing these procedures under intravenous sedation or general anesthesia is recommended, depending on the operator or institutional preference<sup>3</sup> for patient cooperation and comfort.

Besides performing routine postprocedural imaging, closely monitoring the patient's hemodynamic parameters during and after the procedure is highly recommended. Cirrhotic patients are often already in a hy-

perdynamic circulatory state, and the appearance of tachycardia due to hypovolemia may be delayed.<sup>6</sup> Any post-procedural clinical symptoms that suggest a vascular complication should be immediately brought to the clinician's attention. Among patients with hemoperitoneum, the most common symptom after ablation is abdominal pain with increasing intensity.<sup>6</sup> If this occurs along with tachycardia (>100 beats/min) and/or hypotension (systolic blood pressure <90 mmHg or reduction in the systolic blood pressure by >40 mmHg), the clinician should be notified. Additionally, hemorrhagic complications may manifest >8 hours after the procedure; therefore, it is highly recommended that all ablation procedures are performed in an inpatient setting.<sup>6</sup>

## Conclusion

Although percutaneous thermal ablation of hepatic tumors is a safe procedure with a low incidence of significant complications, a spectrum of vascular complications can occur. As with any procedure, a better outcome can be achieved when patients are selected carefully, and the operator is knowledgeable about the array of complications encountered after the procedure. This is important for the early detection and appropriate management of any complications.

### Conflict of interest disclosure

The authors declared no conflicts of interest.

## References

1. Majumdar A, Roccarina D, Thorburn D, Davidson BR, Tsochatzis E, Gurusamy KS. Management of people with early- or very early-stage hepatocellular carcinoma: an attempted network meta-analysis. *Cochrane Database Syst Rev.* 2017;3(3):CD011650. [\[Crossref\]](#)
2. Cucchetti A, Piscaglia F, Cescon M, et al. Cost-effectiveness of hepatic resection versus percutaneous radiofrequency ablation for early hepatocellular carcinoma. *J Hepatol.* 2013;59(2):300-307. [\[Crossref\]](#)
3. Crocetti L, de Baère T, Pereira PL, Tarantino FP. CIRSE standards of practice on thermal ablation of liver tumours. *Cardiovasc Intervent Radiol.* 2020;43(7):951-962. [\[Crossref\]](#)
4. Rhim H, Yoon KH, Lee JM, et al. Major complications after radio-frequency thermal ablation of hepatic tumors: spectrum of imaging findings. *Radiographics.* 2003;23(1):123-134. [\[Crossref\]](#)
5. Takaki H, Yamakado K, Nakatsuka A, et al. Frequency of and risk factors for complications

after liver radiofrequency ablation under CT fluoroscopic guidance in 1500 sessions: single-center experience. *AJR Am J Roentgenol.* 2013;200(3):658-664. [\[Crossref\]](#)

6. Goto E, Tateishi R, Shiina S, et al. Hemorrhagic complications of percutaneous radiofrequency ablation for liver tumors. *J Clin Gastroenterol.* 2010;44(5):374-380. [\[Crossref\]](#)
7. Mendiratta-Lala M, Brook OR, Midkiff BD, et al. Quality initiatives: strategies for anticipating and reducing complications and treatment failures in hepatic radiofrequency ablation. *Radiographics.* 2010;30(4):1107-1122. [\[Crossref\]](#)
8. Rhim H, Dodd GD 3rd, Chintapalli KN, et al. Radiofrequency thermal ablation of abdominal tumors: lessons learned from complications. *Radiographics.* 2004;24(1):41-52. [\[Crossref\]](#)
9. Huang Q, Xu E, Tan L, Zeng Q, Zheng R, Li K. Thermal ablation of hepatocellular carcinoma in patients with abnormal coagulation function. *Int J Hyperthermia.* 2018;34(7):1038-1043. [\[Crossref\]](#)
10. Mulier S, Mulier P, Ni Y, et al. Complications of radiofrequency coagulation of liver tumours. *Br J Surg.* 2002;89(10):1206-1222. [\[Crossref\]](#)
11. Kim YS, Lim HK, Rhim H, Do YS. Hepatic arterial pseudoaneurysm after percutaneous radiofrequency ablation for hepatocellular carcinoma. *Eur J Radiol Extra.* 2006;57(3):85-89. [\[Crossref\]](#)
12. Chiang J, Willey BJ, Del Rio AM, Hinshaw JL, Lee FT, Brace CL. Predictors of thrombosis in hepatic vasculature during microwave tumor ablation of an in vivo porcine model. *J Vasc Interv Radiol.* 2014;25(12):1965-1971. [\[Crossref\]](#)
13. Kim AY, Rhim H, Park M, et al. Venous thrombosis after radiofrequency ablation for hepatocellular carcinoma. *AJR Am J Roentgenol.* 2011;197(6):1474-1480. [\[Crossref\]](#)
14. Kim KR, Thomas S. Complications of image-guided thermal ablation of liver and kidney neoplasms. *Semin Intervent Radiol.* 2014;31(2):138-148. [\[Crossref\]](#)
15. de Baère T, Risse O, Kuoch V, et al. Adverse events during radiofrequency treatment of 582 hepatic tumors. *AJR Am J Roentgenol.* 2003;181(3):695-700. [\[Crossref\]](#)
16. Akahane M, Koga H, Kato N, et al. Complications of percutaneous radiofrequency ablation for hepato-cellular carcinoma: imaging spectrum and management. *Radiographics.* 2005;25(Suppl 1):57-68. [\[Crossref\]](#)
17. Kim YS, Rhim H, Lim HK, Choi D, Lee WJ, Kim SH. Hepatic infarction after radiofrequency ablation of hepatocellular carcinoma with an internally cooled electrode. *J Vasc Interv Radiol.* 2007;18(9):1126-1133. [\[Crossref\]](#)
18. Livraghi T, Solbiati L, Meloni MF, Gazelle GS, Halpern EF, Goldberg SN. Treatment

- of focal liver tumors with percutaneous radio-frequency ablation: complications encountered in a multicenter study. *Radiology*. 2003;226(2):441-451. [\[Crossref\]](#)
19. Akpek S, Ilgit ET, Cekirge S, Yücel C. High-flow arterioportal fistula: treatment with detachable balloon occlusion. *Abdom Imaging*. 2001;26(3):277-280. [\[Crossref\]](#)
20. Curley SA, Marra P, Beaty K, et al. Early and late complications after radiofrequency ablation of malignant liver tumors in 608 patients. *Ann Surg*. 2004;239(4):450-458. [\[Crossref\]](#)
21. Chung MW, Ha SY, Choi JH, et al. Cardiac tamponade after radiofrequency ablation for hepatocellular carcinoma: case report and literature review. *Medicine (Baltimore)*. 2018; 97(49):13532. [\[Crossref\]](#)



# Feasibility study of percutaneous thoracic duct embolization with lower-limb intermittent pneumatic compression devices

Ravivarma Balasubramaniam   
Mona Mossad 

## PURPOSE

To demonstrate intranodal thoracic duct embolization (TDE) for treating chyle leaks following thoracic surgery and the feasibility of applying lower-limb intermittent pneumatic compression devices during TDE.

## METHODS

Between December 2017 and October 2020, 12 consecutive TDEs for post-operative chyle leaks were performed in 11 patients using intranodal lymphangiogram (IL) with an intermittent pneumatic compressive device applied to the lower limb. The procedure's duration, technical/clinical success, and complications were retrospectively evaluated.

## RESULTS

IL was successful at imaging the thoracic duct in all procedures (100%), and TDE had an intention-to-treat success rate of 92% (11/12). No related complications were observed during follow-up, which took place at a mean of 27 days. The time from the commencement of lymphangiogram until visualization of the thoracic duct was a mean of 21.6 min, and the mean overall procedure time was 87.3 min.

## CONCLUSION

This study supports IL-guided TDE as a safe and effective option to treat post-thoracic surgery chyle leaks. We revealed shorter lymphangiogram times compared with previously published studies, and we postulate that the application of intermittent lower-limb pneumatic compressive devices contributed toward this study's results by expediting the return of lymph from the lower limb. This study is the first to illustrate this approach in TDE and advocates for randomized controlled studies to further evaluate the influence of intermittent pneumatic compressive devices on the procedure.

## KEYWORDS

Thoracic duct, embolization, chyle leak, intermittent pneumatic venous compression devices, lymphangiogram

From the Department of Radiology (R.B. ✉ Ravivarma. Balasubramaniam@uhnm.nhs.uk, M.M.), Royal Stoke University Hospital, Staffordshire, England.

Received 14 October 2021; revision requested 15 November 2021; last revision received 16 January 2022; accepted 19 January 2022.



Epub: 24.01.2023

Publication date: 29.03.2023

DOI: 10.5152/dir.2022.21975

Injury to the thoracic duct can occur as a post-operative complication and is encountered in 1% to 9% of transthoracic esophagectomies and in 1.4% to 4% of pulmonary resections.<sup>1-4</sup> This results in a chyle leak, which can lead to respiratory failure, hypovolemia, malnutrition, or septicemia, with a mortality ranging from 3.7% to 46%.<sup>3,5,6</sup> Conservative management with nutritional support, sometimes combined with octreotide, can be trialed; however, for higher-volume chyle leaks, early surgical intervention and ligation of the thoracic duct has been shown to be critical to improving outcomes.<sup>2,3,7,8</sup> Surgical repair of a chyle leak has a success rate of 68% to 90% but carries a mortality rate of 10% to 16%.<sup>3,7-9</sup> In recent times, thoracic duct embolization (TDE) has emerged as a less invasive alternative, with an intention-to-treat success rate of 53% to 100% combined with a significantly lower complication rate.<sup>10-17</sup> It has the advantage of providing comprehensive delineation of the thoracic duct and can better identify the site of the chyle leak; this is of particular relevance given the recognized variance

You may cite this article as: Balasubramaniam R, Mossad M. Feasibility study of percutaneous thoracic duct embolization with lower-limb intermittent pneumatic compression devices. *Diagn Interv Radiol.* 2023;29(2):326-330.

in thoracic duct anatomy.<sup>12,18</sup> TDE entails a lymphangiogram, which is conventionally done via exposure of the pedal lymphatics, followed by cannulation of the cisterna chyli/thoracic duct and subsequent embolization. Recently, ultrasound-guided intranodal access has been demonstrated as an alternative method to support the lymphangiogram to guide TDE, with fewer complications; however, published data on this technique remains limited.<sup>19-24</sup> The transport of lymph is similar to venous return and is primarily regulated by the contraction of the smooth muscles in the lymphatic channels and surrounding skeletal muscles. We theorize that intermittent pneumatic compressive devices, which expedite venous return when used as a prophylaxis in the prevention of deep vein thrombosis, may have a similar influence on the return of lymph and could shorten TDE procedure times.

We detail a study of consecutive intranodal lymphangiogram (IL)-guided TDEs to treat post-thoracic surgery chyle leaks and illustrate the application of intermittent pneumatic compression devices.

## Methods

Permission from the Institutional Review Board of the University Hospital of North Midlands Ethics Committee's Research and Design Department was obtained for this study (protocol number: 210421). A retrospective analysis of 12 procedures in 11 consecutive patients who underwent TDE at our institute between December 2017 and October 2020 was performed. All chyle leaks occurred as a post-operative complication: eight after esophagectomy, two following thoracotomies, and one after video-assisted thoracoscopic surgery. All the operations were performed to treat malignancy, except for one thoracotomy that was undertaken to resect a first rib to treat thoracic outlet syndrome. The thoracic duct was not ligated during any of the operations. There were seven male and four female patients, ranging in age from 25 to 81 years, with a mean age

of 57.5 years. All patients presented with the classic milky white appearance of post-operative pleural fluid. A pleural fluid analysis with a triglyceride content of >1.2 mmol and cholesterol of <5.1 mmol were used to differentiate between a chylothorax and pseudochylothorax. A chylomicrons analysis of the pleural fluid was not available at our institute. Prior to the IL TDE, all patients had a trial of conservative treatment for a minimum of 5 days (fat-free diet and octreotide therapy). The inclusion criteria were that patients had a drain output of >500 mL/day, despite conservative management, and a full blood count with a lymphocytopenia ranging from 0.1 to 1 (normal value is 1.5).

All patients underwent TDE with ultrasound-guided IL, performed by a single interventional radiologist with 3 years of procedural experience. The duration from the initial thoracic surgery to TDE had a range of 2 to 25 days, with a mean of 12.2 days. Chylothorax resolution and removal of the chest drain were considered the endpoint for clinical success. Informed written consent and a surgical safety checklist were completed before commencing the intervention. Prophylactic intravenous antibiotics consisting of 1.2 g of intravenous co-amoxiclav was administered at the initiation of the procedure. Prior to cleaning and draping the patient, bilateral pneumatic compression boots were applied around both of the patient's lower limbs but remained switched off. An ultrasound examination of both groins was performed using a Philips Purewave CX 50 ultrasound machine, and the largest and most superficial inguinal lymph node was targeted. Under ultrasound guidance using an aseptic technique, an inguinal node was punctured using a 22 G 3.5-inch BD spinal needle and a maximum of 20 mL of lipiodol injected. If extravasation was demonstrated, another unilateral inguinal node was targeted, with a maximum of three inguinal nodes punctured in one procedure. After successfully accessing an inguinal node, the ipsilateral intermittent pneumatic compressive sleeve was turned on, and the progression of Lipiodol through the lymphatic system was monitored under intermittent fluoroscopy until visualization of the cisterna chyli or thoracic duct (see Table 1 column for the visualization of cisterna chyle for the duration of intermittent compression device application). At this point, the pneumatic compression device was turned off for the remainder of the procedure to avoid the rapid transit/washout of the contrast and maximize the visualization of the thoracic duct. A maximum sedation of 250 µg of

fentanyl and 7.5 mg of midazolam was then administered before 10–20 mL of 1% lignocaine was infiltrated locally and the cisterna chyli or thoracic duct directly punctured at L1/L2 level using an AccuStick II kit (Boston Scientific; introducer needle with stylet 21 G 15 cm). Once the cisterna chyli/thoracic duct was cannulated, a V18 short taper 0.018 inch × 200 cm control wire (Boston Scientific) was introduced, and the 21 G needle was subsequently exchanged for a Progreat micro-catheter system (2.7 F, 130 cm; Terumo). Visipaque contrast was then injected into the micro-catheter to confirm the position and delineate the site of the chyle leak. A detachable coil was next inserted upstream of the leak (Concerto; detachable coil system with nylon fibers, 4 mm × 8 cm × 0.0125 inch, ev3), followed by a mixture of tissue adhesive glue (Histoacryl, B. Braun) and lipiodol (Ultra fluid, Guerbet) with a mixing ratio of 1:2. The glue was injected along the course of the thoracic duct as the micro-catheter was pulled out under fluoroscopic guidance. Completion X-rays were subsequently obtained of the chest, abdomen, and pelvis for a reference of embolic position (Figure 1).

## Results

### Technique

The site of the chyle leak was identified using IL in each of the 12 cases. In all 11 patients, the chyle leak was treated successfully with TDE using two micro-coils combined with a mixture of cyanoacrylic glue and lipiodol. The overall intention-to-treat success rate was 11/12 (92%), as there was one patient with an abdominal chyle injury that required a repeat procedure 17 days later to achieve successful treatment (Figure 2). In cases where local extravasation of lipiodol from the inguinal node puncture site occurred, clinical follow-up over the ensuing 24 to 48 h was conducted with no local symptoms of pain or swelling reported. There were no long-term post-procedure complications on follow-up, which ranged from 9 to 91 days, with a mean of 27 days.

### Duration

There were no records of the time taken to access the inguinal node for the lymphangiogram under ultrasound guidance. The procedure time from the initiation of the lymphangiogram to visualization of the target lymphatic (thoracic duct or a major tributary) ranged from 9 to 29 min, with a mean of 21.6 min and a standard deviation of ± 6.0 min. The duration from the commencement

### Main points

- Thoracic duct embolization (TDE) is a viable option to surgical ligation in the management of post-operative chyle leaks.
- Ultrasound guided intranodal lymphangiogram is a safe and effective alternative to pedal lymphangiogram to guide TDE.
- Intermittent pneumatic compressive devices may have a role in expediting lower-limb lymphangiography and TDE procedures.

of the lymphangiogram to catheterization of the thoracic duct ranged from 28 to 106 min, with a mean of 55.5 min and a standard deviation of  $\pm 24.2$  min. The time from the beginning of the lymphangiogram to embolization of the thoracic duct ranged from

47 to 124 min, with a mean of 83.1 min and a standard deviation of  $\pm 24.3$  min. Intermittent pneumatic compression devices were activated from the commencement of the lymphangiogram until visualization of the cisterna chyli, with a duration ranging from 9

to 29 min and mean application time of 21.6 min. The overall procedure time from the start of the lymphangiogram to completion of the TDE procedure had a mean of 87.3 min with a standard deviation of  $\pm 23.9$  min (see Table 1 for the individual times).

## Discussion

### Technique

TDE was first illustrated by Cope et al.<sup>10</sup> in 1998 through the transabdominal catheterization of the cisterna chyli guided by a pedal lymphangiogram. In a subsequent study of 42 patients by Cope and Kaiser<sup>11</sup> in 2002, TDE delivered favorable outcomes, with a treatment response of 78%. However, the emergence of computed tomography and magnetic resonance imaging lymphan-



**Figure 1.** Fluoroscopic images of a thoracic duct chyle leak post esophagectomy. (a) Fluoroscopic intranodal lymphangiogram (IL) image delineating the site of the thoracic duct chyle leak (white arrow), (b) fluoroscopic IL image after successful thoracic duct embolization with detachable coil, adhesive glue, and lipiodol (white arrow heads).

**Figure 2.** Abdominal chyle leak post esophagectomy; fluoroscopic intranodal lymphangiogram image showing the site of the abdominal chyle leak (white arrows).

**Table 1.** Procedure times for intranodal lymphangiography and thoracic duct embolization

Patient	Age in years (sex)	Surgery	Site of chyle leak	Visualization of CC	Time to cannulation of TD	Time to embolization of TD	Total procedure time
1	25 (F)	VATS	T11	18	37	67	68
2	69 (M)	Esophagectomy	T12/L1	21	39	76	78
3	-			22	54	80	95
4	58 (M)	Esophagectomy	T10	28	81	105	108
5	63 (M)	Esophagectomy	T11	14	33	56	59
6	54 (M)	Esophagectomy	T10	18	34	57	67
7	81 (F)	Thoracotomy	TD- LSV	20	37	70	72
8	60 (F)	Esophagectomy	T8	23	61	95	102
9	66 (M)	Esophagectomy	T11	28	71	102	104
10	56 (M)	Esophagectomy	T8	29	106	124	126
11	56 (M)	Esophagectomy	T10	9	28	47	49
12	44 (F)	Thoracotomy	T12	29	85	118	119
<b>Mean (SD)</b>	<b>57.5</b>			<b>21.6 (<math>\pm 6.3</math>)</b>	<b>55.5 (<math>\pm 25.27</math>)</b>	<b>83.1 (<math>\pm 25.4</math>)</b>	<b>87.25 (<math>\pm 25.0</math>)</b>

The light line shaded area denotes a repeat procedure on the same patient. CC, cisterna chyli; TD, thoracic duct; VATS, video-assisted thoracoscopic surgery; TD-LSV, junction of the thoracic duct with the left subclavian vein; SD, standard deviation; F, female; M, male.

giogram meant pedal lymphangiography (PL) became less frequently utilized, resulting in diminished clinical experience in the technique.<sup>25-27</sup> This has limited the development of conventional TDE as an alternative to surgical ligation in the management of thoracic duct injuries, and literature on the topic is limited, with research primarily originating from a small number of institutes. Ultrasound-guided intranodal access as an alternative to PL was first demonstrated by Hall and Kremenz<sup>28</sup> in 1967 and replicated by Rajebi et al.<sup>19</sup> in 2011 in a pediatric group. Intranodal lymphangiography complements ultrasound intervention practice, thereby offering scope to broaden access to TDE as a treatment option for chyle leaks. The technique was first utilized as a viable substitute for PL to guide TDE by Nadolski and Itkin<sup>20</sup> in 2012 and has since been replicated in other studies.<sup>10</sup> This is substantiated by our findings, with the thoracic duct visualized and the site of the chyle leak identified in all 12 procedures. Our technical success rate of 100% for IL is consistent with figures from previous studies by Nadolski and Itkin<sup>21</sup>, which attained rates of 98% to 100% employing both PL and IL for TDE. The chyle leak was successfully treated with IL-guided TDE in all 11 patients in our study, with one case requiring a repeat procedure. Our 92% technical success rate was similar to the 86% reported by Ushinsky et al.<sup>22</sup> in treating chyle leaks after head/neck cancer surgery and superior to other smaller IL TDE studies by Kariya et al.<sup>23</sup> and Kim et al.<sup>24</sup>, which accomplished rates of 75% and 67%, respectively. Our study is the largest series of consecutive IL TDEs to treat chyle leaks following thoracic surgery, with results comparable to the largest similar study by Nadolski and Itkin<sup>21</sup>, which reported a technical success rate of 98% in 50 patients, 22 of whom underwent TDE using an IL method. Our overall intention-to-treat success rate of 92% (11/12) supports IL as an alternative to PL for TDE in the treatment of post-operative chyle leaks, being equivalent to the 75–97% stated in previous PL TDE studies, including the two largest studies by Pamarthi et al.<sup>15</sup> (involving 105 patients) and Itkin et al.<sup>16</sup> (involving 106 patients).<sup>17,20-24</sup> Our intention-to-treat rate of 92% is also equivalent to the clinical success rate of surgical ligation, which ranges from 68% to 90%, with the additional benefits of being minimally invasive.<sup>5,7-9</sup> Complications related to TDE include intra-alveolar hemorrhage or pulmonary embolism from the injected lipiodol and infection, which occurs in 0.9–2.9% of cases; this is primarily related to lymphatic exposure in the PL group.<sup>25,29,30</sup>

No complications were reported in our study during a mean follow-up of 27 days.

### Duration

Comparison with other studies on procedure times are limited by a lack of relevant published data. The most applicable study was by Nadolski and Itkin<sup>20</sup> in 2012, which compared the durations of six IL and six PL-guided TDEs. The time taken to visualize the thoracic duct with IL was significantly shorter in our study, with a range of 9 to 29 min and a mean of 21.6 min compared with a range of 23 to 64 min and mean of 40 min reported in the IL-guided TDE group in the study by Nadolski and Itkin.<sup>20</sup> The overall procedure time in our study was also noticeably shorter, with a mean of 87.3 min compared with a mean of 105.3 min in their study.<sup>20</sup> We postulate that utilizing lower-limb intermittent pneumatic compressive devices may have contributed toward our shorter IL and TDE procedure times. The active transport of lymph from nodes follows a similar process to lower-limb venous return and is primarily governed by the contraction of skeletal muscle and smooth muscle in the walls of lymphatic vessels.<sup>31-33</sup> Intermittent pneumatic compressive devices applied to the lower limbs can improve venous return by increasing blood velocity in the deep veins, and they have been utilized as prophylaxis in the prevention of deep vein thrombosis. For our study, we postulate that the use of pneumatic venous compression devices may have had a similar influence on the return of lymph from the lower limbs to the cisterna chyli and may also have contributed toward the reduced mean time for IL and overall TDE procedure time.<sup>34</sup> This rationale is corroborated by a retrospective study by Meisinger et al.<sup>35</sup>, which demonstrated a significantly shorter IL mean time of 29 min with lower-limb pneumatic compression devices compared with 56 min without. Their results are comparable to the 21.6-min IL duration achieved in our study, but their study predominantly involved patients with non-traumatic chyle leaks (7/19) or research cases with no leak (5/19).<sup>35</sup>

The primary limitations of the present study are its retrospective nature and the absence of a randomized control. However, it remains the largest case series demonstrating consecutive IL-guided TDE to treat post-operative chyle leaks with the application of intermittent pneumatic venous compression devices. Large prospective randomized controlled studies evaluating the effect of pneumatic venous compression boots in TDE, using both an IL and PL technique, are

required to further validate the hypothesis proposed. All TDEs were also performed by a single radiologist, which makes assumptions of wide reproducibility less certain. The radiologist also had relatively limited experience, with only 3 years using this technique. As such, it is assumed that operative duration would be reduced for a radiologist of greater experience.<sup>16</sup> Finally, our study has a relatively small sample size; however, this remains the largest study to date on consecutive TDE using IL to treat post-thoracic surgery chyle leaks.

In conclusion, with an intention-to-treat success rate of 92%, our findings endorse IL-guided TDE as a safe alternative to surgical ligation in the management of post-operative chyle leaks. This is the largest study of consecutive IL-guided TDE to treat post-operative chyle leaks after thoracic surgery, illustrating technical and clinical success rates that compare favorably with larger studies performed using a PL method. This study demonstrates significantly shorter lymphangiogram procedure times compared with previous TDE studies and postulates that utilizing lower-limb intermittent pneumatic compressive devices contributed to these outcomes by expediting lymph return toward the cisterna chyli/thoracic duct. This study is the first to illustrate this approach in TDE and recommends that further prospective randomized studies be performed to evaluate the influence of intermittent pneumatic compressive devices on procedure times in TDE.

### Conflict of interest disclosure

The authors declared no conflicts of interest.

### References

1. Brinkmann S, Schroeder W, Junggeburth K, et al. Incidence and management of chylothorax after Ivor Lewis esophagectomy for cancer of the esophagus. *J Thorac Cardiovasc Surg.* 2016;151(5):1398-1404. [\[CrossRef\]](#)
2. Merigliano S, Molena D, Ruol A, et al. Chylothorax complicating esophagectomy for cancer: a plea for early thoracic duct ligation. *J Thorac Cardiovasc Surg.* 2000;119(3):453-457. [\[CrossRef\]](#)
3. Cerfolio RJ, Allen MS, Deschamps C, Trastek VF, Pairolero PC. Postoperative chylothorax. *J Thorac Cardiovasc Surg.* 1996;112(5):1361-1365; discussion 1365-1366. [\[CrossRef\]](#)
4. Bryant AS, Minnich DJ, Wei B, Cerfolio RJ. The incidence and management of postoperative chylothorax after pulmonary resection and thoracic mediastinal lymph node dissection.

- Ann Thorac Surg.* 2014;98(1):232-235; discussion 235-237. [\[CrossRef\]](#)
5. Shah RD, Luketich JD, Schuchert MJ, et al. Postesophagectomy chylothorax: incidence, risk factors, and outcomes. *Ann Thorac Surg.* 2012;93(3):897-903; discussion 903-904. [\[CrossRef\]](#)
  6. Bolger C, Walsh TN, Tanner WA, Keeling P, Hennessy TP. Chylothorax after oesophagectomy. *Br J Surg.* 1991;78(5):587-588. [\[CrossRef\]](#)
  7. Orringer MB, Bluett M, Deeb GM. Aggressive treatment of chylothorax complicating transhiatal esophagectomy without thoracotomy. *Surgery.* 1988;104(4):720-726. [\[CrossRef\]](#)
  8. Maldonado F, Cartin-Ceba R, Hawkins FJ, Ryu JH. Medical and surgical management of chylothorax and associated outcomes. *Am J Med Sci.* 2010;339(4):314-318. [\[CrossRef\]](#)
  9. Slater BJ, Rothenberg SS. Thoracoscopic thoracic duct ligation for congenital and acquired disease. *J Laparoendosc Adv Surg Tech A.* 2015;25(7):605-607. [\[CrossRef\]](#)
  10. Cope C, Salem R, Kaiser LR. Management of chylothorax by percutaneous catheterization and embolization of the thoracic duct: prospective trial. *J Vasc Interv Radiol.* 1999;10(9):1248-1254. [\[CrossRef\]](#)
  11. Cope C, Kaiser LR. Management of unremitting chylothorax by percutaneous embolization and blockage of retroperitoneal lymphatic vessels in 42 patients. *J Vasc Interv Radiol.* 2002;13(11):1139-1148. [\[CrossRef\]](#)
  12. Matsumoto T, Yamagami T, Kato T, et al. The effectiveness of lymphangiography as a treatment method for various chyle leakages. *Br J Radiol.* 2009;82(976):286-290. [\[CrossRef\]](#)
  13. Boffa DJ, Sands MJ, Rice TW, et al. A critical evaluation of a percutaneous diagnostic and treatment strategy for chylothorax after thoracic surgery. *Eur J Cardiothorac Surg.* 2008;33(3):435-439. [\[CrossRef\]](#)
  14. Itkin M, Kucharczuk JC. Thoracic duct embolization (TDE) for nontraumatic chylous effusion: experience in 31 patients. *Chest.* 2010;138(4):654a. [\[CrossRef\]](#)
  15. Pamarthi V, Stecker MS, Schenker MP, et al. Thoracic duct embolization and disruption for treatment of chylous effusions: experience with 105 patients. *J Vasc Interv Radiol.* 2014;25(9):1398-1404. [\[CrossRef\]](#)
  16. Itkin M, Kucharczuk JC, Kwak A, Trerotola SO, Kaiser LR. Nonoperative thoracic duct embolization for traumatic thoracic duct leak: experience in 109 patients. *J Thorac Cardiovasc Surg.* 2010;139(3):584-589; discussion 589-590. [\[CrossRef\]](#)
  17. Nadolski GJ, Itkin M. Thoracic duct embolization for nontraumatic chylous effusion: experience in 34 patients. *Chest.* 2013;143(1):158-163. [\[CrossRef\]](#)
  18. Sachs PB, Zelch MG, Rice TW, Geisinger MA, Risius B, Lammert GK. Diagnosis and localization of laceration of the thoracic duct: usefulness of lymphangiography and CT. *AJR Am J Roentgenol.* 1991;157(4):703-705. [\[CrossRef\]](#)
  19. Rajebi MR, Chaudry G, Padua HM, et al. Intranodal lymphangiography: feasibility and preliminary experience in children. *J Vasc Interv Radiol.* 2011;22(9):1300-1305. [\[CrossRef\]](#)
  20. Nadolski GJ, Itkin M. Feasibility of ultrasound-guided intranodal lymphangiogram for thoracic duct embolization. *J Vasc Interv Radiol.* 2012;23(5):613-616. [\[CrossRef\]](#)
  21. Nadolski GJ, Itkin M. Lymphangiography and thoracic duct embolization following unsuccessful thoracic duct ligation: Imaging findings and outcomes. *J Thorac Cardiovasc Surg.* 2018;156(2):838-843. [\[CrossRef\]](#)
  22. Ushinsky A, Guevara CJ, Kim SK. Intranodal lymphangiography with thoracic duct embolization for the treatment of chyle leaks after head and neck cancer surgery. *Head Neck.* 2021;43(6):1823-1829. [\[CrossRef\]](#)
  23. Kariya S, Komemushi A, Nakatani M, Yoshida R, Kono Y, Tanigawa N. Intranodal lymphangiogram: technical aspects and findings. *Cardiovasc Intervent Radiol.* 2014;37(6):1606-1610. [\[CrossRef\]](#)
  24. Kim SK, Thompson RE, Guevara CJ, Ushinsky A, Ramaswamy RS. Intranodal Lymphangiography with Thoracic Duct Embolization for Treatment of Chyle Leak after Thoracic Outlet Decompression Surgery. *J Vasc Interv Radiol.* 2020;31(5):795-800. [\[CrossRef\]](#)
  25. Guermazi A, Brice P, Hennequin C, Sarfati E. Lymphography: an old technique retains its usefulness. *Radiographics.* 2003;23(6):1541-1558; discussion 1559-1560. [\[CrossRef\]](#)
  26. Okuda I, Udagawa H, Takahashi J, Yamase H, Kohno T, Nakajima Y. Magnetic resonance-thoracic ductography: imaging aid for thoracic surgery and thoracic duct depiction based on embryological considerations. *Gen Thorac Cardiovasc Surg.* 2009;57(12):640-646. [\[CrossRef\]](#)
  27. Kos S, Hauelsen H, Lachmund U, Roeren T. Lymphangiography: forgotten tool or rising star in the diagnosis and therapy of postoperative lymphatic vessel leakage. *Cardiovasc Intervent Radiol.* 2007;30(5):968-973. [\[CrossRef\]](#)
  28. Hall RC, Kremenz ET. Lymphangiography by lymph-node injection. *JAMA.* 1967;202(13):1136-1139.
  29. Dupont H, Timsit JF, Souweine B, Gachot B, Bedos JP, Wolff M. Intra-alveolar hemorrhage following bipedal lymphography. *Intensive Care Med.* 1996;22(6):614-615. [\[CrossRef\]](#)
  30. Bron KM, Baum S, Abrams HL. Oil embolism in lymphangiography. Incidence, manifestations, and mechanism. *Radiology.* 1963;80:194-202. [\[CrossRef\]](#)
  31. Muthuchamy M, Zawieja D. Molecular regulation of lymphatic contractility. *Ann N Y Acad Sci.* 2008;1131:89-99. [\[CrossRef\]](#)
  32. Reddy NP. Lymph circulation: physiology, pharmacology, and biomechanics. *Crit Rev Biomed Eng.* 1986;14(1):45-91. [\[CrossRef\]](#)
  33. Uhl JF, Gillot C. Anatomy of the veno-muscular pumps of the lower limb. *Phlebology.* 2015;30(3):180-193. [\[CrossRef\]](#)
  34. Kakkos SK, Caprini JA, Geroulakos G, et al. Combined intermittent pneumatic leg compression and pharmacological prophylaxis for prevention of venous thromboembolism. *Cochrane Database Syst Rev.* 2016;9(9):CD005258. [\[CrossRef\]](#)
  35. Meisinger QC, O'Brien S, Itkin M, Nadolski GJ. Use of sequential pneumatic compression devices to facilitate propagation of contrast during intranodal lymphangiography. *J Vasc Interv Radiol.* 2017;28(11):1544-1547. [\[CrossRef\]](#)



# Embolization therapy for type 2 endoleaks after endovascular aortic aneurysm repair: imaging-based predictive factors and clinical outcomes on long-term follow-up

Ruben Vandenbulcke   
Sabrina Houthoofd   
Annouschka Laenen   
Pieter-Jan Buyck   
Hozan Mufty   
Inge Fourneau   
Geert Maleux 

From the Department of Department of Radiology (R.V., P.-J.B., G.M. ✉ [geert.maleux@uzleuven.be](mailto:geert.maleux@uzleuven.be)), University Hospitals Leuven, Leuven, Belgium; Department of Vascular Surgery, (S.H., H.M., I.F.), University Hospitals Leuven, Leuven, Belgium; Department of Biostatistics (A.L.), Interuniversity Institute for Biostatistics and Statistical Bioinformatics Centre, Leuven, Belgium.

Received 04 May 2021; revision requested 24 May 2021; last revision received 09 January 2022; accepted 13 February 2022.



Epub: 21.02.2023

Publication date: 29.03.2023

DOI: 10.4274/dir.2022.22352

## PURPOSE

To evaluate the technical, radiological, and clinical outcomes after type 2 endoleak (T2EL) embolization in patients with a growing aneurysm sac after endovascular aortic aneurysm repair (EVAR). Additionally, to determine clinical and imaging-based factors for outcome prediction after embolization of a T2EL.

## METHODS

A single-institution, retrospective analysis was performed of 60 patients who underwent a T2EL embolization procedure between September 2005 and August 2016 to treat a growing aneurysm sac diameter following EVAR. The patients' electronic medical records and all available pre- and post-embolization imaging were reviewed. Statistical analysis methods included logistic regression models for binary outcomes, proportional odds models for ordinal outcomes, and linear regression models for continuous outcomes. The Kaplan–Meier method was used to estimate the overall survival probability.

## RESULTS

Technical, radiological, and clinical success rates after T2EL embolization were 95% (n = 57), 26.7% (n = 16), and 76.7% (n = 46), respectively. Persistent aneurysm sac expansion was found in 31 patients (51.7%). Unsharp or blurred T2EL delineation on pre-interventional computed tomography (CT) was a predictive factor for a post-embolization persistent visible endoleak and persistent growth of the aneurysm sac ( $P = 0.025$ ). Median survival after T2EL embolization was 5.35 years, with no difference observed between patients with persistent sac expansion compared with patients with stable or decreased sac diameter.

## CONCLUSION

Progression of the aneurysm sac diameter was observed in half the study patients, despite technically successful T2EL embolization. Unsharp or blurred T2EL delineation on pre-interventional CT seemed to be an imaging-based predictor for a persistent T2EL and progressive aneurysm sac growth after embolization.

## KEYWORDS

Abdominal aortic aneurysm, catheter angiography, CT angiography, embolization, endoleak

Current international guidelines propose endovascular aortic aneurysm repair (EVAR) as the standard treatment for abdominal aortic aneurysm (AAA) in selected patients with suitable vascular anatomy.<sup>1,2</sup> However, endoleaks, defined as persistent blood circulation in the aneurysm sac, remain the Achilles' heel of EVAR procedures.<sup>3-6</sup> A type 2 endoleak (T2EL), caused by backflow from collateral arteries into the aneurysm sac, has an occurrence rate of approximately 15% after successful EVAR and accounts for approximately half of all endoleaks.<sup>3,7,8</sup> The management of a T2EL remains controversial; some experts propose conservative management as a safe strategy,<sup>9,10</sup> while others have demonstrated T2ELs as a cause of late rupture with a need for reintervention.<sup>4,11</sup> Current guidelines recommend treatment in patients with a T2EL after EVAR associated with aneurysm sac expansion of >10 mm in diameter.<sup>1</sup> Due to the relatively high late-complication rate in patients with a T2EL after EVAR, lifelong radiological surveillance is currently recommended in these patients.<sup>12,13</sup>

Short-term outcome data after T2EL embolization are variable,<sup>3,14-18</sup> and long-term radiological and clinical outcome data are scarce.<sup>19</sup> Additionally, relatively little is known about how predictive pre-embolization imaging factors are for better or worse outcomes.

The aim of this study is to determine the technical and long-term radiological and clinical outcomes after T2EL embolization and to assess clinical and imaging-based factors for outcome prediction after embolization of T2ELs associated with aneurysm sac expansion following EVAR.

## Methods

### Patients

This retrospective study was approved by the Ethics Committee of the University Hospitals KU Leuven (S62135). All consecutive patients who underwent an elective T2EL embolization procedure between Septem-

ber 2005 and August 2016 were included in the study. Inclusion criteria were a T2EL associated with growth of the aneurysm sac diameter by at least 5 mm compared with the diameter prior to EVAR or growth of the aneurysm sac diameter by less than 5 mm compared with the diameter prior to EVAR but associated with a growth of the largest diameter of the T2EL, as measured in the venous phase, compared with previous follow-up computed tomography (CT) imaging; however, our approach to include patients for T2EL embolization is rather aggressive compared with current society guidelines.<sup>9</sup> Patients with a T2EL associated with other types of endoleaks were excluded from the study. The decision to refer the patient for an embolization procedure was made in consensus during multidisciplinary case discussion meetings, which included vascular surgeons and interventional radiologists. The patients' demographics and clinical follow-up data were gathered from their electronic medical records. Radiological documents, including CT scans prior to and after EVAR, as well as angiographic studies and interventional procedures, were studied on a picture archiving and communication system (PACS, Agfa-Gevaert, Mortsel, Belgium). Measurements of the aortic aneurysm and side branches were performed prior to embolization on a graphical CT workstation (Syngo.via, Siemens Healthcare, Forchheim, Germany). Twenty-five patients (42%) were referred from community hospitals to the authors' institution for interventional management of T2ELs. Referred patients' data were collected after contacting the referring physician, and medical records and all available CT scans were reviewed for each patient.

Initial EVAR was performed using the Excluder device (W. L. Gore & Associates, Flagstaff, AZ, USA) on 28 patients (47%), the Zenith device (Cook, Bloomington, IN, USA) on 17 patients (28%), and the Endurant device (Medtronic, Minneapolis, MN, USA) on 9 patients (15%). Other devices were used on 6 patients [lifepath (n = 1), ovation (n = 1), fortron (n = 2), and talent (n = 2)]. All patients received lifelong aspirin at a dose of 80 mg daily after EVAR.

No prophylactic aortic side branch embolization to prevent T2ELs was performed prior to initial EVAR, despite recent insights suggesting pre-emptive aortic side branch embolization may be associated with lower rates of sac enlargement, incidence of T2ELs, and reinterventions.<sup>20</sup>

### Imaging studies

Patients underwent triphasic CT scans and catheter-directed angiography of the endoleak prior to referral for embolization. All CT scans in our institution were obtained using helical multidetector CT scanners; the type of CT scanner used depended on the time period of inclusion. The CT protocol for follow-up imaging after EVAR included a triple-phase technique with unenhanced, arterial, and delayed venous phases. Contrast-enhanced arterial phase images were generated during an injection of 80–120 mL (depending on the renal function of the patient) of non-ionic contrast material at a flow rate of 4 mL/second using bolus tracking with a threshold of 120 Hounsfield units. Delayed venous phase images were obtained 70 seconds after the arterial phase scan. Catheter-directed angiography of the endoleak was performed under local anesthesia through an arterial puncture in the right or left groin. Flush abdominal aortography in anteroposterior and profile views (30 mL of non-ionic iodized contrast medium at a flow rate of 10 mL/second) was performed using a pigtail catheter, followed by selective catheterization of the superior mesenteric artery (SMA) (20 mL of non-ionic iodized contrast medium at a flow rate of 4 mL/second) and the ipsilateral internal iliac artery and contralateral iliac stent-graft limb (10 mL of non-ionic iodized contrast medium at a flow rate of 5 mL/second) using a Simmons 2 catheter.

Patient follow-up after T2EL embolization took place at 1, 6, and 12 months, and yearly thereafter in accordance with the EUROSTAR guidelines for EVAR follow-up,<sup>5</sup> with special attention given to aneurysm sac diameter and persistence or disappearance of the embolized T2EL. Patients were followed up until the end of the study period (January 2019), the patient's death, or conversion by open surgical repair.

### Evaluation of imaging-based risk factors

Measurements performed on the aortic aneurysm and side branches prior to embolization included the maximum diameter of the AAA, maximum axial diameter (perpendicular to the long axis of the abdominal aorta) of the T2EL at the venous phase, patency of the lumbar arteries (LA) and inferior mesenteric artery (IMA). Additionally, the location of the endoleak in the AAA was determined (>75% of the endoleak area located anterior or posterior in the aneurysm sac) to

#### Main points

- Progression of aneurysm sac diameter is common after type 2 endoleak (T2EL) embolization.
- Unsharp (blurred) contours are predictive for a persistent T2EL.
- Greater need for surgical conversion is seen with blurred T2ELs.

show sharp (Figure 1) or unsharp (blurred) T2EL delineation. Blurred delineation was defined as irregular delineation of at least 75% of the endoleak contour (Figure 2). All measurements were performed after consensus by two interventional radiologists with 5 and 20 years of experience, respectively, in vascular radiology and embolization techniques. Progressive expansion or shrinkage of the aneurysm sac was defined as an increase or

decrease, respectively, of 5 mm or more in the maximum aneurysm diameter. An absence of significant change in AAA diameter (<5 mm) was recorded as no change in the aneurysm sac diameter.

Finally, the embolization approach (transarterial versus translumbar/transperitoneal access) was decided at the discretion of the attending interventional radiologist based on the location of the T2EL, the AAA sac,

surrounding tissues, and the maximum axial diameter of the endoleak (measured in axial sections in the delayed phase). The translumbar/transperitoneal approach was the first-line choice if percutaneous access to the T2EL was technically feasible and safe.

#### T2EL embolization technique

Patients' informed consent was obtained by both the referring vascular surgeon and the attending interventional radiologist prior to the embolization procedure. The anticoagulation regimen, including aspirin at a dose of 80 mg daily, was unchanged after the embolization procedure.

#### Transcatheter embolization of the T2EL

Under general anesthesia, a 4 or 5 French (F) sheath was inserted in the right or left common femoral artery, and catheterization of the SMA or ipsilateral internal iliac artery was performed using a 4 or 5 F Simmons 1 or Cobra catheter (Cook Medical, Bloomington, IN, USA; or Terumo Europe, Leuven, Belgium), followed by superselective catheterization using a microcatheter (Cantata 2.5, Cook Medical, Bloomington, IN, USA; or Maestro 2.4, Merit Medical, South Jordan, UT, USA) of the arc of Riolan and IMA or the iliolumbar artery and lower LA where the IMA or iliolumbar artery was the feeding artery of the T2EL, respectively. The microcatheter was advanced as close as possible to or into the nidus of the endoleak, and then embolics were injected in order to completely close the nidus of the T2EL. Embolics used included microcoils (Microtornado, Cook Medical, Bloomington, IN, USA; or Target microcoils, Boston Scientific, Natick, MA, USA), ethylene vinyl-alcohol copolymer (Onyx, Medtronic, Minneapolis, MN, USA), or glue as a 3:1 mixture of ethiodized oil (Lipiodol, Guerbet, Aulnay-sous-Bois, France) and n-butyl cyano-acrylate (Histoacryl, B. Braun, Melsungen, Germany).

#### Translumbar/transperitoneal embolization of the T2EL

With the patient under general anesthesia and in a prone or supine position, an unenhanced cone beam (CB) CT of the AAA was performed (XperCT, Philips Healthcare, Best, the Netherlands) and fused or visually confronted with the pre-interventional contrast-enhanced CT to determine the T2EL in the aneurysm sac. Using CB-CT-based puncture guidance techniques (XperGuide, Philips Healthcare, Best, the Netherlands), the nidus was percutaneously punctured using a sheathed 5 F needle (percutaneous



**Figure 1.** Venous phase, contrast-enhanced axial computed tomography image in a patient with a growing aneurysm sac and a sharply delineated type 2 endoleak (white arrows) posterior to the endograft limbs.



**Figure 2.** Venous phase, contrast-enhanced axial computed tomography image in a patient with a growing aneurysm sac and an unsharply delineated type 2 endoleak (small black arrows) anterior to the endograft limbs.

entry thinwall needle, Cook Medical, Bloomington, IN, USA). A microcatheter (Progreat 2.7, Terumo Europe, Leuven, Belgium) was introduced into the nidus through the 5 F sheath, and angiographic imaging of the nidus, afferent arteries, and efferent arteries was performed. These arteries were embolized with microcoils (Microtornado, Cook Medical, Bloomington, IN, USA; or target microcoils, Boston Scientific, Natick, MA, USA), and finally, the nidus was occluded using a 1:1 mixture of ethiodized oil (Lipiodol, Guerbet, Aulnay-sous-Bois, France) and n-butyl cyano-acrylate (histoacryl, B. Braun, Melsungen, Germany).

### Definitions for outcome after embolization

The outcome of the T2EL embolization was categorized as a technical, radiological, or clinical success. Technical success was defined as the nidus of the T2EL being fully approachable and completely embolized, with no evidence of residual contrast opacification on completion of angiography. Radiological success was determined by the absence of a persistent endoleak and unchanged or decreased diameter of the aneurysm sac at the latest follow-up CT. Finally, clinical success was defined as the absence of late aortic or endoleak-associated complications such as rupture or the need for surgical conversion on long-term follow-up.

### Statistical analysis

Statistical analyses were performed using SAS software (version 9.4 of the SAS System for Windows, Cary, NY, USA). The association between pre-operative characteristics and outcome was analyzed using univariate binary logistic regression models for persistent endoleaks, proportional odds models for ordinal outcomes (decreased/stable/increased aneurysm sac diameter), and linear regression models for continuous outcomes (changes in aneurysm sac diameter). The significance level was established as  $\alpha$ : 0.05. The Kaplan–Meier method was used to estimate the overall survival curve. The comparison between groups (e.g., increased versus stable/decreased aneurysm sac diameter) was performed using the Mann–Whitney U test for continuous variables, the chi-square test or Fisher’s exact test for categorical variables, or the log-rank test for overall survival. Inter- and intra-observer variability is assessed by Cohen’s kappa coefficient. The kappa coefficient takes values between 0 and 1, with higher values indicating better agreement. Interpretation of this statistic suggested by Fleiss characterizes kappa over 0.75 as excel-

lent, 0.40 to 0.75 as fair to good, and below 0.40 as poor.

The univariate Cox proportional-hazards model was fitted to associate persistent T2EL, aneurysm sac diameter increase, or need for reintervention with overall survival.

## Results

Sixty patients who presented with aortic aneurysm sac expansion after EVAR underwent an elective T2EL embolization at our institution, with a median time interval of 2.6 years (interquartile range 1.3–4.9 years) in between index EVAR and T2EL embolization procedure. The median follow-up time of our study population after embolization was 6.43 years (Q1–Q3, 4.93–9.00).

### Demographics and patient characteristics

The patients’ demographics and baseline clinical characteristics prior to embolization of the T2EL are listed in Table 1. The majority of patients in the study population were male (88.3%) with a median age of 79.5 years (range 62–89 years).

### Endoleak characterization and embolization technique/approach

Pre-interventional vascular imaging characteristics, including type and diameter of the AAA, delineation, and diameter at the location of the T2EL within the AAA, as well as data on the embolization procedures, are summarized in Table 2. In addition, the kappa-coefficient [95% confidence interval (CI)] for inter- and intra-observer variability was 0.64 (0.42; 0.85) and 0.88 (0.75; 1.00), respec-

tively. In 36 patients (60%), the indication for T2EL embolization was a mean sac expansion between pre-EVAR and pre-embolization (9.2 mm; 5–27 mm); a minimum increase of the maximum AAA sac diameter (<5 mm) associated with an increase in the diameter of the nidus of the T2EL (>5 mm) was an indication for embolization in 6 patients (10%). Finally, in 18 patients (30%), it was unclear whether the increase in the diameter of the T2EL or of the AAA was the main indication for embolization of the T2EL.

The afferent artery of the T2EL was the LA in 42 patients (70%), the IMA in 10 patients (16.7%), and a combination of the LA and IMA in 8 patients (13.3%).

### Technical, radiological, and clinical success

#### Technical success

In 57 patients (95%), it was possible to embolize the nidus of the T2EL completely, as demonstrated on completion angiography. In 3 patients (5%), incomplete embolization of the nidus of the T2EL was demonstrated on completion angiography; two of these three patients were embolized in a translumbar approach using glue, which resulted in a partial filling of the nidus of the T2EL. However, follow-up CT scans were not able to demonstrate either a persistent T2EL or progressive expansion of the aneurysm sac. The remaining patient was treated using a transcatheter approach for a T2EL fed by a left ilio-lumbar artery. Superselective embolization was performed using glue and resulted in the partial filling of the endoleak. A follow-up unenhanced CT scan revealed a persistent increase in AAA diameter from 86

**Table 1.** Patients’ demographics and baseline clinical characteristics

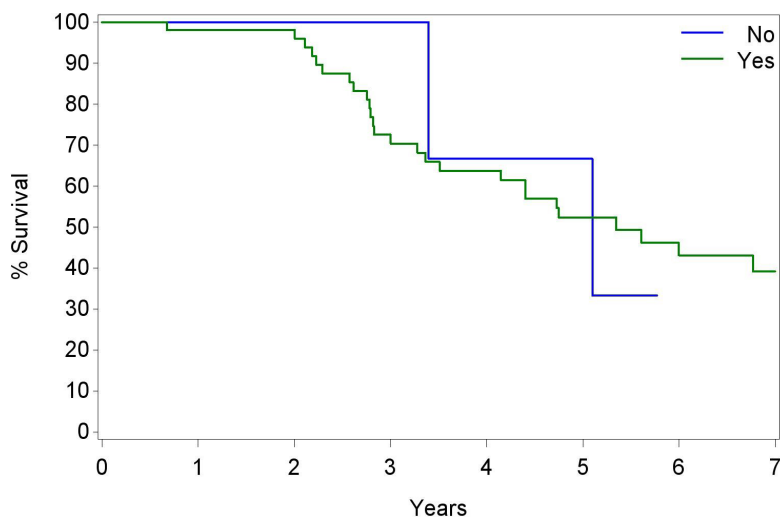
Demographic parameter	Statistic	All
<b>Age</b>	n	60
	Median	79.5
	Q1, Q3	(72.0; 83.0)
<b>Sex</b>		
Male	n (%)	53 (88.33%)
Female	n (%)	7 (11.67%)
Smoking	n (%)	28 (46.67%)
Diabetes	n (%)	4 (6.67%)
Coronary artery disease	n (%)	15 (25%)
Chronic renal insufficiency	n (%)	4 (6.67%)
Arterial hypertension	n (%)	42 (70%)
COPD	n (%)	7 (11.67%)
Hyperlipidemia/hypercholesterolemia	n (%)	28 (46.67%)
Peripheral vascular disease	n (%)	4 (6.67%)

Q1, Q3, first and third quartile; COPD, chronic obstructive pulmonary disease.

**Table 2.** Pre-interventional vascular imaging characteristics and data on the embolization procedures

Pre-interventional vascular imaging characteristics	Statistic	All
<b>Type of abdominal aortic aneurysm</b>		
Infrarenal, aorto-bi-iliac AAA	n (%)	1 (1.67%)
Infrarenal, aorto-left-iliac AAA	n (%)	2 (3.33%)
Infrarenal, aorto-right-iliac AAA	n (%)	6 (10%)
Infrarenal AAA	n (%)	51 (85%)
<b>AAA diameter (mm) prior to type 2 endoleak embolization</b>		
	n	60
	Median	70.5
	Q1, Q3	(63.0; 78.0)
<b>Type 2 endoleak diameter (mm) prior to embolization</b>		
	n	60
	Median	25.0
	Q1, Q3	(18.0; 35.0)
<b>Type of endoleak type 2 delineation</b>		
Blurred (patchy)	n (%)	17 (28.33%)
Sharp	n (%)	43 (71.67%)
<b>Location of type 2 endoleak in AAA</b>		
Anterior	n (%)	12 (20%)
Posterior	n (%)	48 (80%)
<b>Approach to type 2 endoleak</b>		
Transarterial	n (%)	12 (20%)
Translumbar	n (%)	48 (80%)
<b>Embolization material to occlude type 2 endoleak</b>		
Glue (lipiodol and embucrylate)	n (%)	29 (48.33%)
Glue (lipiodol and embucrylate) and microcoils	n (%)	26 (43.33%)
Microcoils	n (%)	3 (5%)
Onyx	n (%)	2 (3.33%)

AAA, abdominal aortic aneurysm; Q1, Q3, first and third quartile.



Number at risk		0	1	2	3	4	5	6	7
No	Yes	56	52	46	33	28	20	14	10

**Figure 3.** No significant difference in overall survival was observed in patients with or without technically successful type 2 endoleak embolization procedure ( $P = 0.9158$ ).

mm prior to embolization to 99 mm at the latest follow-up CT. Long-term clinical follow-up did not reveal any AAA rupture up to the time of patient death due to cardiac decompensation. Kaplan–Meier analysis could not demonstrate a difference in survival between patients with and without technically successful T2EL embolization ( $P = 0.916$ ), as shown in Figure 3. A serious post-embolization complication was observed in 2 patients at 10 and 12 months, respectively, after initially successful translumbar and transcatheter embolization; this was due to infection of the endograft and bilateral psoas abscesses (Figure 4a-c). The responsible microorganisms in the translumbar case were *Staphylococcus hominis* and *Staphylococcus capitis*. Both of these are human skin commensals, suggesting that the infection was inoculated through the percutaneous puncture. These serious infection complications were definitively and successfully resolved with stent-graft resection and surgical aorto-bi-iliac reconstruction with autologous deep vein.

In 4 patients (6.7%), a second embolization procedure was performed 11, 20, 21, and 34 months, respectively, after the initial translumbar T2EL, due to a persistent T2EL in combination with progressive growth of the AAA sac, identified on follow-up CT scan at 6 months, 1 year, 1 year, and 2 years, respectively, after initial T2EL embolization.

### Radiological success

Follow-up with multiphase CT scans was performed in 59 patients (98.3%). In one patient (1.7%), follow-up was performed with duplex ultrasound and an unenhanced CT scan at the referring hospital due to chronic renal insufficiency. Median radiological follow-up after T2EL embolization was 5.3 years (3.5–7.0 years). On follow-up CT scans, a persistent post-embolization T2EL was noted in 35 patients (58.3%). This was associated with an increase in maximum aneurysm sac diameter in 31 patients (51.7%) with a mean increase in maximum sac diameter of 8.3 mm, as summarized in Table 3. Twenty-two patients (36.7%) showed stable aortic diameter, and 7 patients (11.7%) showed a decrease in AAA diameter. Overall, radiological success was observed in 16 patients (26.7%).

Pre-interventional unsharp or blurred T2EL delineation was statistically significant as a predictive factor for a persistent endoleak at follow-up ( $P = 0.025$ ). Other imaging or embolization variables showed no statistically significant difference in radiological or clinical success (Table 4).



**Figure 4.** (a) Venous phase, contrast-enhanced axial computed tomography (CT) image in a patient with a growing aneurysm sac and a sharply delineated type 2 endoleak (small black arrows) posterior to the endograft limbs; the patient was referred for translumbar direct puncture and embolization of the type 2 endoleak. (b) Digital subtraction angiography of the nidus (large black arrows) of the type 2 endoleak after direct translumbar puncture. Also, note the coils (small black arrows) deployed in the proximal left fourth lumbar artery. (c) Follow-up contrast-enhanced CT scan nine months after translumbar endoleak embolization demonstrating the cast of glue (mixture of embucrylate and ethiodized oil) (small black arrows) completely filling the type 2 endoleak. Also note the contrast-enhancing foci in both psoas muscles (large black arrows), suggestive of psoas abscesses.

Blurred T2EL delineation at the pre-embolization CT scan was observed in 17 patients (28.3%), with a mean aneurysm sac diameter increase of 10.9 mm (median 10.0, Q1–Q3, 0.0–15.0, range –6.0–38.0 mm). Of the 17 patients (64.7%) with blurred T2EL delineation, 11 showed an increase in AAA diameter, 5 (29.4%) had a stable AAA diameter, and only 1 patient (5.9%) showed a decrease in AAA diameter after T2EL embolization.

Smoking and hyperlipidemia were associated with radiological success ( $P = 0.010$  and  $P = 0.047$ , respectively), as summarized in Table 4. Kaplan–Meier analysis could not demonstrate a difference in survival between patients with and without radiological success after T2EL embolization ( $P = 0.813$ ), as shown in Figure 5.

**Table 3.** Radiological outcome after type 2 endoleak embolization

Variable	Statistic	All
<b>Technical success</b>		
Yes	n (%)	57 (95.00%)
<b>Persistent endoleak after T2EL embolization</b>		
Yes	n (%)	35 (58.33%)
<b>Change in AAA diameter after T2EL embolization</b>		
Decreased	n (%)	7 (11.67%)
Stable	n (%)	22 (36.67%)
Increased	n (%)	31 (51.67%)
<b>Absolute change in AAA diameter after T2EL embolization</b>		60
	Median	4.5
	Q1, Q3	(0.0; 14.0)
<b>Radiological success after T2EL embolization</b>		
Increased AAA diameter and/or persistent endoleak	n (%)	44 (73.33%)
Stable or decreased AAA diameter and no persistent endoleak	n (%)	16 (26.67%)
<b>Clinical success after T2EL embolization</b>		
Yes	n (%)	46 (76.67%)

T2EL, type 2 endoleak; AAA, abdominal aortic aneurysm; Q1, Q3, first and third quartile.

**Table 4.** Relation between patients' demographics, imaging characteristics, and radiological/clinical outcome

Patients' demographics		Radiological success			Clinical success			
	Statistic	No	Yes	P value	No	Yes	P value	
Sex	Male	n (%)	38 (71.7%)	15 (28.3%)	0.663	12 (22.6%)	41 (77.4%)	0.660
	Female	n (%)	6 (85.7%)	1 (14.3%)		2 (28.6%)	5 (71.4%)	
Smoking	No	n (%)	28 (87.5%)	4 (12.5%)	0.008	11 (34.4%)	21 (65.6%)	0.031
	Yes	n (%)	16 (57.1%)	12 (42.9%)		3 (10.7%)	25 (89.3%)	
Diabetes	No	n (%)	37 (69.8%)	16 (30.2%)	0.173	12 (22.6%)	41 (77.4%)	0.660
	Yes	n (%)	7 (100.0%)	0 (0.0%)		2 (28.6%)	5 (71.4%)	
Chronic renal failure	No	n (%)	42 (75.0%)	14 (25.0%)	0.287	14 (25.0%)	42 (75.0%)	0.564
	Yes	n (%)	2 (50.0%)	2 (50.0%)		0 (0.0%)	4 (100.0%)	
Coronary artery disease	No	n (%)	33 (73.3%)	12 (26.7%)	1.000	12 (26.7%)	33 (73.3%)	0.483
	Yes	n (%)	11 (73.3%)	4 (26.7%)		2 (13.3%)	13 (86.7%)	
Hypertension	No	n (%)	14 (77.8%)	4 (22.2%)	0.755	4 (22.2%)	14 (77.8%)	1.000
	Yes	n (%)	30 (71.4%)	12 (28.6%)		10 (23.8%)	32 (76.2%)	
COPD	No	n (%)	40 (75.5%)	13 (24.5%)	0.370	13 (24.5%)	40 (75.5%)	1.000
	Yes	n (%)	4 (57.1%)	3 (42.9%)		1 (14.3%)	6 (85.7%)	
Hyperlipidemia	No	n (%)	27 (84.4%)	5 (15.6%)	0.039	8 (25.0%)	24 (75.0%)	0.744
	Yes	n (%)	17 (60.7%)	11 (39.3%)		6 (21.4%)	22 (78.6%)	
Peripheral vascular disease	No	n (%)	42 (75.0%)	14 (25.0%)	0.287	13 (23.2%)	43 (76.8%)	1.000
	Yes	n (%)	2 (50.0%)	2 (50.0%)		1 (25.0%)	3 (75.0%)	
Age (at embolization)	n		44	16		14	46	
	Median		79.0	80.0	0.834	77.5	80.0	0.506
	Q1, Q3		(71.5; 83.0)	(72.0; 84.5)		(74.0; 82.0)	(71.0; 84.0)	
<b>Post-embolization persistent endoleak on follow-up CT examination</b>								
<b>Imaging characteristic</b>				<b>Odds ratio (95% CI)</b>	<b>P value</b>	<b>n patients</b>		
Approach		Transarterial vs. direct puncture		0.655 (0.184; 2.335)	0.514	60		
Embolization technique		Global test			0.049	60		
Type 2 endoleak origin		Global test			0.955	60		
Maximal endoleak diameter				0.970 (0.921; 1.023)	0.260	60		
Endoleak contour		Blurred vs. sharp		4.889 (1.226; 19.488)	0.025	60		
Endoleak location in the AAA		Anterior vs. posterior location		2.538 (0.611; 10.551)	0.200	60		
<b>Change in aneurysm sac diameter (increased vs. stable/decreased)</b>								
<b>Imaging characteristic</b>				<b>Odds ratio (95% CI)</b>	<b>P value</b>	<b>n patients</b>		
Approach		Transarterial vs. direct puncture		0.598 (0.180; 1.988)	0.402	60		
Embolization technique		Global test			0.152	60		
Type 2 endoleak origin		Global test			0.127	60		
Maximal endoleak diameter				0.970 (0.923; 1.019)	0.228	60		
Endoleak contour		Blurred vs. sharp		2.159 (0.691; 6.743)	0.186	60		
Endoleak location in the AAA		Anterior vs. posterior location		0.438 (0.131; 1.461)	0.179	60		
<b>Clinical success</b>								
<b>Imaging characteristic</b>				<b>Odds ratio (95% CI)</b>	<b>P value</b>	<b>n patients</b>		
Approach		Transarterial vs. direct puncture		1.667 (0.319; 8.703)	0.545	60		
Embolization technique		Global test			0.882	60		
Type 2 endoleak origin		Global test			0.578	60		
Maximal endoleak diameter				0.992 (0.935; 1.053)	0.801	60		
Endoleak contour		Blurred vs. sharp		0.419 (0.119; 1.473)	0.175	60		
Endoleak location in the AAA		Anterior vs. posterior location		1.667 (0.319; 8.703)	0.545	60		

COPD, chronic obstructive pulmonary disease; Q1, Q3, first and third quartile; CI, confidence interval; CT, computed tomography; AAA, abdominal aortic aneurysm.

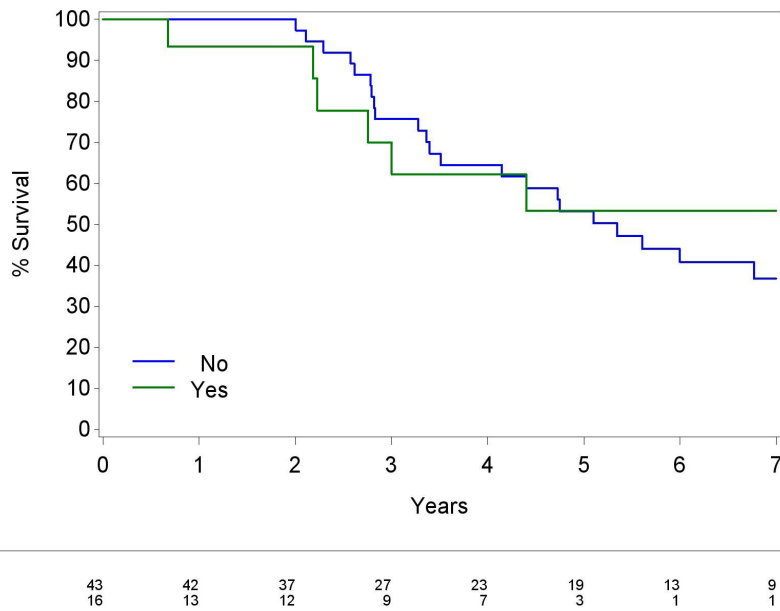


**Figure 5.** No significant difference in overall survival was observed in patients with or without radiological success after type 2 endoleak embolization procedure ( $P = 0.8125$ ).

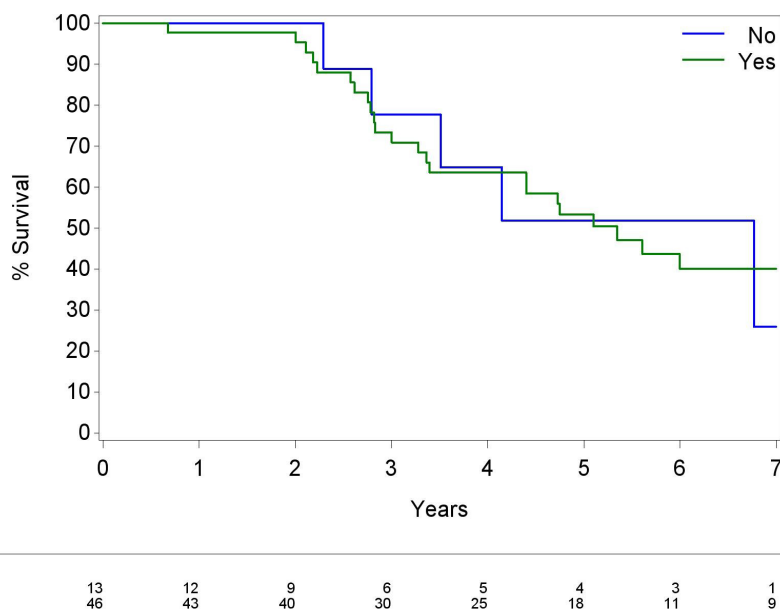


**Figure 6.** No significant difference in overall survival was observed in patients with or without clinical success after type 2 endoleak embolization procedure ( $P = 0.8045$ ).

### Clinical success

Clinical success was achieved in 46 patients (76.7%). Overall, 11 patients (18.3%) were referred for surgical conversion after T2EL embolization. In 3 patients (5%), late rupture of the AAA occurred post-T2EL embolization. All 3 patients showed an increase in AAA diameter and had a persistent T2EL at their follow-up CT scans. In two of these three patients, an additional type 1 endoleak, which was not visible on the CT scan,

was identified during surgery. Two patients who presented with stable or decreased AAA diameter underwent open surgery 12 and 10 months, respectively, after T2EL embolization, in connection with an infected endograft. However, no difference in overall survival was found between patients with and without clinical success after T2EL embolization ( $P = 0.805$ ), as summarized in Figure 6.

Patients showing an increase in AAA diameter after T2EL embolization had a greater

need for surgical conversion ( $P = 0.043$ ); this applied to 9 patients in this subgroup, compared with only 2 conversions in patients with a stable or decreased AAA diameter. Patients with the combination of blurred pre-embolization T2EL delineation and a persistent post-embolization AAA diameter increase also had a greater need for surgical conversion ( $P = 0.022$ ); this was the case in 5 patients (45.5%), compared with 6 out of 49 patients (12.2%) without this combination of imaging characteristics (the residual group) who required surgical conversion.

Median survival after T2EL embolization in our study population was 5.35 years (3.51–7.07, +/-95% CI). The 2-year survival rate was 98.25% (88.19%–99.75%), the 5-year survival rate was 53.23% (38.38%–66.03%), and the 10-year survival rate was 21.24% (8.67%–37.48%) (Figure 7). There was no mortality related to the embolization procedure or to persistent aneurysm growth late after embolization or to secondary aortic interventions. Smoking was the only clinical parameter associated with clinical success after T2EL embolization ( $P = 0.037$ ). No statistical difference in overall success could be demonstrated between patients with ( $n = 29$ ) and without ( $n = 31$ ) a persistent increase in maximum sac diameter after T2EL embolization ( $P = 0.561$ ). Last, univariate analyses for overall survival could not demonstrate any parameter associated with a higher risk for increased mortality, as summarized in Table 5.

## Discussion

This study confirms that embolization therapy for a T2EL in patients with a progressive expansion of the AAA sac after EVAR is feasible and relatively safe. In 95% of included patients, the nidus of the T2EL could be accessed with catheters or needles and completely embolized. This is in line with other studies showing a primary technical success rate between 58% and 100%.<sup>18,21,22</sup> In addition, these high technical success rates are found irrespective of the access route to the T2EL, including transcatheter or translumbar/transperitoneal access,<sup>14,18,21,23–26</sup> or the type of embolic agent used.<sup>26–28</sup> Complications related to the embolization procedure are uncommon, with an incidence ranging from 0% to 10%, and may include septic, ischemic, and neurological events.<sup>19</sup> In the presented case studies, two (3.2%) stent-graft infections occurred, most probably related to contamination during direct percutaneous puncture.<sup>29,30</sup> Curative surgical intervention with stent-graft resection and aorto-bi-iliac reconstruction with autologous deep vein,

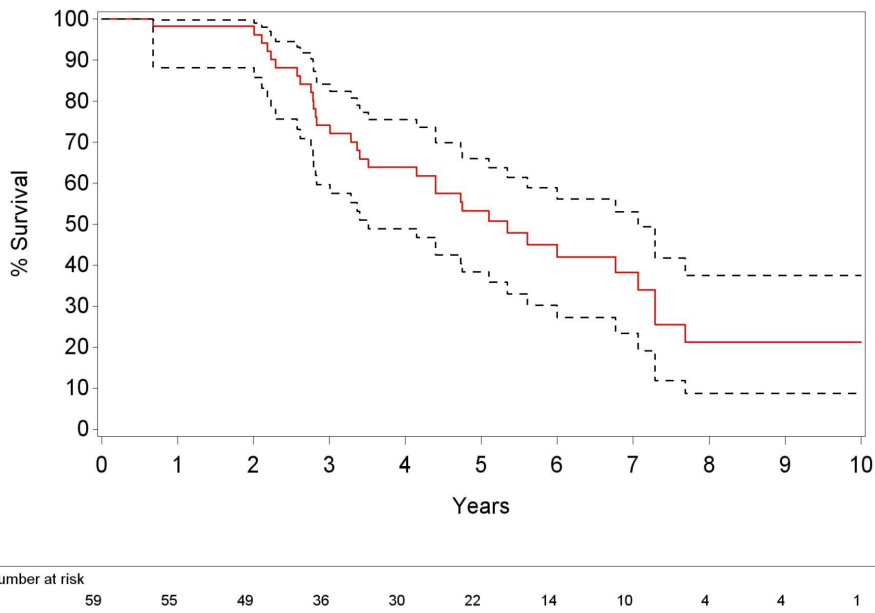


**Figure 7.** Kaplan–Meier analysis shows estimated 2-year survival in 98.25% (88.19%–99.75%) of patients, 5-year survival in 53.23% (38.38%–66.03%), and 7-year survival in 38.24% (23.35%–52.97%) after type 2 endoleak embolization.

**Table 5.** Univariate analysis for overall survival

Parameter	Hazard ratio	P value
Persistent type 2 endoleak	0.849 (0.421; 1.710)	0.646
Aneurysm sac diameter increase	1.234 (0.602; 2.529)	0.566
Need for reintervention	0.886 (0.341; 2.306)	0.805

as performed in the two reported cases, provided by far the best outcome.<sup>31</sup> Sella et al.<sup>32</sup> described another infectious complication related to translumbar direct T2EL percutaneous puncture, namely osteomyelitis and discitis of L3–L4 vertebral bodies.

Despite the high technical success rate, the long-term radiological and clinical success rates are moderate. In half the embolized patients in this study, persistent expansion of the aneurysm sac was observed after embolization therapy. Combined complete disappearance of the T2EL and stable or decreased AAA diameter was observed in about a quarter of embolized patients. These results are rather disappointing, as the failure of the aneurysm sac to regress after EVAR is associated with higher long-term mortality;<sup>33</sup> however, the presented results match with those found by Arenas Azofra et al.<sup>14</sup> Therefore, long-term follow-up after T2EL embolization seems mandatory.<sup>34</sup>

Both pre-interventional imaging and clinical parameters for a higher risk of persistent aneurysm sac expansion after T2EL embolization were analyzed, showing unsharp or blurred delineation of the nidus of the T2EL to be predictive of a persistent T2EL

after embolization ( $P = 0.025$ ). Potentially, the nidus in these T2ELs might have been much larger than identified on CT scans or angiography, and embolization with liquids might not have covered the whole volume of the leak, resulting in high recurrence rates of the T2ELs. Dudeck et al.<sup>23</sup> found the volume of the nidus to be a predictor for late T2EL recurrence; however, in this study, the maximum diameter of the nidus as visualized by CT scan was not predictive of late recurrence ( $P = 0.801$ ); Mursalin et al.<sup>21</sup> reported the endoleak appearance time on the final operative angiogram and attenuation of the endoleak cavity on the first postoperative CT scan as strong image-based predictors of a persistent T2EL after embolization. In addition, two pre-interventional clinical parameters were identified as predictors for a better outcome. Smoking was found to be a protective factor against a persistent T2EL, aneurysm sac expansion, and the need for late surgical conversion, while hyperlipidemia was associated with better radiological success. These findings are in line with the data presented by Koole et al.<sup>35</sup>, showing fewer late T2ELs during post-embolization follow-up in smokers. These findings might be related to the decreased endoleak per-

fusion associated with atherosclerotic injury of small- and medium-sized afferent and efferent arteries of the T2EL and an increased tendency of coagulation, which might further narrow or occlude afferent and efferent arteries. However, in a univariate analysis, Sarac et al.<sup>19</sup> found continued tobacco use and hyperlipidemia to be associated with continued sac expansion and more secondary embolization procedures, respectively.

Clinical success, defined as the absence of late aortic or endoleak-associated complications, such as rupture or need for surgical conversion, was 76%, which is in line with the results of Sarac et al.<sup>19</sup>, who found freedom from second embolization in 76% of patients. The main indication for late surgical conversion was persistent AAA sac expansion despite embolization therapy in patients potentially considered fit for surgery, which was performed in nearly 20% of the study population. In addition, 3 patients (5%) underwent urgent surgical conversion due to AAA rupture. In two of these three patients, a concomitant type 1 endoleak was identified perioperatively. These observations may confirm the findings of Madigan et al.<sup>36</sup> and Aziz et al.<sup>37</sup>, revealing an unexpected type 1 or 3 endoleak in association with a known T2EL in 20% of patients converted to surgical repair for the T2EL. Funaki et al.<sup>22</sup> found that type 3 endoleaks were believed to be T2ELs in 7 out of 25 patients (28%). Finally, in 1 patient (1.6%), rupture was associated with an isolated T2EL and expanding AAA sac, which is in line with a 1% to 2% rate of rupture for AAA after EVAR with a persistent T2EL.<sup>7,9,15</sup>

The present study reveals an estimated overall survival rate of 53% and 21% at 5 and 10 years of follow-up, respectively. Additionally, no difference in survival was found between patients with or without AAA sac expansion after T2EL embolization. These findings are in line with the outcomes found by Walker et al.<sup>10</sup> based on a multicenter EVAR registry, concluding that overall all-cause mortality and aneurysm-related mortality are unaffected by the presence of a T2EL. It should be noted that we did not encounter 30-day mortality in the 11 patients treated by surgical conversion for sac expansion associated with a persistent T2EL after embolization therapy.

We also analyzed a subgroup of patients presenting with blurred T2EL delineation prior to embolization that was associated with persistent aneurysm sac expansion after embolization. This subgroup had a significantly higher risk for late surgical conversion com-

pared with other included patients without these two imaging characteristics ( $P = 0.022$ ). Potentially, patients in this specific subgroup might be selected as good candidates for early conversion to surgery if no response to embolization therapy is identified on the first follow-up CT scan.

Finally, this study also has some limitations. First, this is a retrospective, single-center study with a limited number of included patients treated over a period of more than 10 years. However, the inclusion and exclusion criteria for referral to embolization therapy did not change over that time. Second, several clinical and radiological parameters for better or worse outcomes were analyzed; however, these parameters were based on the authors' interests, not on predefined lists. Third, the radiological techniques used to access the nidus of the T2EL and the embolics used for endoleak occlusion were at the discretion of the attending interventional radiologist, without any randomization. Fourth, the evaluation of the endoleak's configuration in sharp or unsharp delineation needs to be proven in future studies and might be dependent on the experience of the reading physicians, as the interobserver agreement for endoleak configuration was rather fair. Lastly, no comparison was made with a control group.

In conclusion, this retrospective study demonstrates a high technical success rate of T2EL embolization, with moderate long-term radiological and clinical outcomes. Blurred delineation of the T2EL is associated with a significantly higher risk of persistent post-embolization T2EL. Although no difference in overall survival was observed between patients with or without persistent AAA sac expansion after T2EL embolization, patients with blurred T2EL delineation prior to embolization, associated with persistent aneurysm sac expansion after embolization, were at a significantly higher risk of requiring late surgical conversion as a definitive treatment for the T2EL and persistent sac expansion.

#### Conflict of interest disclosure

The authors declared no conflicts of interest.

#### References

1. Wanhainen A, Verzini F, Van Herzele I, et al. Editor's Choice- European Society for Vascular Surgery (ESVS) 2019 Clinical Practice Guidelines on the Management of Abdominal

- Aorto-iliac Artery Aneurysms. *Eur J Vasc Endovasc Surg.* 2019;57(1):8-93. Erratum in: *Eur J Vasc Endovasc Surg.* 2020;59(3):494. [\[CrossRef\]](#)
2. Chaikof EL, Dalman RL, Eskandari MK, et al. The Society of Vascular Surgery practice guidelines on the care of patients with an abdominal aortic aneurysm. *J Vasc Surg.* 2018; 67(1):2-77. [\[CrossRef\]](#)
3. Chung R, Morgan RA. Type 2 endoleaks post-EVAR: current evidence for rupture risk, intervention and outcomes of treatment. *Cardiovasc Intervent Radiol.* 2015;38(3):507-522. [\[CrossRef\]](#)
4. Jones JE, Atkins MD, Brewster DC, et al. Persistent type 2 endoleak after endovascular repair of abdominal aortic aneurysm is associated with adverse late outcomes. *J Vasc Surg.* 2007;46(1):1-8. [\[CrossRef\]](#)
5. van Marrewijk C, Buth J, Harris PL, Norgren L, Nevelsteen A, Wyatt MG. Significance of endoleaks after endovascular repair of abdominal aortic aneurysms: the EUROSTAR experience. *J Vasc Surg.* 2002;35(3):461-473. [\[CrossRef\]](#)
6. Cierci E, De Rango P, Isernia G, et al. Type II endoleak is an enigmatic and unpredictable marker of worse outcome after endovascular aneurysm repair. *J Vasc Surg.* 2014;59(4):930-937. [\[CrossRef\]](#)
7. Sidloff DA, Stather PW, Choke E, Bown MJ, Sayers RD. Type II endoleak after endovascular aneurysm repair. *Br J Surg.* 2013;100(10):1262-1270. [\[CrossRef\]](#)
8. Avgerinos ED, Chaer RA, Makaroun MS. Type II endoleaks. *J Vasc Surg.* 2014; 60(5):1386-1391. [\[CrossRef\]](#)
9. Sidloff DA, Gokani V, Stather PW, Choke E, Bown MJ, Sayers RD. Type II endoleak: conservative management is a safe strategy. *Eur J Vasc Endovasc Surg.* 2014;48(4):391-399. [\[CrossRef\]](#)
10. Walker J, Tucker LY, Goodney P, et al. Type II endoleak with or without intervention after endovascular aortic aneurysm repair does not change aneurysm-related outcomes despite sac growth. *J Vasc Surg.* 2015;62(3):551-561. [\[CrossRef\]](#)
11. El Batti S, Cochenec F, Roudot-Thoraval F, Becquemain JP. Type II endoleaks after endovascular repair of abdominal aortic aneurysm are not always a benign condition. *J Vasc Surg.* 2013;57(5):1291-1297. [\[CrossRef\]](#)
12. Patel R, Sweeting MJ, Powell JT, Greenhalgh RM; EVAR trial investigators. Endovascular versus open repair of abdominal aortic aneurysm in 15-years' follow-up of the UK endovascular aneurysm repair trial 1 (EVAR trial 1): a randomised controlled trial. *Lancet.* 2016;388(10058):2366-2374. [\[CrossRef\]](#)
13. Ultee KHJ, Büttner S, Huurman R, et al.

- meta-analysis of the outcome of treatment for type II endoleak following endovascular aneurysm repair. *Eur J Vasc Endovasc Surg.* 2018;56(6):794-807. [\[CrossRef\]](#)
14. Arenas Azofra E, Rey VM, Marcos FÁ, Al-Sibbai AZ, García FV, Pérez MA. Results of transarterial embolization for treating type 2 endoleaks: a single-center experience. *Ann Vasc Surg.* 2020;66:104-109. [\[CrossRef\]](#)
15. Ultee KHJ, Büttner S, Huurman R, et al. Editor's choice - systematic review and meta-analysis of the outcome of treatment for type II endoleak following endovascular aneurysm repair. *Eur J Vasc Endovasc Surg.* 2018;56(6):794-807. [\[CrossRef\]](#)
16. Jouhannet C, Alsac JM, Julia P, et al. Reinterventions for type 2 endoleaks with enlargement of the aneurysmal sac after endovascular treatment of abdominal aortic aneurysms. *Ann Vasc Surg.* 2014;28(1):192-200. [\[CrossRef\]](#)
17. Gallagher KA, Ravin RA, Meltzer AJ, et al. Midterm outcomes after treatment of type II endoleaks associated with aneurysm sac expansion. *J Endovasc Ther.* 2012;19(2):182-192. Erratum in: *J Endovasc Ther.* 2012;19(3):A6.
18. Nevala T, Biancari F, Manninen H, et al. Type II endoleak after endovascular repair of abdominal aortic aneurysms: effectiveness of embolization. *Cardiovasc Intervent Radiol.* 2010;33(2):278-284. [\[CrossRef\]](#)
19. Sarac TP, Gibbons C, Vargas L, et al. Long-term follow-up of type II endoleak embolization reveals the need for close surveillance. *J Vasc Surg.* 2012;55(1):33-40. [\[CrossRef\]](#)
20. Yu HYH, Lindström D, Wanhainen A, Tegler G, Hassan B, Mani K. Systematic review and meta-analysis of prophylactic aortic side branch embolization to prevent type II endoleaks. *J Vasc Surg.* 2020;72(5):1783-1792. [\[CrossRef\]](#)
21. Mursalin R, Sakamoto I, Nagayama H, et al. Imaging-Based Predictors of Persistent Type II endoleak after endovascular abdominal aortic aneurysm repair. *AJR Am J Roentgenol.* 2016;206(6):1335-1340. [\[CrossRef\]](#)
22. Funaki B, Birouti N, Zangan SM, et al. Evaluation and treatment of suspected type II endoleaks in patients with enlarging abdominal aortic aneurysms. *J Vasc Interv Radiol.* 2012;23(7):866-872; quiz 872. [\[CrossRef\]](#)
23. Dudeck O, Schnapauff D, Herzog L, et al. Can early computed tomography angiography after endovascular aortic aneurysm repair predict the need for reintervention in patients with type II endoleak? *Cardiovasc Intervent Radiol.* 2015;38(1):45-52. [\[CrossRef\]](#)
24. Yang RY, Tan KT, Beecroft JR, Rajan DK, Jaskolka JD. Direct sac puncture versus transarterial embolization of type II endoleaks: an evaluation and comparison of outcomes. *Vascular.* 2017;25(3):227-233. [\[CrossRef\]](#)

25. Stavropoulos SW, Park J, Fairman R, Carpenter J. Type 2 endoleak embolization comparison: translumbar embolization versus modified transarterial embolization. *J Vasc Interv Radiol.* 2009;20(10):1299-1302. [\[CrossRef\]](#)
26. Zener R, Oreopoulos G, Beecroft R, Rajan DK, Jaskolka J, Tan KT. Transabdominal direct sac puncture embolization of type II endoleaks after endovascular abdominal aortic aneurysm repair. *J Vasc Interv Radiol.* 2018;29(8):1167-1173. [\[CrossRef\]](#)
27. Marcelin C, Le Bras Y, Petitpierre F, et al. Safety and efficacy of embolization using Onyx<sup>®</sup> of persistent type II endoleaks after abdominal endovascular aneurysm repair. *Diagn Intervent Imaging.* 2017;98(6):491-497. [\[CrossRef\]](#)
28. Lagios K, Karaolani G, Bazinas T, Perdikides T, Bountouris I. Translumbar infusion of n-butyl cyanoacrylate for the treatment of type II endoleaks. *J Vasc Interv Radiol.* 2018;29(6):826-832. [\[CrossRef\]](#)
29. Harlock JA, Qadura M, Lee G, Szalay DA. Infected aortic stent graft with *Propionibacterium acnes*. *Vasc Endovascular Surg.* 2013;47(5):394-396. [\[CrossRef\]](#)
30. Li B, Tan KT, MacDonald ME, Byrne J. Aortic graft infection with enteric organism after embolization of late type II endoleak. *J Vasc Surg Cases Innov Tech.* 2019;5(1):61-64. [\[CrossRef\]](#)
31. Antonello RM, D'Oria M, Cavallaro M, et al. Management of abdominal aortic prosthetic graft and endograft infections. A multidisciplinary update. *J Infect Chemother.* 2019;25(9):669-680. [\[CrossRef\]](#)
32. Sella D, Frey G, Giesbrandt K. Osteomyelitis and discitis following translumbar repair of a type II endoleak. *Cardiovasc Intervent Radiol.* 2016;39(3):458-461. [\[CrossRef\]](#)
33. O'Donnell TFX, Deery SE, Boitano LT, et al. Aneurysm sac failure to regress after endovascular aneurysm repair is associated with lower long-term survival. *J Vasc Surg.* 2019;69(2):414-422. [\[CrossRef\]](#)
34. D'Oria M, Mastrorilli D, Ziani B. Natural history, diagnosis, and management of type II endoleaks after endovascular aortic repair: review and update. *Ann Vasc Surg.* 2020;62:420-431. [\[CrossRef\]](#)
35. Koole D, Moll FL, Buth J, et al. The influence of smoking on endovascular abdominal aortic aneurysm repair. *J Vasc Surg.* 2012;55(6):1581-1586. [\[CrossRef\]](#)
36. Madigan MC, Singh MJ, Chaer RA, Al-Khoury G, Makaroun MS. Occult type I or III endoleaks are common cause of failure of type II endoleak treatment after endovascular aortic repair. *J Vasc Surg.* 2019;69:432-439. [\[CrossRef\]](#)
37. Aziz A, Menias CO, Sanchez LA, et al. Outcomes of percutaneous endovascular intervention for type II endoleak with aneurysm expansion. *J Vasc Surg.* 2012;55(5):1263-1267. [\[CrossRef\]](#)



# Long-term outcomes of combined radiofrequency ablation and multipronged ethanol ablation for the treatment of unfavorable hepatocellular carcinoma

Ming Liu   
Xiao-Ju Li   
Xiao-Er Zhang   
Ming Kuang   
Xiao-Yan Xie   
Guang-Liang Huang 

## PURPOSE

To evaluate the local efficacy, safety, and long-term outcomes of combined radiofrequency ablation (RFA) and multipronged ethanol ablation (EA) in the treatment of unfavorable hepatocellular carcinoma (HCC) and to determine the prognostic factors for survival.

## METHODS

Between August 2009 and December 2017, 98 patients with 110 unfavorable HCC nodules who underwent combined RFA and multipronged EA were retrospectively enrolled in the study. Unfavorable HCC was defined as a medium (3.1–5.0 cm) or large (5.1–7.0 cm) HCC nodule, a tumor located at a high-risk site, or a perivascular tumor. The treatment response, overall survival (OS), and recurrence-free survival (RFS) were analyzed. The Kaplan–Meier method and Cox proportional hazards regression model were used to evaluate the prognostic factors.

## RESULTS

Complete ablation was obtained in 80.9% (89/110) of the tumors after initial treatment. Major complications were observed in 3 (3.1%) patients. The cumulative incidence of local tumor progression (LTP) was 23.5% at five years, and no variable was found to be an independent predictive factor for LTP. The five-year OS and RFS rates were 41.9% and 34.0%, respectively. Multivariate analysis showed that the serum alpha-fetoprotein level, tumor size, presence of residual tumor after ablation, and extrahepatic metastases were significant prognostic factors for OS ( $P = 0.023$ ,  $P = 0.030$ ,  $P = 0.001$ , and  $P = 0.010$ , respectively). Tumor type and the number of tumors were predictive factors for RFS ( $P = 0.029$  and  $P = 0.001$ , respectively). A perivascular tumor was not an independent predictive factor for OS or RFS.

## CONCLUSION

Combined RFA and multipronged EA is a safe and effective treatment for unfavorable HCC, especially for perivascular tumors.

## KEYWORDS

Combine, ethanol, hepatocellular carcinoma, radiofrequency ablation, survival

From the Department of Medical Ultrasonics (M.L., X-J.L., X-E.Z., M.K., X-Y.X., G-L.H. ✉ huanggl9@mail.sysu.edu.cn), The First Affiliated Hospital of Sun Yat-Sen University, Institute for Diagnostic and Interventional Ultrasound, Guangzhou, China; Department of Liver Surgery (M.K.), The First Affiliated Hospital of Sun Yat-Sen University, Guangzhou, China.

Received 22 August 2021; revision requested 11 October 2021; last revision received 01 February 2022; accepted 16 February 2022.



Epub: 13.02.2023

Publication date: 29.03.2023

DOI: 10.4274/dir.2022.22832

**H**epatocellular carcinoma (HCC) is the fifth most common cancer and a major cause of cancer-related death worldwide.<sup>1,2</sup> Patients with early-stage HCC can be cured by therapies such as hepatic resection, liver transplantation, or ablation. Radiofrequency ablation (RFA) has recently become a treatment option for HCC.<sup>3</sup>

Despite the success of RFA treatment for small tumors, the local tumor complete ablation (CA) rates decline markedly for HCC tumors with a diameter >3 cm; meanwhile, the local tumor recurrence rate for RFA is higher than that for resection because RFA alone can only induce a limited volume of coagulated necrosis.<sup>4</sup> A perivascular tumor location has been

You may cite this article as: Liu M, Li XJ, Zhang XE, Kuang M, Xie XY, Huang GL. Long-term outcomes of combined radiofrequency ablation and multipronged ethanol ablation for the treatment of unfavorable hepatocellular carcinoma. *Diagn Interv Radiol.* 2023;29(2):342-349.

reported to be an independent predictive factor for local tumor progression (LTP) after RFA.<sup>5</sup> This finding could be explained to some degree by the “heat-sink” effect, which is a well-known phenomenon that occurs when thermal energy disseminates from the treated lesion because of blood flow in the nearby blood vessels. This has an adverse impact on thermal ablation and induces tumor cells around the major intrahepatic vessels to escape from the thermal energy.

Some studies have shown that combined percutaneous RFA and ethanol ablation (EA) is an effective treatment for HCC in high-risk locations, which is defined as a tumor less than 0.5 cm from the gastrointestinal tract, gallbladder, diaphragm, or large bile duct (including hepatobiliary and bile ducts with a diameter >0.3 cm), a tumor located directly in contact with the liver capsule,<sup>6,8</sup> a tumor near the large vasculature >0.3 cm, or a tumor near to the heart (perivascular tumor).<sup>9,10</sup> A retractable multipronged injection needle was developed to overcome the limitations of the conventional EA technique.<sup>11</sup> The authors’ preliminary study confirms that medium (3.1–5.0 cm) and large (5.1–7.0 cm) HCC nodules can be treated effectively and safely with this combined ablation therapy.<sup>12</sup>

The aim of the current study is to evaluate the local efficacy, safety, and long-term outcomes of combined RFA and EA as a treatment for unfavorable HCC, especially perivascular tumors, and determine the prognostic survival factors. A multipronged injection needle (Quadra-Fuse; Rex Medical, Conshohocken, PA, USA) is used for EA. To the authors’ knowledge, no previous studies have reported long-term outcomes of combined RFA and EA with a multipronged injection needle.

## Methods

An Institutional Review Board of the hospital approved this retrospective study with a

waiver of informed consent for participation in the study [ethical review decision/protocol number: 2012 (68)]. Before treatment, the authors obtained written informed consent from each patient.

### Patients

Between August 2009 and December 2017, a total of 98 patients (86 men, 12 women; mean age  $55.0 \pm 12.7$  years) with 110 unfavorable HCC nodules ( $4.0 \pm 1.0$  cm) who underwent combined RFA and multipronged EA were retrospectively enrolled in the study. In the current study, unfavorable HCC was defined as medium (3.1–5.0 cm) or large (5.1–7.0 cm) HCC tumors, a tumor located at a high-risk site, or perivascular tumors. The diagnosis of HCC was based on a biopsy or the non-invasive diagnostic criteria of the European Association for the Study of the Liver. The inclusion criteria were as follows: (a) adult patients with HCC or recurrent HCC who refused to undergo surgery; (b) single or multiple tumors (no more than three HCC tumors, with the largest lesion 7.0 cm in diameter) without extrahepatic metastasis or macrovascular invasion; (c) liver function classified as Child–Pugh class A or B; (d) platelet count  $>50 \times 10^9/L$  and prothrombin time ratio  $>50\%$ ; and (e) visualization of the HCC nodule at the planning ultrasonography examination for RFA. Patients with liver function classified as Child–Pugh class C, those with uncontrolled coagulopathy, or those with a history of ethanol allergy were excluded from the study.

Tumor diameters were determined as the largest dimension measured using B-mode ultrasound. Tumor numbers were determined from contrast-enhanced ultrasound (CEUS) with SonoVue as a contrast agent and contrast-enhanced computed tomography (CECT) findings. The Barcelona Clinic Liver Cancer (BCLC) staging and treatment strategy was used to make treatment decisions for stage 0–A patients. For BCLC stage B patients, treatment decisions were made based on the results of a multidisciplinary team (MDT). Diagnostic and treatment decisions were made in consensus by the MDT consisting of hepatobiliary surgeons and interventional radiologists.

### Ethanol ablation

A multipronged injection needle was used to inject ethanol. This device included an 18-gauge 20 cm-long puncture needle consisting of an echogenic tip; three retractable tines, each with two evenly spaced

through-holes (four fluid exits); and a connector with extension tubing. With ultrasound guidance, the needle was introduced percutaneously into the tumor center, and the needle tip was positioned at the bottom of the target tumor. An injection–rotation–injection maneuver was used as described in our previous reports.<sup>12,13</sup> The maximal extent of prong deployment was equal to the tumor’s largest diameter. Ethanol was injected until the whole tumor appeared completely hyperechoic. The amount of ethanol was calculated according to the tumor size and was kept between one-quarter and one-third of the estimated tumor volume. During any necessary pause of ethanol injection, 0.5–1.0 mL of heparinized saline solution was injected to prevent thrombosis inside the prongs. After the completion of the injection, the needle was left in the tumor for 1–2 min to prevent possible ethanol reflux before it was removed.

### Radiofrequency ablation

We used the RITA Medical System (RITA Medical System, Mountain View, CA) and the Cool-tip TM RFA System (Cool-tip System, Covidien, Mansfield, MA). The combined ablation procedure was the same as that described in the authors’ previous report for tumors located or not located at high-risk sites.<sup>12,13</sup> For tumors located at high-risk sites, the Cool-tip System was used. For tumors not located at high-risk sites, the RITA Medical System was used. RFA was performed 3–5 min after EA following the manufacturer’s guidelines. During the ablation, the authors tried to obtain an adequate coagulation volume with a sufficient safety margin of 0.5 cm. CEUS was performed approximately 30 min after ablation, providing an initial evaluation of the treatment effect. Additional treatment was performed if any tumor residue was found.

### Assessment of treatment response and follow-up

All complications related to thermal ablation were categorized according to the grading system of the Society of Interventional Radiology.<sup>14</sup>

The initial CA evaluation performed one month after ablation was assessed using CECT and CEUS simultaneously. All patients were scanned using a 64-slice helical CT scanner (Toshiba, Tokyo, Japan) with the following parameters: 0.5 mm  $\times$  64 mm collima-

#### Main points

- Combined radiofrequency ablation (RFA) and multipronged ethanol ablation (EA) is a safe and effective modality for treating unfavorable hepatocellular carcinoma.
- Combined RFA and multipronged EA expand the indication of thermal ablation to tumors of 5 cm in diameter.
- A high serum alpha-fetoprotein level, large tumors, residual tumors after ablation, and extrahepatic metastases have a significant negative effect on overall survival.

tion, 120 kV, and 150–200 mA. Follow-up was conducted at regular intervals post-ablation (at three-month intervals for the first year and biannually thereafter). The evaluation included assessing common blood chemistry parameters, serum alpha-fetoprotein (AFP) levels, and performing an abdominal CECT examination.

CA was defined as non-enhancement in the ablated zone one month after ablation. LTP was defined as the appearance of tumor foci at the edge of the ablation zone after a contrast-enhanced examination documented CA according to the imaging criteria.<sup>14</sup> Intrahepatic distant recurrence (IDR) was defined as the appearance of new intrahepatic tumors in locations other than the treated area. Extrahepatic metastases were defined as the appearance of new metastases in other organs.

### Statistical analysis

Overall survival (OS) was the time interval between ablation treatment and death, the last follow-up date, or the most recent follow-up date before December 31, 2017. Recurrence-free survival (RFS) was the time interval between ablation treatment and the first date of tumor recurrence (local and/or distant recurrence) or the last follow-up date without recurrence.

According to the normality test for continuous variables, variables conforming to a normal distribution are presented as the means  $\pm$  standard deviations, and variables not conforming to a normal distribution are presented as the medians (min–max). Categorical variables were compared using the Pearson chi-squared test and Fisher's exact test.

The cumulative incidences of LTP and the survival curves were estimated by using the Kaplan–Meier method. Univariate and multivariate analyses were performed to determine the significant clinical and biological parameters for predicting LTP, OS, and RFS. In addition, a univariate Cox proportional hazards model was fitted to each variable. All variables with a *P* value  $< \alpha = 0.05$  were included in the multiple analysis using a backward stepwise Cox proportional hazards regression model. A *P* value  $< \alpha = 0.05$  indicated a significant difference. All statistical analyses were conducted using SPSS version 18.0.

## Results

### Patients and tumor profiles

Eighty-six patients (87.8%) infected with hepatitis B or C received antiviral therapy. Forty-nine (50.0%) patients received a first-time diagnosis of HCC, and 49 (50.0%) had recurrence after hepatectomy (*n* = 34), transcatheter arterial chemoembolization (TACE) (*n* = 10), RFA (*n* = 4), or liver transplantation (*n* = 1). Eighty-two tumors (74.5%) were  $>3.0$  cm in diameter. The other 28 tumors were 3.0 cm; however, of these tumors, 20 were located at high-risk sites, and 8 were perivascular. Eighty (72.7%) tumors were located at high-risk sites. Fifty-eight (52.7%) tumors were perivascular. Forty-three tumors were located at high-risk sites and were perivascular simultaneously. Table 1 shows the demographic and tumor characteristic data.

### Tumor response to treatment

After initial treatment, CA was obtained in 80.9% (89/110) of the tumors. The CA

rate was 92.9% (26/28) for tumors 3.0 cm in diameter, 82.6% (57/69) for tumors with sizes of 3.1–5.0 cm, and 46.2% (6/13) for tumors with sizes of 5.1–7.0 cm. The CA rate of the tumors with sizes of 3.1–5.0 cm was similar to that of the tumors 3.0 cm in diameter (*P* = 0.338). The CA rates of tumors 3.0 cm in diameter and tumors with sizes of 3.1–5.0 cm were both higher than the CA rate of tumors with sizes of 5.1–7.0 cm (*P* = 0.002 and *P* = 0.009, respectively). Of the 21 residual tumors in 21 patients, 9 residual tumors in 9 patients achieved CA after an additional 1–3 RFA procedures. Overall, the technical success rate was 89.1% (98/110). Regarding the other 12 residual tumors in 12 patients, 3 patients were treated with TACE, 3 patients were treated with repeated RFA that failed, and 2 patients underwent liver transplantation. The remaining 4 patients also had distant multinodular recurrences that were treated with sorafenib.

**Table 1.** Demographic and tumor characteristic data

Characteristic	Value
Gender (male/female)	86/12
*Age (years)	55.0 $\pm$ 12.7
Hepatitis virus (B/C/none)	85/1/12
Child–Pugh class (A/B)	92/6
#Serum alanine aminotransferase level (U/L)	36.0 (2.9–351.0)
#Serum total bilirubin (umol/L)	14.4 (2.8–90.6)
*Serum albumin (g/L)	39.3 $\pm$ 4.1 (27.8–49.7)
#Prothrombin time (s)	12.4 (10.2–16.6)
#Platelet count ( $\times 10^9$ /L)	137.0 (47.0–407.0)
Serum alpha-fetoprotein level (ng/mL)	
<20 ng/mL	49
20–200 ng/mL	19
>200 ng/mL	30
Number of patients with primary/recurrent tumor	49/49
Number of patients with single/multiple tumor	67/31
#Tumor size (cm)	3.6 (2.0–7.0)
Number of tumors 3.0 cm/3.1–5.0 cm/5.1–7.0 cm	28/69/13
Number of tumors per location	
Located at high-risk sites (yes/no)	80/30
Perivascular (yes/no)	50/60
#Ethanol volume	15.0 (4.0–30.0)
#Ablation time	24.0 (10.0–60.0)
*Values represent continuous variables conforming to a normal distribution, presented as the means $\pm$ standard deviations, *values represent continuous variables not conforming to a normal distribution, presented as the median (min–max).	

## Complications

No ablation-related deaths occurred in the current study. Three patients (3.1%) experienced major complications. One patient suffered from intra-abdominal hemorrhage and remained hospitalized for 27 days after the ablation procedure. This patient initially presented with abdominal pain, then developed an abdominal infection, and was diagnosed with spontaneous peritonitis, which was successfully treated with ultrasound-guided ascites drainage and antibiotics. Another patient developed acute cholecystitis, which resulted in an eight-day hospital stay after treatment. This patient had a history of gallstones, which were successfully treated. The third patient had a tumor seeding in the abdominal wall at 21.4 months after treatment, and this tumor was successfully treated with RFA.

Ablation-related minor complications occurred in 3 patients (3.1%), including 2 cases of pleural effusion and 1 case of portal venous thrombosis that required no medical intervention.

## Local tumor progression

Of the 98 completely ablated tumors, 23 (23.5%) lesions in 23 patients exhibited LTP during the follow-up period of 3.2–98.4 months (median, 31.1 months), and the LTP time was 2.8–64.2 months (median, 12.2 months). The cumulative incidence of LTP was estimated to be 2.3%, 15.9%, and 23.5% at one, three, and five years, respectively. The LTP rate was 29.6% (8/27) for tumors with sizes 3 cm, 23.4% (15/64) for tumors with sizes of 3.1–5.0 cm, and 0% (0/7) for tumors with sizes of 5.1–7.0 cm ( $P = 0.332$ ). Among the 17 examined variables, including sex (male), age (>65 years), Child–Pugh class (A/B), hepatitis B/C virus status (+/–), serum alanine aminotransferase level (>40 U/L), serum total bilirubin level (>17.1  $\mu\text{mol/L}$ ), serum albumin level (>35 g/L), prothrombin time (>14 s), platelet count (>100  $\times 10^9/\text{L}$ ), serum AFP level (<20 ng/mL/20–200 ng/mL >200 ng/mL), tumor type (primary/recurrent), number of tumors (single/multiple), tumor size (3 cm/3.1–5.0 cm/5.1–7.0 cm), tumor location (located at high-risk sites, perivascular), ethanol volume (>14.4 mL), and ablation time (>24 min), no variable was found to be a predictive factor for LTP. Among the 23 patients with LTP, 14 were treated successfully with repeated RFA, 1 was treated with TACE, 1 underwent liver transplantation, and 1 underwent hepatic resection. The remaining 6 patients also had distant multinodular recurrences that were treated with sorafenib.

## Distant recurrence

Distant recurrence included IDR and extrahepatic metastases. Seventy (71.4%) of the 98 patients had IDR, which was identified 3.0–65.1 months after ablation (median, 8.0 months), during the follow-up period, including 19 patients with IDR in the left lobe of the liver, 34 patients with IDR in the right lobe of the liver, and 17 patients with IDR in the whole liver. In addition, 2 patients developed a portal vein tumor thrombus, which occurred after 2.2 months in one patient and after 3 months in the other patient. During the follow-up period, extrahepatic metastases, which were identified 3.0–55.5 months after ablation (median, 7.2 months), developed in 20 (20.4%) of the 98 patients, and the locations of the initial extrahepatic metastases were as follows: the lungs ( $n = 9$ ), lymph nodes ( $n = 6$ ), abdominal wall ( $n = 2$ ), bone ( $n = 1$ ), adrenal gland ( $n = 1$ ), and spleen ( $n = 1$ ).

## Survival analysis

### Overall survival

During the follow-up period, 53 (54.1%) patients died after ablation. The median survival time of patients who died after the procedure was 21.2 months, and the minimum and maximum survival times were 5.1 and 81.3 months, respectively. The interquartile range was 22.2 months. Among the patients who died, 37 (69.8%) deaths were related to HCC progression; 14 (26.4%) were attributed to cirrhosis-related complications, such as variceal bleeding and liver failure; and 2 (3.8%) involved causes unrelated to liver dis-

ease (e.g., one patient had pneumonia, and the other had a stroke). Six (6.1%) patients underwent liver transplantation 4.2–77.5 months after ablation (median, 6.3 months). The reasons for liver transplantation were HCC recurrence in 5 patients and liver failure in 1 patient.

The estimated one-, three-, and five-year OS rates after RFA were 87.3%, 54.3%, and 41.9%, respectively (Figure 1). In the multivariate analysis, the serum AFP level ( $P = 0.023$ ), tumor size ( $P = 0.030$ ), residual tumor ( $P = 0.001$ ), and extrahepatic metastases ( $P = 0.010$ ) were significant independent predictive factors for OS (Table 2).

### Recurrence-free survival

The estimated one-, three-, and five-year RFS rates were 63.1%, 46.9%, and 34.0%, respectively. Estimates of the mean and median RFS were 42.8 months [95% confidence interval (CI): 33.0–52.6] and 31.9 months (95% CI: 11.8–52.0), respectively. In the multivariate analysis, tumor type ( $P = 0.029$ ) and the number of tumors ( $P = 0.001$ ) were significant independent predictive factors for RFS (Table 3).

Table 4 shows the local efficacy and long-term outcome of different tumor and patient types.

## Discussion

One procedure of one radiofrequency electrode produces a necrotic zone of 3.0–5.0 cm in diameter. The form and size of the ablation area may be errant because of the heat-

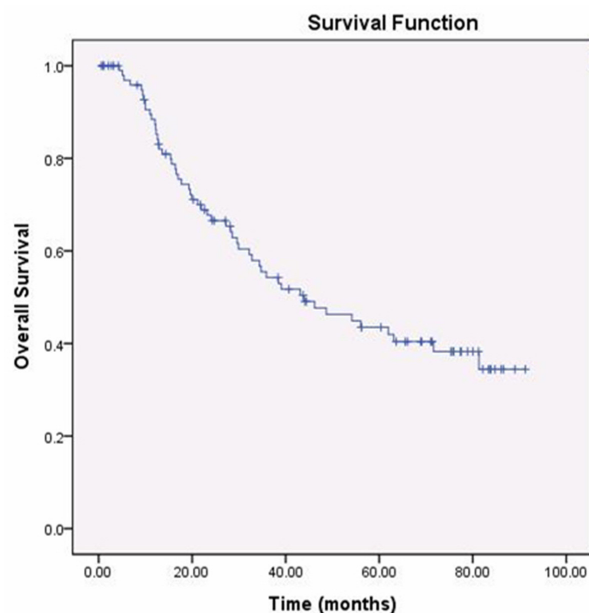


**Figure 1.** A graph showing Kaplan–Meier overall survival estimation for 98 patients who underwent combined radiofrequency ablation and multipronged ethanol ablation for hepatocellular carcinoma.

**Table 2.** Cox survival analysis of predictors for OS in 98 patients with 110 HCCs after combined RFA and multipronged EA

Characteristic	Univariate			Multivariate		
	HR	95%CI	P	HR	95% CI	P
Gender (male)	0.698	0.277–1.750	0.441	-	-	-
Age (>65 years)	0.835	0.452–1.541	0.563	-	-	-
Hepatitis B/C virus (+/-)	0.866	0.344–2.178	0.760	-	-	-
Child–Pugh class (A/B)	0.789	0.244–2.556	0.693	-	-	-
Serum alanine aminotransferase level (>40 U/L)	1.192	0.678–2.093	0.542	-	-	-
Serum total bilirubin (>17.1 umol/L)	1.230	0.683–2.215	0.491	-	-	-
Serum albumin (>35 g/L)	0.912	0.457–1.819	0.793	-	-	-
Prothrombin time (>14 s)	0.972	0.351–2.696	0.957	-	-	-
Platelet count (>100×10 <sup>9</sup> /L)	1.152	0.616–2.155	0.657	-	-	-
Serum alpha-fetoprotein level (ng/mL)	-	-	0.011	-	-	0.023
20 vs. 20–200	1.551	0.731–3.289	0.252	0.396	0.205–0.766	0.006
20 vs. >200	2.513	1.375–4.594	0.003	0.576	0.233–1.423	0.232
Tumor type (primary/recurrent)	0.408	0.232–0.718	0.002	0.592	0.320–1.093	0.094
Number of tumors (single/multiple)	0.384	0.223–0.662	0.001	0.539	0.283–1.028	0.061
Tumor size (cm)			<0.001			0.030
3.0 vs. 3.1–5.0	1.067	0.524–2.171	0.859	0.343	0.134–0.877	0.025
3.0 vs. 5.1–7.0	5.174	2.168–12.349	<0.001	0.349	0.154–0.789	0.011
<b>Tumor location</b>						
Located at high-risk sites (yes/no)	0.948	0.540–1.664	0.853	-	-	-
Perivascular (yes/no)	0.892	0.520–1.529	0.677	-	-	-
Ethanol volume (>14.4 mL)	1.038	0.604–1.781	0.894	-	-	-
Ablation time (>24 min)	1.012	0.575–1.783	0.967	-	-	-
Complication (yes/no)	1.504	0.468–4.883	0.493	-	-	-
Residual tumor (yes/no)	0.201	0.098–0.412	<0.001	0.237	0.103–0.545	0.001
LTP (yes/no)	1.697	0.828–3.477	0.149	-	-	-
IDR	0.305	1.138–1.677	0.004	0.452	0.197–1.041	0.062
Extrahepatic metastases	0.386	0.218–0.685	0.001	0.385	0.186–0.795	0.010

P values of the Cox proportional hazards regression model <0.001. CI, confidence interval; EA, ethanol ablation; HCC, hepatocellular carcinoma; HR, hazard ratio; IDR, intrahepatic distant recurrence; LTP, local tumor progression; OS, overall survival; RFA, radiofrequency ablation.

sink effect, which can lead to an inadequate ablation area and a higher rate of LTP in patients treated with RFA than in those treated with resection. Therefore, the use of RFA for HCC close to large intrahepatic vessels poses a great challenge in clinical practice. Moreover, the use of RFA is still limited for some tumors in other high-risk locations.<sup>15</sup> Several strategies, such as the combined use of RFA and EA or TACE, ablation with artificial hydrothorax and ascites, a no-touch ablation procedure, and irreversible electroporation, have been developed to solve these problems.<sup>16–18</sup>

RFA combined with EA can produce a larger ablation area; with this technique, tumors with diameters of less than 5 cm can be completely ablated with an appropriate safety margin.<sup>19</sup> Factors that contribute to the favorable efficacy of this technique include the following: first, the reduction in the heat-sink

effect produced by the ethanol-induced destruction of the vessels within or around the HCC tumors; and second, the diffusion of hot ethanol into the area not covered by radiofrequency power and the improved thermal conduction associated with the decreased extent of tissue carbonization.<sup>10,20</sup> With this increased safety margin, the likelihood of clearing micrometastases increases, and the risk of LTP decreases.

In this study, the CA rate of tumors with sizes of 3.1–5.0 cm was similar to that of tumors with sizes 3.0 cm. Among the tumors with sizes of 3.1–5.0 cm, 74.3% (52/70) were located at high-risk sites, and 44.3% (31/70) were located at perivascular sites. Among the 31 perivascular tumors, only 2 exhibited residual tumors after treatment, while 3 non-perivascular tumors were residual after treatment. These findings indicate that the use of RFA combined with EA improves

the initial complete necrosis rate of tumors with sizes of 3.1–5.0 cm but not that of tumors 3.0 cm in diameter or larger tumors with sizes of 5.1–7.0 cm. A growing body of literature suggests that RFA is very effective for tumors <3.0 cm, as studies have shown a complete tumor necrosis rate of 90% or more and survival rates comparable to those of patients who underwent surgery for these tumors.<sup>21–25</sup> Our study indicates that adding multipronged EA to RFA significantly improves the local efficacy (CA rate) of ablation for HCC tumors with a size of 3.1–5.0 cm, but this method is not suitable for tumors >5.0 cm in diameter due to the high residual rate.

The current study's 3.1% major complication rate was close to the rates in the previous studies of thermal ablation for HCC (0%–6.1%)<sup>21,25,26</sup> or RFA combined with EA for HCC (0%–4.6%).<sup>12,27</sup> No deaths or serious procedure-related complications resulted from

**Table 3.** Cox survival analysis of predictors for RFS in 86 patients with 98 HCCs after combined RFA and multipronged EA

Characteristic	Univariate			Multivariate		
	HR	95% CI	P	HR	95% CI	P
Gender (male)	0.532	0.164–1.723	0.293	-	-	-
Age (>65 years)	0.719	0.365–1.419	0.342	-	-	-
Hepatitis B/C virus (+/-)	0.938	0.332–2.649	0.903	-	-	-
Child–Pugh class (A/B)	0.650	0.198–2.132	0.478	-	-	-
Serum alanine aminotransferase level (>40 U/L)	0.910	0.490–1.691	0.767	-	-	-
Serum total bilirubin (>17.1 umol/L)	1.325	0.666–2.634	0.423	-	-	-
Serum albumin (>35 g/L)	0.960	0.445–2.072	0.917	-	-	-
Prothrombin time (>14 s)	1.187	0.423–3.335	0.745	-	-	-
Platelet count (>100×10 <sup>9</sup> /L)	1.199	0.589–2.440	0.617	-	-	-
Serum alpha-fetoprotein level (ng/mL)			0.053	-	-	0.117
20 vs. 20–200	1.359	0.594–3.107	0.468	1.437	0.607–3.403	0.410
20 vs. >200	2.282	1.170–4.453	0.016	2.098	1.038–4.240	0.039
Tumor type (primary/recurrent)	0.442	0.238–0.823	0.010	0.488	0.257–0.928	0.029
Number of tumors (single/multiple)	0.264	0.143–0.489	<0.001	0.338	0.177–0.646	0.001
Tumor size (cm)			0.001	-	-	0.053
3.0 vs. 3.1–5.0	1.191	0.563–2.519	0.648	1.498	0.698–3.217	0.300
3.0 vs. 5.1–7.0	7.217	2.292–22.724	0.001	4.809	1.482–15.600	0.009
<b>Tumor location</b>						
Located at high-risk sites (yes/no)	1.044	0.765–1.423	0.787	-	-	-
Perivascular (yes/no)	0.930	0.690–1.255	0.637	-	-	-
Ethanol volume (>14.4 mL)	0.942	0.698–1.271	0.695	-	-	-
Ablation time (>24 min)	0.990	0.522–1.879	0.975	-	-	-
LTP (yes/no)	1.074	0.741–1.556	0.707	-	-	-

P value of the Cox proportional hazards regression model <0.001. CA, complete ablation; CI, confidence interval; EA, ethanol ablation; HCC, hepatocellular carcinoma; HR, hazard ratio; RFA, radiofrequency ablation; RFS, recurrence-free survival; LTP, local tumor progression.

**Table 4.** Local efficacy and long-term outcome of different tumor and patient type

Tumor type	CA	LTP	Patient type	3-year OS	5-year OS	3-year RFS	5-year RFS
Medium tumor	57/69	15/64	Patients with medium tumor	0.564	0.634	0.464	-
Large tumor	6/13	0/7	Patients with large tumor	0.091	0	0	0
Tumor in high-risk locations	70/80	11/70	Patients with tumor in high-risk locations	0.335	0.531	0.429	-
Perivascular tumor	45/50	14/45	Patients with perivascular tumor	0.516	0.570	0.490	-

CA, complete ablation; LTP, local tumor progression; OS, overall survival; RFS, recurrence-free survival.

the combined ablation procedure used in the current study or were reported by other literature.<sup>9,12</sup> Tumors located at high-risk sites or perivascularly were generally successfully treated without complications in the current study (Figures 2, 3), which indicates the minimal invasiveness of this combined therapy. The complication rates of patients with and without perivascular tumors were similar (3/58 vs. 3/52, respectively,  $P = 1.000$ ).

The LTP rate was 23.5% in the current study. This rate is similar to the rates observed in other studies of combined RFA and EA treatment for HCC, which have been reported to be approximately 12.5%–32.6%.<sup>9,10,12,20</sup> Some studies have reported that factors such as tumor size and perivas-

cular tumor location were predisposing factors for LTP.<sup>23,28</sup> However, no such factor was found in the current study. The LTP rates of the patients with and without perivascular tumors were similar (14/58 vs. 9/52, respectively,  $P = 0.379$ ). Because HCC has a relatively high tendency to exhibit intrahepatic vascular invasion, the current study implies that RFA and EA combination therapy is useful for preventing LTP in patients with perivascular tumors. The LTP rate is highest for small tumors and decreases with increasing tumor diameter, which occurs because many large tumors are not completely ablated during the initial treatment.

In recent years, TACE, followed by RFA, has been more widely applied in clinical settings

because TACE can reduce the heat-sink effect of blood flow by lessening hepatic arterial flow. The five-year OS of TACE and RFA has been reported to be approximately 31.0%–46.0%,<sup>29</sup> which was similar to the current data of our study (41.9%). Our results showed that the significant predictive factors for poor OS were a high serum AFP level, tumor size, residual tumor after ablation, and extrahepatic metastases. Tumor size as a predictive factor for OS has been reported in many previous studies.<sup>22,30–32</sup> A high serum AFP level is usually related to tumors with a higher degree of malignancy and is predictive of a high rate of HCC recurrence and poor prognosis after percutaneous ablation. Residual tumor after ablation indicates treatment failure; there-

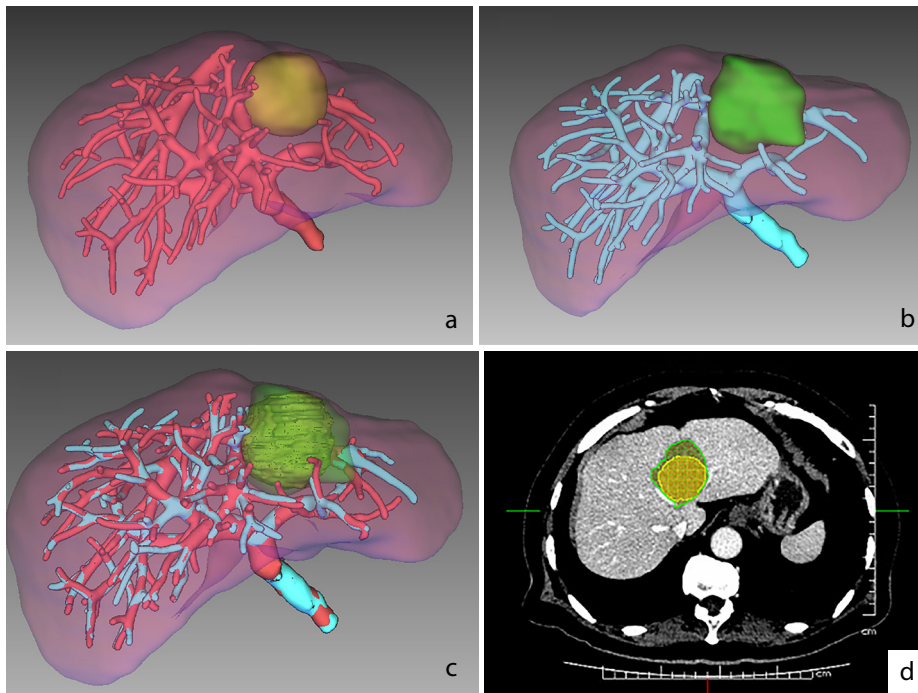


**Figure 2.** A hepatocellular carcinoma tumor located in contact with large vessels (the left and middle hepatic veins) in an 87-year-old man was treated by radiofrequency ablation (RFA) combined with multipronged ethanol ablation: (a) a computed tomography (CT) fusion obtained before performing combined ablation showed a lesion with a diameter of 4.2 cm in segment IV (marked in orange); (b) a CT fusion obtained one month after combined ablation showed the ablation zone (marked in green), which confirmed the complete ablation of the tumor; (c) a CT fusion showed that the tumor was successfully covered by the translucence ablation zone (green); (d) the pre-RFA tumor was overlaid on the post-RFA images. The ablation zone (marked in green line) covered the tumor (marked in yellow line). The minimal ablative margin was 0 cm at the side of the ablation zone in contact with the left and middle hepatic veins.



**Figure 3.** A hepatocellular carcinoma tumor located in contact with large vessels (main portal vein and postcava) in a 32-year-old female was treated with radiofrequency ablation combined with multipronged ethanol ablation: (a) the late arterial phase of pre-treatment computed tomography (CT) showed a lesion with a diameter of 4.1 cm in segment VIII (arrow); (b) the portal venous phase of pre-treatment CT showed that the tumor (arrow) was close to the main portal vein and postcava; and (c) a CT obtained one month after combined ablation showed the ablation zone (arrow), which confirmed the complete ablation of the tumor.

fore, patients undergo other treatments, which may have a poor effect on OS.<sup>32</sup> Multiple tumors were another significant predictor of poor RFS. The possible reasons include the following: first, as the number of tumors increases, the possibility of incomplete tumor removal increases; second, patients with multiple tumors might have a higher incidence of satellite nodules and micro-invasion, resulting in a higher rate of recurrence and worse survival; and, finally, after patients with multiple tumors undergo the combined ablation, when tumors recur, additional treatments are less likely to be performed. It is noteworthy that the presence of perivas-

cular tumors did not predict worse OS or RFS, which implies that combination therapy may overcome some obstacles observed with RFA alone in HCC.

The current study has some limitations. First, a potential risk exists of selection bias because this was a retrospective study. Second, this study included only a single HCC treatment without direct comparisons.

In conclusion, combined RFA and multipronged EA is a safe and effective modality with a five-year OS rate of 41.9% for unfavorable HCC, and this approach was espe-

cially effective in patients with perivascular tumors. The presence of recurrent and multiple tumors had a significant negative effect on OS and RFS. Using this combined method, the authors have expanded the indications for thermal ablation to tumors with a diameter of 5 cm and those in high-risk locations.

### Funding

This study has received funding by the National Natural Science Foundation of China (no: 81530055).

### Conflict of interest disclosure

The authors declared no conflicts of interest.

### References

1. Torre LA, Bray F, Siegel RL, Ferlay J, Lortet-Tieulent J, Jemal A. Global Cancer Statistics, 2012. *CA Cancer J Clin.* 2015;65(2):87-108. [\[CrossRef\]](#)
2. Ferlay J, Soerjomataram I, Dikshit R, et al. Cancer incidence and mortality worldwide: sources, methods and major patterns in GLOBOCAN 2012. *Int J Cancer.* 2015;136(5):359-386. [\[CrossRef\]](#)
3. Kawamura R, Seki T, Umehara H, et al. Combined treatment of large hepatocellular carcinoma with transcatheter arterial chemoembolization and percutaneous ethanol injection with a multipronged needle: experimental and clinical investigation. *Cardiovasc Intervent Radiol.* 2012;35(2):325-333. [\[CrossRef\]](#)
4. Lupo L, Panzera P, Giannelli G, Memeo M, Gentile A, Memeo V. Single hepatocellular carcinoma ranging from 3 to 5 cm: radiofrequency ablation or resection? *HPB (Oxford).* 2007;9(6):429-434. [\[CrossRef\]](#)
5. Lu DS, Raman SS, Limanond P, et al. Influence of large peritumoral vessels on outcome of radiofrequency ablation of liver tumors. *J Vasc Interv Radiol.* 2003;14(10):1267-1274. [\[CrossRef\]](#)
6. Chen J, Peng K, Hu D, et al. Tumor location influences oncologic outcomes of hepatocellular carcinoma patients undergoing radiofrequency ablation. *Cancers (Basel).* 2018;10(10):378. [\[CrossRef\]](#)
7. Hsieh YC, Limquiaco JL, Lin CC, Chen WT, Lin SM. Radiofrequency ablation following artificial ascites and pleural effusion creation may improve outcomes for hepatocellular carcinoma in high-risk locations. *Abdom Radiol (NY).* 2019;44(3):1141-1151. [\[CrossRef\]](#)
8. Lin SM. Local ablation for hepatocellular carcinoma in taiwan. *Liver Cancer.* 2013;2(2):73-83. [\[CrossRef\]](#)
9. Lin JW, Lin CC, Chen WT, Lin SM. Combining radiofrequency ablation and ethanol injection

- may achieve comparable long-term outcomes in larger hepatocellular carcinoma (3.1-4 cm) and in high-risk locations. *Kaohsiung J Med Sci*. 2014;30(8):396-401. [\[CrossRef\]](#)
10. Wong SN, Lin CJ, Lin CC, Chen WT, Cua IH, Lin SM. Combined percutaneous radiofrequency ablation and ethanol injection for hepatocellular carcinoma in high-risk locations. *AJR Am J Roentgenol*. 2008;190(3):187-195. [\[CrossRef\]](#)
  11. Hines-Peralta A, Liu ZJ, Horkan C, Solazzo S, Goldberg SN. Chemical tumor ablation with use of a novel multiple-tine infusion system in a canine sarcoma model. *J Vasc Interv Radiol*. 2006;17(2 Pt 1):351-358. [\[CrossRef\]](#)
  12. Huang G, Lin M, Xie X, et al. Combined radiofrequency ablation and ethanol injection with a multipronged needle for the treatment of medium and large hepatocellular carcinoma. *Eur Radiol*. 2014;24(7):1565-1571. [\[CrossRef\]](#)
  13. Kuang M, Lu MD, Xie XY, et al. Ethanol ablation of hepatocellular carcinoma Up to 5.0 cm by using a multipronged injection needle with high-dose strategy. *Radiology*. 2009;253(2):552-561. [\[CrossRef\]](#)
  14. Ahmed M, Solbiati L, Brace CL, et al. Image-guided tumor ablation: standardization of terminology and reporting criteria--a 10-year update. *J Vasc Interv Radiol*. 2014;25(11):1691-1705. [\[CrossRef\]](#)
  15. Karaman B, Battal B, Sari S, Verim S. Hepatocellular carcinoma review: current treatment, and evidence-based medicine. *World J Gastroenterol*. 2014;20(47):18059-18060. [\[CrossRef\]](#)
  16. Lucchina N, Tsetis D, Ierardi AM, et al. Current role of microwave ablation in the treatment of small hepatocellular carcinomas. *Ann Gastroenterol*. 2016;29(4):460-465. [\[CrossRef\]](#)
  17. Seror O, N'Kontchou G, Nault JC, et al. Hepatocellular carcinoma within milan criteria: no-touch multibipolar radiofrequency ablation for treatment-long-term results. *Radiology*. 2016;280(2):611-621. [\[CrossRef\]](#)
  18. Sutter O, Calvo J, N'Kontchou G, et al. Safety and efficacy of irreversible electroporation for the treatment of hepatocellular carcinoma not amenable to thermal ablation techniques: a retrospective single-center case series. *Radiology*. 2017;284(3):877-886. [\[CrossRef\]](#)
  19. Chen S, Peng Z, Lin M, et al. Combined percutaneous radiofrequency ablation and ethanol injection versus hepatic resection for 2.1-5.0 cm solitary hepatocellular carcinoma: a retrospective comparative multicentre study. *Eur Radiol*. 2018;28(9):3651-3660. [\[CrossRef\]](#)
  20. Cha DI, Lee MW, Rhim H, Choi D, Kim YS, Lim HK. Therapeutic efficacy and safety of percutaneous ethanol injection with or without combined radiofrequency ablation for hepatocellular carcinomas in high risk locations. *Korean J Radiol*. 2013;14(2):240-247. [\[CrossRef\]](#)
  21. Lee DH, Lee JM, Lee JY, et al. Radiofrequency ablation of hepatocellular carcinoma as first-line treatment: long-term results and prognostic factors in 162 patients with cirrhosis. *Radiology*. 2014;270(3):900-909. [\[CrossRef\]](#)
  22. Lee DH, Lee JM, Lee JY, Kim SH, Han JK, Choi BI. Radiofrequency ablation for intrahepatic recurrent hepatocellular carcinoma: long-term results and prognostic factors in 168 patients with cirrhosis. *Cardiovasc Intervent Radiol*. 2014;37(3):705-715. [\[CrossRef\]](#)
  23. Kim YS, Lim HK, Rhim H, et al. Ten-year outcomes of percutaneous radiofrequency ablation as first-line therapy of early hepatocellular carcinoma: analysis of prognostic factors. *J Hepatol*. 2013;58(1):89-97. [\[CrossRef\]](#)
  24. Shiina S, Tateishi R, Arano T, et al. Radiofrequency ablation for hepatocellular carcinoma: 10-year outcome and prognostic factors. *Am J Gastroenterol*. 2012;107(4):569-577. [\[CrossRef\]](#)
  25. Ng KKC, Chok KSH, Chan ACY, et al. Randomized clinical trial of hepatic resection versus radiofrequency ablation for early-stage hepatocellular carcinoma. *Br J Surg*. 2017;104(13):1775-1784. [\[CrossRef\]](#)
  26. Facciorusso A, Serviddio G, Muscatiello N. Local ablative treatments for hepatocellular carcinoma: An updated review. *World J Gastrointest Pharmacol Ther*. 2016;7(4):477-489. [\[CrossRef\]](#)
  27. Chen S, Peng Z, Xiao H, et al. Combined radiofrequency ablation and ethanol injection versus repeat hepatectomy for elderly patients with recurrent hepatocellular carcinoma after initial hepatic surgery. *Int J Hyperthermia*. 2018;34(7):1029-1037. [\[CrossRef\]](#)
  28. Waki K, Aikata H, Katamura Y, et al. Percutaneous radiofrequency ablation as first-line treatment for small hepatocellular carcinoma: results and prognostic factors on long-term follow up. *J Gastroenterol Hepatol*. 2010;25(3):597-604. [\[CrossRef\]](#)
  29. Xu Z, Xie H, Zhou L, Chen X, Zheng S. The combination strategy of transarterial chemoembolization and radiofrequency ablation or microwave ablation against hepatocellular carcinoma. *Anal Cell Pathol (Amst)*. 2019;2019:8619096. [\[CrossRef\]](#)
  30. Tsukamoto M, Yamashita YI, Imai K, et al. Long-term favorable outcomes of radiofrequency ablation for hepatocellular carcinoma as an initial treatment: a single-center experience over a 10-year period. *Anticancer Res*. 2018;38(2):1047-1052. [\[CrossRef\]](#)
  31. Shiina S, Tateishi R, Imamura M, et al. Percutaneous ethanol injection for hepatocellular carcinoma: 20-year outcome and prognostic factors. *Liver Int*. 2012;32(9):1434-1442. [\[CrossRef\]](#)
  32. Ng KK, Poon RT, Lo CM, Yuen J, Tso WK, Fan ST. Analysis of recurrence pattern and its influence on survival outcome after radiofrequency ablation of hepatocellular carcinoma. *J Gastrointest Surg*. 2008;12(1):183-191. [\[CrossRef\]](#)



# Safety and efficacy of flow diverter stents in the treatment of middle cerebral artery aneurysms: a single-center experience and follow-up data

Efe Soydemir   
Cemal Aydın Gündoğmuş   
Derya Türeli   
Nurten Andaç Baltacıoğlu   
Yaşar Bayri   
Feyyaz Baltacıoğlu 

## PURPOSE

This study aims to evaluate the safety and efficacy of flow diverters (FDs) in the treatment of middle cerebral artery (MCA) aneurysms and share the follow-up (F/U) results.

## METHODS

The treatment and F/U results of 76 MCA aneurysms treated with the flow re-direction endoluminal device (FRED), FRED Jr., and pipeline embolization device (PED) FD stents were evaluated retrospectively. The aneurysm occlusion rates were compared between FDs, and the integrated and jailed branches were evaluated through follow-ups. The oversizing of the stent was compared between occluded/non-occluded aneurysms and integrated branches.

## RESULTS

The mean F/U duration was  $32 \pm 6.3$  months, and the mean aneurysm diameter was 4.45 mm. A total of 61 (80.3%) aneurysms were wide-necked; 73 (96.1%) were saccular; 52 (68.4%) were located at the M1 segment; and 36 (45.6%) FREDs, 23 (29.1%) FRED Jr.s, and 19 (24.1%) PEDs were used for treatment. The overall occlusion rates for the 6-, 12-, 24-, 36-, and 60-month digital subtraction angiographies were 43.8%, 63.5%, 73.3%, 85.7%, and 87.5% respectively. The last F/U occlusion rates were 67.6% for FRED, 66.7% for PED, and 60.6% for FRED Jr. ( $P = 0.863$ ). An integrated branch was covered with an FD during the treatment of 63 (82.8%) aneurysms. A total of six (10%) of the integrated branches were occluded without any symptoms at the last F/U appointment. The median oversizing was 0.45 (0–1.30) for occluded aneurysms, and 0.50 (0–1.40) for non-occluded aneurysms ( $P = 0.323$ ). The median oversizing was 0.70 (0.45–1.10) in occluded integrated branches and 0.50 (0–1.40) in non-occluded branches ( $P = 0.131$ ). In-stent stenosis was seen in 22 (30.1%) of the stents at the 6-month F/U and in only 2 (4.7%) at the 24-month F/U. Thus, none of the patients had any neurological deficits because of the in-stent stenosis. Severe in-stent stenosis was seen in two stents.

## CONCLUSION

MCA aneurysms tend to be complex, with integrated branches and potentially wide necks. FD stents are safe and effective in the treatment of MCA aneurysms, and the patency of the side and jailed branches is preserved in most cases. Higher occlusion and lower in-stent stenosis rates are seen with longer F/U durations.

## KEYWORDS

Aneurysm, flow diverter, FRED, MCA, pipeline

From the Department of Radiology (E.S., C.A.G., D.T., F.B.), [feyyazb@amerikanhastanesi.org](mailto:feyyazb@amerikanhastanesi.org), Marmara University Faculty of Medicine, Istanbul, Turkey; Department of Radiology (C.A.G.), Koç University Hospital, Istanbul, Turkey; Department of Radiology (N.A.B., F.B.), VKV Amerikan Hospital, Istanbul, Turkey; Department of Neurosurgery (Y.B.), Marmara University Faculty of Medicine, Istanbul, Turkey.

This study was presented in Annual Congress of Turkish Society of Neuroradiology on 18 February 2021.

Received 19 October 2021; revision requested 29 November 2021; last revision received 27 March 2022; accepted 04 April 2022.



Epub: 02.01.2023

Publication date: 29.03.2023

DOI: 10.4274/dir.2022.211050

You may cite this article as: Soydemir E, Gündoğmuş CA, Türeli D, Andaç Baltacıoğlu N, Bayri Y, Baltacıoğlu F. Safety and efficacy of flow diverter stents in the treatment of middle cerebral artery aneurysms: a single-center experience and follow-up data. *Diagn Interv Radiol.* 2023;29(2):350-358.

**M**iddle cerebral artery (MCA) aneurysms constitute approximately 22% of all cerebral aneurysms. They are generally wide-necked, have accompanying integrated branches, and sometimes have complex anatomy with angulation. Thus, the endovascular treatment of MCA aneurysms is challenging with conventional treatment strategies.<sup>1</sup>

Flow diverter (FD) stents have evolved aneurysm treatment to a different level. They do not just restrict blood flow into the aneurysm sac but also reconstruct the parent artery by remodelling the aneurysm neck. FDs decrease the blood flow into the aneurysm sac with their braided mesh structure. Through this hemodynamic alteration, endothelial remodeling across the neck of the aneurysm enables occlusion of the aneurysm.<sup>2</sup>

Several studies have demonstrated the effectiveness and safety of FDs in the treatment of intracranial aneurysms. Treatment of internal carotid artery (ICA) aneurysms using flow diversion has been widely studied; however, the data intended for cases beyond the circle of Willis, especially MCA aneurysms, is still limited.<sup>3-5</sup>

This study aims to retrospectively evaluate the safety and efficacy of FDs in the treatment of MCA aneurysms and to share the follow-up (F/U) results.

## Methods

This retrospective study was approved by the local ethics committee (protocol no: 09.2020.704). The interdisciplinary consensus among the neuro-interventional radiology and neurosurgery departments was sought in each patient. In addition, written informed consent was given by all the patients for endovascular treatment.

### Patient and aneurysm characteristics

All patients with MCA aneurysms [M1 [(horizontal) and bifurcation (insular)] who were treated with at least one FD stent at a

referral center between May 2013 and December 2019 were enrolled in this study. Most of the M1 aneurysms in this study had integrated branches, and all bifurcation aneurysms had a neck that was hard to by-pass. These were the main factors for choosing FD treatment for the patients. The only exclusion criterion was ruptured aneurysm. One patient with a ruptured blister aneurysm was excluded from the study, and two patients with a total number of three aneurysms were lost during the F/U period. Only procedural and pre-procedural clinical data were analyzed.

In addition to aneurysm location and diameter, the aneurysm morphology (saccular, fusiform, and blister), aneurysm neck size, presence of integrated and jailed branches, and parent artery diameters were recorded. Oversizing was the stent diameter minus the diameter of the proximal parent artery (mm).

### Antiaggregation

All patients were administered with preprocedural dual antiplatelet therapy. Patients under clopidogrel and prasugrel were tested for platelet inhibition using the Multiplate Analyzer (Roche Diagnostics International Ltd, Rotkreuz ZG, Switzerland) before the procedure. The loading doses were 300 mg for clopidogrel 4 days before the procedure, 40 mg for prasugrel 12 h before the procedure, and 180 mg for ticagrelor as a loading dose directly before the operation. This was conducted in both urgent and scheduled procedures without testing. In addition, famotidine was initiated in all patients to prevent possible gastrointestinal tract bleeding, which could potentially lead to the cessation of antiaggregant therapy. Thus, all patients received either dual antiplatelet therapy with 75 mg clopidogrel + 100 mg acetylsalicylic acid (ASA), 180 mg ticagrelor + 100 mg ASA, or 10 mg prasugrel as monotherapy (for  $\geq 6$  months) + ASA (for life).

### Endovascular procedure

All procedures in this study were performed by a single neuroendovascular interventionalist with >10 years of FD experience.

All treatments were performed under general anesthesia. A 6F long introducer sheath was placed to the distal segment of the common carotid artery through femoral access, and a 6F distal access catheter (Navien: Covidien Vascular Therapies, Mansfield, MA, USA or Sofia: MicroVention, Tustin, California, USA) was advanced co-

axially into the ICA as distally as possible. To reveal the anatomy, determine working projections, and measure parent artery diameters, two-dimensional and three-dimensional rotational angiographic images were acquired. Rebar 27 (Covidien Vascular Therapies, Mansfield, MA, USA), Marksman (Covidien Vascular Therapies, Mansfield, MA, USA), or Headway 27 (MicroVention, Tustin, CA, USA) for the pipeline embolization device (PED) (ev3 Neurovascular, Irvine, CA, USA), Headway 27 for the flow re-direction endoluminal device (FRED) (MicroVention, Tustin, CA, USA), and Headway 21 for the FRED Jr. (MicroVention, Tustin, CA, USA) were used in combination with 0.014-inch or 0.016-inch microwires to by-pass the aneurysm neck. The microcatheter was advanced as distally as possible from the neck of the aneurysm. Then, the device was loaded into the microcatheter hub through a hemostatic valve and placed across the target landing zone. The FD device was deployed through a combination of unsheathing, pushing, and maintaining forward tension on the delivery wire of the device, or pulling and loading the microcatheter under continuous fluoroscopy. Simultaneously with the device deployment, stent apposition to the vessel wall was continuously checked. After satisfactory deployment and apposition of the device, a control angiogram was acquired to examine the device lumen and integrated/jailed branch patencies. After device deployment, the perioperative aneurysmal sac filling degree was recorded according to the O'Kelly Marotta (OKM) grading scale.

After the long introducer sheath placement, systemic heparinization was performed with a 5,000 international units intravenous (IV) bolus injection. The target activated clotting time was 2–2.5  $\times$  the baseline. Heparinization was not reversed at the end of the procedures.

### Follow-up treatment

Most of the patients were discharged from the hospital on the second day after the procedure and evaluated clinically on the fifth day. The digital subtraction angiography (DSA) F/U appointments were scheduled at 6, 12, 24, 36, and 60 months after the treatment.

The F/U DSA images were assessed in terms of aneurysm filling, FD stent patency, and integrated/jailed branch patency. The OKM grading scale was used to grade the aneurysmal filling and contrast stagnation

#### Main points

- Middle cerebral artery (MCA) aneurysms tend to be complex.
- Flow diverter stents are safe and effective in the treatment of MCA aneurysms.
- Higher occlusion rates are seen with a longer follow-up time.
- Patency of the side and jailed branches is preserved with flow diverter stents.

phase,<sup>6</sup> and OKM C3 and D grades were accepted as adequate occlusion. The FD stent patency was classified as A: patent; B: <50% stenosis; C: >50% stenosis; D: occluded; and whether the patient was symptomatic or not. Integrated/jailed branch patency was evaluated with regard to the pretreatment images as patent, decreased-caliber, and occluded; it was also determined whether the patient was symptomatic or not.

### Statistical analysis

Descriptive statistics were presented (minimum–maximum) as the median for non-normally distributed variables and as the mean and standard deviation for the normally distributed variables. Categorical variables were reported as frequencies and percentages. The Pearson chi-square test was used to investigate the effect of the FD stent type on aneurysmal occlusion, and the Mann–Whitney U test was used to analyze the effects of oversizing the stent on the aneurysm occlusion and integrated branch patency. The significance level was established as  $\alpha = 0.05$ . The IBM SPSS 21.0 software was used for data analysis.

## Results

### Patient and aneurysm characteristics

A total of 67 patients (52 female; median age, 58 years; age range, 30–75 years) with 76 MCA aneurysms were enrolled in the study. The mean aneurysm diameter was 4.45 mm (range, 1.1–12 mm). Only 5 aneurysms were larger than 10 mm. A total of 61 (80.3%) aneurysms were wide-necked, and 73 (96.2%) were saccular. Furthermore, two aneurysms were blister-like, and one was fusiform in shape. A total of 52 aneurysms (68.4%) were located at the M1 segments, and 24 (31.6%) were located at the MCA bifurcations. The demographics of the treated patients and baseline characteristics of the aneurysms are summarized in Table 1.

### Treatment characteristics

A total number of 79 FD stents were used in this study. The most frequently used device was FRED (45.6%), followed by FRED Jr. (29.1%), and PED (24.1%). Only one aneurysm was treated with Surpass (Stryker Neurovascular, Fremont, CA, USA).

In three cases, a second stent was deployed in a telescopic fashion because of the stent shortening. Coiling was used as an adjunctive technique in four large aneurysms, and an FD stent was used as second-line treatment in four cases (three of them were previously treated with Woven Endo-Bridge (WEB) intra-saccular FD and one with surgical clipping).

### Occlusion rates

A total of 65 patients with 73 aneurysms were followed up with (mean F/U time,  $32.1 \pm 6.3$  months). A total of 63 (86%) aneurysms had  $\geq 12$  months of DSA control, and 45 (62%) aneurysms had  $\geq 24$  months of DSA control. Only 10 (13.6%) aneurysms had a F/U duration of <12 months.

The overall occlusion rates for 6-, 12-, 24-, 36-, and 60-month DSA were 43.8%, 63.5%, 73.3%, 85.7%, and 87.5% respectively.

According to the last F/U time, the mean F/U period was  $24.7 \pm 18.8$  months, and the last F/U occlusion rates were 67.6% for FRED, 66.7% for PED, and 60.6% for FRED Jr. ( $P = 0.863$ ).

Since the flow dynamics differ between side-wall and bifurcation aneurysms, the occlusion rates of M1 and bifurcation aneurysms were compared. A total of 31 (64.6%) M1 aneurysms, and 16 (66.7%) bifurcation aneurysms were occluded on the last F/U ( $P = 0.861$ ) (Table 2).

### Integrated and jailed branches

An integrated branch is any branch arising from the aneurysm sac or neck, while a jailed branch is any branch arising from the parent artery adjacent to the aneurysm and covered with an FD stent. An integrated branch was covered with an FD during the treatment of 63 (82.8%) aneurysms (Figure 1). The most common was the anterior temporal artery, followed by the frontal branches (31.7% and 30.2%, respectively). A percentage of 6.6% (4/60) of the integrated branches at the 6-month F/U and 10% (6/60) at the last F/U were occluded without any symptoms (Table 3).

A total of 12 MCA branches were jailed using an FD. The most common one was also the anterior temporal artery. At the six-month F/U, one jailed branch was occluded without any neurological deficit. A total of 11/12 jailed branches were patent at the 12-month F/U, and 7/8 were patent at the 24-month F/U.

**Table 1.** Demographic data, aneurysm, and treatment characteristics

	n (%)
Age*	57.8 $\pm$ 9
<b>Gender</b>	
Female	52 (77.6)
Male	15 (22.4)
<b>Aneurysm type</b>	
Saccular	73 (96.1)
Blister	2 (2.6)
Fusiform	1 (1.3)
Aneurysm diameter (mm)*	2.5 $\pm$ 2.6
Wide neck	61 (80.3)
Aneurysm neck diameter (mm)*	3.8 $\pm$ 2.8
<b>Aneurysm location</b>	
MCA M1	52 (68.4)
MCA Bifurcation	24 (31.6)
<b>Flow diverter stent</b>	
FRED	36 (45.6)
FRED Jr.	23 (29.1)
PED	19 (24.1)
Surpass	1 (1.3)
Additional coil	4 (5.3)
Integrated branch	63 (82.2)
Jailed branch	12 (15.8)
Follow-up duration (months)*	32.1 $\pm$ 6.3

\*Mean  $\pm$  standard deviation. MCA, middle cerebral artery; FRED (Jr.), flow re-direction endoluminal device (Jr.); PED, pipeline embolization device.

Furthermore, the respective effects of stent oversizing on the aneurysm and integrated branch occlusion were investigated. For both, oversizing was compared between occluded and non-occluded groups. The median oversizing was 0.45 mm (0–1.30 mm) for occluded aneurysms and 0.50 mm (0–1.40 mm) for non-occluded aneurysms ( $P = 0.323$ ). The median oversizing for occluded integrated branches was 0.70 mm (0.45–1.10 mm) and 0.50 mm (0–1.40 mm) for non-occluded branches ( $P = 0.131$ ) (Table 4).

#### FD patency status at F/U

The in-stent stenosis rate was 30.1% at the 6-month F/U and only 4.7% at the 24-month

F/U. Thus, none of the patients had any neurological deficits because of the in-stent stenosis (Figure 2).

Severe in-stent stenosis was seen in two stents at the 24-month DSA.

#### Complications

Procedural complications occurred in 10 cases. The overall procedural complication rate was 14.9%; technical failure occurred in 5 cases, thromboembolic complications occurred in 4 cases, and hemorrhagic complications occurred in 1 case. One patient treated with FRED Jr. had a permanent deficit with a Modified Rankin Scale (mRS) score of 4 (Table 5).

#### Thromboembolic complications

In one patient with a left M1 aneurysm at the frontal branch origin, a partial thrombus not obstructing the flow was formed at the proximal end of the stent immediately after deployment of FRED Jr. Furthermore, total occlusion of the aneurysm sac and a slow flow of the frontal branch was seen. Immediately 2 mg of IV bolus tirofiban was injected. Substantial resolution of the in-stent thrombus with a total recovery of the aneurysm sac and frontal branch flow was seen on the control angiography. Postoperative neurological examination was routine. Even so, IV tirofiban infusion was continued for 24 h, and dual antiplatelet therapy was changed from clopidogrel to ticagrelor + ASA. At the 24-month F/U, the aneurysm sac was still filling (OKM B2).

Another FRED Jr. patient with a left M1 aneurysm was awoken from anesthesia with left-sided central facial palsy and right hemiparesis. An immediate control angiogram of the left ICA revealed total occlusion of the aneurysm and frontal branch. A total dose of 3-mg IV bolus tirofiban was administered, and the thrombus resolved completely. The IV tirofiban infusion was continued for 48 h. The antiaggregant therapy with ASA + clopidogrel was changed to ASA + ticagrelor. The patient's mRS score was 0. Entry remnant (OKM grade C2) of the aneurysm was seen at the 36-month control angiography.

A 75-year-old female with a left M1 aneurysm on the lenticulostriate artery origin was treated with FRED. She became right hemiplegic and aphasic 2 h after she was awoken from anesthesia. The control diffusion-weighted imaging and magnetic resonance imaging showed acute ischemia in the left MCA territory. Immediate control angiography of the left ICA revealed that the left anterior temporal artery, superior trunk (jailed with FRED) of the left MCA, and the aneurysm sac were totally thrombosed. Also, partial in-stent thrombosis was evident, and 2 mg of intraarterial tirofiban was administered directly into the stent lumen. At control angiography after intra-arterial tirofiban injection, minimal residual in-stent thrombus without flow deficiency was seen. Balloon angioplasty to the stent lumen was planned, but the balloon catheter could not be advanced into the stent lumen. The IV tirofiban infusion was continued for 48 h, and the patient was discharged with aphasia and right hemiparesis. At the six-month control angiography, total occlusion of the left MCA was seen. Cortical branches of the MCA were

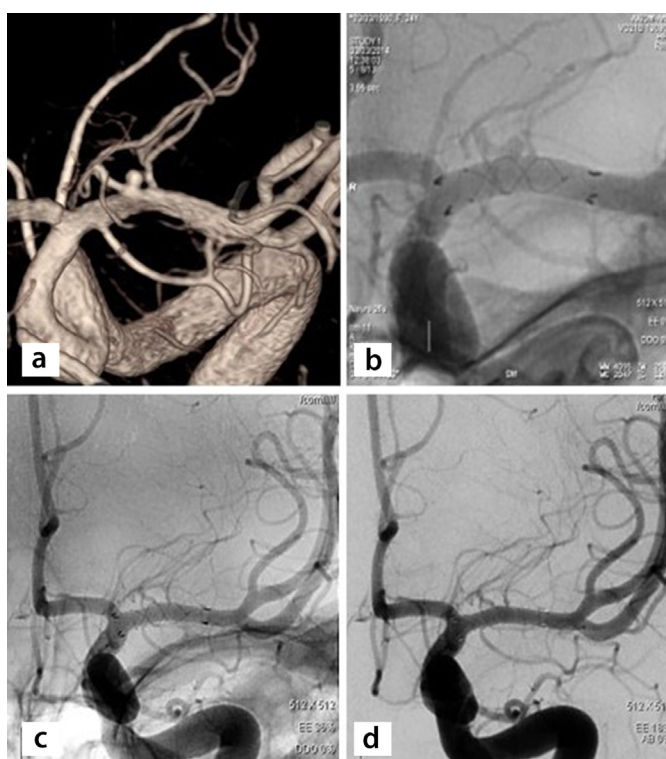


**Figure 1.** Twenty four-years old, female. (a) She had subarachnoid hemorrhage after rupture of a small left MCA M1 aneurysm at the origin of the lenticulostriate artery. (b) The patient is treated with a 3.5 x 17 x 11 mm FRED on the 30<sup>th</sup>-day of bleeding. (c, d) Control angiography on 2<sup>nd</sup>-months shows complete occlusion of the aneurysm and the patent lenticulostriate artery. MCA, middle cerebral artery; FRED, flow re-direction endoluminal device.

Stent	Occlusion n (%)		P
	+	-	
FRED	23 (67.6)	11 (32.4)	0.863
FRED Jr.	14 (60.9)	9 (39.1)	
PED	10 (66.7)	5 (33.3)	
<b>Location</b>			
M1	31 (64.6)	17 (35.4)	0.861
Bifurcation	16 (66.7)	8 (33.3)	

\*Pearson chi-square test, FRED (Jr.), flow re-direction endoluminal device (Jr.); PED, pipeline embolization device. One Surpass patient was excluded.

retrogradely filled via pial collaterals. The patient had an mRS score of 4 (Figure 3).

In the postoperative control Diffusion-weighted Imaging (DWI) of one patient treated with two FRED Jr.s in one session for right MCA bifurcation aneurysm (previously treated with WEB) and right A1–A2 aneu-

rysms, hyperacute infarction at the frontal lobe was detected. There was no major vessel occlusion visible in the immediate control DSA; still, both anterior cerebral artery and MCA flows were sluggish. A total dose of 2 mg IV bolus tirofiban was administered in two turns, with IV infusion for 24 h. Then,

the antiaggregant therapy was changed to ticagrelor + ASA. The patient was discharged without any neurological deficit.

The post-operative DWI of all patients was evaluated for cortical and deep infarcts. Symptomatic patients are discussed above. Among asymptomatic patients, three FRED patients (8.6%) had both cortical and deep millimetric DWI lesions. Two PED patients (10.6%) had both, and one PED patient (5.3%) had only a deep infarct. All FRED Jr. patients had DWI lesions.

#### Technical failures

Technical difficulties occurred in two PED and three FRED patients. In two PED and three FRED patients, the distal landing zone of the stents moved proximally close to the aneurysm neck; hence, a second stent was deployed in a telescopic fashion. In addition, one PED on the right MCA was shortened from the proximal landing zone, and a second stent was deployed.

#### Hemorrhagic complications and mortality

One patient with a left frontal branch origin aneurysm (10.7 mm in diameter) who was treated with FRED developed subarachnoid hemorrhage on postoperative day four. No additional treatment was performed other than decreasing the prasugrel dosage from 10 mg to 5 mg. The patient was discharged with an mRS score of 0 after seven days of hospitalization. The first F/U DSA was at the third month; the sac was still filling and had a slightly decreased diameter. Integrated (frontal artery) and jailed (anterior temporal artery and inferior trunk) branches were patent. However, a 5.4-mm nipple was developed on the posterior side of the aneurysm sac. No further action was taken. At the six-month F/U, the sac was occluded with patent integrated and jailed branches (Figure 4).

There were no treatment-related mortalities in this study.

## Discussion

The endovascular treatment of complex MCA aneurysms is not always possible with standard techniques. Even the recurrence rates of stent-assisted coiling are not negligible.<sup>7</sup> FD stents are widely used to treat intracranial aneurysms with a complex anatomy or recurrent aneurysms despite surgical or endovascular treatments. However, the literature data on the safety and efficacy of FD stent treatment of MCA aneurysms with a

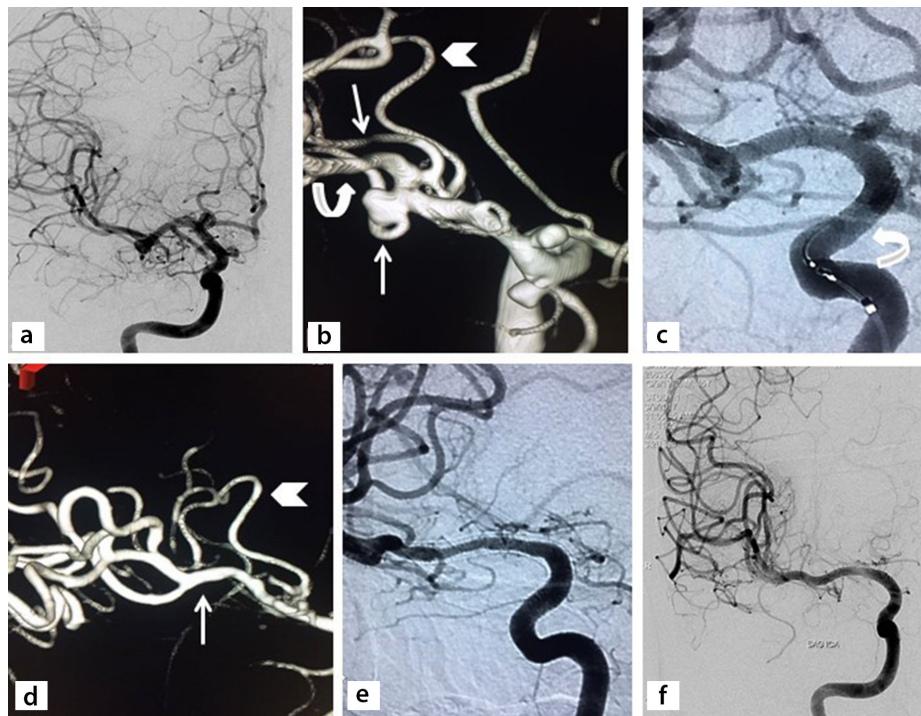


**Figure 2.** Forty five-years old female. (a) Right ICA DSA examination reveals three aneurysms; MCA bifurcation, proximal A1, anterior choroidal artery. (b, c) 3-D angiography shows the inferior trunk as the integrated branch (ascending arrow). All three aneurysms are treated with two successive pipeline stents extending between curved arrows. (d, e) Sixth-month control angiography shows the total occlusion of all aneurysms and the occlusion of the anterior temporal artery and the frontal branch (descending arrow). The patient is neurologically asymptomatic. The other frontal branch jailed by the stent is still patent (arrowhead). There is a medium degree of in-stent stenosis at the level of M1. (f) One-year control DSA examination reveals the total resolution of the stenosis. ICA, internal carotid artery; DSA, digital subtraction angiography; MCA, middle cerebral artery.

Table 3. Distributions of integrated and jailed branches and occlusion rates	
	n (%)
Integrated branch	n = 63
Anterior temporal artery	20 (31.7)
Frontal branches	19 (30.2)
Superior truncus	8 (12.7)
Lenticulostriate artery	8 (12.7)
Others	8 (12.7)
6. month occlusion	4 (6.6)
The last control occlusion	6 (10)
Jailed branch	n = 12
Anterior temporal artery	5 (41.7)
Superior truncus	2 (16.7)
Inferior truncus	2 (16.7)
Others	3 (25)
Jailed branch occlusion*	1 (8.3)

\*Both six-month and the last F/U; F/U, follow-up.

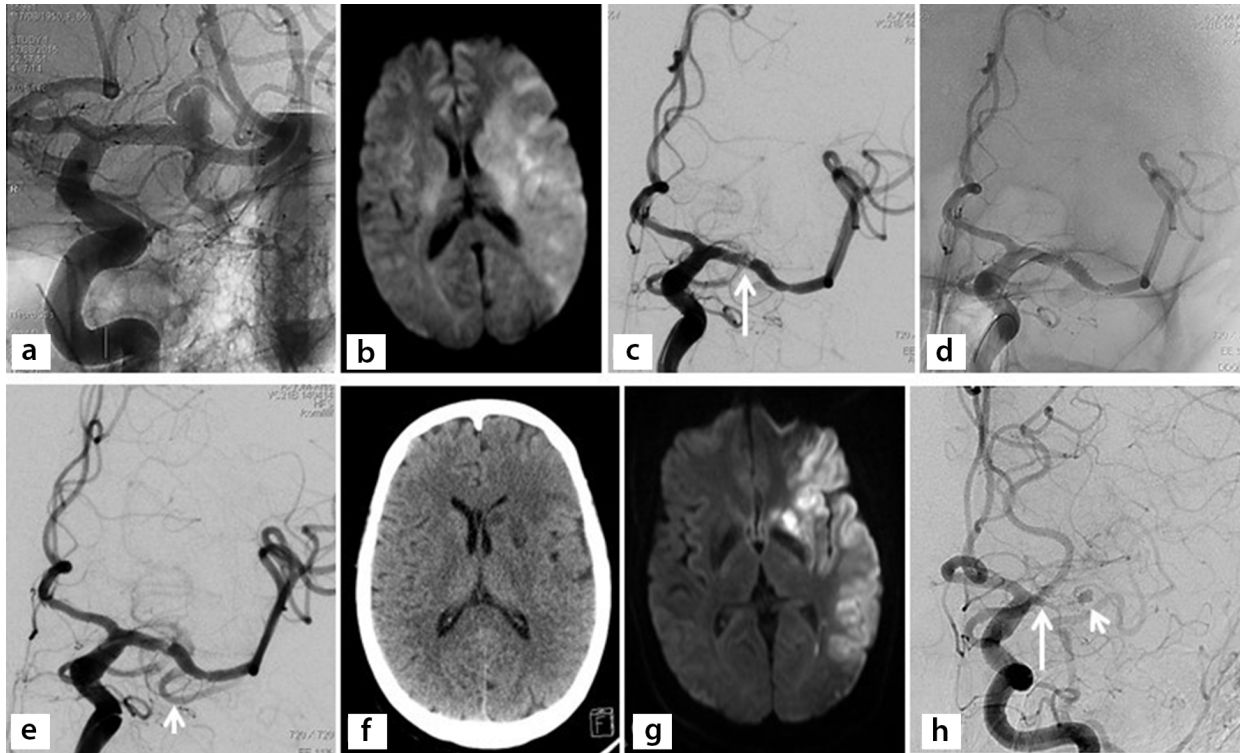


**Figure 3.** Seventy-five-year old, female. (a) Left M1 frontal branch origin aneurysm is treated with FRED. The stent is seen as entirely normal. (b) Two hours after anesthesia, the patient develops aphasia and right hemiparesis. DWI reveals acute ischemic stroke in MCA territory. (c, d) Immediate angiography shows the occlusion of both the frontal branch and the anterior temporal artery, and the aneurysm. There is also a partial thrombus within the stent lumen (long arrow). Also, note the dysmorphic changes -the fish mouth- in the stent. (e) 2 mg of IA tirofiban only enables the slow perfusion of the anterior temporal artery (short arrow). (f, g) Next day CT and DWI show no bleeding, but the acute ischemic changes despite the IV tirofiban infusion. (h) 6<sup>th</sup>-month follow-up DSA shows the total occlusion of the stent (long arrow). The aneurysm is still filling through collaterals to the lenticulostriate arteries (short arrow). FRED, flow re-direction endoluminal device; DW, diffusion-weighted imaging; MCA, middle cerebral artery; CT, computed tomography; DSA, digital subtraction angiography.

**Table 4.** Effect of oversizing the stent on the aneurysm occlusion and integrated branch patency

Aneurysm	Oversizing (mm) Median (minimum–maximum)	<i>P</i>
Occluded	0.45 (0–1.30)	0.323
Non-occluded	0.50 (0–1.40)	
<b>Integrated branch</b>		
Occluded	0.70 (0.45–1.10)	0.131
Non-occluded	0.50 (0–1.40)	

Mann–Whitney U test.

wide neck, complex anatomy, and integrated branches still seems to be limited.

This study investigated the safety and efficacy of FD stents in treating complex MCA aneurysms and compared the treatment success of PED, FRED, and FRED Jr. The median size of the aneurysms enrolled in this study was 4.45 mm (1.1–12 mm). Of the 76 aneurysms included in the study, 71 were small in size (<10 mm). The treatment indications regarding small intracranial aneurysms have not been clearly defined yet. The general opinion is that the treatment decision should not be based on a single parameter. Although the annual rupture rate of small

intracranial aneurysms is relatively low, morbidity and mortality rates are high in cases of rupture.<sup>8–10</sup> Moreover, small MCA aneurysms have a considerable risk of rupture even if they are smaller than 10 mm. Most of the treated aneurysms in this study either had wide necks or integrated branches. These two characteristics were the main parameters for using FD stents in the treatment.

The mean F/U period in this study was 32.1 months. Thus, 86% of the aneurysms had a DSA F/U time of  $\geq 12$  months, and 62% had a DSA F/U time of  $\geq 24$  months.

The total or adequate occlusion (OKM D or C3) rates were 43.8%, 63.5%, 73.3%,

85.7%, and 87.5% for the 6-, 12-, 24-, 36-, and 60-month F/Us, respectively. Excluding an aneurysm from circulation through flow diversion is time-dependent, as mentioned in many studies.<sup>11</sup> Therefore, higher occlusion rates are expected with longer F/U period. A systematic review including 12 studies regarding the treatment of 244 MCA aneurysms with FD stents showed a complete/near-complete occlusion rate of 78.7%, with a mean F/U period of 12 months.<sup>12</sup>

Yavuz et al.<sup>13</sup> reported FD treatment results of 25 aneurysms located at MCA bifurcation and beyond. The study revealed total occlusion rates of 76% and 90% on the 6-month and the last F/U, respectively. In a PED study including 10 complex MCA aneurysms, with a mean F/U period of 7.5 months, a total occlusion rate of 77% was found.<sup>14</sup> Bhogal et al.<sup>9</sup> reported FD treatment results of 15 M1 aneurysms with a median F/U time of 18.7 months. The total occlusion rate was 73%.

In the present study, the 12-month occlusion rate (63.5%) was lower than the occlusion rates in the above-mentioned studies; however, the 24- and 36-months occlusion

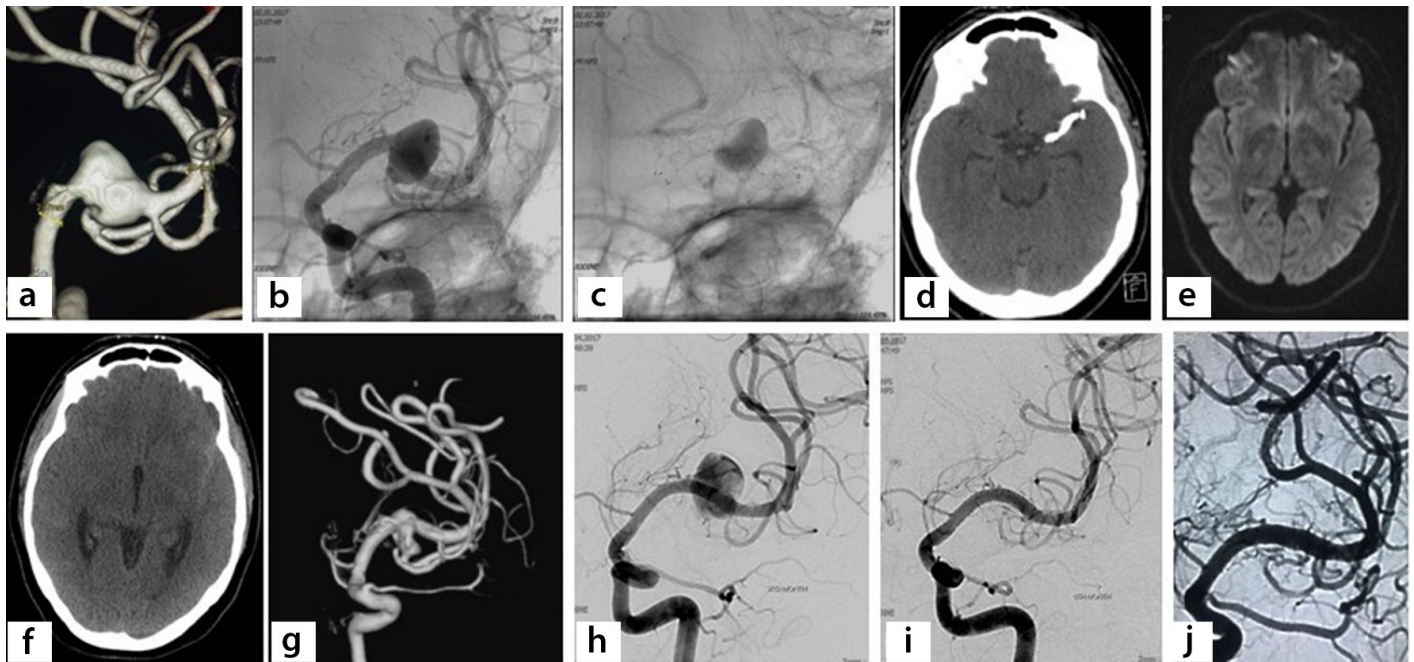


**Figure 4.** Forty one-years old female. (a, b) Left fusiform MCA aneurysm treated with FRED. The temporal branch is directly coming out of from sac. (c) The control angiography after the stent deployment shows prominent stagnation within the sac. (d, e) Control CT and DWI images are unremarkable. (f) The patient has a sudden onset of a severe headache on the 4<sup>th</sup>-day. CT examination reveals subarachnoid hemorrhage. (g) 3-D angiography shows partial thrombosis of the sac with irregular contours. The integrated branch is still patent. (h) Residual, but the slow filling of the sac is seen on 3-month control angiography. (i, j) Six and 12<sup>th</sup>-month follow-ups. No residual filling of the aneurysm. The MCA and the integrated branch are patent. MCA, middle cerebral artery; FRED, flow re-direction endoluminal device; DWI, diffusion-weighted imaging; CT, computed tomography

Table 5. Adverse events	
Procedural complications	n = 67 (%)
Technical	10 (14.9)
Thromboembolic	5 (7.5)
Hemorrhagic	4 (5.9)
In-stent stenosis*	1 (1.5)
	n = 76
6 Month	22/8 (30.1)
12 Month	10/4 (15.9)
24 Month	2/0 (4.7)
Last control	8/2 (11)
Morbidity	1
Mortality	0

\*(Sum/symptomatic).

rates (73.3% and 85.7%, respectively) are consistent with the literature. In the EuFRED study, the subgroup analysis showed that the total occlusion rate of intracranial bifurcation aneurysms was 61.5% at 180 days; this is similar to the results of the present study.<sup>3</sup> The majority of aneurysms in the above studies were located in MCA bifurcation or beyond it. In the present study, 68.4% of aneurysms were located at the M1 segment of MCA, and the occlusion rates for sidewall and bifurcation aneurysms were 64.6% and 66.7%, respectively.

FD treatment of bifurcation and sidewall aneurysms should be evaluated separately because of their hemodynamic differences. A recent meta-analysis investigating FD treatment of sidewall and bifurcation aneurysms reported comparable occlusion rates (69.4% and 73.9% respectively).<sup>15</sup> Another recent study investigating FD treatment of proximal MCA aneurysms reported occlusion rates for sidewall and bifurcation aneurysms (75% and 63% respectively).<sup>16</sup> Both of these studies show that the hemodynamic difference may not alter the occlusion rates to the expected extent. The present study also reveals comparable results.

Integrated branches or perforators mostly accompany the M1 segment aneurysms.

In this study, 82% of the aneurysms were accompanied by an integrated branch. It is the authors' opinion that this is the main reason for the lower first control occlusion rates. Also, the patency of the integrated branch is one of the major concerns regarding FD treatment. The oversizing of the FD to avoid technical failure may delay the occlusion of the aneurysm while contributing to the patency of the integrated branches.

Topcuoglu et al.<sup>17</sup> reported corroborative data showing that 11/17 MCA aneurysms with integrated branches remained open; only 2 of these aneurysms with patent in-

tegrated branches were occluded at the F/U. Based on this argument, the Cekirge and Saatci<sup>18</sup> occlusion grading system might be more practical while assessing the F/U occlusion grade of an aneurysm with integrated branches. The OKM grade C1 and C2 aneurysms were classified as class 5 "stable remodeling" according to the Cekirge and Saatci<sup>18</sup> occlusion grading system at the second control DSA. The effect of oversizing on the aneurysm and integrated branch occlusion was analyzed, and there was no significant difference between occluded/non-occluded aneurysms and integrated branches.

There was no statistically significant difference between the last F/U occlusion rates in the FRED, FRED Jr., and PED patients.

A total of 63 integrated branches were covered in 76 aneurysm treatments; 3 of them were lost to the F/U. The 6-month F/U and last F/U occlusion rates were 6.6% and 10%, respectively. None of the occluded integrated branches were symptomatic. Two studies investigating integrated branch patency after FD treatment of MCA aneurysms and a meta-analysis including 174 MCA branches covered with FD stents reported integrated branch occlusion rates of 10.5%, 20%, and 10.1%, respectively, at the last F/U visit.<sup>12,19,20</sup>

A total of 12 MCA branches were jailed by an FD in the study group. The most common one was the anterior temporal artery. At the six-month F/U, one jailed branch was occluded without any neurological deficit. Any of the other 11 jailed branches were occluded at the 12- or 24-month controls.

In this study group, the overall complication rate was 14.9% (10/67), with one hemorrhagic complication, four thromboembolic complications, and five technical failures. A single-center study regarding FD treatment of MCA bifurcation aneurysms reported a thromboembolic complication rate of 15.3%.<sup>9</sup> Another single-center study emphasized a covered branch status after FD treatment of distal bifurcation aneurysms, with a thromboembolic event rate of 17.6%.<sup>19</sup> Finally, Cagnazzo et al.<sup>12</sup> reported a general complication rate of 20.7% and a thromboembolic event rate of 16.3% in their meta-analysis on FD stent treatment of MCA aneurysms.

The present study's overall and thromboembolic complication rates were 14.9% and 7.5%, respectively; this is consistent with the literature. Even though the data is not statistically significant, FRED Jr. was used in three out of four thromboembolic complications; the other stent used was FRED.

An *in vitro* study suggests that FRED had higher thrombin generation and platelet activation than PED.<sup>21</sup> Both FRED Jr. and FRED are dual-layer stents with a higher metal load than PED. Therefore, this type-two error would probably not occur in series with a more significant number of cases. Interestingly, the lower profile FRED Jr. caused more thromboembolic events than FRED. Therefore, it is critical to test all the patients for clopidogrel and prasugrel resistance, and antiaggregation should be conducted as suggested for each drug.

There are several limitations to this study. First, it is a retrospective study with a relatively small study population to compare the safety and efficacy of different FD stents in treating MCA aneurysms. The low number of bifurcation aneurysms is another limitation. This study reflects a single-center and single-operator experience with FRED, FRED Jr., and PED in flow diversion of MCA aneurysms. Since learning curves tend to differ among operators, the comparison of outcomes of devices may not always apply to all potential interventionalists. Even so, a long F/U period and detailed definitions and solutions to complications may have an impact on the literature.

In conclusion, MCA aneurysms tend to be complex, with integrated branches and potentially wide necks. FD stents are safe and effective in the treatment of MCA aneurysms. The patency of the side and jailed branches is preserved in most cases. Higher occlusion and lower in-stent stenosis rates are seen with longer F/U durations. Oversizing the stent was not found to be a contributor to occlusion of the aneurysm or integrated branch.

### Conflict of interest disclosure

The authors declared no conflicts of interest.

### References

- Zaidat OO, Castonguay AC, Tebeb MS, et al. Middle cerebral artery aneurysm endovascular and surgical therapies: Comprehensive literature review and local experience. *Neurosurg Clin N Am*. 2014;25(3):455-469. [\[CrossRef\]](#)
- Alderazi YJ, Shastri D, Kass-Hout T, Prestigiacomo CJ, Gandhi CD. Flow diverters for intracranial aneurysms. *Stroke Res Treat*. 2014;2014:415653. [\[CrossRef\]](#)
- Killer-Oberpflazer M, Kocer N, Griessenauer CJ, et al. European multicenter study for the evaluation of a dual-layer flow-diverting stent for treatment of wide-neck intracranial aneurysms: the european flow-redirection intraluminal device study. *AJNR Am J Neuroradiol*. 2018;39(5):841-847. [\[CrossRef\]](#)
- Al Kasab S, Guerrero WR, Nakagawa D, Samaniego EA, Ortega-Gutierrez S, Hasan D. Safety and efficacy of the pipeline embolization device use in the outside circle of willis located intracranial aneurysms: a single-center experience. *Interv Neurol*. 2020;8(2-6):83-91. [\[CrossRef\]](#)
- Fiorella D, Gache L, Frame D, Arthur AS. How safe and effective are flow diverters for the treatment of unruptured small/medium intracranial aneurysms of the internal carotid artery? Meta-analysis for evidence-based performance goals. *J Neurointerv Surg*. 2020;12(9):869-873. [\[CrossRef\]](#)
- O'Kelly CJ, Krings T, Fiorella D, Marotta TR. A novel grading scale for the angiographic assessment of intracranial aneurysms treated using flow diverting stents. *Interv Neuroradiol*. 2010;16(2):133-137. [\[CrossRef\]](#)
- Pierot L, Cognard C, Spelle L, Moret J. Safety and efficacy of balloon remodeling technique during endovascular treatment of intracranial aneurysms: Critical review of the literature. *AJNR Am J Neuroradiol*. 2012;33(1):12-15. [\[CrossRef\]](#)
- Briganti F, Leone G, Marseglia M, et al. Endovascular treatment of cerebral aneurysms using flow-diverter devices: A systematic review. *Neuroradiol J*. 2015;28(4):365-375. [\[CrossRef\]](#)

- Bhogal P, AlMatter M, Bäßner H, Ganslandt O, Henkes H, Pérez MA. Flow diversion for the treatment of MCA bifurcation aneurysms-A single centre experience. *Front Neurol*. 2017;8:20. [\[CrossRef\]](#)
- Elsharkawy A, Lehečka M, Niemelä M, et al. Anatomic risk factors for middle cerebral artery aneurysm rupture: computed tomography angiography study of 1009 consecutive patients. *Neurosurgery*. 2013;73(5):825-837. [\[CrossRef\]](#)
- Ye G, Zhang M, Deng L, Chen X, Wang Y. Meta-analysis of the efficiency and prognosis of intracranial aneurysm treated with flow diverter devices. *J Mol Neurosci*. 2016;59(1):158-167. [\[CrossRef\]](#)
- Cagnazzo F, Mantilla D, Lefevre PH, Dargazanli C, Gascou G, Costalat V. Treatment of middle cerebral artery aneurysms with flow-diverter stents: a systematic review and meta-analysis. *AJNR Am J Neuroradiol*. 2017;38(12):2289-2294. [\[CrossRef\]](#)
- Yavuz K, Geyik S, Saatci I, Cekirge HS. Endovascular treatment of middle cerebral artery aneurysms with flow modification with the use of the pipeline embolization device. *AJNR Am J Neuroradiol*. 2014;35(3):529-535.
- Zanaty M, Chalouhi N, Tjoumakaris SI, Gonzalez LF, Rosenwasser R, Jabbour P. Flow diversion for complex middle cerebral artery aneurysms. *Neuroradiology*. 2014;56(5):381-387. [\[CrossRef\]](#)
- Abbasi M, Savasatano LE, Brinjikji W, et al. Endoluminal flow diverters in the treatment of sidewall and bifurcation aneurysm: A systematic review and meta-analysis of complications and angiographic outcomes. *Interv Neuroradiol*. 2022;28(2):229-239. [\[CrossRef\]](#)
- Lauzier DC, Root BK, Kayan Y, et al. Pipeline embolization of proximal middle cerebral artery aneurysms: A multicenter cohort study. *Interv Neuroradiol*. 2022;28(1):50-77. [\[CrossRef\]](#)
- Topcuoglu OM, Akgul E, Daglioglu E, et al. Flow diversion in middle cerebral artery aneurysms: is it really an all-purpose treatment? *World Neurosurg*. 2016;87:317-327. [\[CrossRef\]](#)
- Cekirge HS, Saatci I. A new aneurysm occlusion classification after the impact of flow modification. *AJNR Am J Neuroradiol*. 2016;37(1):19-24. [\[CrossRef\]](#)
- Gawlitza M, Januel AC, Tall P, Bonneville F, Cognard C. Flow diversion treatment of complex bifurcation aneurysms beyond the circle of Willis: a single-center series with special emphasis on covered cortical branches and perforating arteries. *J Neurointerv Surg*. 2016;8(5):481-487. [\[CrossRef\]](#)
- Michelozzi C, Darcourt J, Guenego A, et al. Flow diversion treatment of complex bifurcation aneurysms beyond the circle of Willis: complications, aneurysm sac occlusion, reabsorption, recurrence, and jailed branch

- modification at follow-up. *J Neurosurg.* 2019;131(6):1751-1762. [\[CrossRef\]](#)
21. Girdhar G, Andersen A, Pangerl E, et al. Thrombogenicity assessment of Pipeline Flex, Pipeline Shield, and FRED flow diverters in an in vitro human blood physiological flow loop model. *J Biomed Mater Res A.* 2018;106(12):3195-3202. [\[CrossRef\]](#)



# Microwave ablation as a primary versus secondary treatment for hepatocellular carcinoma

Philip Lee

Ajay Makkena

Mohamed Tantawi

Felipe Velasquez-Botero

John R. Eisenbrey

Colette M. Shaw

## PURPOSE

The purpose of this study was to analyze and compare the outcomes of percutaneous microwave ablation (MWA) when used as a primary vs. secondary treatment for hepatocellular carcinoma (HCC).

## METHODS

The clinical data of 192 patients with HCC treated with MWA between January 2012 and July 2021 were reviewed retrospectively, with 152 patients being treatment naïve (primary treatment) vs. 40 who had residual or recurrent disease following previous trans-arterial chemoembolization or trans-arterial radioembolization (secondary treatment). The primary outcomes were primary technical efficacy, 1- and 3-year local recurrence-free survival (RFS) and overall survival (OS), local recurrence rates, and adverse events. Pre- and post-intervention liver function tests were compared using a Wilcoxon signed rank test. Univariate and multivariate analyses were also performed, looking at prognostic factors associated with OS and local RFS.

## RESULTS

There was no significant difference in 1-year local RFS (primary 93.6% vs. secondary 93.7%;  $P = 0.97$ ) and 3-year local RFS (primary 80.6% vs. secondary 86.5%;  $P = 0.37$ ) rates. There was no significant difference in 1-year OS (primary 82.4% vs. secondary 86.6%;  $P = 0.51$ ) and 3-year OS (primary 68.3% vs. secondary 77.4%;  $P = 0.25$ ) between the two groups. The local recurrence rate (primary 9.8% vs. secondary 14.6%;  $P = 0.37$ ), primary technical efficacy (primary 96.2% vs. secondary 95%;  $P = 0.73$ ), and adverse events (primary 8.0% vs. secondary 11.6%;  $P = 0.45$ ) were also similar between the two groups.

## CONCLUSION

Microwave ablation is safe and effective as a secondary treatment for patients with HCC in a clinical salvage scenario and should be utilized more frequently.

## KEYWORDS

Hepatocellular carcinoma, microwave ablation, primary treatment, secondary treatment, recurrent HCC

From the Department of Radiology (P.L., A.M., M.T., F.V-B., J.R.E., C.M.S. ✉ cshaw@raadocs.com), Thomas Jefferson University, Philadelphia, USA.

Received 10 October 2022; revision requested 22 November 2022; last revision received 16 January 2023; accepted 06 February 2023.



Epub: 01.03.2023

Publication date: 29.03.2023

DOI: 10.4274/dir.2023.221930

The incidence of hepatocellular carcinoma (HCC) recurrence following surgical resection and locoregional therapy (LRT) performed with curative intent is high. Three-year local progression rates after radiofrequency ablation (RFA) vary widely between institutions, ranging from 3.2% to 21.9%.<sup>1-3</sup> Recurrence rates of 50% to 70% (of which 80% to 90% are intrahepatic) have been reported five years after hepatectomy.<sup>4</sup> Such recurrences constitute a significant cause of late mortality.

Trans-arterial therapies have traditionally been recommended in those with large tumors or multifocal disease (intermediate stage). Since some patients' treatment goals are palliative, it is common for patients to undergo more than one treatment, sometimes using combination therapies to achieve disease control.<sup>5</sup> The reported rates of residual disease post-trans-arte-

rial chemoembolization (TACE) vary by study but range from 40% to 70%.<sup>6-9</sup> The failure of TACE or a patient being refractory to treatment has been defined as the development of untreatable progression of HCC despite repeated embolizations.<sup>10-12</sup> Guidelines from international scientific societies recommend switching to systemic therapy in certain patients.<sup>13-15</sup>

While first-line treatment failures are frequently treated with LRT, there is no consensus on when or how these LRTs should be applied. Thermal ablation is an established first-line treatment for small-sized HCCs; however, data evaluating the efficacy of ablation when used as salvage therapy is lacking. Many studies have shown similar outcomes between first-line RFA and microwave ablation (MWA), especially with lesions of less than 3 cm.<sup>16,17</sup> One meta-analysis looked at five original studies comparing RFA and MWA outcomes in 431 patients.<sup>18</sup> In a patient population of very early- or early-stage HCC [Barcelona Clinic Liver Cancer (BCLC)] (stage 0 or A), they found no differences in complete ablation rates, recurrence-free survival (RFS), overall survival (OS), or complication rates. The average ablation time for MWA was significantly shorter than for RFA.<sup>16-25</sup> In most centers in the USA, MWA has replaced RFA for treating HCC. The purpose of this study was to compare treatment outcomes of MWA in naïve tumors with those with residual or recurrent disease following TACE or transarterial radioembolization (TARE).

## Methods

### Patient population

This protocol was approved by the Institutional Review Board of Thomas Jefferson University under protocol no: 21E-073 on February 17<sup>th</sup>, 2021. The requirement for informed consent was waived due to the retrospective nature of the study. In this review, the clinical data of 192 patients (mean age  $66.8 \pm 8.5$  years) with HCC treated with MWA between

January 2012 and July 2021 were reviewed retrospectively.

Ablation was performed under general anesthesia. Probe placement was performed under ultrasound guidance, with secondary computed tomography (CT) utilized in hard-to-visualize tumors, such as those within the dome of the liver. The vast majority of cases involved the treatment of a sole lesion, and no patient had more than two tumors treated in any given session. The standard of care was same-day discharge, with some high-risk patients or those with logistical challenges staying overnight. Of the 192 patients, 152 were treatment naïve (primary treatment), and 40 had received prior TACE or TARE (secondary treatment). Within this patient population, a total of 231 HCC lesions were evaluated, of which, 188 were part of the primary treatment group, and 43 were part of the secondary treatment group. Additional relevant data obtained from electronic medical records included patient demographics, tumor characteristics, primary treatment information, MWA treatment parameters, pre- and post-intervention cross-sectional imaging, and pre- and post-intervention liver function tests.

### Outcome measures

Treatment response was classified according to the 2018 Liver Imaging Reporting and Data System Treatment Response Algorithm.<sup>26</sup> All cases were reviewed at a multidisciplinary liver-tumor board conference. Primary technical efficacy was defined as the percentage of tumors that were reported non-viable on initial 1- to 2-month follow-up imaging. *Residual disease* was defined as a viable tumor in the ablation cavity on the first follow-up imaging on contrast-enhanced multiphase magnetic resonance imaging or CT. Local recurrence was described as a tumor at or immediately adjacent to the ablation cavity following a previously documented successful treatment. Local RFS was calculated from the date of MWA to either the date of recurrence, liver transplant, or the date of the last imaging follow-up. The OS rate was calculated from the date of MWA to either the date of death or censorship at the last follow-up. Adverse events were classified based on criteria developed by the Society of Interventional Radiology Standards of Practice Committee.<sup>27</sup>

### Statistical analysis

Demographic and clinical data of the primary and secondary treatment groups were

compared. Local RFS and OS were compared between the two groups, utilizing a Kaplan–Meier survival analysis with a corresponding log–rank test, with  $P < 0.05$  considered significant. Additionally, 1- and 3-year local RFS and OS were calculated. The rates of local recurrence, primary technical efficacy, and major and minor adverse events were compared using chi-squared tests. Pre- and post-intervention liver function tests were compared using a Wilcoxon signed rank test.

A univariate prognostic factor analysis was performed for both local RFS and OS, analyzing 18 variables. Independent-sample t-tests and chi-squared tests were used for continuous and categorical variables, respectively. All variables found to be significant in the univariate analysis were placed into a binomial logistic regression model for multivariate analysis. All statistical analyses were performed using Statistics for Windows (SPSS) v. 28 statistical software (IBM Corp., Armonk, NY, USA).

## Results

Patient demographics, tumor information, and clinical characteristics are summarized in Table 1. Example cases of a treatment-naïve tumor and secondary treatment are provided in Figures 1 and 2, respectively. The mean follow-up time was 18.2 months (range: 0.3–98.6 months). In the secondary treatment group, 28 lesions were previously treated with TACE, 12 with prior TARE, and three with combination TACE/TARE. The BCLC class and Eastern Cooperative Oncology Group (ECOG) performance status were significantly different between the groups. Sixty-two percent (117/188) of primary treatment patients were BCLC A vs. 42% (18/43) in the secondary treatment group, 16% (30/188) of primary treatment patients were BCLC B vs. 14% (6/43) in the secondary treatment group, 21% (39/188) of primary treatment patients were BCLC C vs. 44% (19/43) in the secondary treatment group, and 1% (2/188) of primary treatment patients were BCLC D vs. none in the secondary treatment group ( $P = 0.014$ ). Seventy-eight percent (147/188) of primary treatment patients were ECOG 0 vs. 56% (24/43) in the secondary treatment group, 14% (27/188) of primary treatment patients were ECOG 1 vs. 21% (9/43) in the secondary treatment group, 6% (12/188) of primary treatment patients were ECOG 2 vs. 23% (10/43) in the secondary treatment group, and 1% (2/188) of primary treatment patients were ECOG 3 vs. none in the secondary treatment group ( $P = 0.003$ ). The likelihood of an overnight stay also signifi-

#### Main points

- Recurrent or residual hepatocellular carcinoma (HCC) following locoregional therapy is still relatively common.
- There are currently no guidelines for the treatment of residual tumors following locoregional therapy.
- Microwave ablation appears safe and effective as a secondary treatment of HCC, with similar local recurrence rates compared with its use as a primary treatment.

cantly varied between the two groups, with 24% (42/175) of primary patients requiring at least an overnight stay vs. 44% (16/36) of secondary patients ( $P = 0.012$ ). Otherwise, the groups were similarly matched across age, gender, *target* tumor size, Child–Pugh score, Model for End-Stage Liver Disease (MELD) score, and baseline liver function tests.

Primary technical efficacy was achieved in 96.8% (152/157) of patients in the primary treatment group and in 95% (38/40) of patients in the secondary treatment group ( $P = 0.58$ ) (Table 2). It should be noted that all MWA was performed on the same system by two treating interventionalists, resulting in a

relatively standardized treatment approach. Five of the seven total incomplete ablations were successfully retreated with either MWA, TACE, or TARE. One of the two remaining patients underwent a transplant shortly afterward, and the other was lost to follow-up. No additional treatments for the study tumor were provided until recurrence was detected on cross-sectional imaging. The percentage of patients in the primary (63/188: 34.0%) and secondary groups (16/43: 37.0%) who went on to liver transplant was equal ( $P = 0.71$ ). The proportion of patients who developed progressive disease at other sites in the liver was similar at 50% (62/125) in the

primary treatment group vs. 62% (16/26) in the secondary treatment group ( $P = 0.42$ ). Although the proportion of patients who developed extra-hepatic metastasis was greater in the secondary treatment group [19% (5/26)] compared with the primary treatment group [7% (8/123)], the difference did not reach statistical significance ( $P = 0.06$ ).

There was no significant difference in OS ( $P = 0.36$ ) or local RFS ( $P = 0.68$ ) between the two groups as measured by a Kaplan–Meier survival analysis with corresponding log-rank tests (Figure 3). A survival analysis was performed using a sample size of 182/188 for primary treatment and 41/43 for secondary treatment after excluding cases with failed primary technical efficacy. The 1-year local RFS in the primary group was 93.6% vs. 93.75% in the secondary group ( $P = 0.97$ ), and the 3-year local RFS in the primary group was 80.58% vs. 86.53% in the secondary group ( $P = 0.37$ ). The 1-year OS in the primary group was 82.39% vs. 86.65% in the secondary group ( $P = 0.51$ ), and the 3-year OS in the primary group was 68.34% vs. 77.45% in the secondary group ( $P = 0.25$ ) (Table 2). The median progression-free survival (PFS) for the primary treatment group was 75.5 months vs. 69.8 months for the secondary treatment group [ratio of 1.08 with a 95% confidence interval (CI) of 0.40 to 2.9]. Similarly, the median OS for the primary treatment group was 95.4 months, while it was undefined in the secondary treatment group.

The rate of adverse events was 8.0% (15/188) in the primary treatment group and 11.6% (5/43) in the secondary treatment group ( $P = 0.45$ ). Events were further subdivided into major and minor adverse events. The rate of major adverse events was 2.7% (5/188) in the primary treatment group vs. 2.3% (1/43) in the secondary treatment group ( $P = 0.88$ ). The rate of minor adverse events was 5.3% (10/188) in the primary treatment group vs. 9.3% (4/43) in the secondary treatment group ( $P = 0.32$ ) (Table 2). Minor adverse events included pain, abdominal wall hematoma, and biliary stricture, all of which were managed conservatively. Major adverse events included the formation of a hepatic abscess that required percutaneous drainage, hepatorenal syndrome, readmission to an outside hospital for fever attributed to post-ablation syndrome, and hepatic encephalopathy necessitating hospital admission, which was treated successfully with medication. One ablation-related death from sepsis occurred in the secondary treatment group.

**Table 1.** Patient demographics and clinical characteristics. Continuous variables are reported as mean  $\pm$  standard deviation, and categorical variables are reported as frequency (%)

	Primary treatment (n = 188)	Secondary treatment (n = 43)	P value
<b>Sex</b>			
Male	143 (76%)	37 (86%)	0.15
Female	45 (24%)	6 (14%)	
Age (years)	67.0 $\pm$ 8.7	66.1 $\pm$ 7.8	0.55
Tumor size (cm)	2.2 $\pm$ 0.8	2.5 $\pm$ 1.3	0.06
<b>Child–Pugh class</b>			
			0.32
A	102 (65%)	25 (64%)	-
B	48 (31%)	14 (36%)	-
C	7 (4%)	0	-
<b>BCLC*</b>			
A	117 (62%)	18 (42%)	0.014
B	30 (16%)	6 (14%)	
C	39 (21%)	19 (44%)	
D	2 (1%)	0	
<b>ECOG*</b>			
0	147 (78%)	24 (56%)	0.003
1	27 (14%)	9 (21%)	
2	12 (6%)	10 (23%)	
3	2 (1%)	0	
<b>Baseline labs</b>			
AFP (ng/mL)	69.8 $\pm$ 241	77.1 $\pm$ 239	0.86
TBili (mg/dL)	1.0 $\pm$ 0.82	1.1 $\pm$ 0.80	0.81
AST (U/L)	53.0 $\pm$ 42.0	69.0 $\pm$ 87.0	0.10
ALT (U/L)	48.0 $\pm$ 43.0	52.0 $\pm$ 69.0	0.61
Albumin (g/dL)	3.9 $\pm$ 0.6	3.9 $\pm$ 0.7	0.62
Platelets ( $\times 10^3/L$ )	143 $\pm$ 78	143 $\pm$ 87	0.99
MELD	10.4 $\pm$ 4.0	11.4 $\pm$ 4.0	0.16
<b>Length of stay*</b>			
Same-day discharge	133 (76%)	20 (56%)	0.012
Overnight stay	42 (24%)	16 (44%)	
Liver transplant	63 (34%)	16 (37%)	0.71

\*Denotes statistical significance. BCLC, Barcelona Clinic Liver Cancer; ECOG, Eastern Cooperative Oncology Group; AFP, alpha-fetoprotein; TBili, total bilirubin; AST, aspartate aminotransferase; ALT, alanine transaminase; MELD, Model for End-Stage Liver Disease.

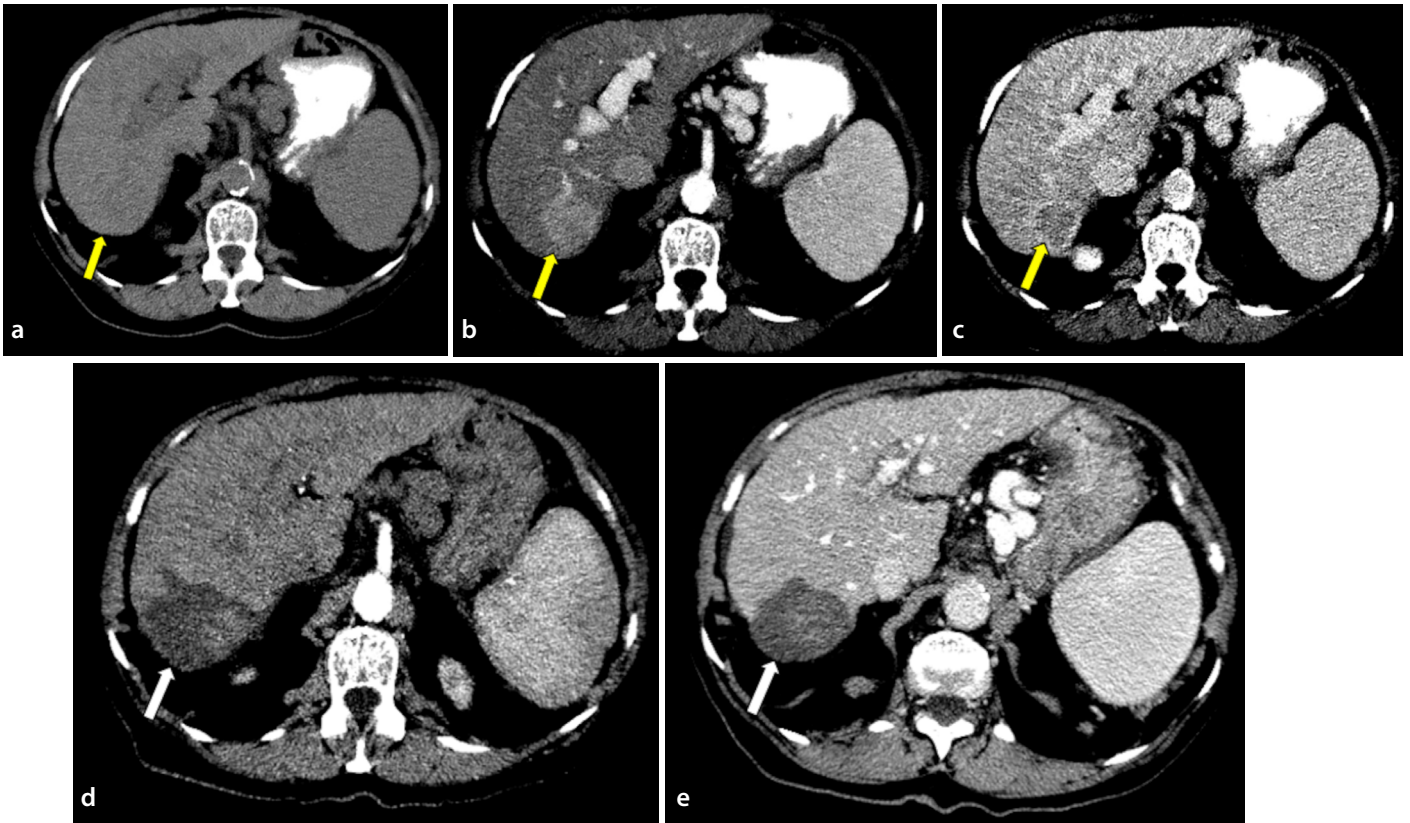


**Figure 1.** Comparison of pre- and post-treatment imaging in a 78-year-old female with a history of hepatocellular carcinoma (HCC) in the context of cirrhosis due to nonalcoholic steatohepatitis after microwave ablation of a segment 6/7 HCC. Pre-treatment computed tomography (CT) with (a) non-contrast, (b) arterial, and (c) portal venous phases show a 3.7 cm segment 6/7 mass demonstrating early-phase arterial hyperenhancement, capsular appearance, and central washout consistent with an Liver Imaging Reporting and Data System 5 HCC (yellow arrow). Post-treatment CT with (d) arterial and (e) portal venous phases demonstrates no enhancement in the treatment cavity consistent with Liver Imaging Reporting and Data System Treatment Response non-viable (white arrow).

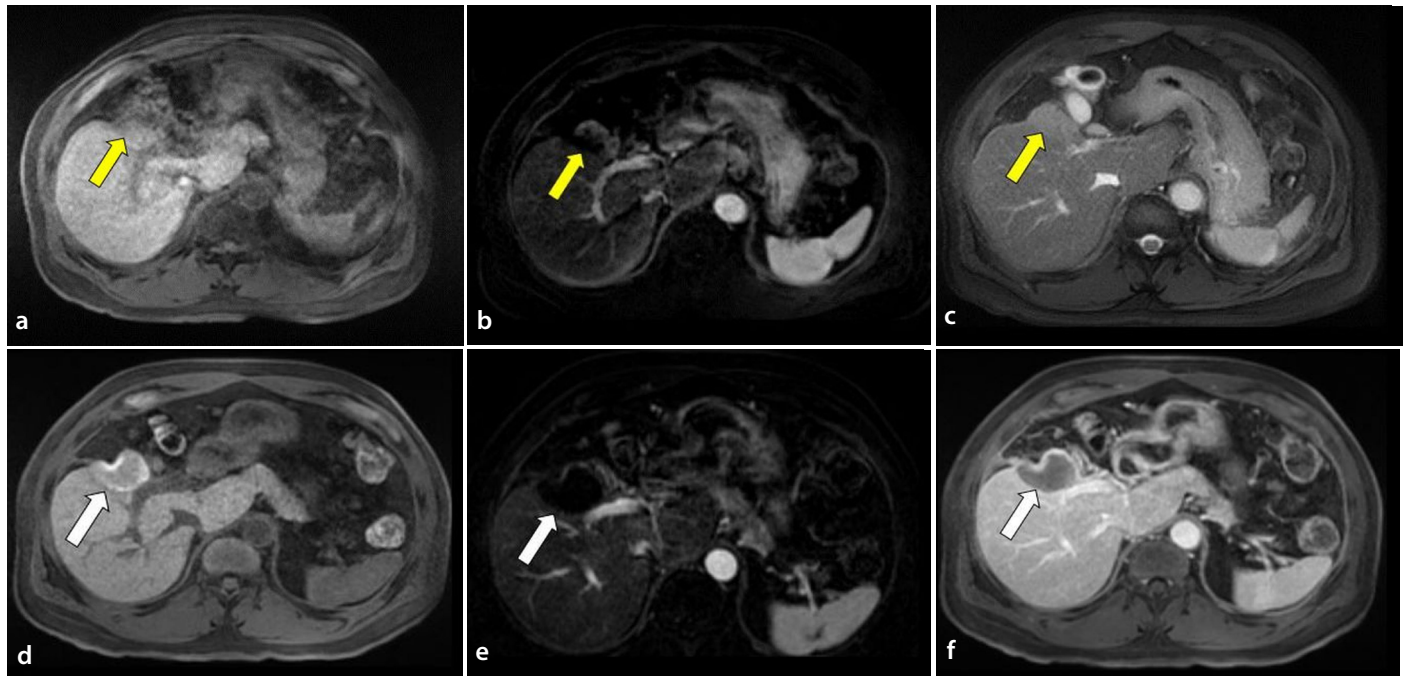


**Figure 2.** Comparison of pre- and post-treatment imaging in a 70-year-old male with a history of hepatocellular carcinoma (HCC) in the context of chronic hepatitis B after microwave ablation of residual disease in segment 5 sixteen months after trans-arterial chemoembolization. Pre-treatment magnetic resonance imaging (MRI) T1-weighted sequences with (a) non-contrast, (b) arterial, and (c) portal venous phases show a residual 3.5 cm nodular enhancing segment-5 lesion with peripheral washout at the anterosuperior and left lateral borders of the treatment cavity consistent with Liver Imaging Reporting and Data System Treatment Response viable (yellow arrow). Post-treatment MRI T1-weighted sequences with (d) non-contrast, (e) arterial, and (f) portal venous phases demonstrate a new ablation cavity with no evidence of arterial phase hyperenhancement or washout consistent with LIRADS-TR non-viable (white arrow).

The local recurrence rates were calculated after excluding cases with failed primary technical efficacy (6/188 for the primary treatment group and 2/43 for the secondary treatment group). The local recurrence rate for the primary treatment group was 9.8%

(18/182) vs. 14.6% (6/41) for the secondary treatment group ( $P = 0.37$ ) (Table 2). The mean follow-up time for the primary group was 18.2 months (range: 0.3–98.6 months) vs. 18.1 months (range: 0.6–89.0 months) in the secondary group. Twelve recurrent le-

sions were retreated with either TACE, TARE, or MWA. The remainder of the patients were treated with systemic therapy or radiation therapy, or they were lost to follow-up.

Pre- and post-intervention tumor marker and liver function tests were compared, with alpha-fetoprotein (AFP) ( $P < 0.001$ ), total bilirubin (TBili) ( $P = 0.043$ ), and albumin ( $P < 0.001$ ) found to be significant (Table 3). Age, Milan criteria, and ablation time were all found to be associated with local RFS by univariate analysis (Table 4). The Milan criteria were an independent predictor of RFS by multivariate analysis, with an odds ratio (OR) of 0.11 (95% CI: 0.018–0.730,  $P = 0.022$ ). Ablation time was an independent predictor of RFS, with an OR of 1.44 (95% CI: 1.053–1.994,  $P = 0.023$ ). The Child–Pugh score, BCLC stage, ECOG status, Milan criteria, AFP, TBili, albumin, platelets, international normalized ratio (INR), MELD score, and length of hospital stay were all found to be associated with OS by univariate analysis (Table 5). The MELD score was an independent predictor of OS by multivariate analysis, with an OR of 0.82 (95% CI: 0.720–0.951,  $P = 0.008$ ).

## Discussion

In the present study, compared with the primary treatment group, the secondary treatment group had a slightly worse ECOG performance status, presented at a more advanced BCLC stage, and had more patients requiring at least an overnight stay post-intervention. They were otherwise similarly matched in terms of age, sex, target tumor size, Child–Pugh score, MELD score, and liver function tests. Despite having a worse baseline ECOG performance status and a more advanced BCLC stage, we found no difference in the 1- and 3-year local RFS and OS rates, local recurrence rates, primary technical effi-

Primary outcomes	Primary treatment (n = 188)	Secondary treatment (n = 43)	P value
1-year OS	82.4%	86.6%	0.51
3-year OS	68.3%	77.4%	0.25
1-year local RFS	93.6%	91.1%, 93.7%	0.97
3-year local RFS	80.6%	84.3%, 86.5%	0.37
Local recurrence rate	18 (9.8%)	6 (14.6%)	0.37
Primary technical efficacy	152 (96.8%)	38 (95%)	0.58
Adverse events	15 (8.0%)	5 (11.6%)	0.45
Major adverse events	5 (2.7%)	1 (2.3%)	0.88
Minor adverse events	10 (5.3%)	4 (9.3%)	0.32

OS, overall survival; RFS, recurrence-free survival.

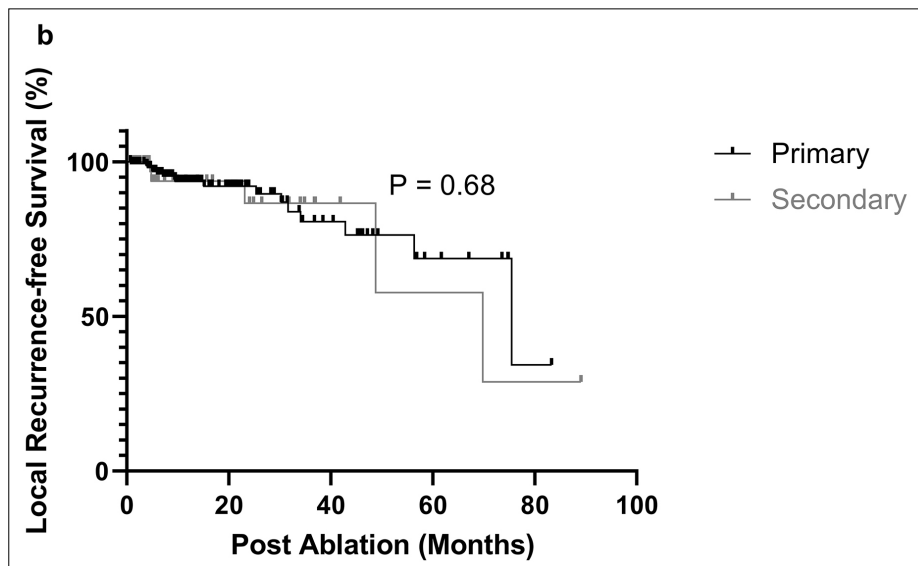
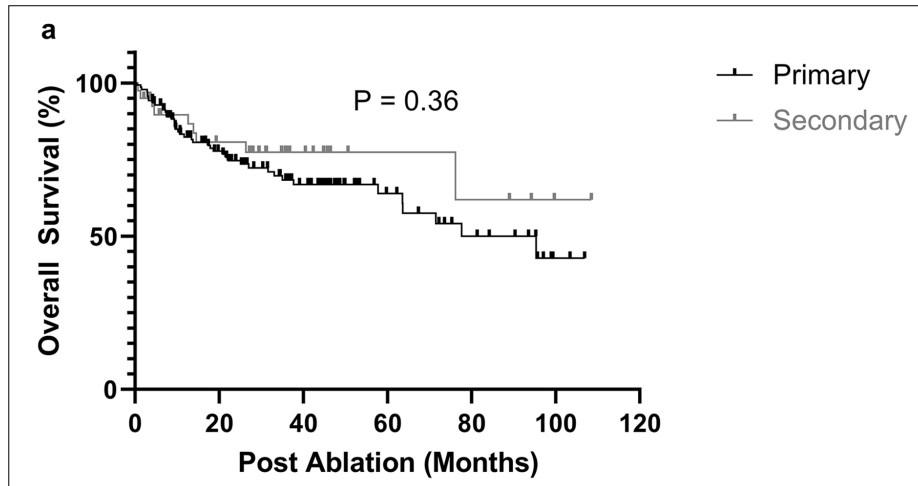


**Figure 3.** (a) Overall survival curves and (b) local recurrence-free survival curves of patients with hepatocellular carcinoma treated with primary vs. secondary microwave ablation.

**Table 3.** Summary of Wilcoxon signed rank test comparing pre- and post-intervention tumor marker and liver function tests

Lab parameter	P value
AFP*	<0.001
TBili*	0.043
AST	0.182
ALT	0.082
Albumin*	<0.001
INR	0.987
MELD	0.974

\*Denotes statistical significance. AFP, alpha-fetoprotein; TBili, total bilirubin; AST, aspartate aminotransferase; ALT, alanine transaminase; INR, international normalized ratio; MELD, Model for End-Stage Liver Disease.

**Table 4.** Univariate and multivariate prognostic factor analyses for local recurrence-free survival

Prognostic factor	Univariate analysis <i>P</i> value	Multivariate analysis odds ratio (95% CI)	<i>P</i> value
Age (<65 vs. >65)*	0.04	2.839 (0.847–9.515)	0.091
Sex	0.58		
Tumor size	0.16		
Child–Pugh	0.95		
BCLC	0.47		
ECOG	0.40		
Milan*	0.038	0.113 (0.018–0.730)	0.022
Ascites (yes/no)	0.40		
AFP	0.95		
TBili	0.82		
AST	0.06		
ALT	0.07		
Albumin	0.98		
Platelets	0.54		
INR	0.69		
MELD	0.99		
Length of stay	0.27		
Ablation time*	0.02	1.449 (1.053–1.994)	0.023

\*Denotes statistical significance. BCLC, Barcelona Clinic Liver Cancer; ECOG, Eastern Cooperative Oncology Group; AFP, alpha-fetoprotein; TBili, total bilirubin; AST, aspartate aminotransferase; ALT, alanine transaminase; INR, international normalized ratio; MELD, Model for End-Stage Liver Disease; CI, confidence interval.

**Table 5.** Univariate and multivariate prognostic factor analyses for overall survival

Prognostic factor	Univariate analysis <i>P</i> value	Multivariate analysis odds ratio (95% CI)	<i>P</i> value
Age	0.14		
Sex	0.85		
Tumor size	0.48		
Child–Pugh*	0.015	1.336 (0.139–12.859)	0.816
BCLC*	<0.001	0.769 (0.239–2.477)	0.554
ECOG*	<0.001	1.053 (0.236–4.703)	0.930
Milan*	0.004	0.727 (0.092–5.735)	0.550
Ascites (yes/no)	0.72		
AFP*	0.20	1.00 (0.999–1.001)	0.950
TBili*	0.004	1.229 (0.596–2.533)	0.664
AST	0.52		
ALT	0.14		
Albumin*	<0.001	1.229 (0.988–8.537)	0.053
Platelets*	0.025	1.002 (0.995–1.008)	0.580
INR*	0.005	4.650 (0.224–96.466)	0.289
MELD*	<0.001	0.828 (0.720–0.951)	0.008
Length of stay*	<0.001	0.871 (0.528–1.437)	0.589
Ablation time	0.48		
Local recurrence	0.07		
Primary technical efficacy	0.06		

\*Denotes statistical significance. BCLC, Barcelona Clinic Liver Cancer; ECOG, Eastern Cooperative Oncology Group; AFP, alpha-fetoprotein; TBili, total bilirubin; AST, aspartate aminotransferase; ALT, alanine transaminase; INR, international normalized ratio; MELD, Model for End-Stage Liver Disease; CI, confidence interval.

cacy rates, or rate of adverse events between patients with HCC treated with MWA as their primary vs. secondary treatment. Across both treatment groups, these primary outcomes were also in line with what has been observed in other studies.<sup>16,18,28,29</sup> However, it should be noted that overall follow-up was limited, with a mean of 18.2 months (range: 0.3–98.6 months), which may have influenced the OS data.

Comparing the baseline and post-ablation lab test results, we found that AFP, TBili, and albumin were significantly different between the primary and secondary treatment groups, instead of “Comparing the baseline and post-ablation lab test results, we found that AFP, TBili, and albumin were significantly different. However, the MELD score, which uses a composite of lab values to predict short-term survival, was unchanged. This supports the idea that while there can be short-term fluctuations in liver function tests, MWA is generally well tolerated, and there was no evidence of any acute decompensation among the patients in this study.

The univariate prognostic factor analysis found that age, Milan criteria, and ablation time were related to local RFS. In the multivariate analysis, the Milan criteria and ablation time were independent predictors, indicating that the stage of the disease is an important factor in patient outcomes. The univariate prognostic factor analysis showed that the Child–Pugh score, BCLC stage, ECOG status, AFP, TBili, albumin, platelets, INR, MELD score, and length of hospital stay were all associated with OS. The MELD score was found to be an independent prognostic factor in the multivariate analysis, which is unsurprising given that this clinical characteristic is known to be closely associated with prognosis.

In this study, approximately 19% (43/231) of patients received MWA as a secondary treatment for residual or recurrent disease following TACE or TARE. Of these, 72.1% (31/43) received TACE, with the remaining receiving TARE or combination TACE/TARE therapy. There is currently no consensus on the optimal use of salvage therapy in such patients. However, TACE/TARE is generally favored in patients with large or invasive tumors as well as in those with evidence of portal vein invasion. MWA is usually preferred in patients with smaller tumors in favorable locations away from major anatomical structures, such as the dome of the liver, gallbladder, or biliary system.<sup>17</sup> The choice of therapy is also essentially operator and institution depend-

ent. A recent study by Chen et al.<sup>30</sup> studied patients with intermediate-stage HCC who were refractory to TACE and compared the OS and RFS of MWA vs. sorafenib as salvage therapy. They found that the MWA group had longer median OS and RFS compared with those of the sorafenib group, suggesting that ablation is a viable option for salvage therapy in such patients.<sup>30</sup>

Recent studies have evaluated the efficacy and safety of new systemic antineoplastic therapies (atezolizumab/bevacizumab) compared with conventional first-line treatment with sorafenib in patients with unresectable HCC, demonstrating significantly increased OS and PFS rates.<sup>31,32</sup> However, to our knowledge, no studies have been conducted comparing the clinical outcomes and disease prognosis associated with the use of local ablative treatments and these newer chemotherapeutic agents in HCC.

In the cohort of patients with a small tumor size (mean:  $2.26 \pm 0.93$  cm), mostly good performance status (ECOG 0 and 1), and primarily early- or intermediate-stage liver disease (BCLC A and B), MWA was equally effective in treating lesions that failed to respond completely to TACE/TARE as it was in treating naïve lesions. We recognize that the population sample size in the secondary treatment group was small and may have contributed to the statistically non-significant results of the primary outcomes. The study group was heterogeneous in terms of disease burden and performance status at presentation. In terms of care goals, treatment intent was curative for some, downstaged to within the Milan criteria for transplant for others, with palliation for those who were not transplant candidates. The analysis did not distinguish between those who had residual disease vs. those with recurrence or between those treated primarily with TACE vs. TARE. While this study showed MWA to be safe and technically effective in a salvage setting, future studies should narrow the focus to include a more specific patient population.

In conclusion, tumor recurrence and its potential impact on survival remain a challenge in patients with HCC treated with hepatectomy and LRTs. Data to guide second-line treatments are very limited. In this retrospective study on clinical experience with MWA as a salvage therapy in patients with residual/recurrent HCC, we showed that despite more advanced tumor stages and poorer performance status at presentation, the survival outcomes and recurrence rates were similar in patients with residual/recur-

rent HCC compared with those in patients who received MWA as a first-line treatment. When used as a second-line treatment, MWA was technically effective and well tolerated.

### Conflict of interest disclosure

The authors declared no conflicts of interest.

### Funding

Grant support from Johnson and Johnson. The publication of this article was made possible in part by support from the Thomas Jefferson University Open Access Fund.

## References

1. Shiina S, Tateishi R, Arano T, et al. Radiofrequency ablation for hepatocellular carcinoma: 10-year outcome and prognostic factors. *Am J Gastroenterol*. 2012;107(4):569-577. [\[CrossRef\]](#)
2. Kono M, Inoue T, Kudo M, et al. Radiofrequency ablation for hepatocellular carcinoma measuring 2 cm or smaller: results and risk factors for local recurrence. *Dig Dis*. 2014;32(6):670-677. [\[CrossRef\]](#)
3. Hao Y, Numata K, Ishii T, et al. Rate of local tumor progression following radiofrequency ablation of pathologically early hepatocellular carcinoma. *World J Gastroenterol*. 2017;23(17):3111-3121. [\[CrossRef\]](#)
4. Minagawa M, Makuuchi M, Takayama T, Kokudo N. Selection criteria for repeat hepatectomy in patients with recurrent hepatocellular carcinoma. *Ann Surg*. 2003;238(5):703-710. [\[CrossRef\]](#)
5. Vogl TJ, Trapp M, Schroeder H, et al. Transarterial chemoembolization for hepatocellular carcinoma: volumetric and morphologic CT criteria for assessment of prognosis and therapeutic success-results from a liver transplantation center. *Radiology*. 2000;214(2):349-357. [\[CrossRef\]](#)
6. Ippolito D, Bonaffini PA, Ratti L, et al. Hepatocellular carcinoma treated with transarterial chemoembolization: dynamic perfusion-CT in the assessment of residual tumor. *World J Gastroenterol*. 2010;16(47):5993-6000. [\[CrossRef\]](#)
7. Kono Y, Lucidarme O, Choi SH, et al. Contrast-enhanced ultrasound as a predictor of treatment efficacy within 2 weeks after transarterial chemoembolization of hepatocellular carcinoma. *J Vasc Interv Radiol*. 2007;18(1 Pt 1):57-65. [\[CrossRef\]](#)
8. Kwan SW, Fidelman N, Ma E, et al. Imaging predictors of the response to transarterial chemoembolization in patients with hepatocellular carcinoma: a radiological-pathological correlation. *Liver Transpl*. 2012;18(6):727-736. [\[CrossRef\]](#)

9. Shaw CM, Eisenbrey JR, Lyshchik A, et al. Contrast-enhanced ultrasound evaluation of residual blood flow to hepatocellular carcinoma after treatment with transarterial chemoembolization using drug-eluting beads: a prospective study. *J Ultrasound Med*. 2015;34(5):859-867. [\[CrossRef\]](#)
10. Lencioni R. Loco-regional treatment of hepatocellular carcinoma. *Hepatology*. 2010;52(2):762-773. [\[CrossRef\]](#)
11. Park JW, Amarapurkar D, Chao Y, et al. Consensus recommendations and review by an International Expert Panel on Interventions in Hepatocellular Carcinoma (EPOIHCC). *Liver Int*. 2013;33(3):327-337. [\[CrossRef\]](#)
12. Yamanaka K, Hatano E, Kitamura K, et al. Early evaluation of transcatheter arterial chemoembolization-refractory hepatocellular carcinoma. *J Gastroenterol*. 2012;47(3):343-346. [\[CrossRef\]](#)
13. European Association for the Study of the Liver. EASL Clinical Practice Guidelines: management of hepatocellular carcinoma. *J Hepatol*. 2018;69(1):182-236. [\[CrossRef\]](#)
14. Heimbach JK, Kulik LM, Finn RS, et al. AASLD guidelines for the treatment of hepatocellular carcinoma. *Hepatology*. 2018;67(1):358-380. [\[CrossRef\]](#)
15. Vogel A, Cervantes A, Chau I, et al. Hepatocellular carcinoma: ESMO Clinical Practice Guidelines for diagnosis, treatment and follow-up. *Ann Oncol*. 2019;30(5):871-873. [\[CrossRef\]](#)
16. Izzo F, Granata V, Grassi R, et al. Radiofrequency ablation and microwave ablation in liver tumors: an update. *Oncologist*. 2019;24(10):990-1005. [\[CrossRef\]](#)
17. Ponniah SA, Zori AG, Cabrera R. Locoregional therapies for bridging and downstaging hepatocellular carcinoma prior to liver transplant. In: Sergi CM, ed. *Brisbane, Liver Cancer*; 2021. [\[CrossRef\]](#)
18. Yu Q, Liu C, Navuluri R, Ahmed O. Percutaneous microwave ablation versus radiofrequency ablation of hepatocellular carcinoma: a meta-analysis of randomized controlled trials. *Abdom Radiol (NY)*. 2021;46(9):4467-4475. [\[CrossRef\]](#)
19. Abdelaziz A, Elbaz T, Shousha HI, et al. Efficacy and survival analysis of percutaneous radiofrequency versus microwave ablation for hepatocellular carcinoma: an Egyptian multidisciplinary clinic experience. *Surg Endosc*. 2014;28(12):3429-3434. [\[CrossRef\]](#)
20. An C, Li WZ, Huang ZM, et al. Small single perivascular hepatocellular carcinoma: comparisons of radiofrequency ablation and microwave ablation by using propensity score analysis. *Eur Radiol*. 2021;31(7):4764-4773. [\[CrossRef\]](#)
21. Kamal A, Elmoety AAA, Rostom YAM, et al. Percutaneous radiofrequency versus microwave ablation for management of

- hepatocellular carcinoma: a randomized controlled trial. *J Gastrointest Oncol.* 2019;10(3):562-571. [\[CrossRef\]](#)
22. Nault JC, Sutter O, Nahon P, et al. Percutaneous treatment of hepatocellular carcinoma: state of the art and innovations. *J Hepatol.* 2018;68(4):783-797. [\[CrossRef\]](#)
  23. Shibata T, Iimuro Y, Yamamoto Y, et al. Small hepatocellular carcinoma: comparison of radio-frequency ablation and percutaneous microwave coagulation therapy. *Radiology.* 2002;223(2):331-337. [\[CrossRef\]](#)
  24. Som A, Reid NJ, DiCapua J, et al. Microwave ablation as bridging therapy for patients with hepatocellular carcinoma awaiting liver transplant: a single center experience. *Cardiovasc Intervent Radiol.* 2021;44(11):1749-1754. [\[CrossRef\]](#)
  25. Viesti Violi N, Duran R, Guiu B, et al. Efficacy of microwave ablation versus radiofrequency ablation for the treatment of hepatocellular carcinoma in patients with chronic liver disease: a randomised controlled phase 2 trial. *Lancet Gastroenterol Hepatol.* 2018;3(5):317-325. [\[CrossRef\]](#)
  26. Chernyak V, Fowler KJ, Kamaya A, et al. Liver imaging reporting and data system (LI-RADS) version 2018: imaging of hepatocellular carcinoma in at-risk patients. *Radiology.* 2018;289(3):816-830. [\[CrossRef\]](#)
  27. Khalilzadeh O, Baerlocher MO, Shyn PB, et al. Proposal of a new adverse event classification by the society of interventional radiology standards of practice committee. *J Vasc Interv Radiol.* 2017;28(10):1432-1437. [\[CrossRef\]](#)
  28. Xu Y, Shen Q, Wang N, et al. Microwave ablation is as effective as radiofrequency ablation for very-early-stage hepatocellular carcinoma. *Chin J Cancer.* 2017;36(1):14. [\[CrossRef\]](#)
  29. Swan RZ, Sindram D, Martinie JB, Iannitti DA. Operative microwave ablation for hepatocellular carcinoma: complications, recurrence, and long-term outcomes. *J Gastrointest Surg.* 2013;17(4):719-729. [\[CrossRef\]](#)
  30. Chen S, Shi M, Shen L, et al. Microwave ablation versus sorafenib for intermediate-stage hepatocellular carcinoma with transcatheter arterial chemoembolization refractoriness: a propensity score matching analysis. *Int J Hyperthermia.* 2020;37(1):384-391. [\[CrossRef\]](#)
  31. Cheng AL, Qin S, Ikeda M, et al. Updated efficacy and safety data from IMbrave150: Atezolizumab plus bevacizumab vs. sorafenib for unresectable hepatocellular carcinoma. *J Hepatol.* 2022;76(4):862-873. [\[CrossRef\]](#)
  32. Ahmed F, Onwumeh-Okwundu J, Yukselen Z, et al. Atezolizumab plus bevacizumab versus sorafenib or atezolizumab alone for unresectable hepatocellular carcinoma: a systematic review. *World J Gastrointest Oncol.* 2021;13(11):1813-1832. [\[CrossRef\]](#)



# Percutaneous cholecystoduodenal stent as a definite treatment for acute cholecystitis in elderly or comorbid patients: a bicentric retrospective study

Tae Yun Lee\*   
 Jong Woo Kim\*   
 Dong Jae Shim   
 Doyoung Kim   
 Young Chul Yoon   
 Edward Wolfgang Lee 

\*Equally contributed as co-first author.

## PURPOSE

To investigate the safety and efficacy of percutaneous cholecystoduodenal stent (CDS) placement to prevent recurrence of acute cholecystitis in patients who were unfit for cholecystectomy.

## METHODS

Between April 2016 and January 2022, 46 patients [median age (range) = 81 (37–99) years; men = 15] with acute cholecystitis who were unfit for surgery underwent percutaneous cholecystostomy followed by a CDS placement in two institutions. Plastic stents of three different materials were used [polyethylene, polyurethane (PU), and polycarbonate (PCB)-based PU]. Clinical outcomes, including technical and clinical success rates and early (<30 days) and delayed adverse events, were retrospectively assessed by stent type.

## RESULTS

CDS placement was technically successful in 39 patients. Clinical success, defined as cholecystostomy catheter removal, was achieved in 35 of 39 patients. Immediate complications, such as acute pancreatitis and peritonitis, occurred in two patients. Two patients experienced recurrent cholecystitis during a 113-day follow-up (range, 3–1,723). Three-stent groups had significantly different delayed complications on Fisher's exact test ( $P = 0.021$ ). The Bonferroni post-hoc analysis showed the PCB-PU group tended to have fewer complications than the PU group ( $P = 0.060$ ).

## CONCLUSION

CDS placement is applicable in treating acute cholecystitis patients who were initially unfit for surgery, but further investigation is needed. Although it was not statistically significant, a PCB-PU stent can be suitable for this use because it tends to have fewer delayed complications and is equipped with a drawstring and side holes.

## KEYWORDS

Biliary system, catheter, gallbladder, percutaneous, stent

Department of Surgery (T.Y.L., Y.C.Y.), Incheon St. Mary's Hospital, College of Medicine, The Catholic University of Korea, Seoul, Republic of Korea; Department of Radiology (J.W.K.), Chung-Ang University H.C.S. Hyundai Hospital, Namyangju, Korea; Department of Radiology (D.J.S.  inharad@naver.com, D.K.), Incheon St. Mary's Hospital, College of Medicine, The Catholic University of Korea, Seoul, Republic of Korea; Department of Radiology, Division of Interventional Radiology (E.W.L.), UCLA Medical Center, David Geffen School of Medicine at UCLA, Los Angeles, CA, USA.

Received 11 November 2022; revision requested 23 December 2022; accepted 08 February 2023.



Epub: 08.03.2023

Publication date: 29.03.2023

DOI: 10.4274/dir.2023.222003

The standard treatment of acute cholecystitis, laparoscopic cholecystectomy, carries risks of general anesthesia and surgery.<sup>1-3</sup> Due to those risks, surgeons often hesitate to perform this surgery on elderly or comorbid patients. Percutaneous cholecystostomy does not require general anesthesia and is known to be safe, so it is usually implemented as a bridge to surgery or definite treatment in elderly and comorbid patients.<sup>1,4</sup> However, maintaining the external drainage catheter can cause adverse events (AEs), including dislocation, bile leakage, or infection, and substantially impair the patient's quality of life. Patients treated only by temporary cholecystostomy and antibiotics for acute cholecystitis experienced a 1-year and 3-year recurrence of acute cholecystitis of 35% and 46%, respectively.<sup>2</sup> For these patients, cholecystoduodenal or cystic duct stent (CDS) can be a beneficial alternative treatment. Only one previous clinical study of 33 patients and several case reports have been

You may cite this article as: Lee TY, Kim JW, Shim DJ, Kim D, Yoon YC, Lee EW. Percutaneous cholecystoduodenal stent as a definite treatment for acute cholecystitis in elderly or comorbid patients: a bicentric retrospective study. *Diagn Interv Radiol.* 2023;29(2):367-372.

published on percutaneous CDS placement; thus, this topic requires more extensive clinical studies.<sup>2,5-9</sup> Furthermore, no dedicated devices are available for this procedure, and the most appropriate type of stent is unknown. Additionally, recent literature on endoscopic CDS supports the efficacy of CDS.<sup>10</sup> Technical success rates were reported to be high in both percutaneous (91%) and endoscopic (6%–100%) approaches and had significant clinical success rates (>80%).<sup>2,9-13</sup> This study aims to investigate the safety and efficacy of percutaneous CDS placement for patients with acute cholecystitis who are unfit for cholecystectomy and to assess its clinical outcomes.

## Methods

### Patients

The Institutional Review Board of Incheon St. Mary Hospital (approval no: OC21RA-DI0153) and the Institutional Review Board of Chung-Ang University H.C.S. Hyundai Hospital (approval no: BI0-IRB 2021-006) approved this retrospective study. Due to its retrospective nature, the requirement of informed consent was waived. Between April 2016 and January 2022, patients that presented with acute cholecystitis and were ineligible for surgery were candidates for the placement of a CDS. Medical records and radiological images of these patients were retrospectively reviewed. All patients were diagnosed with acute cholecystitis based on right upper abdominal tenderness, laboratory findings, and imaging studies, including ultrasonography or computed tomography, and were treated with percutaneous cholecystostomy.<sup>14</sup> Several days after improving the acute inflammatory condition, a surgeon and an anesthesiologist assessed the patient's surgical eligibility. Patients who did not qualify for surgery were referred to interventional radiology for CDS placement. Indi-

cations for CDS placement included patients who were elderly (>80 years old), at high risk for general anesthesia due to comorbidity, or had a poor performance status (Eastern Cooperative Oncology Group III or IV). Patients younger than 19 years old were not considered for this study. Immediate post-procedural AEs (<30 days) were evaluated using the Cardiovascular and Interventional Radiology Society of Europe (CIRSE) classification system.<sup>15</sup> Delayed AEs were recorded regarding stent fracture, dislocation, and recurrent cholecystitis.

### Procedure

Three dedicated interventional radiologists conducted the procedure (with 3, 8, and 10 years of experience, respectively). The placement of CDS was performed under conscious sedation with fentanyl (1 µg/kg) and midazolam (0.05 mg/kg). After subcutaneous injection of 2% lidocaine at the cholecystostomy site, the cholecystostomy catheter was exchanged with an 8 Fr vascular sheath with a tip marker (Super Sheath R/O, Boston Scientific, Marlborough, MA or Brite Tip sheath, Cordis, Miami Lakes, FL). Cystic duct cannulation was attempted with appropriate-shaped catheters, including 4 or 5 Fr Cobra (Cook, Bloomington, IN), 5 Fr Kumpe (Cook), or Davis (Jungsung Medical, Seoul, Korea) with 0.035- or 0.032-inch regu-

lar guidewires (Terumo, Tokyo, Japan). After cannulating the cystic duct with a guidewire up to the jejunum, 5 to 8 Fr plastic stents were placed over the guidewire (Figure 1). Pushers enclosed in a ureteral double-J set were used to insert the stent into the gallbladder. Initially, 11 patients underwent placement of a polyethylene stent, which was not equipped with a drawstring. However, the rest of the patients underwent placement of a double-J ureteral stent fitted with a drawstring. The double-J catheter shape and location were adjusted with drawstrings. A 10.2 Fr cholecystostomy catheter was immediately placed over the wire used for the stent placement to assist with procedure-associated symptom relief and prevent recurrent cholecystitis due to stent malfunction. After several days without clinical symptoms of fever or pain, a capping test and transcatheter cholecystography were performed to evaluate stent patency. In the case of a negative capping test and confirmed stent patency, the temporary catheter was removed, and the patient was discharged from the hospital. Outpatient clinic follow-ups were recommended for patients every six months or after any unexpected events. Regular stent exchanges or surgery were not considered unless there was any event of recurrent cholecystitis.

### Main points

- Cholecystoduodenal stents (CDS) were successfully placed in 39 of 46 patients, and external drainage catheters were successfully removed in 35 of 39 patients.
- Immediate complications presented as recurrent cholecystitis occurred in two patients during a 113-day follow-up (range, 3–1,723).
- A polycarbonate-based polyurethane stent seems more suitable for this use.
- CDS placement could be a safe and effective treatment for preventing recurrent cholecystitis in surgically ineligible patients.

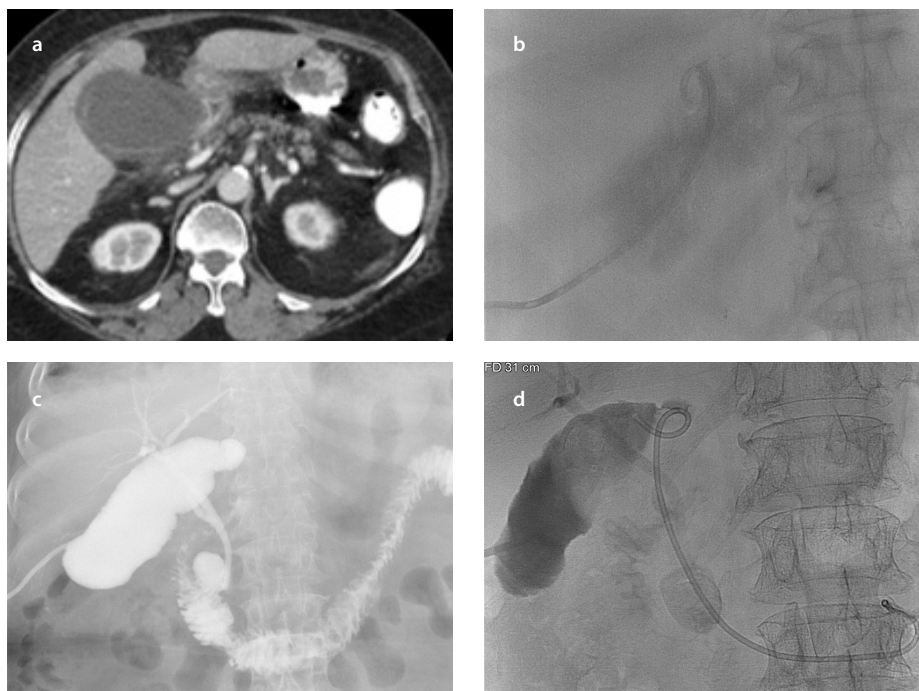


**Figure 1.** Successful cholecystoduodenal stent placement. (a) An 80-year-old woman with type 2 diabetes mellitus and atrial fibrillation presented with right upper abdominal pain. Computed tomography shows a distended gallbladder with mural wall thickening, suggestive of acute cholecystitis. (b) A percutaneous cholecystostomy catheter that was placed via transperitoneal access under ultrasonography and fluoroscopy guidance. (c) A transcatheter cholecystography showing patent cystic duct and duodenal diverticulum 17 days after cholecystostomy. (d) After cannulation of the cystic duct with a 5 Fr catheter and a 0.035-inch guidewire, a polyethylene stent (7 Fr, 12 cm) was placed over the guidewire.

## Materials and types of stents

During the first two years, patients were treated with a 7 Fr, 12–15 cm polyethylene stent (double-J and single-J, Zimmon, Cook, Bloomington, IN) traditionally used for endoscopic insertion. The polyethylene stent was not equipped with a drawstring or side holes. A single-J stent, usually used for pancreatic duct stents and with side holes, was subsequently utilized for the above papilla placement in two patients. During the next two years, patients were treated with a polyurethane (PU) double-J (5–8 Fr, 20–30 cm, Endo-Sof, Cook, Bloomington, IN) catheter for a ureteral stent, which had a drawstring and multiple side holes. While using the PU stent, a high incidence of stent fracture and dislocation was noticed. Therefore, both institutions used polycarbonate (PCB)-based PU stents (6–8 Fr, 14 cm Inlay Optima, BD, Franklin Lakes, NJ) for the rest of the duration. A photograph of the three stents is presented in Figure 2. Depending on the situation, the stent size and length were decided at the operators' discretion.

## Statistical analysis

Normality was tested with the Shapiro–Wilk test. The differences in AE rates between the three stent groups (polyethylene, PU, and PCB-PU) were compared using Fisher's exact test. Post-hoc tests between groups were performed by implementing Bonferroni's methods. Statistical analysis and adjustment of *P* values for multiple comparisons were conducted with R software (version 4.0.3, The R Foundation for Statistical Computing, Vienna, Austria; RVAideMemoire Package). Two-tailed *P* values of less than 0.050 were considered statistically significant. Subgroup analysis on technical success and AEs in transhepatic and transperitoneal access groups was performed using chi-square or Fisher's exact test.

## Results

During the six-year study period, 46 patients underwent an attempt to place a CDS via percutaneous access in two hospitals (41 patients at Incheon St. Mary's Hospital and 5 patients at Chung-Ang University H.C.S. Hyundai Hospital). Polyethylene stents were attempted in 11 patients with double-J (*n* = 9) or single-J (*n* = 2) stents. PU double-J stents were attempted in 14 patients, and PCB-PU stents were attempted in 21 patients. Collectively, 39 patients successfully received CDS (Figure 3). Clinical success, defined as removing the cholecystostomy catheter, was

achieved in 35 of 39 patients. The median periods from percutaneous cholecystostomy to CDS and from CDS to cholecystostomy catheter removal were 16 (0–794) and 5 (0–41) days, respectively. Percutaneous catheters were kept in seven technically unsuccessful patients and four clinically unsuccessful patients. Furthermore, one of seven technically unsuccessful patients underwent cholecystectomy during the follow-up period. The patients' characteristics are presented in Table 1.

The detailed causes of clinical failures included: contrast medium obstruction during transcatheter cholecystography in two patients (Figure 4), pancreatitis leading to stent removal in one patient, and advanced protrusion of the single-J stent against the duodenal wall in one patient initially intended to be placed above the papilla. In the patient with the protruding stent, concerns of a duodenal ulcer formation by the abutting stent tip resulted in stent removal. An immediate postprocedural AE occurred in 16 patients, including 14 minor (CIRSE classification I and II) and 2 major (CIRSE classification III) AEs.

The most common AE was abdominal pain (*n* = 8), followed by fever (*n* = 4) and vomiting (*n* = 2). All patients with minor AEs were treated with conservative management and recovered without sequelae. Major AEs were present in one patient with pancreatitis and another patient with biloma and peritonitis. The patient with pancreatitis was treated with stent removal and conservative management and recovered. The patient with biloma underwent percutaneous drainage and recovered. During the follow-up period (median, 113 days; range, 3–1,737), the most common delayed AEs were stent dislocation (*n* = 7) and fracture (*n* = 7, Figure 5), followed by recurrent cholecystitis (*n* = 2). Twelve patients died of their disease progression, and 34 patients were still alive at the time of the last evaluation. Clinical outcomes are displayed in Table 2. Delayed AEs occurred differently in the three stent groups (*P* = 0.021). However, subsequent post-hoc analysis showed no significant difference in the groups with the Bonferroni method (polyethylene vs. PU: *P* = 0.117; polyethylene vs.

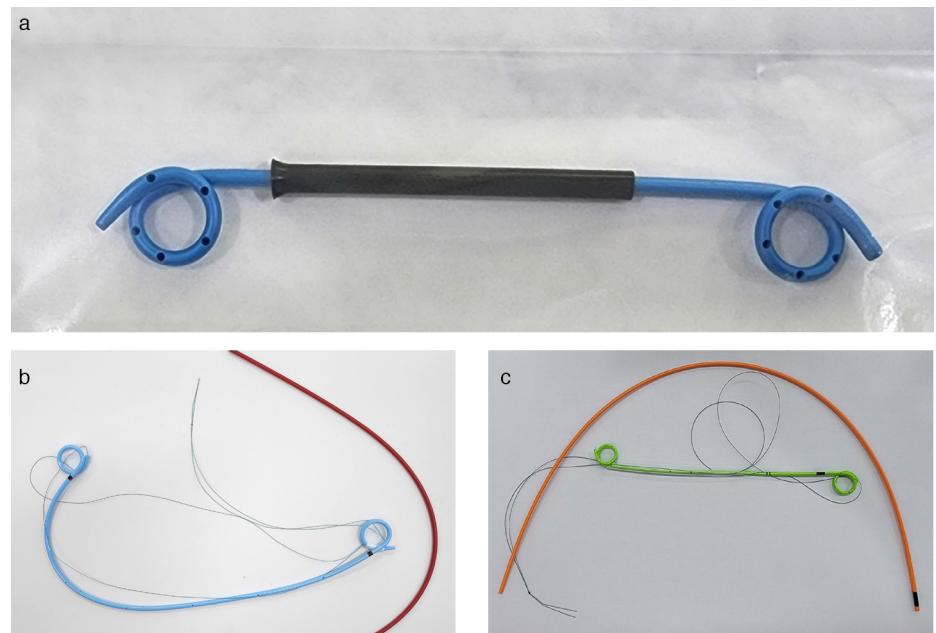


**Figure 2.** Photographs of three double-J stents. (a) Polyethylene stent (Zimmon, Cook, 7 Fr, 7 cm). (b) Polyurethane (Endo-Sof, Cook, 8 Fr, 26 cm) with pusher. (c) Polycarbonate-based polyurethane (Inlay Optima, Bard, 6 Fr, 14 cm) with pusher.

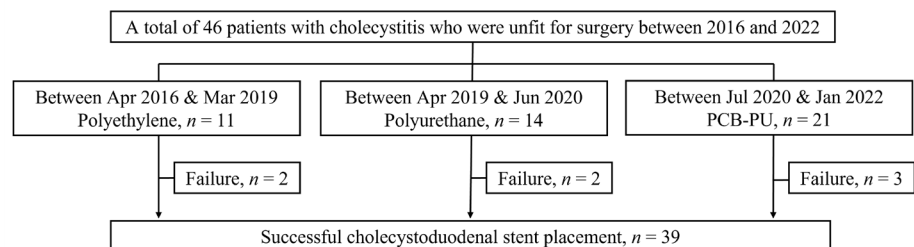


**Figure 3.** Flow chart of patient selection. PCB-PU, polycarbonate-based polyurethane

PCB-PU:  $P > 0.999$ ; PU vs. PCB-PU:  $P = 0.060$ ). The subgroup analysis showed no significant differences in the technical success rate (transhepatic and transperitoneal access: 15/19 vs. 24/27,  $P = 0.424$ ) and AEs rates (5/19 vs. 12/27,  $P = 0.215$ ) in transhepatic and transperitoneal access groups.

## Discussion

This bicentric retrospective study successfully placed CDSs in 85% of the patients. Major AEs occurred in 5% of technically successful patients, and all patients recovered without operative treatment. Recurrent cholecystitis occurred in 6% of clinically successful patients after a median follow-up of 113 days. The three-catheter groups seemed to experience different delayed AEs ( $P = 0.021$ ), although a post-hoc analysis could not reveal the differences.

Patients with an increased perioperative risk often require a permanent cholecystostomy catheter to avoid recurrent cholecystitis.<sup>2</sup> Patients with a long-term catheter can be afflicted by insertion site discomfort, local infection, and recurrent cholecystitis due to occlusion and may require routine catheter replacements. Furthermore, the catheter can frequently dislocate from the gallbladder and necessitate reinsertion.<sup>16</sup> Patients with a non-independent lifestyle could be more vulnerable to sepsis secondary to recurrent cholecystitis. Hersey et al.<sup>2</sup> reported on the safety and efficacy of CDS placement with 33 patients in 2015. Additionally, several cases have been published.<sup>2,17</sup> This present study is in concurrence with the previous study and demonstrated similar outcomes regarding clinical success rate and complications.<sup>2</sup> Major AEs, such as pancreatitis and peritonitis, occurred in two patients. The presumed cause of pancreatitis was either mechanical trauma during the procedure or an anomalous pancreaticobiliary ductal union. Peritonitis was caused by bile leakage during the stent insertion process. The patient underwent CDS placement 10 days after a cholecystostomy. Tract maturation over 2–3 weeks post-cholecystostomy might prevent bile peritonitis.<sup>18</sup>

Due to the lack of a dedicated stent for this purpose, polyethylene stents were initially adopted. These stents are typically used for endoscopic insertion and resist peristalsis and bile. However, polyethylene stents have a smaller inner lumen diameter than PU stents and are not equipped with side holes, pushers, or a drawstring. The next type used was the double-J ureteral stent made of PU. Although they were used off-label, they pro-

vided a larger inner diameter than the polyethylene stent and had side holes, pushers, and a drawstring. However, the double-J PU stents frequently fractured and dislocated during follow-up. Finally, PCB-PU stents were introduced to provide the benefit of a ureteral stent and resistance to peristalsis and bile. The PCB-PU stents seemed more suitable for this usage than other ureteral stents.

Although transhepatic access can be advantageous regarding tract maturation, the transperitoneal route was preferred in this study because it provides a favorable angle for cystic duct cannulation. Transhepatic access often formed an acute angle between the cholecystostomy tract direction and gallbladder axis and the angle made it difficult to cannulate the cystic duct. Transperitoneal

**Table 1.** Characteristics of patients who underwent percutaneous cholecystoduodenal stent placement as a treatment of acute cholecystitis

Characteristics	Value <sup>a</sup>
Total number of patients	46
Age (y)	81 (37–99)
Sex (M:F)	15:31
<b>Predisposing condition</b>	
Cerebral injury/dementia	23 (50)
Cardiac disease	6 (13)
Old age (>80 y)	6 (13)
Hepatic/renal disease	5 (11)
Malignancy	5 (11)
Other medical condition <sup>b</sup>	1 (2)
<b>ECOG</b>	
1	12 (26)
2	10 (22)
3	12 (26)
4	12 (26)
Charlson comorbidity index	6 (4–10)
<b>ASA score</b>	
2	28 (61)
3	18 (39)
<b>Access</b>	
Transhepatic	19 (41)
Transperitoneal	27 (59)
Time interval from cholecystostomy to stent, d	16 (0–794)
Follow-up period, months	4 (0–57)

<sup>a</sup>Data are presented as numbers with percentages in parentheses or medians with ranges in parentheses;

<sup>b</sup>myasthenia gravis. ASA, American Society of Anesthesia; ECOG, Eastern Cooperative Oncology Group; M, male; F, female.

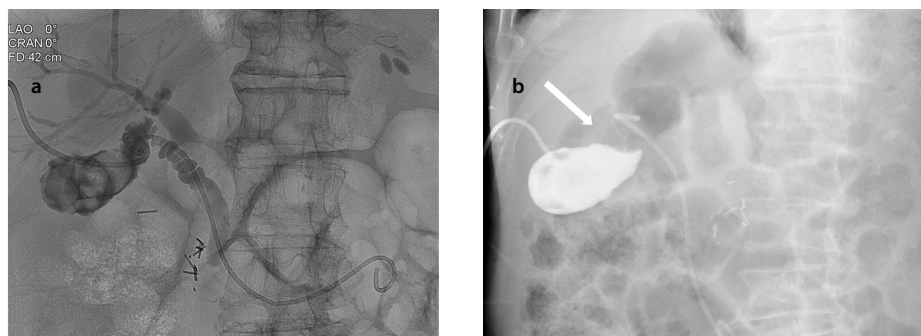


**Figure 4.** A case of clinical failure. (a) An 82-year-old man with gastric cancer and chronic kidney disease successfully underwent cholecystoduodenal stent (polyurethane, 7 Fr 12 cm). (b) Follow-up transscatheter cholecystography showing obstruction at the infundibulum by gallstone (arrow); the patient had abdominal pain. The patient was discharged from the hospital with a percutaneous cholecystostomy catheter.

**Table 2.** Comparison of outcomes for cholecystoduodenal stent placement in patients with acute cholecystitis by stent type

	Total	Polyethylene	Polyurethane	PCB-PU
Number of patients	46	11	14	21
Technical success	39	11	12	16
Clinical success	35	7	12	16
<b>Immediate AE (&lt;30 d)</b>				
Minor	14	6	3	5
Major	2	1 <sup>a</sup>	1 <sup>b</sup>	0
<b>Delayed AE</b>				
Dislocation	7	3	2	2
Fracture of stent	7	0	7	0
Recurrent cholecystitis	2	0	0	2
Total	16	3	9	4

<sup>a</sup>One patient with pancreatitis; <sup>b</sup>one patient with biloma and peritonitis. AE, adverse event; PCB-PU, polycarbonate-based polyurethane.

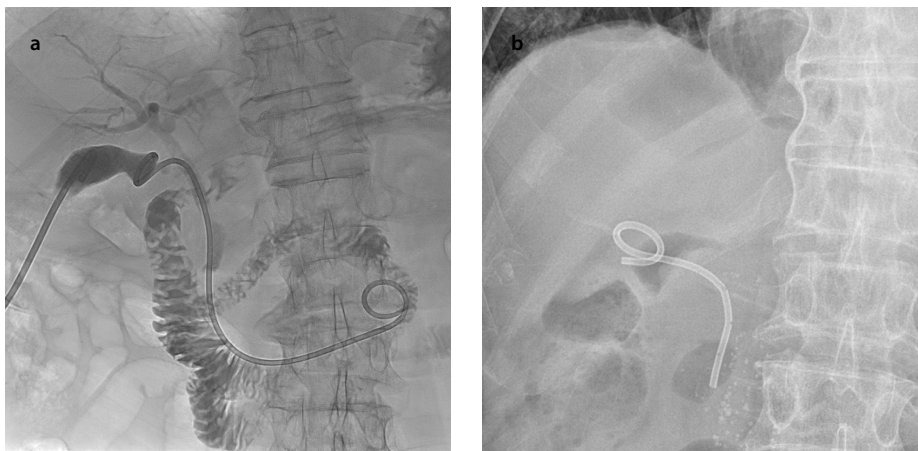


**Figure 5.** A case of delayed stent fracture. (a) A 66-year-old woman with a history of traumatic subdural hematoma received a cholecystoduodenal stent (polyurethane, 6 Fr 20 cm). (b) A plain radiograph at a regular 26-month follow-up of stenting showing a stent fracture; however, the patient had no associated symptoms.

access could have a higher risk of AEs such as bile peritonitis. However, rates of technical success ( $P = 0.424$ ) and AEs ( $P = 0.215$ ) were not significantly different in transhepatic and transperitoneal access groups. In patients with stent fractures, no fracture-associated symptoms were observed. Stent fractures occurred in the second portion of the duodenum, the stent's most angulated and hinged portion. The fractured distal portion of the stent passed through bowel movement, and proximal portions effectively functioned after the fracture.

Limitations of this study include an indication bias due to its retrospective nature, although we conducted the procedure consecutively. Additionally, the numbers in each patient group were small. Another limitation of this study is that it could be controversial whether side holes and a drawstring in stents help preserve patency

and stent placement. The placement of CDS could be beneficial for surgically inapplicable patients. However, cholecystectomy remains a more reliable treatment of cholecystitis for any surgically eligible patients. Therefore, indications for CDS and surgical qualification should be carefully evaluated during the initial and follow-up treatment.

In conclusion, the use of CDSs could be applicable but still needs further investigation in treatment algorithms of acute cholecystitis patients who were initially ineligible for surgery. Although it was not statistically significant, a PCB-PU stent could be suitable for this indication because it tends to have fewer delayed complications and is equipped with a drawstring and side holes.

#### Acknowledgements

We thank Hohee Lee of Incheon St. Mary Hospital for assistance with technical support.

#### Conflict of interest disclosure

The authors declared no conflicts of interest.

#### References

- Gallagher JR, Charles A. Acute cholecystitis: a review. *JAMA*. 2022;327(10):965-975. [CrossRef]
- Hersey N, Goode SD, Peck RJ, Lee F. Stenting of the cystic duct in benign disease: a definitive treatment for the elderly and unwell. *Cardiovasc Intervent Radiol*. 2015;38(4):964-970. [CrossRef]
- Huang SZ, Chen HQ, Liao WX, et al. Comparison of emergency cholecystectomy and delayed cholecystectomy after percutaneous transhepatic gallbladder drainage in patients with acute cholecystitis: a systematic review and meta-analysis. *Updates Surg*. 2021;73(2):481-494. [CrossRef]
- Zarour S, Imam A, Kouniavsky G, Lin G, Zbar A, Mavor E. Percutaneous cholecystostomy in the management of high-risk patients presenting with acute cholecystitis: timing and outcome at a single institution. *Am J Surg*. 2017;214(3):456-461. [CrossRef]
- Comin JM, Cade RJ, Little AF. Percutaneous cystic duct stent placement in the treatment of acute cholecystitis. *J Med Imaging Radiat Oncol*. 2010;54(5):457-461. [CrossRef]
- Brown NI, Jhamb A, Brooks DM, Little AF. Percutaneous placement of permanent metallic stents in the cystic duct to treat obstructive cholecystitis. *J Vasc Interv Radiol*. 2015;26(12):1860-1865. [CrossRef]
- Bonner BC, Brown NI, Joseph VP, Chandrasegaram MD. Cholecystoduodenal stenting: an option in complicated acute calculous cholecystitis in the elderly comorbid patient. *Case Rep Surg*. 2018;2018:1609601. [CrossRef]
- Gatenby P, Flook M, Spalding D, Tait P. Percutaneous transhepatic cholecystoduodenal stent for empyema of the gallbladder. *Br J Radiol*. 2009;82(978):108-110. [CrossRef]
- Kubota K, Abe Y, Inamori M, et al. Percutaneous transhepatic gallbladder stenting for recurrent acute acalculous cholecystitis after failed endoscopic attempt. *J Hepatobiliary Pancreat Surg*. 2005;12(4):286-289. [CrossRef]
- Lee TH, Park DH, Lee SS, et al. Outcomes of endoscopic transpapillary gallbladder stenting for symptomatic gallbladder diseases: a multicenter prospective follow-up study. *Endoscopy*. 2011;43(8):702-708. [CrossRef]
- Maekawa S, Nomura R, Murase T, Ann Y, Oeholm M, Harada M. Endoscopic gallbladder stenting for acute cholecystitis: a retrospective study of 46 elderly patients aged 65 years or older. *BMC Gastroenterol*. 2013;13:65. [CrossRef]

12. Higa JT, Irani SS. endoscopic methods for gallbladder drainage. *Curr Treat Options Gastroenterol*. 2019;17(3):357-366. [\[CrossRef\]](#)
13. Elmunzer BJ, Novelli PM, Taylor JR, Piraka CR, Shields JJ. Percutaneous cholecystostomy as a bridge to definitive endoscopic gallbladder stent placement. *Clin Gastroenterol Hepatol*. 2011;9(1):18-20. [\[CrossRef\]](#)
14. Mori Y, Itoi T, Baron TH, et al. Tokyo Guidelines 2018: management strategies for gallbladder drainage in patients with acute cholecystitis (with videos). *J Hepatobiliary Pancreat Sci*. 2018;25(1):87-95. [\[CrossRef\]](#)
15. Filippiadis DK, Binkert C, Pellerin O, Hoffmann RT, Krajina A, Pereira PL. CIRSE quality assurance document and standards for classification of complications: the CIRSE classification system. *Cardiovasc Intervent Radiol*. 2017;40(8):1141-1146. [\[CrossRef\]](#)
16. Heo J, Jung MK, Cho CM, et al. What makes acute cholecystitis recur after removing the percutaneous cholecystostomy tube? *Medicine (Baltimore)*. 2022;101(5):e28767. [\[CrossRef\]](#)
17. Kumar S, Sharma P, Muthu R, Mohakund S. Management of empyema of gallbladder with percutaneous cholecysto-duodenal stenting in a case of hilar cholangiocarcinoma treated with common bile duct metallic stenting. *Indian J Radiol Imaging*. 2011;21(4):298-300. [\[CrossRef\]](#)
18. Kallini JR, Patel DC, Linaval N, Phillips EH, Van Allan RJ. Comparing clinical outcomes of image-guided percutaneous transperitoneal and transhepatic cholecystostomy for acute cholecystitis. *Acta Radiol*. 2021;62(9):1142-1147. [\[CrossRef\]](#)



# Did radiation exposure increase with chest computed tomography use among different ages during the COVID-19 pandemic? A multi-center study with 42028 chest computed tomography scans

Mehmet Coşkun   
Atilla H. Çilengir   
Kenan Çetinoğlu   
Merve Horoz   
Ayberk Sinci   
Betül Demircan   
Engin Uluç   
Fazıl Gelal 

## PURPOSE

To determine whether radiation exposure increased among different ages with chest computed tomography (CT) use during the coronavirus disease-2019 (COVID-19) pandemic.

## METHODS

Patients with chest CT scans in an 8-month period of the pandemic between March 15, 2020, and November 15, 2020, and the same period of the preceding year were included in the study. Indications of chest CT scans were obtained from the clinical notes and categorized as infectious diseases, neoplastic disorders, trauma, and other diseases. Chest CT scans for infectious diseases during the pandemic were compared with those with the same indications in 2019. The dose-length product values were obtained from the protocol screen individually.

## RESULTS

The total number of chest CT scans with an indication of infectious disease was 21746 in 2020 and 4318 in 2019. Total radiation exposure increased by 573% with the use of chest CT for infectious indications but decreased by 19% for neoplasia, 12% for trauma, and 43% for other reasons. The mean age of the patients scanned in 2019 was significantly higher than those scanned during the pandemic (64.6 vs. 50.3 years). A striking increase was seen in the 10–59 age group during the pandemic ( $P < 0.001$ ). The highest increase was seen in the 20–29 age group, being 18.6 fold. One death was recorded per 58 chest CT scans during the pandemic. Chest CT use was substantially higher at the beginning of the pandemic.

## CONCLUSION

Chest CT was excessively used during the COVID-19 pandemic. Young and middle-aged people were exposed more than others. The impact of COVID-19-pandemic-related radiation exposure on public health should be followed carefully in future years.

## KEYWORDS

COVID-19 pandemic, CT, pneumonia, radiation, thoracic

From the Clinic of Radiology (M.C. ✉ dr.mehmetcoskun@hotmail.com), University of Health Science Turkey, Dr. Behçet Uz Children Disease and Surgery Training and Research Hospital, İzmir, Turkey; Department of Radiology (A.H.Ç.), İzmir Democracy University, İzmir, Turkey; Clinic of Radiology (K.Ç.), Merkezefendi State Hospital, Manisa, Turkey; Clinic of Radiology (M.H.), Çiğli Regional Training and Research Hospital, İzmir, Turkey; Department of Radiology (A.S., E.U., F.G.), İzmir Katip Çelebi University, Atatürk Training and Research Hospital, İzmir, Turkey; Clinic of Pediatrics (B.D.), Bakırçay University Çiğli Regional Training and Research Hospital, İzmir, Turkey.

Received 14 October 2021; revision requested 02 November 2021; last revision received 16 January 2022; accepted 28 January 2022.



Epub: 27.01.2023

Publication date: 29.03.2023

DOI: 10.5152/dir.2022.211043

The World Health Organization declared the coronavirus disease-2019 (COVID-19) as a pandemic on March 11, 2020.<sup>1</sup> While the disease has an asymptomatic or milder course in children and young adults, it is relatively mortal in those over 65.<sup>2-4</sup> Men have an increased risk of mortality compared with women.<sup>3</sup>

There was no clear consensus on the diagnosis of the disease in the early stage of the pandemic, so imaging methods were widely used for detection.<sup>5</sup> After the development of test kits, real-time reverse transcriptase polymerase chain reaction (RT-PCR) became the standard diagnostic test for COVID-19.<sup>6</sup> Currently, imaging is not indicated for patients suspected to have COVID-19 with mild clinical features.<sup>7</sup> Over 95% of patients with COVID-19 infection

survive, and radiation exposure limits even the usage of basic X-ray-based methods in thoracic imaging.<sup>8</sup> However, RT-PCR has disadvantages, such as limited availability, false negative results, and a relatively long test-to-result time.<sup>9,10</sup> Additionally, RT-PCR tests only verify the presence of the virus without suggesting the course and severity of the disease.<sup>11,12</sup>

Chest X-rays are not sensitive regarding the detection of viral pneumonia.<sup>7</sup> However, chest computed tomography (CT) scans play a key role for patients suspected to have COVID-19 pneumonia and contribute to an accurate diagnosis in the triage phase.<sup>13</sup> The decision to isolate the patient is an urgent issue, and CT rules out pneumonia within seconds.<sup>7,13</sup> Furthermore, CT can reveal the presence of pneumonia and can predict the prognosis by indicating the degree of pulmonary involvement and vascular complications.<sup>12</sup> Despite these benefits, it contains relatively high radiation, leading to an increase in the cumulative dose of the patients which are exposed.<sup>13,14</sup>

Radiation does not affect all age groups equally. Young people are more radiosensitive and have an increased risk of cancer with excessive use of CT scans.<sup>15</sup> Demonstration of the increased radiation exposure among different age groups during the pandemic may be useful to highlight potential radiation-induced diseases.

The present study tries to determine whether radiation exposure increased among different ages with chest CT use during the COVID-19 pandemic.

## Methods

### Study design

This retrospective study was approved by the University of Health Science Turkey, Dr. Behçet Uz Pediatrics and Surgery Training and Research Hospital Clinical Research Ethics Committee (approval number: 2021/02.25-513). Written informed consent was obtained before CT acquisition. It was

#### Main points

- During the coronavirus disease-2019 pandemic, excess use of chest computed tomography (CT) caused increased radiation exposure.
- A sharp rise in chest CT use was seen in young people.
- At the beginning of the outbreak, CT use was higher.

conducted in two third-level referral pandemic hospitals (center 1, an adult hospital serving about 3 million adults annually in outpatient services; and center 2, a children's hospital serving about 0.5 million children annually in outpatient services). All patients with chest CT in the 8-month period of the pandemic between March 15, 2020, and November 15, 2020, and the same dates of the preceding year were included. The first case was reported in our country on March 11, 2020. Chest CT scans performed on dates other than in these ranges and non-chest CT scans were excluded.

The patients' diagnoses were obtained from the hospital registration system using International Classification of Diseases-10 codes. The indications of chest CT examinations were determined from the clinical notes as follows: infectious disease, neoplastic disorders, trauma, or other diseases (the majority of other diseases were vascular diseases, including pulmonary thromboembolism, aortic aneurysm, and dissection). Chest CT scans performed with the indication of infectious diseases were used in the statistical analysis, as the study's aim was to determine the radiation exposure related to the imaging of infections, mainly of COVID-19. The patients' demographic information and the date of examination were recorded. Those below the age of 18 were defined as children. Each chest CT scan was counted separately when a patient had more than one.

### Calculation of radiation dose

The standard-dose non-contrast CT was used for infectious indications. The intravenous contrast (350 mg/mL iodine) was administered at a dose of 1 mL/kg of body weight if there was any suspicion of vascular disease, hilar, or mediastinal mass. The scanners and acquisition protocols for standard-dose non-contrast CTs were as follows: center 1 used a 128-slice CT scanner (SOMATOM Definition AS, Siemens, Erlangen, Germany), with a tube voltage of 120 kVp, a maximum tube current of 100 mA with automated exposure control, gantry rotation time of 0.5 s, pitch factor of 1.0, acquisition slice thickness of 0.6 mm; and center 2 used a 32-slice CT scanner (SOMATOM go.Now, Siemens, Erlangen, Germany), with a tube voltage of 110 kVp, a maximum tube current of 100 mA with automated exposure control, gantry rotation time of 1 s, pitch factor of 1.0, acquisition slice thickness of 1 mm. The total tube output during one scan was recorded from the patient's protocol screen as the dose-length product (DLP). The effective

radiation doses (mSv) were calculated using the following formula:  $DLP \times \text{conversion factor} = \text{effective dose}$ , where age-specific conversion factors used were: 0.039 (0–1 year), 0.026 (1–5 years), 0.018 (5–10 years), and 0.014 (>10 years old).<sup>16</sup>

### Statistical analysis

Two years' data were compared using the Statistical Package for the Social Sciences (SPSS™) version 20.0 (IBM Corp., Armonk, NY, USA). In descriptive statistics, continuous variables were reported with mean  $\pm$  standard deviation, while categorical variables were presented with numbers and percentages as n (%). In the examination-based analysis, Pearson's chi-squared test was used for the comparison of chest CT use by indications. Demographic data were found to be normally distributed by the Kolmogorov-Smirnov test. The ages of the patients scanned with an indication of infectious diseases in 2019 were compared with those scanned with the same indication in the pandemic using the t-test. Ages were grouped by decades. The gender and age groups of the patients were compared using Pearson's chi-squared test. Chest CT use with an indication of infectious disease in the centers in 2019 was compared with chest CT use with the same indication in the centers in 2020 using Pearson's chi-squared test. The ages of the patients who had repeated chest CT scans with an indication of infectious diseases in 2020 were compared with the ages of the patients who had a single chest CT scan with an indication of infectious diseases in the same period using the t-test. A *P* value of <0.05 was statistically significant.

## Results

A total of 36502 patients were included in the study. There were 19557 men and 16945 women. The mean age was  $54.9 \pm 19.9$  years. The total number of chest CT scans was 42028.

In 2019, 12212 patients had chest CT, comprising 6466 men and 5746 women. The mean age was  $61.1 \pm 18.6$  years. The total number of chest CT scans was 13832. In 2020, 24290 patients had chest CT, comprising 13091 men and 11199 women. The mean age was  $51.8 \pm 19.9$  years. The total number of chest CT scans was 28196 (Table 1).

Chest CT examinations were grouped by indication. The numbers of chest CT scans with different indications were as follows: 4318 (31.22%) infectious diseases, 3654 (26.42%) neoplasia, 2020 (14.6%) trauma,

and 3840 (27.76%) other diseases in 2019; and 21746 (77.12%) infectious diseases, 2794 (9.91%) neoplasia, 1644 (5.83%) trauma, and 2012 (7.14%) other diseases in 2020. Chest CT use with an indication of infectious disease was five times higher in 2020 than in the preceding year. The number of chest CT scans with indications of neoplasia, trauma, and other diseases decreased by 24%, 19%, and 48%, respectively, in 2020. Chest CT use with an indication of infectious diseases was significantly higher in 2020 ( $P < 0.001$ ) (Table 2). The mean effective radiation doses per scan with an indication of infectious diseases were  $3.15 \pm 1.73$  mSv and  $3.58 \pm 1.56$  mSv in 2019 and 2020, respectively. The total radiation exposure of chest CT scans with an indication of infectious diseases was 13586.28 mSv in 2019, while it was 77867.24 mSv in 2020, an increase of 5.73 times in the pandemic. The total radiation exposure of chest CT scans for neoplastic diseases, trauma, and other reasons decreased by 19%, 12%, and 43%, respectively (Table 3). The data of 24915 (88.36%) chest CT scans in 2020 were accessible to determine the referring clinics. They were mostly ordered from the emergency departments with a rate of 77.58%, followed by infectious diseases, medical oncology, and chest diseases with rates of 8.89%, 5.41%, and 2.90%, respectively.

The demographic data of the patients who underwent chest CT with the indication of infectious disease in 2019 and during the pandemic were also compared. There was no significant difference by gender ( $P = 0.202$ ). The mean ages of the patients with chest CT in 2019 and 2020 were  $64.6 \pm 19.1$  and

$50.3 \pm 20$ , respectively. The difference was statistically significant ( $P < 0.001$ ). A dramatic increase in chest CT use was found in the 10–59 age group ( $P < 0.001$ ). The highest increase was 18.6 times and seen in the 20–29 age group (Table 4). The number of chest CT examinations increased 5.1 times in the adult hospital and 4.1 times in the children's hospital. The difference in the rate of increase between the two hospitals was not statistically significant ( $P = 0.081$ ).

There were 18534 patients with 21746 chest CT scans in the infectious disease group in 2020, of whom 373 died, a mortality rate of 2.01%. One death was recorded per 58 chest CT scans during the pandemic. Chest CT use was substantially higher at the beginning of the pandemic. The numbers of chest CT scans were 631 in April 2019 and 606 in May 2019, while they were 3537 and 2353 in the same months of 2020, respectively. Chest CT use was relatively stable in 2019. However, chest CT use traced a zigzag pattern in the pandemic, and it decreased permanently after a second peak in August 2020 (Figure 1).

The number of patients who underwent repeated chest CT with an indication of infectious diseases was 548 in 2019 and 2301 in 2020, respectively. The maximum number of repetitions was 12 in 2019 and 17 in 2020 for a single patient (Table 5). The demographic data of the patients who, in 2020, had repeated chest CT scans with the indication of infectious disease were compared with those who had single chest CT scans with the same indication. The mean ages of repeated and non-repeated patients' groups were  $55.7 \pm 19.5$  and  $48 \pm 19.8$ , respectively. The mean age of the patients who had repeated chest

CT was significantly higher than that of the patients who had a single chest CT scan in 2020 ( $P < 0.001$ ).

## Discussion

The present study showed that radiation exposure increased significantly with chest CT during the COVID-19 pandemic. In the first year of the pandemic, compared with the preceding year, the increase in overall chest CT use to image infection was about five-fold. Interestingly, young adults were scanned more frequently, and the most prominent increase was observed in the 20–29 age group with 18.6 times. The number of repeated scans also increased 4.2 times during the pandemic. To the best of the authors' knowledge, this is the first study addressing increased radiation exposure by age groups with the increased use of chest CT in the COVID-19 pandemic.

Levin et al.<sup>17</sup> reported a logarithmic linear relationship between the infection fatality rate and age. The age-specific fatality rate was extremely low in children (0.002%) and increased to 0.4% at age 55, 1.4% at age 65, 4.6% at age 75, and 15% at age 85.<sup>17</sup> In a study by Grasselli et al.<sup>18</sup>, older age and male gender were the independent risk factors for death. But COVID-19 infection was more common in middle-aged adults.<sup>4</sup> Moreover, chest CT was often used in triage during the pandemic.<sup>13</sup> These findings explain the more frequent use of chest CT among young and middle-aged people. Chest CT use was more common in men, both in 2019 and 2020. Only 2% of the patients with an indication of infectious disease who had chest CT in 2020 died. This rate (2.01%) was below than the expected mortality of the disease.<sup>17</sup> These results suggest redundant CT use carried out almost as a screening test.

The Fleischner Society did not recommend CT as a screening test and noted that CT should be used for moderate to severe disease with worsening respiratory status.<sup>7</sup> Still, several factors caused excessive CT use during the pandemic. Hospitalization was higher during the pandemic, and most (63%) of the centers used chest CT for hospitalized patients with COVID-19.<sup>8</sup> Chest CT was frequently used as an initial test because of the limited availability of RT-PCR test kits at the beginning of the pandemic. Early studies underlined false negative RT-PCR test results.<sup>9,19</sup> In the meta-analysis of Islam et al.<sup>20</sup>, chest CT had a higher sensitivity than RT-PCR. The pooled sensitivity and specificity of chest CT were 87.9% and 80.0%, respectively.<sup>20</sup> The

**Table 1.** Characteristics of the patient population

Parameters	Number of patients who had chest CT in 2019 n = 12212 (%)	Number of patients who had chest CT in 2020 n = 24290 (%)	Total n = 36502
<b>Men</b>	6466 (52.9%)	13091 (53.9%)	19557
<b>Women</b>	5746 (47.1%)	11199 (46.1%)	16945
<b>Mean age (<math>\pm</math> SD)</b>	61.1 ( $\pm$ 18.6)	51.8 ( $\pm$ 19.9)	54.9 ( $\pm$ 19.9)

CT, computed tomography; SD, standard deviation.

**Table 2.** Comparison of chest CT scans by indications by years

Indications	The number of chest CT scans		P value
	In 2019 n = 13832 (%)	In 2020 n = 28196 (%)	
Infectious diseases	4318 (31.22%)	21746 (77.12%)	<0.001
Neoplastic disorders	3654 (26.42%)	2794 (9.91%)	
Trauma	2020 (14.60%)	1644 (5.83%)	
Other diseases	3840 (27.76%)	2012 (7.14%)	

CT, computed tomography.

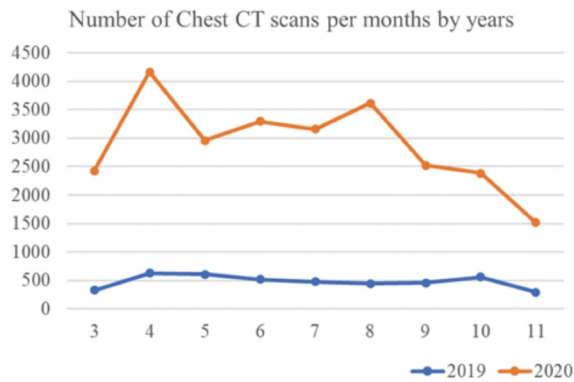


**Figure 1.** Comparison of the number of chest computed tomography scans with the indication of infectious diseases by months. \*Showing half of 3<sup>rd</sup> and 11<sup>th</sup> months. CT, computed tomography.

Indications	Total radiation exposure (mSv)		
	In 2019	In 2020	Change
Infectious diseases	13586.28 (31.36%)	77867.24 (78.23%)	+573%
Neoplastic disorders	11224.30 (25.91%)	9120.59 (9.16%)	-19%
Trauma	6405.92 (14.79%)	5648.76 (5.67%)	-12%
Other diseases	12104.27 (27.94%)	6904.10 (6.94%)	-43%
Total	43320.77	99540.69	+230%

mSv, millisievert.

Parameters	The number of chest CT scans in 2019	The number of chest CT scans in 2020	Fold	P value
Men	2293	11778	5.1	<b>0.202</b>
Women	2025	9968	4.9	
Mean age (± SD)	64.6 (± 19.1)	50.3 (± 20)		<0.001
<b>Age groups by tens</b>				
1 (0-9)	68	72	1.1	
2 (10-19)	41	734	17.9	
3 (20-29)	171	3186	<b>18.6</b>	
4 (30-39)	187	3448	18.4	
5 (40-49)	327	3478	10.6	
6 (50-59)	618	3251	5.3	<0.001
7 (60-69)	915	3074	3.4	
8 (70-79)	978	2650	2.7	
9 (80-89)	801	1566	2	
10 (90-99)	212	281	1.3	
11 (100-110)	0	6	n/a	

CT, computed tomography; SD, standard deviation; n/a, non-applicable.

The number of repetitions	Number of patients who had multiple chest CT	
	In 2019	In 2020
2	370	1730
3-5	160	536
6-10	17	30
11+	1	5

CT, computed tomography.

other potential factors of increased CT use were the unknown course of the disease in the early stages of the pandemic, the tendency to immediately diagnose pneumonia, and peaks during the pandemic. In the present study, it was observed that CT scans were mostly used in the early period of the pandemic and had decreased by September 2020. The increased use of facial masks, which could decrease contagion, the accumulation of knowledge about the disease course, the increased availability of test kits, and the shortening of the RT-PCR test process may have reduced chest CT use later in 2020.

Another factor for the greater radiation exposure was the increased number of patients with repetitive scans. In the cohort of Cristofaro et al.<sup>21</sup>, each patient positive for COVID-19 was scanned with chest CT an average of 2.78 times. The maximum repetition number was 10 between March and October 2020.<sup>21</sup> Yurdaisik et al.<sup>22</sup> showed that 43% of the patients had repetitive scans at the start of the pandemic. They did not find an age difference between the patients with single and multiple scans.<sup>22</sup> In the present study, the number of patients with repetitive scans increased by 4.2 times. The maximum repetition was 17 during the pandemic. Repeated CT scans were observed in older patients. Age correlated with severe disease course, which could have increased the requirement for rescans.

A significant decrease (57.4%) was seen in trauma admissions during the COVID-19 pandemic.<sup>23</sup> Head CT use due to traumatic brain injury decreased by about 40% in emergency departments during the pandemic.<sup>24</sup> Emergency surgeries were also reduced by 59%.<sup>25</sup> Netherland Cancer Registration data showed a 26% decrease in cancer diagnoses except for skin cancers within the first months of the pandemic.<sup>26</sup> Reprioritization of non-emergency services, including diagnostic specialists, and the lockdown of the population dramatically disrupted cancer referrals.<sup>27</sup> Deferrable, non-urgent procedures, even in oncologic practice, were delayed.<sup>28,29</sup> Chest imaging was encouraged to exclude COVID-19 risk for maximal safety before surgeries.<sup>30</sup> Chest CT was recommended for any patient needing emergency surgery and undergoing an abdominal CT scan in the early stage of the pandemic.<sup>31</sup> But the Royal College of Radiologists does not recommend routine preoperative CT screening. Instead, CT use should be limited, and preoperative chest CT should be considered only if positive CT findings would change the

patient's immediate surgical management.<sup>32</sup> The Royal College of Surgeons advises an RT-PCR screening within 72 h of surgery for patients who are candidates for elective surgery.<sup>33</sup> While these factors reduced the use of chest CT for non-infectious reasons, COVID-19 screening increased radiation exposure. In the present study, the total radiation exposure decreased by 12% for trauma, 19% for oncological screening, and 43% for other reasons but increased by 573% for infectious diseases in two referral centers when compared with the preceding year. It can be speculated that the 573% increase in radiation exposure was highly related to the COVID-19 pandemic. The impact of the COVID-19 pandemic on radiation exposure should be followed carefully in future years, especially considering that middle-aged people were excessively exposed.

Using low-dose chest CT protocols has been a controversial issue during the pandemic. The Atomic Energy Study Group determined wide variations in CT use across the centers in 28 countries. Homayounieh et al.<sup>8</sup> reported that approximately half of the centers did not have a dedicated CT protocol for patients with COVID-19, and 20% of the centers used multiphase CT, which was found to be associated with higher radiation exposure. Approximately two-thirds of the centers used standard-dose CT without contrast, while 20% of the centers performed reduced-dose CT without contrast.<sup>8</sup> Kang et al.<sup>14</sup> proposed a dose reduction from a median effective dose of 1.81 mSv to 0.203 mSv without a significant decrease in the image quality. Tabatabaei et al.<sup>13</sup> compared standard-dose ( $6.60 \pm 1.47$  mSv) and low-dose ( $1.80 \pm 0.42$  mSv) CTs and found there was an excellent inter-reader agreement with Kappa scores of 0.81–0.84 in both standard- and low-dose examinations. But decreasing radiation dose increases the noise and limits the discrimination of ground glass opacity typical in COVID-19 pneumonia. Shiri et al.<sup>34</sup> reported diminished lesion detectability in about 60% of the cases with low-dose CT. The quality scores for all other patterns, including consolidation, crazy paving, nodular infiltrations, and bronchovascular thickening, decreased by reducing the radiation dose.<sup>34</sup> Variations in patient sizes and the lack of reduction technologies, such as current iterative reconstructions, also limited the usage of low-dose CT.<sup>8</sup> In the present study, the standard-dose CT was used to avoid underdiagnosis risk with dose reduction. The mean effective dose per scan was slightly elevated during the pandemic (3.58

mSv in 2020 vs. 3.15 mSv in 2019). The majority of chest CT scans (77.58%) were ordered from the emergency department, where the technologists are prone to scan longer. Therefore, increased scan length may have increased the mean effective dose per scan during the pandemic.

The International Commission on Radiological Protection (ICRP) approved three fundamental principles of radiological protection, namely justification, optimization, and the application of dose limits. "Justification" is a necessity before imaging. In justification, the process including radiation should be beneficial for the patient, and the expected benefits should compensate for the costs, including the radiation detriment. In optimization, the number of people exposed and the magnitude of individual procedures should all be kept as low as reasonably achievable (the ALARA principle).<sup>35</sup> The International Atomic Energy Agency recommends that the decision process of an imaging procedure should be shared between the referring physicians and the radiologists. The referring consultant should bring the medical aspect with the history of the patient, and the radiologist should consider the appropriateness of the request, urgency of the procedure, characteristics of the exposure, relevant information from any previous procedures, and alternative methods that do not use ionizing radiation.<sup>36</sup> Some suggestions for reducing radiation exposure are that the radiologists should take an active role in the decision-making process and national guidelines should be developed to clarify the roles of the radiologists and referring physicians, and the three principles of ICRP should be implemented.

There were several limitations of this study. The retrospective design had the potential for bias. The lack of PCR correlation may be a second limitation; however, this would not reduce the value of the study since the primary goal was to determine the increased radiation exposure during the pandemic. The PCR tests had not been performed for all patients with chest CT in 2020. Probably the most important limitation was that chest CT use may have been affected by local factors, such as the intense admissions of COVID-19 cases, peak periods, and insufficiencies in healthcare services, including the lack of experience of the clinicians. Therefore, the results might not be generalized. Still, this limitation can be justified by the lack of consistent and eligible guidelines on chest CT use, especially in the early period of the pandemic globally. In addition, the hospital-

ization ratio or rate of intensive care admission to suggest redundant CT use could not be reached. However, the mortality statistics that could suggest overuse in the study population were obtained.

In conclusion, chest CT was excessively used during the COVID-19 pandemic. Young and middle-aged people were exposed more than others. Awareness should be raised about radiation exposure with CT scans. The clinical benefits should outweigh the potential risks, and CT use should be kept low. The impact of the COVID-19 pandemic-related radiation exposure on public health should be followed carefully in future years.

### Conflict of interest disclosure

The authors declared no conflicts of interest.

### Data sharing statement

Data generated or analyzed during the study are available from the corresponding author by request via e-mail.

## References

1. World Health Organization. WHO Director-General's opening remarks at the media briefing on COVID-19 - 11 March 2020. [updated 2020 Mar 11; cited 2021 July 21]. [\[CrossRef\]](#)
2. Mantovani A, Rinaldi E, Zusi C, Beatrice G, Saccomani MD, Dalbeni A. Coronavirus disease 2019 (COVID-19) in children and/or adolescents: a meta-analysis. *Pediatr Res*. 2021;89(4):733-737. [\[CrossRef\]](#)
3. Biswas M, Rahaman S, Biswas TK, Haque Z, Ibrahim B. Association of sex, age, and comorbidities with mortality in COVID-19 patients: a systematic review and meta-analysis. *Intervirolgy*. 2020:1-12. [\[CrossRef\]](#)
4. Provisional Death Counts for Coronavirus Disease 2019 (COVID-19). [updated 2020 July 19; cited 2021 July 20]. [\[CrossRef\]](#)
5. Wu Z, McGoogan JM. Characteristics of and important lessons from the coronavirus disease 2019 (COVID-19) outbreak in China: summary of a report of 72 314 cases from the chinese center for disease control and prevention. *JAMA*. 2020;323(13):1239-1242. [\[CrossRef\]](#)
6. Tang YW, Schmitz JE, Persing DH, Stratton CW. Laboratory diagnosis of COVID-19: current issues and challenges. *J Clin Microbiol*. 2020;58(6):e00512-e00520. [\[CrossRef\]](#)
7. Rubin GD, Ryerson CJ, Haramati LB, et al. The role of chest imaging in patient management during the COVID-19 pandemic: a multinational consensus statement from the Fleischner Society. *Chest*. 2020;158(1):106-116. [\[CrossRef\]](#)

8. Homayounieh F, Holmberg O, Umairi RA, et al. Variations in CT utilization, protocols, and radiation doses in COVID-19 pneumonia: results from 28 countries in the IAEA study. *Radiology*. 2021;298(3):E141-E151. [\[CrossRef\]](#)
9. Ai T, Yang Z, Hou H, et al. Correlation of Chest CT and RT-PCR testing for coronavirus disease 2019 (COVID-19) in China: a report of 1014 cases. *Radiology*. 2020;296(2):E32-E40. [\[CrossRef\]](#)
10. Yang Y, Yang M, Shen C, et al. Evaluating the accuracy of different respiratory specimens in the laboratory diagnosis and monitoring the viral shedding of 2019-nCoV infections. *medRxiv*. 2020. [\[CrossRef\]](#)
11. Kalra MK, Homayounieh F, Arru C, Holmberg O, Vassileva J. Chest CT practice and protocols for COVID-19 from radiation dose management perspective. *Eur Radiol*. 2020;30(12):6554-6560. [\[CrossRef\]](#)
12. Yang R, Li X, Liu H, et al. Chest CT severity score: an imaging tool for assessing severe COVID-19. *Radiol Cardiothorac Imaging*. 2020;2(2):e200047. [\[CrossRef\]](#)
13. Tabatabaei SMH, Talari H, Gholamrezanezhad A, et al. A low-dose chest CT protocol for the diagnosis of COVID-19 pneumonia: a prospective study. *Emerg Radiol*. 2020;27(6):607-615. [\[CrossRef\]](#)
14. Kang Z, Li X, Zhou S. Recommendation of low-dose CT in the detection and management of COVID-2019. *Eur Radiol*. 2020;30(8):4356-4357. [\[CrossRef\]](#)
15. Pearce MS, Salotti JA, Little MP, et al. Radiation exposure from CT scans in childhood and subsequent risk of leukaemia and brain tumours: a retrospective cohort study. *Lancet*. 2012;380(9840):499-505. [\[CrossRef\]](#)
16. Thomas KE, Wang B. Age-specific effective doses for pediatric MSCT examinations at a large children's hospital using DLP conversion coefficients: a simple estimation method. *Pediatr Radiol*. 2008;38(6):645-656. [\[CrossRef\]](#)
17. Levin AT, Hanage WP, Owusu-Boaitey N, Cochran KB, Walsh SP, Meyerowitz-Katz G. Assessing the age specificity of infection fatality rates for COVID-19: systematic review, meta-analysis, and public policy implications. *Eur J Epidemiol*. 2020;35(12):1123-1138. [\[CrossRef\]](#)
18. Grasselli G, Greco M, Zanella A, et al. Risk factors associated with mortality among patients with COVID-19 in intensive care units in Lombardy, Italy. *JAMA Intern Med*. 2020;180(10):1345-1355. Erratum in: *JAMA Intern Med*. 2021;181(7):1021. [\[CrossRef\]](#)
19. Younes N, Al-Sadeq DW, Al-Jighefee H, et al. Challenges in laboratory diagnosis of the novel coronavirus SARS-CoV-2. *Viruses*. 2020;12(6):582. [\[CrossRef\]](#)
20. Islam N, Ebrahimzadeh S, Salameh JP, et al. Thoracic imaging tests for the diagnosis of COVID-19. *Cochrane Database Syst Rev*. 2021;3(3):CD013639. [\[CrossRef\]](#)
21. Cristofaro M, Fusco N, Petrone A, et al. Increased radiation dose exposure in thoracic computed tomography in patients with Covid-19. *Radiation*. 2021;1(2):153-161. [\[CrossRef\]](#)
22. Yurdaisik I, Nurili F, Aksoy SH, Agirman AG, Aktan A. Ionizing radiation exposure in patients with Covid-19: more than needed. *Radiat Prot Dosimetry*. 2021;194(2-3):135-143. [\[CrossRef\]](#)
23. Kamine TH, Rembisz A, Barron RJ, Baldwin C, Kromer M. Decrease in trauma admissions with COVID-19 pandemic. *West J Emerg Med*. 2020;21(4):819-822. [\[CrossRef\]](#)
24. Agarwal M, Udare A, Alabousi A, et al. Impact of the COVID-19 pandemic on emergency CT head utilization in Ontario-an observational study of tertiary academic hospitals. *Emerg Radiol*. 2020;27(6):791-797. [\[CrossRef\]](#)
25. Surek A, Ferahan S, Gemicci E, Dural AC, Donmez T, Karabulut M. Effects of COVID-19 pandemic on general surgical emergencies: are some emergencies really urgent? Level 1 trauma center experience. *Eur J Trauma Emerg Surg*. 2021;47(3):647-652. [\[CrossRef\]](#)
26. Dinmohamed AG, Visser O, Verhoeven RHA, et al. Fewer cancer diagnoses during the COVID-19 epidemic in the Netherlands. *Lancet Oncol*. 2020;21(6):750-751. Erratum in: *Lancet Oncol*. 2020. [\[CrossRef\]](#)
27. Sud A, Jones ME, Broggio J, et al. Collateral damage: the impact on outcomes from cancer surgery of the COVID-19 pandemic. *Ann Oncol*. 2020;31(8):1065-1074. [\[CrossRef\]](#)
28. Chiu PWY, Ng SC, Inoue H, et al. Practice of endoscopy during COVID-19 pandemic: position statements of the Asian Pacific Society for Digestive Endoscopy (APSDE-COVID statements). *Gut*. 2020;69(6):991-996. [\[CrossRef\]](#)
29. Simonato A, Giannarini G, Abrate A, et al. Clinical pathways for urology patients during the COVID-19 pandemic. *Minerva Urol Nefrol*. 2020;72(3):376-383. [\[CrossRef\]](#)
30. Obek C, Doganca T, Argun OB, Kural AR. Management of prostate cancer patients during COVID-19 pandemic. *Prostate Cancer Prostatic Dis*. 2020;23(3):398-406. [\[CrossRef\]](#)
31. The Royal College of Surgeons of Edinburgh. Intercollegiate General Surgery Guidance on COVID-19 UPDATE. [updated 2020 March 27; cited 2021 November 21]. [\[CrossRef\]](#)
32. The Royal College of Radiologists. Statement on use of CT chest to screen for COVID-19 in pre-operative patients: 30 April 2020. [updated 2020 April 30; cited 2021 November 22]. [\[CrossRef\]](#)
33. Royal College of Surgeons of England. Intercollegiate guidance for pre-operative chest CT imaging for elective cancer surgery during the COVID-19 pandemic. [updated 2020 May 15; cited 2021 November 22]. [\[CrossRef\]](#)
34. Shiri I, Akhavanallaf A, Sanaat A, et al. Ultra-low-dose chest CT imaging of COVID-19 patients using a deep residual neural network. *Eur Radiol*. 2021;31(3):1420-1431. [\[CrossRef\]](#)
35. The 2007 Recommendations of the International Commission on Radiological Protection. ICRP publication 103. *Ann ICRP*. 2007;37(2-4):1-332. [\[CrossRef\]](#)
36. International Atomic Energy Agency. Justification and optimization. [updated 2021; cited 2021 December 5]. [\[CrossRef\]](#)



# Multivariate analysis based on the maximum standard unit value of $^{18}\text{F}$ -fluorodeoxyglucose positron emission tomography/computed tomography and computed tomography features for preoperative predicting of visceral pleural invasion in patients with subpleural clinical stage IA peripheral lung adenocarcinoma

Yun Wang<sup>†</sup>

Deng Lyu<sup>†</sup>

Taohu Zhou

Wenting Tu

Li Fan

Shiyuan Liu

<sup>†</sup>Yun Wang and Deng Lyu contributed equally to this work.

From the Department of Radiology (Y.W., D.L., W.T., L.F.)  
✉ fanli0930@163.com, S.L. ✉ radiology\_cz@163.com),  
Second Affiliated Hospital of Navy Medical University,  
Shanghai, China; Department of Radiology (T.Z.), Weifang  
Medical University, School of Medical Imaging,  
Weifang, China.

Received 13 November 2022; revision requested 23  
December 2022; last revision received 30 January 2023;  
accepted 02 February 2023.



Epub: 21.02.2023

Publication date: 29.03.2023

DOI: 10.4274/dir.2023.222006

## PURPOSE

Preoperative prediction of visceral pleural invasion (VPI) is important because it enables thoracic surgeons to choose appropriate surgical plans. This study aimed to develop and validate a multivariate logistic regression model incorporating the maximum standardized uptake value ( $\text{SUV}_{\text{max}}$ ) and valuable computed tomography (CT) signs for the non-invasive prediction of VPI status in subpleural clinical stage IA lung adenocarcinoma patients before surgery.

## METHODS

A total of 140 patients with subpleural clinical stage IA peripheral lung adenocarcinoma were recruited and divided into a training set ( $n = 98$ ) and a validation set ( $n = 42$ ), according to the positron emission tomography/CT examination temporal sequence, with a 7:3 ratio. Next, VPI-positive and VPI-negative groups were formed based on the pathological results. In the training set, the clinical information, the  $\text{SUV}_{\text{max}}$ , the relationship between the tumor and the pleura, and the CT features were analyzed using univariate analysis. The variables with significant differences were included in the multivariate analysis to construct a prediction model. A nomogram based on multivariate analysis was developed, and its predictive performance was verified in the validation set.

## RESULTS

The size of the solid component, the consolidation-to-tumor ratio, the solid component pleural contact length, the  $\text{SUV}_{\text{max}}$ , the density type, the pleural indentation, the spiculation, and the vascular convergence sign demonstrated significant differences between VPI-positive ( $n = 40$ ) and VPI-negative ( $n = 58$ ) cases on univariate analysis in the training set. A multivariate logistic regression model incorporated the  $\text{SUV}_{\text{max}}$  [odds ratio (OR): 1.753,  $P = 0.002$ ], the solid component pleural contact length (OR: 1.101,  $P = 0.034$ ), the pleural indentation (OR: 5.075,  $P = 0.041$ ), and the vascular convergence sign (OR: 13.324,  $P = 0.025$ ) as the best combination of predictors, which were all independent risk factors for VPI in the training group. The nomogram indicated promising discrimination, with an area under the curve value of 0.892 [95% confidence interval (CI), 0.813–0.946] in the training set and 0.885 (95% CI, 0.748–0.962) in the validation set. The calibration curve demonstrated that its predicted probabilities were in acceptable agreement with the actual probability. The decision curve analysis illustrated that the current nomogram would add more net benefit.

## CONCLUSION

The nomogram integrating the  $\text{SUV}_{\text{max}}$  and the CT features could non-invasively predict VPI status before surgery in subpleural clinical stage IA lung adenocarcinoma patients.

## KEYWORDS

Computed tomography, lung adenocarcinoma, nomogram, positron emission tomography, visceral pleural invasion

You may cite this article as: Wang Y, Lyu D, Zhou T, Tu W, Fan L, Liu S. Multivariate analysis based on the maximum standard unit value of  $^{18}\text{F}$ -fluorodeoxyglucose positron emission tomography/computed tomography and computed tomography features for preoperative predicting of visceral pleural invasion in patients with subpleural clinical stage IA peripheral lung adenocarcinoma. *Diagn Interv Radiol.* 2023;29(2):379-389.

The Global Cancer Statistics 2020 estimate that lung cancer incidence is 11.4%, with lung cancer being the world's second most prevalent type of malignant tumor and leading cause of cancer death, with an estimated 1.8 million deaths (18%) worldwide in 2020.<sup>1</sup> Lung adenocarcinoma accounts for the largest proportion of non-small cell lung cancer (NSCLC).<sup>1</sup>

Visceral pleural invasion (VPI) in lung cancer is defined as a tumor that invades beyond the visceral pleural elastic layer (PL1) and exposes the pleural surface (PL2); it is one of the poor prognostic factors.<sup>2</sup> According to the eighth edition of the tumor-node-metastasis (TNM) staging criteria, when cT1N0M0 lung adenocarcinoma has pathologically positive VPI, the tumor (T) stage is upgraded from T1 to T2, and the TNM stage is upgraded from IA to IB.<sup>2</sup>

According to recent studies, lobectomy surgery results in a better prognosis and lower intrathoracic recurrence for patients with clinical T1 stage tumors (including T1a) and pathologically confirmed positive VPI.<sup>3</sup> For patients with T1-sized VPI-positive lung cancer, more extensive lymph node dissection rather than lymph node sampling is required.<sup>4</sup> However, the conventional intraoperative diagnosing of VPI is time-consuming and inexact, with a reported accuracy of 56.5%.<sup>5</sup> The gold standard for diagnosis still relies on postoperative elastic fiber staining to evaluate VPI,<sup>2</sup> but postoperative pathology cannot guide preoperative surgical planning. Therefore, if the VPI status can be accurately assessed using preoperative imaging methods, it may significantly impact the surgical plan.

Previous studies have explored using computed tomography (CT) findings to predict VPI status.<sup>6-15</sup> Subpleural lung adenocarcinoma presenting as pure ground-glass

nodules (pGGNs) do not enter the visceral pleura due to their low invasiveness.<sup>11-13</sup> In addition, VPI-positive status is never observed in lung cancer without a relationship with the pleura.<sup>13,14</sup> However, it is challenging to accurately determine the VPI status of lung cancers related to the adjacent pleura on CT, such as pleural tags or those in direct contact with the pleura. Positive predictive values range from 44.1% to 56.4%, indicating that approximately half of the CT-based predictions are false positives.<sup>15</sup> Therefore, finding novel and quickly available methods to improve efficiency is critical.

<sup>18</sup>F-fluorodeoxyglucose (<sup>18</sup>F-FDG) positron emission tomography (PET)/CT can reflect the glucose metabolism, the morphological characteristics of the tumors, and the anatomical relationship between adjacent structures, which is of great value for the TNM staging of tumors.<sup>16</sup> Recent studies have indicated that <sup>18</sup>F-FDG PET/CT has high accuracy in predicting the invasiveness,<sup>17</sup> the lymph node metastasis,<sup>18</sup> and the spread through air spaces<sup>19</sup> of clinical T1 stage NSCLC before surgery. However, establishing and validating a multivariate logistic regression model incorporating the maximum standardized uptake value ( $SUV_{max}$ ) and the relevant CT signs for predicting the VPI status of clinical stage IA lung adenocarcinoma, excluding pGGNs and tumors unrelated to the pleura, is rare. A nomogram is based on multivariate regression analysis, integrating multiple predictors to transform complex regression equations into visual graphics, making the results of the prediction model more readable and convenient for evaluating patients. Because a nomogram is intuitive and easy to understand, it has been widely used in preoperative nodal staging, predicting invasiveness, and giving a lung cancer prognosis.<sup>20-22</sup> Therefore, this study aims to explore whether tumor metabolism information and CT features could accurately predict VPI in clinical stage IA lung adenocarcinoma based on a nomogram.

## Methods

This retrospective study was approved by the Shanghai Changzheng Hospital Ethical Review Board of the hospital (decision number: CZ-20210528-01). Due to the retrospective nature of this study, informed consent was waived.

### Patients

Between February 2015 and June 2022, 328 patients with clinical stage IA lung ade-

nocarcinoma who underwent <sup>18</sup>F-FDG PET/CT examination before surgery and surgical resection were recruited. The inclusion criteria were as follows: (i) tumors clinically diagnosed as clinical T1 stage with a tumor size smaller than 30 mm<sup>23</sup> and (ii) tumors without pathological lymph node or distant metastasis. The exclusion criteria were as follows: (i) postoperative pathological diagnosis of atypical adenomatous hyperplasia (n = 1) or adenocarcinoma in situ (n = 1); (ii) no report of VPI status (n = 20); (iii) pGGNs (n = 14); (iv) neither directly in contact with the pleural surface nor had pleural tags (n = 107); (v) the minimum distance between the lesion and the pleura (DLP) >10 mm (n = 24); (vi) had treatment prior to <sup>18</sup>F-FDG PET/CT examination (n = 5); (vii) had a surgery and an examination interval of longer than 14 days (n = 6); and (viii) poor image quality or incomplete clinical data (n = 10). A total of 140 patients were included in our research (Figure 1). The patients were classified into a training and validation set with a 7:3 ratio based on the PET/CT examination temporal sequence. The training set included 98 patients between February 2015 and January 2020; the temporal validation set comprised 42 patients between April 2020 and June 2022.

### Equipment and parameters

Whole-body PET/CT tomography was performed using a Siemens Biograph Truepoint 64 PET/CT. The fasting blood glucose level of the patient was less than 10 mmol/L before the examination. After measuring the patient's body weight, the patient was given an intravenous injection of <sup>18</sup>F-FDG (Shanghai Atomic Kexing Pharmaceutical Co., Ltd.) 3.70–5.55 MBq/kg (0.10–0.15 mCi/kg) body weight with a radiochemical purity >95%, followed by a 300 mL water drink. The patient was instructed to lie down and rest for 60 min in a dark room. After emptying the bladder, the body scan ranged from the base of the skull to the middle of the femur, scanning 5–7 beds, 2–3 min/bed, with a reconstruction matrix of 192 × 192. The PET images were attenuated by CT images and reconstructed iteratively. The body CT scanning parameters were as follows: tube voltage 120 kV, tube current 160 mAs, scanning layer thickness 3.75 mm, reconstruction matrix 512 × 512, and pitch 0.8 s. The chest high-resolution computed tomography (HRCT) scan parameters were as follows: tube voltage 120 kV, tube current 150 mAs, scanning layer thickness 5 mm, reconstruction layer thickness and layer interval 1 mm, reconstruction matrix 512 × 512, and pitch

### Main points

- <sup>18</sup>F-fluorodeoxyglucose positron emission tomography/computed tomography is valuable in the non-invasive diagnosis of visceral pleural invasion (VPI) in subpleural clinical stage IA lung adenocarcinoma patients.
- The maximum standardized uptake value ( $SUV_{max}$ ), the solid component pleural contact length, the pleural indentation, and the vascular convergence sign are independent predictors of VPI.
- A nomogram incorporating  $SUV_{max}$  and independent computed tomography features improves predictive performance.

0.8 s. The lung window images were reconstructed by a high-resolution algorithm (B70f), and the mediastinal window images were reconstructed using a standard algorithm (B40f).

### Clinical and pathological data collection

Patients' clinical data, including age, gender, smoking history, preoperative carcinoembryonic antigen (CEA) level, surgical type, histological subtype, and tumor location, were reviewed.

The resected tissues were stained with hematoxylin and eosin, and the pathological diagnoses were performed by two pathologists with at least 10 years of experience. The specific elastic fiber stain was performed if the VPI status could not be determined accurately. Additionally, VPI was classified as no pleural invasion beyond the elastic layer (PL0), tumor invasion beyond the elastic layer (PL1), and tumor invasion to the surface of the visceral pleura (PL2), with PL1 and PL2 indicating the presence of VPI.<sup>2</sup>

### Image evaluation

The <sup>18</sup>F-FDG PET/CT images were imported into the software (RadiAnt DICOM Viewer 4.2.1, Medixant, Poland) and analyzed by two independent radiologists with seven years of experience who were blinded to the patho-

logical information. The lung window [width: 1.500 Hounsfield scale (HU), level: -500 HU], mediastinal window (width: 300 HU, level: 50 HU), multiplanar reformation (MPR), and maximal intensity projection were used to analyze the lesion. For quantitative indicators, the average measurements of two independent radiologists were used as the final data. For qualitative analysis, disagreements were discussed until a consensus was reached.

First, the tumor density type was classified as solid or part solid. The tumor size (the longest length of the tumor, T) and the solid component size (the longest length of the consolidation part, C) were measured at the lung window on the MPR images, and the proportion of the consolidation part was calculated (C/T ratio, CTR).<sup>24</sup>

Second, the tumor-pleura relationship was classified as a pleural attachment (directly contacting the pleura) or pleural tags (without abutting the pleura). Pleural tags were defined as one or multiple high-density linear strands connecting the tumor margin and the pleura (Figures 2-4).<sup>8</sup> The minimum vertical DLP was measured on the MPR images at the lung window for tumors with pleural tags (Figures 5, 6).<sup>6</sup> The pleural indentation sign was defined as the deviation of the pleura from its original position due to

tumor traction at the lung window, which can be observed in tumors with pleural tags or pleural attachment (Figures 2, 7).<sup>14</sup> The longest interface length of the whole tumor

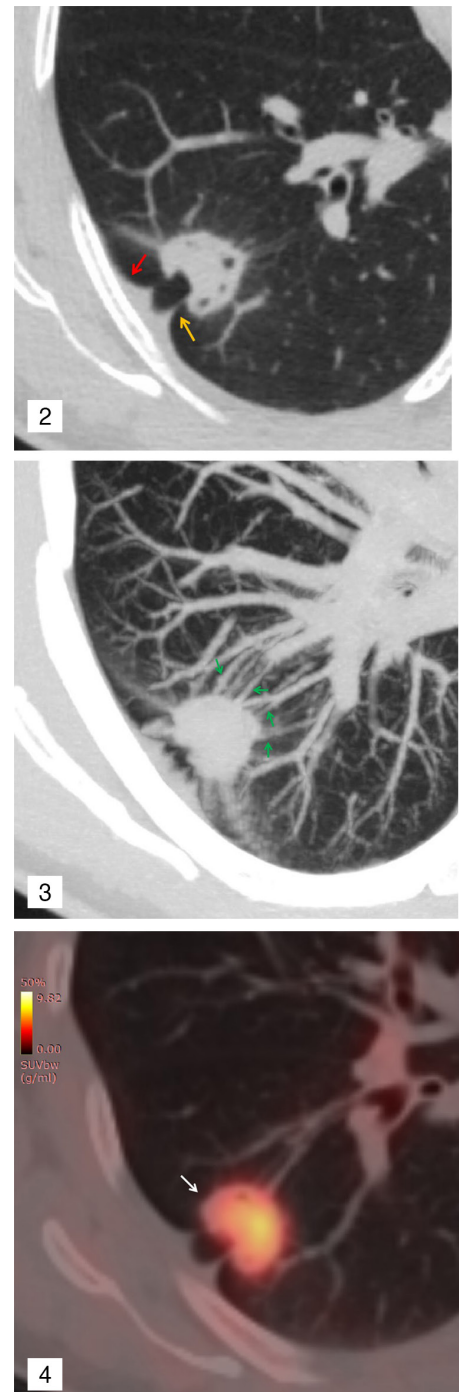


**Figure 2-4.** A 46-year-old female with invasive lung adenocarcinoma in the right lower lobe and positive for visceral pleural invasion. The axial non-contrast computed tomography (Figure 2) shows a solid nodule with multiple pleural tags (yellow arrow) and adjacent pleural indentation (red arrow). The maximal intensity projection (Figure 3) shows a vascular convergence sign (green arrow). The positron emission tomography/computed tomography fusion image (Figure 4) shows that the maximum standardized uptake value of the nodule is 6.38.

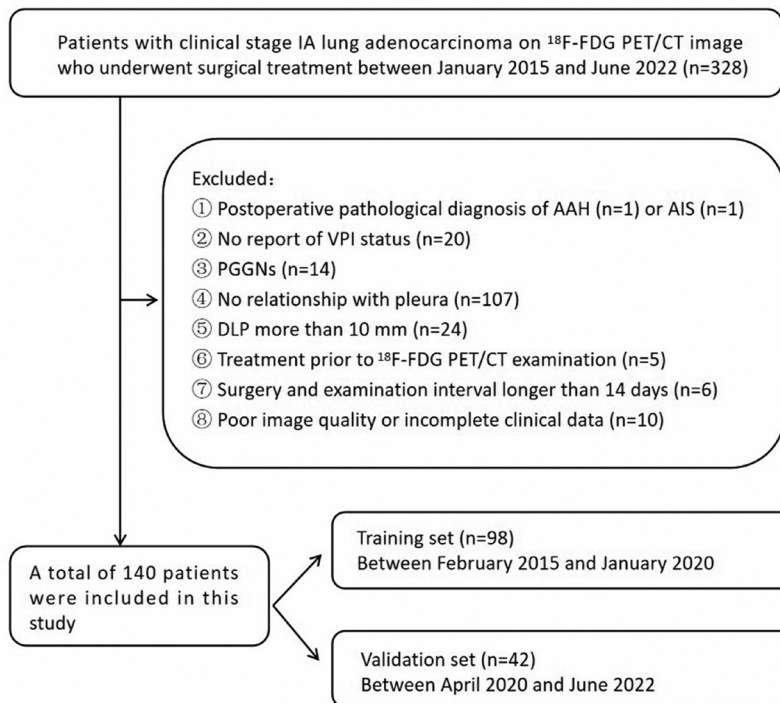


**Figure 1.** The flow chart for patient selection. AAH, atypical adenomatous hyperplasia; AIS, adenocarcinoma in situ; DLP, minimum distance between lesion and pleura; VPI, visceral pleural invasion; <sup>18</sup>F-FDG, <sup>18</sup>F-fluorodeoxyglucose; PET/CT, positron emission tomography/computed tomography; PGGN, pure ground-glass nodules.

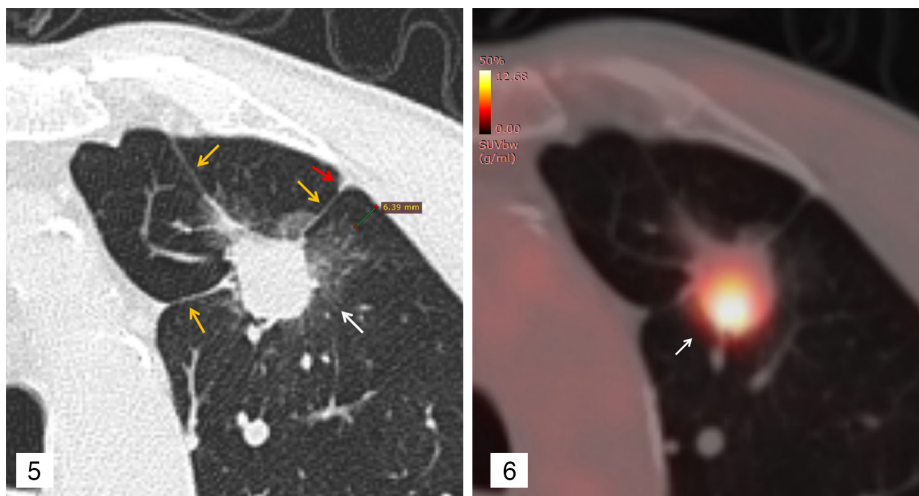


**Figure 5, 6.** A 72-year-old male with invasive lung adenocarcinoma in the left upper lobe and positive for visceral pleural invasion. The axial non-contrast computed tomography (**Figure 5**) shows a part-solid nodule with multiple pleural tags (yellow arrow) and adjacent pleural indentation (red arrow), with the minimum distance between the lesion and pleura being 6.39 mm. The positron emission tomography/computed tomography fusion image (**Figure 6**) shows that the uptake of <sup>18</sup>F-fluorodeoxyglucose is concentrated in the solid component area, and the maximum standardized uptake value of the nodule is 14.91.

and solid component was measured for tumors with pleural attachment by drawing a straight line at the lung window on the MPR images (Figure 7).<sup>10</sup> The solid interface length was 0 mm for a part-solid nodule without the solid component contacting the tumor.

Third, the presence or absence of lobulation, spiculation, vascular convergence, and air bronchogram signs were analyzed for all tumors. Lobulation is defined as a petaloid or wavy appearance at the tumor's margins. Spiculation refers to short, thin linear strands radiating around the surface of the tumor. Vascular convergence is the convergence of pulmonary vessels around the tumor towards the lesion (Figure 3).<sup>22</sup> Air bronchogram refers to air-filled bronchus manifesting as natural, dilated/distorted, or cut-off within the lesions.<sup>25</sup>

Fourth, the <sup>18</sup>F-FDG metric was measured by setting the region of interest covering the tumor on the PET/CT fusion images slice by slice and automatically generating the SUV<sub>max</sub>.

### Statistical analysis

R software (version 4.1.0, <http://www.Rproject.org>) and IBM SPSS Statistics (version 20.0, USA) software were utilized for the statistical analysis. The Shapiro–Wilk test was used to examine the normality of numeric variables. The normally distributed numerical variables were represented as the mean ± standard deviation, and the comparison between the two groups was carried out by using the two independent samples

t-test. Non-normally distributed data were described as the median and the 25% and 75% quartiles, and the Mann–Whitney U test was performed. Pearson's chi-squared test or Fisher's exact test was used for categorical variables analysis. Variables significantly different ( $P < 0.05$ ) in the univariate analysis were involved in the multivariate analysis of logistic regression, and a backward stepwise selection was applied by using the likelihood-ratio test with the Akaike information criterion (AIC) as the stopping rule to select the best combination of variables to build the prediction model in the training set and the corresponding nomogram. Spearman's rank correlation was used to analyze the correlation between the tumor size, the solid component size, the CTR, and the SUV<sub>max</sub>. The interobserver agreement of numeric and categorical variables was assessed using the intraclass correlation coefficient (ICC) and κ-statistic, respectively. The receiver operating characteristic (ROC) curve with the corresponding area under the curve (AUC) value was used to evaluate the discrimination ability of the prediction model and each risk factor in predicting VPI in the training and validation set. The calibration curve and Hosmer–Lemeshow test were used to evaluate the goodness-of-fit of the prediction model, and a  $P$  value of greater than 0.05 indicated a good goodness-of-fit. The decision curve analysis (DCA) was used to evaluate the clinical utility of the nomogram. Multivariate binary logistic regression, nomogram, validation, and calibration plots were done with the “rms” package of R software. The ROC

was performed by the “pROC” package, and the DCA was performed with the function of “ggDCA”.

## Results

### Baseline characteristics of the study cohorts

Among the 140 clinical stage IA lung adenocarcinomas, 57 cases were VPI-positive, and 83 were VPI-negative. The baseline characteristics of the training and validation sets were similar ( $P > 0.05$ ) (Table 1).

### Clinical and <sup>18</sup>F-fluorodeoxyglucose positron emission tomography/computed tomography features by visceral pleural invasion status in the training group

Clinical features showed no significant differences in age ( $P = 0.460$ ), gender ( $P = 0.359$ ), tumor location ( $P = 0.453$ ), smoking status ( $P = 0.349$ ), and CEA level ( $P = 1.000$ ) between the VPI-negative and VPI-positive groups in the training cohort (Table 2).

For <sup>18</sup>F-FDG PET/CT characteristics, the consistency of measurements between the two observers was good (ICCs ranged from 0.962 to 0.998), and the consistency of qualitative evaluation indicators was strong (a Kappa value of 0.879 to 0.971). The interobserver agreement assessment results of each index are shown in Supplementary File 1. The Spearman correlation analysis showed no linear correlation between the tumor size and the SUV<sub>max</sub>. The solid component size was positively correlated with the SUV<sub>max</sub> ( $r_s$ : 0.721,  $P < 0.001$ ), while the CTR was positively correlated with the SUV<sub>max</sub> ( $r_s$ : 0.742,  $P < 0.001$ ). The univariate analysis showed that the SUV<sub>max</sub>, the CTR, the solid component size, the solid pleural contact length, the density type, the pleural indentation, the spiculation, and the vascular convergence sign significantly differed between the VPI-positive and the VPI-negative groups in the training set ( $P < 0.05$ ). The solid nodules, the pleural indentation, the spiculation, and the vascular convergence signs were more common in the VPI-positive group ( $P < 0.001$ ). The VPI-positive group presented a significantly higher SUV<sub>max</sub>, larger solid component size, greater CTR, and longer solid pleural contact length than the VPI-negative group ( $P < 0.05$ ; Table 2).

### Nomogram development and evaluation

Variables significantly different in the univariate analysis were involved in the multivariate logistic regression analysis. Based

**Table 1.** Baseline features of patients in the training and validation cohort

Characteristics	Total (n = 140)	Training cohort (n = 98)	Validation cohort (n = 42)	P value
Age <sup>b</sup>	60.50 ± 9.52	60.23 ± 9.51	61.12 ± 9.61	0.616
<b>Gender</b>				
Female	90 (64.29%)	64 (65.31%)	26 (61.90%)	0.700
Male	50 (35.71%)	34 (34.69%)	16 (38.10%)	
<b>VPI status</b>				
Negative	83 (59.29%)	58 (59.18%)	25 (59.52%)	0.970
Positive	57 (40.71%)	40 (40.82%)	17 (40.48%)	
<b>Location<sup>a</sup></b>				
Right upper lobe	49 (35.00%)	34 (34.69%)	15 (35.71%)	0.727
Right middle lobe	15 (10.71%)	9 (9.18%)	6 (14.29%)	
Right lower lobe	28 (20.00%)	22 (22.45%)	6 (14.29%)	
Left upper lobe	25 (17.85%)	18 (18.37%)	7 (16.67%)	
Left lower lobe	23 (16.44%)	15 (15.31%)	8 (19.04%)	
<b>Smoking status</b>				
Non smoker	112 (80.00%)	78 (79.59%)	34 (80.95%)	0.854
Smoker	28 (20.00%)	20 (20.41%)	8 (19.05%)	
<b>CEA<sup>a</sup>, µg/L</b>				
<5	135 (96.43%)	96 (97.96%)	39 (92.86%)	0.159
≥5	5 (3.57%)	2 (2.04%)	3 (7.14%)	
<b>Surgery type</b>				
Sublobar resection	27 (19.29%)	18 (18.37%)	9 (21.43%)	0.674
Lobectomy	113 (80.71%)	80 (81.63%)	33 (78.57%)	
<b>Pathological grade<sup>a</sup></b>				
MIA	4 (2.86%)	4 (4.08%)	0 (0.00%)	0.316
IA	136 (97.14%)	94 (95.92%)	42 (100.00%)	
SUV <sub>max</sub>	1.84 (1.22, 3.78)	1.80 (1.04, 3.84)	1.88 (1.27, 3.53)	0.297
Tumor size (mm)	24.10 (19.20, 28.95)	23.80 (18.40, 28.70)	26.20 (20.40, 29.40)	0.193
Solid component size (mm)	17.15 (10.85, 23.35)	16.40 (9.67, 21.80)	19.00 (12.70, 26.70)	0.068
CTR (%)	78.14 (53.35, 95.98)	74.31 (47.51, 93.75)	83.76 (66.30, 100.00)	0.106
Pleural contact length (mm)	7.87 (0.00, 16.55)	7.24 (0.00, 15.80)	9.12 (0.00, 17.30)	0.612
Solid pleural contact length (mm)	2.84 (0.00, 10.65)	0.00 (0.00, 10.10)	4.40 (0.00, 13.80)	0.255
DLP (mm)	0.00 (0.00, 3.36)	0.00 (0.00, 3.50)	0.00 (0.00, 2.71)	0.467
<b>Density type</b>				
Part solid	108 (77.14%)	77 (78.57%)	31 (73.81%)	0.539
Solid	32 (22.86%)	21 (21.43%)	11 (26.19%)	
<b>Tumor–pleura relationship</b>				
Pleural tags	64 (45.71%)	45 (45.92%)	19 (45.24%)	0.941
Pleural attachment	76 (54.29%)	53 (54.08%)	23 (54.76%)	
<b>Pleural indentation</b>				
Absent	54 (38.57%)	34 (34.69%)	20 (47.62%)	0.150
Present	86 (61.43%)	64 (65.31%)	22 (52.38%)	
<b>Lobulation<sup>a</sup></b>				
Absent	13 (9.29%)	11 (11.24%)	2 (4.76%)	0.344
Present	127 (90.71%)	87 (88.76%)	40 (95.24%)	
<b>Spiculation</b>				
Absent	105 (75.00%)	72 (73.47%)	33 (78.57%)	0.523
Present	35 (25.00%)	26 (26.53%)	9 (21.43%)	
<b>Air bronchogram</b>				
Absent	55 (39.29%)	41 (41.84%)	14 (33.33%)	0.345
Present	85 (60.71%)	57 (58.16%)	28 (66.67%)	
<b>Vascular convergence</b>				
Absent	116 (82.86%)	83 (84.69%)	33 (78.57%)	0.378
Present	24 (17.14%)	15 (15.31%)	9 (21.43%)	

The P value represents the univariate analysis. Data are presented as n (%). <sup>a</sup>Fisher exact test; <sup>b</sup>mean ± standard deviation, the two independent samples t-test. VPI, visceral pleural invasion; CEA, carcinoembryonic antigen; MIA, minimally invasive adenocarcinoma; IA, invasive adenocarcinoma; CTR, consolidation-to-tumor ratio; SUV<sub>max</sub>, maximum standardized uptake value; DLP, minimum distance between lesion and pleura.

on the principle of AIC value minimization, a prediction model was constructed by a backward stepwise selection of variables, including the  $SUV_{max}$ , the solid component pleural contact length, the pleural indentation, and the vascular convergence sign as the best combination of prediction variables. The  $SUV_{max}$  [odds ratio (OR): 1.753, 95% confidence interval (CI) 1.232–2.496,  $P = 0.002$ ], the solid component pleural contact length (OR: 1.101, 95% CI 1.007–1.204,  $P = 0.034$ ), the pleural indentation (OR: 5.075, 95% CI 1.065–24.172,  $P = 0.041$ ), and the vascular convergence sign (OR: 13.324, 95% CI 1.379–128.691,  $P = 0.025$ ) were independent risk factors for VPI (Table 3). Figures 2 to 8 show the representative cases.

Based on the regression coefficients of the variables included in this model, a nomogram was constructed to evaluate the VPI risk intuitively (Figure 9). The sensitivity, specificity, accuracy, and the AUC for the prediction model in the training set were 82.5%, 79.31%, 80.61%, and 0.892 (95% CI 0.813–0.946), respectively, using the optimal cut-off value of 0.35. The prediction model achieved good discrimination performance in the validation set with sensitivity, specificity, accuracy, and AUC values of 100%, 76.00%, 85.71%, and 0.885 (95% CI, 0.748–0.962), respectively. Figures 10 and 11 present the ROCs for the training and validation cohorts. Table 4 shows the cut-off values and predictive performance of each independent risk factor for predicting VPI in the training and validation cohort. The calibration curve demonstrated that the predicted probabilities were in acceptable agreement with the actual probabilities for the training and validation cohorts, and the Hosmer–Lemeshow test showed good goodness of fit, with  $P$  values of 0.648 and 0.051, respectively (Figures 12, 13). The DCA showed that the prediction model adds more net benefit than the “treat all” or “treat none” approach (Figures 14, 15). Supplementary Figures 1, 2 give an example of the clinical application of this nomogram.

## Discussion

The present study developed a prediction model as a non-invasive method to detect VPI status in clinical stage IA lung adenocarcinoma. The nomogram incorporating the  $SUV_{max}$ , the solid component pleural contact length, the pleural indentation, and the vascular convergence sign provided a scoring system to help predict VPI status before surgery and had excellent discrimination and acceptable calibration, with an AUC of 0.892 in the training set and 0.885 in the validation set.

The visceral pleura contains abundant lymphatic channels, and the subpleural lymphatic system (peripheral lymphatic system) communicates with the axial lymphatic system distributed around the bronchi and pulmonary vessels.<sup>26</sup> Therefore, lung cancer patients with VPI-positive status have a higher probability of hilar and mediastinal lymph node metastasis via the axial lymphatic system<sup>27</sup> and are more prone to skip N2 lymph node metastasis.<sup>28</sup> Thus, lobectomy and extensive lymph node dissection are required for VPI-positive patients.<sup>3,4</sup> Therefore, accurately predicting VPI before surgery is of great clinical significance.

For qualitative indicators, the present study found that the spiculation sign was more common in the VPI-positive group. Spiculation is associated with tumor cell infiltration into adjacent blood and lymphatic vessels, suggesting lung adenocarcinoma is

more aggressive.<sup>29</sup> However, the spiculation sign was not an independent risk factor for VPI prediction in the present study, similar to the previous literature report.<sup>30</sup> As previously reported,<sup>6,31</sup> VPI was significantly related to the pleural indentation in the authors’ study. The mechanism could be that as the tumor grows, the development of reactive fibrous hyperplasia of the tumor, to a certain extent, may cause the adjacent pleura to retract, thereby increasing the risk of VPI.<sup>32</sup> In addition to the pleural indentation sign, the vascular convergence sign was an independent risk factor in the present study, and no previous study reported similar results. It was speculated that it might be related to the pathological basis of the vascular convergence sign, which was also caused by the reactive fibrous hyperplasia of the tumor.<sup>33</sup> As tumor invasiveness increased, reactive fibrous hyperplasia increased, and traction

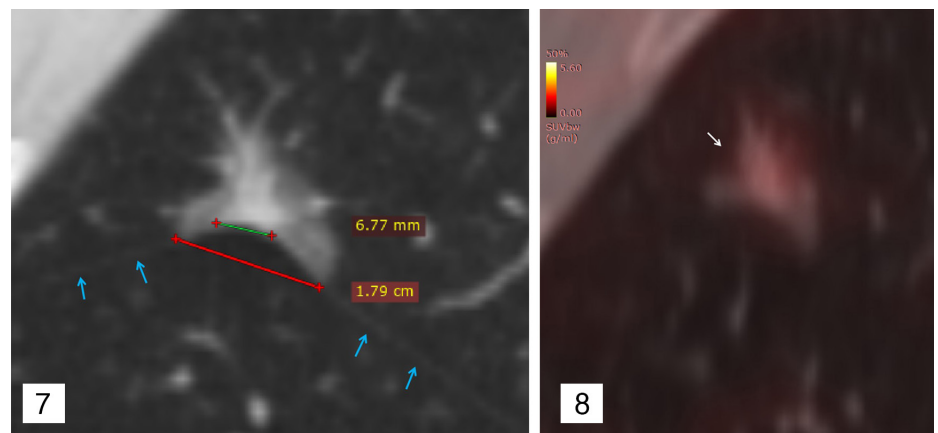


**Figure 7, 8.** A 61-year-old male with invasive lung adenocarcinoma in the right upper lobe and negative for visceral pleural invasion. The sagittal non-contrast computed tomography (Figure 7) shows a part-solid nodule with interlobar fissure attachment (blue arrow) and adjacent interlobar pleural indentation, with the longest interface length of the whole tumor and solid component being 1.79 cm and 6.77 mm, respectively. The image (Figure 8) shows the maximum standardized uptake value of the nodule is 0.95.

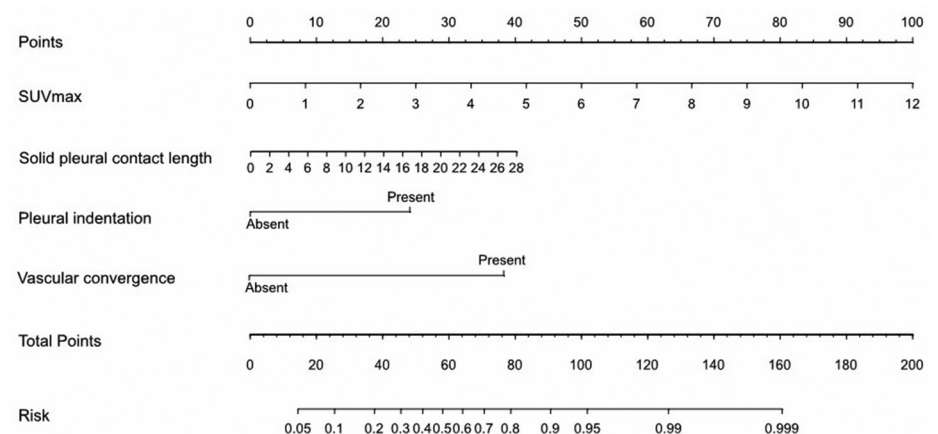


**Figure 9.** A  $^{18}F$ -fluorodeoxyglucose positron emission tomography/computed tomography fusion nomogram for the non-invasive prediction of visceral pleural invasion for patients with clinical stage IA peripheral lung adenocarcinoma, which incorporated the maximum standardized uptake value, the solid component contact length, the pleural indentation, and the vascular convergence sign.

**Table 2.** Clinical characteristics and <sup>18</sup>F-fluorodeoxyglucose positron emission tomography/computed tomography features of patients in the training cohort

Characteristics	Total (n = 98)	VPI-negative (n = 58)	VPI-positive (n = 40)	P value
Age <sup>b</sup>	60.23 ± 9.51	60.83 ± 9.78	59.38 ± 9.16	0.460
<b>Gender</b>				
Female	64 (65.31%)	40 (68.97%)	24 (60.00%)	0.359
Male	34 (34.69%)	18 (31.03%)	16 (40.00%)	
<b>Location<sup>a</sup></b>				
Right upper lobe	34 (34.69%)	17 (29.31%)	17 (42.50%)	0.453
Right middle lobe	9 (9.18%)	4 (6.90%)	5 (12.5%)	
Right lower lobe	22 (22.45%)	14 (24.14%)	8 (20.00%)	
Left upper lobe	18 (18.37%)	13 (22.41%)	5 (12.5%)	
Left lower lobe	15 (15.31%)	10 (17.24%)	5 (12.5%)	
<b>Smoking status</b>				
Non smoker	78 (79.59%)	48 (82.76%)	30 (75.00%)	0.349
Smoker	20 (20.41%)	10 (17.24%)	10 (25.00%)	
<b>CEA<sup>a</sup>, µg/L</b>				
<5	96 (97.96%)	57 (98.28%)	39 (97.50%)	1.000
≥5	2 (2.04%)	1 (1.72%)	1 (2.50%)	
SUV <sub>max</sub>	1.80 (1.04, 3.84)	1.28 (0.86, 1.99)	3.36 (1.97, 6.23)	<0.001
Tumor size (mm)	23.80 (18.40, 28.70)	23.85 (17.50, 28.60)	23.75 (19.60, 28.90)	0.513
Solid component size (mm) <sup>b</sup>	16.09 ± 7.63	13.58 ± 7.43	19.75 ± 6.41	<0.001
CTR (%)	74.31 (47.51, 93.75)	63.90 (37.14, 76.17)	92.08 (77.71, 100.00)	<0.001
Pleural contact length (mm)	7.24 (0.00, 15.80)	3.35 (0.00, 15.50)	9.90 (0.00, 17.65)	0.301
Solid pleural contact length (mm)	0.00 (0.00, 10.10)	0.00 (0.00, 6.69)	5.77 (0.00, 16.75)	0.009
DLP (mm)	0.00 (0.00, 3.50)	0.56 (0.00, 3.57)	0.00 (0.00, 3.38)	0.547
<b>Density type</b>				
Part solid	77 (78.57%)	53 (91.38%)	24 (60.00%)	<0.001
Solid	21 (21.43%)	5 (8.62%)	16 (40.00%)	
<b>Tumor-pleura relationship</b>				
Pleural tags	45 (45.92%)	29 (50.00%)	16 (40.00%)	0.329
Pleural attachment	53 (54.08%)	29 (50.00%)	24 (60.00%)	
<b>Pleural indentation</b>				
Absent	34 (34.69%)	30 (51.72%)	4 (10.00%)	<0.001
Present	64 (65.31%)	28 (48.28%)	36 (90.00%)	
<b>Lobulation<sup>a</sup></b>				
Absent	11 (11.22%)	7 (12.07%)	4 (10.00%)	1.000
Present	87 (88.78%)	51 (87.93%)	36 (90.00%)	
<b>Spiculation</b>				
Absent	72 (73.47%)	51 (87.93%)	21 (52.50%)	<0.001
Present	26 (26.53%)	7 (12.07%)	19 (47.50%)	
<b>Air bronchogram</b>				
Absent	41 (41.84%)	26 (44.83%)	15 (37.50%)	0.470
Present	57 (58.16%)	32 (55.17%)	25 (62.50%)	
<b>Vascular convergence</b>				
Absent	83 (84.69%)	57 (98.28%)	26 (65.00%)	<0.001
Present	15 (15.31%)	1 (1.72%)	14 (35.00%)	

The P value represents the univariate analysis. Data are presented as n (%). <sup>a</sup>Fisher exact test. <sup>b</sup>mean ± standard deviation, the two independent samples t-test. VPI, visceral pleural invasion; CEA, carcino-embryonic antigen; CTR, consolidation-to-tumor ratio; SUV<sub>max</sub>, maximum standardized uptake value; DLP, minimum distance between lesion and pleura.

on adjacent pulmonary vessels or the pleura became more obvious.

For quantitative indicators, there was no linear correlation between the tumor size and the  $SUV_{max}$ . According to the Spearman correlation analysis, while the solid component size and the CTR had a relatively high degree of positive correlation with the  $SUV_{max}$ . This may be related to the larger proportion of part-solid nodules (78.57%) in the training set included in the present study. The tumor cells in the solid component area of the part-solid nodules were denser than in the ground glass area, so the  $^{18}F$ -FDG uptake value was greater in the solid component area. Additionally, the  $SUV_{max}$ , the solid component size, the CTR, and the solid pleural contact length were significantly greater in the VPI-positive group ( $P < 0.05$ ) than in the VPI-negative group, but the tumor size and the whole tumor pleural contact length did not show a difference between the two groups. The results indicate that the solid component represents the more aggressive part of the tumor, consistent with clinical T staging depending on the solid component's size rather than the tumor's overall size, in tumors less than 3 cm.<sup>23</sup> In this study, the analysis found that the  $SUV_{max}$  and the solid pleural contact length were independent risk factors for predicting VPI among quantitative indicators, similar to previous stud-

ies.<sup>34,35</sup> This result suggests that whether a solid component contacts the pleura and its contact length should also be an important consideration when determining VPI status. However, solid components in tumors may also correspond to fibroblast proliferation, alveolar collapse, inflammatory cell infiltration, and tumor-secreted mucus.<sup>36</sup> In some cases in the authors' study, although the solid component accounted for a large proportion, the  $SUV_{max}$  value was low, and the adjacent visceral pleura was not invaded (Supplementary Figures 1 to 2). Therefore, diagnostic efficacy for VPI status is limited when only considering the solid component size and the CTR. The  $SUV_{max}$  reflected the  $^{18}F$ -FDG metabolism of tumors, representing the activity of tumor cell proliferation, and was a better indicator of tumor invasiveness in previous studies.<sup>16-19</sup> Furthermore, previous results found no VPI-positive status in clinical IA lung adenocarcinoma with the  $SUV_{max}$  less than 1.3,<sup>34</sup> indicating that an extremely low  $SUV_{max}$  can represent less invasiveness, which has a high negative predictive value.<sup>34</sup> Similar to the previous study, the authors' results also found that VPI-positive status was not observed in patients with an  $SUV_{max}$  of less than 1.4 in the training group. However, contrary to previous reports,<sup>6,30</sup> there was no significant difference in the DLP between the two groups. This may be because the pro-

portion of tumors directly in contact with the pleura (pleura attachment) included in this study was comparable between the VPI-positive and VPI-negative groups in the training set, while the type of tumors in direct contact with the pleura (DLP = 0 mm) was more prevalent in the VPI-positive group in previous studies.<sup>6,30</sup> The different results are due to selection bias, and further verification is required after collecting large sample cases in the future.

There were two previous studies on predicting VPI status in lung adenocarcinoma based on  $^{18}F$ -FDG PET/CT, but both of them only analyzed the risk factors related to VPI-positive status and did not validate the model. Tanaka et al.<sup>34</sup> studied the value of HRCT and  $^{18}F$ -FDG PET/CT in predicting the pleural invasion of lung adenocarcinoma in direct contact with the pleura. In the subgroup analysis, including whole tumors size less than 3 cm, the multivariate analysis showed that the  $SUV_{max}$  and the whole tumor contact length with the pleura were independent risk factors for predicting pleural invasion. The predictive performance of only the  $SUV_{max}$  (AUC value 0.844) was comparable to the multivariate model (AUC value 0.845–0.857). Unlike the present study, the previous study included pGGNs and 11 cases with pathological parietal pleural invasion. The study by Chen et al.<sup>35</sup> focused on subso-

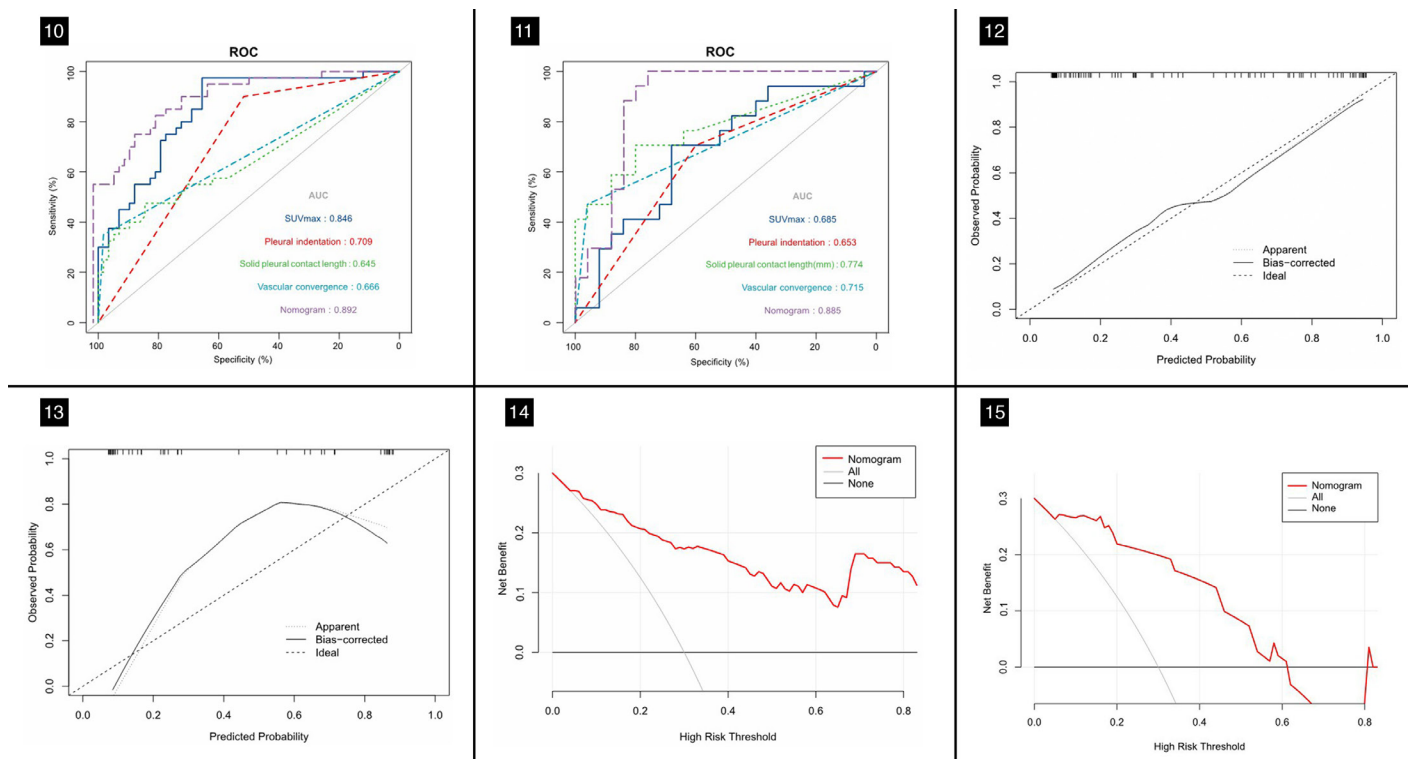


**Figure 10-15.** Receiver operating characteristic curves for the nomogram in the training set (Figure 10) and the validation set (Figure 11). Calibration curves of the nomogram in the training set (Figure 12) and the validation set (Figure 13). Decision curve analysis of the nomogram in the training set (Figure 14) and the validation set (Figure 15).

id nodules, including pGGNs, and the multivariate analysis revealed that the DLP and the  $SUV_{max}$  were independent risk factors for predicting VPI. The AUC value of the combined model, including the two variables, was 0.90. However, Chen et al.<sup>35</sup> did not indicate whether the tumors included were related to the pleura, especially in the VPI-negative group. The present study excluded tumors presenting as pGGNs and tumors unrelated to the pleura that do not invade the visceral pleura, unlike in previous reports.<sup>11-13</sup> Therefore, the authors' results were more objective in including cases with potential VPI-positive status to study the predictive performance of the  $SUV_{max}$  combined with the CT features. The different results may be due to the different inclusion criteria of the study.

A previous study showed that  $^{18}F$ -FDG liver metrics (the  $SUV_{max}$  and the  $SUV_{mean}$ ) obtained from PET/CT studies of the same patient scanned on the same machine at different time periods were highly repeatable and might reliably be used in following patients longitudinally.<sup>37</sup> The  $SUV_{max}$  values in the present study were all obtained from a single  $^{18}F$ -FDG PET/CT device in the same hospital; standardized image acquisition and post-processing were adopted, avoiding the differences brought by the hardware

and post-processing software of the PET/CT equipment. It is worth noting that standardized image acquisition and post-processing of  $^{18}F$ -FDG PET/CT and accurate measurement of the  $SUV_{max}$  are key factors in the pre-operative assessment of whether lung cancer has invaded the visceral pleura.

This study has several limitations. First, the study was retrospective, resulting in inevitable selection bias. Second, although internal validation of the model yielded good discrimination, the generalization of this nomogram needs to be verified on external data. Third, VPI status in some cases lacks clear PL1 and PL2 pathological grades. Therefore, the clinical application and generalization of the model still need to be further improved and validated by multicenter studies.

In conclusion, the nomogram incorporating the  $SUV_{max}$  and the independent CT features (including the solid component pleural contact length, the pleural indentation, and the vascular convergence sign) showed good value for predicting VPI status in clinical stage IA lung adenocarcinoma in this preliminary study. As a non-invasive quantitative method,  $^{18}F$ -FDG PET/CT holds the potential to help in the surgical decision-making process and additional treatment of clinical stage IA lung adenocarcinoma.

## Acknowledgements

The authors thank Dr. Zhengwei Zhang of the Department of Pathology, Second Affiliated Hospital of Navy Medical University, Shanghai 200003, China, for his selfless and valuable assistance in interpreting the pathological results of this study.

## Conflict of interest disclosure

The authors declared no conflicts of interest.

## Funding

This research was funded by National Key R&D Program of China (2022YFC2010000, 2022YFC2010002), Key Program of National Natural Science Foundation of China (81930049), National Natural Science Foundation of China (82171926, 82202140), Shanghai Sailing Program (20YF1449000), Shanghai Science and Technology Innovation Action Plan Program (19411951300), Clinical Innovative Project of Shanghai Changzheng Hospital (2020YLCYJ-Y24), Program of Science and Technology Commission of Shanghai Municipality (21DZ2202600).

**Table 3.** Multivariate logistic regression analysis of independent risk factors for predicting visceral pleural invasion status in the training cohort

Characteristics	B	SE	Wald	P value	OR (95% CI)
$SUV_{max}$	0.562	0.180	9.711	0.002	1.753 (1.232–2.496)
Solid pleural contact length	0.097	0.046	4.491	0.034	1.101 (1.007–1.204)
Pleural indentation	1.624	0.796	4.159	0.041	5.075 (1.065–24.172)
Vascular convergence	2.590	1.157	5.008	0.025	13.324 (1.379–128.691)
Constant	–3.915	0.875	20.033	0.000	0.020

B, regression coefficients; SE, standard error; Wald, Wald  $\chi^2$  value; OR, odds ratio; CI, confidence interval;  $SUV_{max}$ , maximum standardized uptake value.

**Table 4.** The predictive efficacy of nomogram and single predictive factor for predicting visceral pleural invasion

Variable	Cut-off	Cohort	AUC (95% CI)	Accuracy (%)	Sensitivity (%)	Specificity (%)
Nomogram	0.35	Training	0.892 (0.813–0.946)	80.61	82.50	79.31
		Validation	0.885 (0.748–0.962)	85.71	100.00	76.00
$SUV_{max}$	1.43	Training	0.846 (0.759–0.911)	78.57	97.50	65.52
		Validation	0.685 (0.523–0.819)	69.05	70.59	68.00
Solid pleural contact length (mm)	8.92	Training	0.645 (0.542–0.739)	69.39	47.50	84.48
		Validation	0.744 (0.619–0.889)	76.19	70.59	80.00
Pleural indentation	0.50	Training	0.709 (0.608–0.796)	67.35	90.00	51.72
		Validation	0.653 (0.490–0.793)	64.29	70.59	60.00
Vascular convergence	0.50	Training	0.666 (0.564–0.758)	72.45	35.00	98.28
		Validation	0.715 (0.555–0.844)	76.19	47.06	96.00

$SUV_{max}$ , maximum standardized uptake value; AUC, area under the curve; CI, confidence interval.

## References

- Sung H, Ferlay J, Siegel RL, et al. Global Cancer Statistics 2020: GLOBOCAN estimates of incidence and mortality worldwide for 36 cancers in 185 countries. *CA Cancer J Clin.* 2021;71(3):209-249. [CrossRef]
- Goldstraw P, Chansky K, Crowley J, et al. The IASLC lung cancer staging project: proposals for revision of the TNM stage groupings in the forthcoming (Eighth) edition of the TNM classification for lung cancer. *J Thorac Oncol.* 2016;11(1):39-51. [CrossRef]
- Zhang T, Zhang JT, Li WF, et al. Visceral pleural invasion in T1 tumors ( $\leq 3$  cm), particularly T1a, in the eighth tumor-node-metastasis classification system for non-small cell lung cancer: a population-based study. *J Thorac Dis.* 2019;11(7):2754-2762. [CrossRef]
- Wo Y, Zhao Y, Qiu T, et al. Impact of visceral pleural invasion on the association of extent of lymphadenectomy and survival in stage I non-small cell lung cancer. *Cancer Med.* 2019;8(2):669-678. [CrossRef]
- Takizawa H, Kondo K, Kawakita N, et al. Autofluorescence for the diagnosis of visceral pleural invasion in non-small-cell lung cancer. *Eur J Cardiothorac Surg.* 2018;53(5):987-992. [CrossRef]
- Qi LP, Li XT, Yang Y, et al. Multivariate analysis of pleural invasion of peripheral non-small cell lung cancer-based computed tomography features. *J Comput Assist Tomogr.* 2016;40(5):757-762. [CrossRef]
- Yang S, Yang L, Teng L, et al. Visceral pleural invasion by pulmonary adenocarcinoma  $\leq 3$  cm: the pathological correlation with pleural signs on computed tomography. *J Thorac Dis.* 2018;10(7):3992-3999. [CrossRef]
- Hsu JS, Han IT, Tsai TH, et al. Pleural tags on CT scans to predict visceral pleural invasion of non-small cell lung cancer that does not abut the pleura. *Radiology.* 2016;279(2):590-596. [CrossRef]
- Onoda H, Higashi M, Murakami T, et al. Correlation between pleural tags on CT and visceral pleural invasion of peripheral lung cancer that does not appear touching the pleural surface. *Eur Radiol.* 2021;31(12):9022-9029. [CrossRef]
- Heidinger BH, Schwarz-Nemec U, Anderson KR, et al. Visceral pleural invasion in pulmonary adenocarcinoma: differences in CT patterns between solid and subsolid cancers. *Radiol Cardiothorac Imaging.* 2019;1(3):e190071. [CrossRef]
- Ahn SY, Park CM, Jeon YK, et al. Predictive CT features of visceral pleural invasion by T1-sized peripheral pulmonary adenocarcinomas manifesting as subsolid nodules. *AJR Am J Roentgenol.* 2017;209(3):561-566. [CrossRef]
- Zhao Q, Wang JW, Yang L, Xue LY, Lu WW. CT diagnosis of pleural and stromal invasion in malignant subpleural pure ground-glass nodules: an exploratory study. *Eur Radiol.* 2019;29(1):279-286. [CrossRef]
- Shi J, Li F, Yang F, et al. The combination of computed tomography features and circulating tumor cells increases the surgical prediction of visceral pleural invasion in clinical T1N0M0 lung adenocarcinoma. *Transl Lung Cancer Res.* 2021;10(11):4266-4280. [CrossRef]
- Kim HJ, Cho JY, Lee YJ, et al. Clinical significance of pleural attachment and indentation of subsolid nodule lung cancer. *Cancer Res Treat.* 2019;51(4):1540-1548. [CrossRef]
- Kim H, Goo JM, Kim YT, Park CM. CT-defined visceral pleural invasion in T1 Lung adenocarcinoma: lack of relationship to disease-free survival. *Radiology.* 2019;292(3):741-749. [CrossRef]
- Kandathil A, Kay FU, Butt YM, Wachsmann JW, Subramaniam RM. Role of FDG PET/CT in the eighth edition of TNM staging of non-small cell lung cancer. *Radiographics.* 2018;38(7):2134-2149. [CrossRef]
- Li XF, Shi YM, Niu R, et al. Risk analysis in peripheral clinical T1 non-small cell lung cancer correlations between tumor-to-blood standardized uptake ratio on 18F-FDG PET-CT and primary tumor pathological invasiveness: a real-world observational study. *Quant Imaging Med Surg.* 2022;12(1):159-171. [CrossRef]
- Zhai X, Guo Y, Qian X. Combination of fluorine-18 fluorodeoxyglucose positron-emission tomography/computed tomography ( $^{18}\text{F}$ -FDG PET/CT) and tumor markers to diagnose lymph node metastasis in non-small cell lung cancer (NSCLC): a retrospective and prospective study. *Med Sci Monit.* 2020;26:e922675. [CrossRef]
- Wang XY, Zhao YF, Yang L, Liu Y, Yang YK, Wu N. Correlation analysis between metabolic tumor burden measured by positron emission tomography/computed tomography and the 2015 World Health Organization classification of lung adenocarcinoma, with a risk prediction model of tumor spread through air spaces. *Transl Cancer Res.* 2020;9(10):6412-6422. [CrossRef]
- Xie Y, Zhao H, Guo Y, et al. A PET/CT nomogram incorporating SUVmax and CT radiomics for preoperative nodal staging in non-small cell lung cancer. *Eur Radiol.* 2021;31(8):6030-6038. [CrossRef]
- Jin C, Cao J, Cai Y, Wang L, Liu K, Shen W, Hu J. A nomogram for predicting the risk of invasive pulmonary adenocarcinoma for patients with solitary peripheral subsolid nodules. *J Thorac Cardiovasc Surg.* 2017;153(2):462-469. [CrossRef]
- Song C, Guo Z, Yu D, et al. A prognostic nomogram combining immune-related gene signature and clinical factors predicts survival in patients with lung adenocarcinoma. *Front Oncol.* 2020;10:1300. [CrossRef]
- Travis WD, Asamura H, Bankier AA, et al. The IASLC lung cancer staging project: proposals for coding T categories for subsolid nodules and assessment of tumor size in part-solid tumors in the forthcoming eighth edition of the TNM classification of lung cancer. *J Thorac Oncol.* 2016;11(8):1204-1223. [CrossRef]
- Suzuki K, Koike T, Asakawa T, et al. A prospective radiological study of thin-section computed tomography to predict pathological noninvasiveness in peripheral clinical IA lung cancer (Japan Clinical Oncology Group 0201). *J Thorac Oncol.* 2011;6(4):751-756. [CrossRef]
- Tu W, Sun G, Fan L, et al. Radiomics signature: a potential and incremental predictor for EGFR mutation status in NSCLC patients, comparison with CT morphology. *Lung Cancer.* 2019;132:28-35. [CrossRef]
- Imai K, Minamiya Y, Saito H, et al. Detection of pleural lymph flow using indocyanine green fluorescence imaging in non-small cell lung cancer surgery: a preliminary study. *Surg Today.* 2013;43(3):249-254. [CrossRef]
- Inoue M, Minami M, Shiono H, Sawabata N, Ideguchi K, Okumura M. Clinicopathologic study of resected, peripheral, small-sized, non-small cell lung cancer tumors of 2 cm or less in diameter: pleural invasion and increase of serum carcinoembryonic antigen level as predictors of nodal involvement. *J Thorac Cardiovasc Surg.* 2006;131(5):988-993. [CrossRef]
- Gorai A, Sakao Y, Kuroda H, et al. The clinicopathological features associated with skip N2 metastases in patients with clinical stage IA non-small-cell lung cancer. *Eur J Cardiothorac Surg.* 2015;47(4):653-658. [CrossRef]
- Jin C, Cao J, et al. A nomogram for predicting the risk of invasive pulmonary adenocarcinoma for patients with solitary peripheral subsolid nodules. *J Thorac Cardiovasc Surg.* 2017;153(2):462-469. [CrossRef]
- Deng HY, Li G, Luo J, Alai G, Zhuo ZG, Lin YD. Novel biologic factors correlated to visceral pleural invasion in early-stage non-small cell lung cancer less than 3 cm. *J Thorac Dis.* 2018;10(4):2357-2364. [CrossRef]
- Zhao LL, Xie HK, Zhang LP, et al. Visceral pleural invasion in lung adenocarcinoma  $\leq 3$  cm with ground-glass opacity: a clinical, pathological and radiological study. *J Thorac Dis.* 2016;8(7):1788-1797. [CrossRef]
- Gruden JF. What is the significance of pleural tags? *AJR Am J Roentgenol.* 1995;164(2):503-504. [CrossRef]
- Zhang Y, Qiang JW, Ye JD, Ye XD, Zhang J. High resolution CT in differentiating minimally invasive component in early lung adenocarcinoma. *Lung Cancer.* 2014;84(3):236-241. [CrossRef]
- Tanaka T, Shinya T, Sato S, et al. Predicting pleural invasion using HRCT and 18F-FDG

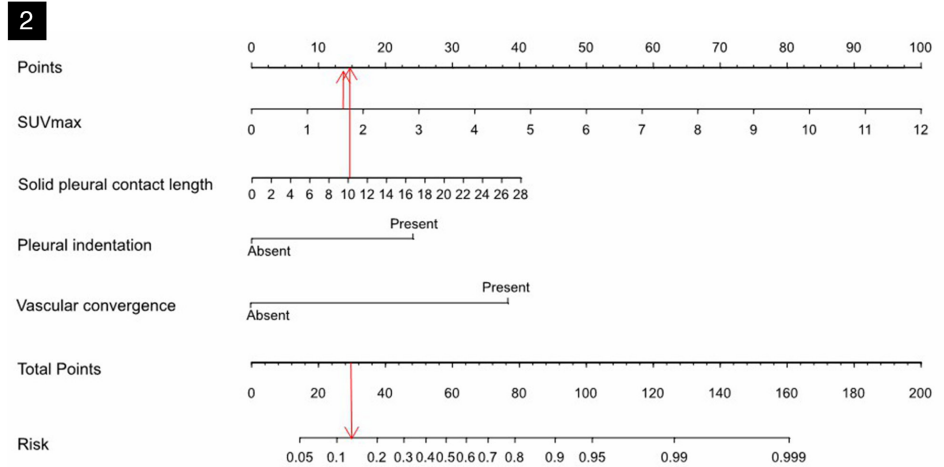
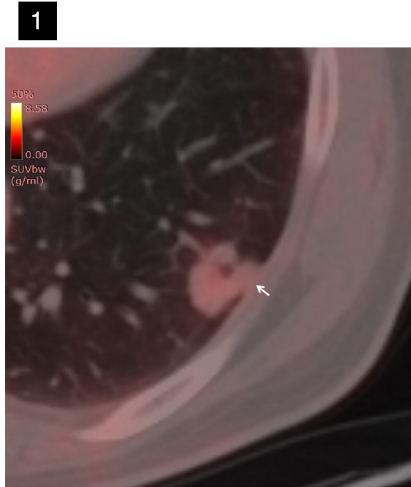
PET/CT in lung adenocarcinoma with pleural contact. *Ann Nucl Med.* 2015;29(9):757-765. [CrossRef]

35. Chen Z, Jiang S, Li Z, Rao L, Zhang X. Clinical value of 18F-FDG PET/CT in prediction of visceral pleural invasion of subsolid nodule stage I lung adenocarcinoma. *Acad Radiol.*

2020;27(12):1691-1699. [CrossRef]

36. Park CM, Goo JM, Lee HJ, Lee CH, Chun EJ, Im JG. Nodular ground-glass opacity at thin-section CT: histologic correlation and evaluation of change at follow-up. *Radiographics.* 2007;27(2):391-408. [CrossRef]

37. Civelek A, Rana A, Malayeri et al. Intra and inter test reproducibility and comparison of PET-MRI and PET-CT derived 18F-FDG metric measurements. *J Nucl Med.* 2017;58(1):1343. [CrossRef]



**Supplementary Figures 1, 2.** A 66-year-old male with invasive lung mucinous adenocarcinoma in the left lower lobe and negative for visceral pleural invasion. The positron emission tomography/computed tomography fusion image shows a solid nodule with pleural attachment (white arrow), without adjacent pleural indentation and vascular convergence, the solid component pleural contact length is 10.1 mm, and the maximum standardized uptake value of the nodule is 1.68 (Supplementary Figure 1). An example of the nomogram in clinical application (Supplementary Figure 2).

### Supplementary file 1

#### Observer agreement

#### Methods

The strengths of the relation between the two sets of measurements were assessed with intraclass-correlation coefficients (ICC). Observer agreement for the assessment of tumor-pleura relationship, pleural indentation, density type, lobulation, spiculation, air bronchogram and vascular convergence sign was calculated and evaluated using kappa-statistics.

#### Results

The relation between the two sets of measurements was strong for maximum standardized uptake value [ICC: 0.987, 95% confidence interval (CI) 0.970 ~ 0.994,  $P < 0.001$ ], tumor size (ICC: 0.970, 95% CI 0.958 ~ 0.978,  $P < 0.001$ ), solid component size (ICC: 0.963, 95% CI 0.949 ~ 0.973), minimum distance between lesion and pleura (ICC: 0.962, 95% CI 0.948 ~ 0.973), pleural contact length (ICC: 0.996, 95% CI 0.995 ~ 0.997) and solid pleural contact length (ICC: 0.998, 95% CI 0.997 ~ 0.998). Observer agreement for assessment of tumor-pleura relationship, pleural indentation, density type, lobulation, spiculation, air bronchogram and vascular convergence sign was excellent, with kappa values were 0.971, 0.879, 0.940, 0.877, 0.925, 0.955, 0.921, respectively.



# Sacroiliac joint involvement in osteochondromatosis: identifying its prevalence and characteristics from cross-sectional imaging

Sevtap Arslan   
Adalet Elçin Yıldız   
Fatma Bilge Ergen   
Üstün Aydıngöz 

## PURPOSE

Apart from a few case reports, sacroiliac joint (SIJ) involvement in osteochondromatosis has not been studied. We aimed to determine the prevalence and characteristics of such involvement using cross-sectional imaging.

## METHODS

In this retrospective study, three observers (one junior radiologist and two musculoskeletal radiologists) independently reviewed computed tomography (CT) or magnetic resonance imaging (MRI) of patients in our database who had osteochondromatosis ( $\geq 2$  osteochondromas across the skeleton) for SIJ involvement. The final decision was reached by the consensus of the two musculoskeletal radiologists in a later joint session.

## RESULTS

Of the 36 patients with osteochondromatosis in our database, 22 (61%) had cross-sectional imaging covering SIJs (14 females, 8 males; age range 7–66 years; mean age 23 years; 13 MRI, 9 CT). Of these, 16 (73%) had intra-articular osteochondromas. For identifying SIJ osteochondromas on cross-sectional imaging, interobserver agreement was substantial [ $\kappa = 0.67$ ; 95% confidence interval (CI): 0.34, 1.00] between the musculoskeletal radiologists and moderate ( $\kappa = 0.59$ ; 95% CI: 0.23, 0.94) between the junior radiologist and the final consensus decision of the two musculoskeletal radiologists. In the cohort with cross-sectional imaging, the anatomical variations of the accessory SIJ (n = 6, 27%) and iliosacral complex (n = 2, 9%) were identified in six different patients with (n = 2) and without (n = 4) sacroiliac osteochondromas.

## CONCLUSION

Cross-sectional imaging shows frequent (73%) SIJ involvement in osteochondromatosis, which, although a rare disorder, nevertheless needs to be considered in the differential diagnosis of such SIJ anatomical variants as the accessory SIJ and iliosacral complex. Differentiating these variants from osteochondromas is challenging in patients with osteochondromatosis.

## KEYWORDS

Computed tomography, magnetic resonance imaging, osteochondroma, osteochondromatosis, sacroiliac joint

From the Clinic of Radiology (S.A. ✉ sevtap.arslan@gmail.com), Afyonkarahisar Suhu State Hospital, Afyonkarahisar, Turkey; Department of Radiology (A.E.Y., F.B.E., Ü.A.), Hacettepe University Faculty of Medicine, Ankara, Turkey.

Received 20 September 2021; revision requested 28 October 2021; last revision received 09 December 2021; accepted 29 December 2021.



Epub: 10.02.2023

Publication date: 29.03.2023

DOI: 10.5152/dir.2022.211018

Although solitary osteochondroma is the most common bone tumor, osteochondromatosis, also known as hereditary multiple exostoses, is a rare disease that manifests with the occurrence of multiple ( $\geq 2$ ) osteochondromas in bones featuring endochondral ossification.<sup>1</sup> It has an autosomal dominant inheritance pattern with a slight male preponderance and a reported prevalence of 1/1,000 to 1/50,000.<sup>2</sup> Since the disease has different penetrance rates between sexes (almost complete penetrance in males and incomplete penetrance in females), not all patients with osteochondromatosis have a family history,<sup>2</sup> and diagnosis is usually made upon detection of multiple osteochondromas in patients with or without familial history. Osteochondromas remain clinically silent unless they cause a palpable mass, compression of the nearby structures, bone deformity, or fractures. Although rare with solitary osteochondromas (1%), malignant transformation may occur in 3% to 25% of cases with osteochondromatosis.<sup>3</sup>

You may cite this article as: Arslan S, Yıldız AE, Ergen FB, Aydıngöz Ü. Sacroiliac joint involvement in osteochondromatosis: identifying its prevalence and characteristics from cross-sectional imaging. *Diagn Interv Radiol.* 2023;29(2):390-395.

Recently, we observed sacroiliac joint (SIJ) involvement in several patients with osteochondromatosis. We also realized that some SIJ anatomical variations (namely, the accessory SIJ and iliosacral complex), which can mimic sacroiliitis and are being increasingly recognized,<sup>4</sup> might be challenging (and might even be mistaken for) in the diagnosis of SIJ involvement in osteochondromatosis. Although flat bones, in particular the ilium and scapula, are commonly affected in patients with osteochondromatosis,<sup>2</sup> there is almost no data in the literature, apart from a few case reports,<sup>5,6</sup> regarding the prevalence of SIJ involvement in osteochondromatosis. In this study, we aimed to investigate the prevalence of SIJ involvement in patients with osteochondromatosis and how such involvement compares with SIJ anatomical variations.

## Methods

### Ethics approval

This retrospective observational study conducted in a tertiary health care center was approved by the Institutional Review Board with a waiver of informed consent (protocol number: GO 21/521). All procedures performed in this study involving human participants were in accordance with the ethical standards of the institutional research committee and with the 1964 Helsinki declaration and its later amendments or comparable ethical standards.

The reporting of this study conforms to the Strengthening the Reporting of Observational Studies in Epidemiology guidelines.<sup>7</sup>

### Consent to participate/consent for publication

Approval from the Institutional Review Board was obtained, and in keeping with the policies for a retrospective review, informed consent was not required.

#### Main points

- Our study demonstrated a high prevalence of intra-articular involvement in osteochondromatosis (73% for the sacroiliac joints), which is considered to be a rare condition.
- Differentiation of sacroiliac joint (SIJ) osteochondromas from anatomical variants is challenging on cross-sectional imaging.
- Knowledge of the frequent SIJ involvement can change the management of patients with osteochondromatosis presenting with low-back pain.

### Study population

We searched our institutional electronic patient records for osteochondromatosis (i.e.,  $\geq 2$  osteochondromas across the skeleton) over the 88-month period from January 2014 through April 2021 by using the following key words: osteochondromatosis, multiple osteochondromas, exostoses, or hereditary exostoses. Having multiple osteochondromas (i.e.,  $\geq 2$ ) with or without familial history was used as the diagnostic criterion for osteochondromatosis. Our hospital information system featuring electronic patient records was used to investigate the family history, clinical follow-up, and surgical history of identified patients.

### Imaging assessment

SIJ involvement with osteochondromas was investigated on cross-sectional imaging [computed tomography (CT) or magnetic resonance imaging (MRI)] independently by three observers (one junior radiologist, who had just finished a 5-year residency, and two radiologists with 14 and 25 years of dedicated musculoskeletal radiology experience, respectively). The final decision for the presence of osteochondromas within the SIJs was reached by consensus of the two musculoskeletal radiologists in a later joint session. The SIJ variations of the accessory SIJ and iliosacral complex, as defined by Prassopoulos et al.<sup>8</sup> and El Rafei et al.<sup>9</sup>, were also noted during the consensus session of the two musculoskeletal radiologists.

An SIJ osteochondroma was defined on CT or MRI either as a sessile or pedunculated cartilage-capped bony overgrowth (with intralesional continuity of the medullary cavity of the parent bone) from the iliac or sacral side of the SIJ protruding into the synovial (cartilaginous) and/or ligamentous portions of the joint.<sup>10</sup>

All imaging studies (i.e., radiographs, CT, and MRI) in all patients with osteochondromatosis were reviewed by the junior radiologist to detect the number and location of osteochondromas across the skeleton. Locations outside the SIJs were labeled as craniofacial, spine (including the sacrum outside the coverage of the SIJs), chest wall, shoulder girdle, elbow (including the three long bones around the elbow), hand and wrist, pelvic girdle (including the ilium outside the coverage of the SIJs), knee (including the patella and the three long bones around the knee), and foot and ankle.

### Statistical analysis

Data analysis was performed by using IBM SPSS Statistics 23.0 (Armonk, NY, USA) and free online resources on the GraphPad Software (San Diego, CA, USA) website ([www.graphpad.com/quickcalcs](http://www.graphpad.com/quickcalcs)). Descriptive analyses were based on frequencies and means of the variables. The Mann–Whitney U test was used to compare the differences of non-categorical continuous data (i.e., age and number of osteochondromas) between independent groups. Fisher's exact test was used to compare the differences in categorical data (i.e., sex and family history) between independent groups. A *P* value less than 0.05 was considered statistically significant. Interobserver agreement was assessed with kappa statistics.<sup>11</sup>

## Results

Thirty-six patients with osteochondromatosis (23 females, 13 males) were identified in our database. Their ages ranged between 5 and 71 years (mean, 21 years; median, 16 years); the age data of patients were taken as their age at the time of their cross-sectional imaging covering the SIJs or, where such imaging was not available, from the time of their latest imaging study. Each patient had at least two osteochondromas (range, 2–76; mean, 32) across their skeleton (Table 1).

Of the 36 patients with osteochondromatosis, 22 (61%) had cross-sectional imaging covering SIJs (14 females, 8 males; age range 7–66 years; mean age, 23 years; median age, 17 years; 13 MRI, 9 CT). Nine of these 22 patients had dedicated sacroiliac MRI; the remainder had their SIJs covered in examinations such as abdominopelvic CT, stone protocol abdominal CT, abdominal CT-angiography, spinal MRI, and pelvic/hip MRI. Indications for cross-sectional imaging studies were follow up of painful osteochondromas, low-back pain, abdominal pain, trauma, or post-operative assessment.

Of the 22 patients with SIJ cross-sectional imaging, 16 (73%) had intra-articular osteochondromas (all but two based on the iliac side) involving one ( $n = 5$ ) or both ( $n = 11$ ) of the SIJs (Figures 1, 2). The hereditary background of this condition was established in 22 (61%) of the 36 patients with osteochondromatosis [14 (64%) of 22 patients with sacroiliac cross-sectional imaging and 9 (56%) of 16 patients with SIJ involvement]. The characteristics of patients with osteochondromatosis, who had their SIJs covered in a cross-sectional imaging examination, are given in Table 2. All patients with SIJ osteo-

chondromas also had osteochondromas in the pelvic girdle. SIJ osteochondromas were significantly more common in younger patients with osteochondromatosis ( $P = 0.012$ ). The total number of osteochondromas across the skeleton was significantly higher in patients with SIJ osteochondroma than those without ( $P = 0.001$ ). Sex and positive family history were not discriminators for the presence of SIJ osteochondromas ( $P = 1.000$  and  $P = 0.350$ , respectively).

In the cohort with cross-sectional imaging, the anatomical variations of accessory SIJ ( $n = 6$ , 27%) and iliosacral complex ( $n = 2$ , 9%) were identified in six different patients with ( $n = 2$ ) and without ( $n = 4$ ) sacroiliac osteochondromas (Figure 3).

For identifying SIJ osteochondromas on cross-sectional imaging, interobserver agreement was substantial [ $\kappa = 0.67$ ; 95% confidence interval (CI): 0.34, 1.00] between the musculoskeletal radiologists and moderate ( $\kappa = 0.59$ ; 95% CI: 0.23, 0.94) between

the junior radiologist and the final consensus decision of the two musculoskeletal radiologists.

## Discussion

This study shows that SIJ involvement is common (73%) in patients with osteochondromatosis. Considering the multiplicity of lesions found within the SIJs, SIJ involvement in osteochondromatosis might even be more prevalent than the occurrence of a solitary (intra-articular) osteochondroma of the SIJ. Thus far, only two solitary osteochondromas of the SIJ have been reported,<sup>5,6</sup> along with a single case of osteochondromatosis with SIJ involvement.<sup>6</sup>

Osteochondromas can increase in size and number during skeletal development;<sup>2</sup> therefore, the prevalence of SIJ involvement can be expected to increase with age. However, in this study, the age of patients with SIJ involvement was significantly lower than

that of patients without SIJ involvement, and we detected SIJ osteochondromas in three patients aged 7 and 8 years old. In addition, in this study, the number of osteochondromas across the skeleton was found to be significantly higher in patients with osteochondromatosis involving SIJ osteochondromas than in those without. This finding might imply that SIJ involvement is more common in patients with a greater number of osteochondromas; however, the entire skeleton was not imaged in all of our patients. In addition, smaller sessile osteochondromas might not be amenable to detection on radiographs. Therefore, these figures might not truly reflect the actual number of osteochondromas.

Several anatomical variations of the SIJ, including the accessory SIJ, iliosacral complex, isolated synostosis, unfused ossification center, bipartite iliac bony plate, and semicircular defect, have been described.<sup>8,9</sup> Among these variations, the accessory SIJ and iliosacral complex may mimic SIJ osteochondromas, in particular, the sessile (broad-based) type. The accessory SIJ has a reported prevalence of 1.7% to 19.1%,<sup>8,9,12,13</sup> and the prevalence of the iliosacral complex is reportedly 2.6% to 11%.<sup>8,9,13</sup> Both of these variations are usually seen on the iliac surface at the posterosuperior (ligamentous) portion of the SIJ at the level of the first and second sacral foramina. The iliosacral complex, which indicates a marked prominence of the ilium across a concave recess of the sacrum,<sup>9</sup> is mostly bilateral (Figure 4a, b); the accessory SIJ is reported to be associated with degenerative changes (Figure 4c), in contradistinction to the iliosacral complex.<sup>8,9</sup> We observed that iliosacral complexes generally protrude with shallow angles from the iliac bone, whereas osteochondromas are either pedunculated (with a stalk narrower than the bulk of the lesion) or, when sessile, show steeper angles at their take-off from their base than iliosacral complexes. Nevertheless, distinguishing an osteochondroma from an iliosacral complex is not straightforward. Considering the rarity of osteochondromatosis and the frequency of these variations, different SIJ anatomy is more likely to be a variation rather than an osteochondroma. However, patients with osteochondromatosis may be asymptomatic until they are incidentally diagnosed, and they may present with low-back pain and undergo sacroiliac MRI. As the early diagnosis of osteochondromatosis may dramatically change the treatment and follow-up algorithms, the correct identification of SIJ osteochondromas is especially important in

**Table 1.** Characteristics of all patients ( $n = 36$ ) with osteochondromatosis

Characteristic	
Age, <sup>a</sup> years [mean, (range)]	21 [5–71]
Sex (F:M)	23:13
Family history, n (%)	22 (61%)
Number of osteochondromas, <sup>b</sup> mean (range)	32 (2–76)
<b>Involvement sites,<sup>c</sup> n (%)</b>	
Craniofacial (n = 6)	0 (0%)
Spine (n = 32)	12 (38%)
Chest wall (n = 31)	17 (55%)
Shoulder girdle (n = 32)	29 (91%)
Elbow (n = 17)	3 (18%)
Hand and wrist (n = 20)	19 (95%)
Pelvic girdle (n = 32)	28 (88%)
SIJ <sup>d</sup> (n = 22)	16 (73%)
Knee (n = 34)	34 (100%)
Foot and ankle (n = 27)	24 (89%)
<b>Malignant transformation,<sup>e</sup> n (%)</b>	
3 (8%)	
<b>Other indications for surgical treatment,<sup>f</sup> n</b>	
Painful lesion	12 (39)
Bone deformity	9 (12)
Spinal cord compression	2 (2)
Fracture	1
Radial head dislocation	1

<sup>a</sup>Age data of patients was taken as their age at the time of their cross-sectional imaging covering the SIJs or, where such imaging was not available, from the time of their latest imaging study.

<sup>b</sup>Minimum number of osteochondromas across the skeleton identified on available imaging studies.

<sup>c</sup>Numbers in parentheses below denote patients having imaging studies covering these areas. Spine includes the sacrum outside the coverage of the SIJs, elbow includes the three long bones around the elbow, pelvic girdle includes the ilium outside the coverage of the SIJs, and knee includes the patella and the three long bones around the knee.

<sup>d</sup>This only takes into account cross-sectional imaging (CT or MRI), not radiographs, on which it is not possible to reliably ascertain the presence of SIJ osteochondromas.

<sup>e</sup>Four lesions in three patients, who had SIJ osteochondromas, were surgically excised and histologically proven to be secondary chondrosarcoma (scapula, 1; ilium, 1; fibula, 1; toe phalanx, 1). The mean age at the time of malignancy diagnosis was 31 years (range, 15–46 years).

<sup>f</sup>These indications for surgical treatment in 23 patients exclude malignant transformation, mentioned above. Nine patients had more than one surgery for different indications. Numbers in parentheses are the total number of surgeries for the mentioned indications. SIJ, sacroiliac joint; F, female; M, male; CT, computed tomography; MRI, magnetic resonance imaging.

these patients. Therefore, before a diagnosis of variant anatomy is made, the possibility of an SIJ osteochondroma should be considered, and osteochondromas should be searched for elsewhere in the skeleton. In this study, all patients with SIJ osteochondromas had osteochondromas in the pelvic girdle. Thus, patients with osteochondromatosis presenting with low-back pain and featuring osteochondromas in the pelvic girdle should also be evaluated for SIJ osteochondromas along with other causes of low-back pain. In addition, considering the hereditary background of this condition, undiagnosed relatives of osteochondromatosis

patients presenting with low-back pain would benefit from evaluation with sacroiliac MRI for possible SIJ osteochondromas.

Osteochondromas typically display intral-lesional continuity of the medullary cavity of the parent bone and project away from the epiphysis. However, neither the latter feature in a flat bone, such as the ilium (where the overwhelming majority of osteochondromas in our study were based) nor the former characteristic (since both accessory SIJs and the iliosacral complex also feature a protrusion with a continuation of the medullary

cavity) are necessarily helpful for diagnosis. A helpful finding for differentiating osteochondromas from the accessory SIJ and the iliosacral complex, which is more common at the ligamentous (rather than the cartilaginous) portion of the SIJ, is the cartilage “cap” on osteochondromas. However, prominent vessels on the surface of the iliosacral complex described in a previous study<sup>9</sup> and edematous changes at the accessory SIJ should not be confused with the cartilage cap. The mushroom shape of pedunculated osteochondromas is also useful in differential diagnosis. Nevertheless, some accessory SIJs

**Table 2.** Characteristics of osteochondromatosis patients with a cross-sectional imaging study covering SIJs (n = 22)

Characteristic		P
<b>Patients with SIJ osteochondromas, n (%)</b>		
Overall	16 (73%)	
CT (n = 9)	9	
MRI (n = 13)	7	-
Bilateral	11 (69%)	
Unilateral	5 (31%)	
<b>Age, years [mean, (range)]</b>		
With SIJ osteochondromas	17 [7–42]	0.012 <sup>d</sup>
Without SIJ osteochondromas	37 [16–66]	
<b>Sex (F:M)</b>		
With SIJ osteochondromas	10:6	1.000 <sup>e</sup>
Without SIJ osteochondromas	4:2	
<b>Patients with family history, n (%)</b>		
With SIJ osteochondromas	9 (56%)	0.350 <sup>e</sup>
Without SIJ osteochondromas	5 (83%)	
<b>Number of osteochondromas,<sup>a</sup> mean (range)</b>		
With SIJ osteochondromas	44 (17–76)	0.002 <sup>d</sup>
Without SIJ osteochondromas	13 (2–30)	
<b>SIJ anatomical variations, n<sup>b</sup> (%)</b>		
Accessory SIJ (n = 6) <sup>c</sup>		
With SIJ osteochondromas (n = 3)	5 (23%)	
Without SIJ osteochondromas (n = 3)	2 (13%)	
Iliosacral complex (n = 2) <sup>c</sup>	3 (50%)	-
With SIJ osteochondromas (n = 0)	2 (9%)	
Without SIJ osteochondromas (n = 2)	0 (0%)	
	2 (33%)	

<sup>a</sup>Indicates minimum number of osteochondromas across the skeleton.

<sup>b</sup>Numbers in the right column denote patients.

<sup>c</sup>These numbers denote all instances of anatomical variations seen either on the right or the left side.

<sup>d</sup>Mann–Whitney U test.

<sup>e</sup>Fisher’s exact test. SIJ, sacroiliac joint; F, female; M, male; CT, computed tomography; MRI, magnetic resonance imaging.

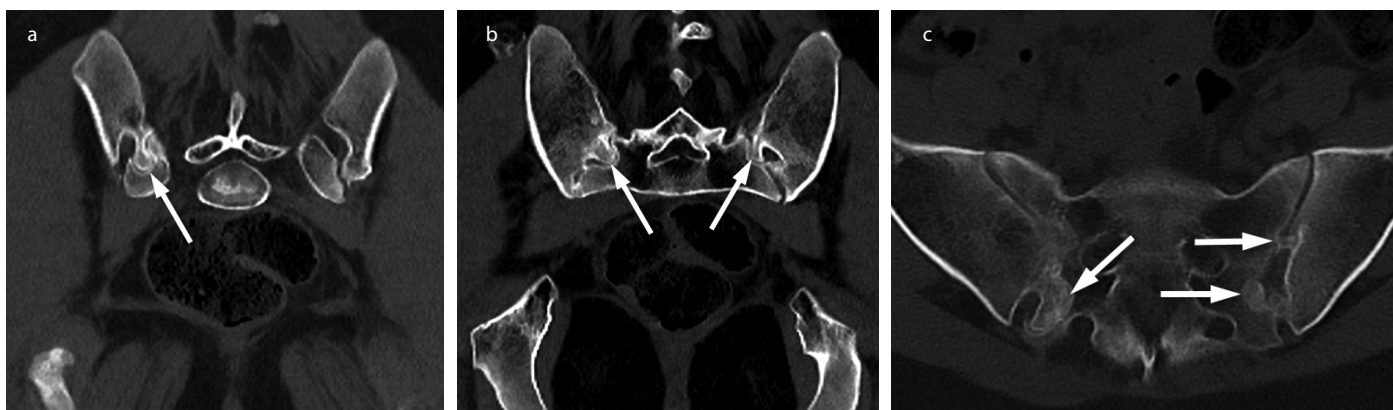


**Figure 1.** A 16-year-old girl with osteochondromatosis. Oblique coronal reformatted (a, b) and axial (c) pelvic computed tomography images show ilium-based sacroiliac joint osteochondromas (arrows) on both sides.

mentioned in the literature<sup>8</sup> clearly showed a mushroom shape as well. Furthermore, patients with osteochondromatosis may have SIJ variations. In this study, the anatomical variations of accessory SIJs (n = 6, 27%) and the iliosacral complex (n = 2, 9%) were identified in six different patients with (n = 2) and without (n = 4) sacroiliac osteochondromas. In view of the aforementioned conditions, differentiating these variants from osteo-

chondromas can be challenging in patients with osteochondromatosis. In general, MRI is better than CT at showing the cartilaginous cap in osteochondromas, whereas the greater spatial resolution of CT renders it more helpful than MRI in identifying bony contours of especially small osteochondromas and accessory SIJs.

Although the prevalence of intra-articular involvement in osteochondromatosis is not established, it is considered to be rare.<sup>14,15</sup> The frequent SIJ involvement shown in our study is remarkable in this regard. SIJ involvement has been described in dysplasia epiphysealis hemimelica (Trevor disease),<sup>16,17</sup> which, although featuring intra-articular osteochondroma-like (or, more accurately, osteocarti-

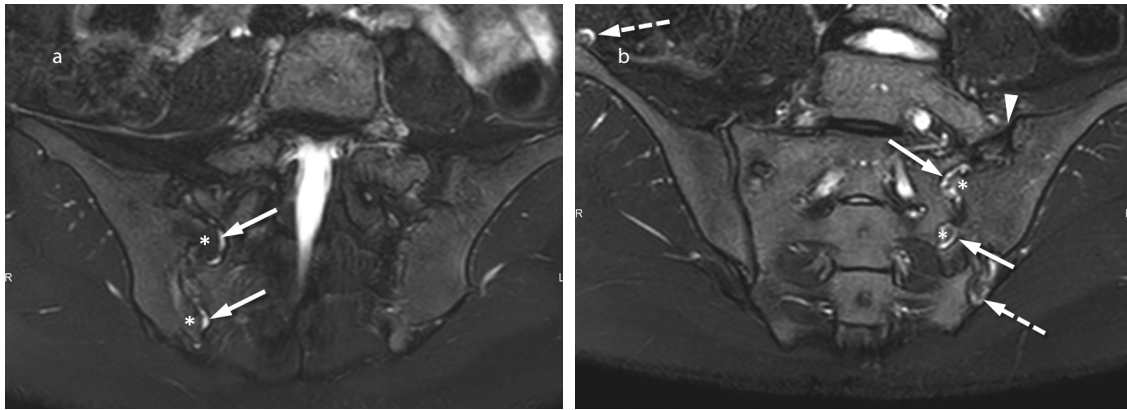


**Figure 2.** A 17-year-old girl with multiple hereditary exostoses (osteochondromatosis). Coronal T2-weighted magnetic resonance images with fat saturation (a, b) show bilateral sacroiliac joint osteochondromas (asterisks), all but one ilium-based (the inferior osteochondroma on the left is sacrum-based). Note cartilage caps on intra-articular (solid arrows) and extra-articular (dashed arrows) osteochondromas. Note also the left-sided pseudoarthrosis (arrowhead) of a lumbosacral transitional vertebra.

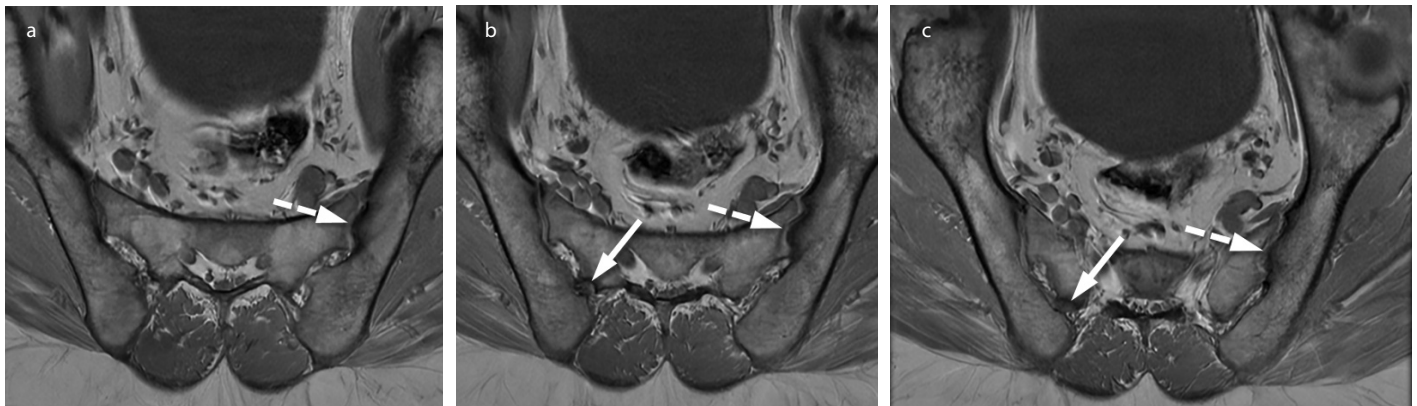


**Figure 3.** A 31-year-old man with multiple hereditary exostoses (osteochondromatosis). Oblique axial T1-weighted magnetic resonance images (a-c) show an accessory sacroiliac joint on the right (solid arrows) and an iliosacral complex on the left (dashed arrows). No sacroiliac joint osteochondromas were identified.

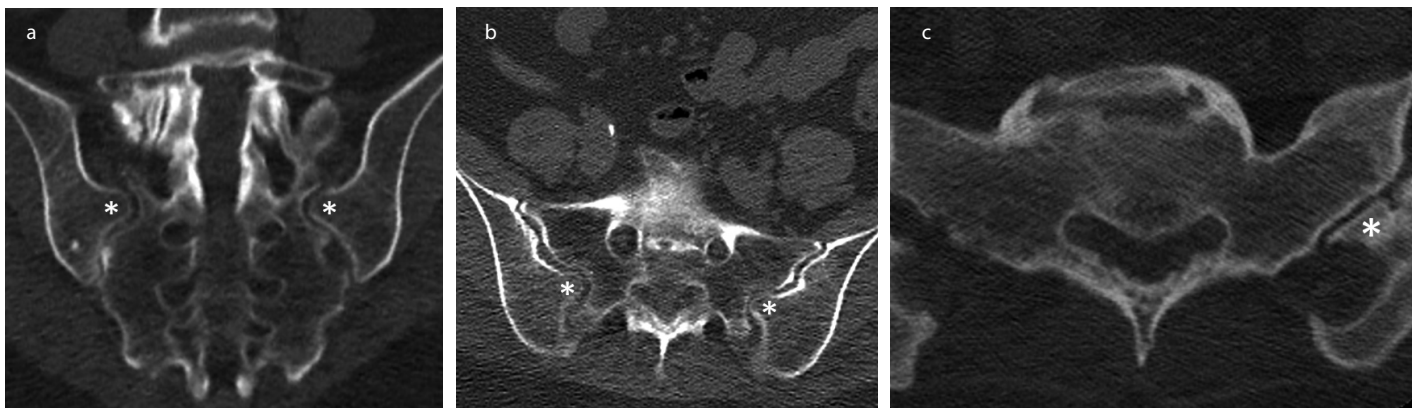


**Figure 4.** Anatomical variants in two patients without osteochondromatosis (outside the study group). Bilateral iliosacral complexes (a, b; asterisks) on oblique coronal reformatted (a) and axial (b) computed tomography (CT) images in a 66-year-old woman who underwent the pelvic CT exam for total hip arthroplasty control. An accessory sacroiliac joint (c; asterisk) on axial CT image in a 38-year-old woman who underwent the lumbar spinal CT exam for posterior spinal fixation hardware control.

laginous) lesions, has a different mechanism than osteochondromatosis.<sup>18</sup> Trevor disease, characterized by osteocartilaginous epiphyseal lesions, is a very rare clinical entity with about 150 reported cases.<sup>18</sup> The most common sites of disease are epiphyses and epiphyseal equivalents of the lower limb. Although bilateral involvement has been reported,<sup>19</sup> the distribution of the lesions usually fits a hemimelic pattern with the involvement of multiple joints in the same extremity. The SIJ is an uncommon location for Trevor disease and has been reported in only two cases.<sup>16,17</sup> Unilateral involvement of the SIJ and multiple lesions on the epiphyses and epiphyseal equivalents in the same extremity appear to be reliable findings in differentiating between osteochondromatosis and Trevor disease.<sup>18</sup> None of our cases featured these findings.

Our study has several limitations. First, the small number of patients with osteochondromatosis who had undergone cross-sectional imaging covering their SIJs in our study limits its power. Nevertheless, as the first study to look into SIJ involvement in osteochondromatosis, it features a cohort of patients (n = 36), 61% of whom had cross-sectional imaging of the SIJs. Second, there is selection bias, as the observers were aware while reviewing the radiological examinations that the patients had osteochondromatosis. However, this did not prevent us from factoring in the already-established anatomical variations of the SIJs that might have mimicked osteochondromatosis. Third, the presence of osteochondromas involving the SIJs might have been obscured by some of the SIJ anatomical variations. Fourth, the presented cases were treated in a tertiary health care center; therefore, our study may not reflect the true prevalence of SIJ involvement in osteochondromatosis. Fifth, we do not have histologic proof of osteochondromas involving the SIJ, as none of these patients needed to undergo surgery in this area. However, when an iliosacral complex is located at the cartilaginous portion of the joint, it would also be covered with a cartilage cap (the joint cartilage), and even histology might not be very helpful in differentiating it from a sessile osteochondroma. The same is valid for an accessory SIJ, which might be overlined by cartilage (in a synchondrotic accessory joint). Finally, the

relationship between SIJ osteochondromas and low-back pain could not be definitively ascertained due to the retrospective design of the study. Therefore, we were not able to further elaborate on the clinical significance of SIJ involvement in osteochondromatosis.

In conclusion, this study investigated the SIJ involvement in osteochondromatosis. Cross-sectional imaging shows such involvement to be frequent (73%). Although a rare disorder, osteochondromatosis nevertheless needs to be considered during daily radiological reporting practice in the differential diagnosis of such SIJ anatomical variants as the accessory SIJ and iliosacral complex. However, differentiating these variants from osteochondromas can be challenging in patients with osteochondromatosis. Patients with SIJ osteochondromas commonly display other osteochondromas in the pelvis, which might help ascertain osteochondromatosis in a focused imaging examination such as sacroiliac MRI. Knowledge of the frequency of SIJ involvement can change the management of patients with osteochondromatosis presenting with low-back pain.

#### Conflict of interest disclosure

The authors declared no conflicts of interest.

#### References

1. Bovée JV. Multiple osteochondromas. *Orphanet J Rare Dis.* 2008;3:3. [\[CrossRef\]](#)
2. D'Arienzo A, Andreani L, Sacchetti F, Colangeli S, Capanna R. Hereditary multiple exostoses: current insights. *Orthop Res Rev.* 2019;11:199–211. [\[CrossRef\]](#)
3. Sonne-Holm E, Wong C, Sonne-Holm S. Multiple cartilaginous exostoses and development of chondrosarcomas—a systematic review. *Dan Med J.* 2014;61(9):A4895. [\[CrossRef\]](#)
4. Toussirot E, Aubry S, Runge M. Unilateral Accessory sacroiliac joint with bone marrow edema mimicking sacroiliitis. *J Rheumatol.* 2018;45(9):1327–1328. [\[CrossRef\]](#)
5. Agrawal A, Dwivedi SP, Joshi R, Gangane N. Osteochondroma of the sacrum with a correlative radiographic and histological evaluation. *Pediatr Neurosurg.* 2005;41(1):46–48. [\[CrossRef\]](#)
6. Güner G, Güner S, Elmali N, Ertem K. Anterior sacroiliac fusion: a new video-assisted endoscopic technique. *Surg Laparosc Endosc.* 1998;8(3):233–236. [\[CrossRef\]](#)

7. von Elm E, Altman DG, Egger M, et al. The Strengthening the reporting of observational studies in epidemiology (STROBE) statement: guidelines for reporting observational studies. *Lancet.* 2007;370(9596):1453–1457. [\[CrossRef\]](#)
8. Prassopoulos PK, Faffia CP, Voloudaki AE, Gourtsoyiannis NC. Sacroiliac joints: anatomical variants on CT. *J Comput Assist Tomogr.* 1999;23(2):323–327. [\[CrossRef\]](#)
9. El Rafei M, Badr S, Lefebvre G, et al. Sacroiliac joints: anatomical variations on MR images. *Eur Radiol.* 2018;28(12):5328–5337. [\[CrossRef\]](#)
10. Puhakka KB, Melsen F, Jurik AG, Boel LW, Vesterby A, Egund N. MR imaging of the normal sacroiliac joint with correlation to histology. *Skeletal Radiol.* 2004;33(1):15–28. [\[CrossRef\]](#)
11. Landis JR, Koch GG. The measurement of observer agreement for categorical data. *Biometrics.* 1977;33(1):159–174. [\[CrossRef\]](#)
12. Ehara S, el-Khoury GY, Bergman RA. The accessory sacroiliac joint: a common anatomic variant. *AJR Am J Roentgenol.* 1988;150(4):857–859. [\[CrossRef\]](#)
13. Tok Umay S, Korkmaz M. Frequency of anatomical variation of the sacroiliac joint in asymptomatic young adults and its relationship with sacroiliac joint degeneration. *Clin Anat.* 2020;33(6):839–843. [\[CrossRef\]](#)
14. Porter DE, Benson MK, Hosney GA. The hip in hereditary multiple exostoses. *J Bone Joint Surg Br.* 2001;83(7):988–995. [\[CrossRef\]](#)
15. El-Fiky TA, Chow W, Li YH, To M. Hereditary multiple exostoses of the hip. *J Orthop Surg (Hong Kong).* 2009;17(2):161–165. [\[CrossRef\]](#)
16. Segal LS, Vrahas MS, Schwentker EP. Dysplasia epiphysealis hemimelica of the sacroiliac joint: a case report. *Clin Orthop Relat Res.* 1996;(333):202–207. [\[CrossRef\]](#)
17. Karam AR, Birjawi GA, Saghieh S, Tawil A, Khoury NJ. Generalized dysplasia epiphysealis hemimelica with contralateral sacro-iliac joint involvement. *Skeletal Radiol.* 2008;37(12):1147–1152. [\[CrossRef\]](#)
18. Degnan AJ, Ho-Fung VM. More Than epiphyseal osteochondromas: updated understanding of imaging findings in dysplasia epiphysealis hemimelica (Trevor disease). *AJR Am J Roentgenol.* 2018;211(4):910–919. [\[CrossRef\]](#)
19. Merzoug V, Wicard P, Dubouset J, Kalifa G. Bilateral dysplasia epiphysealis hemimelica: report of two cases. *Pediatr Radiol.* 2002;32(6):431–434. [\[CrossRef\]](#)



# Quantitative analysis of the olfactory system in pediatric epilepsy: a magnetic resonance imaging study

Ali Haydar Baykan

Elçin Aydın

Şükrü Şahin

Erman Altunışık

## PURPOSE

Olfactory dysfunction is a well-known complication in epilepsy. Studies have demonstrated that olfactory bulb volume (OBV), olfactory tract length (OTL), and olfactory sulcus depth (OSD) can be reliably evaluated using magnetic resonance imaging (MRI). In this study, we compared the OBV, OTL, and OSD values of children with epilepsy and those of healthy children (controls) of similar age. Our aim was to determine the presence of olfactory dysfunction in children with epilepsy and demonstrate the effects of the epilepsy type and treatment on olfactory function in these patients.

## METHODS

Cranial MRI images of 36 patients with epilepsy and 108 controls (3–17 years) were evaluated. The patients with epilepsy were divided into groups according to the type of disease and treatment method. Subsequently, OBV and OSD were measured from the coronal section and OTL from the sagittal section. The OBV, OTL, and OSD values were compared between the epilepsy group, subgroups, and controls.

## RESULTS

OBV was significantly reduced in the children with epilepsy compared with the control group ( $P < 0.001$ ). No significant difference between the healthy children and those with epilepsy was determined in terms of OTL and OSD. Although OBV was moderately positively correlated with age in the control group ( $r = 0.561$ ,  $P < 0.001$ ), it was poorly correlated with age in children with epilepsy ( $r = 0.393$ ,  $P = 0.018$ ).

## CONCLUSION

The results of our study indicate that OBV decreases in children with epilepsy, but epilepsy type and treatment method do not affect OBV, OTL, or OSD ( $P > 0.05$ ).

## KEYWORDS

Epilepsy, magnetic resonance imaging, olfactory bulb, olfactory sulcus, olfactory tract

From the Department of Radiology (A.H.B. ✉ drbaykan@yahoo.com), Adiyaman University Faculty of Medicine, Adiyaman, Turkey; Department of Radiology (E.A.), University of Health Sciences Turkey, Tepecik Training and Research Hospital, İzmir, Turkey; Department of Radiology (Ş.Ş.), Adiyaman Training and Research Hospital, Adiyaman, Turkey; Department of Neurology (E.A.I.), Adiyaman University Faculty of Medicine, Adiyaman, Turkey.

Received 30 March 2021; revision requested 28 April 2021; last revision received 23 August 2021; accepted 15 October 2021.



Epub: 20.03.2023

Publication date: 29.03.2023

DOI: 10.5152/dir.2022.21287

Epilepsy is a chronic neurological disease that affects people of all ages.<sup>1</sup> The incidence of epilepsy in children varies from 41 to 187 per 100,000, with approximately 30,000 children being diagnosed with epilepsy every year.<sup>2</sup> Olfactory abnormalities in epilepsy are well documented. Clinically, these abnormalities present as olfactory auras or olfactory performance deficits such as odor detection impairment.<sup>3</sup> The olfactory system consists of primary olfactory nerves in the nasal cavity, the olfactory bulb, olfactory tract, and connections extending to the central nervous system. The olfactory nerves traverse the cribriform plate and form olfactory bulbs intracranially, and the olfactory tracts connect the olfactory bulbs to the brain. The olfactory bulbs and tracts are located under the olfactory sulcus on the lower surface of the frontal lobe. Nerve fibers originate from the olfactory tract and extend to the amygdala, olfactory tubercle, and parahippocampal gyrus.<sup>4</sup> Olfactory bulb volume (OBV), olfactory tract length (OTL), and olfactory sulcus depth (OSD) can be reliably evaluated using magnetic resonance imaging (MRI),<sup>5,6</sup> and OBV is clinically important for measuring olfactory function.<sup>7</sup>

You may cite this article as: Baykan AH, Aydın E, Şahin Ş, Altunışık E. Quantitative analysis of the olfactory system in pediatric epilepsy: a magnetic resonance imaging study. *Diagn Interv Radiol.* 2023;29(2):396-401.

To date, studies on the olfactory system in epilepsy have generally focused on adults,<sup>3,8,9</sup> however, few published studies relate to the imaging findings of the olfactory system (such as OBV measurement) in adults with epilepsy.<sup>8,9</sup> To the best of our knowledge, no study has provided a quantitative analysis of the olfactory system (such as OBV, OSD, or OTL measurement) in childhood epilepsy. Therefore, in the present study, we aim to compare the quantitative measurements of olfactory anatomical structures (OBV, OSD, and OTL) between patients diagnosed with childhood epilepsy and healthy controls.

## Methods

### Participants

This study had a retrospective design (local ethics committee approval no: 2019/2-28) and involved 36 patients with epilepsy who underwent cranial MRI between January 2016 and August 2020. Informed consent was not obtained because the study was in a retrospective design. Only patients diagnosed with primary epilepsy were included in the study group. Patients with uncontrolled epilepsy, intellectual disability, or a history of hypoxic ischemic encephalopathy, trauma, meningoencephalitis, prematurity, endocrinopathy, metabolic disease, or neurodegenerative disease were excluded. Cases with inadequate MRI images were also excluded. Patients with normal brain MRI reports were included in the study. The patients that met the study criteria were divided into three groups according to the International League Against Epilepsy 2017 criteria: generalized onset, focal onset, and unclassified. The generalized-onset group contained 23 patients, the focal-onset group 8 patients, and the unclassified group 5 patients.

#### Main points

- There is a correlation between decreased olfactory bulb volume (OBV) and the presence of some neurodegenerative diseases, such as dementia and Alzheimer disease. To date, studies on the olfactory system in epilepsy have focused on adults.
- A quantitative analysis of the olfactory system can be reliably undertaken using magnetic resonance imaging. In this study, OBV values of pediatric patients with epilepsy were decreased.
- The decrease in OBV in children with epilepsy reflects not only the olfactory function of OBV but also the destructive effect of childhood epilepsy on the nervous system.

The patients were also categorized according to the treatment they were receiving: those in remission who were not receiving any medical treatment at that time ( $n = 9$ ), those using a single antiepileptic agent ( $n = 20$ ), and those using two or more antiepileptic agents ( $n = 7$ ). The control group consisted of 108 children aged 3 to 17 years who underwent brain MRI for reasons other than epilepsy (e.g., tension-type headache, transient non-specific benign vertigo attacks, or somatization) and were reported to have normal findings. Patients and controls were divided into three age-range groups as follows: group 1, young children (3–6 years); group 2, children (7–11 years); and group 3, adolescents (12–17 years). Patients and controls were compared in these three groups.

### Magnetic resonance imaging studies

The MRI studies were evaluated by two radiologists with 12- and 10-years' experience. The radiologists did not know which group the studies belonged to. Two radiologists performed the measurements separately, and the mean value was used for analysis. Images were obtained using a 1.5 T scanner (Achieva, Philips Medical Systems, Best, Netherlands) with a head coil. Images in the coronal section were obtained perpendicular to the cribriform plate. Examination sequences were composed of balanced fast-field echo (B-FFE) three-dimensional (3D) images in the coronal plane [repetition time (TR), 6.5 ms; echo time (TE), 3.4 ms; field of view (FOV) 180 180 mm; number of signals averaged (NSA), 2; thickness, 1 mm; gap, 0 mm; slices, 75; matrix, 308 308 mm] and sagittal 3D T1-weighted images (TR, 8.2 ms; TE, 4.0 ms; FOV, 140 156 mm; NSA, 4; thickness, 1.2 mm; gap, 0.2 mm; slices, 40; matrix, 252 278 mm). The MRI scan time was 4–5 min.

### Image analysis

OBV, OTL, and OSD were measured in all patients. On the coronal B-FFE 3D images, the olfactory bulb was visualized as a hypointense round or ovoid structure surrounded by cerebrospinal fluid superior to the anterior cribriform plate (Figures 1, 2). The relatively abrupt change in diameter defined the proximal border of the bulb (on coronal plane B-FFE 3D images). Volume measurements were obtained using manual segmentation based on the contour stack principle and calculated using the Philips Extended MR workspace (version 2.6.3.5) post-processing software package (Philips Medical Systems). OSD was measured on coronal B-FFE 3D images, and the maximum depth

was recorded (Figure 3). Olfactory tract measurements were performed on the plane on which the olfactory tract was most clearly seen on sagittal 3D T1 reformatted images (Figure 4).

### Statistical analysis

To perform the statistical analysis, SPSS v25.0 software was used. The Kolmogorov–Smirnov test was used to determine whether the data were distributed normally. The control and epilepsy groups were compared using the independent sample t-test. The Mann–Whitney U test was used to compare the epilepsy and control groups in small groups. The Kruskal–Wallis test was used for a comparison of more than two groups in terms of OBV, OTL, and OSD values. When parametric tests were used, mean and standard deviation (SD) values were given, and when non-parametric tests were used, median, minimum, and maximum values were given. The demographic characteristics of the epilepsy and control groups are presented as mean  $\pm$  SD, and categorical variables are expressed as counts and percentages. The relationship between OBV, OSD, and OTL measurements and age was assessed using Pearson's correlation coefficient.

The intraclass correlation coefficient (ICC) was used in the study because of its ability to compare quantitative measurements among observers. The ICC test was calculated using a two-way random absolute single measurement model with a 95% confidence interval. Interobserver agreement in OBV, OSD, and OTL measurements was evaluated using Bland–Altman plots, which were produced through SPSS software. The average difference and 95% limits of agreement (mean difference  $\pm$  1.96 SD) are specified. The statistically significant level was accepted as  $P < 0.05$ .

## Results

The ICC, indicating agreement in interobserver measurements, was good to excellent and ranged from 0.73 to 0.96 (Table 1). Of the cases diagnosed with epilepsy, 20 were boys (55%) and 16 (45%) were girls, and the mean age was  $7.53 \pm 3.60$  years. The control group consisted of 108 cases, of which 60 were boys (55%) and 48 were girls (45%) (mean age  $8.23 \pm 4.55$ ). OBV was significantly decreased in patients with epilepsy compared with the control group (Table 2), but no significant difference was identified in terms of right and left OTL and OSD between the epilepsy and control groups ( $P = 0.188$ ,  $0.726$  and  $P = 0.920$ ,  $0.845$ , respectively).

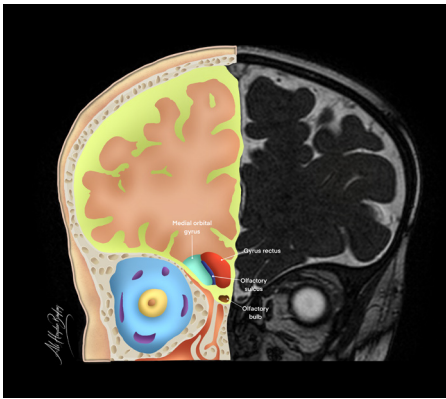


**Figure 1.** Illustration of the olfactory system on coronal plane magnetic resonance imaging. The medial orbital gyrus (green area), gyrus rectus (red area), olfactory sulcus (blue area), and olfactory bulb (brown area) are depicted at the side of the illustration.

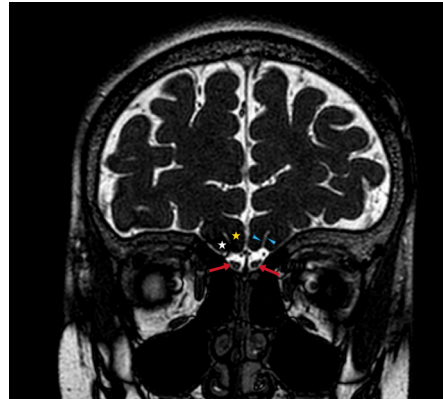


**Figure 2.** Coronal three-dimensional balanced fast-field echo magnetic resonance images of a 6-year-old girl showing the right and left olfactory bulb as a hypointense ovoid structure (arrows). The olfactory sulcus is displayed as a hyperintense line between the medial orbital gyrus (white star) and gyrus rectus (yellow star). Note the hyperintense cerebrospinal fluid surrounding the olfactory bulbs.

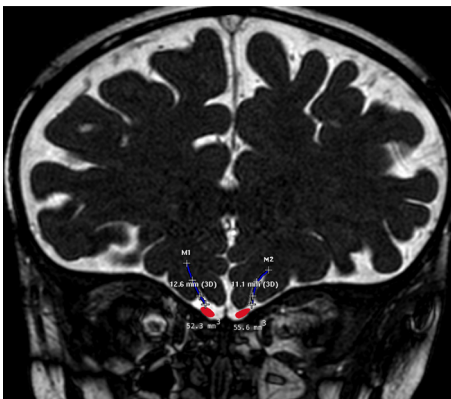


**Figure 3.** Olfactory bulbs (red area) and olfactory sulcus (blue line) are shown on coronal three-dimensional (3D) balanced fast-field echo magnetic resonance imaging. A semi-automatic measurement of the olfactory bulb volume using manual segmentation and multiplanar reformatting on the 3D workstation. To minimize the possibility of errors in volumetric measurements, the images were magnified as much as possible. The volumes are given in mm<sup>3</sup>, and the line measurements are given in mm.

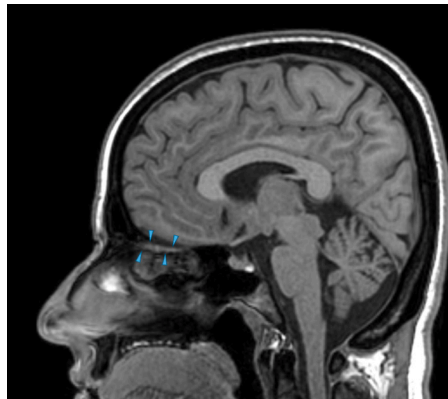


**Figure 4.** A sagittal T1-weighted magnetic resonance image revealing the boundaries of the right olfactory tract (arrowheads).

In addition, no significant difference was detected when the right and left OSD values were compared within the epilepsy and control groups ( $P = 0.334$ ,  $P = 0.445$ , respectively) nor between the right and left OTL in the epilepsy and control groups ( $P = 0.947$ ,  $P = 0.402$ , respectively). Pearson's correlation coefficients were calculated, and a weak positive correlation was observed between age and OBV in the epilepsy group ( $r = 0.393$ ,  $P = 0.018$ ), and there was a moderate positive correlation between OBV and age in the control group ( $r = 0.561$ ,  $P < 0.001$ ). The right and left OTL and OSD values were not correlated with age ( $r = 0.095$ ;  $P = 0.256$ ,  $r = 0.001$ ;  $P = 0.993$ ,  $r = 0.921$ ;  $P = 0.275$ ,  $r = 0.583$ ;  $P = 0.488$ , respectively). The right and left OBV, OTL, and OSD values did not significantly differ according to sex in either group (patients:  $P = 0.445$ ,  $P = 0.585$ ,  $P = 0.432$ ,  $P = 0.266$ ,  $P = 0.504$ ,  $P = 0.581$ ; controls:  $P = 0.112$ ,  $P = 0.990$ ,  $P = 0.643$ ,  $P = 0.975$ ,  $P = 0.681$ ,  $P = 0.922$ , respectively).

No significant difference in OBV, OTL, and OSD was identified among the patients with generalized-onset, focal-onset, or unclassifiable epilepsy (Table 3). Furthermore, no significant difference was found in these three parameters among the single therapy, multiple therapy, and non-therapy groups (Table 4). When all age groups were compared, there was no significant relationship between the right and left OTL and OSD values of the patient and control groups ( $P = 0.643$ ,  $P = 0.921$ ,  $P = 0.141$ ,  $P = 0.143$ , respectively). However, OBV values decreased in the epilepsy group in all age groups (Table 5). Bland–Altman graphics representing the relationship between the differences in measurements and the mean values identified by the two radiologists are presented in Figures 5 and 6.

## Discussion

Olfactory deficits (odor identification, recognition memory, discrimination, and perception threshold) are more prominent in patients with epilepsy than in healthy individuals.<sup>3</sup> Khurshid et al.<sup>3</sup> conducted a meta-analysis on epilepsy and smell by screening 21 articles, revealing that olfactory deficits varied according to epilepsy types and were most prominent in temporal and mixed frontal lobe epilepsy. Impaired smell identification in patients with temporal lobe epilepsy before seizures, as well as those with a history of temporal lobectomy, demonstrates the effect of the temporal lobe on the sense of smell.<sup>3</sup>

**Table 1.** Intraclass correlation coefficient estimates of two observers

Variables	ICC (95% CI)
Right OBV	0.89 (0.81–0.93)
Left OBV	0.96 (0.94–0.97)
Total OBV	0.96 (0.94–0.97)
Right OTL	0.90 (0.63–0.96)
Left OTL	0.88 (0.72–0.94)
Right OSD	0.73 (0.57–0.83)
Left OSD	0.84 (0.73–0.90)

OBV, olfactory bulb volume; OTL, olfactory tract length; OSD, olfactory sulcus depth; CI, confidence interval; ICC, intraclass correlation coefficient.

**Table 2.** Comparison of the epilepsy and control groups

Variables	Epilepsy (n = 36) (mean ± SD)	Control (n = 108) (mean ± SD)	P
Right OBV	54.60 ± 11.29	66.30 ± 13.44	<0.001
Left OBV	52.66 ± 10.82	66.25 ± 17.13	<0.001
Total OBV	106.61 ± 16.69	132.55 ± 28.27	<0.001
Right OTL	24.30 ± 3.08	25.16 ± 3.43	0.188
Left OTL	24.55 ± 3.29	24.17 ± 3.19	0.726
Right OSD	10.09 ± 1.98	10.13 ± 1.65	0.920
Left OSD	9.95 ± 1.64	10.02 ± 1.89	0.845

Independent two samples t-test was used. SD, standard deviation; OBV, olfactory bulb volume; OTL, olfactory tract length; OSD, olfactory sulcus depth.

**Table 3.** Comparison of the parameters among the epilepsy subgroups according to seizure type

Variables	Generalized onset (n = 23) median (min–max)	Focal onset (n = 8) median (min–max)	Unclassified (n = 5) median (min–max)	P
Right OBV	53.44 (37.08–65.55)	56.70 (52.44–70.09)	47.39 (41.29–62.99)	0.193
Left OBV	51.87 (29.08–74.68)	54.43 (37.96–74.65)	54.73 (37.39–63.79)	0.754
Total OBV	102.93 (71.16–133.16)	114.96 (90.40–140.12)	102.50 (78.68–124.65)	0.367
Right OTL	23.60 (18.13–30.14)	26.80 (21.58–29.80)	23.32 (20.96–26.46)	0.161
Left OTL	25.35 (17.89–29.86)	23.91 (21.62–27.52)	22.53 (19.57–25.93)	0.337
Right OSD	9.52 (6.32–14.20)	10.72 (9.12–13.04)	11.09 (8.86–11.67)	0.320
Left OSD	9.93 (6.31–14.30)	9.60 (8.14–13.57)	10.19 (8.92–11.61)	0.808

OBV, olfactory bulb volume; OTL, olfactory tract length; OSD, olfactory sulcus depth (Kruskal–Wallis test was used), min, minimum; max, maximum

**Table 4.** Comparison of the parameters among the epilepsy subgroups according to treatment

Variables	Single antiepileptic (n = 20) median (min–max)	Multiple antiepileptics (n = 9) median (min–max)	No therapy (n = 7) median (min–max)	P
Right OBV	57.79 (37.08–70.09)	50.41 (41.29–62.81)	53.45 (46.45–63.32)	0.214
Left OBV	51.90 (39.72–74.68)	51.87 (29.08–66.72)	52.24 (41.32–63.79)	0.729
Total OBV	106.54 (76.80–140.12)	102.12 (71.16–129.42)	106.69 (92.08–124.65)	0.397
Right OTL	23.51 (18.13–29.80)	25.87 (19.88–30.14)	23.61 (21.71–27.13)	0.670
Left OTL	24.70 (17.89–29.74)	24.08 (18.63–29.86)	24.26 (20.68–28.18)	0.728
Right OSD	10.87 (7.32–14.20)	9.67 (6.82–11.24)	9.01 (6.32–13.04)	0.418
Left OSD	10.01 (6.31–14.30)	8.98 (6.73–11.56)	10.59 (8.92–13.57)	0.100

OBV, olfactory bulb volume; OTL, olfactory tract length; OSD, olfactory sulcus depth (Kruskal–Wallis test was used), min, minimum; max, maximum

**Table 5.** Comparison of epilepsy and control groups by age group

Age groups	Variables	Epilepsy (n = 14, 12, 10) median (min–max)	Control (n = 46, 31, 31) median (min–max)	P
3–6 years (group 1)	Right OBV	54.13 (37.08–63.32)	62.21 (35.87–85.79)	0.009
	Left OBV	47.70 (29.08–74.68)	59.34 (34.10–102.97)	0.009
	Total OBV	98.62 (71.16–133.16)	122.15 (73.51–188.76)	0.005
7–11 years (group 2)	Right OBV	55.23 (41.29–65.55)	63.37 (38.98–92.47)	0.009
	Left OBV	50.87 (37.39–74.65)	64.19 (41.19–95.46)	0.011
	Total OBV	106.51 (78.68–140.12)	126.51 (87.56–182.11)	0.002
12–17 years (group 3)	Right OBV	54.95 (41.17–70.09)	77.55 (51.40–98.74)	<0.001
	Left OBV	56.78 (51.24–66.72)	75.66 (43.56–121.04)	0.004
	Total OBV	111.99 (95.39–129.53)	155.96 (94.95–205.51)	0.001

OBV, olfactory bulb volume, min, minimum; max, maximum

The olfactory bulb is the first key station that relays odor information from the periphery. It ends in the olfactory tract and is closely related to the olfactory sulcus in the frontal lobe. OBV is a criterion for evaluating olfactory function and is smaller in patients with anosmia than in those with hyposmia.<sup>10</sup> In patients with posttraumatic and postinfectious (as in sinusitis) odor loss, a significant correlation was reported between olfactory recovery and the initial OBV measurement (the more prominent the initial OBV, the more meaningful the improvement in olfactory function).<sup>7</sup> One study revealed that OBV varied according to age, and although there was no obvious difference in adults until the age of 40 years, OBV started to decrease in the 60–70-years age group.<sup>7</sup> In the same study, the OBV cut-off value was determined as 40 mm<sup>3</sup> for adults without smell dysfunction.<sup>7</sup>

In the only pediatric study, quantitative measurements of OBV, OTL, and OSD were performed in healthy children, and these values were observed to increase with age without sex difference.<sup>11</sup> OBV decreased in

posttraumatic and postinfectious olfactory disorders, congenital anosmia, and neurodegenerative diseases (e.g., Parkinson, Alzheimer, and Behçet diseases).<sup>5,7,12–15</sup> In a study conducted on patients with mesial temporal lobe epilepsy, OBV was significantly lower in this group than in the control group, and the mean OBV of patients with hyposmia (epilepsy) was significantly lower than that of patients with normosmia.<sup>9</sup>

In an experimental study, the development of epilepsy was reported in mice in which olfactory bulbectomy had been performed.<sup>16</sup> In other studies, increased excitability in the amygdala was revealed after olfactory bulbectomy in mice.<sup>17,18</sup> These studies suggest that the olfactory bulb may play a role in suppressing epileptic discharges rather than being an epileptic focus. In humans, the presence of reflex epilepsy provoked by smell<sup>19</sup> suggests that the olfactory bulb may be involved in the etiopathogenesis of epilepsy.

Doğan et al.<sup>13</sup> reported that OBV decreased in Behçet disease, but they did not

find a difference in OSD compared with the control group. OSD was reported to be lower than that of controls in certain diseases, such as schizophrenia, migraine, Parkinson disease, and major depression.<sup>8,12,14,20–22</sup> Although OBV has previously been reported to decrease in cases of olfactory dysfunction that develop because of upper respiratory tract infection and in patients with allergic rhinitis, in the same studies, no significant difference in OSD was observed compared with controls.<sup>23,24</sup> Few studies have been published on OTL. One study revealed that OTL is decreased in patients with essential tremor compared with controls.<sup>25</sup> Kumar et al.<sup>26</sup> induced olfactory hallucination in 11 children with focal epilepsy by stimulating the olfactory bulb or tract using subdural electrodes.

Although the olfactory nerve is a pure sensory nerve, it also exhibits volume loss in cases where extrapyramidal motor function is impaired, such as Parkinson disease, systemic diseases such as Behçet, psychosomatic disorders such as restless legs syndrome,<sup>27</sup> and neurogenic abnormal discharges such as epilepsy. Thus, in many systemic diseases in which olfactory function is not clinically impaired, OBV decreases or the olfactory system may be affected.

In this study, the OBV value increased with age in both children with epilepsy and healthy children, but this increase was lower in the epileptic group than in the control group. This result might indicate that the development of the olfactory bulb is slowed in children with epilepsy.

This study has certain limitations, such as its retrospective design, evaluation of cases based on medical files, absence of an evaluation of the olfactory aura or disease duration in patients with epilepsy, absence of odor testing, and the sample not including any patient with a history of epilepsy surgery.

In conclusion, the quantitative analysis of the olfactory system can be reliably undertaken using MRI. In this study, there was a decrease in the OBV values of pediatric patients with epilepsy. The literature suggests the presence of a correlation between reduced OBV and presence of neurodegenerative diseases, and OBV is not only associated with olfactory function but also reflects the devastating effect of diseases on the nervous system. Further research investigating different diseases in wider populations might better reveal the relationship between OBV and neurodegeneration.

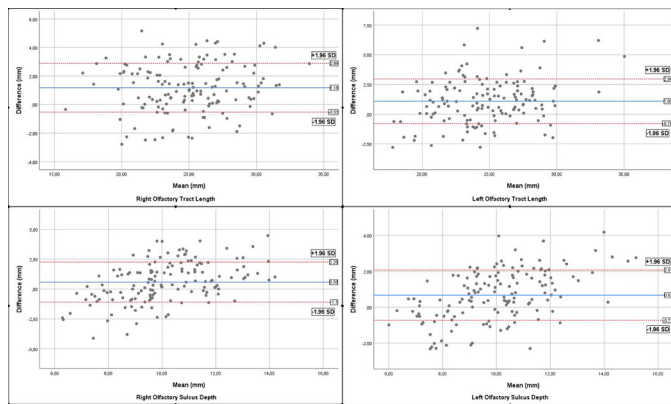


**Figure 5.** Bland–Altman graphics of the interobserver agreement for olfactory tract length and olfactory sulcus depth. The difference between the two observers is plotted on the y-axis and the mean value of the measurements on the x-axis. A continuous line indicates mean difference. Dashed upper and lower lines indicate the upper and lower limits of the 95% fit limits (mean  $\pm$  variability estimate = 1.96 standard deviation).

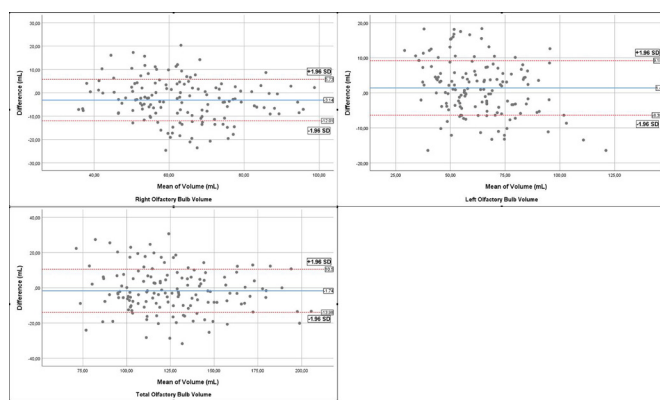


**Figure 6.** Bland–Altman graphics of the interobserver agreement for olfactory bulbus volumes. The difference between the two observers is plotted on the y-axis and the mean value of the measurements on the x-axis. A continuous line indicates mean difference. Dashed upper and lower lines indicate the upper and lower limits of the 95% fit limits (mean  $\pm$  variability estimate = 1.96 standard deviation).

## Conflict of interest disclosure

The authors declared no conflicts of interest.

## References

1. Friedman MJ, Sharieff GQ. Seizures in children. *Pediatr Clin North Am.* 2006;53(2):257-277. [\[CrossRef\]](#)
2. Camfield P, Camfield C. Incidence, prevalence and aetiology of seizures and epilepsy in children. *Epileptic Disord.* 2015;17(2):117-123. [\[CrossRef\]](#)
3. Khurshid K, Crow AJD, Rupert PE, et al. A quantitative meta-analysis of olfactory dysfunction in epilepsy. *Neuropsychol Rev.* 2019;29(3):328-337. [\[CrossRef\]](#)
4. Shepherd GM. The synaptic organization of the brain: Oxford university press; 2004. [\[CrossRef\]](#)
5. Hummel T, Witt M, Reichmann H, Welge-Luessen A, Haehner A. Immunohistochemical, volumetric, and functional neuroimaging studies in patients with idiopathic Parkinson's disease. *J Neural Sci.* 2010;289(1-2):119-122. [\[CrossRef\]](#)
6. Kim JY, Lee WY, Chung EJ, Dhong HJ. Analysis of olfactory function and the depth of olfactory sulcus in patients with Parkinson's disease. *Mov Disord.* 2007;22(11):1563-1566. [\[CrossRef\]](#)
7. Rombaux P, Huart C, Deggouj N, Duprez T, Hummel T. Prognostic value of olfactory bulb volume measurement for recovery in postinfectious and posttraumatic olfactory loss. *Otolaryngol Head Neck Surg.* 2012;147(6):1136-1141. [\[CrossRef\]](#)
8. Hummel T, Henkel S, Negoias S, et al. Olfactory bulb volume in patients with temporal lobe epilepsy. *J Neurol.* 2013;260(4):1004-1008. [\[CrossRef\]](#)
9. Türk BG, Metin B, Tekeli H, et al. Evaluation of olfactory and gustatory changes in patients with mesial temporal lobe epilepsy. *Seizure.* 2020;75:110-114. [\[CrossRef\]](#)
10. Haehner A, Rodewald A, Gerber JC, Hummel T. Correlation of olfactory function with changes in the volume of the human olfactory bulb. *Arch Otolaryngol Head Neck Surg.* 2008;134(6):621-624. [\[CrossRef\]](#)
11. Sahin S, Baykan AH, Altunisik E, Vural CA, Sahin FD, Inan I. Quantitative analysis of healthy olfactory sulcus depth, olfactory tract length and olfactory bulb volume in the paediatric population: a magnetic resonance study. *Folia Morphol (Warsz).* 2021;80(1):33-39. [\[CrossRef\]](#)
12. Gudziol V, Buschhüter D, Abolmaali N, Gerber J, Rombaux P, Hummel T. Increasing olfactory bulb volume due to treatment of chronic rhinosinusitis—a longitudinal study. *Brain.* 2009;132(Pt 11):3096-3101. [\[CrossRef\]](#)
13. Doğan A, Muluk NB, Asal N, et al. Olfactory bulb volume and olfactory sulcus depth in patients with Behçet's disease. *J Laryngol Otol.* 2018;132(12):1088-1092. [\[CrossRef\]](#)
14. Tanik N, Serin HI, Celikbilek A, Inan LE, Gundogdu F. Associations of olfactory bulb and depth of olfactory sulcus with basal ganglia and hippocampus in patients with Parkinson's disease. *Neurosci Lett.* 2016;620:111-114. [\[CrossRef\]](#)
15. Li J, Gu CZ, Su JB, et al. Changes in olfactory bulb volume in Parkinson's disease: a systematic review and meta-analysis. *PLoS One.* 2016;11(2):e0149286. [\[CrossRef\]](#)
16. Jiang Y, Pun RY, Peariso K, Holland KD, Lian Q, Danzer SC. Olfactory bulbectomy leads to the development of epilepsy in mice. *PLoS One.* 2015;10(9):e0138178. [\[CrossRef\]](#)
17. Cain DP, Corcoran ME. Kindling in olfactory-lesioned rats. *Behav Biol.* 1978;22(2):264-268. [\[CrossRef\]](#)
18. Watanabe S, Nakanishi H, Shibata S, Ueki S. Changes in amygdaloid afterdischarges and kindling effect following olfactory bulbectomy in the rat. *Physiol Behav.* 1982;28(4):687-692. [\[CrossRef\]](#)
19. Ilik F, Pazarli AC. Reflex epilepsy triggered by smell. *Clin EEG Neurosci.* 2015;46(3):263-265. [\[CrossRef\]](#)
20. Negoias S, Hummel T, Symmank A, Schellong J, Joraschky P, Croy I. Olfactory bulb volume predicts therapeutic outcome in major depression disorder. *Brain Imaging Behav.* 2016;10(2):367-372. [\[CrossRef\]](#)
21. Doğan A, Bayar Muluk N, Şahan MH, Asal N, Inal M, Ergün U. Olfactory bulb volume and olfactory sulcus depth in migraine patients: an MRI evaluation. *Eur Arch Otorhinolaryngol.* 2018;275(8):2005-2011. [\[CrossRef\]](#)
22. Nishikawa Y, Takahashi T, Takayanagi Y, et al. Orbitofrontal sulcogyral pattern and olfactory sulcus depth in the schizophrenia spectrum. *Eur Arch Psychiatry Clin Neurosci.* 2016;266(1):15-23. [\[CrossRef\]](#)
23. Hang W, Liu G, Han T, Zhang J, Zhang Q. [Olfactory bulb volume and depth of olfactory sulcus in olfactory dysfunction patients after upper respiratory tract infection]. *Zhonghua Er Bi Yan Hou Tou Jing Wai Ke Za Zhi.* 2015;50(6):488-492. [\[CrossRef\]](#)
24. Zhang Q, Liu G, Hang W. [Olfactory bulb volume and depth of olfactory sulcus in patients with allergic rhinitis]. *Lin Chung Er Bi Yan Hou Tou Jing Wai Ke Za Zhi.* 2014;28(24):1956-1960. [\[CrossRef\]](#)
25. Altunışık E, Baykan AH. Decreased olfactory bulb volume in patients with restless legs syndrome. *Anadolu Psikiyatri Dergisi.* 2020;21(5):537-543. [\[CrossRef\]](#)
26. Kumar G, Juhász C, Sood S, Asano E. Olfactory hallucinations elicited by electrical stimulation via subdural electrodes: effects of direct stimulation of olfactory bulb and tract. *Epilepsy Behavior.* 2012;24(2):264-268. [\[CrossRef\]](#)
27. Altunisik E, Baykan AH. Comparison of the olfactory bulb volume and the olfactory tract length between patients diagnosed with essential tremor and healthy controls: findings in favor of neurodegeneration. *Cureus.* 2019;11(10):e5846. [\[CrossRef\]](#)



# Radiomics analysis for predicting malignant cerebral edema in patients undergoing endovascular treatment for acute ischemic stroke

Xuehua Wen

Xingfei Hu

Yanan Xiao

Junfa Chen

## PURPOSE

Radiomics analysis is a promising image analysis technique. This study aims to extract a radiomics signature from baseline computed tomography (CT) to predict malignant cerebral edema (MCE) in patients with acute anterior circulation infarction after endovascular treatment (EVT).

## METHODS

In this retrospective study, 111 patients underwent EVT for acute ischemic stroke caused by middle cerebral artery (MCA) and/or internal carotid artery occlusion. The participants were randomly divided into two datasets: the training set ( $n = 77$ ) and the test set ( $n = 34$ ). The clinico-radiological profiles of all patients were collected, including cranial non-contrast-enhanced CT, CT angiography, and CT perfusion. The MCA territory on non-contrast-enhanced CT images was segmented, and the radiomics features associated with MCE were analyzed. The clinico-radiological parameters related to MCE were also identified. In addition, a routine visual radiological model based on radiological factors and a combined model comprising radiomics features and clinico-radiological factors were constructed to predict MCE.

## RESULTS

The areas under the curve (AUCs) of the radiomics signature for predicting MCE were 0.870 ( $P < 0.001$ ) and 0.837 ( $P = 0.002$ ) in the training and test sets, respectively. The AUCs of the routine visual radiological model were 0.808 ( $P < 0.001$ ) and 0.813 ( $P = 0.005$ ) in the training and test sets, respectively. The AUCs of the model combining the radiomics signature and clinico-radiological factors were 0.924 ( $P < 0.001$ ) and 0.879 ( $P = 0.001$ ) in the training and test sets, respectively.

## CONCLUSION

A CT image-based radiomics signature is a promising tool for predicting MCE in patients with acute anterior circulation infarction after EVT. For clinicians, it may assist in diagnostic decision-making.

## KEYWORDS

Computed tomography, malignant cerebral edema, middle cerebral artery, radiomics, stroke

From the Department of Radiology (X.W., Y.X., J.C. [✉ cjf2002@126.com](mailto:cjf2002@126.com)), Center for Rehabilitation Medicine, Zhejiang Provincial People's Hospital, Affiliated People's Hospital, Hangzhou Medical College, Zhejiang, China; Department of Radiology (X.H.), The First People's Hospital of Daishan, Zhejiang, China.

Received 10 January 2022; revision requested 16 November 2022; last revision received 24 January 2023; accepted 02 February 2023.



Epub: 17.02.2023

Publication date: 29.03.2023

DOI: 10.4274/dir.2023.221764

The safety and efficacy of endovascular treatment (EVT) for anterior circulation large vessel occlusive stroke (LVOS) have been verified in randomized controlled trials. However, nearly 45% of the cases with LVOS cannot recover after EVT.<sup>1,2</sup> Recent evidence has revealed that malignant cerebral edema (MCE) commonly occurs after EVT, and the development of MCE may reduce the benefit–risk ratio of EVT.<sup>3–5</sup> MCE is a severe complication of stroke that occurs in approximately 10% of all patients with stroke. The prognosis for MCE is poor, with a mortality rate of 80% when treated conservatively.<sup>6</sup> Early decompressive surgery effectively lowers mortality and improves the clinical outcomes of patients with MCE.<sup>7</sup> The addition of decompressive craniectomy to the best medical therapy can reduce the mortality rate of MCE by 50%–75%.<sup>8</sup> Hence, the early identification of patients at a high risk of MCE is critical for therapeutic decision-making. The imaging predictors for MCE that have been studied so far primarily involve the characterization of the infarction size, neurovascular condition, and brain perfusion of the patient.<sup>7</sup>

You may cite this article as: Wen X, Hu X, Xiao Y, Chen J. Radiomics analysis for predicting malignant cerebral edema in patients undergoing endovascular treatment for acute ischemic stroke. *Diagn Interv Radiol.* 2023;29(2):402–409.

Diffusion-weighted imaging (DWI) is a valuable technique for identifying the ischemic core. Rapid sequence magnetic resonance imaging (MRI) using DWI and fluid-attenuated inversion recovery sequences has gradually emerged as a new screening modality in people with suspected acute ischemic stroke (AIS), especially where there might be delays in obtaining full sequence brain imaging. However, some limitations still exist, such as limited access at some emergency departments and the contraindications of MRI examination for some patients. Computed tomography (CT) is a commonly used imaging technique in clinical practice for diagnosing and treating AIS. However, some reported prognostic variables (i.e., MCE) are imprecise when using conventional CT methods (i.e., cranial CT scan).<sup>7</sup> Therefore, new approaches that can promptly identify MCE are needed.

Conventional CT images contain information that cannot be evaluated visually but may be assessed using image analysis tools. Image textures correspond to the brightness value and the position of image pixels. Image texture analysis is a quantitative image analysis method that can improve the accuracy of the diagnostic or classification information extracted from different imaging methods, such as ultrasound, CT, and MRI.<sup>9</sup> The correlation between the radiomics signature based on image textures and the progression of MCE after EVT is not fully known. This study hypothesized that the radiomics signature might be an early predictor of MCE in patients with acute anterior circulation infarction after EVT. Furthermore, this study evaluated the predictive potential of a single radiomics signature and a model comprising a radiomics signature as well as clinical factors and routine radiological parameters for MCE.

## Methods

This retrospective study was approved by the Zhejiang Provincial People's Hospital's Ethics Committee (approval number: 2020QT038), and informed consent was waived due to its retrospective nature. The clinical data and radiological findings of all

subjects were obtained from the medical records and the picture archiving and communication system of our hospital.

### Study population

The clinical and radiological data of patients diagnosed with AIS caused by middle cerebral artery (MCA) and/or internal carotid artery (ICA) occlusion and who had undergone EVT were retrospectively reviewed from the institutional databases between January 2018 and August 2021. Finally, a total of 111 patients were included (Figure 1).

The inclusion criteria were as follows: (1) patients were diagnosed with AIS and underwent EVT; (2) baseline cranial non-contrast-enhanced CT (NCCT), CT angiography (CTA), CT perfusion (CTP) images, and the follow-up CT/MRI images in case of neurological deterioration or within three days after EVT were available; and (3) patients had a causative occlusion of the MCA and/or ICA. The exclusion criteria were as follows: (1) the presence of AIS in the areas supplied by the posterior circulation or bilateral acute ischemic lesions demonstrated by neuroimaging; (2) a modified Rankin Scale score of over

two before admission; (3) the presence of symptomatic intracranial hemorrhage; and (4) difficulty in image interpretation due to incomplete images or artifacts.

### Endpoint

The primary endpoint was the occurrence of MCE, defined as a midline shift of over 5 mm at the pineal gland or septum pellucidum on the follow-up imaging, with the need for decompressive hemicraniectomy.<sup>3,10-12</sup>

### Imaging protocol

All participants underwent baseline CTP and NCCT scans and had follow-up CT or MRI. CTP and NCCT were performed using a 640-slice CT (Aquilion ONE TSX-301A, Toshiba).

The whole-brain NCCT was performed in one rotation (detector width: 16 cm). Moreover, CTP was acquired after the administration of a contrast agent (50 mL; Omnipaque, GE Healthcare) through intravenous (IV) injection at a rate of 6 mL/s, followed by 50 mL of saline (acquisition parameters: scanning width, 5 mm; scanning coverage, 240 mm; 128 mAs; and 120 kV). At 7 s after the

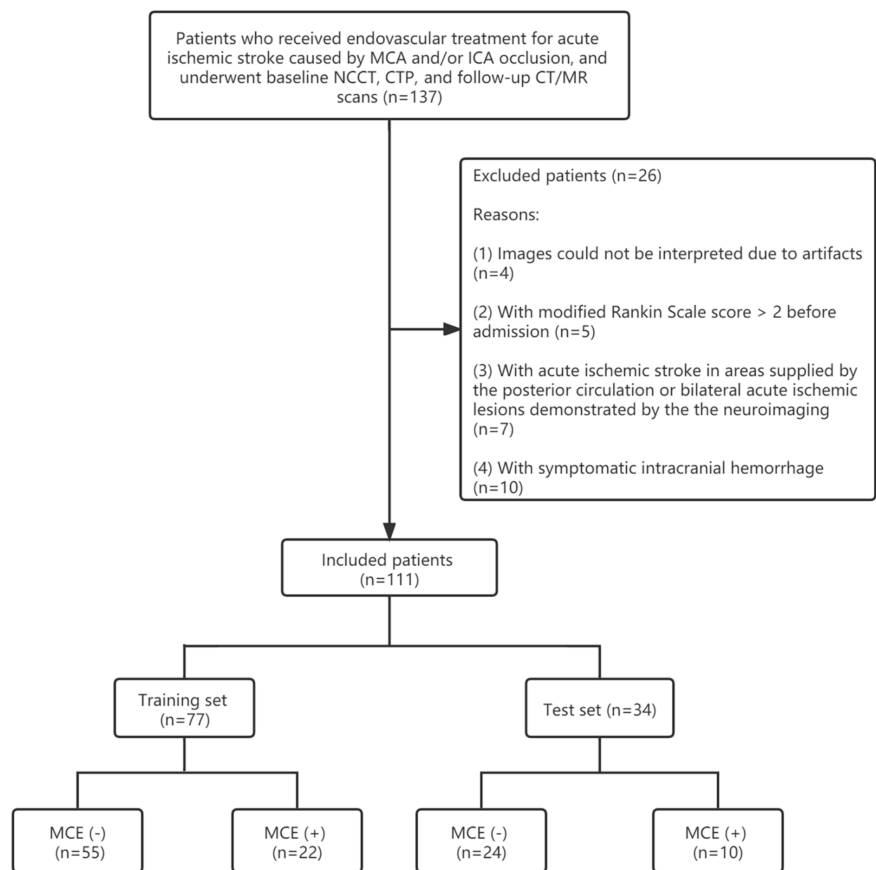


**Figure 1.** Flowchart of patient enrollment. MCA, middle cerebral artery; ICA, internal carotid artery; NCCT, non-contrast enhanced computed tomography; CTP, computed tomography perfusion; CT, computed tomography; MR, magnetic resonance; MCE, malignant cerebral edema.

### Main points

- The development of malignant cerebral edema (MCE) may reduce the benefit–risk ratio of endovascular treatment (EVT).
- Computed tomography-based radiomics analysis may be used to predict MCE.
- A radiomics signature was built to screen patients at high risk of MCE after EVT.

injection of the contrast agent, a pulsed full rotation scan was performed with 18 time points acquired over 1 min and a total image acquisition time of 9.5 s. Multiphase CTAs, including venous peak phase, venous late phase, and arterial peak phase images, were generated from CTP images using MIStar (Apollo Medical Imaging Technology).

### Clinical and routine radiological assessment

The baseline neurological status of patients at admission was evaluated using the National Institutes of Health Stroke Scale (NIHSS). The recanalization status after EVT was assessed using the modified Thrombolysis in Cerebral Infarction grading system.

Radiological images, including baseline NCCT, CTP, and CTA, as well as follow-up images, were reviewed and evaluated by two neuroradiologists (H and X, with 6 and 10 years of clinical experience, respectively). Any discordant interpretations between the two raters were resolved by consensus through discussion.

The Alberta Stroke Program Early CT Score (ASPECTS) was calculated by subtracting the score of the low-density regions from a total score of 10 on NCCT images.<sup>13</sup>

On CTA images, the thrombosis burden was quantified to assess the clot in the anterior circulation using the clot burden score (CBS), which starts at 10 and is deducted

based on the loss of contrast opacification on CTA.<sup>14</sup> The leptomeningeal collateral status was evaluated on a 0–3 scale: 0, absent collateral filling; 1,  $\leq 50\%$  collateral filling; 2,  $>50\%$  but  $<100\%$  collateral filling; and 3,  $\geq 100\%$  collateral filling when compared with the non-occluded side.<sup>15</sup>

On CTP images, the ischemic core was defined by a decrease in the relative cerebral blood flow to less than 30% of normal. The ischemic lesion was defined as brain tissues with a delay time (DT) of  $>3$  s based on MIStar.

### Image preprocessing and radiomics feature selection

Radiomics analysis was conducted based on baseline cranial NCCT (Figure 2).

Image data preprocessing, including gray-level discretization, intensity normalization, and image interpolation, was carried out using the AK software (version 3.0.0. R, Artificial Intelligence Kit, GE Healthcare).

The region of interest (ROI) of the whole MCA territory was manually segmented on a 3D volume of interest on NCCT images using the ITK-SNAP software (www.itksnap.org). The intra- and inter-rater agreement on the ROI segmentation was evaluated using intraclass correlation coefficients. Rater H segmented the ROIs twice within a 2 month interval. Intra-rater ICC was determined by comparing the two measurements of rater H. Inter-rater ICC was calculated by comparing

the ROIs in 30 randomly selected patients (measured by raters X and H).

The extracted features included haralick, histogram, formfactor, gray level co-occurrence matrix, run-length matrix, and gray level size-zone matrix. For each patient, 396 features were extracted, which were then standardized to remove the unit limits of the data. Dimension reduction was carried out using the correlation test, Mann–Whitney U test, and analysis of variance. The features were further selected using the least absolute shrinkage and selection operator (LASSO).

### Development of the radiomics signature

Multivariate logistic regression analysis was used to construct the radiomics signature, which was then used to predict MCE based on selected features using the LASSO. Subsequently, the radiomics score (rad-score) of each patient was calculated. The formula was derived from the training set data and was then used to determine the rad-score of the patient in the test set. The predictive efficiency of the radiomics signature was evaluated using the receiver operating characteristic (ROC) curves in both the training and test sets.

### Development of the prediction model for malignant cerebral edema

All parameters (i.e., sex, age, history of hypertension, atrial fibrillation, hyperlipidemia, diabetes mellitus, alcohol abuse, smoking, baseline NIHSS, hyperdense vessel sign of the MCA, ASPECTS, collateral score, occlusion site, CBS, ischemic lesion volume, ischemic core volume, IV-type plasminogen activator (tPA), time from onset to groin puncture, reperfusion grade, and the radiomics signature) were screened to identify variables associated with MCE. Furthermore, multivariate regression analysis was performed to construct a prediction model for MCE. The model calibration was assessed using the Hosmer–Lemeshow test. The ROC curve was used to evaluate the predictive ability of the model.

### Statistical analysis

The MedCalc v15.2.2, SPSS v21.0, and Microsoft R Open v3.3.1 software were used for statistical analyses. Descriptive statistics were presented as median (first quartile and third quartile) for non-normally distributed variables, and the mean  $\pm$  standard deviation was used for the normally distributed variables. Categorical variables were report-

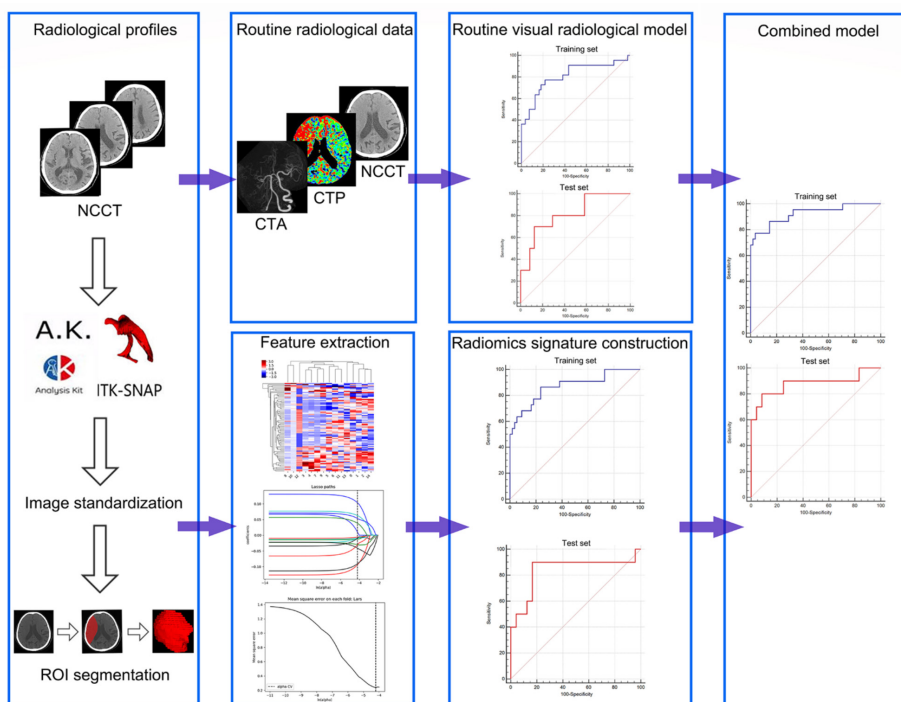


**Figure 2.** Workflow of radiomics analysis. NCCT, non-contrast enhanced computed tomography; CTA, CT angiography; CTP, CT perfusion; ROI, region of interest.

ed as frequencies (percentages). The LASSO analysis was conducted based on the minimum criterion by 10 fold cross-validation. The Student's t-test, Mann-Whitney U test, Pearson's chi-square test, and Fisher's exact test were used to identify MCE-associated variables. The Youden index in the ROC analysis was used to determine the best cut-off point of CTP parameters and NCCT ASPECTS for identifying patients with MCE. Multivariate regression analysis was performed to establish the radiomics signature, the routine visual radiological model, and the combined model for predicting MCE. The ROC curves were compared using the method developed by DeLong et al.<sup>16</sup> The significance level was established as  $\alpha = 0.05$ .

## Results

### The intra- and inter-rater reliability

The intra-rater agreement on the ROI segmentation between the two measurements

from the same rater was 0.896 ( $P < 0.001$ ). The inter-rater agreement between the two raters was 0.842 ( $P < 0.001$ ).

### Baseline characteristics

A total of 111 patients were randomly split into two datasets at a ratio of 7:3<sup>17</sup> as follows: the training set ( $n = 77$ ) and the test set ( $n = 34$ ). There were no significant differences in the clinical or routine radiological characteristics between the two sets (Table 1). The rad-score, ASPECTS, ischemic core volume, DT >3 s lesion volume, and IV-tPA were significantly different between the MCE (+) and MCE (-) groups in the training set (Table 2).

### The radiomics signature

After identifying 187 features using the Mann-Whitney U test and analysis of variance, 22 features were retained after the Spearman correlation analysis. Moreover, the LASSO analysis was performed, and 15

features remained (Supplementary Table 1). The rad-score was obtained using the LASSO model, with a linear combination of the 15 features (Supplementary Materials). The values of the 15 features of each subject were placed into the calculation formula, and the rad-score was obtained to indicate the predictive efficiency for MCE.

The sensitivity, specificity, and AUC of the radiomics signature for predicting MCE in the training set were 86.36%, 76.36%, and 0.870 [95% confidence interval (CI): 0.773–0.967], respectively (Figure 3). The radiomics signature showed satisfying goodness-of-fit ( $P = 0.361$ ). The sensitivity, specificity, and AUC in the test set were 90.00%, 83.33%, and 0.837 (95% CI: 0.655–1), respectively (Figure 3).

### The routine visual radiological model

The routine radiological parameters for the prediction of MCE were as follows: 1) ASPECTS with an AUC of 0.800 (95% CI, 0.683–0.917;  $P < 0.001$ ); 2) ischemic core volume with an AUC of 0.793 (95% CI, 0.675–0.910;  $P < 0.001$ ); and 3) DT >3 s lesion volume with an AUC of 0.725 (95% CI, 0.580–0.870;  $P = 0.002$ ). The best cut-off values for the ASPECTS, ischemic core volume, and DT >3 s lesion volume were 7, 37, and 235, respectively (Table 3).

The sensitivity, specificity, and AUC of the routine visual radiological model based on the above radiological parameters were 77.27%, 78.18%, and 0.808 (95% CI: 0.687–0.929), respectively, in the training set (Figure 3). The routine visual radiological model showed satisfying goodness-of-fit ( $P = 0.200$ ). The sensitivity, specificity, and AUC in the test set were 70.00%, 87.50%, and 0.813 (95% CI: 0.649–0.976), respectively (Figure 3).

### The combined model

The combined model for predicting MCE included the rad-score, ASPECTS, ischemic core volume, DT >3 s lesion volume, and IV-tPA.

In the training set, the sensitivity, specificity, and AUC of the combined model were 77.27%, 96.36%, and 0.924 (95% CI: 0.850–0.998), respectively (Figure 3). The combined model showed satisfying goodness-of-fit ( $P = 0.662$ ). In the test set, the sensitivity, specificity, and AUC were 80.00%, 91.67%, and 0.879 (95% CI: 0.712–1), respectively (Figure 3).

The participants were divided into high- and low-risk groups according to the optimal diagnostic cut-off value of the model (0.390). The number of patients with MCE (+) was significantly different between the high- and low-risk groups in the training set ( $P < 0.001$ ).

Variable	Training set (n = 77)	Test set (n = 34)	P value
Male gender, n (%)	49 (63.6%)	22 (64.7%)	0.914
Age (years), mean $\pm$ SD	72.1 $\pm$ 13.7	70.6 $\pm$ 12.7	0.575
Hypertension, n (%)	54 (70.1%)	24 (70.6%)	0.961
Diabetes mellitus, n (%)	11 (14.3%)	5 (14.7%)	1.000
Hyperlipidemia, n (%)	16 (20.8%)	3 (8.8%)	0.123
Atrial fibrillation, n (%)	40 (51.9%)	14 (41.2%)	0.295
Smoking, n (%)	21 (27.3%)	11 (32.4%)	0.586
Alcohol abuse, n (%)	15 (19.5%)	9 (26.5%)	0.410
Baseline NIHSS, median (Q1, Q3)	17 (13–21)	17 (14–20)	0.951
ASPECTS on NCCT, median (Q1, Q3)	8 (5–10)	8 (6–9)	0.748
HVS of MCA, n (%)	43 (55.8%)	14 (41.2%)	0.154
Collateral score, median (Q1, Q3)	1 (1–1)	1 (1–2)	0.054
<b>Vessel occlusion</b>			
Isolated MCA occlusion, n (%)	46 (59.7%)	18 (52.9%)	0.504
Isolated ICA occlusion, n (%)	5 (6.5%)	2 (5.9%)	1.000
Tandem ICA + MCA occlusion, n (%)	26 (33.8%)	14 (41.2%)	0.454
CBS, median (Q1, Q3)	6 (4–6)	5 (4–6)	0.165
<b>Baseline CTP</b>			
Ischemic core volume (mL), median (Q1, Q3)	36 (9–84)	26 (10–63)	0.550
DT >3 s lesion volume (mL), median (Q1, Q3)	144 (85–231)	133 (67–237)	0.916
<b>Treatment characteristics</b>			
IV-tPA, n (%)	26 (33.8%)	7 (20.6%)	0.161
Onset to groin puncture in hours, median (Q1, Q3)	5.1 (3.5–7.6)	5.5 (3.7–7.3)	0.703
mTICI $\geq$ 2b, n (%)	72 (93.5%)	30 (88.2%)	0.452

SD, standard deviation; NIHSS, National Institutes of Health Stroke Scale; Q1, first quartile; Q3, third quartile; NCCT, non-contrast-enhanced computed tomography; ASPECTS, Alberta Stroke Program Early CT Score; HVS, hyperdense vessel sign; MCA, middle cerebral artery; ICA, internal carotid artery; CBS, clot burden score; CTP, computed tomography perfusion; DT, delay time; IV-tPA, intravenous-tPA; mTICI, modified thrombolysis in cerebral infarction.

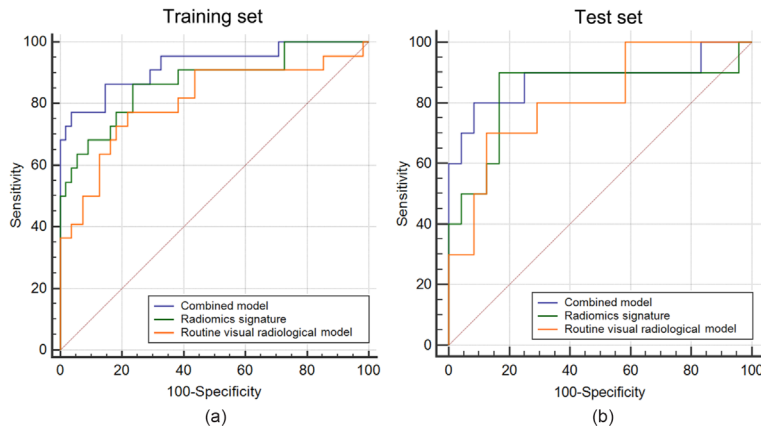


**Figure 3.** (a) The ROC curve of the radiomics signature [AUC, 0.870 (0.773–0.967)], routine visual radiological model [AUC, 0.808 (0.687–0.929)], and combined model [AUC, 0.924 (0.850–0.998)] for predicting MCE in the training set. (b) The ROC curve of the radiomics signature [AUC, 0.837 (0.655–1)], routine visual radiological model [AUC, 0.813 (0.649–0.976)], and combined model [AUC, 0.879 (0.712–1)] for predicting MCE in the test set. ROC, receiver operating characteristic; AUC, area under the curve; MCE, malignant cerebral edema.

Table 2. Comparison between patients with MCE (+) and MCE (-) in the training set			
Variable	MCE (n = 22)	non-MCE (n = 55)	P value
Male gender, n (%)	15 (68.2%)	34 (61.8%)	0.600
Age (years), mean ± SD	73.0 ± 13.4	71.8 ± 13.9	0.731
Hypertension, n (%)	15 (68.2%)	39 (70.9%)	0.813
Diabetes mellitus, n (%)	3 (13.6%)	8 (14.5%)	1.000
Hyperlipidemia, n (%)	6 (27.3%)	10 (18.2%)	0.371
Atrial fibrillation, n (%)	13 (59.1%)	27 (49.1%)	0.428
Smoking, n (%)	5 (22.7%)	16 (29.1%)	0.571
Alcohol abuse, n (%)	6 (27.3%)	9 (16.4%)	0.342
Baseline NIHSS, median (Q1, Q3)	18 (15–21)	17 (13–22)	0.436
ASPECTS on NCCT, median (Q1, Q3)	5 (3–7)	8 (7–10)	<0.001*
HVS of MCA, n (%)	13 (59.1%)	30 (54.5%)	0.717
Collateral score, median (Q1, Q3)	1 (1–1)	1 (1–1)	0.850
<b>Vessel occlusion</b>			
Isolated MCA occlusion, n (%)	10 (45.5%)	36 (65.5%)	0.106
Isolated ICA occlusion, n (%)	1 (4.6%)	4 (7.3%)	1.000
Tandem ICA + MCA occlusion, n (%)	11 (50%)	15 (27.3%)	0.057
CBS, median (Q1, Q3)	5 (4–6)	6 (4–7)	0.154
<b>Baseline CTP</b>			
Ischemic core volume (mL), median (Q1, Q3)	85 (42–134)	22 (8–55)	<0.001*
DT >3 s lesion volume (mL), median (Q1, Q3)	246 (130–304)	120 (77–192)	0.002*
<b>Treatment characteristics</b>			
IV-tPA, n (%)	2 (9.1%)	24 (43.6%)	0.004*
Onset to groin puncture in hours, median (Q1, Q3)	5.5 (2.9–8.3)	5.0 (3.5–7.5)	0.839
mTICI ≥2b, n (%)	19 (86.4%)	53 (96.4%)	0.137
Rad-score, mean ± SD	3.54 ± 13.62	-2.59 ± 2.10	0.048*

\*represents  $P < 0.05$ . MCE; malignant cerebral edema; SD, standard deviation; NIHSS, National Institutes of Health Stroke Scale; Q1, first quartile; Q3, third quartile; NCCT, non-contrast-enhanced computed tomography; ASPECTS, Alberta Stroke Program Early CT Score; HVS, hyperdense vessel sign; MCA, middle cerebral artery; ICA, internal carotid artery; CBS, clot burden score; CTP, computed tomography perfusion; DT, delay time; IV-tPA, intravenous-tPA; mTICI, modified thrombolysis in cerebral infarction.

Additionally, the results showed that the patients categorized into the high-risk group in the test set were all patients with MCE (+) (Figure 4).

The AUCs of the radiomics signature and the combined model were significantly different ( $P = 0.049$ ). The AUCs of the combined model and the routine visual radiological model were also significantly different ( $P = 0.020$ ). However, there was no significant difference in the AUC between the radiomics signature and the routine visual radiological model ( $P = 0.354$ ) (Table 4).

## Discussion

MCE is a life-threatening condition with high mortality rates. It is usually secondary to the acute occlusion of the proximal MCA trunk or the distal ICA.<sup>18</sup> Pathophysiologically, early damage to cerebrovascular autoregulation in the tissues surrounding the infarction, increased vascular permeability, and the loss of the integrity of the endothelial basal layer altogether play important roles in the progression of MCE.<sup>19,20</sup> The early detection of MCE and the use of decompressive surgery can improve the clinical outcomes of patients with MCE.<sup>21,22</sup> However, the current methods for detecting MCE are mainly reactive: waiting for signs of clinical deterioration and mass effect to appear before surgical intervention. Therefore, the identification of early predictors for MCE is of high importance.

Texture feature analysis is widely used in radiomics, which allows the quantification of internal heterogeneity that may not be perceived by the naked eye, thus promoting the identification and classification of different tissues.<sup>23</sup> Until recently, few studies have performed texture analysis of cerebral infarction. CT radiomics based on texture features showed good performance in identifying hyperacute or AIS lesions, assessing the extent of ischemic lesions, and determining the time from symptoms onset in basal ganglia infarction.<sup>24–26</sup> Kuang et al.<sup>27</sup> developed an automated method to compute the ASPECTS on NCCT images from patients with AIS. Additionally, texture analysis based on MRI effectively identified the presence of ischemic stroke lesions and detected hemorrhagic transformation in patients with AIS.<sup>28,29</sup> Furthermore, in patients with stroke, the texture features of brain MRI may provide early markers for poststroke cognitive impairment.<sup>30</sup> The potential of texture features for predicting MCE in patients with AIS caused by MCA and/or ICA occlusion after EVT was evaluated. By constructing a radiomics model, it was found

that the radiomics signature based on texture features was a valuable tool for identifying patients at a high risk of MCE after EVT, with AUCs of 0.870 and 0.837 in the training and test sets, respectively.

By analyzing the correlation between clinico-radiological factors and MCE, it was found that the ASPECTS on NCCT, ischemic core volume, DT >3 s lesion volume, and IV-tPA were correlated with MCE. The ASPECTS, ischemic core volume, and DT >3 s lesion volume can indicate the extent of ischemia or infarct lesion. Compared with patients with MCE (-), patients with MCE (+) showed lower ASPECTS, larger ischemic core volume, and larger DT >3 s lesion volume. This finding suggested that ischemia or infarction core during the early stage was more severe in pa-

tients with MCE (+) than in patients with MCE (-), which was consistent with the findings of Tracol et al.<sup>31</sup> A midline shift of over 3.9 mm and an infarct volume of more than 220 mL are predictors of severe brain edema and herniation.<sup>32</sup> This study's results further showed that the proportion of the use of IV-tPA in patients with MCE (+) was lower than that in patients with MCE (-). It suggested that IV-tPA could reduce the incidence of MCE, which was in line with the findings of Fuhrer et al.<sup>33</sup> Treatment with IV-tPA lowered the odds of experiencing MCE, with a reduced odds ratio of 0.88 (95% CI: 0.83–0.94).

With the development of analytical approaches and high-throughput technology, the multiparameter approach has recently become a useful tool for improving diagnos-

tic performance.<sup>34</sup> Therefore, this study built a model combining the radiomics signature, clinical factors, and routine visual radiological factors to predict MCE. Parameters related to MCE, such as the radiomics signature, ASPECTS, ischemic core volume, DT >3 s lesion volume, and use of IV-tPA, were included in this model. The combined model exhibited better differentiation capabilities than the radiomics signature or the routine visual radiological model, with AUCs of 0.924 and 0.879 in the training and test sets, respectively.

The limitations of this study should be noted. First, information and selection biases may exist due to the retrospective nature of this study. Therefore, the validation of the results in a prospective study is required. Second, the sample size was considerably small, and the proposed models were not externally validated. Third, the difference between the combined model and radiomics signature or the routine visual radiological model was small, with only borderline statistical significance between the combined model and radiomics signature. Therefore, a large-scale, multicenter study is required to validate the proposed multimodal diagnostic approach. Despite the abovementioned limitations, a prediction model for MCE after EVT was established in this study by combining the radiomics signature, clinical factors, and routine radiological factors, which may facilitate the accurate early prediction of MCE in patients with acute anterior circulation infarction after EVT.

In conclusion, this study constructed a model for predicting MCE in patients with acute anterior circulation infarction after EVT. These findings may contribute to the accurate and early prediction of MCE and assist clinical decision-making.

#### Conflict of interest disclosure

The authors declared no conflicts of interest.

#### Funding

This work was supported by grants-in-aid from the health commission of Zhejiang province (grant number: 2022RC105) and the excellent scientific research foundation of Zhejiang Provincial People's Hospital (grant number: ZRY2021A007).

#### References

- Goyal M, Menon BK, van Zwam WH, et al. Endovascular thrombectomy after large-vessel ischaemic stroke: a meta-analysis of individual patient data from five randomised trials. *Lancet*. 2016;387(10029):1723-1731. [CrossRef]

	AUC (95% CI)	P value	Best cut-off value	Sensitivity (%)	Specificity (%)
ASPECTS	0.800 ± 0.060 (0.683–0.917)	<0.001*	7	81.82	67.27
Ischemic core volume	0.793 ± 0.060 (0.675–0.910)	<0.001*	37	86.36	67.27
DT >3 s lesion volume	0.725 ± 0.074 (0.580–0.870)	0.002*	235	59.09	90.91

\*represents  $P < 0.05$ . MCE, malignant cerebral edema; AUC, area under the curve; ROC, receiver operating characteristic; NCCT, non-contrast enhanced computed tomography; ASPECTS, Alberta Stroke Program Early CT Score; DT, delay time; CI, confidence interval; CTP, computed tomography perfusion.

Variable	Difference between the areas (95% CI)	P value
Combined model vs. radiomics signature	0.0537 (0.0001–0.107)	0.049*
Combined model vs. routine visual radiological model	0.1160 (0.0179–0.213)	0.020*
Radiomics signature vs. routine visual radiological model	0.0620 (-0.0691–0.193)	0.354

\*represents  $P < 0.05$ . ROC, receiver operating characteristic; CI, confidence interval.

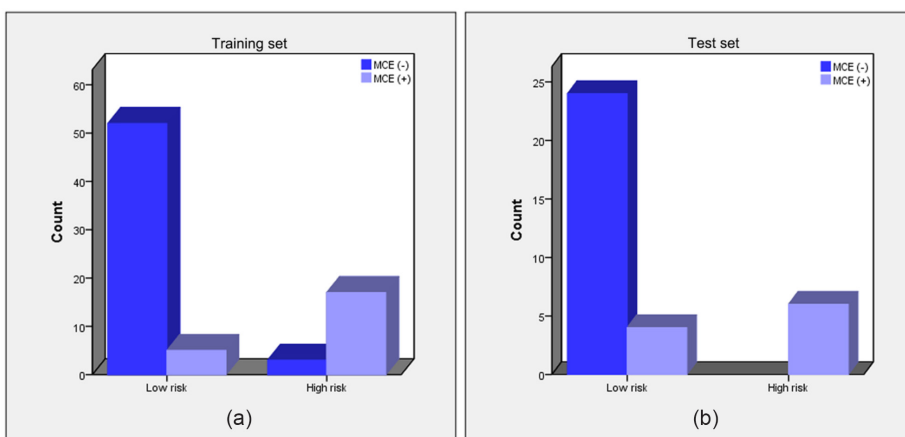


**Figure 4.** (a, b) Classification performance of the combined model in the training and test sets. MCE, malignant cerebral edema.

2. ZiW, Wang H, Yang D, et al. Clinical effectiveness and safety outcomes of endovascular treatment for acute anterior circulation ischemic stroke in China. *Cerebrovasc Dis*. 2017;44(5-6):248-258. [\[CrossRef\]](#)
3. Huang X, Yang Q, Shi X, et al. Predictors of malignant brain edema after mechanical thrombectomy for acute ischemic stroke. *J Neurointerv Surg*. 2019;11(10):994-998. [\[CrossRef\]](#)
4. Kimberly WT, Dutra BG, Boers AMM, et al. Association of reperfusion with brain edema in patients with acute ischemic stroke: a secondary analysis of the MR CLEAN trial. *JAMA Neurol*. 2018;75(4):453-461. [\[CrossRef\]](#)
5. Davoli A, Motta C, Koch G, et al. Pretreatment predictors of malignant evolution in patients with ischemic stroke undergoing mechanical thrombectomy. *J Neurointerv Surg*. 2018;10(4):340-344. [\[CrossRef\]](#)
6. Oppenheim C, Samson Y, Manaï R, et al. Prediction of malignant middle cerebral artery infarction by diffusion-weighted imaging. *Stroke*. 2000;31(9):2175-2181. [\[CrossRef\]](#)
7. Minnerup J, Wersching H, Ringelstein EB, et al. Prediction of malignant middle cerebral artery infarction using computed tomography-based intracranial volume reserve measurements. *Stroke*. 2011;42(12):3403-3409. [\[CrossRef\]](#)
8. Kürten S, Munoz C, Beseoglu K, et al. Decompressive hemicraniectomy for malignant middle cerebral artery infarction including patients with additional involvement of the anterior and/or posterior cerebral artery territory—outcome analysis and definition of prognostic factors. *Acta Neurochir (Wien)*. 2018;160(1):83-89. [\[CrossRef\]](#)
9. Sikiö M, Köhli P, Ryymin P, et al. MRI texture analysis and diffusion tensor imaging in chronic right hemisphere ischemic stroke. *J Neuroimaging*. 2015;25(4):614-619. [\[CrossRef\]](#)
10. Kauw F, Bennink E, de Jong HWAM, et al. DUST Investigators; DUST (Dutch Acute Stroke Study) investigators are as follows. Intracranial cerebrospinal fluid volume as a predictor of malignant middle cerebral artery infarction. *Stroke*. 2019;50(6):STROKEAHA119024882. [\[CrossRef\]](#)
11. Walcott BP, Miller JC, Kwon CS, et al. Outcomes in severe middle cerebral artery ischemic stroke. *Neurocrit Care*. 2014;21(1):20-26. [\[CrossRef\]](#)
12. Du M, Huang X, Li S, et al. A nomogram model to predict malignant cerebral edema in ischemic stroke patients treated with endovascular thrombectomy: an observational study. *Neuropsychiatr Dis Treat*. 2020;16:2913-2920. [\[CrossRef\]](#)
13. Mokin M, Primiani CT, Siddiqui AH, Turk AS. ASPECTS (Alberta Stroke Program Early CT Score) measurement using Hounsfield unit values when selecting patients for stroke thrombectomy. *Stroke*. 2017;48(6):1574-1579. [\[CrossRef\]](#)
14. Puetz V, Dzialowski I, Hill MD, et al. Intracranial thrombus extent predicts clinical outcome, final infarct size and hemorrhagic transformation in ischemic stroke: the clot burden score. *Int J Stroke*. 2008;3(4):230-236. [\[CrossRef\]](#)
15. Tan IY, Demchuk AM, Hopyan J, et al. CT angiography clot burden score and collateral score: correlation with clinical and radiologic outcomes in acute middle cerebral artery infarct. *AJNR Am J Neuroradiol*. 2009;30(3):525-531. [\[CrossRef\]](#)
16. DeLong ER, DeLong DM, Clarke-Pearson DL. Comparing the areas under two or more correlated receiver operating characteristic curves: a nonparametric approach. *Biometrics*. 1988;44(3):837-845. [\[CrossRef\]](#)
17. Shu Z, Fang S, Ding Z, et al. MRI-based radiomics nomogram to detect primary rectal cancer with synchronous liver metastases. *Sci Rep*. 2019;9(1):3374. [\[CrossRef\]](#)
18. Vassileva E, Stoyanov P, Vavrek E, Stamenova P. Unexpected arterial recanalization after decompressive hemicraniectomy. *J Stroke Cerebrovasc Dis*. 2013;22(8):e661-3. [\[CrossRef\]](#)
19. Bosche B, Dohmen C, Graf R, et al. Extracellular concentrations of non-transmitter amino acids in peri-infarct tissue of patients predict malignant middle cerebral artery infarction. *Stroke*. 2003;34(12):2908-2913. [\[CrossRef\]](#)
20. Dohmen C, Bosche B, Graf R, et al. Identification and clinical impact of impaired cerebrovascular autoregulation in patients with malignant middle cerebral artery infarction. *Stroke*. 2007;38(1):56-61. [\[CrossRef\]](#)
21. Thomalla G, Hartmann F, Juettler E, et al. Clinical Trial Net of the German Competence Network Stroke. Prediction of malignant middle cerebral artery infarction by magnetic resonance imaging within 6 hours of symptom onset: A prospective multicenter observational study. *Ann Neurol*. 2010;68(4):435-445. [\[CrossRef\]](#)
22. Cho DY, Chen TC, Lee HC. Ultra-early decompressive craniectomy for malignant middle cerebral artery infarction. *Surg Neurol*. 2003;60(3):227-32; discussion 232-233. [\[CrossRef\]](#)
23. Castellano G, Bonilha L, Li LM, Cendes F. Texture analysis of medical images. *Clin Radiol*. 2004;59(12):1061-1069. [\[CrossRef\]](#)
24. Peter R, Korfiatis P, Blezek D, et al. A quantitative symmetry-based analysis of hyperacute ischemic stroke lesions in noncontrast computed tomography. *Med Phys*. 2017;44:192-199. [\[CrossRef\]](#)
25. Oliveira MS, Fernandes PT, Avelar WM, et al. Texture analysis of computed tomography images of acute ischemic stroke patients. *Braz J Med Biol Res*. 2009;42(11):1076-1079. [\[CrossRef\]](#)
26. Yao X, Mao L, Lv S, et al. CT radiomics features as a diagnostic tool for classifying basal ganglia infarction onset time. *J Neurol Sci*. 2020;412:116730. [\[CrossRef\]](#)
27. Kuang H, Najm M, Chakraborty D, et al. Automated ASPECTS on noncontrast CT scans in patients with acute ischemic stroke using machine learning. *AJNR Am J Neuroradiol*. 2019;40(1):33-38. [\[CrossRef\]](#)
28. Ortiz-Ramón R, Valdés Hernández MDC, González-Castro V, et al. Identification of the presence of ischaemic stroke lesions by means of texture analysis on brain magnetic resonance images. *Comput Med Imaging Graph*. 2019;74:12-24. [\[CrossRef\]](#)
29. Kassner A, Liu F, Thornhill RE, Tomlinson G, Mikulis DJ. Prediction of hemorrhagic transformation in acute ischemic stroke using texture analysis of postcontrast T1-weighted MR images. *J Magn Reson Imaging*. 2009;30(5):933-941. [\[CrossRef\]](#)
30. Betrouni N, Yasmina M, Bombois S, et al. Texture features of magnetic resonance images: an early marker of post-stroke cognitive impairment. *Transl Stroke Res*. 2020;11(4):643-652. [\[CrossRef\]](#)
31. Tracol C, Vannier S, Hurel C, et al. Predictors of malignant middle cerebral artery infarction after mechanical thrombectomy. *Rev Neurol (Paris)*. 2020;176(7-8):619-625. [\[CrossRef\]](#)
32. Park J, Goh DH, Sung JK, et al. Timely assessment of infarct volume and brain atrophy in acute hemispheric infarction for early surgical decompression: strict cutoff criteria with high specificity. *Acta Neurochir (Wien)*. 2012;154(1):79-85. [\[CrossRef\]](#)
33. Fuhrer H, Schönenberger S, Niesen WD, et al. Endovascular stroke treatment's impact on malignant type of edema (ESTIMATE). *J Neurol*. 2019;266(1):223-231. [\[CrossRef\]](#)
34. Birkhahn M, Mitra AP, Cote RJ. Molecular markers for bladder cancer: the road to a multimarker approach. *Expert Rev Anticancer Ther*. 2007;7(12):1717-1727. [\[CrossRef\]](#)

## Supplementary Materials

Least absolute shrinkage and selection operator (LASSO) is a powerful algorithm for regression analysis with high dimensional predictors. In our study, we used LASSO to select the most important predictive features in the training set based on the “glmnet” package in R statistical software version 3.3.1. There were 15 most valuable radiomics features left following LASSO. Details of the 15 radiomics features are shown in Supplementary Table 1. The multivariate logistic regression was used to build the model of LASSO. At last, a formula was generated using a linear combination of selected features that were weighted by their respective LASSO coefficients.

Supplementary Table 1. Information of radiomics features selected by least absolute shrinkage and selection operator		
Category	Feature	Description
RLM	HighGreyLevelRunEmphasis_AllDirection_offset1_SD	The grey level run-length matrix (RLM) is defined as the numbers of runs with pixels of gray level $i$ and run length $j$ for a given direction $\theta$ . RLMs is generated for each sample image segment having directions ( $0^\circ, 45^\circ, 90^\circ$ & $135^\circ$ ).
	LongRunEmphasis_angle0_offset4	
	LongRunHighGreyLevelEmphasis_AllDirection_offset4_SD	
	LongRunLowGreyLevelEmphasis_angle45_offset4	
	ShortRunEmphasis_angle45_offset7	
GLCM	Inertia_AllDirection_offset4_SD	The grey level co-occurrence matrix (GLCM) represents the joint probability of certain sets of pixels having certain grey-level values. It calculates how many times a pixel with grey-level $i$ occurs jointly with another pixel having a grey value $j$ , by varying the displacement vector $d$ between each pair of pixels.
	differenceVariance	
	sumEntropy	
Histogram	MinIntensity	Histogram parameters are concerned with properties of individual pixels. They describe the distribution of voxel intensities within the computed tomography image through commonly used and basic metrics.
	Percentile10	
	VoxelValueSum	
	ClusterShade_AllDirection_offset7_SD	
Form factor	Compactness2	Form factor parameters include descriptors of the three-dimensional size and shape of the lesion region.
	Sphericity	
GLSZM	HighIntensitySmallAreaEmphasis	The gray level size zone matrix (GLSZM) is the starting point of Thibault matrices. For a texture image $f$ with $N$ gray levels, it is denoted $GSf(s, g)$ and provides a statistical representation by the estimation of a bivariate conditional probability density function of the image distribution values. It is calculated according to the pioneering Run Length Matrix principle: the value of the matrix $GSf(s, g)$ is equal to the number of zones of size $s$ and of gray level $g$ . The resulting matrix has a fixed number of lines equal to $N$ , the number of gray levels, and a dynamic number of columns, determined by the size of the largest zone as well as the size quantization.

### Rad-score calculation formula

$$\begin{aligned}
 \text{Rad-score} = & -0.8398 + 0.8269 \times \text{MinIntensity} \\
 & -0.5822 \times \text{Percentile10} \\
 & -0.3390 \times \text{VoxelValueSum} \\
 & -0.5025 \times \text{ClusterShade\_AllDirection\_offset7\_SD} \\
 & -1.6389 \times \text{Inertia\_AllDirection\_offset4\_SD} \\
 & +0.7927 \times \text{differenceVariance} \\
 & +0.2364 \times \text{sumEntropy} \\
 & +0.0480 \times \text{HighGreyLevelRunEmphasis\_AllDirection\_offset1\_SD} \\
 & +0.0517 \times \text{LongRunEmphasis\_angle0\_offset4} \\
 & +0.2528 \times \text{LongRunHighGreyLevelEmphasis\_AllDirection\_offset4\_SD} \\
 & +7.4376 \times \text{LongRunLowGreyLevelEmphasis\_angle45\_offset4} \\
 & -0.3203 \times \text{ShortRunEmphasis\_angle45\_offset7} \\
 & +0.4199 \times \text{Compactness2} \\
 & -0.2494 \times \text{Sphericity} \\
 & -0.7987 \times \text{HighIntensitySmallAreaEmphasis}
 \end{aligned}$$



# Less known but important complications and associated anomalies of Abernethy malformation

Ayşe Rüksan Ütebey   
Furkan Ufuk   
Muhammed Raşid Aykota 

Dear Editor,

We read with interest the article "Abernethy malformation: a comprehensive review" by Kumar et al.<sup>1</sup> published in *Diagnostic and Interventional Radiology*. We congratulate the authors for their comprehensive and instructive article on this unusual anomaly. Abernethy malformation is an extremely rare anomaly characterized by portal venous blood passing into the systemic circulation bypassing the liver.<sup>1,2</sup> Abernethy malformation can cause pulmonary hypertension, hepatic encephalopathy, hepatopulmonary syndrome, and heart failure.<sup>2</sup> Moreover, Abernethy malformation is associated with multiple congenital anomalies (such as cardiovascular and skeletal anomalies) and acquired complications (such as benign and malignant primary hepatic tumors). Therefore, it is essential to recognize this anomaly and follow up regarding these complications.<sup>1,2</sup> Although complications and abnormalities accompanying Abernethy malformation are described in detail in Kumar et al.'s<sup>1</sup> article, we would like to make a contribution to this article.

According to the pathophysiology, Abernethy malformation can also cause the following clinical consequences: the decrease in hepatic glucose uptake may increase the blood's glucose level and cause hyperinsulinism and, consequently, hypoglycemia attacks, especially in the pediatric population.<sup>3,4</sup> Moreover, there are accompanying osteoporosis cases in patients with Abernethy malformation, primarily due to liver enzymes' role in vitamin D metabolism.<sup>3,5</sup> In addition to the anomalies related to Abernethy malformation stated by Kumar et al.<sup>1</sup> it has been shown in the literature that visceral arterial and venous aneurysms can be found (Figure 1).<sup>2,6</sup> The awareness of this unusual entity is crucial for the prevention and close monitoring of possible complications, such as abdominal hemorrhage.

## KEYWORDS

Cirrhosis, congenital, diagnosis, liver, portal hypertension, portal vein

From the Department of Radiology (A.R.Ü., F.U. ✉ furkan.ufuk@hotmail.com), Pamukkale University Faculty of Medicine, Denizli, Turkey, Department of Surgery (M.R.A.), Pamukkale University Faculty of Medicine, Denizli, Turkey.

Received 11 March 2021; Accepted 9 January 2022.



Epub: 02.01.2023

Publication date: 29.03.2023

DOI: 10.5152/dir.2022.211146

You may cite this article as: Ütebey AR, Ufuk F, Aykota MR. Less known but important complications and associated anomalies of Abernethy malformation. *Diagn Interv Radiol.* 2023;29(2):410-411.

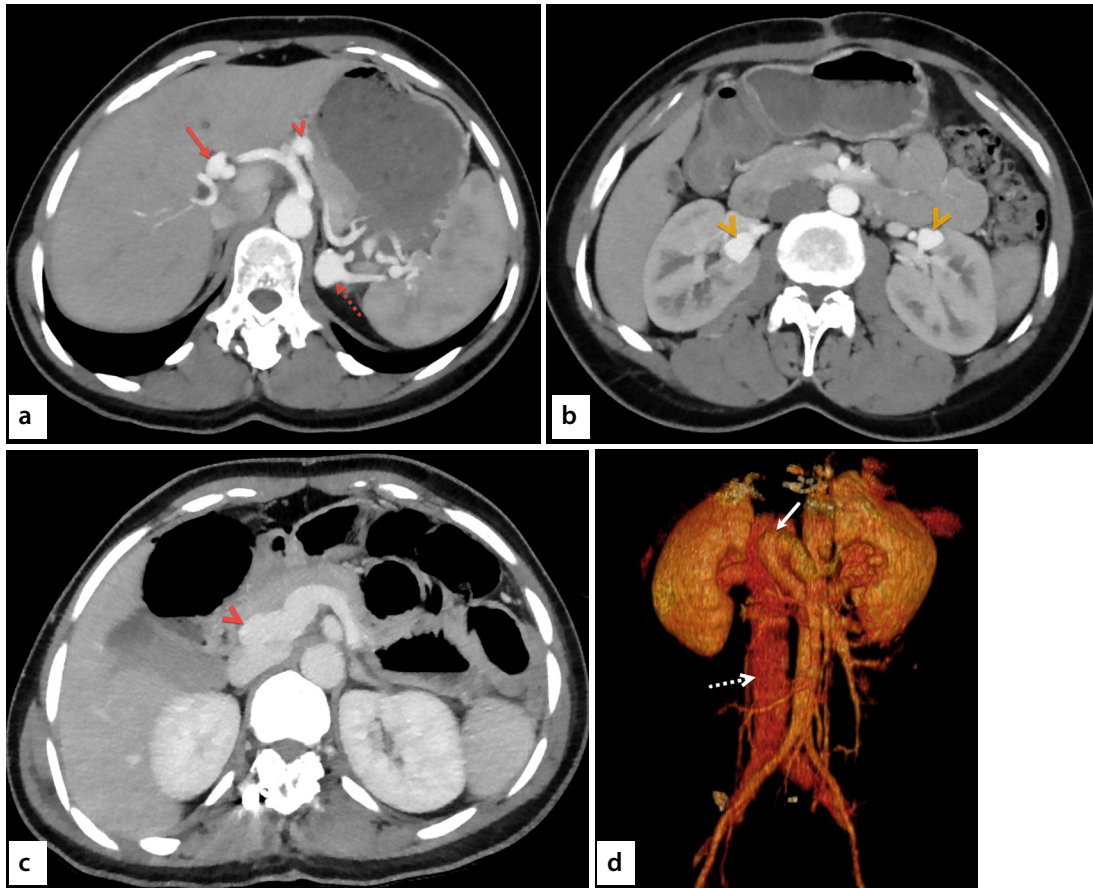


**Figure 1.** A 29-year-old female was presented to the emergency room with a stab injury. In her medical history, she had scoliosis surgery 12 years ago. Dynamic contrast-enhanced abdominal computed tomography (CT) was obtained. (a, b) Axial abdominal CT angiography images show multiple visceral arterial aneurysms, including hepatic artery (red arrow), proximal part of the splenic artery (red arrowhead), distal part of the splenic artery (dashed red arrow), and bilateral renal arteries (orange arrowheads). (c) Axial contrast-enhanced abdominal CT image in the portal venous phase shows the drainage of portal vein into the vena cava inferior (arrowhead). (d) Three-dimensional volumetric image of the abdominal CT demonstrates the drainage of portal vein into the vena cava inferior (arrow) and enlargement of the vena cava inferior (dashed arrow).

### Conflict of interest disclosure

The authors declared no conflicts of interest.

### References

1. Kumar P, Bhatia M, Garg A, Jain S, Kumar K. Abernethy malformation: a comprehensive review. *Diagn Interv Radiol.* 2022;28(1):21-28. [\[CrossRef\]](#)
2. Ogul H, Bayraktutan U, Yalcin A, et al. Congenital absence of the portal vein in a patient with multiple vascular anomalies. *Surg Radiol Anat.* 2013;35(6):529-534. [\[CrossRef\]](#)
3. Bas S, Guran T, Atay Z, et al. Premature pubarche, hyperinsulinemia and hypothyroxinemia: novel manifestations of congenital portosystemic shunts (Abernethy malformation) in children. *Horm Res Paediatr.* 2015;83(4):282-287. [\[CrossRef\]](#)
4. Senniappan S, Pitt K, Shah P, et al. Postprandial hyperinsulinaemic hypoglycaemia secondary to a congenital portosystemic shunt. *Horm Res Paediatr.* 2015;83(3):217-220. [\[CrossRef\]](#)
5. Peček J, Fister P, Homan M. Abernethy syndrome in Slovenian children: Five case reports and review of literature. *World J Gastroenterol.* 2020;26(37):5731-5744. [\[CrossRef\]](#)
6. Kong Y, Zhang H, Liu C, et al. Abernethy malformation with multiple aneurysms: incidentally found in an adult woman with Caroli's disease. *Ann Hepatol.* 2013;12(2):327-331. [\[CrossRef\]](#)



# Letter to the Editor: “Prospective assessment of VI-RADS score in multiparametric MRI in bladder cancer: accuracy and the factors affecting the results”

Furkan Ufuk   
Ahmet Baki Yağcı 

Dear Editor,

We read the article titled “Prospective assessment of VI-RADS score in multiparametric MRI in bladder cancer: accuracy and the factors affecting the results” by Oğuz et al.<sup>1</sup>, published online in Diagnostic and Interventional Radiology. We congratulate the authors on this prospective magnetic resonance imaging (MRI) study in patients with bladder cancer. We want to make a few contributions and comments on this research article.

First, it is noteworthy that the number of cases accepted on the Vesical Imaging Reporting and Data System (VI-RADS) 3, according to the MRI evaluation in this study, was considerably higher than the studies in the current literature.<sup>2-6</sup> The proportion of patients with a VI-RADS score of 3 in Oğuz et al.’s<sup>1</sup> study was 38.75%. However, in prospective studies in the current literature, the proportion of patients with a VI-RADS score of 3 was 13.4% in Del Giudice et al.’s<sup>2</sup> study, 18.2% in Erkoc et al.’s<sup>3</sup> study, 6.9% in Metwally et al.’s<sup>4</sup> study, 19.2%–20.5% in Akcay et al.’s<sup>5</sup> study, and 8.8%–18.7% in Ueno et al.’s<sup>6</sup> study. Moreover, Oğuz et al.<sup>1</sup> reported that 93.5% (29/31) of the patients with a score of VI-RADS 3 had histopathologically non-muscle invasive bladder cancer, which is quite different from the literature. Many studies have shown that bladder tumors with a VI-RADS 3 score are in the gray zone and can indicate muscle-invasive and non-muscle-invasive bladder cancer at a similar rate. For example, Metwally et al.<sup>4</sup> reported that of the 24 patients with a VI-RADS score of 3, 13 (54.2%) had histopathologically non-muscle invasive bladder cancer, while 11 (45.8%) had muscle-invasive bladder cancer. Similarly, Akcay et al.<sup>5</sup> reported that of the 15 patients with a VI-RADS score of 3, 7 (46.7%) had histopathologically non-muscle invasive bladder cancer, while 8 (53.3%) had muscle-invasive bladder cancer. We suggest that this difference between the literature and Oğuz et al.’s<sup>1</sup> study may be due to an MRI assessment error.

Second, Oğuz et al.<sup>1</sup> reported that the second observer for interobserver agreement evaluated only 20 random patients. However, the VI-RADS scores of these 20 patients were not specified. According to our clinical practice, the VI-RADS scores of the tumors are very important in terms of the interobserver agreement. For example, an excellent interobserver agreement is expected in evaluating tumors with a VI-RADS score of 1 or 5. In contrast, a significant decrease in the agreement is scheduled for those with a VI-RADS score of 3. Therefore, the authors need to indicate the VI-RADS scores of the 20 patients they evaluated.<sup>1</sup>

Finally, the authors noted that patients without muscle tissue in the transurethral resection of bladder tumor (TUR-BT) sample underwent a second TUR-BT after the first resection but did not specify the number or proportion of these patients. Akcay et al.<sup>5</sup> reported that 10 of 83 patients (12%) had insufficient TUR-BT. We suggest that reporting the number of inadequate TUR-BT procedures in this study will contribute to the literature.<sup>1</sup>

## Conflict of interest disclosure

The authors declared no conflicts of interest.

## KEYWORDS

Bladder, cancer, invasive, magnetic resonance imaging, tumor

From the Department of Radiology (F.U. ✉ furkan.ufuk@hotmail.com, A.B.Y.), Pamukkale University Faculty of Medicine, Denizli, Turkey.

Received 07 April 2022; accepted 30 May 2022.



Epub: 28.12.2022

Publication date: 29.03.2023

DOI: 10.4274/dir.2022.221568

You may cite this article as: Ufuk F, Yağcı AB. Letter to the Editor: “Prospective assessment of VI-RADS score in multiparametric MRI in bladder cancer: accuracy and the factors affecting the results”. *Diagn Interv Radiol.* 2023;29(2):412-413.

## References

1. Oğuz U, Bekçi Y, Öğreden E, et al. Prospective assessment of VI-RADS score in multiparametric MRI in bladder cancer: Accuracy and the factors affecting the results. *Diagn Interv Radiol.* 2022;28(5):396-402. [\[CrossRef\]](#)
2. Del Giudice F, Flammia RS, Pecoraro M, et al. The accuracy of Vesical Imaging-Reporting and Data System (VI-RADS): an updated comprehensive multi-institutional, multi-readers systematic review and meta-analysis from diagnostic evidence into future clinical recommendations. *World J Urol.* 2022;40(7):1617-1628. [\[CrossRef\]](#)
3. Erkoç M, Otunçtemur A, Bozkurt M, et al. The efficacy and reliability of VI-RADS in determining candidates for repeated transurethral resection in patients with high-risk non-muscle invasive bladder cancer. *Int J Clin Pract.* 2021;75(9):e14584. [\[CrossRef\]](#)
4. Metwally MI, Zeed NA, Hamed EM, et al. The validity, reliability, and reviewer acceptance of VI-RADS in assessing muscle invasion by bladder cancer: a multicenter prospective study. *Eur Radiol.* 2021;31(9):6949-6961. [\[CrossRef\]](#)
5. Akçay A, Yagci AB, Celen S, Özlülerden Y, Türk NS, Ufuk F. VI-RADS score and tumor contact length in MRI: A potential method for the detection of muscle invasion in bladder cancer. *Clin Imaging.* 2021;77:25-36. [\[CrossRef\]](#)
6. Ueno Y, Tamada T, Takeuchi M, et al. VI-RADS: Multiinstitutional Multireader Diagnostic Accuracy and Interobserver Agreement Study. *AJR Am J Roentgenol.* 2021;216(5):1257-1266. [\[CrossRef\]](#)